EVALUATION OF CO_2 TRAPPING MECHANISMS AT THE SACROC NORTHERN PLATFORM: SITE OF 35 YEARS OF CO_2 INJECTION

By

Weon Shik Han

Submitted in Partial Fulfillment
of the Requirements for the

Doctorate of Philosophy in Earth and Environmental Science
With Dissertation in Hydrology

The New Mexico Institute of Mining and Technology
Socorro, New Mexico

May, 2008

ABSTRACT

The main purpose of this study is to assess the potential fate of CO_2 when it is injected in the deep subsurface for storage. In the coming year (2008), over 20 field geologic sequestration tests are being designed and scheduled for deployment in the United States. An additional 23 are ongoing or slated for deployment soon in other countries. For large-scale geologic sequestration to be deployed and sustainable over the long-term, a meaningful assessment of CO_2 trapping mechanisms is essential. Therefore, the chapters in this dissertation are each part of a detailed study of the physical and chemical processes associated with CO_2 trapping mechanisms.

First, two integrated equations of state (EOS) algorithms were assembled to evaluate multiphase transport of carbon dioxide (CO_2). One integrated EOS is based on Redlich and Kwong's original algorithm developed in 1949, and the other is based on a more recent algorithm developed by Span and Wagner in 1996. Both algorithms calculate solubility, compressibility factor, density, viscosity, fugacity, and enthalpy of CO_2 in gaseous and supercritical phases, and mixtures or solutions of CO_2 in water, as functions of pressure and temperature. In general, the predictions of thermophysical properties for both algorithms are close, except for a contrast in the predicted fugacity coefficient of CO_2, which subsequently propagates to a contrast in predicted solubility in water/brine.

To facilitate a general comparison of these EOS algorithms, one-dimensional flow models were developed. Simulation results suggest that dissolution rates of separate-phase CO_2 predicted from the two EOS algorithms are significantly different, resulting in markedly different CO_2 migration patterns.

Finally, a specific case study of CO_2 trapping mechanisms and related processes was carried out using numerical simulation. The site of the case study was the SACROC (Scurry Area Canyon Reef Operators Committee) Unit in the Permian Basin of Texas, the oldest continuous CO_2 enhanced oil recovery (EOR) site in the United States. SACROC has been subjected to CO_2 injection for 35 years, and thus provides an excellent field laboratory for this analysis. Not all CO_2 injected for EOR has been recovered, and thus some is trapped in the subsurface. A comprehensive numerical model was developed for analyzing the range of possible trapping mechanisms and other related physical and chemical effects of the injected CO_2. Data used to parameterize the three-dimensional model includes spatial distributions of seismic- and core-derived porosity and permeability that were estimated by the Texas Bureau of Economic Geology.

Two separate models were developed for the analysis of CO_2 trapping mechanism. The first model was designed for simulating CO_2 trapping mechanisms in a reservoir saturated with brine. The other model was designed for simulating CO_2 trapping mechanisms in a reservoir saturated with both brine and oil.

CO_2 trapping mechanisms in the brine-only model show a distinctive set of stages. In Stage I (1972~2002), the same as the original injection period, hydrostratigraphic trapping is dominant. In Stage II (2002~2017), residual trapping

dramatically increases. In Stage III (2017 to several hundreds years), solubility trapping becomes important because over time both the residual and mobile CO_2 dissolve in the brine. Finally, at stage IV (~after several thousand years), mineral trapping is predicted to be greater than any other mechanisms. In sum, the major CO_2 trapping mechanisms were hydrostratigraphic (mobile), residual, and solubility trapping during 200 years.

However, in the brine (28%) plus oil (72%) model, the CO_2 trapping mechanisms do not vary much over time. Separate-phase CO_2 is stored as a free (mobile) form due to its high saturation, but it behaves like residual (immobile) CO_2 because of the smaller contrast between fluid densities of oil and CO_2. Further, CO_2 mobility is hindered by other fluids such as brine and oil in model due to the reduction of relative permeability. In sum, both oil trapping and hydrostratigraphic (mobile) trapping were dominant mechanisms during 200 years.

The combined results of these two model analyses suggest that injecting CO_2 into brine formations below oil reservoirs will provide several advantages in terms of CO_2 storage capacity and protection from potential leakage.

Results of this dissertation are intended to provide insight regarding effective approaches for geologic CO_2 sequestration. Specifically, understanding the potential range of CO_2 trapping mechanisms in typical reservoirs may help scientists and engineers evaluate sequestration operations to maximize trapping and minimize risks.

ACKNOWLDGEMENTS

This dissertation would not have been possible without the support from mentors, colleagues, friends, family, and the New Mexico Institute of Mining and Technology.

First, I would like to acknowledge my research advisor, Dr. Brian McPherson who always respected my ideas and helped me pursue this dissertation. He was not only an advisor, professor and boss these past four years, but also trusted friend. Because of the opportunity to work with Dr. Brian McPherson, I was able to participate in the Southwest Regional Sequestration Partnership and collaborate with many researchers from various universities, national laboratories, research institutes, companies, and geological surveys. My academic advisor, Dr. John Wilson, also provided critical advice and helped me to improve conceptual thinking and "big picture" questions. Further, he encouraged me to be a self-confident and independent researcher. I also thank my dissertation committee members at the New Mexico Institute of Mining and Technology and Los Alamos National Laboratory for their guidance and support. Dr. Peter Lichtner, despite his busy schedule, always responded to my queries about reactive transport modeling and gave me useful guidance. Many discussions with Dr. Peter Lichtner were most critical in finishing Chapters 6 and 7. Dr. Fred Phillips supplied me with abundant literature to read. Especially, references associated with quantification of natural heterogeneity were

really helpful to finish Chapter 6. Finally, Dr. Peter Mozley helped me with his strong background on carbonate sedimentology.

Other professors and researchers from various places helped me finish this dissertation. Dr. Robert Bowman advised diverse issues associated with career, culture, and study. Both Dr. Dana Scholle and Dr. Peter Scholle from the New Mexico Bureau of Geology helped me understand the geology of my study area (SACROC, Texas) with their knowledge of carbonate geology in the Permian basin. Mike Raines, who was the former Kinder Morgan geologist, provided me the valuable field data of SACROC field. The discussion with Mike Raines was most valuable in finishing Chapter 5. Fred Wang from the Texas Bureau of Economic Geology provided the high-resolution geo-cellular model. With this model, I was able to finish Chapter 6 and 7. Dr. Juliana Fessenden from Los Alamos National Laboratory shared the carbon isotope data collected during RECES (Research Experience in Carbon Sequestration) Field Trip. I would like to thank to Dr. Long Nghiem and Bob Brugman from Computer Modeling Group Ltd. for helping with the use of CMG's GEM simulator. Finally, I was fortunate to have a chance to study in classes and share ideas with the brilliant graduate students at New Mexico Institute of Mining and Technology during my Ph.D. period.

This dissertation was fully supported by the National Energy Technology Laboratory under the United States Department of Energy. The Petroleum Research Recovery Center and Graduate Student Association of New Mexico Institute of Mining and Technology provided some funds for travel and research.

TABLE OF CONTENTS

LIST OF TABLES

LIST OF FIGURES

LIST OF APPENDICES

This dissertation is accepted on behalf of the
Faculty of the Institute by the following committee:

John L Wilson

Academic Advisor

Brian McPherson

Research Advisor

Peter Lichtner

11 / 20 / 2009

Date

I release this document to the New Mexico Institute of Mining and Technology

Ukon Shik Han 11/20/2009

Student's Signature Date

CHAPTER 1

INTRODUCTION

1.1. Application of Numerical Simulation to Quantifying CO_2 Trapping Mechanisms.

Four CO_2 trapping mechanisms are recognized as the most important for geologic sequestration. These include hydrostratigraphic (mobile), residual, solubility, and mineral trapping and are summarized in Figure 1.1 (Bachu et al. 1994; Hitchon, 1996; Orr, 2004). First, supercritical CO_2 can be stored as a mobile phase below a low permeability formation. This trapping mechanism is called "hydrostratigraphic trapping". Second, supercritical CO_2 can be trapped in pores existing as an immobile phase due to capillary forces, called "residual trapping". The time scale of both hydrostratigraphic and residual trapping is generally considered as less than one hundred years (Juanes et al. 2006). Third, both mobile (free-flowing) and immobile (residual) CO_2 can subsequently dissolve into reservoir fluids, and this trapping mechanism is called "solubility trapping". The time scale of solubility trapping is generally regarded as between a hundred and a thousand years (Zerai et al. 2006). Finally, CO_2 dissolution will decrease the pH of the reservoir fluid and induce associated dissolution of the primary host rock and lead to subsequent precipitation of carbonate minerals, this mechanism is called "mineral trapping". The time scale of

mineral trapping is generally regarded as greater than a thousand years (Xu et al., 2004).

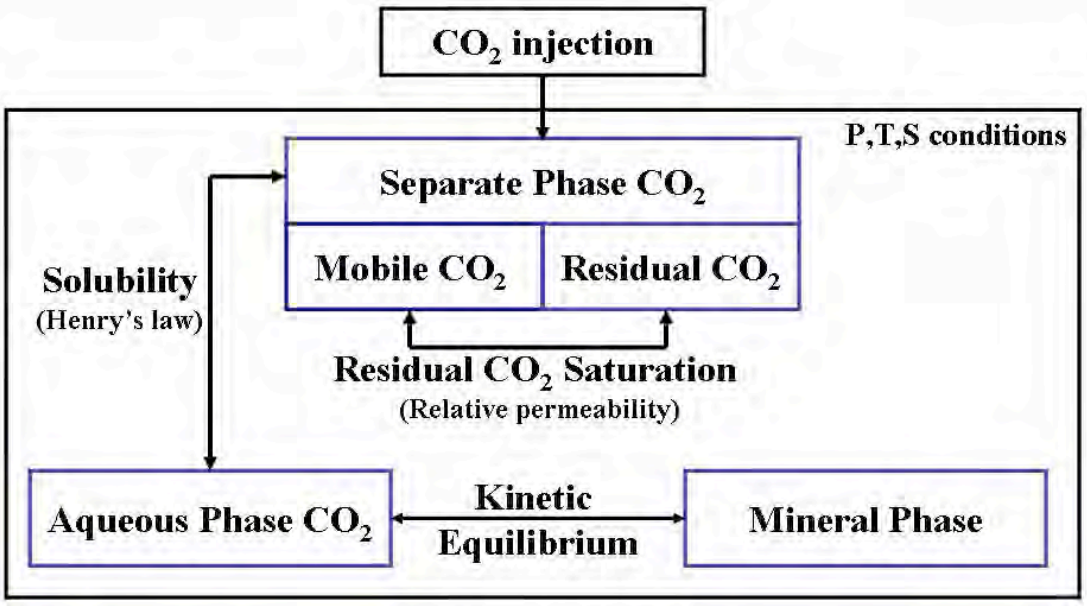

Figure 1.1. A schematic diagram showing the sequential CO_2 trapping mechanisms.

1.1.1. Hydrostratigraphic (mobile) and Residual Trappings

Depending on depth and associated pressure and temperature conditions, injected CO_2 will be stored as separate-phase CO_2 (either supercritical or gas) in the targeted formation (Figure 1.1). During the CO_2 injection process, the separate-phase CO_2 (typically non-wetting phase) displaces brine (typically wetting phase) similar to a drainage process. After CO_2 injection stops, CO_2 will migrate laterally through preferential paths and upward due to the buoyancy-driven force caused by its low density relative to reservoir fluid. However, some of the CO_2 will be trapped in pores and will not migrate. Migrating CO_2 is defined as free (mobile) CO_2 and trapped CO_2 is defined as residual (immobile) CO_2. Whether CO_2 will migrate or be trapped is determined by residual CO_2 saturation in the relative permeability among the phases

(Figure 1.1); relative permeability in numerical simulation is implemented through functional relationships that include hysteretic effects.

In detail, the drainage curve is used to describe the process when a non-wetting phase (CO_2) displaces a wetting phase (brine) while the imbibition curve is used to describe the process when a wetting phase (brine) displaces a non-wetting phase (CO_2). Hysteresis implies that the drainage and imbibition processes are not identical. Generally, relative permeability value of the non-wetting phase (CO_2) in the imbibition curve reaches the zero although its saturation in the imbibition curve is still greater than zero. When the relative permeability value of the non-wetting phase (CO_2) in the imbibition curve becomes zero, its saturation is defined as the residual CO_2 saturation (Figure 1.1). During the imbibition process, the non-wetting phase (CO_2) is trapped in pores where its saturation becomes less than the value of residual CO_2 saturation.

At the field scale, drainage processes occur at the front of the migrating CO_2 plume where separate-phase CO_2 displaces brine. At the same time, imbibition processes occur at the tail of the migrating CO_2 plume where brine displaces separate-phase CO_2. At the tail of separate-phase CO_2 plume (where imbibition occurs), separate-phase CO_2 becomes trapped within pores where CO_2 saturation is less than residual CO_2 saturation. The field scale effects of relative permeability are discussed in Chapter 7.

Several different models that mathematically describe relative permeability functions with hysteresis effects have been developed (Land, 1968; Killough, 1976; Carlson, 1981; Lenhard and Parker, 1987; Lenhard and Oostrom, 1998; Blunt, 2000).

Recently, some of these models have been employed in CO_2 sequestration simulations to evaluate residual trapping (Kumar et al. 2005; Ozah et al. 2005; Spiteri et al. 2005; Juan et al. 2006; Doughty, 2007).

1.1.2. Solubility (Aqueous) Trapping

Separate-phase CO_2, existing as both mobile and residual CO_2, will dissolve into brine depending on ambient reservoir conditions such as pressure, temperature, and salinity. Solubility trapping is defined as CO_2 stored in solution in a reservoir fluid. In numerical simulation, solubility-trapped CO_2 can be predicted with appropriate CO_2 solubility algorithms (Figure 1.1). Generally, two important parameters, the fugacity coefficient and the Henry's law constant, are required to predict CO_2 solubility. The generalized Henry's Law relationship is given by:

$$K\Phi P=\gamma X_{CO2} \qquad \text{(Eq. 1.1)}$$

Where X_{CO2} is the mole fraction of CO_2, P is the partial pressure of CO_2, Φ is the fugacity coefficient, K is the equilibrium constant, and γ is the activity coefficient correcting for non-ideal solution behavior.

The fugacity coefficient (Φ) of CO_2 can be derived from cubic approximations to the real gas equation of state (Redlich and Kwong, 1949; Soave, 1972; Peng and Robinson, 1976; Kerrick and Jacobs, 1981; Prausnitz et al. 1986). It also can be derived from thermodynamic parameter correlations (Duan et al. 1992), or the Helmholtz free energy function (Span and Wagner, 1996). Although the formulation of Span and Wanger, (1996) is regarded by many workers to be one of the most accurate algorithms for predicting the CO_2 fugacity coefficient, direct

application of this algorithm in numerical simulation is not practical due to the high degree of polynomial equations and its requirement to switch to iterative computation (Appendix II). Therefore, often, researchers adapt a lookup table to increase the efficiency of computation (Pruess and Spycher, 2007; Lichtner, *Written Communication*, 2007). Based on a review of CO_2 sequestration literature, cubic equations or thermodynamic parameter correlations (Duan et al. 1992; Duan and Sun, 2003) are more commonly used in CO_2 sequestration simulations. The comparison study of fugacity coefficients between Duan and Sun (2003) and Span and Wagner (1996) indicates that the difference is within experimental uncertainty (Duan, *Written Communication*, 2004).

In additional to the fugacity coefficient, accurate algorithms for calculating CO_2 solubility had been developed (Zawisza and Malesinska, 1981; Reid et al. 1987; Enick and Klara, 1990; Battistelli et al. 1997; Diamond and Akinfiev, 2003; Spycher et al. 2003; Duan and Sun, 2003; Spycher and Pruess, 2005; Portier and Rochelle, 2005; Duan et al. 2006). Recently, numerous fugacity and solubility algorithms have been introduced in CO_2 sequestration simulations to account for solubility trapping (Weir, 1996; Cole, 2000; McPherson and Cole, 2000; Pruess and Garcia, 2002; Garcia, 2003; Xu et al. 2003; Doughty and Pruess, 2004; Lagneau et al. 2005; Gaus et al. 2005; Ketzer et al. 2005; Kervevan et al. 2005; Zerai et al. 2006; McPherson et al. 2008). Within these studies, the solubility algorithms of Duan and Sun, (2003) and Duan et al. (2006) have been applied more than other algorithms.

1.1.3. Mineral Trapping

Dissolution of separate-phase CO_2 in reservoir fluid will decrease pH, which may induce dissolution of the primary host rock and supply dissolved cations and bicarbonate species in the reservoir fluid. The dissolved bicarbonate species may subsequently react with the existing cations (Na^+, Ca^{2+}, Mg^{2+}, Fe^{2+}, and Al^{3+}) to precipitate carbonate minerals such as dolomite ($CaMg(CO_3)_2$), dawsonite ($NaAl(CO_3)(OH)_2$), siderite ($FeCO_3$), and ankerite ($CaFe_xMg_{1-x}(CO_3)_2$). The precipitation of such minerals is generally considered as the last or permanent stage of CO_2 sequestration. To account for mineral trapping, several different reactive transport simulators such as TOUGHREACT, EQ3/6, CMG'GEM-GHG, ChemTOUGH, SCALE2000, PHREEQC, Hytec, CRUNCH, and Geochemist's Workbench, have been introduced (Wolery and Daveler, 1992; White, 1995; Bethke, 1996; van der Lee, 1997; Parkhurst and Appelo, 1999; Steefel, 2001; Azaroual et al. 2004; Nghiem et al. 2004a; Xu et al. 2006).

1.1.4. Time Scale of CO_2 Trapping Mechanisms

In the previous section, the definitions and processes of individual CO_2 trapping mechanisms were introduced. The goal of this section is to evaluate the time frame when a certain mechanism will be dominant during geological CO_2 sequestration. The developed simulation is simplified but it will provide a general idea for the time scale of CO_2 trapping mechanisms. The complex simulation is performed in Chapter 7.

As a simple example using a generic model, a simulation was developed to quantify the timing of different CO_2 trapping mechanisms including

hydrostratigraphic (mobile), residual, solubility and mineral trapping. The model does not include heterogeneity or complex chemical reactions. For this analysis, the CMG's GEM-GHG simulator was used (Computer modeling Group, 2006).

The number of grid elements is 12,167 (23x23x23), illustrated in Figure 1.2a. The approximate size of this model is 250 m wide by 250 m long by 230 m thick. To reduce complexity, homogenous porosity (0.2) and 10^{-14} m^2 of horizontal permeability (K_x=K_y) were assigned with a permeability anisotropy ratio (K_z/K_x) of 0.1. The initial reservoir pressure was assigned to be hydrostatic from top (14.05 MPa) to bottom (16.21 MPa); the initial reservoir temperature was assigned uniform at 60 ºC. Because both pressure and temperature exceed the critical point for CO_2, the injected CO_2 starts out as a supercritical phase in the model. Top and bottom boundaries were assumed to be no-flow conditions and lateral boundaries were assumed to be hydrostatic conditions. Brine concentration was assumed to be 100,000 ppm.

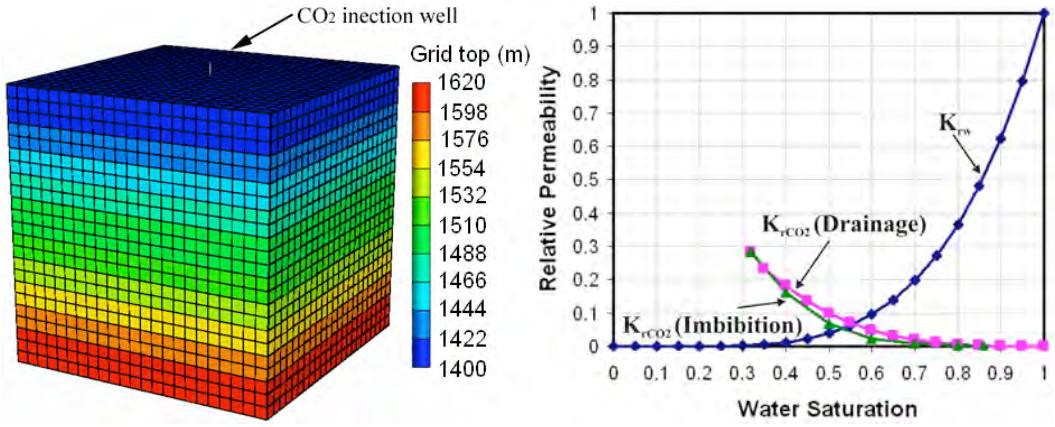

(a) (b)

Figure 1.2. (a) Model structure describing a generic target formation for CO_2 sequestration processes. (b) Generic relative permeability curves of both brine and supercritical CO_2 with hysteresis effect.

The generic relative permeability curves are developed with Land-type hysteresis effect as shown in Figure 1.2b (Land, 1965). The effect of capillary pressure between CO_2 and brine are ignored.

The simplified ten chemical reactions are included to predict mineral trapping and the associated chemical reactions:

$$
\begin{aligned}
&H_2O = H^+ + OH^- \\
&CO_2 + H_2O = H^+ + HCO_3^- \\
&CO_2 + H_2O = 2H^+ + CO_3^{2-} \\
&Al(OH)^{2+} + H^+ = Al^{3+} + H_2O \\
&Al(OH)_2^+ + 2H^+ = Al^{3+} + 2H_2O \qquad \text{(Eq. 1.2)} \\
&Al(OH)_3 + 3H^+ = Al^{3+} + 3H_2O \\
&Al(OH)_4^- + 4H^+ = Al^{3+} + 4H_2O \\
&Calcite + H^+ = Ca^{2+} + HCO_3^- \\
&Kaolinite + 6H^+ = 5H_2O + 2SiO_2 + 2Al^{3+} \\
&Anorthite + 8H^+ = Ca^{2+} + 2Al^{3+} + 2SiO_2(aq) + 4H_2O
\end{aligned}
$$

The chosen chemical parameters are similar to Nghiem et al., (2004b) and provided in Table 1.1.

Table 1.1. Mineral reaction parameters

Mineral	Log k (mol/m^{2}s) at 25°C	Surface Area (m^2/m^3)	Volume fraction
Calcite	-8.80	88	0.0088
Anorthite	-12.0	88	0.0088
Kaolinite	-13.0	17600	0.0176

Approximately 3700 tonnes of CO_2 were injected at the center of the model at a depth of 1570 m during 10 years (Figure 1.2a). Finally, the simulated duration of the model is 1000 years.

Figure 1.3 shows the sequences of dominant trapping mechanisms. During the injection period (10 years), most of the injected CO_2 exists as a form of mobile

(free) CO_2. From 0 to 10 years, hydrostratigraphic (mobile) trapping becomes a dominant mechanism.

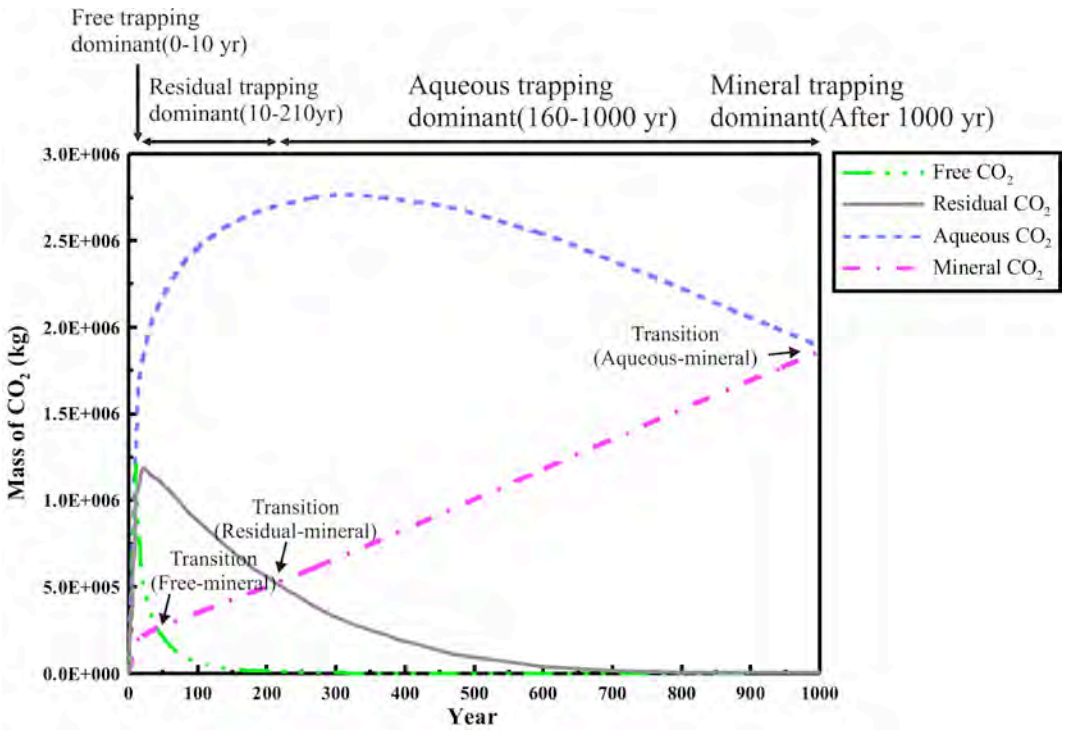

Figure 1.3. Analyses of time scale representing dominant CO_2 trapping mechanisms.

After stopping injection, CO_2 migrates either horizontally or vertically from the injection well. However, some of the CO_2 cannot migrate and becomes trapped in pores due to capillarity. Therefore, the amount of residual CO_2 increases abruptly after 10 years. Results of this analysis also indicate that the residual trapping mechanism becomes dominant from 10 to 210 years. Concurrently, both mobile and residual CO_2 dissolve into reservoir fluid. The amount of CO_2 trapped by dissolution dramatically increases until 300 years because the reservoir fluid is undersaturated with respect to CO_2. After 300 years, the reservoir fluid becomes supersaturated with respect to CO_2 and the solubility trapping asymptotically approaches its maximum.

The solubility trapping mechanism is dominant during the entire simulation period. Mineral trapping is regarded as the final trapping mechanism because reactions between reservoir fluid and minerals are very slow. During the CO_2 injection period, dissolution of minerals dominates because of a high CO_2 partial pressure and low pH conditions. After injection ceases, minerals gradually precipitate with time. After about 1000 years, mineral trapping is dominant.

In summary, the analysis of CO_2 sequestration mechanisms using a generic model indicates that

(1) Hydrostratigraphic (mobile) and residual trapping mechanisms are generally dominant up to 100 years after injection. (the hydrostratigraphic trapping mechanism is dominant during the injection period and the residual trapping mechanism becomes dominant after stopping CO_2 injection).

(2) The solubility trapping mechanism is generally dominant between 100 and 1000 years.

(3) The mineral trapping mechanism is generally dominant after 1000 years.

1.2. Review of the Previous Research

During the last 10 years, scientific and engineering research has attempted to describe the subsurface migration and trapping mechanisms of injected CO_2 using numerical models (Table 1.2). Early research generally considered hydrostratigraphic (mobile) and solubility trapping mechanisms using either multiphase transport codes

(e.g, TOUGH2) or compositional oil simulators (e.g., ECLIPSE, STARS, and others) after coupling appropriate CO_2 equations of state algorithms. Mineral trapping has not been studied in detail because it requires coupled reactive transport codes with multiphase transport codes. Alternatively, another general approach to study mineralization is to use reaction path modeling without considering multiphase effects. More recently, codes capable of simulating chemical reactions and transport of CO_2 together have been developed (e.g., TOUGHREACT and GEM-GHG). These codes are able to simulate hydrostratigraphic (mobile), residual, solubility, and mineral trapping mechanisms together.

In this section, previous research associated with CO_2 sequestration simulation studies are discussed (Table 1.2).

Weir et al. (1996) numerically evaluated the amount of injected CO_2, which escaped above a cap-rock after injecting CO_2 at a rate of 100 kg/s during 10 years into a 3 km deep aquifer. A two-dimensional model with three formations (lower formation, confining layer, and upper formation) was developed. By varying the permeability of the confining layer, they attempted to estimate how much CO_2 could migrate though the confining layer. They found that 12% of CO_2 escaped to the surface through a confining layer of 10^{-15} m^2 permeability, but no CO_2 escaped to the surface through a confining layer of 10^{-17} m^2 permeability. Although they ignored the capillary and hysteresis effects, the simulation results indicated that a low permeability seal should overlie any target CO_2 storage formation. For this simulation, Weir et al. (1996) used the TOUGH2 simulator after modifying its equations of state module for CO_2 sequestration purposes (Table 1.3).

Table 1.2. Historical overview of CO_2 sequestration research approaching with numerical methods.

Numerical modeling	Scale	Dimension	Fluid in Storage formation	Simulator	Trapping mechanisms considered			
					Hydrostratigraphic	Residual	Solubility	Mineral
Weir et al. (1996)	Field (Generic)	2D	Pure water	Modified TOUGH2 (Weir et al. 1995)	X		X	
Van der Meer (1996)	Field (Wabamum Lake, Alberta)	2D	Brine	CMG's STAR ECLIPSE SIMBEST II	X		X	
McPherson and Cole (2000)	Basin (Powder River Basin, Wyoming)	2D	Pure water	Modified TOUGH2 (Cole, 2000)	X		X	
Pruess et al. (2001)	Field Batch reaction (Glauconitic sandstone aquifer, Alberta)	1D 0D	Brine	TOUGH2 (Pruess et al. 1999) TOUGH-REACT (Xu et al., 2004)			X	X
Pruess and Garcia (2002)	Field (Generic)	1D	Brine	TOUGH2 (Pruess et al. 1999)	X		X	
Xu et al. (2003)	Field (Generic, Gulf coast sediment)	1D	Brine	TOUGHREACT/ ECO2 (Xu et al. 2004)	X		X	X
Xu et al. (2004)	Batch reaction (Generic)	0D	Brine	TOUGHREACT (Xu et al. 2004)			X	X
Doughty and Pruess (2004)	Field (Frio formation, Texas)	3D	Brine	TOUGH2 (Pruess et al. 1999)	X		X	
Cipolli et al. (2004)	Batch reaction (Serpentinite aquifer, Genova, Italy)	0D	Brine	EQ3/6 (Wolery and Daveler, 1992)			X	X
Nghiem et al. (2004a)	Field (Generic)	3D	Brine	CMG's GEM-GHG (Nghiem et al. 2004a)	X		X	X
White et al. (2005)	Field (Colorado Plateau, Utah)	2D	Brine	Chem-TOUGH (White, 1995)	X		X	X
Xu et al. (2005)	Field (Generic)	1D	Brine	TOUGHREACT (Xu et al. 2004)			X	X
Zwingmann et al. (2005)	Batch reaction (Niigata basin, Japan)	0D	Brine	EQ3/6 (Wolery and Daveler, 1992)				X
Kumar et al. (2005)	Field (Generic)	3D	Brine	CMG's GEM-GHG (Nghiem et al. 2004a)	X	X	X	X
Mo and Akervoll, (2005)	Field (Generic)	3D	Brine	ECLIPSE (Schlumberger, 2003)	X	X	X	
Kervevan et al. (2005)	Batch reaction (Generic)	0D	Brine	SCALE2000 (Azaroual et al. 2004)			X	X

Table 1.2. *Continued*.

Numerical modeling	Scale	Dimension	Fluid in Storage formation	Simulator	Trapping mechanisms considered			
					Hydrostratigraphic	Residual	Solubility	Mineral
Ozah et al. (2005)	Field (Generic)	3D	Brine	CMG's GEM-GHG (Nghiem et al. 2004)	X	X	X	X
Gaus et al. (2005)	Field (Caprock at Sleipner, North Sea)	1D	Brine	PHREEQC (Parkhurst and Appelo, 1999)			X	X
Lagneau et al. (2005)	Field (Dogger, Paris basin and Bunter, North Sea)	2D	Brine	Hytec (van der Lee et al. 2003)			X	X
Knauss et al. (2005)	Field (Frio formation)	1D	Brine	CRUNCH (Steefel, 2001)			X	X
Spiteri et al. (2005)	Field (PUNQ-S3)	3D	Brine			X		
Juanes et al. (2006)	Field (PUNQ-S3)	3D	Brine	ECLIPSE- 100 (Schlumberger, 2005)		X		
Zerai et al. (2006)	Field (Rose Run sandstone, Ohio)	0D	Brine	Geochemist's Workbench (Bethke, 1996)			X	X
Bryant et al. (2006)	Field (Generic)	2D	Brine	CMG's GEM-GHG (Nghiem et al. 2004)	X		X	
Andre et al. (2007)	Field (Dogger aquifer, Paris basin, France)	1D	Brine	TOUGHREACT (Xu et al. 2004) SCALE2000 (Azaroual et al. 2004)	X		X	

Historically, oil simulators have been widely used for enhanced oil recovery (EOR) analyses. Due to the similarity between EOR and CO_2 sequestration, petroleum researchers have used oil simulators to model CO_2 sequestration processes. Van der Meer (1996) developed an aquifer-scale model representing the Lower Mannville siliciclastic aquifer in the Wabamun Lake area of Alberta and simulated CO_2 sequestration processes using different oil simulators such as CMG's STARS, ECLIPSE, and SIMBEST II. In this research, all three simulators generally provided similar results. However, it was suggested that both CMG's STARS, which determined CO_2 solubility from user-defined K-values (detailed discussion about K-value approach is in section 5.5.3.2), and ECLIPSE, which determined CO_2 solubility from gas-solution ratios, overestimated CO_2 solubility.

Later, Pruess et al. (2004) performed similar comparison. They created eight different problems associated with CO_2 sequestration processes and compared simulation results from 10 groups in six countries:

(1) Lawrence Berkeley National Laboratory (LBNL), USA: TOUGH2/ EOS7C, TOUGH2/ECO2, TOUGHREACT, and TOUGH2-FLAC3D
(2) University of Stuttgard, Germany: MuFTE_UG
(3) CSIRO Petroleum, Australia: TOUGH2/ECO2
(4) Institut Français du Petrole (IFP), France: SIMUSCOPP
(5) Stanford University, USA: Internal Research code
(6) Alberta Research Council (ARC), Canada: CMG's GEM
(7) Los Alamos National Laboratory (LANL): FLOTRAN and ECLIPSE 300
(8) Lawrence Livermore National Laboratory (LLNL), USA: NUFT
(9) Industrial Research Limited (IRL), New Zealand: CHEM-TOUGH2
(10) Pacific Northwest National Laboratory (PNNL): STOMP

Results of intercomparison reveal general agreement in most problems. However, they also have disagreement due to the sensitivities of fluid properties.

McPherson and Cole (2000) evaluated the residence time and the migration of injection CO_2 in the Powder River basin where advective groundwater flow is driven by topographically controlled regional groundwater flow. Their model represented the realistic configuration of formations at the basin scale. In addition, permeability fields of formations were determined after calibrating modeled surface heat flow to observed data. For this simulation, they used a modified TOUGH2 with equations of state from Cole (2000) in Table 1.3. The simulation result indicated that injected CO_2 migrated ~23 km away from the injection location after 1000 years due to the topographically driven groundwater flow. Therefore, regional scale groundwater flow may accelerate the escape of stored CO_2 from the storage site.

Table 1.3. Selected equations of state algorithms adapted in CO_2 sequestration simulators

	Fluid Density	Viscosity	CO_2 Density	Viscosity	Fugacity Coefficient	Solubility	Fluid-CO_2 Density
Weir et al. (1996)	IFC (1967)	IFC (1967)	Redlich and Kwong (1949)	Vesovic (1990)	Prausintz (1969)	Zawisza and Malesinska (1981)	Anderson et al. (1992)
Cole (2000)	IFC (1967)	IFC (1967)	Redlich and Kwong (1949)	Fenghour (1998)	Prausintz (1969)	Reid et al. (1987)	Anderson et al. (1992)
Garcia (2003)	Battistelli et al. (1997)	Phillips et al. (1981)	Correlation with Altunin (1975)	Correlation with Altunin (1975)	Correlation with Spycher et al. (2003)	Prausnitz et al. (1986)	Garcia (2001)
Talman et al. (2004)	IFC (1967)	IFC (1967)	Span and Wagner (1996)	Vesovic (1990)	Span and Wagner (1996)		
McPherson et al. (2008)	Batzle and Wang (1992)	Palliser and McKibbin (1998)	Span and Wagner (1996)	Vesovic (1990)	Span and Wagner (1996)	Duan and Sun (2003)	Anderson et al. (1992)

Pruess et al. (2001) defined CO_2 capacity factors (*CF*) in different phases such as gas (*g*), liquid (*l*), and solid (*s*) and made a preliminary evaluation of sequestration

capacity using a volumetric estimation. The quantitative measure of *CF* is defined below:

$$CF_g = S_g$$

$$CF_l = \frac{S_l \rho_l X_l^{CO2}}{\rho_g} \qquad \text{(Eq. 1.3)}$$

$$CF_s = \frac{v_s \rho_s X_s^{CO2}}{\phi \rho_g}$$

where, S_β is the saturation of phase β (=*g*, *l*, and *s*), ρ_β is density of phase β, X_β^{CO2} is the mass fraction of CO_2 in phase β, V_s is the fraction of reservoir volume occupied by solid phase, and ϕ is porosity. Without considering the effect of hydrodynamic instabilities, heterogeneity, capillary, and buoyancy effect, they concluded that gas phase capacity factor ranged from about 40 % for media with large permeability ($>10^{-15} m^2$), to below 20 % for less permeable media. In addition, the liquid phase capacity factor strongly depended on salinity more than the pressure and temperature in reservoir.

Pruess and Garcia (2002) simulated CO_2 discharge along a fault zone and investigated the effects of salinity on the CO_2 migration patterns using TOUGH2 coupled with ECO2 (Table 1.3; Garcia, 2003). For this simulation, they treated the fault as a one-dimensional and homogeneous unit. Any chemical and mechanical processes induced by CO_2 transport were ignored. By exploring the dynamics of CO_2 discharge through the fault, they determined five stages of CO_2 discharge processes, illustrated in Figure 1.4.

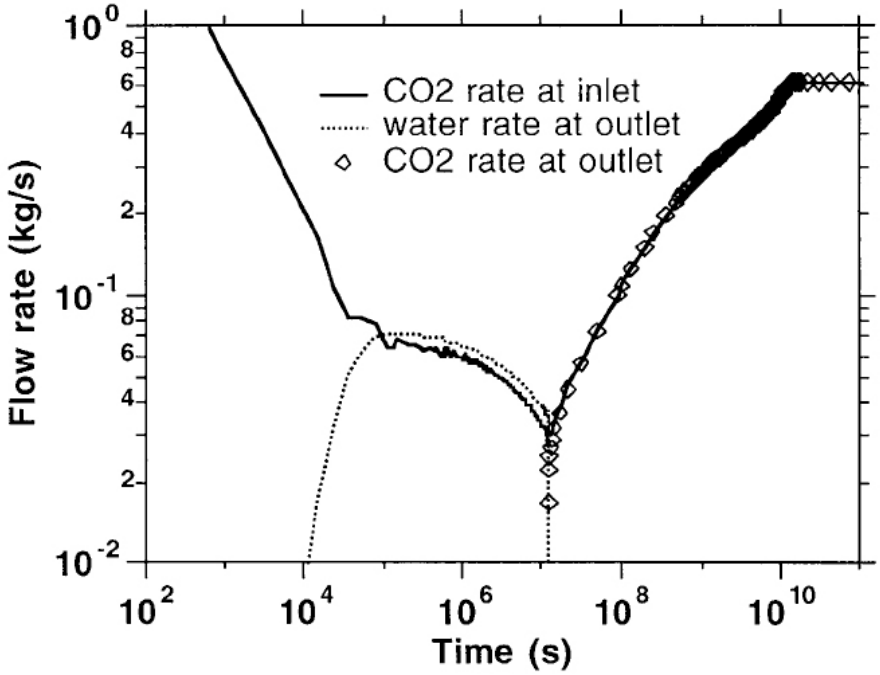

Figure 1.4. CO_2 discharge rate in the modeled fault zone (Pruess and Garcia, 2002).

(1) Stage I ($0\sim10^4$ s): CO_2 at a bottom boundary causes a rapid increase of pressure and creates two-phase conditions (water and supercritical CO_2). At the end of stage I, the pressure pulse reaches the top of the fault and water discharge begins.

(2) Stage II ($10^4\sim10^5$ s): Water discharge continues at a top boundary due to the pressure pulse from bottom boundary.

(3) Stage III ($10^5\sim10^7$ s): the CO_2 plume front migrates from the bottom to the top boundary. At the end of stage III, the CO_2 plume front reaches the top boundary.

(4) Stage IV ($10^7\sim10^{10}$ s): The residual water in the fault starts to dry out into CO_2. Later, at the end of Stage IV, the residual water completely dissolves into the CO_2 plume.

(5) Stage V (10^{10} s ~): Steady state CO_2 flows in the fault without a water phase.

Pruess (2004) further investigated the migration pattern of CO_2 through the fault. Previous simulations only accounted for a two-phase conversion between supercritical-phase CO_2 and aqueous-phase CO_2. However, when CO_2 escapes through a fault, a three-phase fluid zone (aqueous / supercritical CO_2 / gaseous CO_2) might form due to the radical drop of pressure. The simulation revealed that coexistence of three-phase CO_2 caused a drop in fluid mobility induced by phase interference. Subsequently, the drop of fluid mobility reduced the upward rate of CO_2 flow and enhanced the lateral migration of the CO_2 plume. As a result, the CO_2 plume broadened laterally and gave rise to more dispersed CO_2 discharge at the land surface.

Although previous models could account for both hydrostratigraphic (mobile) and solubility trapping mechanisms, they could not simulate mineral trapping mechanisms because such models require coupling multiphase transport codes with reactive transport codes. Therefore, Xu et al. (2003) coupled TOUGHREACT and TOUGH/ECO2 and attempted to estimate the amount of hydrostratigraphic, solubility, and mineral-trapping mechanisms using a one-dimensional model with radial coordination system.

Later, Xu et al. (2004) performed reaction-path model analyses to estimate a CO_2 storage capacity in three different rocks: (1) glauconitic sandstone in the Alberta sedimentary basin, (2) Gulf Coast rocks in Texas, and (3) dunite consisting essentially of olivine. Their simulation predicted that CO_2 storage capacity varied with rock

type. For example, dunite had the largest storage capacity and glauconitic sandstone had the smallest storage capacity. In addition, they found that CO_2 trapping minerals were case-dependent. For glauconitic sandstone, most of CO_2 was trapped as ankerite and siderite. For the Gulf Coast strata, the dominant trapped minerals were dawsonite and ankerite. Finally, for dunite, the dominant trapping minerals were magnesite and siderite. Although Xu et al. (2004) nicely compared the mineralizations at different rock types, they were limited by a lack of kinetic data for dawsonite. In Xu's study, the kinetic rate of dawsonite was assigned to be equal to that of K-feldspar. Recently, kinetic data for dawsonite was measured at 80ºC as a function of pH from 3 to 10 (Hellevang et al., 2005). In this dissertation, I adapted the measured kinetic data to develop the SACROC model in Chapters 6 and 7.

Doughty and Pruess (2004) attempted to investigate how natural heterogeneity can affect CO_2 migration. They stochastically created a three-dimensional model representing fluvial/deltaic Frio Formations with TProGS (Figure 1.5a; Carle and Fogg, 1996; 1997). Both CO_2 migration and partitioning were simulated with TOUGH2/ECO2. However, chemical reactions between CO_2 and rock minerals were not considered.

Their simulation results clearly showed that buoyancy-driven CO_2 dominantly migrated through a preferential flow path. The other emphasis was the role of relative permeability curves, which determined residual CO_2 saturation. Both generic and Frio-like relative permeability curves had been implemented in their study (Figure 1.5b). The result indicated that the CO_2 plumes tended to be more immobile when using Frio-like curves, which had 0.24 of residual CO_2 saturation. However,

their model did not account for the hysteretic effect. Later, several models were developed to account for hysteresis effects (Kumar et al. 2005; Ozah et al. 2005; Juanes et al. 2006; Doughty, 2007).

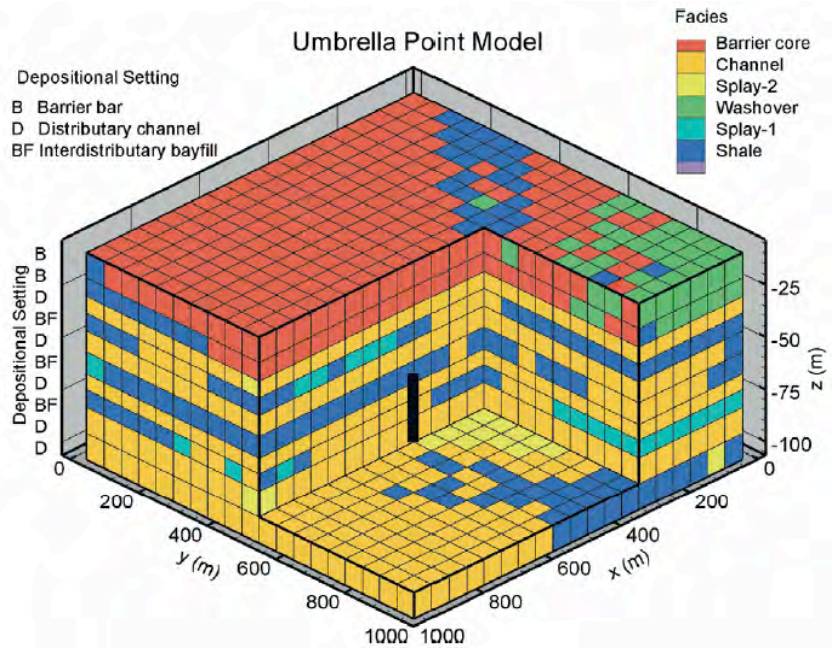

(a)

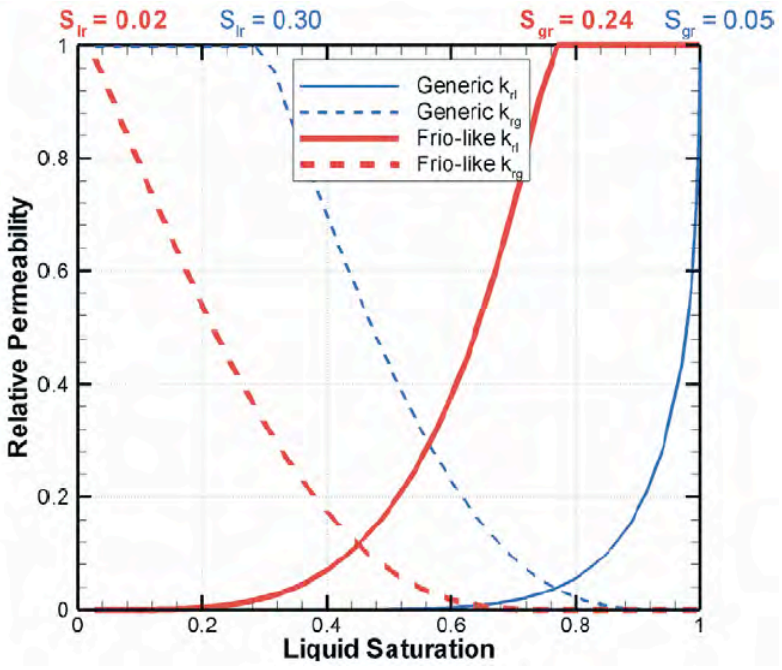

(b)

Figure 1.5. (a) Geologic model describing fluvial/deltaic Frio formations (Doughty and Pruess, 2004), (b) Relative permeability curves (Doughty and Pruess, 2004).

Previously, Xu et al. (2004) performed numerical simulations for evaluating the storage capacity of (1) glauconitic sandstone in the Alberta sedimentary basin, (2) Gulf Coast rocks in Texas, and (3) ultramafic rock (dunite) and indicated that dunite had the largest mineral sequestration capacity (100 kg/m^3) when compared to the sedimentary rocks. Similarly, Cipolli et al. (2004) performed reaction path modeling using EQ3/6 after collecting geochemical data, including isotopes, and suggested that the ultramafic rock affected by serpentinization had a high CO_2 sequestration capacity through mineral fixation of magnesite. Further, CO_2 sequestration into ultramafic rocks continues to be investigated (McGrail et al. 2006; Matter et al. 2006).

Nghiem et al. (2004a) coupled chemical reaction equations into a commercially available compositional reservoir simulator. The coupled simulator (GEM-GHG) was specially designed for simulating CO_2 trapping mechanisms in saline aquifers and was capable of predicting hydrostratigraphic (mobile), residual, solubility, and mineral trapping at the same time. The algorithms and coupling schemes of GEM-GHG are different from TOUGH2/TOUGHREACT. First of all, its solution scheme uses an adaptive-implicit scheme based on the finite difference method. The adaptive-implicit scheme is based on the principle that some grids are solved implicitly while the remaining grids are solved explicitly. Compared to GEM-GHG, TOUGH2/TOUGHREACT, which uses an integrated finite different scheme (Narasimhan and Witherspoon, 1976), is only able to use one solution scheme, either an implicit or an explicit scheme. Second, GEM-GHG simultaneously coupled transport and chemical reaction equations using Newton's method. Compared to GEM-GHG, TOUGHREACT solves both equations sequentially. There are pros and cons to both approaches. A detailed discussion about solution schemes is provided by several

studies (Yeh and Tripathi, 1989; Steefel and MacQuarrie, 1996; Carrayrou et al. 2004; Jacques et al. 2006). In addition, a detailed discussion for GEM-GHG simulator is provided in Chapter 5.

White et al. (2005) evaluated the storage capacity of a hypothetical CO_2 injection site on Colorado Plateau, Utah. They created a two-dimensional model using both TOUGH2 and ChemTOUGH (White, 1995). Their code was able to predict all of CO_2 trapping mechanisms except for residual trapping. Their capacity estimation indicated that about 21 % of injected CO_2 was permanently sequestered as mineral, 52 % was sequestered as both gas and dissolved in brine, and 17 % had leaked to the surface after 1000 years.

Xu et al. (2005) studied mineral sequestration with the data from a Gulf coast aquifer. They developed a one-dimensional model with two formations such as sandstone and shale layers. In their simulation, most of the CO_2 was sequestered as ankerite and dawsonite in the sandstone layer with the capacity of 90 kg/m^3 after 100,000 years. In addition, the diffusion of both Na^+ and Fe^{2+} from shale to sandstone formation was an important factor for precipitation of ankerite and dawsonite.

Zwingmann et al. (2005) estimated both solubility and mineral trapping for the Niigata basin, Japan, where CO_2 injection would be carried out on a small-scale. They collected several groundwater samples from the targeted formation and adjusted its concentration for formation conditions. Using adjusted brine concentration, they estimated CO_2 storage capacity at Niigata basin using EQ3/6. Their simulation indicated that about 2.0 mol/kg H_2O (90 $kgCO_2/m^3$ H_2O) and 21.3 mol/kg H_2O (940 $kgCO_2/m^3$ H_2O), respectively, was stored in the aqueous phase and in minerals after 10^8 years.

Kumar et al. (2005) evaluated all CO_2 sequestration mechanisms at the same time using a three-dimensional heterogeneous simulation using the GEM-GHG modeling package (Nghiem et al. 2004a).

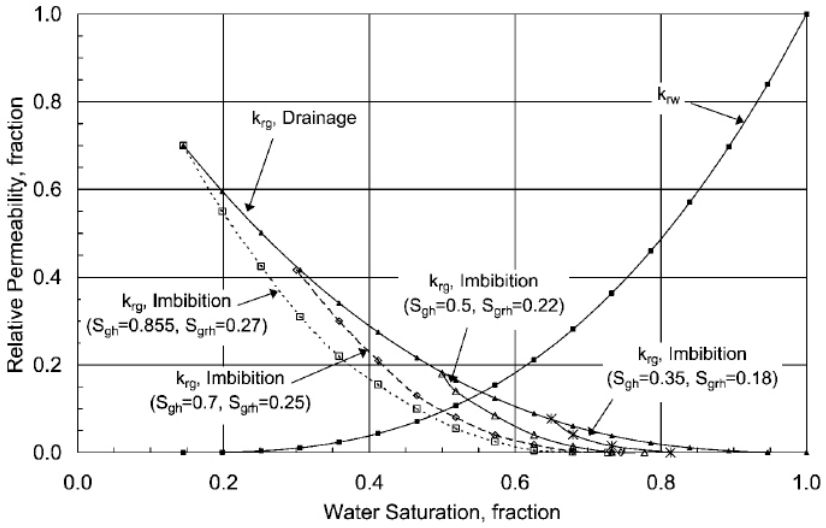

(a)

Parameter Varied	Results/Comments
Layered Permeability—Injection for 50 Years	
Temperature = 43.33°C Temperature = 60°C* Temperature = 76.66°C Temperature = 93.33°C Temperature = 110°C	Increase in temperature leads to increased dissolution of gas into brine
Mean permeability = 10 md Mean permeability = 100 md* Mean permeability = 1000 md	Increase in mean permeability leads to greater injectivity as well as greater migration of CO_2
Salinity = 0 ppm Salinity = 50,000 ppm Salinity = 100,000 ppm* Salinity = 200,000 ppm Salinity = 300,000 ppm	Increase in salinity leads to decreased dissolution of gas into brine
K_v/K_h = 0 K_v/K_h = 0.001* K_v/K_h = 0.01 K_v/K_h = 0.1 K_v/K_h = 1	Increase in K_v/K_h value leads to upward migration of gas and finally its migration along seal
S_{gr} = 0.05 S_{gr} = 0.15 S_{gr} = 0.25* S_{gr} = 0.35 S_{gr} = 0.5	Low value for S_{gr} leads to increased gas migration and dissolution in brine, while high value leads to increased trapping as residual gas
Dip = 0° Dip = 1°* Dip = 2.5° Dip = 5°	Increase in dip leads to increased gas migration and dissolution into brine
Stochastic Permeability—Injection for 50 Years (Correlation Lengths: $\Delta x = \Delta y$ = 127 m, Δz = 1.27 m)	
Mean permeability = 10 md (other properties correlated) Mean permeability = 1000 md (other Properties correlated)	Increase in mean permeability leads to increased injectivity and dissolution into brine

(b)

Figure 1.6. (a) Relative permeability with hysteresis effect (Kumar et al. 2005), (b) Summary of sensitivity analyses (Kumar et al. 2005).

Compared to previous research, Kumar et al. (2005) accounted for residual trapping with Land-type hysteresis effect (Figure 1.6a; Land, 1968). The most significant finding in their work was that the effect of residual trapping mechanism was greater than any other trapping mechanisms. Further, both Juanes et al. (2006) and Doughty (2007) also continued investigations of residual trapping mechanism. Additionally, Kumar et al. (2005) performed a sensitivity analysis using diverse parameters such as temperature, mean permeability, salinity, anisotropy ratio, residual CO_2 saturation, and formation dip after ignoring mineral trapping. The results of sensitivity analyses are summarized in Figure 1.6b.

Ozah et al. (2005) tested the feasibility of CO_2-H_2S mixture injection and the application of horizontal wells. Injecting pure CO_2 generally increases the cost. One possible method of reducing cost is to sequester impure CO_2. Their results indicated that solubility of H_2S was greater than CO_2. Therefore, CO_2-H_2S gas mixture migrated at shorter distance in the aquifer than pure CO_2. However, this simulation ignored the effect of mineralization processes, which might impact CO_2 plume migration by changing rock permeability. The impact to the mineralization by injecting impure CO_2 has been discussed in detail by Knauss et al. (2005). Ozah et al. (2005) also indicated that the application of horizontal wells would increase the volume of stored CO_2 by facilitating higher injection rates.

Mo et al. (2005) investigated residual trapping using ECLIPSE. However, their study ignored both solubility and mineral trapping. They suggested that the amount of residual-trapped CO_2 is dependent on the sweep efficiency controlled by mobility ratio, capillary pressure and aquifer heterogeneity. In detail, the buoyancy-driven migration of CO_2 will be determined by the ratio between gravity and viscosity forces. For example, if the gravitational force is greater, an upward migrating CO_2

plume does not disperse with higher CO_2 saturation ratio. However, if the viscous force is greater, upward migrating CO_2 plume disperses more with less CO_2 saturation. Therefore, higher viscous force implies that more CO_2 can be stored as residual CO_2 form. To account for the effect of viscous force, they performed sensitivity analyses varying both injection rate and vertical permeability.

Kervevan et al. (2005) performed reaction path modeling using SCALE2000 developed by Azaroual et al. (2004). They focused on evaluating the relative importance of activity coefficients, equilibrium constants, and fugacity, which all vary with temperature, pressure, and salinity. For this analysis, they adapted the Pitzer model for activity coefficient calculation (Pitzer, 1973) and accounted for the effect of both pressure and temperature on calculating equilibrium constants (Monnin, 1990), after correcting the infinite dilute molal volume and molal compressibility (Johnson et al. 1992). Finally, they corrected the CO_2 fugacity based on Duan et al. (1992; 2003). Their analyses indicated that both fugacity and activity correction had a strong impact on the precision of geochemical modeling.

Gaus et al. (2005) performed reactive transport simulation using PHREEQC (Parkhurst and Appelo, 1999) to evaluate seal integrity of caprock at Sleipner, North Sea. For this analysis, they created a conceptual model similar to Xu et al. (2005) and assumed that diffusion is the only transport mechanism in caprock. Because of the density contrast between supercritical CO_2 and brine, supercritical CO_2 will migrate vertically. When supercritical CO_2 reaches the lower boundary of the caprock, it will dissolve into the caprock formation water and subsequently diffuse into the caprock. Simulation results showed that the diffusion of CO_2-saturated brine into caprock

induced chemical reactions with caprock minerals. However, diffusion-induced mineral reactions only occur about 2 m inward from the bottom of caprock after 3000 years indicating diffusion does not significantly affect CO_2 migration through caprock.

Knauss et al. (2005) evaluated the feasibility of impure CO_2 injection similar to Ozah et al. (2005). Knauss et al. (2005) considered complex chemical reactions without considering the effects of supercritical CO_2 transport while Ozah et al. (2005) considered relatively simple chemical reactions with the effect of supercritical CO_2 transport. In Knauss et al. (2005), injecting H_2S with CO_2 does not significantly affect the CO_2 sequestration process compared to pure CO_2 injection. However, injecting SO_2 with CO_2 triggered the drop of pH below 1 causing significant mineral changes.

Lagneau et al. (2005) developed two models representing both the carbonate aquifer of the Dogger (Paris basin) and the sandstone aquifer of the Bunter (North Sea). The purpose of their research was to evaluate the feasibility and limitations of reactive transport simulations for the field scale CO_2 sequestration studies. For this analysis, they used Hytec, a reactive transport code initially developed for transport of chemical solutions and colloidal particles in column systems (van der Lee, 1997). The analysis pointed out several limitations of applying the reactive transport code. The listed limitations were associated with the lack of:

(1) Aquifer properties data

(2) Thermodynamic and kinetic data under an appropriate P-T condition

(3) The reactivity data of supercritical CO_2 with host rock.

Both Spiteri et al. (2005) and Juanes et al. (2006) investigated residual trapping associated with hysteresis effects. Because of the similarity of two papers, Juanes et al. (2006) is discussed here. They modified the black oil simulator (ECLIPSE) to simulate residual trapping. Previously, both Kumar (2005) and Ozah (2005) modeled residual trapping with Land-type hysteresis effects (1968). In a different fashion, Juanes et al. (2006) used the Killough (1976) hysteresis model for modification of relative permeability curves. In their model, the effect of capillary pressure was ignored because the characteristic capillary length is much smaller than the grid resolution (Aziz and Settari, 1979; Spiteri et al. 2005). Their simulation results revealed that residual trapping occurred during the upward migration of the CO_2 plume, but only after injection had stopped (Figure 1.7).

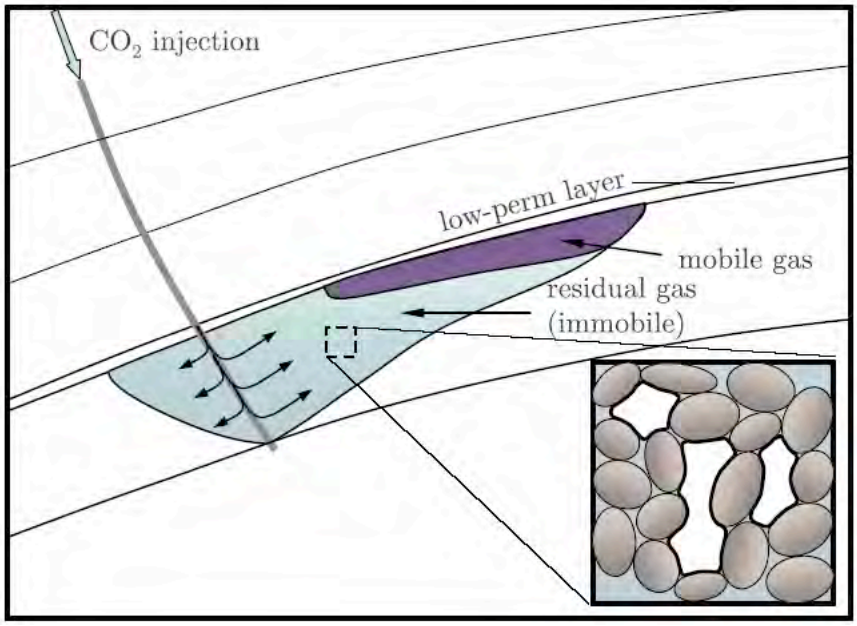

Figure 1.7. Schematic diagram of the trail of residual CO_2 that is left behind (Juanes et al. 2006).

Additionally, the relative roles of CO_2 injection rate, alternating water injection, bottom hole pressure, and grid resolution, and their effects on CO_2 residual trapping were evaluated. In these analyses, higher CO_2 injection rate resulted in more effective CO_2 sequestration because the build-up of pressure helped CO_2 to invade smaller pores, which had high capillary entry pressures. However, lower CO_2 injection rates made CO_2 reach the formation top earlier. Water alternating with CO_2 injection increased the effectiveness of CO_2 sequestration because the injected water more effectively displaced CO_2 at the tail of CO_2 plume. Consequently, more CO_2 was trapped as residual form in pores. Finally, simulation with coarser grids overestimated the sweep and subsequent residual trapping.

Zerai et al. (2006) estimated CO_2 storage capacity in carbonate rock, sandstone rock, and carbonate+sandstone rock in the Rose Run sandstone, Ohio using Geochemist's Workbench (Bethke, 1996). Both equilibrium and kinetic reaction path modeling were performed without considering the effects of flow. In their analysis, the equilibrium model indicated that both siderite and dawsonite were potentially important for mineral trapping of CO_2. The kinetic model indicated that solubility trapping was dominant within tens to hundreds of years and mineral trapping would be the major trapping mechanism over hundreds to thousands of years. In addition, model results showed that mineral trapping is sensitive to pH and to the saturation indices of minerals, which vary with the CO_2 fugacity, brine-to-rock ratio, initial brine concentration, and kinetic rate.

Both Kumar et al. (2005) and Ozah et al. (2005) emphasized the importance of residual trapping. They suggested that residual trapping could be maximized by

letting CO_2 rise toward the top seal of the aquifer but not reach it. Bryant et al. (2006) developed numerical simulation with 40,000 grid blocks to test in which conditions residual trapping could be maximized. For this analysis, several fine scale geostatistical realizations of permeability were generated and the effect of capillary pressure, anisotropy and dip angle were examined. They found that: (1) CO_2 rises through the preferential flow paths in heterogeneous rock rather than through fingering due to the instability of the CO_2 displacement front, (2) when the effect of capillary pressure is considered, the vertical migration of CO_2 is retarded and CO_2 plume tends to disperse laterally and (3) if formation beds are not horizontal, capillary pressure and anisotropy can cause the CO_2 to move predominantly up-dip, along the bedding plane, rather than vertically.

Andre et al. (2007) developed a one-dimensional radial numerical model representing the carbonate Dogger aquifer in France. They performed reactive transport simulations using both TOUGHREACT (Xu et al. 2006) and SCALE2000 (Azaroual et al. 2004). Two injection scenarios were investigated, first with CO_2-saturated water and second with pure supercritical CO_2. The simulation results showed that CO_2-saturated water injection caused a decrease of pH to 3.6, resulting in significant damage to reservoir rocks. However, the injection of supercritical CO_2 did not affect the reservoir rock much because of the relatively small solubility of supercritical CO_2. Therefore, the predicted pH was about 4.8 after the buffering effect of carbonate rock. Additionally, they found a drying out zone near the injection well where residual brine vaporizes into supercritical CO_2 causing the saturation of supercritical CO_2 to reach 1.0. Consequently, the vaporization process

of brine led to precipitating salts and dramatically reduced permeability near the injection well.

1.3. Research Motivation and Objectives

Diverse research has attempted to quantify CO_2 trapping mechanisms using numerical codes (Table 1.2). Early on, researchers focused on developing and integrating CO_2 equations of state predicting density, fugacity coefficient, viscosity, enthalpy, and solubility for appropriate pressure and temperature conditions. Consequently, researchers were able to predict the storage and migration behavior of both supercritical and dissolved CO_2.

However, flow and transport codes coupled with equations of state were not able to account for mineral trapping. To simulate mineral trapping, researchers attempted to couple flow and transport codes with reaction codes. Even before starting CO_2 sequestration studies, researchers studying geothermal fields had already developed codes to simultaneously simulate chemical reaction and fluid transport (Lichtner, 1985; Lichtner, 1987; Steefel and Lasaga, 1994). With similar approaches, researchers studying CO_2 sequestration started to couple chemical reaction codes to flow and transport codes and equations of state (Nghiem et al. 2004a; Xu et al. 2006). Several codes such as TOUGHREACT and CMG's GEM-GHG are currently available for simulating CO_2 transport and corresponding water-rock interaction.

Recently, research has emphasized the importance of residual trapping. Land-type hysteresis models were included in relative permeability function to quantify residual trapping.

In Table 1.2, the historical development of CO_2 sequestration modeling is listed. However, these studies appear to possess several limitations.

(1) Most previous models did not describe all of the CO_2 trapping mechanisms at the same time. Rather, models focused on one or two mechanisms.

(2) Most of the previous models simplified their dimension into either one- or two-dimensions after ignoring heterogeneity effects.

(3) Although some of the models used a three-dimensional grid, spatial heterogeneity measured from the field was generally disregarded.

Therefore, the first objective of this dissertation study is to develop a comprehensive model that accounts for all CO_2 trapping mechanisms including hydrostratigraphic (mobile), residual, solubility, and mineral trapping. Another objective is to demonstrate the application of high-resolution geo-cellular model in CO_2 sequestration simulation. High-resolution geo-cellular model, which applied to this study, is the model comprising of a broad field of expertise such as geologic data (core data, well-log data, sedimentologic and stratigraphic interpretation) and geophysical data (seismic attributes and rock physics data). The high-resolution geo-cellular model with 9 million elements (Δx=several tens meter, Δy=several tens meter, and Δz=several meter) was built as a framework to perform numerical simulation of CO_2 trapping mechanisms in this study. However, the cost of simulating flow simulations on a large number of high-resolution geo-cellular model is computationally expensive. Therefore, we applied one of the upscaling techniques, renormalization, to acquire the reasonable number of elements. The final objective of

this research is to quantify the various CO_2 trapping mechanisms using upscaled geo-cellular model describing northern platform SACROC, a site of 35 years of CO_2 injection.

1.4. Chapter Descriptions

Chapter 1 ("Introduction") addresses the previous modeling approaches to quantify CO_2 trapping mechanisms and describes the overall direction of this dissertation to readers.

The purpose of Chapter 2 ("Two equations of state assembled for basin analysis of multiphase CO_2 flow under deep sedimentary basin condition") is to present two equations of state (EOS) algorithms assembled for multiphase flow and transport of carbon dioxide (CO_2). One is a modified Redlich-Kwong EOS, "MRKEOS," that employs modification of the attractive term from the original van der Waals equation developed in 1873 (van der Waals, 1873; Kerrick and Jacobs 1981; Weir et al, 1996; Cole, 2000). The other EOS algorithm that we coded and implemented, "SWEOS," is an EOS for CO_2 originally developed by Span and Wagner (1996), who based their algorithm on an empirical representation of the fundamental equation of Helmholtz energy. Both were modified for the application to sedimentary basin studies of multiphase CO_2 flow processes, including carbon sequestration applications. Source code for both algorithms are provided in Appendices, including "stand-alone" Matlab © scripts for interactive calculation of fluid properties at specified P-T conditions and FORTRAN subroutines for inclusion in existing FORTRAN multiphase fluid simulation packages (e.g. TOUGH2).

In Chapter 3 ("Comparison of two different equations of state for application of carbon dioxide sequestration"), we simulated and compared CO_2 migration patterns using the previously developed two EOS algorithms—both MRKEOS and SWEOS. In general, the results of thermophysical properties for both EOS algorithms are consistent, except for a contrast in the predicted fugacity coefficient of CO_2, which subsequently propagates to a contrast in predicted solubility. However, in simulations of CO_2 migration, dissolution rates of separate-phase CO_2 predicted from the two EOS algorithms were significantly different, even for small contrasts in predicted fluid properties from EOS algorithms, resulting in markedly different migration patterns. I also examined reservoir seal integrity using both EOS algorithms. Simulations indicate that the distance that separate-phase CO_2 will migrate through an unfractured seal varies linearly with the amount of injected CO_2, logarithmically with permeability, and inversely with porosity. More general sensitivity analyses were conducted to investigate how individual parameters including brine density, viscosity, and CO_2 solubility in brine, affect CO_2 flow and transport. General results indicate that both brine density and CO_2 solubility are critical factors.

Chapter 4 ("Principal reservoir description associated with geology and oil production history in SACROC, site of 35 years of CO_2 injection") provides an overview description of SACROC (Scurry Area Canyon Reef Operator's Committee) Unit where CO_2 has been injected the last 35 years since 1972. The SACROC Unit became very attractive to researchers associated with CO_2 sequestration because its 35 year CO_2 injection history confirms that CO_2 is trapped by an effective sealing

unit. Despite its attraction, researchers had a difficult time finding relevant reference materials for describing this site because most of the papers were published before 1980, some even before 1960, and were primarily published in petroleum associated journals. Therefore, this chapter is intended to provide general information associated with geology and injection/production histories of the SACROC Unit.

Chapter 5 ("Description of GEM-GHG simulator") introduces mathematical representations of CMG's GEM-GHG simulator, which is a multi-dimensional, finite-difference, isothermal, geochemical, and compositional simulator. Although GEM-GHG is specifically designed for simulating CO_2 sequestration processes, its original version (GEM) is developed for compositional behavior of oil reservoirs. Therefore, the mathematical representations of governing equations within GEM are different than other conventional groundwater simulators. Furthermore, simulating CO_2 sequestration requires equations of state capable of calculating the thermophysical property changes of fluids at deep reservoir pressures and temperatures. Finally, Chapter 5 also describes how flow equations are coupled with chemical reaction equations. Although the TOUGH2 simulator is extensively used in both Chapters 2 and Chapter 3, the mathematical description of TOUGH2 simulator is not provided here. Rather, we refer the readers to the TOUGH2 manual for a detailed description (Pruess, 1999).

Chapter 6 ("Evaluation of CO_2 trapping mechanisms at the SACROC northern platform, Permian basin, Texas, site of 35 years of CO_2 injection: 1. Analyses of field data for model preparation") addresses how the Texas Bureau of Economic Geology quantified the natural heterogeneity at the SACROC northern platform using

geophysical data. In their work, porosity distributions were defined from both seismic survey and wire log analyses. Permeability distributions were calculated from seismically calibrated porosity values using empirical equations derived from rock fabric classification. This high-resolution geo-cellular model was adapted to simulate CO_2 trapping mechanisms for a case study of SACROC. However, the original high-resolution geo-cellular model consisted of over 9 million elements. Therefore, it was necessary to upscale to acquire a reasonable number of elements for simulating CO_2 trapping mechanisms. In this study, we upscaled the about 9.4 million elements down to 15,470 elements using a "renormalization" technique (King, 1989). Further, we analyzed both water chemistry and $\delta^{13}C$ isotope data collected from various sources. Both analyses suggest that the Wolfcamp shale acts as a suitable seal at SACROC.

In Chapter 7 ("Evaluation of CO_2 trapping mechanisms at SACROC northern platform, Permian basin, Texas, site of 35 years of CO_2 injection: 2. Model Development"), the development of two models that evaluate CO_2 trapping mechanisms at the SACROC northern platform using the upscaled geo-cellular model is described. The first model was designed for simulating CO_2 trapping mechanisms in a reservoir saturated with brine. In this model, relatively complicated chemical reactions are included to accurately predict mineralization with complexation reactions. Therefore, researchers studying CO_2 sequestration with backgrounds of either hydrology or geochemistry will be interested in this work. The other model was designed for simulating CO_2 trapping mechanism in a reservoir saturated with both brine and oil. In this model, for the sake of computational efficiency, relatively

simple chemical reactions are included with the additional oil phase. The latter model provides relatively realistic representation of CO_2 trapping mechanisms at the SACROC field because this field is an oil reservoir subjected to a long history of CO_2-enhanced oil recovery. Researchers working on CO_2 sequestration with backgrounds in petroleum will be interested in this work. In summary, we compared CO_2 trapping mechanisms in both cases and investigated how the different reservoir fluids can affect the CO_2 trapping.

Conclusions and recommendations are presented in Chapter 8.

References

Altunin, V.V., 1975. Thermophysical Properties of Carbon Dioxide. Publishing House of Standards, Moscow (in Russian).

Andersen, G., Probst, A. Murray, L., Butler, S., 1992. An accurate PVT model for geothermal fluids as represented by H_2O-CO_2-NaCl mixtures. Proceedings of the 17th Workshop on Geothermal Reservoir Engineering, Stanford, California, 17, 239–248.

Andre, L., Audigane, P., Azaroual, M., Menjoz, A., 2007. Numerical modeling of fluid-rock chemical interactions at the supercritical CO_2-liquid interface during CO_2 injection into a carbonate reservoir, the Dogger aquifer (Paris Basin, France). Energy Conversion and Management 48(6), 1782-1797.

Azaroual, M., Kervevan, C., Durance, M.V., Brochot, S., Durst, P., 2004. SCALE2000 (V3.1), User's manual (in French), BRGM. ISBN 2-7159-0939-X.

Aziz, K., Settari, A., 1979. Petroleum Reservoir Simulation, Elsevier, New York. p.476.

Bachu, S., Gunter, W.D., Perkins, E.H., 1994. Aquifer disposal of CO_2: Hydrodynamic and mineral trapping. Energy Conversion and Management 35(4), 269-279.

Battistelli, A., Calore, C., Pruess, K., 1997. The simulator TOUGH2/EWASG for modelling geothermal reservoirs with brines and non-condensable gas. Geothermics 26(4), 437-464.

Batzle, M., Wang, Z., 1992. Seismic properties of pore fluids. Geophysics 57, 1396-1408.

Bethke, C.M., 1996. Geochemical Reaction Modeling. University Press, New York. p.397.

Blunt, M.J., 2000. An empirical model for three-phase relative permeability. Society of Petroleum Engineers Journal 67950.

Bryant, S.L., Lakshminarasimhan, S., Pope. G.A., 2006. Buoyancy-dominated multiphase flow and its impact on geological sequestration of CO_2. Society of Petroleum Engineers Journal 99938.

Carle, S.F., Fogg, G.E., 1996. Transition probability based indicator geostatistics. Mathematical Geology 28, 437-464.

Carle, S.F., Fogg, G.E., 1997. Modeling spatial variability with one and multidimensional continuous-lag Markov chains. Mathematical Geology 29, 891-917.

Carlson, F.M., 1981. Simulation of relative permeability hysteresis to the nonwetting phase. Society of Petroleum Engineers Journal 10157.

Carrayrou, J., Mose, R., Behra, P., 2004. Operator-splitting procedures for reactive transport and comparison of mass balance errors. Journal of Contaminant Hydrology 68, 239-268.

Cipolli, F., Gambardella, B., Marini, L., Ottonello, G., Zuccolini, M.V., 2004. Geochemistry of high-pH waters from serpentinites of the Gruppo di Voltri (Genova, Italy) and reaction path modeling of CO_2 sequestration in serpentinite aquifers. Applied Geochemistry 19, 787-802.

Cole, B. S., 2000. Sequestration of Supercritical Carbon Dioxide in Deep Sedimentary Basin Aquifers: A Numerical Model. Master's Thesis, New Mexico Institute of Mining and Technology, p.124.

Computer Modeling Group, 2006. User's Guide GEM, Advanced Compositional Reservoir Simulator (version 2006). Computer Modeling Group Ltd.

Diamond, L.W., Akinfiev, N.N., 2003. Solubility of CO_2 in water from -1.5 to 100ºC and from 0.1 to 100 MPa: evaluation of literature data and thermodynamic modeling. Fluid Phase Equilibria 208, 265-290.

Doughty, C., 2007. Modeling geologic storage of carbon dioxide: Comparison of non-hysteretic and hysteretic characteristic curves. Energy Conversion and Management 48, 1768-1781.

Doughty, C., Pruess, K., 2004. Modeling supercritical carbon dioxide injection in heterogeneous porous media. Vadose Zone Journal 3, 837-847.

Duan, Z., Moller, N., Weare, J.H., 1992. An equation of state for the CH_4-CO_2-H_2O system: I. Pure systems from 0 to 1000ºC and 0 to 8000 bar. Geochimica et Cosmochimica Acta 56, 2605-2617.

Duan, Z., Sun , R., 2003. An improved model calculating CO_2 solubility in pure water and aqueous NaCl solutions from 273 to 533 K and from 0 to 2000 bar. Chemical Geology 192, 257-271.

Duan, Z., Sun, R., Zhu, C., Chou, I.-M., 2006. An improved for the calculation of CO_2 solubility in aqueous solutions containing Na^+, K^+, Ca^{2+}, Mg^{2+}, Cl^-, and SO_4^{2-}. Marine Chemistry 98, 131-139.

Enick, R.M., Klara, S.M., 1990. CO_2 solubility in water and brine under reservoir condition. Chemical Engineering Communications 90, 23-33.

Fenghour, A., Wakeham, W. A., Vesovic, V., 1998. The viscosity of carbon dioxide. Journal of Physical and Chemical Reference Data 27(1), 31–44.

Garcıa, J.E., 2001. Density of aqueous solutions of CO_2. Technical Report LBNL-49023, Lawrence Berkeley National Laboratory, Berkeley, CA.

Garcıa, J. E., 2003. Fluid Dynamics of Carbon Dioxide Disposal into Saline Aquifers. Ph.D Thesis, University of California, Berkeley, 136pp.

Gaus, I., Azaroual, M., Czernichowski-Lauriol, I., 2005. Reactive transport modeling of the impact of CO_2 injection on the clayey caprock at Sleipner (North Sea). Chemical Geology 217, 319-337.

Hellevang, H., Aagaard, P., Oelkers, E.H., Kvamme, B., 2005. Can Dawsonite permanently trap CO_2? Environmental Science and Technology 39, 8281-8287.

Hitchon, B., 1996. Aquifer Disposal of Carbon Dioxide. B. Hitchon (Eds.), Sherwood Park, Alberta, Canada. Geoscience publishing.

International Formulation Committee, 1967. A Formulation of the Thermodynamic Properties of Ordinary Water Substance. IFC Secretariat, Düsseldorf, Germany.

Jacques, D., Simunek, J., Mallants, D., van Genuchten, M.Th., 2006. Operator-splitting errors in coupled reactive transport codes for transient variably saturated flow and contaminant transport in layered soil profiles. Journal of Contaminant Hydrology 88, 197-218.

Johnson, J.W., Oelkers, E.H., Helgeson, H.C., 1992. SUPCRT92; a software package for calculating the standard molal thermodynamic properties of minerals, gases, aqueous species, and reactions from 1 to 5000 bar and 0 to 1000 degrees C. Computers and Geosciences 18(7), 899-947.

Juanes, R. Spiteri, E.J., Orr, F.M., Blunt, M.J., 2006. Impact of relative permeability hysteresis on geological CO_2 storage. Water Resources Research 42, doi:10.1029/2005WR004806.

Kerrick, D.M., Jacobs, G.K., 1981. A modified Redlich- Kwong equation for H_2O, CO_2, and H_2O-CO_2 mixtures at elevated pressures and temperatures. American Journal of Sciences 281, 735-767.

Kervevan C.M., Azaroual, M., Durst, P., 2005. Improvement of the calculation accuracy of acid gas solubility in deep reservoir brines: Application to the geological storage of CO_2. Oil & Gas Science and Technology 60(2), 357-379.

Ketzer, J.M., Carpentier, B., Le Gallo, Y., Le Thiez, P., 2005. Geological sequestration of CO_2 in mature hydrocarbon fields: Basin and reservoir numerical modeling of the Forties field, North Sea. Oil & Gas Science and Technology 60(2), 259-273.

Killough, J.E., 1976. Reservoir simulation with history-dependent saturation functions. Society of Petroleum Engineers Journal 5106.

King, P.R., 1989. The use of renormalization for calculating effective permeability. Transport in Porous Media 4, 37-58.

Knauss, K.G., Johnson, J.W., Steefel, C.I., 2005. Evaluation of the impact of CO_2, co-contaminant gas, aqueous fluid and reservoir rock interactions on the geologic sequestration of CO_2. Chemical Geology 217, 339-350.

Kumar, A., Noh, M., Pope, G.A., Sepehrnoori, K., Bryant, S.L., Lake, L.W., 2005. Reservoir simulation of CO_2 storage in deep saline aquifer. Society of Petroleum Engineers Journal 89343.

Lagneau, V., Pipart, A., Catalette, H., 2005. Reactive transport modeling of CO_2 sequestration in deep saline aquifers. Oil & Gas Science and Technology 60(2), 231-274.

Land, C.S., 1968. Calculation of imbibition relative permeability for two and three-phase flow from rock properties. Society of Petroleum Engineers Journal 1942.

Lenhard, R.J., Oostrom, M., 1998. A parametric model for predicting relative permeability-saturation-capillary pressure relations of oil-water systems in porous media with mixed wettability. Transport in Porous Media 31(1), 109-131.

Lenhard, R.J., Parker, J.C., 1987. A model for hysteretic constitutive relations governing multiphase flow: 2. Permeability-saturation relations, Water Resources Research 23(12), 2197-2206.

Lichtner, P.C., 1985. Continuum model for simultaneous chemical reactions and mass transport in hydrothermal systems. Geochimica et Cosmochimica Acta 43, 779-800.

Lichtner, P.C., 1987. Fluid flow and mineral reactions at high temperature and pressures. Journal of the Geological Society, London 144, 313-326.

Matter, J.M., Takahashi, T., Goldberg, D., 2006. Experimental evaluation of in situ CO_2-water-rock reactions during CO_2 injection in basaltic rocks: Implications for geologic CO_2 sequestration. Geochemistry Geophysics Geosystems 8(2), Q02001, doi:10.1029/2006GC001427

McGrail, B.P., Schaef, H.T., Ho, A.M., Chien, Y.-J., Dooley, J.J., Davidson, C.L., 2006. Potential for carbon dioxide sequestration in flood basalts. Journal of Geophysical Research 111, B12201, doi:10.1029/2005JB004169.

McPherson, B.J., Cole, B.S., 2000. Multiphase CO_2 flow, transport and sequestration in the Powder River basin, Wyoming, USA. Journal of Geochemical Exploration 69-70, 65-69.

McPherson, B.J., Han, W.S., Cole, B.S., 2008. Two equations of state assembled for basic analysis of multiphase CO_2 flow in deep sedimentary basin condition. Computers and Geosciences (In Press).

Mo, S., Zweigel, P., Lindeberg, E., Akervoll, I., 2005. Effect of geologic parameters on CO_2 storage in deep saline aquifers. Society of Petroleum Engineers Journal 93952.

Monnin, C. 1990. The influence of pressure on the activity coefficients of the solutes and on the solubility of minerals in the systems Na-Ca-Cl-SO_4-H_2O to 200^{o}C and 1 kbar and to high NaCl concentration. Geochimica et Cosmochimica Acta 54, 3265-3282.

Narasimhan, T.N., Witherspoon, P.A., 1976. An integrated finite difference method for analyzing fluid flow in porous media. Water Resources Research 12(1), 57-64.

Nghiem, L., Sammon, P., Grabenstetter, J., Ohkuma, H., 2004a. Modeling CO_2 storage in aquifers with a fully-coupled geochemical EOS compositional simulator. Society of Petroleum Engineers Journal 89474.

Nghiem, L., Shrivastava, V., Kohse, B., Sammon, P., 2004b. Simulation of CO_2 EOR and sequestration processes with a geochemical EOS compositional simulator. Petroleum Society's 5th Canadian International Petroleum Conference. Paper 2004-051.

Orr, Jr. F.M., 2004. Storage of carbon dioxide in geologic formations. Society of Petroleum Engineers Journal 88842.

Ozah, R.C., Lakshminarasimhan, S., Pope, G.A., Sepehrnoori, K., Bryant, S.L., 2005. Numerical simulations of the storage of pure CO_2 and CO_2-H_2S gas mixtures in deep saline aquifers. Society of Petroleum Engineers Journal 97255.

Palliser, C., McKibbin, R., 1998. A model for deep geothermal brines, III: Thermodynamic properties - enthalpy and viscosity. Transport in Porous Media 33, 155-171.

Parkhurst, D.L., Appelo, C.A.J., 1999. User's guide to PHREEQC (version 2) – A computer program for speciation batch-reaction, one-dimensional transport,

and inverse geochemical calculations: U.S. Geological Survey Water-Resources Investigation Report 99-4259, p.312.

Peng, D.Y., Robinson, D.B., 1976. A new-constant equation of state. Industrial and Engineering Chemistry 15(1) 58-64.

Phillips, S.L., Igbene, A., Fair, J.A., Ozbek, H., Tavana, M., 1981. A technical databook for geothermal energy utilization. Lawrence Berkeley National Laboratory, Berkeley, CA., REP LBL-12810.

Pitzer, K.S., 1973. Thermodynamics of electrolytes. I. Theoretical basis and general equations. Journal of Physical Chemistry 12, 268-277.

Portier, S., Rochelle, C., 2005. Modeling CO_2 solubility in pure water and NaCl-type waters from 0 to 300ºC and from 1 to 300 bar application to the Utsira formation at Sleipner. Chemical Geology 217, 187-199.

Prausintz, J.M., 1969. Molecular Thermodynamics of Fluid-Phase Equilibria, Prentice-Hall Inc., Englewood Cliffs, New Jersey.

Prausnitz, J.M., Lichtenthaller, R.N., De Azedevo, E.G., 1986. Molecular Thermodynamics of Fluid Phase Equilibria. Prentice Hall, New York.

Pruess, K., 2004. Numerical simulation of CO_2 leakage from a geologic disposal reservoir, including transitions from super- to subcritical conditions, and boiling to liquid CO_2. Society of Petroleum Engineers Journal 86098.

Pruess, K., Garcia, J., 2002. Multiphase flow dynamics during CO_2 disposal into saline aquifers. Environmental Geology 42, 282-295.

Pruess, K., Garcia, J., Kovscek, T., Oldenburg, C., Rutqvist, J., Steefel, C., Xu, T., 2004. Code intercomparison builds confidence in numerical simulation models for geologic disposal of CO_2. Energy 29, 1431-1444.

Pruess, K., Oldenburgh, C., Moridis, G., 1999. TOUGH2 user's guide, version 2.0. Lawrence Berkeley National Laboratory, Berkeley, California: Report LBNL-43134.

Pruess, K., Spycher, N., 2007. ECO2N – A fluid property module for the TOUGH2 code for studies of CO_2 storage in saline aquifer. Energy Conversion and Management 48, 1761-1767.

Pruess, K., Xu, T., Apps, J., Garcia, J., 2001. Numerical modeling of aquifer disposal of CO_2. Society of Petroleum Engineers Journal 66537.

Redlich, O., Kwong, J.N.S., 1949. On the thermodynamics of solutions. V. an equation of state. Fugacities of gaseous solution. Chemistry Review 44, 233-244.

Reid, R.C., Prausnitz, J.M., Poling, B.E., 1987. The Properties of Gases and Liquids. Fourth edition, McGraw-Hill, Inc., New York.

Schlumberger, 2003. Eclipse Technical Description, v.2003.

Schlumberger, 2005. Eclipse Technical Description, v.2005A, report, Abingdon, U.K.

Soave, G., 1972. Equilibrium constants from a modified Redlich-Kwong equation of state. Chemical Engineering Sciences 27, 1197-1203.

Span, R., Wagner, W., 1996. A new equation of state for carbon dioxide covering the fluid region from the triple-point temperature to 1100 K at pressures up to 800 MPa. Journal of Physical and Chemical Reference Data 25(6), 1509-1596.

Spiteri, E.J., Juanes, R., Blunt, M.J., Orr, F.M. Jr., 2005. Relative permeability hysteresis: Trapping models and application geological sequestration. Society of Petroleum Engineers Journal 96448.

Spycher, N., Pruess, K., 2005. CO_2-H_2O mixtures in the geological sequestration of CO_2. II. Partitioning in chloride brines at 12-100ºC and up to 600 bar. Geochimica et Cosmochimica Acta 69(13), 3309-3320.

Spycher, N., Pruess, K., Ennis-King, J., 2003. CO_2-H_2O mixtures in the geological sequestration of CO_2. I. Assessment and calculation of mutual solubilities from 12 to 100ºC and up to 600 bar. Geochimica et Cosmochimica Acta 67(16), 3015-3031.

Steefel, C.I. 2001. GIMRT, version 1.2: Software for modeling multicomponent, multidimensional reactive transport. User's guide, LLNL Report UCRL-MA-143182.

Steefel, C.I., Lasaga, A.C., 1994. A coupled model for transport of multiple chemical species and kineteic precipitation/dissolution reactions with application to reactive flow in single phase hydrothermal systems. American Journal of Science 294, 529-592.

Steefel, C.I., MacQuarrie, K.T.B., 1996. Approaches to modeling reactive transport in porous media, in: P.C. Lichtner, C.I. Steefel, E.H. Oelkers (Eds.), Reactive Transport in Porous Media, Reviews in Mineralogy 34, 83-125.

Talman, S.J., Adams, J.J., Chalaturnyk, R.J., 2004. Adapting TOUGH2 for general equation of state with application to geological storage of CO_2. Computers and Geosciences 30, 543-552.

Van der Lee, J., 1997. Modelisation du comportement geochimique et du transport des radionucleides. Ph. D., dissertation. Ecole nationale superieure des mines de Paris.

Van der Lee, J., De Windt, Lagneau, L., Goblet, P., 2003. Module-oriented modeling of reactive transport with hytec. Computers and Geosciences 29, 265-275.

Van der Meer, L.G.H., 1996. Computer modelling of underground CO_2 storage. Energy Conversion and Management 37(6-8), 1155-1160.

Van der Waals, J.D. (1873) De continuiteit van den gas- en vloeistoftoestand. Ph. D. dissertation, University Leiden, p.134.

Vesovic, V., Wakeham, W.A., Olchowy, G.A., Sengers, J.V., Watson, J.T.R., Millat, J., 1990. The transport properties of carbon dioxide. Journal of Physical and Chemical Reference Data 19(3), 763–808.

Weir, G.J., White, S.P., Kissling, W.M., 1996. Reservoir, storage and containment of greenhouse gases. Transport in Porous Media 23, 37-60.

White, S.P., 1995. Multiphase non-isothermal transport of systems of reacting chemicals. Water Resources Research 31(7), 1761-1772.

White, S.P., Allis, R.G., Moore, J., Chidsey, T., Morgan, C., Gwynn, W., Adams, M., 2005. Simulations of reactive transport of injected CO_2 on the Colorado Plateau, Utah, USA. Chemical Geology 217, 387-405.

Wolery, T.J., Daveler, S.A., 1992. EQ6, A computer program for reaction path modeling of aqueous geochemical systems: Theoretical manual, user's guide, and related documentation (version 7.0). Report UCRL-MA-110662 PT IV. Lawrence Livermore National Laboratory, Livermore.

Xu, T., Apps, J.A., Pruess, K., 2003. Reactive geochemical transport simulation to study mineral trapping for CO_2 disposal in deep arenaceous formations. Journal of Geophysical Research 108(B2), 2071, doi:10.1029/2002JB001979.

Xu, T., Apps, J.A., Pruess, K., 2004. Numerical simulation of CO_2 disposal by mineral trapping in deep aquifers. Applied Geochemistry 19, 917-936.

Xu, T., Apps, J.A., Pruess, K., 2005. Mineral sequestration of carbon dioxide in a sandstone-shale system. Chemical Geology 217, 295-318.

Xu, T., Sonnenthal, E., Spycher, N., Pruess, K., 2006. TOUGHREACT-A simulation program for non-isothermal multiphase reactive geochemical transport in variably saturated geologic media: Applications to geothermal injectivity and CO2 geological sequestration. Computers and Geosciences 32, 145-165.

Yeh, G.T., Tripathi, V.S., 1989. A critical evaluation of recent development in hydrogeochemical transport models of reactive multichemical components. Water Resources Research 25(1), 93-108.

Zawisza, A., Malesinska, B., 1981. Solubility of carbon dioxide in liquid water and of water in gaseous carbon dioxide in the range 0.2-5 MPa at temperature up to 473 K. Journal of Chemical and Engineering Data 26(4), 388-391.

Zerai, B., Saylor, B.Z., Matisoff, G., 2006. Computer simulation of CO_2 trapped through mineral precipitation in the Rose Run Sandstone, Ohio. Applied Geochemistry 21, 223-240.

Zwingmann, N., Mito, S., Sorai, M., Ohsumi, T., 2005. Preinjection characterization and evaluation of CO_2 sequestration potential in the Haizume formation, Niigata basin, Japan: Geochemical modelling of water-minerals-CO_2 interaction. Oil & Gas Science and Technology 60(2), 249-258.

CHAPTER 2

TWO EQUATIONS OF STATE ASSEMBLED FOR BASIC ANALYSIS OF MULTIPHASE CO_2 FLOW UNDER DEEP SEDIMENTARY BASIN CONDITION

2.1. Introduction and Background

Disposal and long-term sequestration of anthropogenic "greenhouse gases" such as CO_2 is a proposed approach to reducing global warming. Deep, regional-scale aquifers in sedimentary basins are possible sites for sequestration, given their ubiquitous nature. One approach to evaluating such geologic sequestration is to use numerical models of geologic basins, including multiphase flow of CO_2 and groundwater. The models would be used to evaluate potential storage capacities and residence times in potential aquifer storage sites and to study migration patterns and rates away from injection sites.

Simulation of such processes requires realistic representations of thermodynamic properties (density, fugacity, enthalpy, viscosity) of water, separate-phase CO_2 (gas and supercritical phases), and aqueous mixtures of CO_2 over the range of temperatures and pressures anticipated in a given geologic setting. In addition, capillary pressure and relative permeability must be treated. Finally, an adequate representation of the solubility of CO_2 as a function of temperature and pressure

needs to be included, in addition to appropriate phase changes in response to evolving pressure and temperature conditions.

Two different equations of state (EOS) algorithms are assembled and compared for primary thermodynamic state conditions of supercritical/gas phase CO_2, including density, fugacity, and enthalpy. One is a modified Redlich-Kwong EOS, "MRKEOS," that employs modification of the attractive term from the original van der Waals equation developed in 1873 (van der Waals, 1873; Kerrick and Jacobs 1981; Weir et al. 1996; Cole, 2000). The other EOS algorithm that we coded and implemented, "SWEOS," is an EOS for CO_2 originally developed by Span and Wagner (1996), who based their algorithm on an empirical representation of the fundamental equation of Helmholtz energy. Both EOS codes use identical methods for calculating viscosity and capillary pressure for single (supercritical/gas) or mixed phase (water/CO_2) fluids. In the case of mixed phase CO_2-water systems, both codes employ the same approach for determining relative permeability and different approaches for calculating solubility of CO_2 in the water phase.

For the benefit of other workers, both EOS algorithms' source codes are provided in Appendix III, IV, V, and VI. The FORTRAN versions provided here were specifically adapted for the TOUGH2 simulator developed by Pruess (1991) at the Lawrence Berkeley Laboratory, although the routines may be adapted for any FORTRAN flow code that simulates coupled multiphase fluid and heat flux in the subsurface. For the sake of accommodating users who wish to use or test either or both algorithms immediately, we provide "stand-alone" versions in the form of interactive Matlab © scripts.

2.2. Assumptions

The following assumptions were made in the development of the two EOS algorithms presented in this study:

1) The multiphase form of the Darcy equation adequately describes multiphase fluid flow in porous media.
2) The phases present are in local chemical and thermal equilibrium.
3) Molecular diffusion is negligible relative to advective transport.
4) Energy changes caused by acceleration and viscous dissipation are negligible.
5) The system is composed of two components, liquid H_2O and CO_2.
6) Dissolution of water in CO_2 is not considered; for the mixed phase, dissolution of CO_2 in water is considered only. Thus, other processes such as near-well formation dehydration (typically called "dry-out") following CO_2 injection cannot be evaluated.

2.3. Constitutive Relationships

Appropriate governing equations for multiphase flow of CO_2 and groundwater require constitutive relationships that express parameters as functions of a set of primary thermodynamic variables. These constitutive relationships are provided in the EOS algorithms. A summary of these relationships includes the following:

1) Relative permeabilities are functions of fluid phase saturations.
2) Capillary pressures are functions of fluid phase saturations.

3) Fluid phase densities, enthalpies, fugacities, and viscosities are functions of pressure, temperature, and fluid phase composition.

4) At equilibrium, CO_2 partitions between fluid phases according to Henry's law.

5) Thermal conductivity of gaseous/supercritical CO_2 is considered negligible relative to that of the rock matrix and liquid.

The governing equations for which the EOS applies are assumed to have two supplemental constraints:

1) Fluid phase saturations sum to unity or

$$\sum_{\beta=l,g} S_\beta = 1 \qquad \text{(Eq. 2.1)}$$

2) In each fluid phase, component mass fractions sum to unity or

$$\sum_{\alpha=\substack{H_2O,\\ CO_2}} X_\beta^\alpha = 1 \qquad \text{(Eq. 2.2)}$$

2.4. Primary Variables

From Gibbs' phase rule, the number of thermodynamic degrees of freedom, F, in a system consisting of N_α components distributed amongst N_β phases is

$$F = N_\alpha + 2 - N_\beta \qquad \text{(Eq. 2.3)}$$

This equation pertains only to the intensive properties of the system. Information regarding the relative amounts of phases in the system is provided through the phase saturations. Since only ($N_\beta - 1$) of the phase saturations are independent (Eq. 2.1), the total number of degrees of freedom, F_T, is reduced to (N_α +

1) or

$$F_T = F + N_\beta - 1 = (N_\alpha + 2 - N_\beta) + N_\beta - 1 = N_\alpha + 1 \qquad \text{(Eq. 2.4)}$$

The appropriate choice of the (N_α + 1) primary variables depends on the phases present. The approach used in the TOUGH2 simulator, is to use pressure, temperature, and the mass fraction of the component dissolved in water as the primary variables for those volume elements containing only one phase (Pruess, 1991). If two-phase conditions develop, the primary variables are switched to pressure, temperature, and saturation of the gaseous phase.

Equation of state module in TOUGH2 handles this problem by using pressure, temperature, and the mass fraction of the component dissolved in water as the primary variables for only one phase. If two-phase conditions develop, TOUGH2 "switches" the primary variables to pressure, temperature, and saturation of the gaseous phase. However, this simple "switching" method failed to represent the physics of the more rigorous model of CO_2 flow and transport applied in this study. Convergence of the numerical solution failed if this primary variable "switching" method was employed. Weir et al. (1996) and White (Personal communication, 1999) also had similar convergence problems using TOUGH2 to model the injection and transport of large quantities of CO_2.

Later, Wu and Forsyth, (2001) showed that the selection of primary variables depends in general on the sensitivity of the system of equations to at given phase and flow conditions. Therefore, we developed the two codes to accommodate a set of "four persistent primary variables" (pressure, temperature, dissolved mass fraction of

CO_2, and saturation of gaseous/supercritical CO_2) rather than use "a primary variable-switching method". These persistent primary variables remain independent even as phase conditions change. Adding a fourth primary variable makes computation slightly more difficult because it represents an additional unknown to be solved for implicitly. However, the advantage of defining four persistent primary variables is that with the phase saturation constraint Eq. (2.1), a three-phase system can be fully defined. This allows CO_2 mass to be explicitly partitioned between the gaseous and liquid phases using the source/sink term of multiphase flow equations.

However, the primary variable-switching method continuously applied to numerical simulation associated with CO_2 sequestration (Pruess and Garcia, 2002; Pruess, 2004). Therefore, it is difficult to evaluate which methods between "the four persistent primary variables" and "the primary variable-switching" method take advantages of (1) computational efficiency, (2) robustness, and (3) simplicity in evaluating other secondary variables and setting up the linearized equations at this point.

Similar to this work, Talman et al. (2004) also developed an EOS based on Span and Wagner (1996). They chose density and temperature as primary variables, rather than temperature and pressure. As a result, processing time is faster than that for SWEOS. However, a change in the original TOUGH2 simulator code was required. In addition to changing the original TOUGH2 code, there are practical difficulties in estimating the density values as the input parameter when simulating deep reservoirs; density variation is not a linear function of pressure and temperature. Thus, we elected to maintain use of temperature and pressure as primary variables.

2.5. Interphase Mass Transfer

In the EOS developed in this study, we assume that, when present, the gas phase consists purely of CO_2. During each time step, the solubility of CO_2 at the prevailing pressure and temperature is calculated for each node or cell, using the Henry's law relationship (discussed in section 2.6.2.1). This value represents the solubility of CO_2 in water if it were in equilibrium with separate-phase CO_2 at the prevailing pressure and temperature. This solubility is then compared to the actual concentration in the liquid phase in that cell.

If the actual concentration is greater than the calculated solubility, then a sink of aqueous-phase CO_2 "component" and a source of the separate-phase CO_2 "component," both equal in magnitude to the excess concentration, are included in the mass balance equations. Similarly, if the concentration is less than the calculated solubility, then a source of aqueous-phase CO_2 component and a sink of the separate-phase CO_2 component, both equal in magnitude to the difference between actual concentration and calculated solubility, are added to the component mass balance equations. In this manner, phases are allowed to completely disappear and reappear depending on pressure and temperature conditions. This "kinetic" type method of interphase mass transfer maintains mass balance errors to be generally quite small, typically less than 3%. The source code documents the interphase mass transfer routines we developed for the algorithm.

2.6. Thermophysical Properties

We provide two EOS algorithms, each drawing on several sources for evaluation of different properties, as detailed schematically in Figure 2.1. For example, the density, fugacity, and enthalpy of MRKEOS are calculated from the modified Redlich-Kwong (MRK) EOS that employs modification of the attractive term from van der Waals equation (Kerrick and Jacobs, 1981; Weir et al. 1996; Cole, 2000). In SWEOS, the density, fugacity and enthalpy of separate-phase CO_2 are calculated using the approach originally developed by Span and Wagner (1996). As detailed in Figure 2.1, both EOS codes use the same approach for calculating viscosity (Vesovic et al. 1990) and capillary pressure (Parker et al. 1987) for single (supercritical/gas) or mixed phase (water/CO_2) fluids. Also illustrated in Figure 2.1 is that for the case of mixed phase CO_2-water systems, both codes employ the same approach for determining relative permeability (Parker et al. 1987) and different approaches for calculating solubility of CO_2 in the water phase: SWEOS uses the solubility approach of Diamond and Akinfiev (2003), while MRKEOS draws on the approach of Reid et al. (1987). Both the relative permeability and capillary formulations are not described here, but rather refer the reader to Parker et al. (1987) and Cole (2000) for details.

The following sections detail the relationships used to calculate thermophysical properties of the CO_2/H_2O fluid system, including specific density, specific enthalpy, compressibility factor, and dynamic viscosity in each EOS.

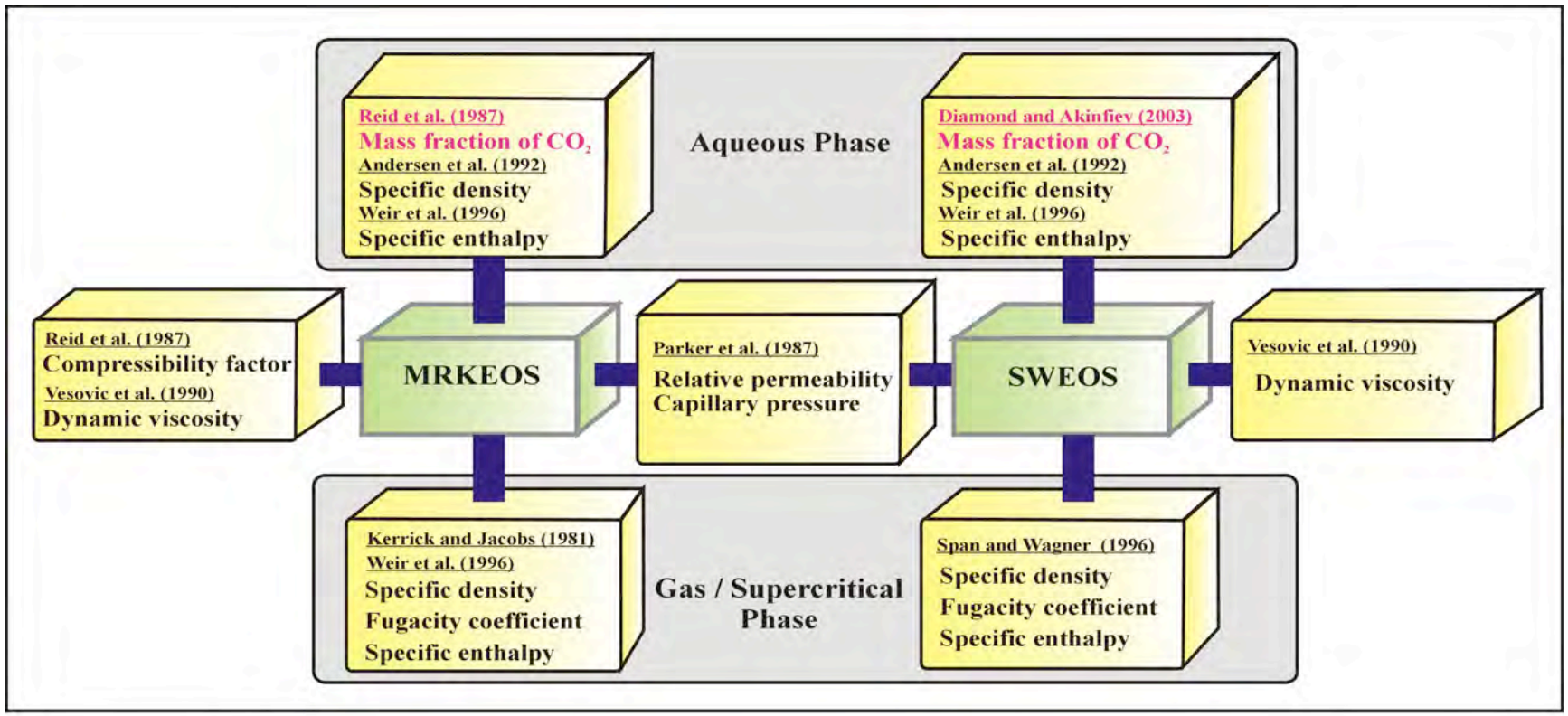

Figure 2.1. A schematic diagram for comparing the MRKEOS and SWEOS components

As summarized in Figure 2.1, both EOS developed in this study draw on the formulations of Carnahan and Starling (1972), Jacobs and Kerrick (1981), Kerrick and Jacobs (1981), Reid et al. (1987), Patel and Eubank (1988), Vesovic et al. (1990), Andersen et al. (1992), Span and Wagner (1996), Weir et al. (1996), and Fenghour et al. (1998). Jacobs and Kerrick (1981) also assembled an EOS algorithm for H_2O–CO_2 mixtures, but the new set of algorithms we assembled for this study adapt subsequent advances made by Reid et al. (1987), Fenghour et al. (1998), Patel and Eubank (1988), Vesovic et al. (1990), Span and Wagner (1996), and Weir et al. (1996), as detailed in the following sections.

The MRKEOS and SWEOS codes are valid for pressures ranging from 0.1 MPa to greater than 100 MPa, and temperatures ranging from approximately 15°C to greater than 100°C. These pressure and temperature ranges adequately cover those anticipated in a typical geologic basin. However, we do not discuss phase behavior in detail, but rather refer the reader to Spycher at al. (2003) for a detailed discussion of CO_2-water phase diagram and associated phase states at different thermodynamic conditions; Pruess (2004) also provides a useful discussion of phase transitions at different pressure-temperature conditions.

2.6.1 Gaseous/Supercritical CO_2

This subsection summarizes the relationships employed to calculate the thermophysical properties of gaseous/supercritical CO_2 necessary to characterize its flow as a separate-phase in the subsurface. These properties include specific density, specific fugacity, specific enthalpy, and dynamic viscosity, all functions of pressure

and temperature. Additionally, relationships for the compressibility factor for gaseous/supercritical CO_2 are developed only in MRKEOS.

2.6.1.1. Specific Density

The first step in adequately characterizing the properties of a pure gas is to determine its density behavior as a function of temperature and pressure.

In MRKEOS, the density is acquired from modified Redlich-Kwong EOS. Redlich and Kwong (1949) modified the attractive portion of the van der Waals equation to reflect its temperature dependence as follows:

$$P = \frac{RT}{v-b} - \frac{a}{\sqrt{T}\,v(v+b)} \qquad \text{(Eq. 2.5)}$$

The Redlich-Kwong (RK) equation produces acceptable agreement with experimental data for several gases. Numerous empirical modifications to the RK equation have been published (e.g., Carnahan and Starling, 1972; Soave, 1972; de Santis et al. 1974; Hederer et al. 1976; Peng and Robinson, 1976; Fuller, 1976), most of which propose the different form of attractive term as function of temperature.

In developing a modified Redlich–Kwong (MRK) EOS explicitly for CO_2 at elevated temperatures and pressures, Kerrick and Jacobs (1981) chose to use the repulsive term from the Carnahan and Starling (1972) version of the RK, but further modified the attractive term (*a(P,T)*) to depend on both temperature and pressure. The EOS of Kerrick and Jacobs (1981) is as follows:

$$P = \frac{RT\left(1+y+y^2-y^3\right)}{v(1-y)^3} - \frac{a(P,T)}{\sqrt{T}\,v(v+b)} \qquad \text{(Eq. 2.6)}$$

In this equation, the term on the left is the modified version of the repulsive term by Carnahan and Starling (1972), and the term on the right is the modified version of the attractive term by Kerrick and Jacobs (1981).

The attractive term takes the form

$$a(P,T) = c(T) + \frac{d(T)}{v} + \frac{e(T)}{v^2} \qquad \text{(Eq. 2.7)}$$

where *c*, *d*, and *e* are second-order polynomial functions of temperature with empirically-derived coefficients. To extend the EOS of Kerrick and Jacobs (1981) to lower temperatures (i.e., closer to those expected in a typical sedimentary basin), Weir et al. (1996) further modified the attractive term as follows:

$$a(P,T) = c(T) + \frac{d(T)}{v} + \frac{e(T)}{v^2} + \frac{f(T)}{v^3} \qquad \text{(Eq. 2.8)}$$

where *c*, *d* , *e* and *f* are second order polynomial functions of temperature defined in Table 2.1 (Weir et al. 1996).

Combining Eq (2.6) with (2.8) and using the relations provided in Table 2.1 provides an EOS for CO_2 that is valid for the temperature and pressure conditions expected in a typical sedimentary basin. The complete EOS derived is Eq. (2.9) in Table 2.1 (Kerrick and Jacobs, 1981; Weir et al. 1996).

By taking the derivative of Eq. (2.9) with respect to the molar volume (*v*), we used the Newton Method in our algorithm to iterate for the molar volume of CO_2. Noting that the molar density of CO_2 is simply the inverse of the molar volume, the specific density of CO_2 can be determined from the relationship ($\rho = \frac{M_W}{v}$).

Table 2.1. Coefficients of the MRKEOS; from Weir et al. (1996) and Eq. (2.9), (2.10), (2.12).

$c(T)=c_1(=2.39534\times10^{1})+c_2(=-4.55309\times10^{-2})T+c_3(=3.65168\times10^{-5})T^2$

$d(T)=d_1(=-4.09844\times10^{-3})+d_2(=1.23158\times10^{-5})T+d_3(=-8.99791\times10^{-9})T^2$

$e(T)=e_1(=2.89224\times10^{-7})+e_2(=-8.02594\times10^{-10})T+e_3(=-7.30975\times10^{-13})T^2$

$f(T)=f_1(=-6.43556\times10^{-12})+f_2(=2.01284\times10^{-14})T+f_3(=-2.17304\times10^{-17})T^2$

$$P=\frac{RT\left(1+y+y^2-y^3\right)}{v\left(1-y\right)^3}-\frac{c(T)+\dfrac{d(T)}{v}+\dfrac{e(T)}{v^2}+\dfrac{f(T)}{v^3}}{\sqrt{T}\,v\left(v+b\right)} \qquad (2.9)$$

$$Z=\frac{1+y+y^2-y^3}{\left(1-y\right)^3}-\frac{a(P,T)}{RT^{1.5}\left(v+b\right)} \qquad (2.10)$$

$$\begin{aligned}\ln\phi \;=\; & \frac{8y-9y^2+3y^3}{\left(1-y\right)^3}-\ln Z-\frac{c(T)}{RT^{1.5}\left(v+b\right)}+\left[\frac{c(T)}{bRT^{1.5}}\ln\left(\frac{v}{v+b}\right)\right]- \\ & \frac{d(T)}{vRT^{1.5}\left(v+b\right)}-\frac{d(T)}{bvRT^{1.5}}+\left[\frac{d(T)}{b^2RT^{1.5}}\ln\left(\frac{v+b}{v}\right)\right]- \\ & \frac{e(T)}{v^2RT^{1.5}\left(v+b\right)}-\frac{e(T)}{2bv^2RT^{1.5}}+\frac{e(T)}{b^2vRT^{1.5}}-\left[\frac{e(T)}{b^3RT^{1.5}}\ln\left(\frac{v+b}{v}\right)\right]- \\ & \frac{f(T)}{v^3RT^{1.5}\left(v+b\right)}-\frac{f(T)}{3bv^3RT^{1.5}}+\frac{f(T)}{2b^2v^2RT^{1.5}}-\frac{f(T)}{b^3vRT^{1.5}}+\left[\frac{f(T)}{b^4RT^{1.5}}\ln\left(\frac{v+b}{v}\right)\right]\end{aligned} \qquad (2.12)$$

In SWEOS, we employed the density formulation from Span and Wagner (1996). A detailed description and the full equation are provided in Appendix II. In this EOS, density and temperature are assigned as primary variables. Span and Wagner's EOS used density and temperature as primary variables; because the TOUGH2 simulator employs pressure and temperature as primary variables, we used a numerical method to facilitate pressure and temperature as primary variables, following the approach of Diamond and Akinfiev (2003).

A plot of the specific density of CO_2 as a function of pressure along several representative isotherms calculated using MRKEOS and SWEOS is provided in Figure 2.2. For comparison, values of specific density of CO_2 generated from an

EOS developed by the International Union of Pure and Applied Chemistry (IUPAC) (tabulated in Angus et al. 1976) are also plotted.

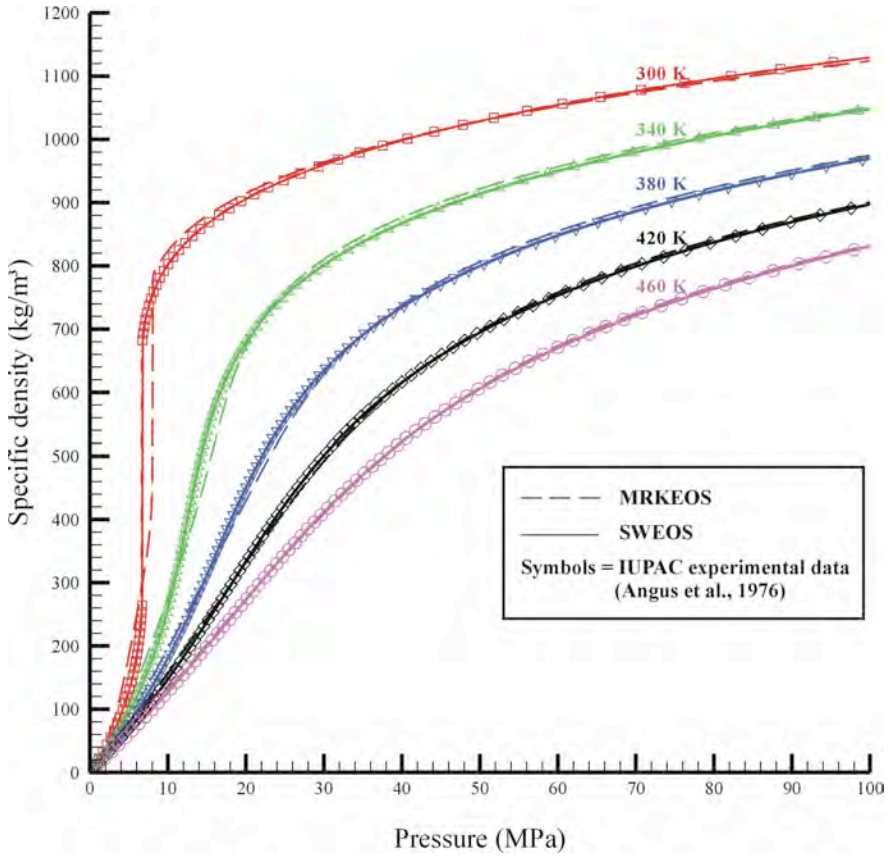

Figure 2.2. Specific density for CO_2 as a function of pressure along several representative isotherms. IUPAC refers to values tabulated in Angus et al. (1976).

2.6.1.2 Compressibility Factor

Substituting the MRKEOS presented as Eq. (2.9) into the ideal gas law $\left(Z = \frac{Pv}{RT}\right)$ and simplifying yields the equation of the compressibility factor for CO_2 used in the algorithm. The equation of the compressibility factor is expressed as Eq. (2.10) in Table 2.1. In SWEOS, the compressibility factor is not provided.

2.6.1.3 Fugacity Coefficient

In MRKEOS, the fugacity coefficient of a gas is calculated using (Prausnitz, 1969)

$$RT\ln\phi = \int_{v}^{\infty}\left[\frac{P}{n} - \frac{RT}{V}\right] dV \; - \; RT\ln Z \; + \; RT(Z-1) \qquad \text{(Eq. 2.11)}$$

Substituting Eq. (2.9) for P in the first term on the right hand side of Eq. (2.11), this equation can be split into three separate integrals. Following Kerrick and Jacobs (1981), evaluating these integrals yields the expression (Eq. 2.12) used to calculate the fugacity coefficient for CO_2 used in the EOS algorithm (Table 2.1).

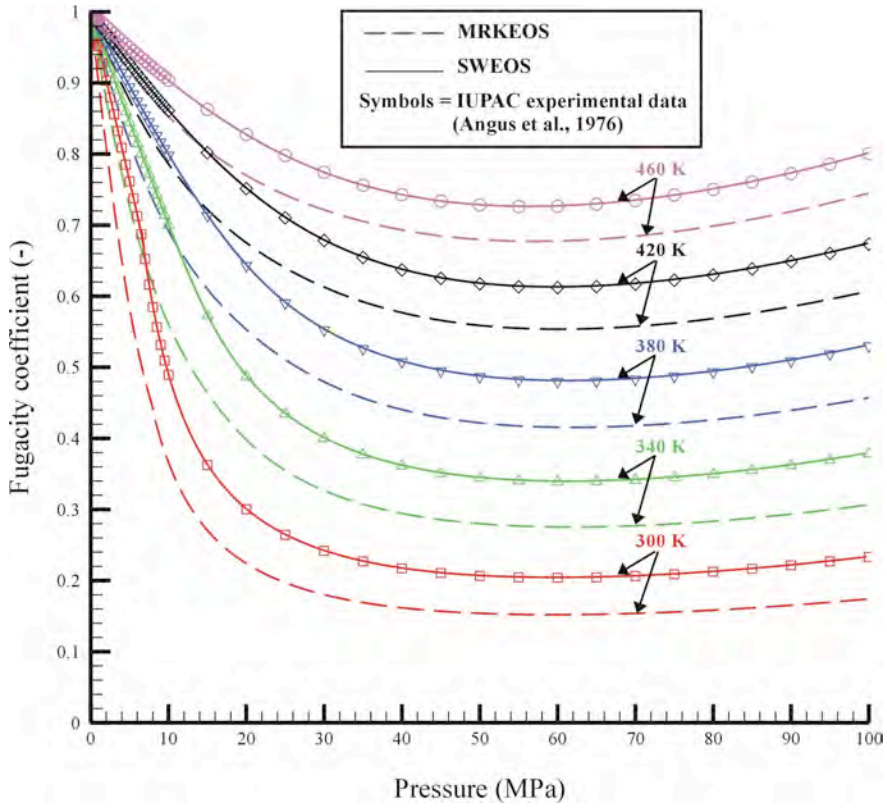

Figure 2.3. Fugacity coefficient for CO_2 as a function of pressure along several representative isotherms. IUPAC refers to values tabulated in Angus et al. (1976).

In SWEOS, the fugacity coefficient is adapted from Span and Wagner (1996), based on calculated values of specific density and temperature (Appendix II). A plot of the fugacity coefficient for CO_2 as a function of pressure along several representative isotherms, calculated using Eq. (2.12) and SWEOS, is provided in Figure 2.3. For comparison, values of the fugacity coefficient for CO_2 generated from the EOS developed by IUPAC (tabulated in Angus et al. 1976) are also plotted.

2.6.1.4. Specific Enthalpy

In MRKEOS, following the work of Weir et al. (1996) and Patel and Eubank (1988), the EOS algorithm calculates the enthalpy of CO_2 using residual properties. After Patel and Eubank (1988), the residual molar internal energy may be defined as:

$$\frac{U - U^*_{ref}}{RT} = \frac{1}{T}\int_0^{\rho}\left(\frac{\partial Z}{\partial \frac{1}{T}}\right)_{\rho}\frac{d\rho}{\rho} + \frac{1}{T}\int_{T_{ref}}^{T}\frac{C^*_V}{R}dT = (A) + (B) \qquad \text{(Eq. 2.13)}$$

Where the asterisk (*) indicates the perfect gas state property value (Patel and Eubank, 1988). *(A)* and *(B)* are defined in Table 2.2.

Once the residual molar internal energy is determined, the residual molar enthalpy may be calculated using (Patel and Eubank, 1988):

$$\frac{H - H^*_{ref}}{RT} = \frac{U - U^*_{ref}}{RT} + Z - \frac{T_{ref}}{T} = (A) + (B) + Z - \frac{T_{ref}}{T} \qquad \text{(Eq. 2.14)}$$

Therefore, the molar enthalpy can be determined by evaluating compressibility factor *Z* from Eq. (2.10) and multiplying through by the quantity *RT*. The specific enthalpy is then calculated by dividing the molar enthalpy by the molecular weight of CO_2.

Table 2.2. Coefficients of the equation for perfect gas state molar heat capacity; adapted from Angus et al. (1976).

N	r_n	
0	0.769441246×10^{1}	$A = \frac{1}{12 b^4 R T^{1.5}} \left(\begin{array}{l} b^3\rho\left(-18d_1 - 6d_2T + 6d_3T^2\right) + b^2\rho\left(18e_1 + 6e_2T - 6e_3T^2\right) + \\ b\rho\left(-18f_1 - 6f_2T + 6f_3T^2\right) + b^3\rho^2\left(-9e_1 - 3e_2T + 3e_3T^2\right) + \\ b^2\rho^2\left(9f_1 + 3f_2T - 3f_3T^2\right) + b^3\rho^3\left(-6f_1 - 2f_2T + 2f_3T^2\right) + \\ \ln\left(1+b\rho\right)\left(\begin{array}{l} b^3\left(-18c_1 - 6c_2T + 6c_3T^2\right) + b^2\left(18d_1 + 6d_2T - 6d_3T^2\right) + \\ b\left(-18e_1 - 6e_2T + 6e_3T^2\right) + \left(18f_1 + 6f_2T - 6f_3T^2\right) \end{array} \right) \end{array} \right)$
1	-0.249610766×10^{0}	
2	-0.254000397×10^{2}	
3	0.651102201×10^{2}	
4	-0.820863624×10^{2}	
5	0.574148450×10^{2}	$B = \left(\begin{array}{l} \gamma_0 - 1 + \frac{T_{ref}}{T}\left(1-\gamma_0\right) + \frac{\beta\gamma_1}{T}\ln\left(\frac{T}{T_{ref}}\right) + \frac{\beta^2\gamma_2}{T}\left(\frac{1}{T_{ref}} - \frac{1}{T}\right) + \frac{\beta^3\gamma_3}{2T}\left(\frac{1}{T_{ref}^2} - \frac{1}{T^2}\right) + \\ \frac{\beta^4\gamma_4}{3T}\left(\frac{1}{T_{ref}^3} - \frac{1}{T^3}\right) + \frac{\beta^5\gamma_5}{4T}\left(\frac{1}{T_{ref}^4} - \frac{1}{T^4}\right) + \frac{\beta^6\gamma_6}{5T}\left(\frac{1}{T_{ref}^5} - \frac{1}{T^5}\right) + \frac{\beta^7\gamma_7}{6T}\left(\frac{1}{T_{ref}^6} - \frac{1}{T^6}\right) \end{array} \right)$
6	-0.212184243×10^{2}	
7	0.323362153×10^{1}	

β is 304.2 K

In SWEOS, the specific enthalpy is calculated from Span and Wagner (1996), much as we did for fugacity coefficient (Appendix II). A plot of the specific enthalpy for CO_2 as a function of pressure along several representative isotherms, calculated using Eq. (2.14) and SWEOS, is provided in Figure 2.4. For comparison, values of the specific enthalpy for CO_2 generated from the EOS developed by IUPAC (tabulated in Angus et al. 1976) are also plotted.

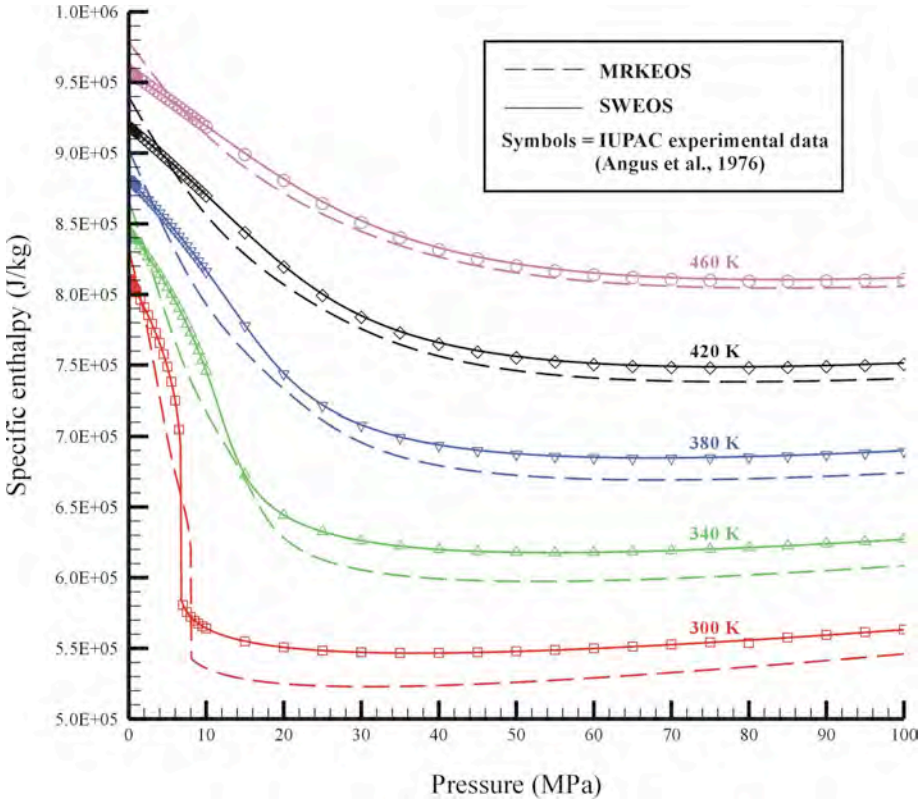

Figure 2.4. Specific enthalpy for CO_2 as a function of pressure along several representative isotherms. IUPAC refers to values tabulated in Angus et al. (1976).

2.6.1.5 Dynamic Viscosity

Based on a large body of available experimental data, Vesovic et al. (1990) developed a correlation for the dynamic viscosity of CO_2 applicable to temperatures ranging from 200 to 1500 K and pressures up to 100 MPa. Subsequently, Fenghour et al. (1998) updated the correlation of Vesovic et al. (1990) based on experimental data. The final dynamic viscosity representation is valid for pressures up to 300 MPa for temperatures ranging from 200 to 1000 K, and for pressures up to 30 MPa for temperatures ranging from 1000 to 1500 K. Based on the work of these authors, the total viscosity of CO_2 as a function of density and pressure may be expressed as the sum of three independent contributions:

$$\eta(\rho,T) = \eta_o(T) + \Delta\eta(\rho,T) + \Delta_c\eta(\rho,T) \qquad \text{(Eq. 2.15)}$$

In Eq. (2.15), $\eta_o(T)$ is the contribution in the limit of zero density arising from two-body molecular interactions, $\Delta_c\eta(\rho,T)$ is the contribution of the critical point enhancement arising from the long range fluctuations that occur in a fluid near its critical point, and $\Delta\eta(\rho,T)$ is the excess viscosity arising from the contribution of all other effects, including many-body collisions, molecular-velocity correlations, and collisional transfer (Vesovic et al. 1990).

From Vesovic et al. (1990), the viscosity in the zero-density limit can be evaluated as a function of temperature only, using

$$\eta_o(T) = \frac{1.00697\sqrt{T}}{\psi_\eta^*(T^*)} \qquad \text{(Eq. 2.16)}$$

where the reduced effective cross-section, ψ^*_η, is calculated using the following empirical relationship:

$$\ln\psi_\eta^*(T^*) = \sum_{i=0}^{4} a_i (\ln T^*)^i \qquad \text{(Eq. 2.17)}$$

where the reduced temperature, $T^* = \frac{kT}{\varepsilon}$, with the energy scaling parameter (ε/k) that is equal to 251.196 K. The coefficients (a_i) of Eq. (2.17) are provided in Table 2.3.

To represent the excess viscosity contribution to the total viscosity, Fenghour et al. (1998) used a power series expansion in density of the form

$$\Delta\eta(\rho,T) = \sum_{i=1}^{n} b_i(T)\rho^i \qquad \text{(Eq. 2.18)}$$

The temperature dependence of the density coefficients, $b_i(T)$, is determined by a functional relationship of the form

$$b_i = \sum_{j=1}^{m} \frac{d_{ij}}{T^{*(j-1)}} \qquad \text{(Eq. 2.19)}$$

By fitting experimental data to Eq. (2.18) and (2.19), Fenghour et al. (1998) determined the coefficients d_{ij} provided in Table 2.3.

Table 2.3. Coefficients of a representation of the viscosity of CO_2 in the limit of zero-density, adapted from Vesovic et al. (1990); coefficients of the representation of the excess viscosity of CO_2 from Fenghour et al. (1998); all other d_{ij} coefficients are equal to zero.

I	0	1	2	3	4
a_i	2.351560×10^{-1}	-4.912660×10^{-1}	5.211155×10^{-2}	5.347906×10^{-2}	-1.537102×10^{-2}
Ij	11	21	64	81	82
d_{ij}	0.4071119×10^{-2}	0.7198037×10^{-4}	0.2411697×10^{-16}	0.2971072×10^{-22}	-0.1627888×10^{-22}

Combining equations Eq. (2.18) and (2.19), the excess viscosity correlation can written explicitly as

$$\Delta\eta(\rho,T) = d_{11}\rho + d_{21}\rho^2 + \frac{d_{64}\rho^6}{T^{*3}} + d_{81}\rho^8 + \frac{d_{82}\rho^8}{T^*} \qquad \text{(Eq. 2.20)}$$

Where $\Delta\eta\ (\rho,T)$ is the excess viscosity in units of μPa s and ρ is the specific density in units of kg/m^3.

Theoretical and experimental evidence indicates that the viscosity of CO_2 diverges at the critical point. However, the contribution of the critical point enhancement to the total viscosity of CO_2 is weak and restricted to a narrow range of conditions near the critical point (Fenghour et al. 1998). Vesovic et al. (1990) show that the relative critical viscosity enhancement, $\Delta\eta_c(\rho,T)/\eta(\rho,T)$, is smaller than 1%

outside the region bounded approximately by 300 K < T < 310 K and 300 kg/m^3 < ρ < 600 kg/m^3 (or in terms of pressure, 7 MPa < P < 9 MPa).

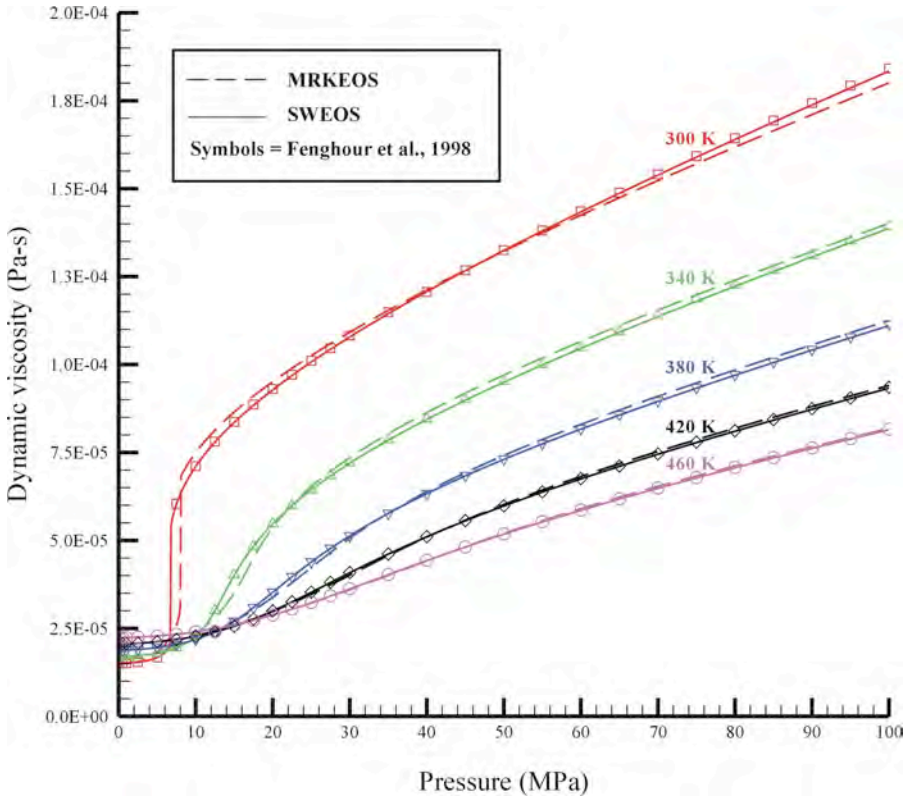

Figure 2.5. Dynamic viscosity of CO_2 as a function of pressure along several representative isotherms. Symbols refer to values tabulated in Fenghour et al. (1998).

To characterize the viscosity of CO_2 in the region near its critical point, Vesovic et al. (1990) present a function to cross over from the singular behavior of the viscosity asymptotically close to the critical point to the nonsingular background behavior far away from the critical point. However, given the narrow range of pressure and temperature conditions for which the critical point enhancement is considered important, its contribution to the total viscosity is neglected in this study, resulting in considerable computational savings. Therefore, in Eq. (2.15) $\Delta_c\eta(\rho,T)$ is

considered to be zero in this study, while $\eta_o(T)$ and $\Delta\eta(\rho,T)$ are evaluated using Eq. (2.16) and Eq. (2.20), respectively.

A plot of the dynamic viscosity of CO_2 as a function of pressure along several isotherms, calculated as outlined above, is provided in Figure 2.5. For comparison, values for the dynamic viscosity of CO_2 from Fenghour et al. (1998) are also plotted. The values for the dynamic viscosity of CO_2 predicted from the equations outlined above compare favorably with those generated by Fenghour et al. (1998), except near the critical point (Figure 2.5).

2.6.2 Aqueous H_2O/CO_2 Mixtures

In this section we summarize the relationships employed to calculate thermophysical properties such as solubility, density, and enthalpy of aqueous mixtures of water and CO_2 necessary to characterize the flow of such mixtures in the subsurface.

2.6.2.1. Solubility

Two different solubility models using a modified Henry's law were applied in each algorithm. The solubility model from Reid et al. (1987) was used in MRKEOS and that from Diamond and Akinfiev (2003), was used in SWEOS.

A fairly good approximation of the solubility of a slightly soluble gas (CO_2) in a volatile liquid solvent (H_2O) can be obtained using Henry's law. Letting subscript *2* represent the gaseous solute and subscript *1* represent the volatile liquid solvent, Henry's law can be written as

$$f_2 = H_{2,1}^{(P_{vp1})} X_2 \qquad X_2 << 1 \qquad \text{(Eq. 2.21)}$$

Where X_2 is the mole fraction of the gaseous solute, f_2 is the fugacity of the slightly soluble gas in equilibrium with the volatile liquid solvent, and $H_{2,1}^{(P_{vp1})}$ is the Henry's Coefficient for the gaseous solute in the volatile liquid solvent (Reid et al. 1987). Henry's Coefficient is defined as

$$H_{2,1}^{P_{vp1}} = \lim_{X_2 \to 0} \left(\frac{f}{X} \right)_2 \qquad \text{(Eq. 2.22)}$$

where the superscript P_{vp1} indicates that as X_2 approaches 0, the pressure of the system equals the vapor pressure of the volatile liquid solvent at the prevailing temperature (Reid et al. 1987).

In cases where the gas pressure is considerable, such as when CO_2 is injected in the subsurface, Eq. (2.21) takes the more general form

$$\ln \left(\frac{f}{X} \right)_2 = \ln H_{2,1}^{P_{vp1}} + \frac{\overline{V_2^{\infty}} \left(P - P_{vp1} \right)}{RT} \qquad \text{(Eq. 2.23)}$$

Where $\overline{V_2^{\infty}}$ is the partial molar volume of the gaseous solute at infinite dilution in the volatile liquid solvent (assumed to be independent of pressure in the interval $P - P_{vp1}$), P is the system pressure, T is the temperature, and R is the universal gas constant (Reid et al. 1987). For Eq. (2.23), one must assume that X_2 is much less than unity, such that the corresponding change of aqueous activity coefficient with change in mole fraction of gaseous solute can be neglected (Zawisza and Malesinska, 1981). The first term in the right hand side of Eq. (2.23) is always dominant, whereas the second term is the Poynting correction arising from the compression of the volatile liquid solvent (Reid et al. 1987).

Solving Eq. (2.23) for the mole fraction of the gaseous solute (X_2) yields the relationship used in the algorithm to determine the solubility of CO_2 in water:

$$X_2 = \exp\left(\ln f_2 - \ln H_{2,1}^{P_{vp1}} - \frac{\overline{V_2^{\infty}}\left(P - P_{vp1}\right)}{RT} \right) \qquad \text{(Eq. 2.24)}$$

The partial molar volume of a gaseous solute at infinite dilution in a volatile liquid solvent ($\overline{V_2^{\infty}}$) is a function of temperature. However, the work of Takenouchi and Kennedy (1964) suggests that it is nearly constant at approximately 3.0 x 10^{-5} m^3/mol below temperatures of approximately 200°C. This constant value was adopted for the current study. One potential limitation of Eq. (2.23) and Eq. (2.24) is associated with the use of actual molar volume, $\overline{V_2^{\infty}}$, which may lead to overestimates of solubility at higher pressure, and it may be appropriate to fit this parameter to match actual solubility data (Enick and Klara, 1990).

The EOS presented here does not calculate vapor pressure of water as a function of temperature. Rather, it is assumed that the flow code to which the EOS is applied will have such capability.

Several authors, including Malinin (1959), Ellis and Goulding (1963), Takenouchi and Kennedy (1964), and Gibb and Van Ness (1971), have published data regarding the solubility of CO_2 in water. Using a piece-wise quadratic fit to these data, O'Sullivan et al. (1985) defined the following temperature dependence of Henry's coefficient for CO_2 (subscript 2) in water (subscript 1):

$$\begin{aligned} H_{2,1}^{P_{vp1}} &= 6400 - 2077.78\tau^2 + 311.11\tau^4, \qquad \tau \geq 0 \\ H_{2,1}^{P_{vp1}} &= 6400 - 2149.14\tau^2 - 195.43\tau^4, \qquad \tau < 0 \end{aligned} \qquad \text{(Eq. 2.25)}$$

where, τ is $\frac{T-170}{100}$.

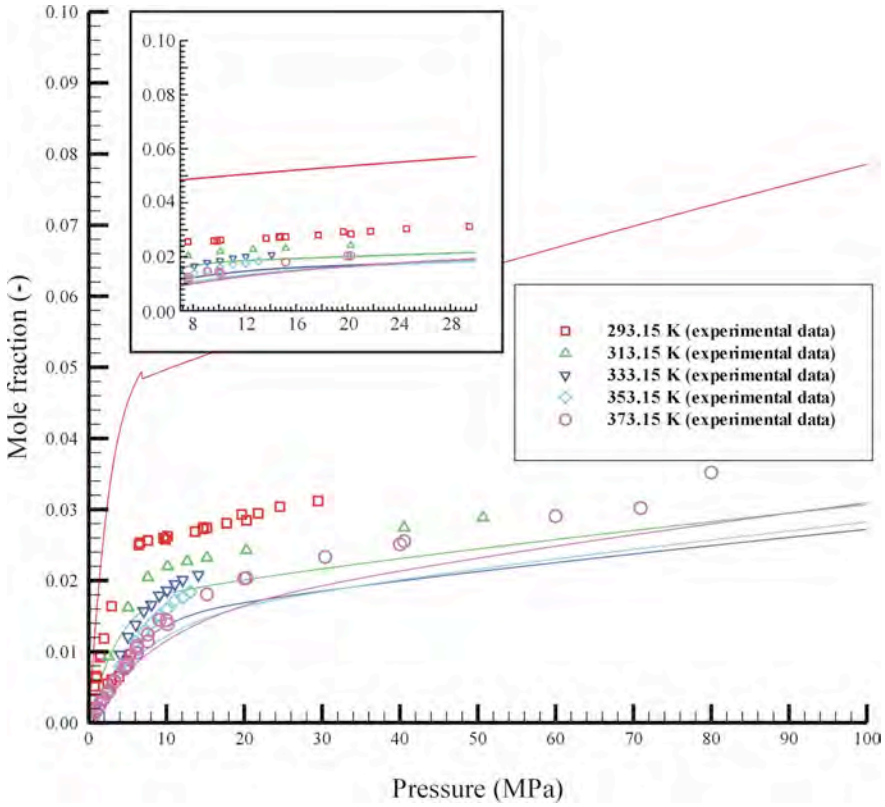

Figure 2.6. Solubility of CO_2 in water as a function of pressure along several representative isotherms, calculated using MRKEOS (sources of solubility data include: Sander, 1912; Kritschewsky et al. 1935; Zel'vinskii, 1937; Wiebe and Graddy 1939, 1940; Bartholome and Friz, 1956; Malinin and Kurovskaya, 1975; Zawisza and Malesinska, 1981; Muller et al. 1988; King et al. 1992; Teng et al. 1997; Bamberger et al. 2000).

Although these functions for Henry's coefficient are adapted from O'Sullivan et al. (1985), we elected not to use the fugacity formulation from that study. O'Sullivan et al. (1985) did not address fugacity corrections. In contrast, we defined fugacity(f_2) of CO_2 in Eq. (2.23) as $f_2 = \phi_2 P$ where ϕ_2 is the fugacity coefficient for CO_2 described in section 2.6.1.3., suggesting that solubilities predicted by

MRKEOS (Figure 2.6) would be less than those calculated using O'Sullivan et al.'s fugacity model.

We implemented a different solubility approach for SWEOS, developed by Diamond and Akinfiev (2003), based on experimental data. Henry's law for the reaction equilibrium between CO_2 and water can be written as

$$X_{CO_2}^{\text{model}} = \frac{f\, X_{CO_2}^{non} \gamma_{non}}{H_{2,1}^{(Pvp1)} \gamma_{CO_2}} \qquad \text{(Eq. 2.26)}$$

To calculate the mole fraction of CO_2 in aqueous phase using Eq. (2.26), γ_{CO_2} and γ_{non} are assumed equal to unity, $X_{CO_2}^{\text{non}}$ is the mole fraction of CO_2 in non-aqueous phase (Diamond and Akinfiev, 2003). The coefficients (b_i) of Eq. (2.27) are provided in Table 2.4.

Table 2.4. Coefficients (b_i, c_i) of corrected CO_2 solubility, adapted from Diamond and Akinfiev (2003); coefficients (d_i) of CO_2 density at saturation pressure, adapted from Anderson et al. (1992); coefficients (e_i) of specific enthalpy of CO_2, adapted from O'Sullivan et al. (1985).

I	0	1	2	3	4	5
b_i	0.1256×10^{-3}	-0.0212×10^{-3}	0.065×10^{-5}	1.121×10^{-5}		
c_i	3.63579×10^{-5}	-4.477820×10^{-6}	1.18833×10^{-4}	5.41469×10^{-5}	7.31010×10^{-3}	-7.49356×10^{-3}
d_i	3.736×10^{1}	-7.109×10^{-2}	-3.812×10^{-5}	3.296×10^{-6}	-3.702×10^{-9}	
e_i	-0.073696×10^{6}	0.56405×10^{6}	0.70363×10^{6}	-0.27882×10^{6}	0.042579×10^{6}	

$$\begin{aligned} X_{CO_2}^{non} &= 1 - \frac{P_{sat}}{P}, && \frac{P_{sat}}{P} > b_1 t + b_2 + b_3 tP + b_4 P \\ X_{CO_2}^{non} &= 1 - (b_1 t + b_2 + b_3 tP + b_4 P), && \frac{P_{sat}}{P} \le b_1 t + b_2 + b_3 tP + b_4 P \end{aligned} \qquad \text{(Eq. 2.27)}$$

Henry's coefficient ($H_{2,1}^{(Pvp1)}$) is calculated from the following equation of state (Akinfiev and Diamond, 2003):

$$H_{2,1}^{(Pvp1)} = \exp\left\{(1-\xi)\ln\frac{f_{H_2O}}{10^6} + \xi\ln\left(\frac{RT}{M_w^{H_2O}\times 10^6}\rho_{H_2O}\right) + 2\times 10^{-3}\rho_{H_2O}\left[c + d\left(\frac{1000}{T}\right)^{0.5}\right]\right\}$$

(Eq. 2.28)

where f_{H_2O} is the fugacity of water, ρ_{H_2O} is the density of water calculated from Hill (1990) (which can also be calculated by this algorithm) and ξ, c, and d are the empirical fitting parameters. After calculating mole fraction ($X_{CO_2}^{\text{model}}$) using Eq. (2.26), Diamond and Akinfiev (2003) reduced error relative to experimental data to less than 2% by applying an empirical correction function.

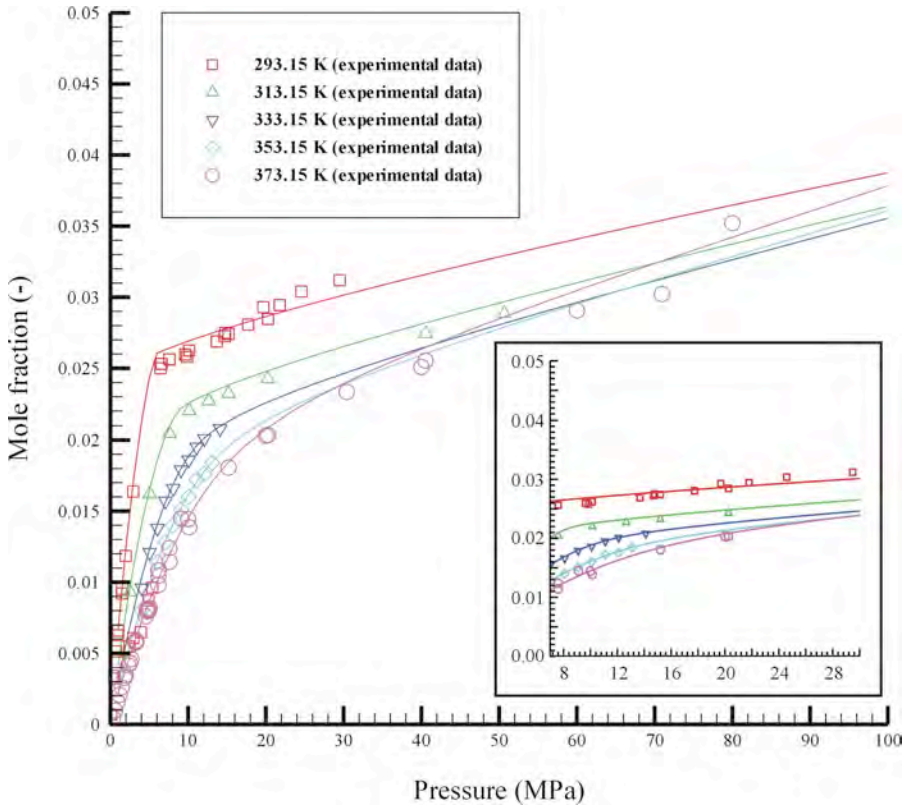

Figure 2.7. Solubility of CO_2 in water as a function of pressure along several representative isotherms, calculated using SWEOS (sources of solubility include: Sander, 1912; Kritschewsky et al. 1935; Zel'vinskii, 1937; Wiebe and Graddy 1939, 1940; Bartholome and Friz, 1956; Malinin and Kurovskaya, 1975; Zawisza and Malesinska, 1981; Muller et al. 1988; King et al. 1992; Teng et al. 1997; Bamberger et al. 2000).

The coefficients (c_i) of Eq. (2.28) are provided in Table 2.4.

$$r^* = c_0 + c_1 t + c_2 t X_{co_2}^{\text{model}} + c_3 t (X_{co_2}^{\text{model}})^2 + c_4 X_{co_2}^{\text{model}} + c_5 (X_{co_2}^{\text{model}})^2 \qquad \text{(Eq. 2.29)}$$

$$X_{CO_2} = X_{co_2}^{\text{model}} (1 + r^*) \qquad \text{(Eq. 2.30)}$$

Therefore, the final corrected mole fraction of CO_2 (X_{CO_2}) can be calculated as above in Eq. (2.30).

A plot of the solubility of CO_2 using SWEOS in water as a function of pressure along several isotherms, calculated as outlined above, is provided in Figure 2.7.

2.6.2.2. Specific Density

As indicated previously, dissolution of CO_2 in water increases the density of water. Based on empirical data and theoretical considerations, Andersen et al. (1992) suggest that the density of aqueous mixtures of CO_2 and water (ρ_{mix}) can be approximated using

$$\rho_{mix} = \frac{\rho_{H_2O}\, \rho_{CO_2}^{sat}}{\left(1 - X_{CO_2}\right)\rho_{CO_2}^{sat} + X_{CO_2}\rho_{H_2O}} \qquad \text{(Eq. 2.31)}$$

Where ρ_{H_2O} is the density of water, $\rho_{CO_2}^{sat}$ is the density of CO_2 at saturation pressure, and X_{CO_2} is the dissolved mole fraction of CO_2. The density of CO_2 at saturation pressure is determined by the following relationship (Andersen et al. 1992). The coefficients (d_i) of Eq. (2.32) are provided in Table 2.4.

$$\rho_{CO_2}^{sat} = \left(\frac{1}{\sum_{i=0}^{4} d_i T^i} \right) 10^6 M_w \qquad \text{(Eq. 2.32)}$$

A comparison of the specific density of aqueous mixtures of water and CO_2 to that of water as a function of pressure along several representative isotherms is provided in Figure 2.8.

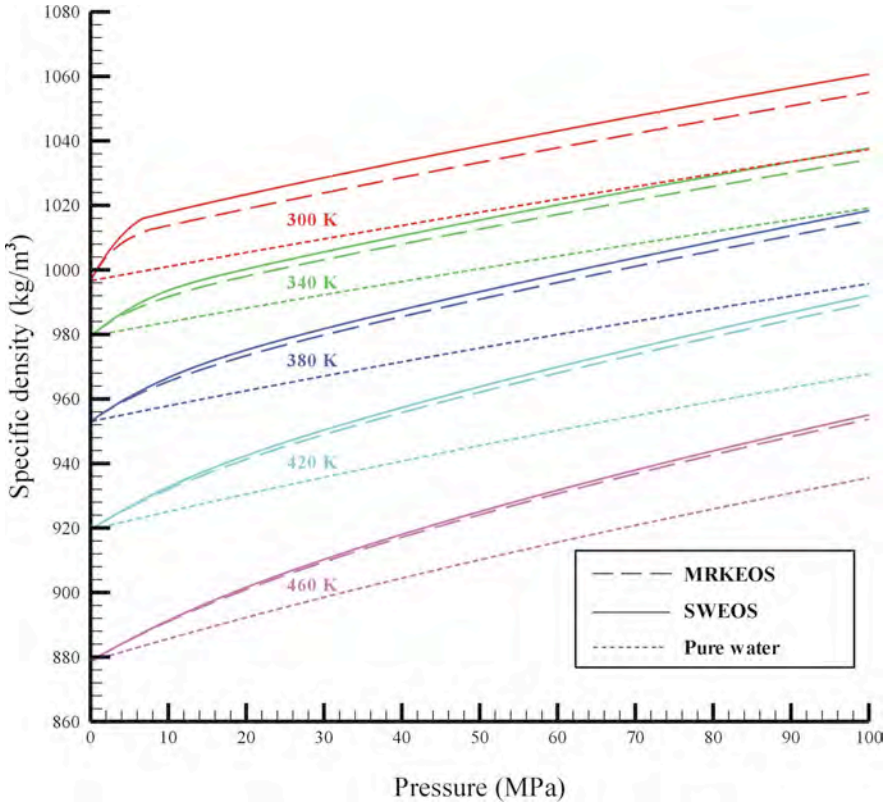

Figure 2.8. Specific density of aqueous mixtures of CO_2 as a function of pressure along several representative isotherms. Density of water calculated using formulation developed by the International Formulation Committee (1967).

2.6.2.3. Specific Enthalpy

Weir et al. (1996) indicate that the specific enthalpy of water and the specific enthalpy of CO_2, plus a specific enthalpy of solution for CO_2, can be used to

determine the specific enthalpy of aqueous mixtures of CO_2 and water with the following relationship:

$$H_{mix} = \left(1 - X_{CO_2}\right)H_{H_2O} + X_{CO_2}\left(H_{sol} + H_{CO_2}\right) \qquad \text{(Eq. 2.33)}$$

Where X_{CO_2} is the dissolved mass fraction of CO_2, H_{sol} is the specific enthalpy of solution for CO_2, and H_{H_2O} and H_{CO_2} are the specific enthalpies of water and CO_2 at the prevailing pressure and temperature, respectively.

O'Sullivan et al. (1985) provide the following relationship for the specific enthalpy of solution for CO_2 (H_{sol}):

$$H_{sol} = \sum_{i=o}^{4} e_i \left(\frac{T}{100}\right)^i \qquad \text{(Eq. 2.34)}$$

2.6.2.4. Dynamic Viscosity

The EOS presented here does not calculate the dynamic viscosity of water; rather, it is assumed that the flow code to which it will be applied includes appropriate formulations.

2.7. Summary and Conclusion

In the MRKEOS, calculations of density, enthalpy, and fugacity are based on a modified Redlich-Kwong (MRK) EOS (Kerrick and Jacobs, 1981; Weir et al. 1996; Cole, 2000). Calculations of SWEOS are based on Span and Wagner EOS (Span and Wagner, 1996). The previous work related to this topic was performed by Weir et al. (1996) who adapted MRKEOS to simulate CO_2 injection into the thick fresh water reservoir.

As shown in previous sections, the MRKEOS results are not entirely consistent with IUPAC results. This discrepancy occurs due to the treatment of the attractive term (Eq. (2.8)) and covolume (b: 5.8×10^{-5}). In particular, values for the fugacity coefficient of CO_2 predicted from Eq. (2.12) appear to be systematically lower than those generated by IUPAC and Span and Wagner (Figure 2.3). Kerrick and Jacobs (1981) showed that treating the attractive term as a function of both pressure and temperature, as done in this study, leads to lower predicted fugacity coefficients than if the attractive term is treated independent of pressure. In addition to the treatment of the attractive term, covolume (b) should vary with pressure and temperature instead of remaining constant. With increasing pressure and temperature the covolume should decrease due to molecules becoming "softer" (Vera and Prausnitz, 1972). Because of those two parameters, the discrepancy is propagated to other thermodynamic properties. For example, the equation for the compressibility factor (Z) has a covolume term in Eq. (2.10). Later, this compressibility factor (Z) is included in the equation of enthalpy in Eq. (2.14). Therefore, values for the enthalpy of CO_2 appear to be lower than those generated by IUPAC and Span and Wagner (Figure 2.4). However, the modified Redlich-Kwong (MRK) EOS is practically more flexible and easy to code such that many researchers still actively use their work. In relation to geologic sequestration, Spycher et al (2003) developed their own version of the MRKEOS to predict the fugacity coefficient and solubility of CO_2 in water, accurate to 2% with respect to experimental data for 12 to 100°C and up to 60 MPa.

The thermodynamic properties from Span and Wagner (1996), which are accurate to within 0.05% over the P-T range of our research interest, including the

near-critical region, are almost identical to IUPAC data sets. Therefore, SWEOS is recommended for routine research instead of MRKEOS. On the other hand, SWEOS is much more cpu-intensive because of its root-finding approach used for determining density as a function of pressure. The upshot is that MRKEOS is computationally faster but less accurate, while SWEOS is more accurate but computationally slower. Figures 2.3, 2.4, 2.6 and 2.7 demonstrate how SWEOS provides more accurate estimates of some parameters, at least with respect to experimental data. For the quantitative analysis of computational intensity, computational analysis was performed using the provided Matlab scripts (Appendix V and VI). Both Matlab scripts calculate CO_2 thermophysical properties. We chose a pressure increment of 0.1 and 1 MPa, with pressure ranging from 0 to 100 MPa at fixed temperature condition. For this simple case, our calculation comparison illustrated that MRKEOS is about 98 times faster than SWEOS for a range of applications. However, our implementation of SWEOS is not necessarily as efficient as it could be. For example, SWEOS could be revised further to compute common subexpressions only once. Additionally, other workers pre-evaluate state-properties from a given EOS on a P-T grid and then interpolate as necessary during a simulation, which would most likely improve speed.

Finally, in both EOS algorithms, the relationships for aqueous solubility of CO_2 are derived for water only. However, most reservoirs below depths of a few hundred meters are saline to some extent. Increasing salinity of water decreases the solubility of CO_2. For example, the solubility of CO_2 in water containing 3% salinity

is approximately 85% of the solubility of CO_2 in pure water (Enick and Klara, 1990). Modification of EOSs for brine conditions are investigated in Chapter 3.

References

Akinfiev, N.N., Diamond, L.W., 2003. Thermodynamic description of aqueous nonelectrolytes at infinite dilution over a wide range of state parameters. Geochimica et Cosmochimica Acta 67(4), 613-629.

Andersen, G., Probst, A. Murray, L., Butler, S., 1992. An accurate PVT model for geothermal fluids as represented by H_2O-CO_2-NaCl mixtures. Proceedings of the 17th Workshop on Geothermal Reservoir Engineering, Stanford, California, 17:239–248.

Angus, S., Armstrong, B., de Reuck, K.M., 1976. International Thermodynamic Tables of the Fluid State: Carbon Dioxide, 1st edn., Pergamon Press, 385 pp.

Bamberger, A., Sider, G., Maurer, G., 2000. High-pressure (vapor+liquid) equilibrium in binary mixtures of (carbon dioxide+water or acetic acid) at temperatures from 313 to 353. Journal of Supercritical Fluids 17, 97-100.

Bartholomé, E., Friz, H., 1956. Löslichkeit von Kohlendioxyd in Wasser bei höheren Drucken (Solubility of carbon-dioxide in water at high pressures). Chemie Ingenieur Technik 28, 706-708.

Carnahan, N.F., Starling, K.E., 1972. Intermolecular repulsions and the equation of state for fluids. American Institute of Chemical Engineering Journal 18, 1184-1189.

Cole, B.S., 2000. Sequestration of supercritical carbon dioxide in deep sedimentary basin aquifers: A numerical model. Master's Thesis, New Mexico Institute of Mining and Technology, 124 pp.

de Santis, R., Breedveld, G.J.F., Prausnitz, J.M., 1974. Thermodynamic properties and aqueous gas mixtures at advanced pressures. Industrial and Engineering Chemistry Process Design and Development 13, 374–377.

Diamond, L.W., Akinfiev, N.N., 2003. Solubility of CO_2 in water from -1.5 to 100°C and from 0.1 to 100MPa: evaluation of literature data and thermodynamic modeling. Fluid Phase Equilibria 208, 265-290.

Ellis, A.J., Goulding, R.M., 1963. The solubility of carbon dioxide above 100°C in water and in sodium chloride solutions. American Journal of Science 261, 47–60.

Enick, R.M., Klara, S.M., 1990. CO_2 solubility in water and brine under reservoir conditions. Chemical Engineering Communications 90, 23–33.

Fenghour, A., Wakeham, W.A., Vesovic, V., 1998. The viscosity of carbon dioxide. Journal of Physical and Chemical Reference Data 27(1), 31–44.

Fuller, G.G., 1976. A modified Redlich-Kwong-Soave equation of state capable of representing the liquid state. Industrial and Engineering Chemistry Fundamentals 15, 254–257.

Gibb, R.E., Van Ness, H.S., 1971. Solubility of gases in liquids in relation to the partial molar volumes of the solute-carbon dioxide-water. Industrial and Engineering Chemistry Fundamentals 10(2), 312–315.

Hederer, H., Peter, S., Wenzel, H., 1976. Calculation of thermodynamic properties from a modified Redlich-Kwong equation of state. Chemical Engineering Journal 11, 183–190.

Hill, P.G., 1990. A unified fundamental equation for the thermodynamic properties of H_2O. Journal of Physical and Chemical Reference Data 19(5), 1233-1274.

International Formulation Committee, 1967. A Formulation of the Thermodynamic Properties of Ordinary Water Substance. IFC Secretariat, Düsseldorf, Germany, 27 pp.

Jacobs, G.K., Kerrick, D.M., 1981. APL and FORTRAN programs for a new equation of state for H_2O, CO_2, and their mixtures at supercritical conditions. Computers and Geosciences 7, 131-143.

Kerrick, D.M., Jacobs, G.K., 1981. A modified Redlich–Kwong equation for H_2O, CO_2, and H_2O-CO_2 mixtures. American Journal of Science 281, 735–767.

King, M.B., Mubarak, A., Kim, J.D., Bott, T.R., 1992. The mutual solubilities of water with supercritical and liquid carbon-dioxide. Journal of Supercritical Fluids 5, 296-302.

Kritschewsky, I.R., Schaworonkoff, N.M., Aepelbaum, V.A., 1935. Gemeinsame Löslichkeit der Gase in Flüssigkeiten unter Druck. 1. Löslichkeit des Kohlendioxyds in Wasser aus seinen Gemischen mit Wasserstoff bei 20 und 30° C und Gesamtdruck bis 30 kg/cm^2 (Mutual solubility of gases in liquids under pressure. 1. Solubility of carbon-dioxide in water from its mixtures with hydrogen at 20 and 30° C and total pressure to 30 kg/cm^2). Zeitschrift für Physikalische Chemie, A 175, 232-238.

Malinin, S.D., 1959. The system water-carbon dioxide at high temperatures and pressures. Geokhimiya 10, 1523–1549.

Malinin, S.D., Kurovskaya, N.A., 1975. Solubility of CO_2 in chlorides solutions at elevated temperatures and CO_2 pressures. Geochemistry International 12, 199-201.

Muller, G., Bender, E., Maurer, G. 1988. Vapor-liquid-equilibrium in the ternary-system ammonia-carbon dioxide-water at high water contents in the range 373 K to 473 K. Berichte der Bunsen-Gesellschaft-Physical Chemistry Chemical Physics 92, 148-160.

O'Sullivan, M.J., Bodvarsson, G.S., Pruess, K., Blakeley, M.R., 1985. Fluid and heat flow in gas-rich geothermal reservoirs. Society of Petroleum Engineers Journal 25, 215–225.

Parker, J.C., Lenhard R.J., Kuppusamy T., 1987. A parametric model for constitutive properties governing multiphase flow in porous media. Water Resources Research 23(4), 618-624.

Patel, M.R., Eubank, P.T., 1988. Experimental densities and derived thermodynamic properties for carbon dioxide-water mixtures. Journal of Chemical and Engineering Data 33, 185–193.

Peng, D., Robinson, D.B., 1976. A new two-constant equation of state. Industrial and Engineering Chemistry Fundamentals 15, 59–64.

Prausnitz, J.M., 1969. Molecular Thermodynamics of Fluid-Phase Equilibria. Prentice-Hall, Inc., Englewood Cliffs, New Jersey, 523 pp.

Pruess, K., 1991. TOUGH2-A general purpose numerical simulator for multiphase fluid and heat flow. Report LBNL - 29400, Lawrence Berkeley National Laboratory, Berkeley, CA.

Pruess, K., 2004. Numerical simulation of CO_2 leakage from a geologic disposal reservoir, including transitions from super- to subcritical conditions, and boiling of liquid CO_2. Society of Petroleum Engineers Journal 86098.

Pruess, K., Garcia, J., 2002. Multiphase flow dynamics during CO_2 disposal into saline aquifers. Environmental Geology 42, 282-295.

Redlich, O., Kwong, J.N.S., 1949. An equation of state. Fugacities of gaseous solutions. Chemical Reviews 44, 233–244.

Reid, R.C., Prausnitz, J.M., Poling, B.E., 1987. The Properties of Gases and Liquids. 4th edn. McGraw-Hill, Inc., New York, 741 pp.

Sander, W., 1912. The solubility of carbon dioxide in water and some other solvents under high pressures. Zeitschrift für Physikalische Chemie, Stoechiom. Verwandtschaftsl. 78, 513-549.

Soave, G., 1972. Equilibrium constants from a modified Redlich-Kwong equation of state. Chemical Engineering Science 27, 1197–1203.

Span, R., Wagner,W., 1996. A new equation of state for carbon dioxide covering the fluid region from the triple-point temperature to 1100 K at pressures up to 800 Mpa. Journal of Physical and Chemical Reference Data 25(6), 1509-1596.

Spycher, N., Pruess, K., Ennis-King, J., 2003. CO_2-H_2O mixtures in the geological sequestration of CO_2. I. Assessment and calculation of mutual solubilities from 12 to 100°C and up to 600 bar. Geochimica et Cosmochimica Acta 67 (16), 3015-3031

Takenouchi, G., Kennedy, G.C., 1964. The binary system H_2O-CO_2 at high temperatures and pressures. American Journal of Science 272, 1055–1074.

Talman, S.J., Adams, J.J., Chalaturnyk, R.J., 2004. Adapting TOUGH2 for general equations of state with application to geological storage of CO_2. Computers and Geosciences 30, 543-552.

Teng, H., Yamasaki, A., Chun, M.K., Lee, H., 1997. Solubility of liquid CO_2 in water at temperatures from 278 K to 293 K and pressures from 6.44 MPa to 29.49 MPa and densities of the corresponding aqueous solutions. Journal of Chemical Thermodynamics 29, 1301-1310.

Van der Waals, J.D. 1873. De continuiteit van den gas en vloeistoftoestand. Ph. D. dissertation, University Leiden, pp. 134.

Vera, J.H., Prausnitz, J.M., 1972. Generalized van der Waals theory for dense fluid. Chemical Engineering Journal 3, 1-13

Vesovic, V., Wakeham, W.A., Olchowy, G.A., Sengers, J.V., Watson, J.T.R., Millat, J., 1990. The transport properties of carbon dioxide. Journal of Physical and Chemical Reference Data 19(3), 763–808.

Weir, G.J., White, S.P., Kissling, W.M., 1996. Reservoir storage and containment of greenhouse gases. Transport in Porous Media 23, 37–60.

Wiebe, R., Graddy, V.L., 1939. The solubility in water of carbon dioxide at 50, 75, and 100°C, at pressures to 700 atmospheres. Journal of the American Chemical Society 61, 315-318.

Wiebe, R., Graddy, V.L., 1940. The solubility of carbon dioxide in water at various temperatures from 12 to 40°C and at pressures to 500 atmospheres: Critical phenomena. Journal of the American Chemical Society 62, 815-817.

Wu, Y.-S., Forsyth, P.A., 2001. On the selection of primary variables in numerical formulation for modeling multiphase flow in porous media. Journal of Contaminant Hydrology 48, 277-304.

Zawisza, A., Malesinska, B., 1981. Solubility of carbon-dioxide in liquid water and of water in gaseous carbon-dioxide in the range 0.2–5MPa and at temperatures up to 473 K. Journal of Chemical and Engineering Data 26, 388-391.

Zel'vinskii, Y. D., 1937. On the solubility of carbon dioxide in water under pressure. Zhurn. Khim. Prom. (in Russian) 14(17-18), 1250-1257.

CHAPTER 3

COMPARISON OF TWO DIFFERENT EQUATIONS OF STATE FOR APPLICATION OF CARBON DIOXIDE SEQUESTRATION

3.1. Introduction

Concerns about the increasing concentration of carbon dioxide (CO_2) in the atmosphere have led to the suggestion of large-scale storage of anthropogenic CO_2 into the subsurface, including oil and gas reservoirs, deep saline aquifers, and coal beds (Bachu, 2000; Orr, 2004). Carbon dioxide may be sequestered in geologic formations by several different mechanisms (Hitchon, 1996). One option is to store it as a separate phase (gas or supercritical phase) under a low-permeability caprock, a process commonly called hydrostratigraphic (mobile) trapping. Another option is to store CO_2 as a dissolved phase in saline groundwater, typically called solubility trapping. This mechanism may increase the acidity of groundwater and dissolve minerals composing the host rock and caprock matrix. Another mechanism is called mineral trapping, which refers to the precipitation of CO_2 by divalent cations in the reservoir brine to form secondary carbonate minerals. The other mechanism is residual gas trapping, which refers to capillary forces (surface tension) that render CO_2 immobile in the reservoir pore space.

Numerical codes that simulate flow and transport of sequestered CO_2 and the concomitant chemical reactions are essential tools for studying CO_2 sequestration and for designing CO_2 disposal operations. Diverse numerical codes include TOUGH2 (Pruess et al. 1999), TOUGHREACT (Xu et al. 2004), PHREEQC (Parkhurst and Appelo, 1999), NUFT (Nitao, 1998), CHRUNCH (Steefel, 2001), chemTOUGH (White, 1995), and GEM-GHG (Nghiem et al. 2004). These codes have been applied in recent studies of CO_2 sequestration (Johnson, 2001; Pruess and Garcia, 2002; Doughty and Pruess, 2004; Nghiem et al. 2004; Gaus et al. 2005; Knauss et al. 2005; White et al. 2005). Additionally, various simulation packages have been evaluated on their capability related to CO_2 sequestration processes (Pruess et al. 2004).

Our study does not focus on comparing overall simulation packages like Pruess et al. (2004), but rather focuses on the implication of employing different EOS algorithms. Generally, numerical codes for CO_2 sequestration include EOS algorithms representing thermophysical properties of gas, liquid, and supercritical phases of H_2O, CO_2, CO_2/H_2O, and $CO_2/NaCl/H_2O$. The decision regarding which EOS algorithms to use is often based on the balance between the accuracy of calculation and computational time. For example, certain numerical codes utilize lookup tables of thermophysical properties rather than explicit formulations, because calculating such properties in real time may be computationally expensive. On the other hand, some direct-calculation EOS algorithms provide similar computational speed like lookup tables, but by employing less accurate formulations. Our literature review suggests that previous studies have not examined how differing individual EOS algorithms might impact simulation results.

This chapter includes four main parts: (1) assembly of different EOS algorithms, (2) a general comparison of EOS algorithms, (3) a sensitivity analysis of seal integrity, (4) an application to a brine system, and (5) an effect of relative permeability.

The EOS assembly section describes individual EOS algorithms and how individual EOS formulations are interrelated. In the general comparison section, the differences in predicted state properties by two EOS algorithms are investigated through one-dimensional simulations. The primary purpose of these simulations was not only to compare the thermophysical properties calculated from each EOS, but rather to discover how any differences in these predicted properties can propagate into contrasts in the flow and transport simulation. In the section about seal integrity, sensitivity analyses were conducted using parameters including as the mass of injected CO_2, permeability, and porosity. Finally, in the section about the application of EOS into brine system, we conducted sensitivity analyses to investigate how brine density, viscosity, and CO_2 solubility may affect the transport of separate CO_2 at various concentrations.

3.2. Assembly of EOS Algorithms

We assembled two integrated EOS algorithms in Figure 2.1. The integrated MRKEOS is based on a Modified Redlich-Kwong algorithm, which employs modification of the attractive term from the van der Waals equation (Kerrick and Jacobs, 1981; Weir *et al.* 1996; Cole, 2000). The integrated SWEOS was based on Span and Wager algorithms (Span and Wagner, 1996), which is an empirical

representation where equations for properties are written based on the fundamental equation of Helmholtz energy. Both integrated EOS algorithms were assembled for calculating thermophysical properties including density, fugacity, enthalpy, viscosity, solubility of CO_2 in gaseous and supercritical phases, and mixtures or solutions of CO_2 in water as functions of pressure and temperature in Figure 2.1. Both codes use the same formulations for relative permeability and capillary pressure without considering hysteresis effects (Parker et al. 1987; Cole, 2000). Cole (2000) calibrated relative permeability curves with experimental data from (Holt et al. 1995) for supercritical CO_2 in a 1.2 m core of Bentheimer sandstone measured at 335.15 K and 20 MPa. In these curves, residual saturation of supercritical CO_2 was 0.1. A capillary function was adapted after changing the interfacial tension between supercritical CO_2 and water. A detailed mathematical representation is not provided here. Rather, we refer the readers to (Parker et al. 1987; Cole, 2000).

The thermophysical properties of pure H_2O were adapted from IFC data (International Formulation Committee, 1967). In addition, both integrated EOS algorithms were designed for the TOUGH2 simulator, which included coupled flow of heat and groundwater (Pruess, 1999).

Our research concerns specific ranges of pressure and temperature, approximately 10 to 40 MPa and 303.15 to 343.15 K, because these conditions are generally applicable to geologic CO_2 sequestration. The thermodynamic properties (density, fugacity coefficient, and enthalpy) predicted from Span and Wagner, (1996) in the integrated SWEOS, accurate within 0.05% over the pressure and temperature range of interest including the near-critical region, are almost identical to IUPAC data

sets (Figure 2.2, 2.3, and 2.4). Moreover, Span and Wagner, (1996) in the integrated SWEOS are available in wider ranges (P: 0.1 MPa-800 MPa, T: 273.15 K and 800 K) compared to Kerrick and Jacobs, (1981), Weir et al. (1996), and Cole, (2000) in the integrated MRKEOS (P: 1 MPa-100 MPa and T: 288.15 K-623.15 K). However, the modeling accuracy and ranges of both integrated EOS algorithms are actually determined by the solubility EOS algorithm because the predictable accuracy and ranges by the solubility EOS algorithm are normally less than density, fugacity coefficient, and enthalpy EOS algorithms. Because the solubility EOS algorithm was adapted from Reid et al. (1987) within the integrated MRKEOS and from Diamond and Akinfiev, (2003) within the integrated SWEOS (Figure 2.1), the modeling accuracy and ranges depend on the chosen solubility EOS algorithms. Therefore, the actual accuracy of the integrated SWEOS is less than 2% with range 0.1 MPa–100 MPa and 273.15 K–373.15 K and that of the integrated MRKEOS over 5% with range 1 MPa–45 MPa and 288.15 K–373.15 K. The discrepancy of predicted solubility values with experimental data are also provided in Figure 2.6 and 2.7.

With the accuracy and available range of the integrated EOS algorithms, the required computational time is also an important factor. Although the integrated SWEOS can predict experimental data with more accuracy, it is more computationally expensive because of the high degree of its polynomial equations and its requirement to switch the primary variables from density and temperature to pressure and temperature. On the other hand, MRKEOS is relatively easier to code and requires much less computation time and hence is used by many researchers.

Quantitative analysis of computation time indicates that MRKEOS is about 98 times faster than SWEOS for a range of applications (see Section 2.7).

3.2.1. Interrelationship of Thermophysical Properties within Integrated EOS Algorithms

Figure 3.1 shows the interrelationship of the individual thermophysical properties within both integrated MRKEOS and SWEOS. In general, pressure and temperature are not ideal primary variables because they make the calculation of thermodynamic conditions difficult near the critical point (Ingebritsen and Sanford, 1998). Consequently, most EOS algorithms do not adapt pressure and temperature as primary variables at the same time. For example, Span and Wagner, (1996) in the integrated SWEOS adapted density and temperature as primary variables, while Kerrick and Jacobs, (1981), Weir et al. (1996), and Cole, (2000) in the integrated MRKEOS adapted molal volume and temperature. Although pressure and temperature are not ideal as primary variables, it is preferable to employ them as such in deep reservoir simulation because density varies nonlinearly with depth. Thus, many simulators, including the TOUGH2 we applied in this study, use pressure and temperature as primary variables. We, therefore, switched the primary variables, density and temperature, to pressure and temperature while solving Span and Wagner, (1996) in the integrated SWEOS and the primary variables, molal volume and temperature, to pressure and temperature while solving Kerrick and Jacobs, (1981), Weir et al. (1996), and Cole, (2000) in integrated MRKEOS (Figure 3.1).

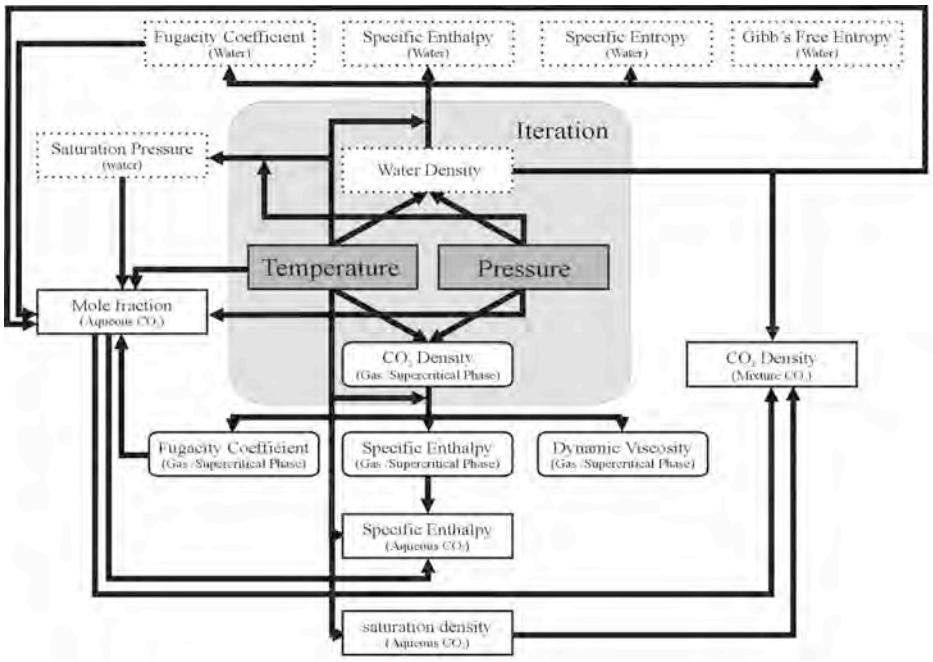

(a) SWEOS

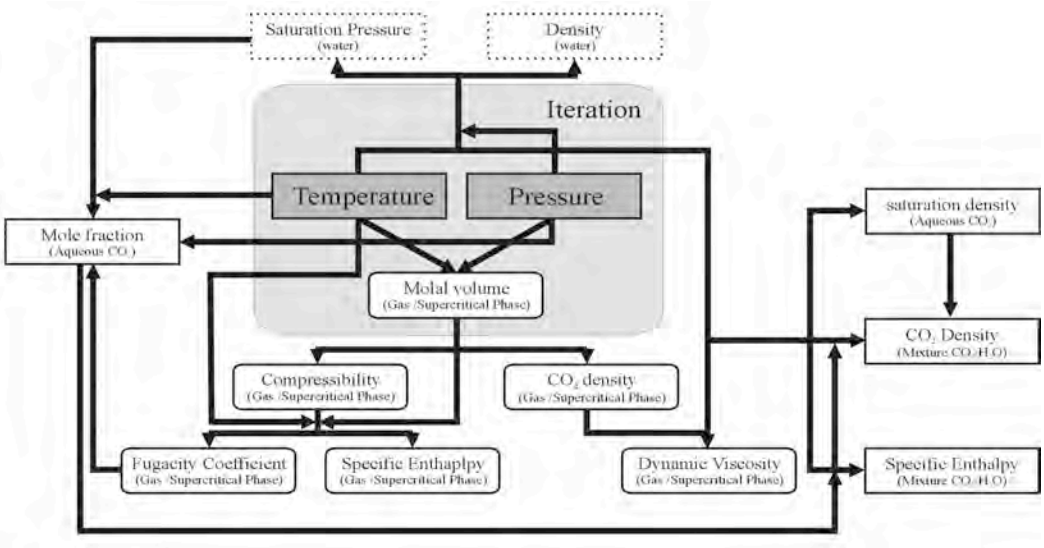

(b) MRKEOS

Figure 3.1. The schematic representation of MRKEOS and SWEOS algorithms. The boxes with dot line, solid line and curvature, respectively, express the thermodynamic properties of water, mixture (CO_2/H_2O), and separate-phase CO_2. The arrows indicate the direction of the input parameters for the subsequent calculation of thermophysical properties. The box with gray color shows the location where the primary variables are switched.

Figures 3.1a and 3.1b describe schematically the interrelation among thermophysical properties, showing how these are closely interrelated within the integrated EOS algorithms. For example, in Figure 3.1a (SWEOS), the calculation of CO_2 density, which requires pressure and temperature as independent variables, is represented by the arrows from the pressure and temperature boxes that converge into the CO_2 density (gas/supercritical phase) box. In another example (Figure 3.1a), the calculation of mole fraction requires pressure, temperature, saturation pressure of water, fugacity coefficient of CO_2, fugacity coefficient of water, and water density as independent variables. These variables are represented by arrows from the corresponding boxes that converge into the mole fraction (aqueous CO_2) box. These examples demonstrate how individual thermophysical properties are closely interrelated within EOS algorithms.

The specific density, fugacity coefficient, and specific enthalpy from both MRKEOS and SWEOS are compared with the experimental data (Figures 2.2, 2.3, and 2.4). Although values of specific density from both MRKEOS and SWEOS show a close agreement with experimental data, values of the fugacity coefficient and specific enthalpy from MRKEOS appear to be systematically lower than those from both IUPAC and SWEOS. This discrepancy between MRKEOS and IUPAC occurs because of the treatment of the attractive term and covolume (see Section 2.7).

Solving for the mole fraction of a gaseous solute generally requires Henry's relation, which depends on the fugacity coefficient. Because of the lower prediction of fugacity coefficients, the mole fraction from MRKEOS does not provide a good fit with solubility data (Figure 2.6).

As described earlier, it should be emphasized that all thermophysical properties are interrelated within the integrated EOS algorithms (Figure 3.1). The errors generated by the discrepancy of the fugacity coefficient from MRKEOS clearly affect the mole fraction calculation. The calculation of both mixture density and mixture enthalpy requires mole fraction as an input parameter (Figure 3.1). The discrepancy is depicted in the mixture density plots (Figure 2.8). The discrepancy of mixture densities originates from the low prediction of fugacity coefficients, which also skews the mole fraction.

Finally, Figure 2.6 illustrates that MRKEOS overestimates the solubility values below 303.15 K (30°C) and underestimates those over 303.15 K (30°C) in pressure range from 7 to 30 MPa. The adequate condition for storing CO_2 as a separate phase must be above the critical temperature (about 304.15 K (31°C)) and pressure (about 7.38 MPa). Thus, when the adequate conditions are met, MRKEOS will underestimate the solubility.

3.2.2. Comparison of CO_2 Migration Patterns using MRKEOS and SWEOS

In this section, we compare the MRKEOS and SWEOS algorithms by examining the effects of the buoyancy-driven distance of separate-phase CO_2 and the gravity-driven distance of aqueous-phase CO_2. In addition, the discrepancy of the dissolution rates of separate-phase CO_2 from MRKEOS and SWEOS is analyzed.

In order to compare quantitatively both EOS algorithms, a one-dimensional vertical model was designed (Figure 3.2). This model has two sedimentary units, each of 100 m thickness. Top and bottom units respectively represent caprock and

storage formations. A detailed description of model parameters is provided in Table 3.1. The model was run without any CO_2 injection to obtain a steady-state solution and the solution was used as the initial condition for CO_2 injection simulation.

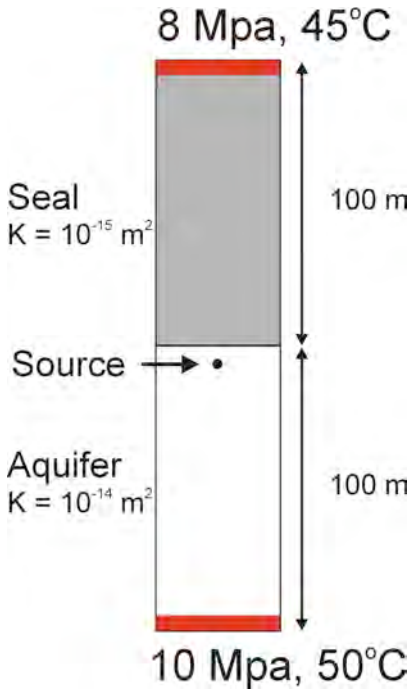

Figure 3.2. The conceptual model developed to describe the migration of both separate- CO_2 and aqueous-phase CO_2.

Table 3.1. Model parameters for describing the migration of both separate- and aqueous-phase CO_2 in Figure 3.2.

Total number of elements	400
Size of each element	Δx=0.5m, Δy=100m, Δz=100m
Initial Pressure condition	estimated from $P = \rho gh$
Initial Temperature condition	estimated from $T = 25 + 0.025 \times h$
Boundary conditions (top and bottom)	constant pressure
Porosity	0.2 (in the entire model)
Permeability:	Seal: 10^{-15} m^2, storage formation: 10^{-14} m^2
Source location	900.25 m
Amount of injected CO_2:	2160 tons of CO_2 over 50 days.

Figures 3.3a and 3.3b are the plots of CO_2 migration curves that represent both separate-phase CO_2 and aqueous-phase CO_2 at several sequential times. In Figure 3.3a, the saturation of separate-phase CO_2 has the highest peak at 1 year (◆) while separate-phase CO_2 penetrates 2 m through the low permeability caprock. The caprock definitively impedes the vertical movement of separate-phase CO_2 at 1 year. However, separate-phase CO_2 gradually penetrates the caprock over time because of the effect of injection pressure and the buoyancy-driven force. The vertical migration of separate-phase CO_2 continues until its saturation ratio becomes below residual CO_2 saturation (0.1).

Another distinct feature of these CO_2 migration curves is that the plume size of separate-phase CO_2 predicted from SWEOS is always smaller than that from MRKEOS (Figure 3.3a). At 1 year (◆), both plumes are almost identical. However, the size discrepancies of these plumes increase with time. This occurs because SWEOS and MRKEOS calculate different values of mass fraction from solubility EOS algorithms. As discussed earlier, mass fraction calculated from SWEOS is always greater than that calculated by MRKEOS for temperatures over 303.15K (30°C) (Figures 2.6 and 2.7). Since the temperature near the injection location is approximately 320.65K (47.5°C) in this model (Figure 3.2), SWEOS will convert more mass of separate-phase CO_2 into aqueous-phase CO_2. Consequently, the size of the separate-phase CO_2 plume from SWEOS always becomes smaller than that from MRKEOS.

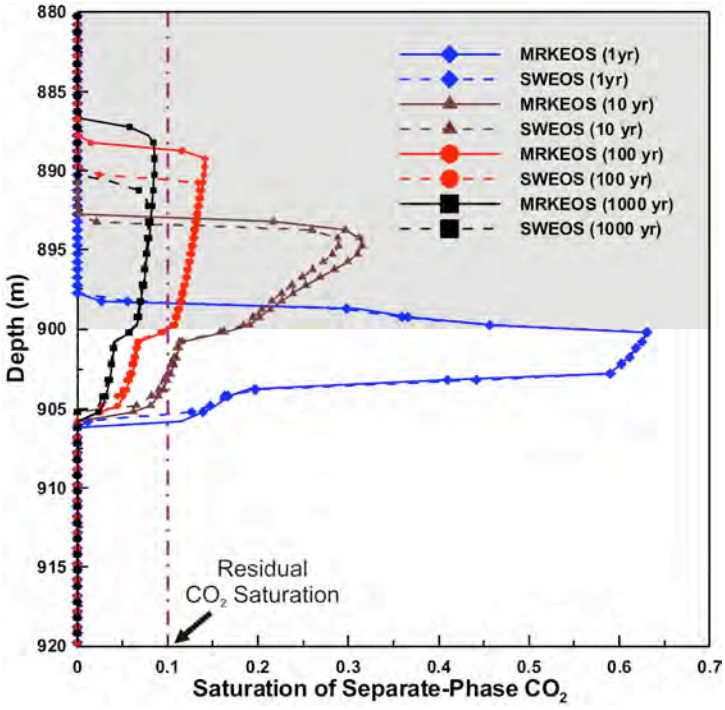

(a)

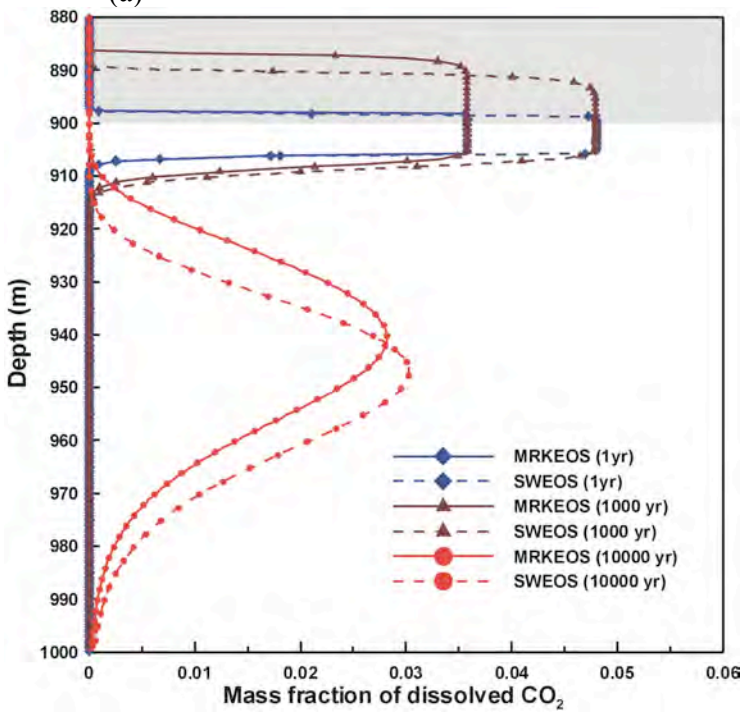

(b)

Figure 3.3. Plots of CO_2 migration from both MRKEOS and SWEOS at 1 yr, 10 yr, 100 yr, and 1000 yr. The gray color zones within both plots represent a seal with low permeability (10^{-15} m^2): (a) saturation of separate-phase CO_2, (b) mass fraction of aqueous-phase CO_2.

We suggest three interesting features in the CO_2 migration curves of aqueous-phase CO_2 (Figure 3.3b). First, it is obvious that the mass fractions of aqueous-phase CO_2 from SWEOS are greater than MRKEOS. For example, the highest peak of mass fraction from MRKEOS and SWEOS are 0.036 and 0.050 at both 1 and 1000 years, respectively.

Second, the rate of gravitational segregation from SWEOS is greater than MRKEOS. Gravitational segregation occurs because the density of water including aqueous-phase CO_2 is greater than that of pure water. The density of water including aqueous-phase CO_2 from both MRKEOS and SWEOS and pure water is compared (Figure 2.8). The density of water including aqueous-phase CO_2 calculated from MRKEOS is consistently greater than pure water. In addition, the density of water including aqueous-phase CO_2 from SWEOS is consistently greater than it is from MRKEOS. Therefore, the plume of aqueous-phase CO_2 from SWEOS will sink faster than that from MRKEOS.

Third, gravitational segregation is dominant after all of the separate-phase CO_2 is converted into aqueous-phase CO_2. This indicates that the relative permeability effect is critical to the migration of CO_2. As more fractions of pores are filled with separate-phase CO_2, the relative permeability of water including aqueous-phase CO_2 decreases. Later, when all separate-phase CO_2 dissolves, there is no reduction by relative permeability. Prior to 1000 years, separate-phase CO_2 still remains in the model (Figure 3.3a) with less downward migration of aqueous-phase CO_2 (Figure 3.3b) indicating the reduction of the relative permeability of water including aqueous-phase CO_2. In our simulation, all of the separate-phase CO_2 is

converted into aqueous-phase CO_2 at 6000 years in MRKEOS and at 4000 years in SWEOS (Figure 3.4). Prior to these times, the downward migration of aqueous-phase CO_2 is retarded due to relative permeability effect. However, the downward migration of aqueous-phase CO_2 increases without separate-phase CO_2. For example, the CO_2 migration curves at 10,000 years show a distinctive downward migration (Figure 3.3b).

The plot of CO_2 mass partitioning provides a useful method to quantify how much CO_2 is stored as dissolved phase and separate phase (Figure 3.4). The total mass of injected CO_2 was 2160 tons during 50 days in this simulation. During the injection period, separate-phase CO_2 was increased and simultaneously converted into aqueous-phase CO_2. After injection ceased, the mass of separate-phase CO_2 dropped while the mass of aqueous-phase CO_2 gradually increased because of the phase conversion from separate-phase CO_2 to aqueous-phase CO_2.

In this model, the mass fractions calculated from solubility EOS algorithms in MRKEOS and SWEOS were 0.038 and 0.050, respectively, at the injection point where approximate pressure and temperature are 9 MPa and 320.65 K (47.5°C) (Figure 3.3b). Although the difference (0.050 – 0.038 = 0.012) of mass fraction calculated from solubility EOS algorithms between MRKEOS and SWEOS is small, the actual mass of CO_2 from both MRKEOS and SWEOS reflects a huge difference (Figure. 3.4a and 3.4b). The value of maximum difference was 259 tons at 2000 years, or 12% of the total injected CO_2 (2160 tons). Further, the EOS algorithms also strongly affect the time when the entire mass of separate-phase CO_2 converts into aqueous-phase CO_2 (Figure 3.4a). In SWEOS, the entire mass of separate-phase CO_2

converted into aqueous-phase CO_2 after 4000 years. Therefore, complete solubility trapping occurred after 4000 years. However, MRKEOS required 6000 years to store CO_2 in a completely aqueous-phase CO_2.

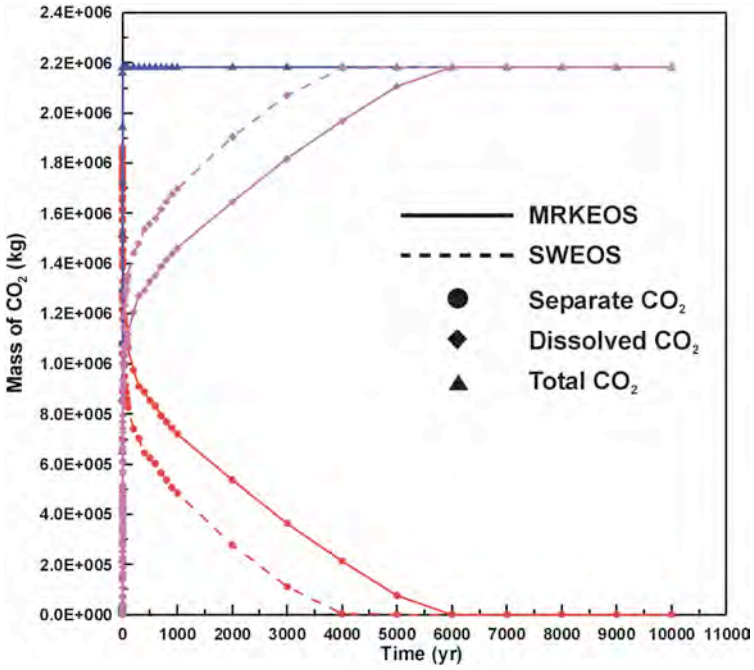

(a)

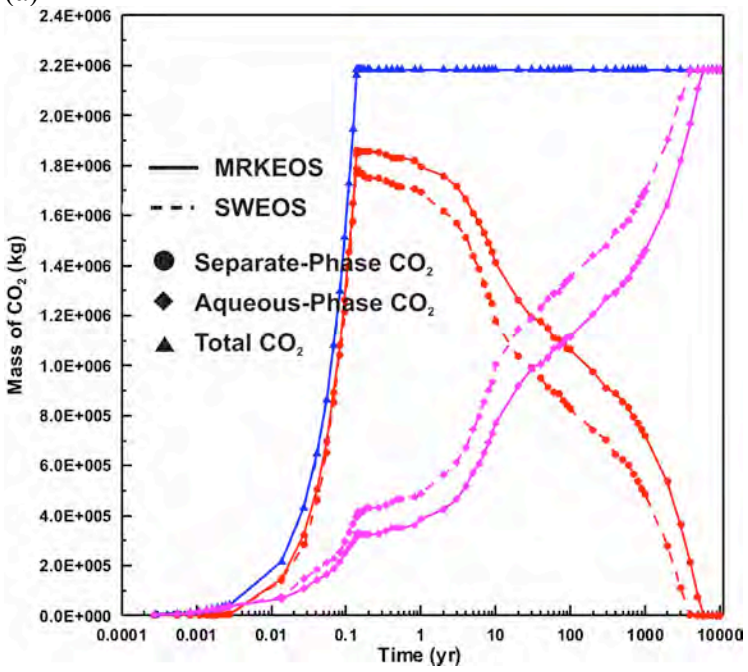

(b)

Figure 3.4. (a) CO_2 mass partitioning between separate- and aqueous-phase CO_2. (b) To emphasize the evolution at initial times, x-axis is plotted with log 10 scale.

Comparison of simulation results from MRKEOS and SWEOS reveals critical differences of actual mass and the time required for complete solubility trapping. These disparities are rooted in predicted differences of both mass fraction and density of water including aqueous-phase CO_2. The dissolved CO_2 mass fraction calculated from SWEOS is always greater than that calculated by MRKEOS for temperatures over 303.15K (30°C) (Figure 2.6 and 2.7). Consequently, the size of the separate-phase CO_2 plume from SWEOS always becomes smaller than that by MRKEOS. Furthermore, the saturation of separate-phase CO_2 from SWEOS reaches residual CO_2 saturation more quickly, thus trapping and holding back the separate-phase CO_2 more quickly, leading to a shorter time before vertical migration of that separate phase CO_2 ceases. Additionally, the density of water including aqueous-phase CO_2 predicted by SWEOS is always greater than that predicted by MRKEOS (Figure 2.8). Therefore, the rate of gravitational segregation from SWEOS is always greater than that predicted by MRKEOS. Because water including aqueous-phase CO_2 from SWEOS segregates faster, separate-phase CO_2 from SWEOS will always meet more CO_2-unsaturated water more quickly and therefore dissolve more quickly. The ultimate result is that separate-phase CO_2 from SWEOS dissolves more quickly and leads to significantly different predictions of migration and timing of solubility trapping processes.

3.3. Factors that Determine Migration/Penetration Distance through Unfractured Caprock

In this section, we detail results of sensitivity analyses designed to quantify the factors that control the distance to which CO_2 may penetrate an unfractured caprock, including: (1) amount of injected CO_2 mass, (2) caprock permeability, and (3) porosity (reservoir capacity). In addition, we also compared the difference in migration/penetration induced by using different EOS algorithms.

3.3.1. Mass of Injected CO_2

The previous conceptual model was applied to conduct a sensitivity analysis with respect to mass of injected CO_2 (Figure 3.2). Results from these simulations are shown in Figure 3.5. In these simulations (Figure 3.5), most injection-induced pressure dissipates within 10 years and subsequently reaches hydrostatic condition. Therefore, the effect of build-up pressure on CO_2 solubility is not significant at longer time scales (~1000 years).

In each simulation, the available volume for storing separate-phase CO_2 is consistent because porosity does not change. A linear increase of injected CO_2 mass corresponds to a linear increase of CO_2 volume. Because this simulation is 1-dimensional, the linear increments of volume translate to a corresponding linear migration/penetration distance (Figure 3.5), even after 1000 years. And, even though changes in relative permeability are not linear, this effect is not significant enough to change the linear correlation between injection amount and migration distance.

Another distinctive feature is that the migration/penetration distance from MRKEOS is greater than that from SWEOS. This is because MRKEOS predicts lower solubility values than SWEOS. Results of this sensitivity analysis suggest that

EOS algorithms that underestimate solubility may overestimate the size of the separate-phase CO_2 plume.

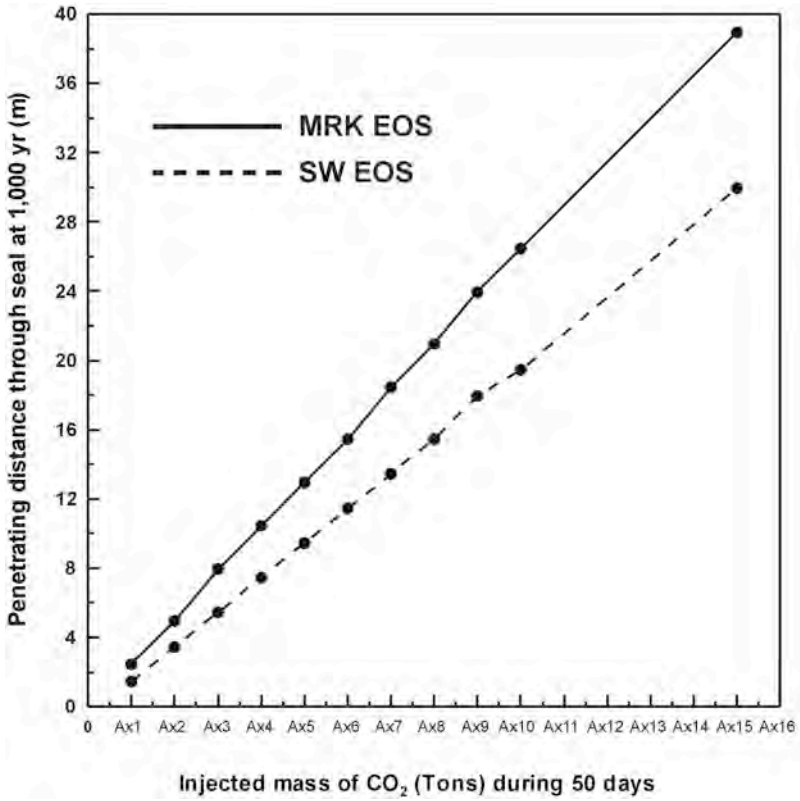

Figure 3.5. The sensitivity analyses of the penetrating distance through seal using the mass of injected CO_2. The y-axis is defined as the migration/penetration distance through the seal at 1000 yr, which is the distance between the injection location (900.25 m) and the plume front of separate-phase CO_2. The x-axis indicates the mass of the injected CO_2 over 50 days. A is the 432 tonnes of injected CO_2.

3.3.2. Caprock Permeability

Because permeability is commonly regarded as the most critical parameter for evaluating the integrity of caprock, it is chosen as the sensitivity parameter. We applied the same conceptual model for this sensitivity analysis (Figure 3.2). Permeability of the CO_2 storage formation was assigned the same value (10^{-14} m^2) for all simulations, but permeability of the caprock was varied from 10^{-16} m^2 to 10^{-11} m^2.

A permeability ratio less than 1 indicates that the formation above acts as a caprock. However, if the permeability ratio is greater than 1 (shaded area of Figure 3.6), this represents a situation in which the formation above no longer serves as a caprock, but rather has been breached by chemical or mechanical processes. We investigate the scenarios with the permeability ratio greater than 1 in order to understand caprock failure associated with CO_2 migration.

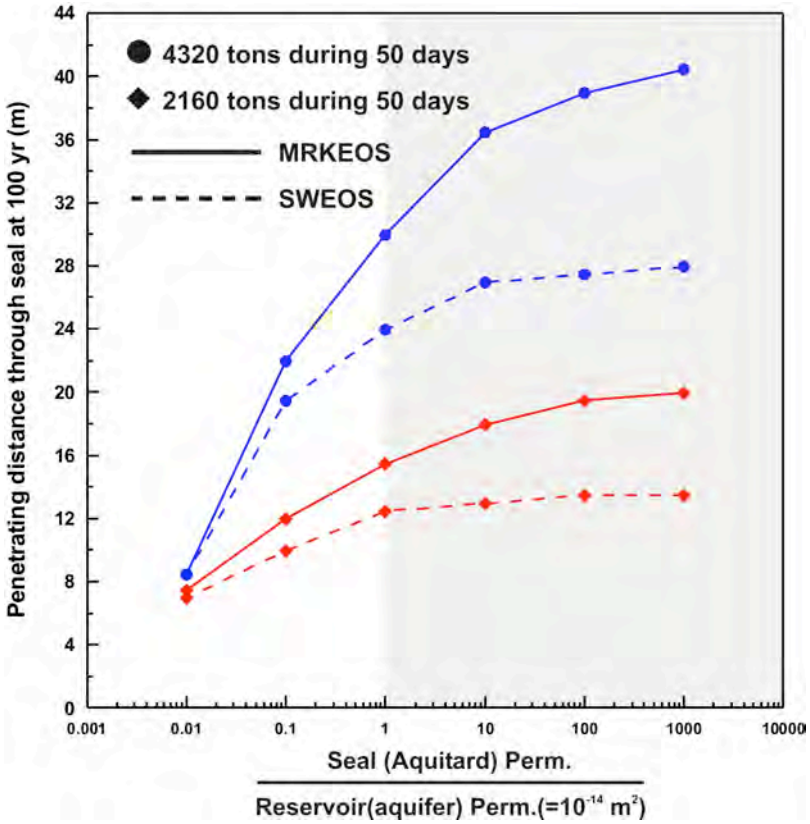

Figure 3.6. The sensitivity analyses of the penetrating distance through caprock using permeability with 2160 tons and 4320 tons of injection scenarios. The y-axis is defined as the migration/penetration distance through the seal at 100 yr, which is the distance between the injection location (900.25 m) and the plume front of separate-phase CO_2. The x-axis is defined as the permeability ratio between the seal (aquitard) and storage formation (aquifer).

As expected, a lower permeability caprock is more effective for preventing upward movement of separate-phase CO_2 (Figure 3.6). For example, using the MRKEOS algorithm with a permeability ratio of 0.01 in the 4320-ton injection scenario produced a migration/penetration distance of separate-phase CO_2 to 8.45 m at 100 years. Further, a migration/penetration distance of separate-phase CO_2 at low permeability is not sensitive to the amount of CO_2 injection. Although the amount of the injected CO_2 is doubled at low permeability, a migration/penetration distance of separate-phase CO_2 does not increase much. In addition, the discrepancy caused by EOS algorithms is minimal. However, a migration/penetration distance of separate-phase CO_2 at higher permeability caprock greatly varies with both the amount of the injected CO_2 and the discrepancy caused by EOS algorithms.

A distinctive feature of CO_2 migration results is that the migration/penetration distance of separate-phase CO_2 logarithmically increases with the permeability ratio and approaches an asymptotic limit of migration/penetration distance (Figure 3.6). For example, the asymptotic limit of the migration/penetration distance predicted from SWEOS reached approximately 13.5 m in the 2160-ton injection scenario, where the CO_2 plume will not migrate beyond this limit (13.5 m) even with a high-permeability caprock.

Generally, separate-phase CO_2 migrates upwards due to the density contrast with surrounding fluids and concurrently dissolves into aqueous-phase CO_2. In detail, separate-phase CO_2 will migrate into a pore, become saturated, and over time the saturation of separate-phase CO_2 will decrease by primary migration and dissolution. Once CO_2 saturation decreases to the residual CO_2 saturation, then it will

only decrease by dissolution. The result of this physical process indicates that vertical migration of separate-phase CO_2 will be impeded, effectively, by both the dissolution process and residual CO_2 saturation. In our simulations with higher permeability caprock, separate-phase CO_2 dissolves more quickly into reservoir fluid, because it reaches a fresh supply of CO_2-unsaturated fluid. Similarly, Ennis-King and Paterson, (2003) also observed that separate-phase CO_2 dissolved quickly at greater vertical permeability. Therefore, the saturation of separate-phase CO_2 reaches residual CO_2 saturation more quickly due to faster migration and dissolution of the separate-phase CO_2. These combined effects limit migration of separate-phase CO_2 to the asymptotic limit, even with a high-permeability caprock.

This asymptotic limit of a migration/penetration distance increases with the increasing mass of injected CO_2 because of the piston displacement process described in the previous section. For example, the asymptotic limit of migration/penetration distance predicted from SWEOS reached approximately 13.5 m in the 2160-ton injection. After increasing the mass of separate-phase CO_2 in the 4320-ton injection, the asymptotic limit reached approximately 28 m. Therefore, if the amount of injected CO_2 is greater than the current injected amounts, separate-phase CO_2 may reach the top of caprock formation. Further, this sensitivity analyses indicate that separate-phase CO_2 stored below poor quality of caprock may not reach (or leak) to the surface if all of separate-phase CO_2 dissolves and its saturation reaches residual CO_2 saturation while it migrates though preferential flow paths.

As expected, the migration/penetration distance calculated from MRKEOS is greater than that from SWEOS because MRKEOS underestimates the solubilities.

3.3.3. Porosity (Reservoir Capacity)

If permeability is a measure that enables the evaluation of the integrity of the caprock, porosity is a measure that allows the capacity of a CO_2 storage formation to be accessed. At the same time, porosity may affect the transport of CO_2 through caprock. Because porosity is a critical parameter for evaluating the CO_2 storage capacity of a target formation and potential CO_2 leakage through caprock, sensitivity analyses of the migration/penetration distance were conducted to evaluate the role of porosity. The same conceptual model (Figure 3.2) was adapted for this particular analysis.

In Figure 3.7, the migration/penetration distances from both MRKEOS and SWEOS are relatively short, 7.45 m at 0.3 porosity, because pore space is large enough to store most of the separate-phase CO_2. However, the migration/penetration distance for both MRKEOS and SWEOS becomes much larger, respectively, 51 m and 45 m at 0.05 porosity. The smaller porosity augments the piston displacement process because of the smaller amount of space available to accommodate the separate-phase CO_2.

Interestingly, the migration/penetration distance inversely (1/n) increases with decreasing porosity (Figure 3.7). This inversely increasing pattern of the migration/penetration distance can be explained with an example: consider one element with 0.4 porosity that is fully saturated with separate-phase CO_2. If the volume of the element is V_T, the separate-phase CO_2 occupies $0.4V_T$ within this element. If porosity is decreased to 0.2, one element can only accommodate $0.2V_T$

volume of separate-phase CO_2. In this case, it is necessary to use two elements to store $0.4V_T$ volume of separate-phase CO_2. Thus, decreasing porosity by half will double the number of required elements to accommodate the original amount of separate-phase CO_2.

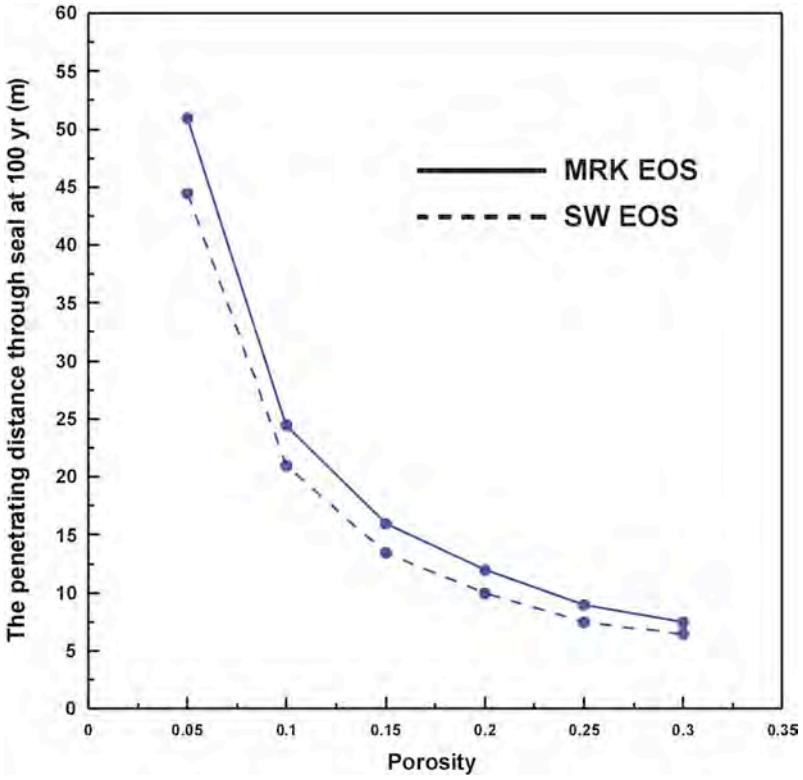

Figure 3.7. The sensitivity analyses of the penetrating distance through caprock using porosity (reservoir capacity). The y-axis is defined as the migration/penetration distance through the seal at 100 yr, which is the distance between the injection location (900.25 m) and the plume front of separate-phase CO_2. The x-axis indicates the change of porosity. Porosity is uniformly distributed in the entire model.

Although separate-phase CO_2 is not at full saturation in our simulation, the simulation results similarly indicate that decreasing porosity by half doubles the migration/penetration distance. Specifically, the migration/penetration distance from SWEOS was 6.45 m at 0.3 porosity. After decreasing porosity to 0.15, the

migration/penetration distance becomes 13.5 m, which is roughly double. In another example, the migration/penetration distance from MRKEOS was 12 m at 0.2 porosity. After decreasing porosity to 0.1, the migration/penetration distance becomes 24.5 m.

In sum, these simulation results suggest that porosity (storage capacity) is also a critical parameter because the amount of pore space available will directly impact any piston-displacement and associated migration/penetration distance.

3.4. Effects of Brine Concentration on Fluid Properties and CO_2 Migration

All analyses discussed above involved pure water—not brine—as the host reservoir fluid, to isolate the roles and effects of the processes of interest without the influence of brine variability on those processes; brine may vary greatly in density, viscosity, and CO_2 solubility depending on concentration. Adams and Bachu (2002) recognized the importance of brine thermophysical properties and provided critical reviews of the current available density and viscosity algorithms for brine. Another available algorithm is ECO2, an integrated EOS module assembled for CO_2 sequestration in brine formations (Garcia, 2003). However, while most of these previous studies considered the accuracy of EOS algorithms with respect to experimental data, they did not consider how variations in individual state properties might affect the flow and transport of sequestered CO_2. Therefore, sensitivity analyses were conducted to investigate how brine density, viscosity, and CO_2 solubility affect the transport of separate-phase CO_2 at various concentrations.

First, we replaced appropriate algorithms for brine density, viscosity, and CO_2 solubility within the integrated SWEOS and named it “BrineEOS”. We did not

modify MRKEOS because the general prediction of state properties from MRKEOS is less accurate than that from SWEOS. Details of this integrated BrineEOS are presented in Table 3.2 and included in Appendix VII, VIII, and IX. The main limitation of most currently adapted EOS algorithms for the integrated BrineEOS is that the EOS algorithms are developed based on the measurement of NaCl solution, a simplification compared to the complexity of natural brine compositions. Figure 3.8 presents plots of density, viscosity, and CO_2 solubility from the adapted EOS algorithms as functions of pressure and concentration at a fixed temperature (323.15 K (50°C)).

Table 3.2. The replaced algorithms for calculating brine density, viscosity, and CO_2 solubility at various pressure, temperature, and salinity conditions.

Properties	Study	Fluid	P (MPa)	T(°C)	S (mol/L)
Density	Batzle and Wang (1992)	NaCl	5 - 100	20 - 350	0- 5.5
Viscosity	Palliser and McKibbin (1998)	NaCl	0.1-300	0.1 - 800	0-17.1
Solubility	Duan and Sun (2003)	NaCl	0 - 200	0.15 - 259.85	0 - 4.3

For our sensitivity analyses with various concentrations, the previous conceptual model (Figure 3.2) was adapted. However, temperature was assigned as a fixed value (323.15 K (50°C)) within the entire model to reduce complexity. In addition, 0 mol, 1 mol, 2 mol, and 3 mol brine concentrations are used as representative concentrations. By assigning a fixed temperature and concentrations with a 1-mol interval, all of the calculated thermophysical properties within this model plot on the lines in Figure 3.8.

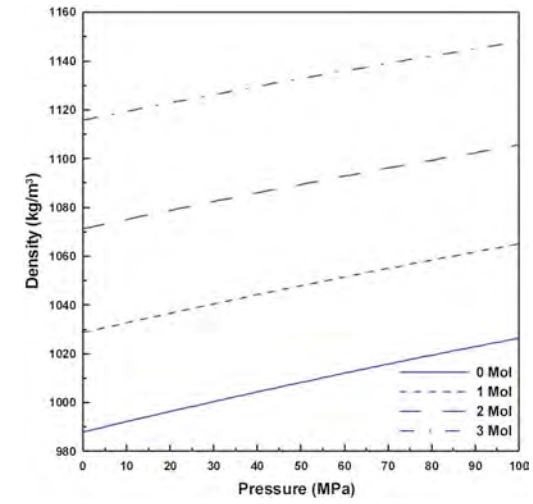

(a)

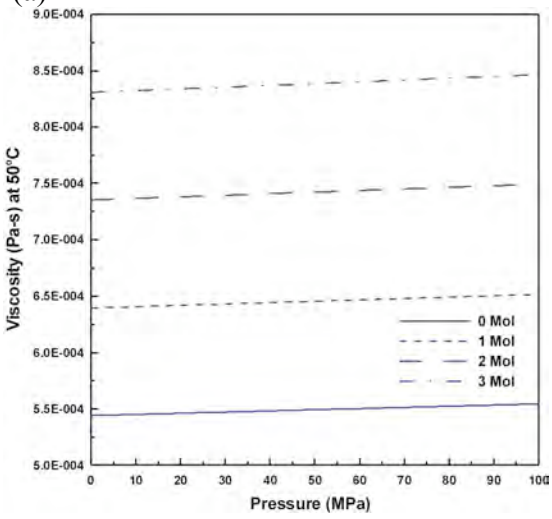

(b)

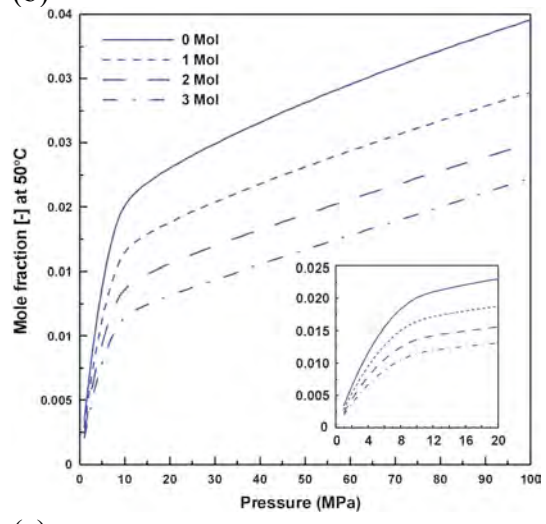

(c)

Figure 3.8. State properties as a function of pressure along several concentrations at fixed temperature (323.15 K (=50°C)): (a) Brine density, (b) Brine viscosity, and (c) CO_2 solubility.

Simulations with 12 different scenarios were conducted to investigate the sensitivity of separate-phase CO_2 flow and transport with respect to effects of (1) brine density, (2) brine viscosity, (3) CO_2 solubility, and (4) all of the above (Table 3.3).

Table 3.3. The representative scenarios for the sensitivity analyses of brine density, viscosity, and CO_2 solubility.

(mol)	I	II	III	IV	V	VI	VII	VIII	IX	X	X1	XII	XIII
Density	1	2	3	0	0	0	0	0	0	0	1	2	3
Viscosity	0	0	0	1	2	3	0	0	0	0	1	2	3
Solubility	0	0	0	0	0	0	1	2	3	0	1	2	3

3.4.1. Effects of Brine Concentration on Density

Scenarios I, II, and III in Table 3.3 indicate that brine density varies with concentration but brine viscosity and CO_2 solubility do not (Figures 3.9a and b). Increasing brine concentration increases brine density (Figure 3.8a) and causes an associated increase in hydrostatic pressure ($P=\rho_{brine}gh$) in the model. CO_2 solubility does not vary with concentration in these scenarios (Table 3.3); it only increases with pressure at fixed temperature (323.15 K (50°C)) (Figure 3.8c). Consequently, increased hydrostatic pressure due to the higher brine concentration causes CO_2 solubility to increase.

In Figure 3.9a, the plume front in high concentration (3 mol) brine does not migrate further than in low concentration (1 mol) brine. This is because separate-phase CO_2 dissolves faster in higher concentrations of brine. Figure 3.9b clearly

shows that all of separate-phase CO_2 in 3 mol brine dissolved completely after 50 years.

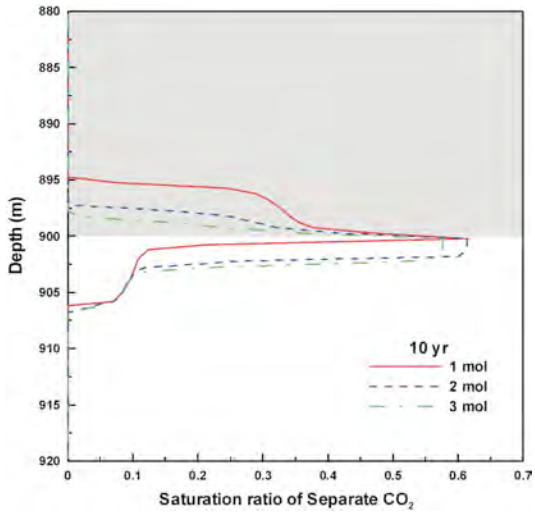

(a)

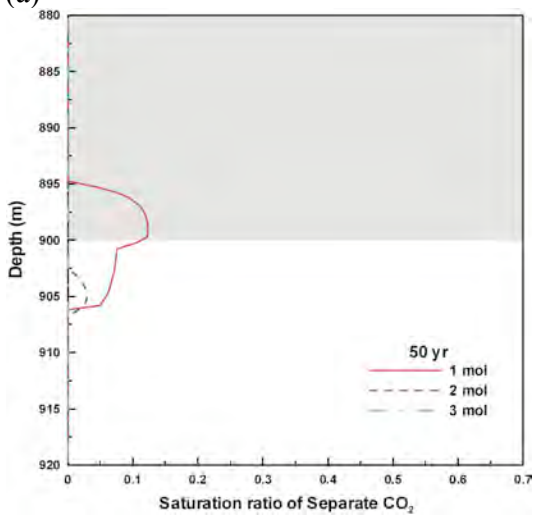

(b)

Figure 3.9. Plots of saturation of separate-phase CO_2 along several concentrations: (a) Scenario I, II, and III at 10 yr, (b) Scenario I, II, and III at 50 yr.

By increasing brine concentration, the density contrasts between separate-phase CO_2 and brine also increases. Therefore, more buoyancy-driven force tends to enhance the vertical movement of separate-phase CO_2. However, the vertical movement of separate-phase CO_2 was retarded in figure 3.9a and 3.9b because of the enhancement of dissolution rate in higher brine concentration. In conclusion, brine

density is a critical parameter and must be considered for quantitatively consistent simulation of CO_2 sequestration.

3.4.2. Effects of Brine Concentration on Viscosity

Scenarios IV, V, and VI in Table 3.3 indicate that brine viscosity varies with concentration but brine density and CO_2 solubility do not. (Figures 3.10a and b). Increasing brine concentration increases brine viscosity (Figure 3.8b).

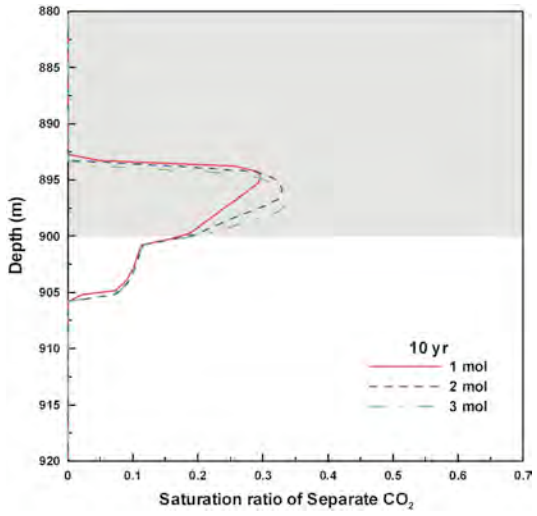

(a)

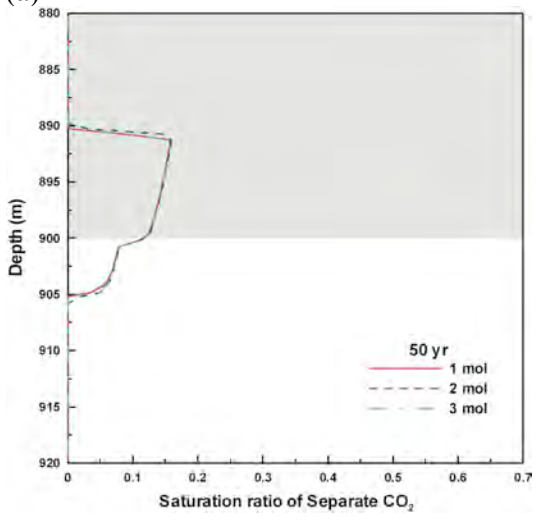

(b)

Figure 3.10. Plots of saturation of separate-phase CO_2 along several concentrations: (a) Scenario IV, V, and VI at 10 yr, (b) Scenario IV, V, and VI at 50 yr.

The sensitivity analyses show that transport of separate-phase CO_2 is not sensitive to viscosity. The increment of density in a 1 mol brine is about 40 kg/m^3 (Figure 3.8a), while the increment of viscosity is minimal, 10^{-4} pa-s (Figure 3.8b), leading to small effects on transport. The plume fronts of separate-phase CO_2 with different concentrations are located in approximately the same position. In sum, the range of potential changes in brine viscosity produces relatively small changes in flow and transport of separate-phase CO_2.

3.4.3. Effects of Brine Concentration on CO_2 Solubility

Scenarios VII, VIII, and IX in Table 3.3 indicate that CO_2 solubility varies with concentration but brine density and viscosity do not (Figures 3.11a and b). As illustrated in Figure 3.8c, CO_2 solubility decreases with increasing concentration, indicating that the dissolution rate of separate-phase CO_2 will be enhanced at low concentrations of brine.

Both Figures 3.11a and b show that the plume of separate-phase CO_2 in 1 mol brine is the smallest plume, reflecting the enhanced dissolution rate. These results suggest that CO_2 solubility is a critical parameter because it dictates dissolution rate, which eventually determines the size and migration/penetration distance of separate-phase CO_2. On the other hand, at higher concentration reducing dissolution rate, migration/penetration distances of separate-phase CO_2 will be increased. The next section provides a brief analysis of these coupled effects on flow and transport of separate-phase CO_2.

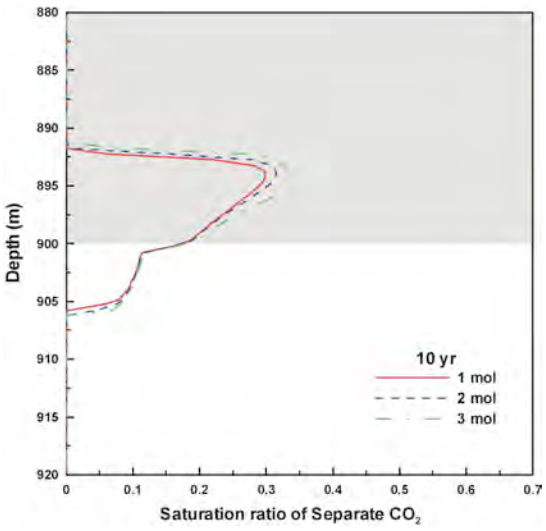

(a)

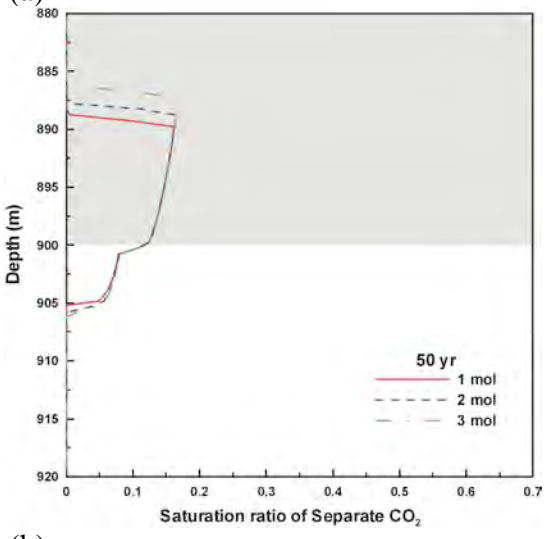

(b)

Figure 3.11. Plots of saturation of separate-phase CO_2 along several concentrations: (a) Scenario VII, VIII, and IX at 10 yr, (b) Scenario VII, VIII, and IX at 50 yr.

3.4.4. Combined Sensitivity of All Parameters

Figures 3.12a and 3.12b present the simulation results from scenarios X, XI, XII, and XIII in which density, viscosity, and CO_2 solubility were permitted to vary with concentrations. Therefore, the transport of separate-phase CO_2 reflects the integrated effects of density, viscosity, and CO_2 solubility due to the changes of brine concentration.

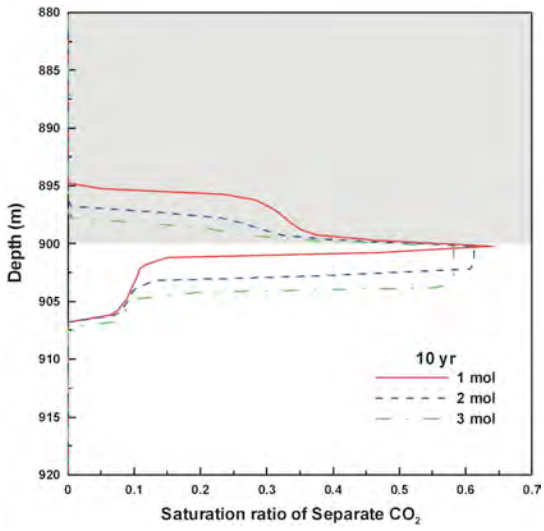

(a)

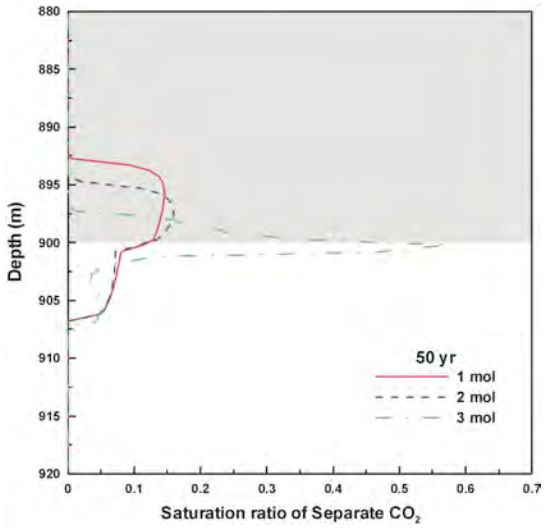

(b)

Figure 3.12. Plots of saturation of separate-phase CO_2 along several concentrations. Brine density, viscosity and CO_2 solubility vary with concentration: (a) Scenario X, XI, XII, and XIII at 10 yr. (b) Scenario X, XI, XII, and XIII at 50 yr.

The plume fronts of separate-phase CO_2 migrate the farthest distance (or reach the highest locations) in 0 mol brine, as shown in both figures, and migrate the least distance (lowest locations) in 3 mol brine. Coupled effects of pressure, solubility, and density discrepancy generate the contrasts of CO_2 migration and transport. Table 3.4

summarizes effects on penetration/migration distance by increasing brine concentration. These coupled effects make the plume fronts of separate-phase CO_2 in 3 mol brine migrate the least distance.

Table 3.4. The lists of effects to the penetration/migration distance of separate-phase CO_2 by increasing brine concentration.

Effect by increasing brine concentration	Effect to the penetration/migration distance of separate CO_2
Increasing brine density	Because the mass of brine overlying separate CO_2 gets heavier, penetration/migration distance of separate CO_2 is retarded
	Because of increasing the density contrast between brine and separate CO_2, buoyancy driven force is increased and penetration/migration distance of separate CO_2 is enhanced
Increasing hydrostatic pressure	CO_2 solubility is increased with pressure. Because increased solubility reduces piston displacement process, migration/penetration distanced retarded
Increasing concentration	CO_2 solubility is decreased with increasing concentration. Because reduced solubility augments piston displacement process, migration/penetration distanced increased

Interestingly, opposite effects occurred from the previous sensitivity analyses of CO_2 solubility. In previous analyses detailed in section 3.4.3, the plume of separate-phase CO_2 in 1 mol brine dissolved faster because CO_2 solubility was greater in low concentrations of brine (Figure 3.11b). However, simulation results show that the plume of separate-phase CO_2 in 3 mol brine dissolved faster (Figure 3.12b). This is because the gravitational segregation rate of aqueous-phase CO_2 is different. In our BrineEOS, the density of brine including aqueous-phase CO_2 was adapted from Andersen, (1992), which included a brine density term in order to calculate the density of brine including aqueous-phase CO_2. As a result, increasing the density of brine increases the segregation rate of brine including aqueous-phase CO_2.

For example, the density of brine including aqueous-phase CO_2 at 3 mol concentration is greater than that at 1 mol. Therefore, aqueous-phase CO_2 at 3 mol concentration will segregate faster. Because aqueous-phase CO_2 at 3 mol concentration segregates faster, the remaining separate-phase CO_2 has more opportunity to contact brine where CO_2 has not been dissolved. In contrast, because aqueous-phase CO_2 at 1 mol concentration segregates slowly and stays with separate-phase CO_2, separate-phase CO_2 hardly dissolves into brine where CO_2 has already been saturated.

In conclusion, results of sensitivity analyses that varied all parameters—brine density, brine viscosity, and CO_2 solubility—indicate that brine density and CO_2 solubility are the most critical parameters for the transport of separate-phase CO_2.

3.5. Effect of Relative Permeability

Although relative permeability is a key factor in determining the subsurface transport of both separate-phase and dissolved-phase CO_2, its function for the application of CO_2 sequestration is not well defined because of the paucity of laboratory data. Recently, the importance of the relative permeability function for numerical simulation has been proven by comparing generic curve with a "Frio-like" curve (Doughty and Pruess, 2004). In addition, Bennion and Bachu (2005) measured relative permeability of both CO_2 and brine from the various cores at Wabamun lake area in Alberta, western Canada.

In our EOS algorithms, we had adapted Cole's (2000) relative permeability function, which is the fitted function of Parker et al (1987) with experimentally

determined data from Holt et al. (1995). These functions approximately matched the experimental data provided by Holt et al. (1995) for supercritical CO_2 in a 1.2 m core of Bentheimer sandstone at a temperature of 62ºC and pressure of 20 MPa (Figure 3.13). For the comparison, relative permeability curves are fitted with the experimentally measured data by Bennion and Bachu, (2005) describing supercritical CO_2 in a 0.16 m core of low permeability carbonate rock collected from Wabamun lake at 41ºC and 22.4 MPa (Figure 3.13).

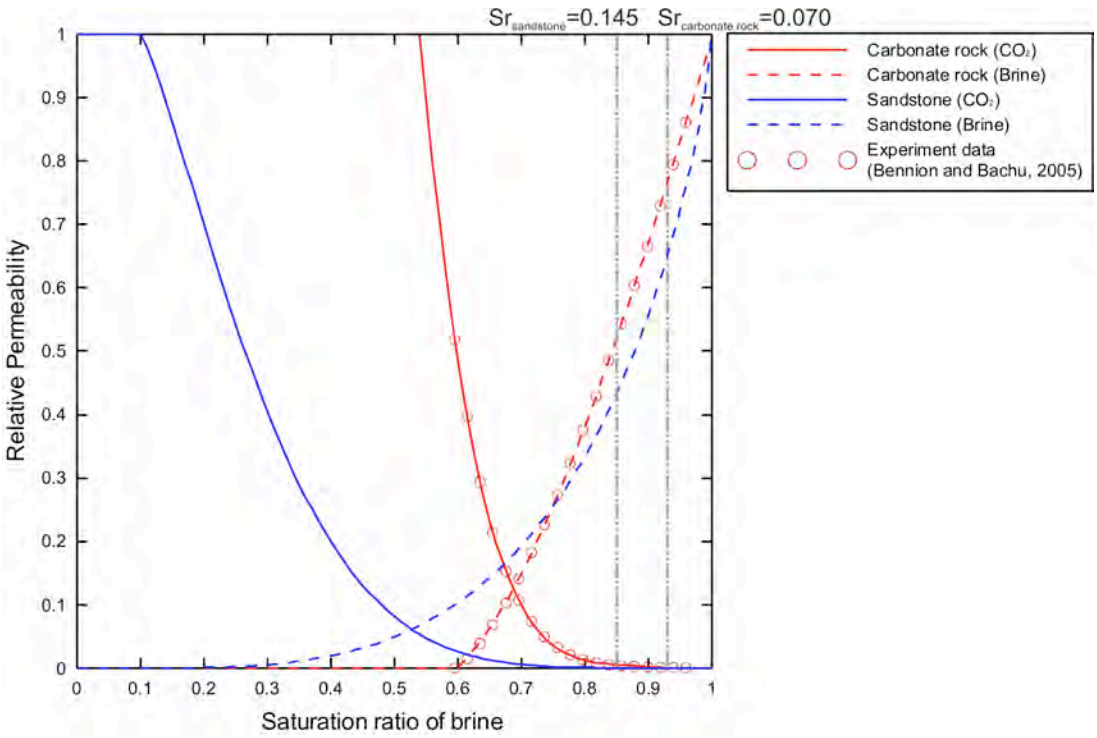

Figure 3.13. Relative permeability curves of both carbonate rock (Bennion and Bachu, 2005) and sandstone (Holt, 1995).

The significant distinction between the two sets of curves is the residual saturation, which is respectively 0.07 and 0.145 in carbonate rock and sandstone (Figure 3.13). Below these saturations, the plumes of separate-phase CO_2 do not

migrate because relative permeability becomes zero. In sum, separate-phase CO_2 in carbonate rock will show greater mobility.

For the test of relative permeability effect, the previous conceptual model with SWEOS was applied to conduct a sensitivity analysis (Figure 3.2). The plume front of separate-phase CO_2 in sandstone is located at 895 m in 5 years with highest accumulation of saturation below the seal (Figure 3.14). However, the plume front of separate-phase CO_2 in carbonate migrates further and is located at 891 m in 5 years. Separate-phase CO_2 in carbonate rock shows greater vertical mobility. At 10 years, the saturation ratio of separate-phase CO_2 in carbonate rock approaches residual saturation (0.07). Eventually, the vertical movement of separate-phase CO_2 stops at 10 years because relative permeability becomes almost zero. Consequently, any movement of separate-phase CO_2 in carbonate rock is not shown at 100 years.

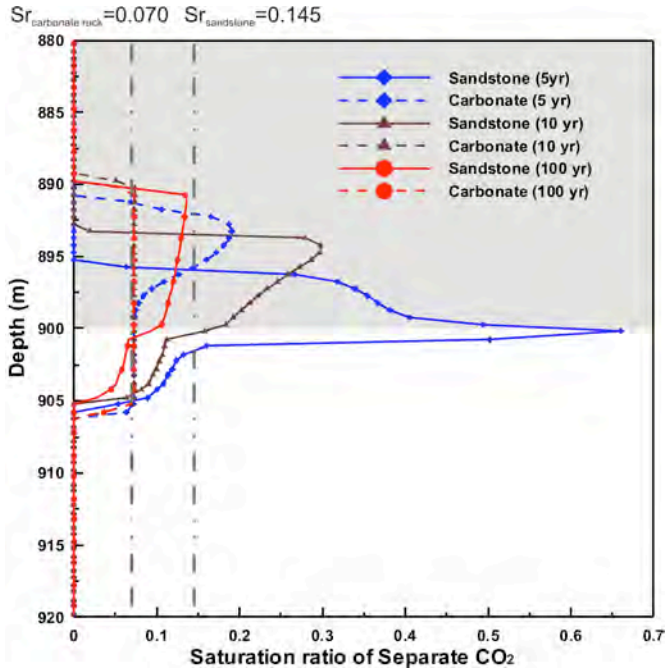

Figure 3.14. Plots of saturation of separate-phase CO_2 from carbonate rock and sandstone at 5 yr, 10 yr, and 100 yr.

The saturation of separate-phase CO_2 in sandstone is greater than residual saturation (0.145) at 10 years (Figure 3.14b). Therefore, the CO_2 plume will migrate further until saturation of separate-phase CO_2 is below residual saturation. Eventually the movement of separate-phase CO_2 in sandstone stops at 100 years.

This study clearly indicates that the migration of separate-phase CO_2 through an unfractured caprock is determined by residual saturation of relative permeability.

3.6. Summary and Conclusion

Although many EOS algorithms have been adapted into diverse numerical codes associated with CO_2 sequestration, no research had considered how EOS algorithms might affect the predicted simulation results.

The primary purpose of this study was not just to compare the thermophysical properties calculated from MRKEOS, SWEOS, and BrineEOS, but rather to identify how differences in predicted physical properties result in differences in prediction of CO_2 flow and transport. Therefore, we designed and developed a one-dimensional model that can describe the buoyancy-driven flow of separate-phase CO_2 and gravitational segregation of aqueous-phase CO_2. This idealized model will not describe completely CO_2 migration with heterogeneity effects. And, a one-dimensional model may provide quantitatively different results than a three-dimensional heterogeneous model, for obvious reasons. However, the general conclusions will be consistent. We also suggest that a one-dimensional model will more aptly isolate critical (fundamental) processes that affect CO_2 migration and

transport. Therefore, it was easier to elucidate how the discrepancy among EOS algorithms may affect the migration of separate-phase CO_2.

In this research, the major conclusions that can be drawn are as follows:

1. The thermophysical properties are sequentially calculated within the integrated EOS algorithms. During this process of sequential calculations, errors generated from the previous EOS calculation propagate into subsequent calculations. For example, the discrepancy of the fugacity coefficient predicted from MRKEOS propagates into the subsequent calculations such as solubility and mixture density.
2. Due to the complexity and computational expense of EOS algorithms, researchers often opt for less accurate (and typically faster) EOS algorithms. However, this approach may cause significant uncertainty in the simulation results. For example, the maximum difference of the CO_2 mass was 12% in our model and the predicted time to obtain complete dissolution of injected CO_2 in water was 4000 years for SWEOS and was 6000 years for MRKEOS.
3. Sensitivity analyses show that variability in the mass of injected CO_2, caprock permeability, and reservoir porosity affects the migration of CO_2 in overlying caprock. The migration/penetration distance of separate-phase CO_2 depends linearly on the injected CO_2 mass, logarithmically on caprock permeability, and inversely (1/n) on reservoir porosity. Finally, the analysis of the migration/penetration distance of separate-phase CO_2 suggests that caprock permeability and reservoir porosity should be thoroughly characterized prior

to CO_2 injection and the maximum amount of injected CO_2 should be reasonably determined based on geologic properties.

4. The changes of thermophysical properties (density, viscosity, and CO_2 solubility) with concentration can significantly affect CO_2 migration. Sensitivity analyses were conducted to investigate how these variations with concentration might affect migration/penetration distance of separate-phase CO_2. Simulation results indicate that both brine density and CO_2 solubility are critical factors. However, the effect of brine viscosity is minimal in most cases.
5. The analysis of relative permeability indicates that the vertical migration of separate-phase CO_2 through an unfractured caprock is determined by residual saturation. When the saturation ratio of separate CO_2 plume becomes less than the residual saturation, the vertical migration of separate CO_2 eventually stops.

Currently, many researchers have attempted to study problems related to CO_2 sequestration. Although many EOS algorithms have been adapted into these diverse simulators, no research considers how EOS algorithms may affect the predicted simulation results. In this work, we only consider two fundamentally different EOS algorithms. However, many other EOS algorithms are still being used without appropriate validation. For better scientific prediction associated with CO_2 sequestration, it is important that studies validating the various EOS algorithms actively progress.

References

Adams, J.J., Bachu, S., 2002. Equations of state for basin geofluids: algorithm review and intercomparison for brines. Geofluid 2, 257-271.

Andersen, G., Probst, A. Murray, L., Butler, S., 1992. An accurate PVT model for geothermal fluids as represented by H_2O-CO_2-NaCl mixtures. Proceedings of the 17th Workshop on Geothermal Reservoir Engineering, Stanford, California, 17,239–248.

Bachu, S., 2000. Sequestration of CO_2 in geological media: criteria and approach for site selection in response to climate change, Energy Conversion and Management 41, 953-970.

Batzle, M., Wang, Z., 1992. Seismic properties of pore fluids. Geophysics 57, 1396-1408.

Bennion, B., Bachu, S., 2005. Relative permeability characteristics for supercritical CO_2 displacing water in a variety of potential sequestration zones in the western Canada sedimentary basin. Society of Petroleum Engineers Journal 95547.

Cole, B.S., 2000. Sequestration of Supercritical Carbon Dioxide in Deep Sedimentary Basin Aquifers: A Numerical Model. Master thesis, New Mexico Institute of Mining and Technology, Socorro, 124pp.

Diamond, L. W., Akinfiev, N. N., 2003. Solubility of CO_2 in water from -1.5 to 100°C and from 0.1 to 100MPa: Evaluation of literature data and thermodynamic modeling. Fluid Phase Equilibria 208, 265-290.

Doughty, C., Pruess, K., 2004. Modeling supercritical carbon dioxide injection in heterogeneous porous media. Vadose Zone Journal 3, 837-847.

Duan, Z. and Sun, R. 2003. An improvement model calculating CO_2 solubility in pure water and aqueous NaCl solutions from 273 to 533 K and from 0 to 2000 bar. Chemical Geology, 193, 257-271.

Ennis-King, J., Paterson, L., 2003. Role of convective mixing in the long-term storage of carbon dioxide in deep saline formations. Society of Petroleum Engineers Journal 84344.

Garcıa, J.E., 2003. Fluid dynamics of carbon dioxide disposal into saline aquifers. Ph.D Thesis, University of California, Berkeley, 136pp.

Gaus, I., Azaroual, M., Czernichowski-Lauriol, I. 2005. Reactive transport modeling of the impact of CO_2 injection on the clayey cap rock at Sleipner (North Sea). Chemical Geology 217, 319-337.

Hitchon, B. 1996. Aquifer disposal of carbon dioxide. Geoscience Publishing, Ltd, Sherwood Park, Alberta, Canada.

Holt, T., Jensen, J. –I., Linderberg, E., 1995. Underground storage of CO_2 in aquifers and oil reservoirs. Energy Conversion and Management 36(6-9), 535-538.

Ingebritsen, S.E., Sanford, W.E., 1998. Groundwater in geologic processes. Cambridge University Press, 341pp.

International Formulation Committee, 1967. A formulation of the thermodynamic properties of ordinary water substance, IFC Secretariat, Dusseldorf, Germany, 27pp.

Johnson, J., Nitao, J., Steefel, C., Knauss, K., 2001. Reactive transport modeling of geologic CO_2 sequestration in saline aquifers: the influence of intra-aquifer shales and the relative effectiveness of structural, solubility, and mineral trapping during prograde and retrograde sequestration. Proceedings of the First National Conference on Carbon Sequestration, Washington, DC, May 14–17, 2001.

Kerrick D.M., Jacobs, G.K., 1981. A modifed Redlich-Kwong equation for H_2O, CO_2, and H_2O-CO_2 mixtures at elevated pressures and temperatures. American journal of science, 281, 753-767.

Knauss, K.G., Johnson, J.W., Steefel, C.I., 2005. Evaluation of the impact of CO_2, co-contaminant gas, aqueous fluid and reservoir rock interactions on the geologic sequestration of CO_2. Chemical Geology 217, 339-350.

Nghiem, L., Sammon, P., Grabenstetter, J., Ohkuma, H., 2004. Modeling CO_2 storage in aquifers with fully-coupled geochemical EOS compositional simulator. Society of Petroleum Engineers Journal 89474.

Nitao, J.J., 1998. User's manual for the USNT module of NUFT code, Version 2.0. Report UCRL-MA-130653. Lawrence Livermore National Laboratory, Lawrence, CA, 65pp.

Orr, F.M. Jr., 2004. Storage of carbon dioxide in geologic formation. Journal of Petroleum Technology 56, 90-97.

Palliser, C., McKibbin, R., 1998. A model for deep geothermal brines, III: Thermodynamic properties-enthalpy and viscosity. Transport in Porous Media 33, 155-171.

Parker, J.C., Lenhard, R.J., Kuppusamy, T., 1987. A parametric model for constitutive properties governing multiphase flow in porous media, Water Resources Research 23(4), 618-624.

Parkhurst, D.L., Appelo, C.A.J., 1999. User's guide to PHREEQC (version 2) - A computer program for speciation batch-reaction, one-dimensional transport, and inverse geochemical calculations: U.S. Geological Survey Water-Resources Investigations Report 99-4259, 312p.

Pruess, K. Garcia, J., 2002. Multiphase flow dynamics during CO_2 disposal into saline aquifers. Environmental Geology 42, 282-195.

Pruess, K. Garcia, J., Kovscek, T., Oldenburg, C., Rutqvist, J., Steefel, C., Xu, T., 2004. Code intercomparison builds confidence in numerical simulation models for geologic disposal of CO_2. Energy 29, 1431-1444.

Pruess, K. Oldenburg, C., Moridis, G., 1999. TOUGH2 user's guide, version 2.0. Lawrence Berkeley National Laboratory, Berkeley, CA, Novermber, Rep LBNL-43134.

Reid, R.C., Prausnitz, J.M., Poling, B.E., 1987. The properties of gases and liquids. 4th edition, McGraw-Hill, Inc., New York.

Span, R., Wager, W., 1996. A new equation of state for carbon dioxide covering the fluid region from the triple-point temperature to 1100 K at pressures up to 800 MPa. Journal of physical chemical reference data, 25(6), 1509-1596.

Steefel, C.I., 2001. CRUNCH. Lawrence Livermore National Laboratory

Weir, G.J., White, S.P., Kissling, W.M., 1996. Reservoir storage and containment of greenhouse gases. Transport in porous media, 23, 37-60.

White, S.P., 1995. Multiphase non-isothermal transport of systems of reacting chemicals. Water Resources Research 31(7), 1761-1772.

White, S.P., Allis, R.G., Moore, J., Chidsey, T., Morgan, C., Gwynn, W., Adams, M., 2005. Simulation of reactive transport of injected CO_2 on the Colorado Plateau, Utah, USA. Chemical Geology 217, 387-405.

Xu, T., Sonnenthal, E., Spycher, N., Pruess, K., 2004. TOUGHREACT user's guide: a simulation program for non-isothermal multiphase reactive geochemical transport in variable saturated geologic media. Lawrence Berkeley National Laboratory Report LBNL-55460, Berkeley, CA, 192pp.

CHAPTER 4

PRINCIPAL RESERVOIR DESCRIPTION ASSOCIATED WITH GEOLOGY AND OIL PRODUCTION HISTORY IN SACROC, SITE OF 35 YEARS OF CO_2 INJECTION

4.1. Introduction

The Scurry Area Canyon Reef Operator's Committee (SACROC) Unit, within the Horseshoe Atoll, is the oldest continuously operated CO_2 enhanced oil recovery (EOR) operation in the United States, having undergone CO_2 injection since 1972. SACROC continues to be flooded by the current operator, Kinder Morgan CO_2 Company. About 93 million tonnes (93,673,236,443 kg) of carbon dioxide have been injected in the SACROC Unit and about 38 million tonnes (38,040,501,080 kg) have been produced (Raines, 2005). A net mass balance suggests that the site has accumulated about 55 million tonnes (55,632,735,360 kg) of CO_2.

For the past several decades, oil industry workers and petroleum geologists have extensively investigated this site for the purpose of enhancing oil recovery (Bergenback and Terriere, 1953; Vest. 1970; Dicharry et al. 1973; Brummett et al. 1976; Graue and Blevins, 1978; Hawkins et al. 1996). Currently, the area has attracted CO_2 sequestration researchers because its 35–year CO_2 injection history confirms that CO_2 is trapped by an effective sealing unit (Holtz et al. 2006; Han et al. 2006; Carey et al. 2007).

4.2. Geologic Description

SACROC is located in the southeastern segment of the "Horseshoe Atoll" within the Midland basin in western Texas (Figure 4.1). The Horseshoe Atoll, 282 km long and 914 m thick with a total area of 15,540 km^2, is a reef mound composed of mixed types of in-place boundstones and bioclastic debris accumulated during the late Paleozoic (Vest, 1970). Within the Horseshoe Atoll, SACROC comprises an area of 356 km^2, with a length of 40 km and a width of 3~15 km.

Geologically, the carbonate reef complex at SACROC is composed of massive amounts of bedded bioclastic limestone and thin shale beds (mm to cm in thickness) representing the Strawn, Canyon, and Cisco Formations of the

Pennsylvanian, and the Wolfcamp Series of the Lower Permian (Raines et al. 2001). The oil at SACROC is produced from the Canyon and Cisco Formations, which are in Pennsylvanian age (Vest, 1970).

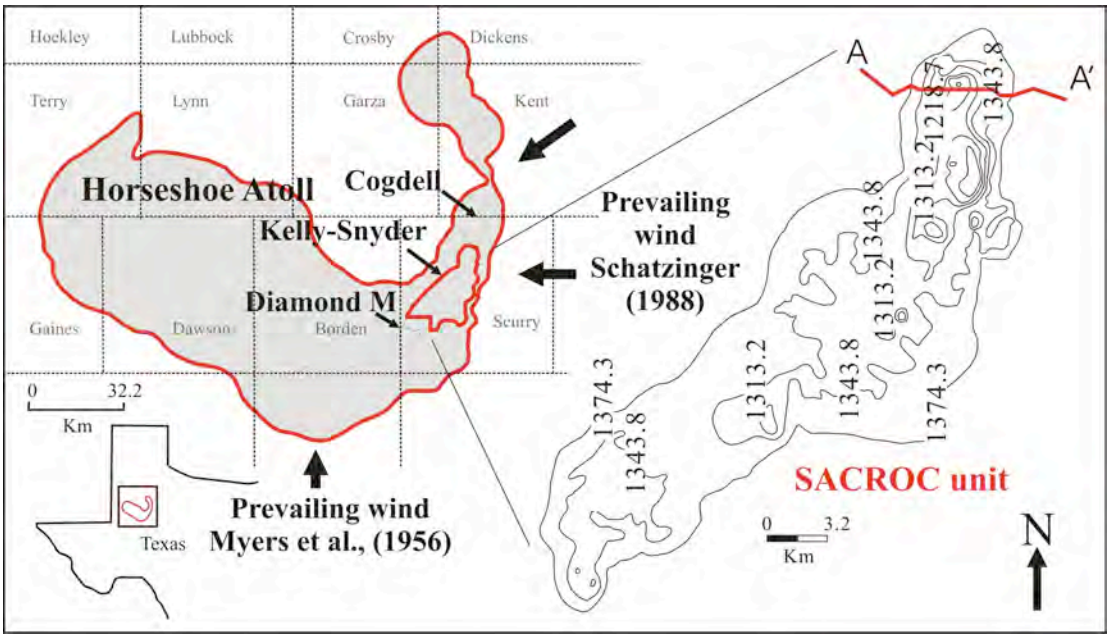

Figure 4.1. SACROC Unit at the Horseshoe Atoll in west Texas and structural contours map of top of carbonate reef modified from Stafford (1954). Contours are m scale.

A cross-section of geologic structure and stratigraphy of the study area is presented in Figure 4.2. The carbonate reef complex developed in the early Strawn (Desmoinesian) while the basin was on the equator. During the formation of the Canyon (Missourian) and Cisco (Virgilian), carbonate sedimentation continued.

Accumulation of carbonate sediments on the SACROC ended during the Wolfcampian due to the drastic influx of fine-grained clastics.

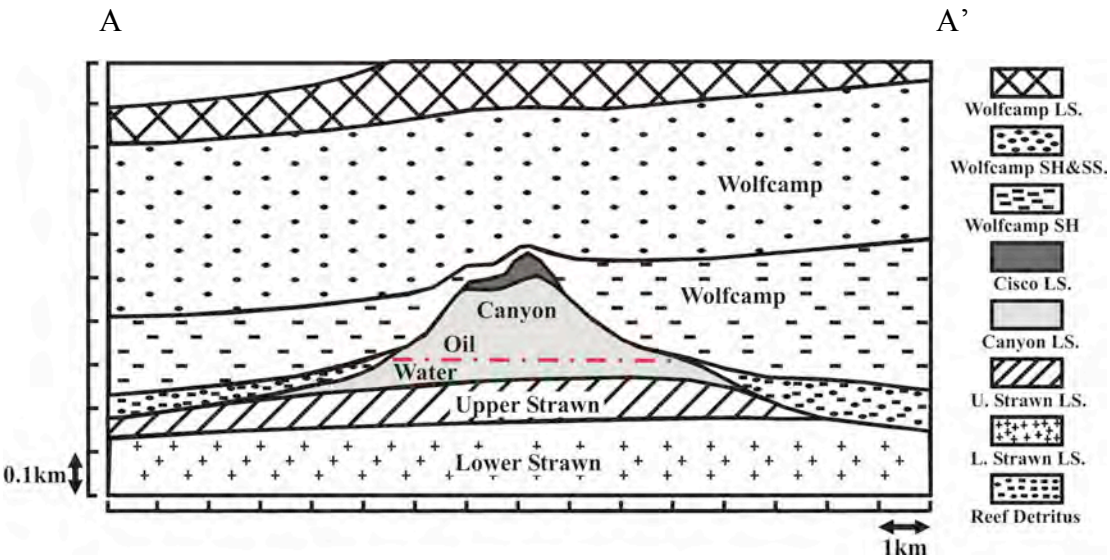

Figure 4.2. A structural and stratigraphic cross-section of profile A-A', located within the SACROC northern platform (Vest, 1970). See Figure 4.1 for a location of profile A-A'.

A majority of the Canyon and Cisco Formations are composed of limestone, but minor amounts of anhydrite, sand, chert, and shale are present locally (Raines et al. 2001). Recently, Carey et al (2007) analyzed core samples from wells 49-5 and 49-6 in the SACROC field and indicated that the limestone was mostly calcite with minor ankerite, quartz, and thin clay lenses. Detailed discussion of the carbonate reef complex related to facies, depositional environment, and petrography is included

in Bergenback and Terriere, (1953), Stafford, (1954), Mayer et al. (1956), Stewart, (1957), Burnside, (1959), Vest, (1970), Schatzinger (1988), and Reid and Reid (1991).

The Wolfcamp shale of the lower Permian provides a low permeability seal above the Pennsylvanian Cisco and Canyon Formations (Raines et al. 2001). Carey et al. (2007) measured the permeability of the shale and indicated that the permeability perpendicular to shale layer is <0.05 mD (k_z) and that parallel to the shale layer is 9 mD (k_x). Further, they performed X-ray diffraction analyses and indicated that the shale is mostly illite and quartz with minor feldspar, carbonate, and pyrite. Based on their mineralogical analysis, CO_2 has not interacted with shale; the carbonate in the shale appears to derive from primarily diagenetic processes. In addition, carbon and oxygen isotope measurement from shale also shows that carbonates in shale are typical marine-originated $\delta^{13}C$ values.

4.2.1. Overview of Geologic Parameters

The original carbonate reef (Cisco and Canyon Formations) was composed of bioclastic limestone with large pore sizes (Bergenback and Terrier, 1953; Myer et al. 1956). These pore spaces were subsequently filled by calcium carbonate cement. During the late Pennsylvanian and early Permian, glacio-eustatic fluctuations exposed

the carbonate reef to meteoric processes above sea level. As a result, the carbonate reef became a highly heterogeneous feature and secondary porosity developed with the presence of karst, vuggy porosity, and microfractures (Figure 4.3a and 4.3b). Later, this secondary porosity was reduced with drusy calcite (Figure 4.3c) and authigenic quartz (Myers et al. 1956), plus minor amounts of karst-related shale fill.

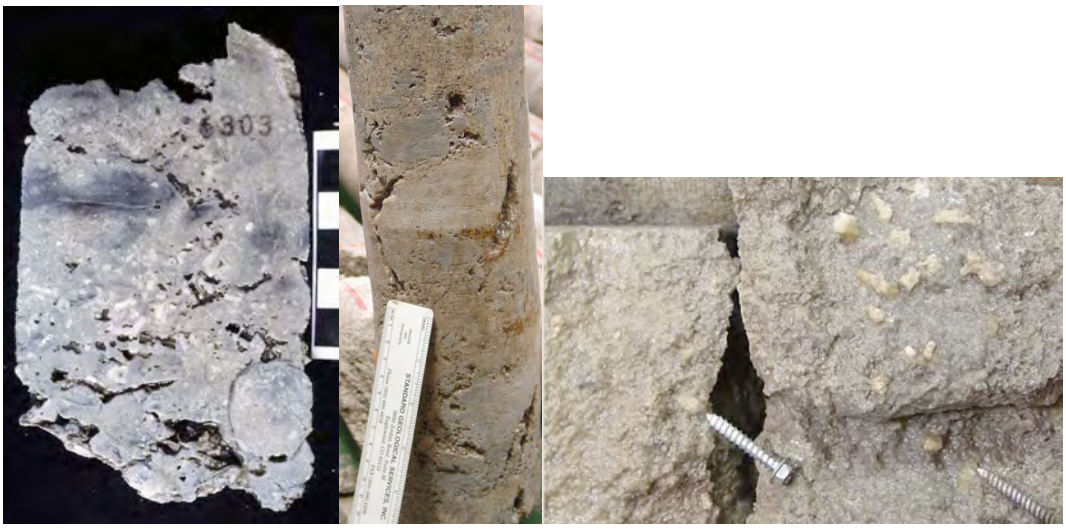

(a) (b) (c)

Figure 4.3. The evidences of meteoric digenesis process in SACROC cores: (a) vuggy porosity from well 17-5 (Raines, 2003), (b) vuggy porosity from well 37-11 (Raines, *Personal Communication*), and (c) calcite crystal growth indicates that fracture are open and reservoir fluid passes through it (Raines, *Personal Communication*).

The change in geologic environment provides for a wide variability in both porosity (0 to 30%) and permeability (0 to 1000 mD). Table 4.1 summarizes the porosity and permeability range from previous studies of this area.

Table 4.1. Overviews of carbonate properties in Cisco and Canyon Formations.

Porosity (%)	Permeability (mD)	References
(0~20)		Bergenback and Terriere, (1953)
6 (0~30)	4.5 (0~85), cracks, fractures 2,500	Myers et al. (1956)
6	(0-85)	Burnside (1959)
10.3	30.6	Vest, (1970)
3.93	19.4	Kane, (1979)
9.41	3.03	Langston et al. (1988)
9.8 (0~22.5)	19 (0.1~1760)	Raines, (2005)
7.6	19.4	Brnak et al. (2006)
Sponge mound facies: 15~20 Phylloid mound facies: <15 Oolitic grainstone facies: 20~30 Peritida mud facies: poor, locally reach 5 Breccia facies: poor, locally reach 10		Schatzinger, (1988)
Oolitic grainstone facies: 25~30 Bioclastic grainstone facies: 20~25 Algal wackestone facies: 15~20	Oolitic grainstone facies: >100 Bioclastic grainstone facies: 10~50 Algal wackestone facies: <10	Cogdell field, Reid and Reid, (1991)

Bergenback and Terriere (1953) megascopically observed porosity from 0–20 % and Myers et al. (1956) observed porosity from 0–30 % after core analysis. Both found that most of the porosity is secondary with mineralization evidence such as calcitization, dolomitization, and silicification. Burnside (1959) indicates that

open fractures markedly influence the permeability. Other studies such as Vest (1970), Kane (1979), Langston et al. (1988), Raines (2005), and Brnak et al. (2006) also provide average porosity and permeability, and the reader is referred to these studies for more detailed discussion.

Schatzinger (1988) divided the eastern part of the Horseshoe Atoll into three zones with respect to the depositional environments. The first zone includes the Cogdell field and northern SACROC (Figure 4.1), both reflecting turbulent environments with deposition of basin-facing ooid shoals. Central and southern SACROC shows intermediate turbulence conditions with deposition of sponge-algal-bryozoan buildups. Finally, the stratigraphy of both the Diamond M field (Figure 4.1) and southern SACROC reflect a low turbulence environment.

Research by Reid and Reid (1991) was more focused on the Cogdell field (Figure 4.1). In their work, the reef limestone was divided into nine zones after fusulinid age-dating and log correlations. Recently, there has been a similar effort to build stratigraphic frameworks and porosity distributions from correlation of fusulinid biostratigraphy in SACROC northern platform (Hawkins et al. 1996). Hawkins et al. (1996) indicate that the biostratigraphic distinction is significant because examination

of core and correlation with logs suggests that porosity patterns are closely related to changes in depositional facies.

4.2.2. Depositional Environments

Carbonate distribution and reef buildup were greatly influenced by the depositional environment such as prevailing winds, climate, ocean currents, and paleolatitude. Several workers have attempted to identify depositional environments from the present distribution of carbonate lithofacies in this area. Initially, Bergenback and Terriere (1953) inferred depositional environments from the distribution of carbonate lithofacies such as calcilutite (calcitic mud) and oolitic limestone, which were respectively deposited in environments with quiet water and strong currents. Myers et al. (1956) discussed the possible theories of atoll growth and concluded that the "winds and currents" theory by Fairbridge (1950) accounted for the shape of the Horseshoe Atoll. Their research deduces that the direction of prevailing wind and currents was from south to north (Figure 4.1). Later, Schatzinger (1988) recognized the spatial variation of oolites, which evidently decrease from north to south, in the eastern portions of the Horseshoe Atoll such as

Cogdell field, SACROC, and Diamond M field, and inferred that sedimentation was influenced by east-northeast prevailing winds (Figure 4.1).

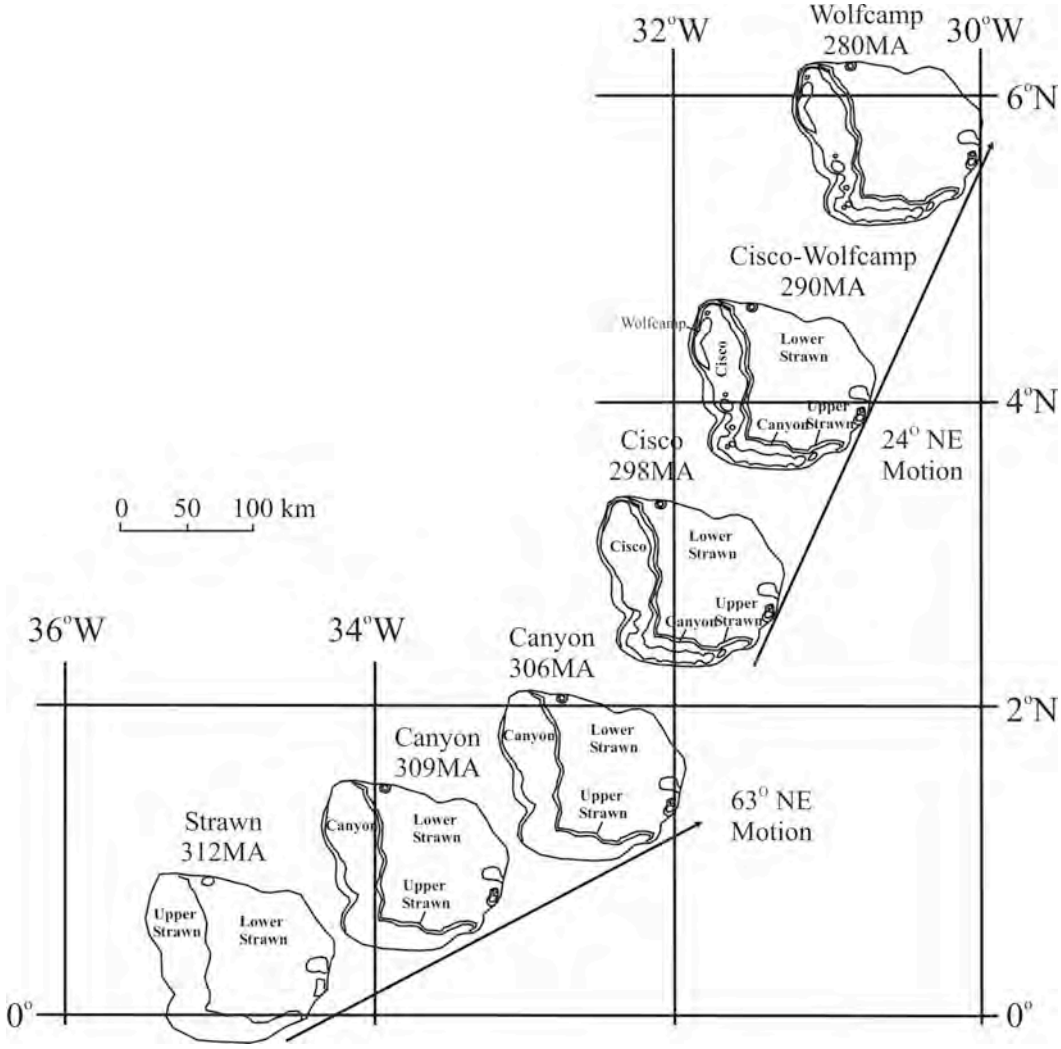

Figure 4.4. The orientation and geologic location of the Horseshoe Atoll through geologic time (Walker et al. 1991).

Walker et al. (1991) tried to identify the distribution of carbonate species and accretion of the Horseshoe Atoll by placing it in its paleolatitude and paleogeographic

orientation (Figure 4.4). According to their research, the carbonate platform was on the equator in the early Strawn (312 Ma). From early Strawn (312 Ma) to middle Canyon (306 Ma), the relative motion of the carbonate platform was north 63 degrees and the platform accumulated at 2 degrees north latitude. From early Cisco (298 Ma) to Wolfcampian (280 Ma), the direction of movement changed to north 24 degrees east. As a result, the platform moved from 2 to 4 degrees North Latitude. Finally, carbonate accumulation stopped during the Wolfcampian at 6 degrees North Latitude due to the influx of fine-grained siliciclastics and dark shales (Walker et al. 1991). During its accumulation, prevailing winds from the northeast had a major impact on the distribution of carbonate facies, showing that the percentage of oolitic carbonate is highest on the northeast-facing edges of the platform.

4.3. Historical Overview of SACROC Petroleum Production

4.3.1. Reservoir Descriptions

The SACROC Unit, comprising about 98% of the Kelly-Snyder field, was discovered by the Standard Oil Company of Texas in November 1948. The original oil in place (OOIP) in this Unit was estimated at approximately 2.73 billion STB (Stock Tank Barrel) in the Canyon reef limestone formation and had a solution gas

content slightly under 1,000 scf/STB, with a bubble point pressure of 1,805 psi (12.45 MPa) (Dicharry et al. 1973). Later, Kane (1979) estimated the OOIP as 2.1 billion STB and van Everdingen and Kriss (1980) as 2.113 billion STB. Table 4.2 summarizes SACROC reservoir parameters.

Table 4.2. Reservoir parameters in SACROC, estimated by Vest (1970).

Rock properties	
Porosity (%)	
Net (>3%)	10.03
Gross	7.11
Permeability (mDarcy)	
Net (>3%)	19.4
Gross	30.6
Fluid Properties	
Gravity of oil (°API)	42 (=0.816 specific gravity)
Sulfur (%)	0.183
Formation volume factor (bbl/bbl @SP)	1.500
Viscosity of oil (cp @SP)	0.375 (=0.375×10^{-5} kg/m-s)
Gas cap	None
Gravity of gas	1.13
Solution gas-oil ratio (CFPB @SP)	1000
Water salinity (mg/l)	159000
Water saturation (%)	28.2
Pressure	
Initial reservoir pressure (psig@-4300ft)	3122 (21.53 MPa@-1310.64m)
Bubble point pressure (psig)	1805 (12.45 MP)
Critical gas-saturation pressure (psig)	±1600 (11.03 MPa)

Table 4.2. *Continued*

Oil producing mechanism	
1948 – 1953	Solution gas drive
1954 – 1971	Artificial water injection drive (Center line)
1972 – Current	Pattern waterflood / CO_2 injection drive
Pay section	
Maximum oil column (ft)	765 (233.17 m)
Average pay thickness (ft)	229 (69.80 m)
Estimated oil in place (billion bbl)	2.73
Estimated total oil recovery (%)	51.7

*SP: Standard pressure, *CFPB: cubic feet per barrel

4.3.2. Solution Gas Drive (Primary Production)

From 1948 to 1951, over 1200 producing wells with 81 individual operators were drilled in the Canyon reef complex (Bayat et al. 1996). Solution gas drive was an early production mechanism.

During this period, the original reservoir pressure (3122 psia = 21.53 MPa) had dropped by over 50% (1560 psi = 11.38 MPa), with only 5% of OOIP produced (Figure 4.5a; Dicharry et al. 1973; Brummett, et al. 1976). Due to the lower oil production and the reduction of reservoir pressure, it became necessary to increase and then maintain reservoir pressure to improve oil recovery.

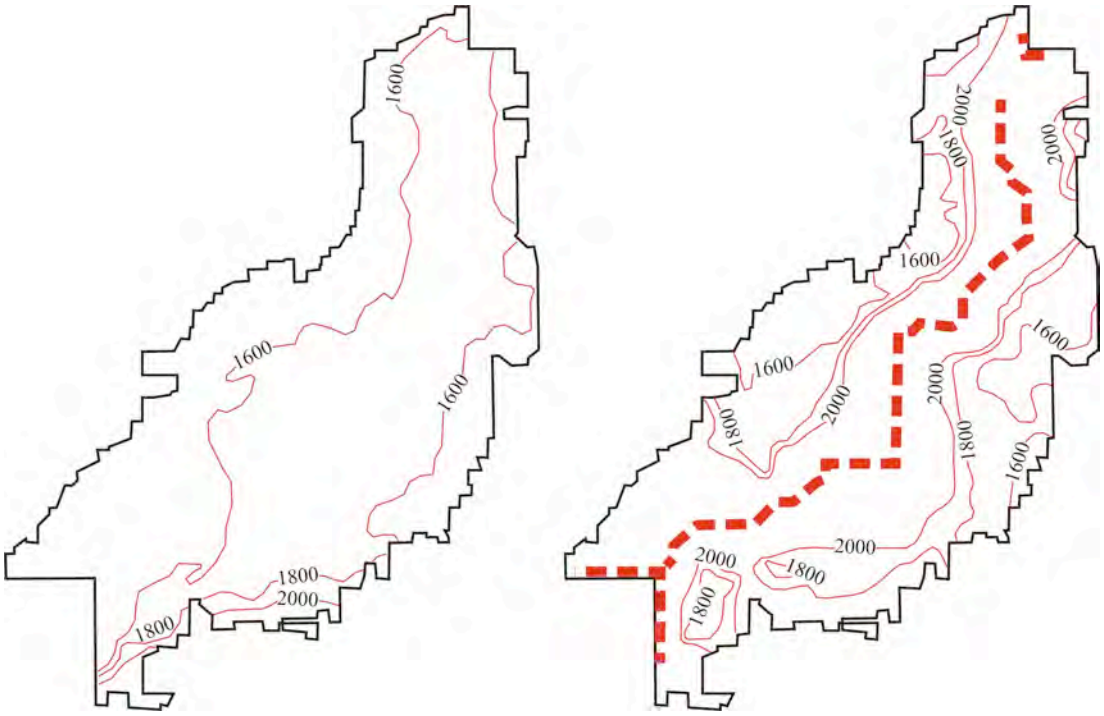

(a) April 1954 (b) April 1970

Figure 4.5. Contour and dotted lines, respectively, indicate the bottom hole pressure (psi) and the location of center-line water injection wells (Dicharry et al. 1973). (a) Five months before starting water injection (September 1954). Only 1 % of reservoir volume is above bubble point pressure (1805 psig=12.45 MPa). (b) Seventeen years later after starting water injection (September 1970). 77 % of the reservoir volume is above bubble point pressure.

4.3.3. Center Line Waterflooding (Secondary Production)

To improve oil production and prevent pressure loss, operators and royalty owners agreed to start a pressure maintenance program, the largest of its kind at the time. In 1953, the Texas Railroad Commission approved the formation of the SACROC (Scurry Area Canyon Reef Operators Committee) Unit. The operation of SACROC Unit was significantly different from that of previous fields in the region.

This was the first approval of a pressure maintenance project by the Texas Railroad Commission. In addition, it was the first approval of a center-to-edge injection project, as opposed to a pattern flood (Burkett, 1979).

In September 1954, the pressure maintenance project started with 53 water injection wells having a injection rate of 132,000 barrels of water per day (BWPD) along the crest of Canyon reef describing the "center-line pattern" injection (Figure 4.5b; Allen and LaRue, 1957; Allen and Thomas, 1959; Dixon and Newton, 1965; Dicharry et al. 1973; Brummett et al. 1976; Bayat et al. 1996). Water was injected throughout the oil section from the reef top to the oil-water contact (Dixon and Newton, 1965). The goal of this "center-line" injection scheme was to increase the reservoir pressure back above the bubble point (1805 psig = 12.45 MPa) and push oil from the center of the SACROC Unit toward the eastern and western boundaries. Soon, the water injection wells at both northern and southern boundaries were added to keep oil from migrating into Fullerton area (NE) (Current Cogdell field) and Diamond M Unit (SW) illustrated in Figure 4.1. As a result, the total number of water injection wells increased to 72.

Between 1969 and 1971, an additional 72 wells were converted to injection wells, resulting in a total of 144 center-line water injection wells because the oil-

producing wells near the center-line converted into water injection wells as the front of waterflooding moves to the margin of SACROC (Burkett, 1979; Kane, 1979). In sum, at the end of the initial water injection period in 1971, 771 million barrels of water had been injected into the Canyon reef formation. Reservoir pressure had increased to 2350 psi (16.20 MPa) in the central portion of the SACROC Unit and 408 million barrels of oil had been produced (Kane, 1979).

Pressure maintenance plan by center-line water flooding permitted a large volume of water to be injected into the thick portion of the Canyon reef, resulting in repressurization of the reservoir. Before waterflooding began, only 1% of the reservoir was above bubble point pressure. Forty-five percent of the area rose above bubble point pressure in less than two years and 77 % was above bubble point pressure after 17 years of water injection (Figure 4.5b). Center-line water injection swept 72 % of the reservoir volume with oil saturation decreasing to 26% (Burkett, 1979).

However, in spite of high sweep efficiency of waterflooding, the mass-balance calculation indicates that approximately 1.2 billion STB of oil was still left at the end of water injection period in 1972 (Dicharry et al. 1973). In addition, the implementation of the repressurization plan eventually resulted in high reservoir

pressure in the center of the unit, but low pressures towards the eastern and western margins (Dicharry et al. 1973). Because of the tremendous volume of oil still left in the reservoir after waterflooding, other enhanced oil recovery (EOR) techniques were considered to improve oil recovery.

4.3.4. Early CO_2 Miscible Enhanced Oil Recovery (Early Tertiary Production)

4.3.4.1. Prior to the CO_2-WAG project

Initially, the SACROC engineering committee considered three enhanced oil recovery techniques: (1) reinjecting dry residue gas, (2) an enriched gas-miscible process, and (3) CO_2-miscible enhanced oil recovery (Dicharry et al.; 1973; Burkett, 1979). The idea of reinjecting dry residue gas was rejected because the average reservoir pressure was too low to afford miscibility between reinjected gas and oil. Recycling dry residue gas failed to increase the reservoir pressure up to the minimum miscibility pressure (MMP). An enriched gas from gasoline plant mixed with propane was also suggested as a promising option. A laboratory study indicated that miscibility could be achieved when about 285 barrels of propane was added to one million standard cubic feet of residue gas. The producing mixture at 2000 psi (13.79 MPa) and 130°F (54.4°C) would have a mobility 19 times greater than that of

SACROC crude oil (Dicharry et al. 1973). However, the high cost of the injected material (propane) made this process less attractive than CO_2 miscible enhanced oil recovery.

After the study was performed, a CO_2-miscible enhanced oil recovery process was chosen to improve oil recovery at SACROC. The summary of several characteristics determined by laboratory (Dicharry et al.; 1973; Burkett, 1979) is as follows:

1. CO_2 will vaporize and subsequently extract lighter hydrocarbons in the crude oil. The lighter hydrocarbons, after contacting CO_2, will be displaced as a gas from the crude oil and will condense to form a bank of light hydrocarbons. After the lighter hydrocarbons are vaporized, the remaining oil in the pore will have a higher density compared to the density of original crude oil.
2. After CO_2 was dissolved in the crude oil, the density of the oil increased. As a result, the density contrast between oil and reservoir fluid (brine) became smaller. This allowed for improved sweep efficiency, due to the lessened tendency for the oil to override the brine.

3. The CO_2 flooding test using 100 ft long sand pack saturated with SACROC reservoir fluid indicated that pressure, temperature, and oil composition conditions conducive to 100% oil displacement did exist in the SACROC reservoir.

4. The reservoir pressure and fluid properties within the SACROC Unit were ideal for the miscible recovery process, after repressurization by waterflood.

5. The mixed volume of CO_2 and oil would be 25% greater than that of the original crude oil due to swelling, which would allow additional oil to be contacted with flood waters.

6. The CO_2 would reduce oil viscosity and surface tension, thus increasing the miscible fluid's mobility.

7. The reaction of injected CO_2 and reservoir fluid will form a weak carbonate acid and cause pH to decrease. Although pH is buffered by carbonate rock, pH of reservoir fluid will still decrease to 4~5. This low pH fluid will induce a chemical disequilibrium between reservoir fluid and host rock. As a result, further chemical reactions will improve the permeability of the reservoir and injectivity.

4.3.4.2. Early CO_2 Source and Supply (Val Verde Basin)

Based on scientific research and engineering calculations, the SACROC committee decided on CO_2 injection as the recovery process. The major task was to find the closest CO_2 sources near SACROC. The closest CO_2 source was Ellenburger hydrocarbon gas fields in the Val Verde basin where CO_2 produced from natural gas fields with CO_2 contamination of 18 to 53% (Newton and McClay, 1977), about 220 miles (354 km) south of SACROC (Figure 4.6). In this field, CO_2 was vented as a byproduct from several gas plants.

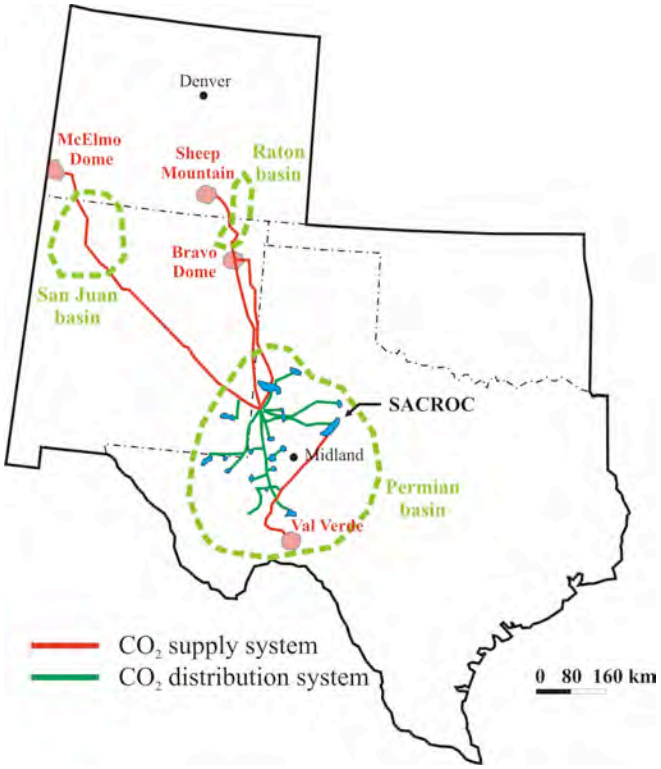

Figure 4.6. CO_2 source and supply system, as of 2005.

Canyon Reef Carriers (CRC) was formed December 1970 to deliver CO_2 from the Val Verde basin to the SACROC Unit. The construction of the 220-mile long CO_2 pipeline was completed in 1971. The system was capable of transporting 200 MMCF/day (Kane, 1979). However, due to operational problems such as compressor malfunctions, the CO_2 pipeline never delivered CO_2 at the planned rate. The maximum CO_2 delivery rate was about 75% of the planned 200 MMCF/day rate until an additional CO_2 compression station was built (Burkett, 1979; Kane, 1979). Design and management of infrastructures are discussed in detail by Newton and McClay (1977) and Gill (1982).

4.3.4.3. Early Designs of a CO_2-WAG Project

The 200 MMCF/day of CO_2 supply rate was not enough to inject into the entire SACROC Unit simultaneously. Rather, this supply rate was equivalent to one-third of the unit's desired volume. Therefore, the SACROC engineering committee decided to divide the CO_2 target area into Phases I, II, and III, as shown in Figure 4.7. Each phase had approximately equal hydrocarbon pore volumes (HCPV).

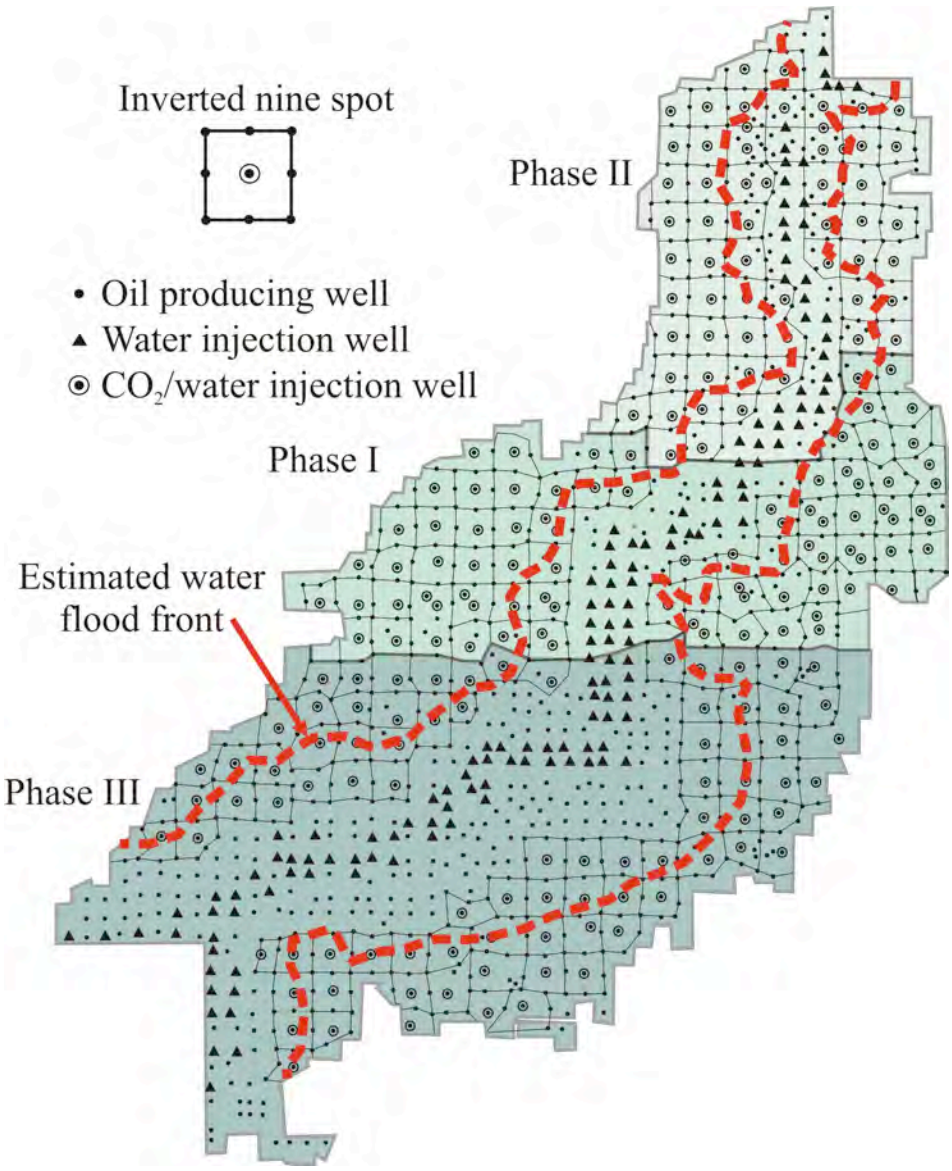

Figure 4.7. Well locations and phase areas in the 1973 SACROC Unit CO_2 development plan (Kane, 1979).

Initially, the plan was to inject a continuous slug of CO_2 equal in volume to 20 % of a Hydrocarbon Pore Volume (HCPV) followed by continuous water injection. The plan included 174 inverted nine-spot patterns (Figure 4.7) in the area where the

water front had not invaded the formation. However, the initial plan was changed to improve the oil recovery (Kane, 1979; Burkett, 1979). The changed plans are summarized here from Burkett, (1979):

1. The area chosen for CO_2 injection was expanded to include 28 additional inverted nine-spot patterns (total 202 inverted nine-spots), including patterns touching the leading edge of the water front (Figure 4.7).

2. To improve the overall oil recovery efficiency, a Water-Alternating-with-Gas (WAG) injection program was chosen (where relatively small volumes of injected fluids alternate between CO_2 and water until the ultimate desired CO_2 volume is obtained) instead of the "continuous slug" method (where the entire volume of CO_2 is injected in one phase and water follows at the end of the program).

3. The "chase volumes" (the amount of water to follow the CO_2 at the end of the injection life cycle) was also changed. After the continuous CO_2 slug volume of 6.0 % HCPV had been injected, the initial plan called for a 2.8 % HCPV slug of chase water (WAG ratio

of 0.47:1). Instead, it was decided to follow the CO_2 with 3.6 % water for a WAG ratio of 0.6:1.

4. Originally, the plan called for CO_2 to be the first injectant in each expansion pattern. However, they instead injected a 6 % HCPV slug of water ahead of the first CO_2 slug. Although the areas near the center-line water injectors were at relatively high pressures, the areas around the carbonate reef flanks had not been repressurized by the existing (centerline) water injection program, due to the long distances between the water injectors and wells in the flank areas. Because the pressures did not reach the minimum miscibility pressure (MMP) of 1600 psi (11.03 MPa) in these remote areas, it was necessary to repressurize each pattern prior to CO_2 injection. Therefore, the primary purpose of having the water slug first was to insure that MMP had been established before CO_2 was introduced into the pattern.

A WAG process had been chosen because it was estimated that a WAG approach would result in improved recovery by one or two percent more than continuous CO_2 injection. In addition, the mobility ratio of water with respect to oil (0.3) is better than that of CO_2 with respect to oil (0.8), since injecting water enhances

the displacement of oil (Burkett, 1979). Additionally, WAG offered an advantage in that it allowed for the total unit to be exposed to CO_2. After injecting CO_2 into the Phase I Area, the available CO_2 could be switched to inject into the second area, while the first area was receiving its water slug.

4.3.4.4. Pre-CO_2 Water Injection

A laboratory study identified that the MMP for CO_2 was 1600 psi (11.03 MPa) in SACROC crude oil (Dicharry et al. 1973). Because a large part of the field did not receive waterflooding support (and associated pressure increases), pressures in the targeted area for the WAG project were typically below the MMP. Therefore, pre-CO_2 water injection was started in Phase I in October 1971 prior to the CO_2 injection. A total of 21.5 million barrels of pre-CO_2 water (representing 3.7 % HCPV) was injected into 56 of 66 nine-spot patterns in Phase 1 (Kane, 1979). Consequently, the average pressure of patterns exceeded of 2400 psi (16 MPa) by April 1973 (Langston et al. 1988). Similarly, pre CO_2-water injection from June 1972 to December 1973 in the Phase II area resulted in an increase in pressure to 2209 psi (15.23MPa). In the Phase III area, pre-CO_2 water injection caused increases in pressure from 1816 psi (12.52 MPa) to 2696 psi (18.59 MPa).

4.3.4.5. Early CO_2 Project

After pre-CO_2 water injection, CO_2 injection was begun in Phase I in January 1972 (Figure 4.7). Although the original reservoir pressure (1600 psi =11.03 MPa) was below minimum miscible pressure (MMP), it rose above the MMP (2400 psi =16.55 MPa) after pre-CO_2 water injection followed by CO_2 injection in April 1973 (Langston et al. 1988). As a result of the increased pressure due to the pre-CO_2 water injection from January 1972 to April 1973, the oil production rate increased by more than three times from 30,000 barrels per day (BBL/D) to 100,000 barrels per day (BBL/D) in Phase I (Bayat et al. 1996). The pre-water injection in Phase II began in June 1972 with a rising oil production rate from 40,000 barrels per day to 80,000 barrels per day (Langston et al. 1988; Bayat et al. 1996). The increase in production rate apparently began after the beginning of CO_2 injection in March, 1974. Finally, pre-CO_2 water injection was begun in April, 1973 in Phase III with production increasing from 30,000 barrels per day to 40,000 barrels per day. At the end of November 1976, 138 million barrels of pre-water was injected in Phase III area (Bayat et al. 1996).

After starting the CO_2-WAG process, significant problems led to changes in the original plan. Initially, all the available CO_2 was planned to be injected into the Phase I area until the first 6% HCPV slug had been injected, and then switched to the Phase II area while the 2.8% HCPV slug of water was being injected into Phase I (Burkett, 1979). However, this plan had to be changed due to the unexpected breakthrough of CO_2 from producing wells in Phase I.

Based on laboratory research, CO_2 breakthrough was supposed to occur in producing wells after three years. However, within six months of the initial CO_2 injection in June 1972, CO_2 breakthrough occurred in the producing wells. Soon the peak of CO_2 production was reached in November 1972 and CO_2 production exceeded the capacity (3000 Mcf/D=84.95 Mm^3/d) of the existing CO_2 removal facility (Kane, 1979). Therefore, it was necessary to curtail oil production until the middle of 1973 to complete additional CO_2 removal facilities.

One of the critical problems was the occurrence of early CO_2 breakthrough causing a large volume of CO_2 in producing wells. Based on extensive research, the main causes of the premature CO_2 breakthrough in the producing wells were found to be the existence of: 1) preferential flow paths for the (CO_2) gas, and 2) low pressure zones, which created an immiscible gas drive. The latter problem was easy to solve,

because the immiscible gas phase could be converted into the miscible phase by controlling reservoir pressure through several methods, including additional pre-CO_2 water injection.

However, dealing with preferential flow paths by reservoir heterogeneity was not an easy problem. Based on field and laboratory studies, it was discovered that CO_2 production could be controlled by both increasing WAG ratio and decreasing the size of the CO_2 slug. In the original design, CO_2 slug volumes were to be 6.0 % HCPV followed by a 3.6 % HCPV slug of chase water. However, this ratio was soon increased to 1:1 (and was increased even more, to 1:3, in late 1973). In addition, the CO_2 slug size was reduced from 6.0 % HCPV to 1.5 % in late 1973 (Kane, 1979). Additionally, the SACROC Engineering committee suggested a zonal injection control program in 1973. Before this program, only 36 of 202 pattern injectors were cased through 50% or more of the reef. To avoid cycling CO_2, to keep produced CO_2 volumes within the limits of the CO_2 removal capacity, and to inject CO_2 into all pay zones in reservoir, a liners across the reef and downhole flow controller were installed.

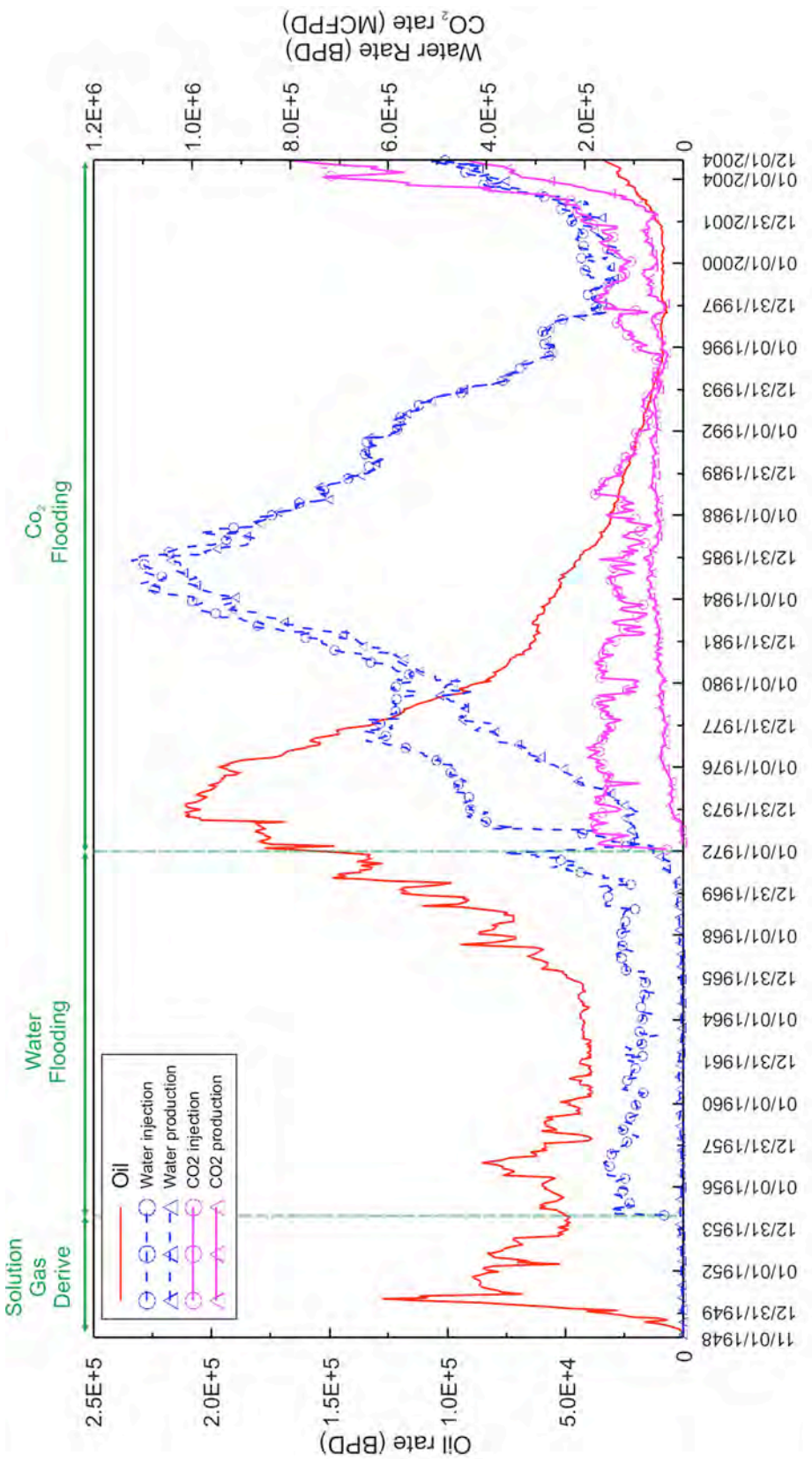

Figure 4.8. Injection and production history of oil, water, and CO_2 (Raines et al., 2005)

4.3.4.6. Evaluation of the Early CO_2 Project

During the period from 1972 to 1985, waterflooding efforts increased for increasing reservoir pressure over MMP prior to CO_2 injection (Figure 4.8), to make CO_2 more miscible in oil. However, in this period, the amount of injected CO_2 was actually relatively small (Figure 4.8) and the CO_2 injection wells were scattered. Moreover, the CO_2 supply was not continuous. Because of the discontinuity of CO_2 injection and the difficulty of maintaining CO_2 supply, the early CO_2 project was not regarded as a "Modern CO_2 operation" (see section 4.4.4 for discussion).

Results of subsequent geologic modeling studies in 1986 indicated that waterflooding already swept all of the oil which could expect from waterflooding area with high porosity and permeability. Moreover, it became difficult to handle the large volume of produced water. Therefore, waterflooding volumes were gradually decreased after 1985.

4.4.4. Modern Concept of CO_2 Miscible Enhanced Oil Recovery (Current Tertiary Production)

After 1995, Pennzoil gradually increased CO_2 injection (Figure 4.8). First, Pennzoil injected CO_2 into two project areas as opposed to previously scattering

injection patterns over the SACROC Unit. Subsequently, Pennzoil started to supply CO_2 from McElmo Dome, a natural CO_2 reservoir in Colorado under a transportation and supply agreement in June 1996 (Raines, *Personal communication*, 2006) and improved the CO_2 supply (Figure 4.6). Table 4.3 is the summary of site characterization at the McElmo Dome.

Table 4.3. Summary of site characterization in McElmo dome in Colorado (Gerling, 1983; Tremain, 1993; Allis et al. 2001).

Area	800 km^2	Avg. Depth	2100 m
Net thickness	21 m	Gross thickness	90 m
Reservoir lithology	Mississippian Leadville Limestone	Seal lithology	Pennsylvanian Paradox salt
Porosity	3-20% (11%)	Permeability	23 mD
Total CO2 reserves	476 billion m^3 (17 trillion cubic feet)		
Gas composition	CO_2: 98.2%, N_2: 1.6%, CH_4: 0.2%		
Water chemistry (mg/kg)	TDS: 27000-44000, Na: 8500-1400, Ca: 800-1900, Mg: 130-400, Fe: 70-135, Cl: 11000-23000, HCO_3: 3300-3900, SO_4: 1400-1900		
Production	6.2-8.8 billion m^3/yr (220-315 billion cubic feet/yr) since 1995		
Cumulative production	92 billion m^3 (3.3 trillion cubic feet) through 1999		

By changing the source of CO_2 from a natural reservoir, operations became more stable because of the continuous CO_2 supply (not relying on the gas plants, which were subject to potential shutdowns due to their own problems). A detailed review of CO_2 production operations from the natural reservoir in Colorado is

discussed by Weeter and Halstead (1981). Finally, Penzoil started to put the CO_2 into regular shaped patterns as injector-centered 5 spots. Previously, regular patterns were not implemented in CO_2 flooding areas.

However, even this operation was not as efficient and effective as modern CO_2 operations. Despite Pennzoil's effort, oil production did not increase dramatically (Figure 4.8). One of the reasons for lack of improved production was that Pennzoil did not ensure that the entire production pattern remained above minimum miscible pressure (MMP) and they did not implement measures to keep oil from migrating outside of the project area. Moreover, Pennzoil targeted oil missed by the waterflooding. However, the areas missed by waterflooding are areas that do not easily transmit fluids (Raines, 2001).

Since Kinder Morgan CO_2 purchased this field from Devon, who acquired Pennzoil following bankruptcy in August 2000, oil production rate increased dramatically (Figure 4.8). After Kinder Morgan CO_2 became the operator of this field, SACROC became a "modern CO_2 operation". A "modern CO_2 operation" is defined by Raines, (2001) as: (1) target residual oil after waterflooding, (2) control reservoir pressure through either pre-CO_2 water injection or the operation of water curtain wells, (3) use smaller (~40 acres) patterns, (4) avoid CO_2 flooding where high

CO_2 relative permeability is observed, (5) perform CO_2 flooding where successful waterflooding was performed.

While Pennzoil was exploring for areas of unswept waterflooding oil, Kinder Morgan CO_2 targeted a post-waterflooded oil (residual-to-waterflood oil) (Raines, 2001; 2005). In addition to the change of its target area, Kinder Morgan CO_2 tried to use a "water curtain" (a row of water injection wells) for the purpose of closing the outer boundary within each injection patterns. A water curtain may help keep fluid pressure at the desired level across the entire pattern, creating a pressure barrier to minimize fluid migration past the production wells, and acts effectively as a physical barrier. In addition, Kinder Morgan CO_2 found that most successful CO_2 flooding has taken place along portions of the oil waterflooding center-lines. As discussed by Raines (2001), 6000 BOPD oil were produced in the middle portion of the old centerline area.

4.5. Summary and Conclusion

SACROC Unit is the world's second oldest continuous CO_2-flooding operations since 1972. Because of its history and the amount of injected CO_2, SACROC Unit is regarded as a valuable example of an anthropogenic analog site of

CO_2 sequestration. Extensive records of injection/production history are available and infrastructure for CO_2 injection already exists. Further, SACROC provides direct evidence of rock properties changes associated with CO_2 injection over time, which is difficult to observe in the laboratory experiments.

However, although the attention of this site is growing because this site has many advantages, researchers have had a difficult time finding relevant materials for describing this site because related articles are relatively old and were primarily published in petroleum-associated journals. Further, the complicated injection/production history makes this site even more difficult for researchers to study.

Therefore, the primary purpose of this chapter was to provide a concise overview of geology and production history in SACROC Unit to other researchers. Additionally, discussion associated with geologic parameters and injection/production performance are used for the decision-making process while developing the numerical model evaluating CO_2 trapping mechanisms in northern platform SACROC described in chapter 6 and 7. Therefore, understanding of chapter 4 will aid to understand the following chapters.

References

Allen, H.H., LaRue, C.R., 1957. SACROC Unit operations. Society of Petroleum Engineers Journal 829.

Allen, H.H., Thomas, J.B., 1959. Pressure maintenance in SACROC Unit operations January 1, 1959. Society of Petroleum Engineers Journal 1259.

Allis, R., White, S., Chidsey, T., Gwynn, W., Morgan, C., Adams, M., Moore, J., 2001. Natural CO_2 reservoirs on the Colorado plateau and southern Rocky Mountains: Candidates for CO_2 sequestration. Proceedings of the First National Conference on Carbon Sequestration, Washington DC, May.

Bayat, M.G., Pickard, C.D., Benvegnu, A.J., Wingate, T.P., Larkin, R., 1996. Linking reservoir characteristics and recovery processes at SACROC-controlling wasteful cycling of fluids at SACROC while maximizing reserves. Second Annual Subsurface Fluid Control Symposium and Conference.

Bergenback, R.E., Terriere, R.T., 1953. Petrography and petrology of Scurry reef, Scurry County, Texas. American Association of Petroleum Geologists Bulletin. 37(5), 1014-1029.

Brnak, J., Petrich, B., Konopczynski, M.R., 2006. Application of smartwell technology to the SACROC CO_2 EOR project: A case study. Society of Petroleum Engineers Journal 100117.

Brummett, Jr., W.M., Emanuel, A.S., Ronquille, J.D., 1976. Reservoir description by simulation at SACROC-a case history. Society of Petroleum Engineers Journal 5536.

Burkett, G.D., 1979. Review of the carbon dioxide enhanced oil recovery project at the SACROC Unit-Kelly-Snyder field, Texas. Chevron Technical Report.

Burnside, R.J., 1959. Geology of part of Horseshoe Atoll in Borden and Howard Counties, Texas. Geological Survey Professional Paper 315-B, 34.

Carey, J.W., Wigand, M., Chipera, S., Woldegabriel, G., Pawar, R., Lichtner, P., Wehner, S., Raines, M., Guthrie, J., 2007. Analysis and performance of oil

well cement with 30 years of CO_2 exposure from the SACROC Unit, west Texas. International Journal of Greenhouse Gas Control 1(1), 75-85.

Dicharry, R.M., Pettyman, T.L., Ronquille, J.D., 1973. Evaluation and design of a CO_2 miscible flood project-SACROC Unit, Kelly-Snyder field. Society of Petroleum Engineers Journal 4083.

Dixon, B.P., Newton, Jr., L.E., 1965. Rejection of large volumes of produced water in secondary operations. Society of Petroleum Engineers Journal 1147.

Fairbridge, R.W., 1950. Recent and Pleistocene coral reefs of Australia. Geology 58(4), 330-401.

Gerling, C.R., 1983. McElmo dome Leadville carbon dioxide field, Colorado. In Fassett, J.E., ed. Oil and gas fields of the four corners area," Four corners geological society, 3, 735-739.

Gill, T.E., 1982. Ten years of handling CO_2 for SACROC unit. Society of Petroleum Engineers Journal 11162.

Graue, D.J., Blevins, T.R., 1978. SACROC tertiary CO_2 pilot project. Society of Petroleum Engineers Journal 7090.

Han, W.S., McPherson, B.J., Raines, M., Sulaiman, A.I., 2006. Comparison of two CO_2 EOS algorithms: Minor contrasts in state properties may translate to significant contrasts in predicted migration histories, Proceedings of the 5th Annual Conference on Carbon Capture & Sequestration, Alexandria, Virginia.

Hawkins, J.T., Benvegnu, A.J., Wingate, T.P., McKamie, J.D., Pickard, C.D., Altum, J.T., 1996. SACROC unit CO_2 flood: Multidisciplinary team improves reservoir management and decreases operating costs. Society of Petroleum Engineers Journal 35359.

Holtz, M. H., Smyth, R.C., McPherson, B.J., Han, W.S., 2006. Subsurface characterization of CO_2 sequestration sites, example from a carbonate reef setting. Proceedings of International Symposium on Site Characterization for CO_2 Geological Storages (CO2SC), Lawrence Berkeley National Laboratory, Berkeley, California.

Kane, A.V., 1979. Performance review of large-scale CO_2-Wag enhanced recovery project, SACROC unit-Kelly-Snyder field. Society of Petroleum Engineers Journal 7091.

Langston, M.V., Hoadley, S.F., Young, D.N., 1988. Definitive CO_2 flooding response in the SACROC Unit. Society of Petroleum Engineers Journal 17321.

Myers, D.A., Stafford, P.T., Burnside, R.J., 1956. Geology of the late Paleozoic Horseshoe Atoll in west Texas. Bureau of Economic Geology Publication 5607, p.113.

Newton, Jr., L.E., McClay, R.A., 1977. Corrosion and operational problems, CO_2 project, SACROC Unit. Society of Petroleum Engineers Journal 6391.

Raines, M. A., 2003. Reef Heterogeneity as Seen by Wireline and Cross-well Seismic in the Pennsylvanian SACROC Unit, Scurry County, Texas. The Permian Basin: Back to Basics West Texas Geological Society Fall Symposium, October 8-10, 2003. Abstract in: Hunt, Tim J. and Lufholm, Peter H. (eds.) The Permian Basin: Back to Basics WTGS Publication # 03-112. West Texas Geological Society, Midland, Texas, p.325.

Raines, M. A., 2005. Kelly-Snyder (Cisco-Canyon) Fields/SACROC Unit. West Texas Geological Society: Oil and gas fields in west Texas v.8, Publication number 05-114, p.69-78. West Texas Geological Society, Midland, Texas.

Raines, M.A., Dobitz, J.K., Wehner, S.C., 2001. A review of the Pennsylvanian SACROC Unit. In J.J. Viveros and S.M. Ingram, eds., The Permian basin: Microns to satellites, looking for oil and gas at all scales: West Texas Geological Society Publication 01-110, p.67-74.

Reid, A.M., Reid, S.A.T., 1991. The Cogdell field study, Kent and Scurry counties, Texas: A post-mortem. In M. Candelaria, eds., The Permian basin plays: tomorrow's technology today. West Texas Geological Society Publication 91-89, 39-66.

Schatzinger, R.A. 1988. Changes in facies and depositional environments along and across the trend of Horseshoe Atoll, Scurry and Kent Counties, Texas. In, B.K., Cunningham, eds., Permian and Pennsylvanian Stratigraphy Midland

basin, west Texas: Studies to aid hydrocarbon exploration. Premian Basin Section, Society for Economic Paleontologists and Mineralogists Publication 88-28, p. 79-95.

Stafford, P.T., 1954. Scurry field: Scurry, Kent and Borden Counties, Texas, Herald, F.A. (ed.) Occurrence of oil and gas in west Texas, Bureau of Economic Geology, Austin, Texas, 5716, p.295-302.

Stewart, R.W., 1957. Reef limestones of the North Snyder oil field, Scurry County, Texas. Ph.D Dissertation. Department of of Geology. Massachusetts Institute of Technology.

Tremain, C., 1993. Low-BTU gas in Colorado. In atlas of major Rocky Mountain gas reservoir. New Mexico Bureau of Mines and Mineral Resources, 172 pp.

Van Everdingen, A.F., Kriss, H.S., 1980. A proposal to improve recovery efficiency. Society of Petroleum Engineers Journal 9088.

Vest, E.L.Jr., 1970. Oil Fields of Pennsylvanian-Permian Horseshoe Atoll, West Texas *in* Halbouty, Michael T. (ed.) Geology of Giant Petroleum Fields, AAPG Memoir # 14. American Association of Petroleum Geologists, Tulsa Oklahoma, pp. 185-203.

Walker, D.A., Golonka, J., Reid, A.M., 1991. The effects of late Paleozic paleolatitute and paleogeography on carbonate sediment in the Midland basin, Texas. *in* Candelaria, M. (ed.) Permian basin plays, tomorrow's technology today. West Texas Geological Society Publication 91-89, p. 141-162.

Weeter, R.F., Halstead, L.N., 1981. Production of CO_2 from a reservoir-A new concept. Society of Petroleum Engineers Journal 10283.

CHAPTER 5

DESCRIPTION OF GEM-GHG SIMULATOR

5.1. Introduction

CMG's GEM (Generalized Equation of State Module) simulator is a multi-dimensional, finite-difference, isothermal compositional simulator that can model three-phases (oil, water, gas) and multi-components (CO_2, N_2, C1, C2, C3, C4, C5, C6, C7+ and et al.).

One of the numerical solution schemes in GEM is an adaptive-implicit solution scheme (Collins et al. 1992). The adaptive-implicit scheme is based on the idea that some grids are solved implicitly while the remaining grids are solved explicitly. Generally, the fully explicit scheme is fast and easy to code relative to other schemes. However, its solution is often unstable when the size of time step exceeds a certain limit. Therefore, it is conditionally stable. The fully implicit scheme is unconditionally stable with any time step but it is often intensive with computational time because the generated linear algebraic equations must be solved simultaneously, using an iterative solution method or a direct matrix solution technique (Aziz and Sttari, 1979; Wang and Anderson, 1982; Zheng and Bennett, 2002). The adaptive-implicit scheme increases solution stability by adapting the implicit scheme in certain grid blocks and reduces the simulation time by adapting the

explicit scheme in the rest of the blocks. Because of this specific advantage, the adaptive-implicit scheme has been widely used for reservoir simulation (Thomas and Thurnau, 1981; Bertiger and Kelsey, 1985; Byer et al. 1999; Caillabet et al. 2003).

In the adaptive-implicit scheme, a specific criterion will dictate when a grid block is switched from explicit to implicit. Russell, (1989) has suggested the Courant-Friedrichs-Lewy (CFL) criteria for the adaptive-implicit scheme in black oil simulation. Later, CFL criteria relevant to compositional simulation were developed (Grabenstetter et al. 1991). GEM uses the latter stability test algorithm to decide which grids must be solved in fully implicit or explicit modes.

The GEM simulation package adapts both the Peng-Robinson (Peng and Robinson, 1976) and Soave-Redlich-Kwong (Soave, 1972) equations of state (EOS) to calculate thermodynamic properties such as densities and fugacity coefficients of gas and oil mixture components. The phase equilibrium of the components can be obtained by solving from either Henry's relation or thermodynamic-equilibrium equations ("flash" calculation). Generally, flash calculations of phase equilibrium are complicated and require an iterative procedure. Therefore, flash equilibrium equations are usually decoupled from flow equations to reduce the complexity and increase the flexibility of the solution method (Collins et al. 1992). The decoupled flash equilibrium equations are solved in GEM using the quasi-Newton successive substitution method (QNSS) (Nghiem, 1983).

Recently, the GEM simulator has been developed into a fully coupled geochemical and compositional EOS simulator known as GEM-GHG (Nghiem et al. 2004). The GEM-GHG package is designed for simulating (1) flow and transport in

porous media, (2) phase equilibrium between oil, gas, and aqueous phases, (3) chemical equilibrium reactions between aqueous species, and (4) kinetic reactions of minerals. In general, GEM-GHG is designed for simulating CO_2 trapping mechanisms such as hydrostratigraphic (mobile), aqueous, mineral, and residual gas trapping. Many researchers have performed numerical simulations related to CO_2 sequestration processes with GEM-GHG (Noh et al. 2004; Basbug et al. 2005; Kumar et al. 2004; Calabrese et al. 2005; Ozah et al. 2005; Bryant et al. 2006; Han and McPherson, 2007). The following sections discuss the mathematical representation of GEM-GHG, including its flow governing equations, chemical reactions, equations of state and the changes of rock properties (Figure 5.1).

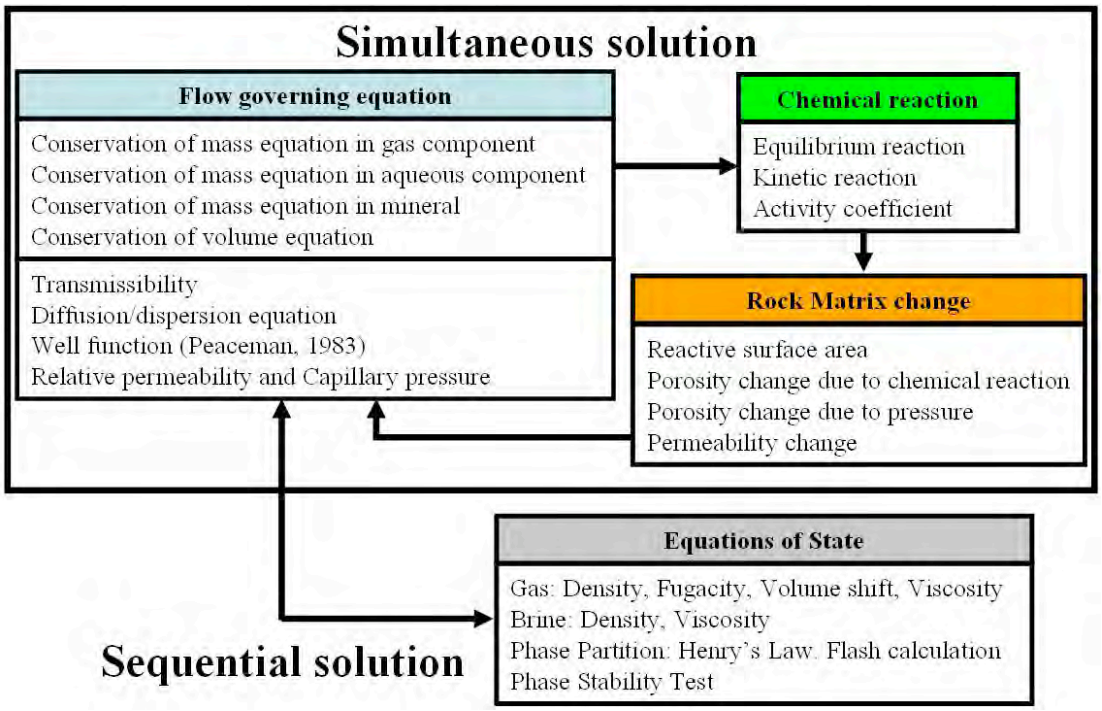

Figure 5.1. The schematic representation of the solution procedure of GEM-GHG.

5.2. Mathematical Representation of General Conservation Equations

This section summarizes the governing equations of multiphase flow. The following derivations of general conservation equations are based on Chen et al. (2006). Table 5.1 defines the parameters involved in the governing equations. Multiphase flow equations can be extended from the single-phase flow equation. The general single-phase equation is

$$\frac{\partial(\phi\rho)}{\partial t} = \nabla\cdot\left(\frac{\rho}{\mu}k(\nabla p - \rho G\nabla z)\right) + q. \qquad \text{(Eq. 5.1)}$$

We present general equations for two-phase flow (e.g. water and oil) equations accounting that the fluids are immiscible. The general two-phase immiscible flow equations are

$$\frac{\partial(\phi\rho_w S_w)}{\partial t} = \nabla\cdot\left(\frac{\rho}{\mu}kk_{rw}(\nabla p_w - \rho_w G\nabla z)\right) + q_w, \qquad \text{(Eq. 5.2)}$$

$$\frac{\partial(\phi\rho_o S_o)}{\partial t} = \nabla\cdot\left(\frac{\rho}{\mu}kk_{ro}(\nabla p_o - \rho_o G\nabla z)\right) + q_o, \qquad \text{(Eq. 5.3)}$$

Additionally, the relations of saturation and capillary pressure are

$$S_w + S_o = 1, \qquad \text{(Eq. 5.4)}$$

$$p_c = p_o - p_w. \qquad \text{(Eq. 5.5)}$$

Compositional flow involves many components and mass transfer between phases. In a compositional model, a finite number of hydrocarbon components are used to represent the composition of reservoir fluids. Several inherent assumptions include:

(1) Three phases (water, oil, and gas) are considered;

(2) No mass interchanges between the water phase and the hydrocarbon phases;

(3) Diffusive effects are neglected.

Instead of using concentration, it is more convenient to employ mole fraction for each component in compositional flow, because phase equilibrium relations are generally determined in terms of mole fraction.

The molar densities in the gas and oil phases are

$$m_g = \sum_{i=1}^{N_c} m_{ig}, \qquad \text{(Eq. 5.6)}$$

$$m_o = \sum_{i=1}^{N_c} m_{io}. \qquad \text{(Eq. 5.7)}$$

The mole fractions of component *i* in the gas and oil phases are

$$x_{ig} = \frac{m_{ig}}{m_g}, \qquad \text{(Eq. 5.8)}$$

$$x_{io} = \frac{m_{io}}{m_o}. \qquad \text{(Eq. 5.9)}$$

The algebraic constraints of mole fraction are

$$\sum_{i=1}^{N_c} x_{ig} = \sum_{i=1}^{N_c} x_{io} = 1. \qquad \text{(Eq.5.10)}$$

The volumetric velocities of each phase are expressed as Darcy's law, or

$$u_g = -\frac{kk_{rg}}{\mu_g}\left(\nabla p_g - \rho_g G \nabla z\right), \qquad \text{(Eq. 5.11)}$$

$$u_w = -\frac{kk_{rw}}{\mu_w}\left(\nabla p_w - \rho_w G \nabla z\right), \qquad \text{(Eq. 5.12)}$$

$$u_o = -\frac{kk_{ro}}{\mu_o}\left(\nabla p_o - \rho_o G \nabla z\right). \qquad \text{(Eq. 5.13)}$$

The mass conservation equations of each component in the fluid phase are

$$\frac{\partial(\phi m_w S_w)}{\partial t} + \nabla \cdot (m_w u_w) = q_w, \qquad \text{(Eq. 5.14)}$$

$$\frac{\partial\left(\phi\left(x_{io} m_o S_o + x_{ig} m_g S_g\right)\right)}{\partial t} + \nabla \cdot \left(x_{io} m_o u_o + x_{ig} m_g u_g\right) = x_{io} q_o + x_{ig} q_g . \qquad \text{(Eq. 5.15)}$$

Finally, the relations of saturation and capillary pressure are

$$S_w + S_o + S_g = 1, \qquad \text{(Eq. 5.16)}$$

$$p_{cow} = p_o - p_w, \; p_{cgo} = p_g - p_o . \qquad \text{(Eq. 5.17)}$$

Table 5.1. Parameters for the general mass conservation equations.

g	Gas	x_i	Mole fraction of component i in the phase
k	Permeability	G	Gravity
k_r	Relative permeability	N_c	Total number of component in the phase
m_i	Molar density of component i in the phase	S	Saturation
o	Oil	Z	Depth
p	Pressure	ϕ	Porosity
p_c	Capillary pressure	μ	Viscosity
q	Sink/source	∇	Divergence operator
w	Water	ρ	Density

5.3. Mathematical Representation of Conservation Equations Describing Gaseous, Aqueous, and Mineral Phases in GEM-GHG

The previous section summarized the governing equations of general multiphase flow equations. In this section, we introduce the governing equations used to simulate the flow and transport of CO_2 with chemical reactions in both GEM and GEM-GHG. A more detailed description is given in Collins et al. (1992), Nghiem et al. (2004), and the GEM user manual (Computer Modeling Group, 2006). The governing equations describing the compositional EOS simulator in porous

media coupled with chemical reactions are based on conservation of mass in gaseous, aqueous, and mineral components. The following paragraph details the governing equations; Table 5.2 defines the parameters involved in the governing equations.

Table 5.2. Parameters for the mass conservation equations for GEM-GHG.

g	Gas	J_{ja}	Diffusion/dispersion of aqueous component
k	Permeability	N_{ig}	Moles of gas component per grid volume
k_r	Relative permeability	N_{ja}	Moles of aqueous component per grid volume
$m_{ig,g}$	Mole fraction of gas component in gas phase	N_{km}	Moles of mineral per grid volume
$m_{ig,w}$	Mole fraction of gas component in aqueous phase	Z	Depth
$m_{ja,w}$	Mole fraction of aqueous component in aqueous phase	ϕ	Porosity
P	Pressure	μ	Viscosity
p_{cwg}	Capillary pressure	ρ	Density
q	Sink/source	$\sigma_{ig,aq}$	Reaction rate between gaseous and aqueous component
s	Saturation	$\sigma_{ja,aq}$	Reaction rate between aqueous and aqueous component
t	Time	$\sigma_{ja,mn}$	Reaction rate between aqueous and mineral component
w	Water	$\sigma_{km,mn}$	Mineral reaction rate
G	Gravity	∇	Divergence operator
J_{ig}	Diffusion/dispersion of gas component		

The conservation of mass equation for gaseous components (g) is

$$\nabla \cdot \left(\frac{\rho_g k k_{rg} m_{ig,g}}{\mu_g} \right) (\nabla p + \nabla p_{cwg} - \rho_g G \nabla z)$$

$$+\nabla \cdot \left(\frac{\rho_w k k_{rw} m_{ig,w}}{\mu_w} \right) \left(\nabla P + \nabla P_{cwg} - \rho_w G \nabla z \right)$$

$$+\nabla \cdot J_{ig} + \sigma_{ig,aq} + q = \frac{\partial N_{ig}}{\partial t}. \qquad \text{(Eq. 5.18)}$$

The conservation of mass equation for aqueous components (aq) is

$$\nabla \cdot \left(\frac{\rho_w k k_{rw} m_{ja,w}}{\mu_w} \right) (\nabla p - \rho_w G \nabla z) + \nabla \cdot J_{ja}$$

$$+ \sigma_{ja,aq} + \sigma_{ja,mn} + q = \frac{\partial N_{ja}}{\partial t}. \qquad \text{(Eq. 5.19)}$$

The conservation of mass equation for minerals (*m*) is

$$\sigma_{km,mn} = \frac{\partial N_{km}}{\partial t}. \qquad \text{(Eq. 5.20)}$$

Finally, the relations of saturation and capillary pressure must be determined.

$$S_w + S_g = 1, \qquad \text{(Eq. 5.21)}$$

$$p_{cwg} = p_g - p_w. \qquad \text{(Eq. 5.22)}$$

5.4. Discretization of Conservation Equations in GEM-GHG

The above governing equations must be discretized to apply a finite difference scheme. After defining the transmissibility (*T*), Eq. (5.18), (5.19), and (5.20) are written again. Table 5.3 defines the parameters involved in the governing equations.

The conservation of mass equation for gaseous components (*g*) is

$$\Delta T_g^u m_{ig,g}^u (\Delta p^{n+1} + \Delta p_{cwg}^u - \rho_g^u G \Delta z) + \Delta T_w^u m_{ig,w}^u (\Delta p^{n+1} - \rho_g^u G \Delta z)$$

$$+ \Delta(A J_{ig}) + V \sigma_{ig,aq}^{n+1} + q_{ig}^{n+1} = \frac{V}{\Delta t} (N_{ig}^{n+1} - N_{ig}^n) \qquad i=1,\ldots,n_g \,.$$

(Eq. 5.23)

The conservation of mass equation for aqueous components (*aq*) is

$$\Delta T_w^u m_{ja,w}^u (\Delta p^{n+1} - \rho_w^u G \Delta z) + \Delta(A J_{ja}) + V \sigma_{ja,aq}^{n+1} + V \sigma_{ja,mn}^{n+1} + q_{ja}^{n+1}$$

$$= \frac{V}{\Delta t} (N_{ja}^{n+1} - N_{ja}^n) \qquad j=n_g+1,\ldots,n_{aq}. \qquad \text{(Eq. 5.24)}$$

The conservation of mass equation for minerals (*m*) is

$$V\sigma_{km,mn}^{n+1} = \frac{V}{\Delta t}(N_{km}^{n+1} - N_{km}^{n}) \qquad k=n_{aq}+1,\ldots,n_s\ . \qquad \text{(Eq. 5.25)}$$

with saturations

$$S_w = \sum_{ja=1}^{n_a} N_{ja}/(\phi\rho_w), \qquad \text{(Eq. 5.26)}$$

$$S_g + S_w = 1. \qquad \text{(Eq. 5.27)}$$

The governing equations (Eq. 5.23, 5.24 and 5.25) are expressed with pressure (P) and moles (N). Saturations (S) of phases are solved from Eq. (5.26) and (5.27). Mass conservation equations governing gaseous (Eq. 5.23) and aqueous components (Eq. 5.24) include transmissibility (T). However, the mass conservation equation describing minerals (Eq. 5.25) does not include transmissibility, indicating that minerals only react with aqueous components without regard to movement.

Table 5.3. Parameters for the discretized mass conservation equations for GEM-GHG.

n_g	Total number of gaseous components		
n_a	Total number of aqueous components		
n_m	Total number of minerals		
n_{aq}	$= n_g + n_a$		
n_s	$= n_g + n_a + n_m = n_{aq} + n_m$		
A	Cross-sectional area	g	Gravity
J_{ig}	Diffusion / dispersion of gas component	d	Depth
J_{ja}	Diffusion/dispersion of aqueous component	t	Time step
N_{ig}	Moles of gas component per grid volume	$m_{ig,g}$	Mole fraction of gas component in gas phase
N_{ja}	Moles of aqueous component per grid volume	$m_{ig,w}$	Mole fraction of gas component in aqueous phase
N_{km}	Moles of minerals per grid volume	$m_{ja,w}$	Mole fraction of aqueous component in aqueous phase
P	Water pressure	$\sigma_{ih,aq}$	Reaction rate between gaseous and aqueous component
P_{cwg}	Capillary pressure between water and gas	$\sigma_{ja,aq}$	Reaction rate between aqueous and aqueous component
q_{ig}	Well molar flow rate of gas component	$\sigma_{ja,mn}$	Reaction rate between aqueous and mineral component
q_{ja}	Well molar flow rate of aqueous component	$\sigma_{km,mn}$	Mineral reaction rate
T_g	Transmissibility of gas phase	ρ_g	Density of gas
T_w	Transmissibility of aqueous phase	ρ_w	Density of water
V	Grid block volume	Δ	Difference operator

The superscript (n) refers to the previous time level, while the superscript ($n+1$) refers to the new time level. The superscript (u) is the term for determining a finite different scheme.

For example, if u is equal to current time (n), the finite different scheme becomes implicit pressure, explicit composition and saturation (IMPECS). The IMPECS equations are

$$\Delta T_g^n m_{ig,g}^n (\Delta p^{n+1} + \Delta p_{cwg}^n - \rho_g^n G\Delta z) + \Delta T_w^n m_{ig,w}^n (\Delta p^{n+1} - \rho_g^n G\Delta z)$$

$$+\Delta(AJ_{ig}) + V\sigma_{ig,aq}^{n+1} + q_{ig}^{n+1} = \frac{V}{\Delta t}(N_{ig}^{n+1} - N_{ig}^n) \qquad i=1,\ldots,n_g \ ,$$

(Eq. 5.28)

$$\Delta T_w^n m_{ja,w}^n (\Delta p^{n+1} - \rho_w^n G\Delta z) + \Delta(AJ_{ja}) + V\sigma_{ja,aq}^{n+1} + V\sigma_{ja,mn}^{n+1} + q_{ja}^{n+1}$$

$$= \frac{V}{\Delta t}(N_{ja}^{n+1} - N_{ja}^n) \qquad i=n_g+1,\ldots,n_{aq}. \qquad \text{(Eq. 5.29)}$$

In the IMPECS scheme, the transmissibility (T), capillary pressure (p_{cwg}), and gravity (ρ) terms are evaluated at the previous time level (n) from the gridblock that it treated with IMPECS.

If u is equal to the new time ($n+1$), the finite different scheme becomes a fully implicit scheme, or

$$\Delta T_g^{n+1} m_{ig,g}^{n+1} (\Delta p^{n+1} + \Delta p_{cwg}^{n+1} - \rho_g^{n+1} G\Delta z) + \Delta T_w^{n+1} m_{ig,w}^{n+1} (\Delta p^{n+1} - \rho_g^{n+1} G\Delta z)$$

$$+\Delta(AJ_{ig}) + V\sigma_{ig,aq}^{n+1} + q_{ig}^{n+1} = \frac{V}{\Delta t}(N_{ig}^{n+1} - N_{ig}^n) \qquad i=1,\ldots,n_g \ ,$$

(Eq. 5.30)

$$\Delta T_w^{n+1} m_{ja,w}^{n+1} (\Delta p^{n+1} - \rho_w^{n+1} G\Delta z) + \Delta(AJ_{ja}) + V\sigma_{ja,aq}^{n+1} + V\sigma_{ja,mn}^{n+1} + q_{ja}^{n+1}$$

$$= \frac{V}{\Delta t}(N_{ja}^{n+1} - N_{ja}^n) \qquad i=n_g+1,\ldots,n_{aq}. \qquad \text{(Eq. 5.31)}$$

In the fully implicit (FI) scheme, the transmissibility (T), capillary pressure (p_{cwg}), and gravity (ρ) terms are evaluated at the new time level ($n+1$). In both methods (IMPECS and FI), pressure is always solved implicitly.

Table 5.4. Parameters of sub-terms in the conservation mass equations (Eq. 5.32, 5.33, and 5.34).

D_{iq}^{*u}	Molecular diffusion coefficient of component i in phase q	r_w	Well radius
F_q^u	Formation resistivity factor of phase q	u_q	Velocity of phase q
K	Intrinsic permeability	Δx	Grid-block size in x direction
P	Water pressure	Δy	Grid-block size in y direction
P_w	Bottom hole pressure	Δm_{iq}	Changes of mole fraction of component i in phase q
S	Skin factor	Δz	Grid-block size in z direction
h	Perforation length	α_q	Dispersivity of phase q
k_{rq}	Relative permeability of phase q	ρ_q	Density of phase q
r_0	Effective drainage radius	μ_q	Viscosity of phase q

Many of the sub-terms in the governing equations involve empirical relationships. The transmissibility of phase q (gas or water) is defined in Eq. (5.32),

$$T_q = \frac{Kk_{rq}\Delta y\Delta z}{\Delta x}\left(\frac{\rho_q}{\mu_q}\right). \qquad \text{(Eq. 5.32)}$$

The diffusion/dispersion terms (J_{iq}) of components i in phase q is defined as

$$J_{iq} = \rho_q^u \Delta y_{iq}^{n+1}\left(\frac{D_{iq}^{*u}}{F_q^u} + \alpha_q\left|u_q\right|^n\right), \qquad \text{(Eq. 5.33)}$$

and the parameters in this equation are defined in Table 5.4. Well-flow rate (q_{iq}^{n+1}) of component i in phase q is defined as (Peaceman, 1978; 1983),

$$q_{iq}^{n+1} = \frac{2\pi Kh}{\ln\left(\frac{r_0}{r_w}\right) + S}\left(\frac{k_{rq}\rho_q y_{iq}}{\mu_q}\right)^{n+1}\left(p_w^{n+1} - p^{n+1}\right), \qquad \text{(Eq. 5.34)}$$

and the parameters in this equation are also defined in Table 5.4.

5.5. Equations of State (EOS)

This section summarizes the equations of state (EOS) to calculate thermodynamic properties of gas, oil, and brine phases. The GEM-GHG simulator relies on cubic EOSs for predicting densities, fugacity coefficients, and Z factors of gas and oil (Soave, 1972; Peng and Robinson, 1976). Viscosities of both gas and oil phases were calculated from Jossi et al. (1962). The EOSs initially calculate density and viscosity of a pure component. In the subsequent calculations, the effect of mixing components is added to the density and viscosity values of pure components by mixing rules.

Both brine density and viscosity are, respectively, calculated from algorithms outlined by Rowe and Chou (1970) and Kestin et al. (1981). Like many EOS algorithms, both EOS initially calculate density and viscosity of pure water. Subsequently, both density and viscosity of pure water are corrected to account for salinity effects.

The solubility of the gas component in brine is calculated by Henry's Law after determining the fugacity coefficient using the approach of Michelson and Heidemann (1981). In a mixture component system, Henry's Law cannot predict phase partitioning. Therefore, phase partitioning in both oil-gas and oil-gas-water

systems are calculated by flash calculations (Nghiem et al. 1983; Nghiem and Li, 1984).

The general description of EOSs in both GEM and GEM-GHG is discussed in the following section. A further detailed overview of the EOS calculations for the composition simulation is summarized in Whitson and Brule (2000).

5.5.1. Gas and Liquid Phase (Gas and Oil Phases)

5.5.1.1. Density Algorithm

Many different types of cubic EOS's have been introduced since van der Waals initial work in the late 1800s (van der Waals, 1873; Redlich and Kwong, 1949; Soave, 1972; Abbott, 1973; Fuller, 1976; Peng and Robinson, 1976). The original van der Waals EOS consists of both a repulsive term and an attractive term. Most of the modified EOSs retain the original van der Waals repulsive term and modify only the denominator in the attractive term.

Both GEM and GEM-GHG are able to predict the density of pure and mixture components by adapting either Peng-Robison or Soave-Redlich-Kwong EOS (Soave, 1972; Peng and Robinson, 1976). Because the Peng-Robinson EOS has been used to develop the SACROC model described in Chapters 6 and 7, its mathematical representation is described below. The Peng-Robinson EOS terms include,

$$P = \frac{RT}{v-b} - \frac{a}{v^2 + vb}, \qquad \text{(Eq. 5.35)}$$

$$\sqrt{a} = \sqrt{a_c \alpha}, \qquad \text{(Eq. 5.35.1)}$$

$$\sqrt{a_c} = \frac{\sqrt{\Omega_a}(RT_c)}{\sqrt{P_c}}, \qquad \text{(Eq. 5.35.2)}$$

$$\sqrt{\alpha} = 1 + k(1 - \sqrt{\frac{T}{T_c}}), \qquad \text{(Eq. 5.35.3)}$$

$$b = \frac{\Omega_b R T_c}{P_c}, \qquad \text{(Eq. 5.35.4)}$$

$$k = 0.37464 + 1.54226\omega - 0.26992\omega^2, \qquad \text{(Eq. 5.35.5)}$$

and the parameters of these terms are defined in Table 5.5.

Table 5.5. Parameters for Peng and Robinson equation of state.

P	Pressure	a_c	Acentric factor
P_c	Critical pressure	b	Coefficients in Peng and Robinson EOS accounting for the mixture effect
R	Ideal gas constant	d_{ij}	Interaction coefficient
T	Temperature	x_i	Mole fraction of component i
T_c	Critical temperature	Ω_a	0.45724
V	Molar volume	Ω_b	0.07780
V_c	Critical volume of component i	θ:	Exponents for computing interaction coefficients between components
a	Coefficients in Peng and Robinson EOS accounting for the mixture effect		

Densities of the mixture components are calculated using a mixing rule (Eq. 5.35.6, 5.35.7, and 5.35.8) with empirically determined interaction parameters (Eq. 5.35.9). The calculation of mixing effects requires finding appropriate coefficients a and b for mixture components in the Peng-Robinson EOS, including

$$a = \sum_i x_i S_i, \qquad \text{(Eq. 5.35.6)}$$

$$b = \sum_i x_i b_i, \qquad \text{(Eq. 5.35.7)}$$

$$S_i = \sqrt{a_i} \sum_j x_j (1 - d_{ij}) \sqrt{a_j}. \qquad \text{(Eq. 5.35.8)}$$

The empirically determined interaction coefficients (d_{ij}) between components are estimated from (Oellrich et al. 1981; Mehra, 1981; Li et al. 1985)

$$d_{ij} = 1 - \left| \frac{2\sqrt{v_c(i)v_c(j)}}{v_c(i) + v_c(j)} \right|^{\theta} . \qquad \text{(Eq. 5.35.9)}$$

Noting that the molar density of a component is simply the inverse of the molar volume, the specific density of a component is determined from equation (Eq. 5.36) below,

$$\rho = \frac{M_w}{v}. \qquad \text{(Eq. 5.36)}$$

5.5.1.2. Fugacity Algorithm

The fugacity (f_i) of component i in the mixture is calculated from Michelson and Heidemann (1981),

$$f_i = \phi_i x_i P, \qquad \text{(Eq. 5.37)}$$

$$\ln\phi_i = \frac{b_i}{b}(Z-1) - \ln(Z-B) - \frac{1}{2.8284}\frac{A}{B}\left(\frac{2S_i}{a} - \frac{b_i}{b}\right)\ln\left(\frac{Z+2.4142B}{Z-0.4142B}\right), \qquad \text{(Eq. 5.37.1)}$$

$$Z = \frac{Pv}{RT}, \qquad \text{(Eq. 5.37.2)}$$

$$A = \frac{ap}{(RT)^2}, \qquad \text{(Eq. 5.37.3)}$$

$$B = \frac{bP}{RT}, \qquad \text{(Eq. 5.37.4)}$$

$$b = \sum_i x_i b_i, \qquad \text{(Eq. 5.37.5)}$$

$$S_i = \sqrt{a_i} \sum_j x_j (1 - d_{ij}) \sqrt{a_j}\,, \qquad \text{(Eq. 5.37.6)}$$

and the parameters for these expressions are defined in Table 5.6.

Table 5.6. Parameters for fugacity algorithm.

a	Coefficients in Peng and Robinson EOS accounting for the mixture effect	f_i	Fugacity of component i
b	Coefficients in Peng and Robinson EOS accounting for the mixture effect	x_i	Mole fraction of component i
d_{ij}	Interaction coefficient in (eq. 5.35.9)	ϕ_I	Fugacity coefficient of component i

5.5.1.3. Volume Shift Algorithm

Modifications of cubic EOS's such as Redlich-Kwong and Peng-Robinson require changing the denominator in the attractive term. This modification generally causes a change in fugacities and subsequently affects equilibrium calculations for pure or mixture components. Therefore, Peneloux et al. (1982) suggested a volume shift technique (Eq. 5.38), which does not disturb the calculation of an equilibrium constant (Eq. 5.38.4), including

$$\nu_{corr} = \nu - c\,, \qquad \text{(Eq. 5.38)}$$

$$c = xt\Omega_b \frac{RT_c}{p_c}, \qquad \text{(Eq. 5.38.1)}$$

with parameters for these expressions defined in Table 5.7.

For the multi-component vapor/liquid system, the volume shift calculation becomes

$$\nu_{corr}^L = \nu^L - \sum_{i=1}^{N} x_i^L c_i \text{ and } \nu_{corr}^v = \nu^v - \sum_{i=1}^{N} x_i^v c_i\,. \qquad \text{(Eq. 5.38.2)}$$

The corresponding fugacities are expressed as

$$(f_i^v)_{corr} = (f_i^v)\exp\left(-c_i \frac{p}{RT}\right) \text{ and } (f_i^L)_{corr} = (f_i^L)\exp\left(-c_i \frac{p}{RT}\right) .$$

(Eq. 5.38.3)

Eq. (5.38.3) indicates that the fugacity ratio (equilibrium constant) is invariant after volume shifting, or

$$\left(\frac{f_i^v}{f_i^L}\right)_{corr} = \left(\frac{f_i^v}{f_i^L}\right) = K_i. \qquad \text{(Eq. 5.38.4)}$$

The volume shift technique is available for improving the prediction of thermodynamic properties in both GEM and GEM-GHG. The volume shift parameters for individual components are defined by Jhaveri and Youngren (1988). Furthermore, volume shift parameters that depend on temperature can be calculated using the modified Rackett equation (Kokal and Sayegh, 1990).

Table 5.7. Parameters for volume shift algorithm.

T	Dimensionless individual translation value	x	Mole fraction
ν	Molar volume from Peng and Robins EOS	Ω_b	Equation of state parameter in Peng and Robinson
ν_{corr}	Corrected molar volume		

5.5.1.4. Viscosity Algorithm

Five methods are available to calculate the viscosity of both pure and mixture components in GEM and GEM-GHG. Among them, the Jossi-Stiel-Thodos correlation method is introduced below. The mixture viscosity (μ) by Jossi et al. (1962) is

$$\left[\left(\mu - \mu^*\right)\xi + 10^{-4}\right]^{0.25}$$

$$= 0.1023 + 0.023364\rho_r + 0.058533\rho_r^2 - 0.040758\rho_r^3 + 0.0093324\rho_r^4,$$

(Eq. 5.39)

$$\rho_r = \rho\left[\sum_{i=1}^{n_c} x_i v_{c_i}^{\alpha}\right]^{1/\alpha}, \qquad \text{(Eq. 5.39.1)}$$

$$\xi = \frac{\left(\sum_i x_i T_{c_i}\right)^{1/6}}{\left(\sum_i x_i Mw_i\right)^{1/2}\left(\sum_i x_i P_{c_i}\right)^{2/3}}, \qquad \text{(Eq. 5.39.2)}$$

$$\mu^* = \frac{\sum_i \left(x_i \mu_i^* Mw_i^{0.5}\right)}{\sum_i \left(x_i Mw_i^{0.5}\right)}. \qquad \text{(Eq. 5.39.3)}$$

The low pressure viscosity (μ_i^*) of pure component *i* is in Eq. (5.39.4) (Stiel and Thodos, 1961)

$$\mu_i^* \xi_i = \left[4.610 T_{r_i}^{0.618} - 2.04\exp(-0.449 T_{r_i}) + 1.94\exp(-4.058 T_{r_i}) + 0.1\right] \times 10^{-4},$$

(Eq. 5.39.4)

$$\xi_i = T_{c_i}^{1/6} Mw_i^{-1/2} P_{c_i}^{-2/3}, \qquad \text{(Eq. 5.39.5)}$$

$$T_{r_i} = \frac{T}{T_{c_i}}, \qquad \text{(Eq. 5.39.6)}$$

with the parameters in these expressions defined in Table 5.8.

Table 5.8. Parameters for viscosity algorithm.

M_{wi}	Molecule weight of pure component *i*	α	Mixing exponent parameter
P	Pressure	μ^*	Low pressure viscosity of mixture
P_c	Critical pressure of pure component *i*	μ_i^*	Low pressure viscosity of pure component *i*
T	Temperature	ν	Critical molar volume
T_c	Critical temperature of pure component *i*	ρ_r	Reduced molar volume
x_i	Mole fraction of component *i*		

5.5.2. Aqueous Phase (Brine Phase)

5.5.2.1. Density Algorithm

GEM-GHG adapted the algorithm of brine density from Rowe and Chou (1970). Initially, the molar volume of pure water (v_{H2O}) is calculated from

$$\nu_{H_2O} = A(T) - B(T)P - C(T)P^2, \qquad \text{(Eq. 5.40)}$$

$$A(T) = 5.916365 - 0.010357694T + 0.9270048\times10^{-5}T^2 - 1127.522T^{-1} + 100674.1T^{-2}, \qquad \text{(Eq. 5.40.1)}$$

$$B(T) = 0.5204914\times10^{-2} - 0.10482101\times10^{-4}T + 0.8328532\times10^{-8}T^2 - 1.1702939T^{-1} + 102.2783T^{-2}, \qquad \text{(Eq. 5.40.2)}$$

$$C(T) = 0.118547\times10^{-7} - 0.6599143\times10^{-10}T. \qquad \text{(Eq. 5.40.3)}$$

After calculating the molar volume of pure water (ν_{H_2O}), molecular weight and molar volume are modified to account for effects of salinity (Eq. 5.41 and 5.42). The total aqueous component (n_{aq}) in saline water is the sum of the dissolved gaseous component (n_h), the aqueous species (n_a), and H_2O. The molecular weight of the total aqueous components (n_{aq}) is determined from the sum of the product of mole fractions and molecule weight (Eq. 5.41), or

$$M_{aq} = \sum_{i=1}^{n_{aq}} y_{i,aq} M_i \,. \qquad \text{(Eq. 5.41)}$$

In a similar manner, the molar volume accounting for the effect of salinity becomes

$$v_{aq} = \sum_{i=1}^{n_h} y_{i,aq} \nu_i^{\infty} + y_{H_2O}\nu_{H_2O} + \sum_{i=1}^{n_a} y_{i,aq} \bar{\nu}\,. \qquad \text{(Eq. 5.42)}$$

The parameters for Eq. (5.41) and (5.42) are defined in Table 5.9.

Table 5.9. Parameters for brine density algorithm.

M_{aq}	Molecular weight of total aqueous component (brine)	ν_{H_2O}	Molar volume of pure water
M_i	Molecular weight of component *i*	ν_i^{∞}	Molar volume of gaseous components at infinite dilution *i*
$y_{i,aq}$	Mole fraction of component *i* in aqueous phase	$\overline{\nu_i}$	Partial molar volume of ions in solution

Finally, the molar density of brine can be calculated from Eq. (5.36).

5.5.2.2. Viscosity Algorithm

Both GEM and GEM-GHG adapted a modified Kestin's algorithm to calculate brine viscosity as a function of pressure, temperature, and salinity after pressure corrections (Kestin et al. 1981; Whitson and Brule, 2000). The modified Kestin's algorithm is appropriate for pressures from 0.1 to 30 MPa, temperatures from 20 to 150 ºC, and concentrations from 0 to 5.4 moles, and includes the following expressions:

$$\mu = (1 + A_0 P)\mu^*, \qquad \text{(Eq. 5.43)}$$

$$\mu^* = \mu^0 \exp(A_1 + A_2 A_3), \qquad \text{(Eq. 5.43.1)}$$

$$\mu^0 = 1.002 \exp(A_3), \qquad \text{(Eq. 5.43.2)}$$

$$A_0 = 10^{-3}\left(0.8 + 0.01(T - 90)\exp(-0.25s)\right), \qquad \text{(Eq. 5.43.3)}$$

$$A_1 = \left(3.324s + 3.624 \times 10^{-1} s^2 - 1.879 \times 10^{-2} s^3\right) \times 10^{-2}, \qquad \text{(Eq. 5.43.4)}$$

$$A_2 = \left(-3.96s + 1.02s^2 - 7.02 \times 10^{-2} s^3\right) \times 10^{-2}, \qquad \text{(Eq. 5.43.5)}$$

$$A_3 = \frac{1}{96+T}\begin{pmatrix} 1.2378(20-T) - 1.303\times10^{-3}(20-T)^2 + 3.06\times10^{-6}(20-T)^3 \\ +2.55\times10^{-8}(20-T)^4 \end{pmatrix},$$

(Eq. 5.43.6)

with the parameters in these expressions defined in Table 5.10.

Table 5.10. Parameters for brine viscosity algorithm.

P	Pressure	μ	Viscosity of brine
T	Temperature	μ^0	Viscosity of pure water
s	Salinity (NaCl molality)		

5.5.3. Thermodynamic Equilibrium: CO_2 Solubility

Both GEM and GEM-GHG are capable of calculating thermodynamic equilibrium using either Henry's Law or "Flash Calculations". GEM was originally developed for oil reservoir simulations, and thus its fluid phase options include groundwater (or brine) with complex hydrocarbon oils of multiple components.

In GEM-GHG, CO_2 is included as an additional fluid component to multi-component hydrocarbon (oil) plus water or brine. If a simulation model includes only CO_2 and water (or brine), then Henry's Law is used to assign CO_2 phase partition. If the fluid components also include oil, then "flash calculations" are used for phase partition. Such flash calculations are discussed in section 5.5.3.2.

5.5.3.1. CO_2 Solubility in Brine (Henry's Law)

CO_2 solubility can be modeled from Henry's law, or

$$p\phi_i = H_i x_i . \qquad \text{(Eq. 5.44)}$$

The fugacity coefficient (ϕ_i) of component *i* is calculated from Michelson and Heidemann (1981) in Eq. (5.37.1). The Henry's law constant (*H*) is calculated from,

$$\ln(H_i) = \ln(H_i^{ref}) + \frac{\nu_i^{\infty}(P - P_{ref})}{RT}. \qquad \text{(Eq. 5.45)}$$

Parameters within Eq. (5.44) and (5.45) are defined in Table 5.11.

The Henry's law constant was adjusted for the salinity effect (Li and Nghiem, 1986). Additionally, vapor pressure and molar volume of pure water have to be calculated. The detailed calculation procedure is explained in the GEM user manual (Computer Modeling Group, 2006).

Table 5.11 Parameters for calculating CO_2 solubility in brine.

H_i	Henry's law constant for component *i*	X_i	Mole fraction of component *i* in the aqueous phase
H_i^{ref}	Henry's constant of component *i* at reference pressure (P_{ref})	ϕ_i	Fugacity coefficient of component *i*
P	Pressure	ν_i^{∞}	Molar volume at infinite dilution of component *i* (Lyckman et al. 1965)
P_{ref}	Reference pressure		

5.5.3.2. Flash Calculation

Flash evaporation is a vaporization process that occurs when saturated liquid in a closed system undergoes a pressure reduction. If the saturated liquid is a single-component liquid, a portion of the liquid immediately flashes into the vapor phase. Similarly, a flash calculation usually requires an iterative solution predicting the amounts of flashed vapor and residual liquids in an equilibrium state at a given pressure and temperature condition.

Generally, the procedure requires solving the Rachford-Rice equation derived from the equilibrium reaction of fugacity and material balance equations (Rachford

and Rice, 1952). In both GEM and GEM-GHG, the flash calculation is decoupled from the transport equation and solved using Quasi Newton Successive Substitution (Nghiem and Heidemann, 1982).

The thermodynamic equilibrium reaction for two phases between vapor and liquid systems can be written with the equilibrium constant (K_i), or

$$x_i^V \leftrightarrow x_i^L \text{ and } K_i = \frac{x_i^V}{x_i^L}. \qquad \text{(Eq. 5.46)}$$

When the reaction reaches the equilibrium condition, the Gibbs free energy becomes zero, or

$$G_i = \ln K_i - \ln \phi_i^L + \ln \phi_i^V = 0 \qquad i=1,\ldots,N_c. \qquad \text{(Eq. 5.47)}$$

The total component material balance can be derived with several definitions of mole fractions. The total material balance is $N=N_L+N_V$, the vapor fraction is $f_V = \frac{N_V}{N}$, and the liquid fraction is $f_L = \frac{N_L}{N}$. The total component material balance is given by $z_i = f_L x_i^L + f_V x_i^V$. Substituting the liquid fraction, total mole balance, and equilibrium equation into the total component material balance yields

$$z_i = f_L x_i^L + f_V x_i^V = \frac{N_L}{N} x_i^L + f_V x_i^V = \frac{N - N_V}{N} x_i^L + f_V x_i^V = \frac{N - Nf_V}{N} x_i^L + f_V x_i^V$$

$$= \left(1 - f_v + f_V K_i\right) x_i^L. \qquad \text{(Eq. 5.48)}$$

Both the liquid and vapor mole fractions of component *i* are expressed as equilibrium constant, or

$$x_i^L = \frac{z_i}{\left[1 + f_v(K_i - 1)\right]} \qquad i=1,\ldots,N_c, \qquad \text{(Eq. 5.49)}$$

$$x_i^V = \frac{K_i z_i}{\left[1 + f_v(K_i - 1)\right]}, \qquad \text{(Eq. 5.50)}$$

where x_i^V is the vapor mole fraction of component *i,* x_i^L is the liquid mole fraction of component *i,* z_i is the global mole fraction of component *i,* and f_v is the vapor mole fraction of the system.

The summations of each mole fraction must be unity ($\sum_i x_i^L = \sum_i x_i^V = 1$). Therefore, a primary constraint can be expressed as $\sum_i (x_i^V - x_i^L) = 0$. By substituting both liquid and vapor mole fractions into this constraint, the material balance equation, also called the Rachford-Rice equation, can be expressed as

$$\sum_i \left(\frac{K_i z_i}{1 + f_v(K_i - 1)} - \frac{z_i}{1 + f_v(K_i - 1)} \right) = 0, \qquad \text{(Eq. 5.51)}$$

$$G_{n_c} = \sum_i \frac{z_i(K_i - 1)}{1 + f_v(k_v - 1)}. \qquad \text{(Eq. 5.52)}$$

For the initial estimation of K_i, the following empirical relationship is used (Wilson, 1968):

$$\ln K_i = 5.37(1 + \omega_i)\left(1 - \frac{T_{c_i}}{T}\right) + \ln\left(\frac{P_{c_i}}{P}\right), \qquad \text{(Eq. 5.53)}$$

where, ω_i is the acentric factor of component.

The feed composition (z_i), estimated equilibrium constant (K_i), and vapor fraction (f_v) can be calculated using an iterative method. Nghiem et al. (1983) solved this iteratively using a Quasi-Newton Successive Substation method (QNSS) for K_i, f_v, x_i, and y_i. The realistic vapor fraction (f_v) from solution must be between 0 and 1, where $f_v=0$ corresponds to a bubble point condition, f_v=1 corresponds to a dewpoint condition, and $0<f_v<1$ indicates a two phase condition.

Additionally, the equilibrium constant of component *i* in a three phase system, such as liquid, gas, and water, can be predicted using a flash calculation. The Rachford-Rice equation for three phases includes

$$K_{iv} = \frac{x_i^V}{x_i^L}, \qquad \text{(Eq. 5.54)}$$

$$K_{iw} = \frac{x_i^W}{x_i^L}, \qquad \text{(Eq. 5.55)}$$

$$\sum_{i=1}^{N_c}\left(x_i^V - x_i^L\right) = \sum_{i=1}^{N_c}\frac{(K_{iv}-1)z_i}{f_L + f_V K_{iv} + f_w K_{iw}} = 0, \qquad \text{(Eq. 5.56)}$$

$$\sum_{i=1}^{N_c}\left(x_i^W - x_i^L\right) = \sum_{i=1}^{N_c}\frac{(K_{iw}-1)z_i}{f_L + f_V K_{iv} + f_w K_{iw}} = 0. \qquad \text{(Eq. 5.57)}$$

5.5.3.3. Phase Stability Test

To solve for phase equilibrium using a flash calculation, three restrictions must be satisfied (Baker et al. 1982; Whitson and Brule, 2000):

(1) Material balance must be satisfied (Equation 5.48).

(2) Chemical potentials for each component must be the same in all phases, which means that there are no driving forces to cause a net movement of any components. Because chemical potential can be expressed as fugacity, the constraint becomes $f_{Vi} = f_{Li}$.

(3) Gibbs energy of mixture components must be the smallest at the system's temperature and pressure.

These three criteria can determine whether a mixture will actually split into two phases at specific temperature and pressure conditions.

Flash calculations described in section 5.3.3.2 may find an equilibrium state satisfying criteria (1) and (2), but not necessarily (3). Therefore, the Gibbs tangent-plane technique has been suggested to satisfy criterion (3) (Baker et al. 1982; Michelsen, 1982). The Gibbs tangent-plane technique is used to find a valid tangent plane (global minimum point), which does not intersect the Gibbs energy surface anywhere except at the points of tangency. A comprehensive description of Gibbs tangent-plane techniques is explained by Baker et al. (1982). The implementation of numerical algorithms is introduced by Michelsen (1982).

In both GEM and GEM-GHG, stability tests were performed using the Gibbs tangent-plane technique prior to flash calculations (Nghiem and Li., 1984). Stability tests determine whether a mixture composition is thermodynamically stable. If the test indicates a stable condition, the system will be single phase. Conversely, if the test indicates an unstable condition, a two-phase flash calculation will be initialized using an estimated K value.

5.6. Chemical Reactions

5.6.1. Constitutive Relation

The GEM-GHG simulator can evaluate the chemical reactions among chemical species in the aqueous phase and the dissolution/precipitation of minerals. To describe the chemical reactions, it is useful to define the number of chemical reactions and to define the number of components in gas, aqueous, and mineral phases (Table 5.12).

Table 5.12. Constitutive relation for calculating chemical reactions.

n_{aq}^{r}	Number of equilibrium reactions between components in the aqueous phase
n_{nm}^{r}	Number of kinetic reactions between aqueous components and minerals
n_g	Number of components in the gas phase
n_{aq},	Number of components in the aqueous phase
n_{aq}^{pri}	Number of primary components in the aqueous phase
$n_{aq}^{\sec}$	Number of secondary components in the aqueous phase
n_m	Number of mineral components
n_{ct}	Total number of components (=n_{aq}+n_g+n_m+*1*)

Because H_2O is also regarded as an independent component, the total number of components becomes $n_{ct}=n_{aq}+n_g+n_m+1$. Further, aqueous components can be divided into primary and secondary components, or

$$n_{aq} = n_{aq}^{pri} + n_{aq}^{\sec}. \qquad \text{(Eq. 5.58)}$$

Number of secondary components always equals the number of reactions ($n_{aq}^{\sec} = n_{aq}^{r}$). Therefore, the number of primary components always becomes equal to the difference between the total number of species and the number of chemical reactions, or

$$n_{aq}^{pri} = n_{aq} - n_{aq}^{\sec} = n_{aq} - n_{aq}^{r}. \qquad \text{(Eq. 5.59)}$$

5.6.2. Equilibrium Reactions Governing Aqueous Components

The aqueous reaction is modeled as a mass-action equation with the equilibrium constant, or

$$Q_i = \prod_{k=1}^{n_{aq}} a_k^{\nu_k^i} = K_{eq,i},\ i=1,\ldots,\ n_{aq}^{r}, \qquad \text{(Eq. 5.60)}$$

with the parameters in this expression defined in Table 5.13.

Table 5.13. Parameters for calculating equilibrium reactions and activity coefficient.

I	Ionic strength	a_k	Activity component k
$K_{eq,i}$	Chemical equilibrium constant for aqueous reaction i	$\overset{o}{a}$	Ion size parameters
Q_i	Activity product of reaction i	ν_k^i	Stoichiometric coefficients of component k in aqueous reaction i
Z	Ion charge		

The equilibrium constant is a function of temperature and is extrapolated using a cubic function (Kharaka et al. 1989),

$$K_{eq} = \exp(a_0 + a_1 T + a_2 T^2 + a_3 T^3 + a_4 T^4)\,. \qquad \text{(Eq. 5.61)}$$

The mole fraction of the aqueous component is calculated using activity coefficients, or

$$a_i = r_i m_i \qquad \text{i=1,…., } n_{aq}\,. \qquad \text{(Eq. 5.62)}$$

The GEM-GHG simulator implements both the modified Debye-Huckel and B-dot models. The modified Debye-Huckel model,

$$\log r_i = -\frac{A z_i^2 \sqrt{I}}{1 + \overset{o}{a}_i B\sqrt{I}} \text{ and } I = \frac{1}{2}\sum_i m_i z_i^2\,, \qquad \text{(Eq. 5.63)}$$

is the most common equation used to solve for activity coefficients. The coefficients for the modified Debye-Huckel model are listed in Table 5.14.

Later, Helgeson and Kirkham (1974) developed a modified activity model called the B-dot model. This model accounts for activity coefficients over a wide range of temperatures. Because reservoir conditions for CO_2 injection vary with temperature, the B-dot model,

$$\log r_i = -\frac{A z_i^2 \sqrt{I}}{1 + \overset{o}{a}_i B\sqrt{I}} + \dot{B} I\,, \qquad \text{(Eq. 5.64)}$$

will be more applicable to a CO_2 sequestration simulation. The coefficients for the B-dot model are also summarized in Table 5.14.

The Pitzer model (Pitzer, 1987) was often adapted in geochemical modeling because it accurately modeled the behavior of electrolyte solutions at high ionic strength. Compared to the Debye-Huckle formulation, which only describes the electrostatic and hydration effects, the Pitzer model additionally accounts for aqueous complexing and ion pairing effects. Previously, several studies indicate that the Pitzer model predicted activity coefficients similar to those of experimental data at high ionic strength fluid (Bethke, 1996; Lichtner and Felmy, 2003; Zhang, 2005).

Therefore, several reactive transport codes such as SOLMINEQ.88 (Kharaka et al. 1988), Phrqpitz (Plummer et al. 1988), EQ/EQ6 (Wolery, 1992), REACT (Bethke, 1994), GMIN (Felmy, 1995) and Lichtner (2001) included a generally accepted form of Pitzer model, which is formulated by Harvie et al. (1984).

Table 5.14. Debye-Huckel and B-dot coefficients with various temperatures.

Temperature (ºC)	A	B	$\dot{B}$
0	0.4913	0.3247	0.0174
10	0.4976	0.3261	
20	0.5050	0.3276	
25			0.0410
30	0.5135	0.3291	
40	0.5336	0.3307	
50	0.5450	0.3325	
60	0.5573	0.3343	0.0440
70	0.5706	0.3362	
80	0.5848	0.3381	
90	0.5998	0.3401	
100	0.6417	0.3422	0.0460
125	0.6898	0.3476	
200	0.8099	0.3533	0.0470
250	0.9785	0.3792	0.0340
300	1.2555	0.3965	0.0000
350	1.9252	0.4256	

In CO_2 sequestration processes, the fluid in CO_2 injection formations has a high ionic strength. Therefore, the Pitzer model will accurately predict activity coefficients compared to other methods. However, the model is limited because of the lack of interaction parameters for trace element complexes (Langmuir and Melchior, 1985). Moreover, at the elevated temperature there are limitations estimating activity coefficients with current data. Compared to the Pitzer model, the Debye-Huckel-type models are easy to apply and incorporate new species in the calculations because they require fewer coefficients. Moreover, the Debye-Huckel-type models can easily estimate activity coefficient under high temperature conditions.

Although the Pizter model is more accurate, researchers associated with CO_2 sequestration frequently used Debye-Huckel-type equations (Kumar et al. 2004; Xu et al. 2004; Gaus et al. 2005; Hellevang et al. 2005; Knauss et al. 2005; Zerai, 2006; Andre et al. 2007). Recently, Kervevan et al. (2005) and Andre et al. (2007) applied the Pitzer model to simulate CO_2 sequestration processes.

5.6.3. Kinetic Reactions Governing Dissolution/Precipitation of Minerals

Mineral dissolution/precipitation due to chemical reactions with aqueous phase components are governed by the rate of reaction derived from Transition State Theory (Lasaga, 1984; Lasaga, 1995),

$$r_i = \hat{A}_i k_i \left[1 - \frac{Q_i}{K_{eq,i}}\right], \qquad \text{(Eq. 5.65)}$$

with parameters in this expression defined in Table 5.15.

Generally, kinetic rate constants of most minerals are experimentally measured at several representative temperature conditions. Therefore, it is necessary

to extrapolate kinetic rate constants for other temperature conditions. An Arrhenius equation is used to calculate the rate constants at different temperatures:

$$k = k_0 \exp\left[-\frac{E_a}{R}\left(\frac{1}{T}-\frac{1}{T_0}\right)\right] \quad . \qquad \text{(Eq. 5.66)}$$

Table 5.15. Parameters for calculating kinetic reactions.

$\hat{A}_i$	Reactive surface area of mineral *i*	k_i	Kinetic rate constant of mineral *i*
E_a	Activation energy for reaction	k_0	Reaction rate constant at reference temperature (25ºC)
$K_{eq,i}$	Chemical equilibrium constant of mineral *i*	r_i	Reaction rate (+: precipitation, -: dissolution)
Q_i	Activity product of mineral *i*	ν_k^i	Stoichiometric coefficients of component *k* in aqueous reaction *i*
Z	Ion charge		

5.6.4. Coupling Equations Governing Porosity and Permeability

Although the reactive surface area is important in quantifying mineral-water reactions, measurements of the reactive surface area are not simple. Moreover, the reactive surface area concurrently changes with chemical reactions representing precipitation and/or dissolution. To quantify the variation of reactive surface area, Lichtner (1988) has an equation that relies on the ratio of mineral volume fraction,

$$\hat{A} = \hat{A}_0 \frac{\bar{v}}{\bar{v}_0} . \qquad \text{(Eq. 5.67)}$$

The parameters in Eq. (5.67) are defined in Table 5.16.

However, in contrast, the GEM-GHG simulator uses a mole ratio. In each time step, the ratio between initial and current number of moles is updated. The product of the initial reactive surface area and the ratio of moles determines the reactive surface area at the current time, or

$$\hat{A} = \hat{A}_0 \frac{N}{N_0}. \qquad \text{(Eq. 5.68)}$$

Porosity varies as a function of precipitation and dissolution reactions. In addition, pressure changes also affect porosity because the rock matrix has elastic properties. Porosity change due to chemical reactions is implemented in GEM-GHG as

$$\hat{\phi}^* = \phi^* + \sum_{i=1}^{n_m} \left(\frac{N_i}{\rho_i} - \frac{N_i^0}{\rho_i} \right). \qquad \text{(Eq. 5.69)}$$

After updating porosity with effects of precipitation/dissolution, porosity is corrected for the appropriate pressure conditions, or

$$\phi = \hat{\phi}^* \left(1 + c\left(P - P^* \right) \right). \qquad \text{(Eq. 5.70)}$$

Finally, permeability changes induced by porosity changes are calculated using a form of the Kozeny-Carman equation,

$$\frac{k}{k^0} = \left(\frac{\phi}{\phi^0} \right)^3 \left(\frac{1-\phi^0}{1-\phi} \right)^2. \qquad \text{(Eq. 5.71)}$$

Table 5.16. Parameters for calculating reactive surface area, porosity, and permeability.

$\hat{A}$	Reactive surface area at current time	k^0	Permeability at t=0
$\hat{A}_0$	Reactive surface area at t=0	ϕ	Porosity
N	Number of moles in the mineral at current time	ϕ^*	Porosity without the effect of precipitation/dissolution at a reference pressure
N_0	Number of moles in the mineral at t=0	$\hat{\phi}^*$	Porosity including the effect of precipitation/dissolution at a reference pressure
P	Pressure at reference state	$\bar{v}$	Mineral volume fraction at current time
c	Rock compressibility	$\bar{v}_0$	Mineral volume fraction at t=0
k	Permeability including the effect of porosity change	ρ_i	Mineral molar density

5.7. Summary and Conclusion

Mathematical representations of CMG's GEM-GHG simulator, which is a multi-dimensional, finite-difference, isothermal, geochemical, and compositional simulator are introduced in this chapter. Although GEM-GHG is specifically designed for simulating CO_2 sequestration processes, its original version (GEM) is developed for simulating compositional oil simulation. Therefore, the mathematical representations of governing equations within GEM are different from other conventional groundwater simulators. Further, injected CO_2 in deep subsurface will exist as separate-phase or dissolved-phase depending on the pressure, temperature, and composition of the formation water. Therefore, simulating CO_2 sequestration requires equations of state capable of calculating the thermophysical property changes of fluids. Finally, dissolution of CO_2 also increases the acidity of the formation water due to the release of H^+, and produces bicarbonate ions, HCO_3^-, leading to secondary reactions with complex feedbacks that buffer the aqueous solution properties and mineral reactivity. To simulate the chemical reaction between dissolved CO_2 and rock matrix, the appropriate chemical reaction codes has to couple with transport codes.

As discussed above, the modeling associated with CO_2 sequestration includes diverse numerical techniques such as multiphase transport, reactive transport, and compositional modeling. Many modelers probably are familiar with one or two techniques but not all of techniques. Therefore, this chapter was written for introducing clearly and concisely how such physical and chemical processes associated with CO_2 sequestration are treated in numerical model (GEM-GHG).

Finally, understanding this chapter will help to understand better how the model is developed for evaluate CO_2 trapping mechanisms in northern platform SACROC described in chapter 6 and 7.

References

Abbott, M.M., 1973. Cubic equation of state. AIChE Jounal 596.

Andre, L., Audigane, P., Azaroual, M., Menjoz, A., 2007. Numerical modeling of fluid-rock chemical interactions at the supercritical CO_2-liquid interface during CO_2 injection into a carbonate reservoir, the Dogger aquifer (Paris basin, France). Energy Conversion and Management 48(6), 1782-1797.

Aziz, K., Settari, A., 1979. Petroleum Reservoir Simulation. Elsevier, New York, 476pp.

Baker, L.E., Pierce, A.C., Luks, K.D., 1982. Gibbs energy analysis of phase equilibria. Society of Petroleum Engineers Journal 9806.

Basbug, B., Gumrah, F., Oz, B., 2005. Simulating the effects of deep saline aquifer properties on CO_2 sequestration. Petroleum society, Canadian Institute of Mining, Metallurgy & Petroleum, Paper 2005-139, 1-15.

Bertiger, W.I., Kelsey, F.J., 1985. Inexact adaptive Newton Method, Society of Petroleum Engineers Journal 13501.

Bethke, C.M., 1994. The Geochemist's Workbench^{TM}, version 2.0, A user guide to Rxn, Act2, Tact, React, and Gtplot. Hydrology Program, University of Illinois.

Bethke, C.M., 1996. Geochemical Reaction Modeling. Oxford University Press, New York, NY, 397pp.

Bryant, S.L., Lakshminarasimhan, S., Pope, G.A., 2006. Buoyancy-dominated multiphase flow and its impact on geological sequestration of CO_2. Society of Petroleum Engineers Journal 99938.

Byer, T.J., Edwards, M.G., Aziz, K., 1999. A preconditioned adaptive implicit method for reservoirs with surface facilities. Society of Petroleum Engineers Journal 51895.

Caillabet, Y., Magras, J.-F., Ricois, O., 2003. Large compositional reservoir simulations with parallelized adaptive implicit method. Society of Petroleum Engineers Journal 81501.

Calabrese, M., Masserano, F., Blunt, M.J., 2005. Simulation of physical-chemical processes during carbon dioxide sequestration in geological structures. Society of Petroleum Engineers Journal 95820.

Chen, Z., Huan, G., Ma, Y., 2006. Computational Methods for Multiphase Flows in Porous Media. SIAM Computational Science & Engineering. 531pp.

Collins, D.A., Nghiem, L.X., Li, Y.-K., Grabenstetter, J.E., 1992. An efficient approach to adaptive-implicit compositional simulation with an equation of state. Society of Petroleum Engineers Journal 15133.

Computer Modeling Group, 2006. User's guide GEM, Advanced compositional reservoir simulator (version 2006). Computer modeling Group Ltd.

Felmy, A.R., 1995. GMIN, a computerized chemical equilibrium program using a constrained minimization of the Gibbs free energy: Summary report, Special Publication of Soil Science Society of America 42, 377-407.

Fuller, G.G., 1976. A modified Redlich-Kwong-Soave equation of state capable of representing the liquid state. Industrial and Engineering Chemistry 15, 254.

Gaus, I., Azaroual, M., Czernichowski-Lauriol, I., 2005. Reactive transport modeling of the impact of CO_2 injection on Clayey cap rock at Sleipner (North Sea). Chemical Geology 217, 319-337.

Grabenstetter, J., Li, Y.-K., Collins, D.A., Nghiem, L.X., 1991. Stability-based switching criterion for adaptive-implicit compositional reservoir simulation. Society of Petroleum Engineers Journal 21225.

Han, W.S., McPherson, B.J., 2007. Evaluation of CO_2 storage mechanisms at SACROC, site of 35 years of CO_2 injection, Proceedings of the 6th annual conference on carbon capture & sequestration, Pittsburgh, Pennsylvanian.

Harvie, C.E., Moller, N., Weare, J.H., 1984. The prediction of mineral solubilities in natural waters: The Na-K-Mg-Ca-H-Cl-SO_4-OH-HCO_3-CO3-H_2O-system to high ionic strengths at 25°C. Geochimica et Cosmochimica Acta 48(4), 723-751.

Helgeson, H.C., Kirkham, D.H., 1974. Theoretical prediction of the thermodynamic behavior of aqueous electrolytes at high pressures and temperatures, II. Debye-Huckel parameters for activity coefficients and relative partial molal properties. American Journal of Science 274, 1199-1261.

Hellevang, H., Aagaard, P., Oelkers, E.H., Kvamme, B., 2005. Can dawsonite permanently trap CO_2? Environmental Science and Technology 39, 8281-8287.

Jhaveri, B.S., Youngren, G.K., 1988. Three-parameter modification to the Peng-Robinson equation of state to improve volumetric prediction. Society of Petroleum Engineers Journal 13118.

Jossi, J.A., Stiel, L.I., Thodos, G., 1962. The viscosity of pure substances in the dense gaseous and liquid phases. AIChe Journal 8(1), 59-62.

Kervevan, C., Azaroual, M., Durst, P., 2005. Improvement of the calculation accuracy of acid gas solubility in deep reservoir brines: Application to the geological storage of CO_2. Oil & Gas Science and Technology 60(2), 357-379.

Kestin, J., Khalifa, H.E., Correia, R.J., 1981. Tables of the dynamic and kinematic viscosity of aqueous NaCl solutions in the temperature range 20-150°C and pressure range 0.1-35 MPa, Journal of Physical and Chemical Reference Data. 10, 71-87.

Kharaka, Y.K., Gunter, W.D., Aggarwal, P.K., Perkins, E., DeBraal, J.D., 1989. SOLMINEQ.88: A computer program for geochemical modeling of water-rock reactions. U.S. Geological Survey Water-Resources Investigations Report 88-4227.

Knauss, K.G., Johnson, J.W., Steefel, C.I., 2005. Evaluation of the impact of CO_2, co-contaminant gas, aqueous fluid and reservoir rock interactions on the geologic sequestration of CO_2. Chemical Geology 217, 339-350.

Kokal, S.L., Sayegh, S.G., 1990. Gas-saturated bitumen density predictions using the volume-translated Peng-Robinson equation of state. Journal of Canadian Petroleum Technology 29(5), 77-82.

Kumar, A., Noh, M., Pope, G.A., Bryant, S., Lake, L.W., 2004. Reservoir simulation of CO_2 storage in deep saline aquifers. Society of Petroleum Engineers Journal 89343.

Langmuir, D., Melchior, D., 1985. The geochemistry of Ca, Sr, Ba, and Ra sulfates in some deep brines from the Palo Duro basin, Texas. Geochimica et Cosmochimica Acta 49(11), 2423-2432.

Lasaga, A.C., 1984. Chemical kinetics of water-rock interactions. Journal of Geophysical Research 89, 4009-4025.

Lasaga, A.C., 1995. Fundamental approaches in describing mineral dissolution and precipitation rates. Reviews in Mineralogy 31, 23-86.

Li, Y.-K., Nghiem, L.X., 1986. Phase equilibria of oil, gas, and water/brine mixtures from a cubic equation of state and Henry's law. Canadian Journal of Chemical Engineering 486-496.

Li, Y.-K., Nghiem, L.X., Siu, A., 1985. Phase behavior computations for reservoir fluids: Effects of pseudo-components on phase diagrams and simulation results. Journal of Canadian Petroleum Technology 24(6), 29-36.

Lichtner, P.C., 1988. The quasi-stationary state approximation to coupled mass transport and fluid-rock interaction in a porous media. Geochimica et Cosmochimica Acta 52, 143-165.

Lichtner, P.C., 2001. FLOTRAN: User's manual, Los Alamos National Laboratory report, LA-UR-02-2349.

Lichtner, P.C., Felmy, A., 2003. Estimations of Hanford SX tank waste compositions from historically derived inventories. Computers and Geosciences 29(3), 371-383.

Lyckman, E.W., Eckert, C.A., Prausnitz, J.M., 1965. Generalized liquid volumes and solubility parameters for regular solution applications. Chemical engineering science 20, 703-706.

Mehra, R.K., 1981. The computation of multi-phase equilibrium in compositional reservoir studies. Ph.D. thesis, University of Calgary.

Michelsen, M.L., 1982. The isothermal flash problem. Part I. Stability. Fluid Phase Equilibria 9(1), 1-19.

Michelsen, M.L., Heidemann, R.A., 1981. Calculation of critical points from cubic two-constant equations of state. AIChE Journal 27(3), 521-523.

Nghiem, L., 1983. A new approach to quasi-newton methods with application to compositional modeling. Society of Petroleum Engineers Journal 12242.

Nghiem, L., Aziz, K., Li, Y.K., 1983. A robust iterative method for flash calculatios using the Soave-Redlich-Kwong or the Peng-Robinson equation of state. Society of Petroleum Engineers Journal 8285.

Nghiem, L., Heidemann, R.A., 1982. General acceleration proceduce for multiphase flash calculations with application to oil-gas-water systems. Paper presented at the Second European Symposium on enhanced Oil Recovery, Paris, France.

Nghiem, L., Li, Y.-K., 1984. Computation of multiphase equilibrium phenomena with an equation of state. Fluid Phase Equilibria 17, 77-95.

Nghiem, L., Sammon, P., Grabenstetter, J., Ohkuma, H., 2004. Modeling CO_2 storage in aquifers with a fully-coupled geochemical EOS compositional simulator. Society of Petroleum Engineers Journal 89474.

Noh, M., Lake, L.W., Bryant, S.L., Araque-Martinez, A., 2004. Implications of coupling fractional flow and geochemistry for CO_2 injection in aquifers. Society of Petroleum Engineers Journal 89341.

Oellrich, L., Plocker, U., Prausnitz, J.M., Knapp, H., 1981. Equations of state methods for computing phase equilibria and enthalpies. International Chemical Engineering 21(1), 1-15.

Ozah, R.C., Lakshminarasimhan, S., Pope, G.A., Sepehrnoori, K., Bryant, S.L., 2005. Numerical simulation of the storage of pure CO_2 and CO_2-H_2S gas mixtures in deep saline aquifers. Society of Petroleum Engineers Journal 97255.

Peaceman, D.W., 1978. Interpretation of well-block pressures in numerical reservoir simulation. Society of Petroleum Engineers Journal 6893

Peaceman, D.W., 1983. Interpretation of well-block pressures in numerical reservoir simulation with nonsquare grid blocks and anisotropic permeability. Society of Petroleum Engineers Journal 10528.

Peneloux, A., Rauzy, E., Freze, R., 1982. A consistent correction for Redlich-Kwong-Soave volumes. Fluid Phase Equilibria 8, 7-23.

Peng, D.Y., Robinson, D.B., 1976. A new two-constant equation of state. Industrial and Engineering Chemistry Fundamentals 15, 59-64.

Pitzer, K.S., 1987. A thermodynamic model for aqueous solutions of liquid-like density. In I.S.E. Carmichael and H.P. Eugster (eds.), Thermodynamic modeling of geological materials: Minerals Fluids and Melts. Reviews in Mineralogy 17, 97-142.

Plummer, L.N., Parkhurst, D.L., Fleming, G.W., Dunkle, S.A., 1988. PHRQPITZ, a computer program incorporating Pitzer's equations for calculation of geochemical reactions in brines. U.S. Geologiccal Survey Water-Resources Investigation Report 88-4153.

Redlich, O., Kwong, J.N.S., 1949. On the thermodynamics of solutions. V.An equation of state/ Fugacities of gaseous solutions. Chemistry Review 44, 233–244.

Rachford, H.H., Rice, J.D., 1952. Procedure for use of electrical digital computers in calculating flash vaporization hydrocarbon equilibrium. Society of Petroleum Engineers Journal 952327.

Rowe, A.M., Chou, J.C.S., 1970. Pressure-volume-temperature-concentration relation of aqueous NaCl solutions. Journal of Chemical and Engineering Data 15, 61-66.

Russell, T.F., 1989. Stability analysis and switching criteria for adaptive implicit methods based on the CFL condition. Society of Petroleum Engineers Journal 18413.

Soave, G., 1972. Equilibrium constants from a modified Redlich-Kwong equation of state. Chemical Engineering Science 27, 1197-1203.

Stiel, L.I., Thodos, G., 1961. The viscosity of nonpolar gases at normal pressures. AIChE Journal 7, 611-615.

Thomasa, G.W., Thurnau, D.H., 1981. Reservoir simulation using an adaptive implicit method. Society of Petroleum Engineers Journal 10120.

Van der Waals, J.D., 1873. Continuity of the gaseous and liquid state of matter. Ph. D. Dissertation, University of Leiden, Leiden, Germany, 134 pp.

Wang, H.F., Anderson, M.P., 1982. Introduction to groundwater modeling: Finite difference and finite element methods. Academic Press, 238 pp.

Whitson, C.H., Brule, M.R., 2000. Phase behavior. SPE Monograph 20, Society of Petroleum Engineers, Dallas, Texas

Wilson, G., 1968. A modified Redlich-Kwong equation of state, application to general physical data calculations. Paper 15C presented at the AIChE National Meeting, Cleveland, OH, May 4-7.

Wolery, T.J., 1992. EQ3/EQ6, a software package for geochemical modeling of aqueous systems, package overview and installation guide (version 7.0). Lawrence Livermore National Laboratory Report UCRL-MA-110662(1).

Xu, T., Apps, J.A., Pruess, K., 2004. Numerical simulation of CO_2 disposal by mineral trapping in deep aquifers. Applied Geochemistry 19, 917-936.

Zerai, B., Saylor, B.Z., Matisoff, G., 2006. Computer simulation of CO_2 trapped through mineral precipitation in the Rose Run sandstone, Ohio. Applied Geochemistry 21, 223-240.

Zheng, C., Bennett, G.D., 2002. Applied Contaminant Transport Modeling, second edition. A John Wiley & Sons, Inc.

Zhang, G., Zheng, Z., Wan, J., 2005. Modeling reactive geochemical transport of concentrated aqueous solutions. Water Resources Research 41, W02018, doi:10.1029/2004WR003097.

CHAPTER 6

EVALUATION OF CO_2 TRAPPING MECHANISMS AT THE SACROC NORTHERN PLATFORM, PERMIAN BASIN, TEXAS, SITE OF 35 YEARS OF CO_2 INJECTION:

1. ANALYSES OF FIELD DATA FOR MODEL PREPARATION

6.1. Introduction

Chapter 6 addresses how the natural heterogeneity at the SACROC northern platform is quantified using geophysical and geologic data. Both porosity and permeability vary naturally as a result of complex geological processes such as structural deformation, sedimentary deposition, and diagenesis. The variability of these rock properties greatly affects the subsurface migration of injected CO_2 and trapping mechanisms such as hydrostratigraphic (mobile), residual, solubility, and mineral trapping. Furthermore, chemical reactions (precipitation/dissolution) induced by CO_2 injection will cause changes in rock properties.

Although quantification of natural heterogeneity using diverse techniques has been discussed in detail in the hydrology and petroleum literature (Lake and Carroll, 1986; Lake et al. 1991; Anderson, 1996; Koltermann and Gorelick, 1996; de Marsily et al. 2005), the application of these techniques to CO_2 sequestration processes has not yet been widely performed.

Therefore, we successfully adapted the high-resolution geocellular model describing reservoir heterogeneity to facilitate a detailed numerical modeling study of the sequestration processes. The high-resolution geocellular model, which was applied to this study, is a model comprising a broad field of expertise in geologic data (core data, well-log data, sedimentologic and stratigraphic interpretation) and geophysical data (seismic attributes and rock physics data). Therefore, the high-resolution geocellular model includes detailed heterogeneity and helps us to better understand the subsurface migration of injection CO_2.

In this section, porosity distributions were determined from both seismic survey and wire log analyses. Permeability distributions were calculated from seismically calibrated porosity values using empirical equations derived from rock-fabric classification. The original high-resolution geocellular model consisted of over 9.4 million elements. Therefore, it was necessary to upscale in order to acquire a reasonable number of elements for simulating CO_2 trapping mechanisms. Further, we analyzed both water chemistry and $\delta^{13}C$ isotope data gathered in the SACROC field. Both analyses suggest that the Wolfcamp shale acts as a suitable seal at SACROC.

6.2. Description of Geology and Petroleum Production at SACROC

6.2.1. Overview of SACROC Site

The Scurry Area Canyon Reef Operations Committee Unit (SACROC), within the Horseshoe Atoll, is the oldest continuously operated CO_2 enhanced oil recovery operation in the United States, having undergone CO_2 injection since 1972. Until 2005, about 93 million tonnes (93,673,236,443 kg) of CO_2 have been injected and

about 38 million tonnes (38,040,501,080 kg) have been produced. As a result, a simple mass balance suggests that the site has accumulated about 55 million tonnes (55,632,735,360 kg) of CO_2 (Raines, 2005). Currently, SACROC continues to be flooded by the current owner/operator, Kinder Morgan CO_2.

6.2.2. Geologic Descriptions

SACROC is located in the southeastern segment of the Horseshoe Atoll within the Midland basin of west Texas (Figure 4.1). Within the Horseshoe Atoll, SACROC comprises an area of 356 km^2 with a length of 40 km and a width of 3–15 km (Vest, 1970).

Geologically, the carbonate reef complex at SACROC is composed of massive amounts of bedded bioclastic limestone and thin shale beds representing the Strawn, Canyon, and Cisco Formations of the Pennsylvanian, and the Wolfcamp Series of the Lower Permian (Vest, 1970). Among these formations, most of the CO_2 for enhanced oil recovery is injected into Cisco and Canyon Formations, which were deposited during the Pennsylvanian age.

The Strawn Formation in the carbonate reef complex started to form in the early Desmoinesian while the basin was on the equator (Walker et al. 1991). During the Missourian and Virgilian, carbonate sedimentation of the Canyon and Cisco Formations continued. Accumulation of carbonate sediments on the SACROC ended during the Wolfcampian due to the drastic influx of fine-grained clastics.

The Canyon and Cisco Formations are mostly composed of limestone, but minor amounts of anhydrite, sand, chert, and shale are present locally (Raines et al.

2001). Recently, Carey et al. (2007) analyzed core samples from wells 49-5 and 49-6 in the SACROC field and indicated that the limestone was mostly calcite with minor ankerite, quartz, and thin clay lenses. Detailed discussions of the carbonate reef complex in the SACROC related to facies, depositional environment, and petrography are provided by BergenBack and Terriere (1953), Stafford (1954), Myers et al. (1956), Stewart (1957), Burnside (1959), Vest (1970), Schatzinger (1988), Reid and Reid (1991), and Walker et al. (1991).

The Wolfcamp shale of the lower Permian acts as a seal above the Canyon and Cisco Formations (Raines et al. 2001). Analysis of X-ray diffraction results indicates that the shale is mostly illite/smectite and quartz with minor feldspar, carbonate, and pyrite. Based on mineralogical analysis, Carey et al. (2007) concluded that the CO_2 had not interacted with shale.

6.2.3. Injection and Production History

The SACROC Unit was discovered by the Standard Oil Company of Texas in November 1948. The original oil in place (OOIP) in this unit was estimated to be approximately 2.73 billion stock tank barrels (STB) in the Canyon Reef limestone formation (Dicharry et al. 1973). The reservoir parameters are detailed in Table 4.2.

From 1948 to 1951, over 1200 producing wells with 81 operators were drilled in the Canyon Reef complex (Bayat et al. 1996). The solution gas drive was an early producing mechanism. During this period, the original reservoir pressure (3122 psia = 21.53 MPa) dropped by over 50% (1560 psi = 11.38 MPa) with only 5% of OOIP produced (Dicharry et al. 1973; Brummett, et al. 1976).

To improve oil production and prevent pressure loss, a water injection project was suggested. In September 1954, one of the largest pressure maintenance projects started with 53 water injection wells having an injection rate of 132,000 barrels of water per day (BWPD) along the crest of Canyon reef, describing a "center-line pattern" injection (Allen and LaRue, 1957; Allen and Thomas, 1959; Dixon and Newton, 1965; Dicharry et al. 1973; Brummett et al. 1976; Bayat et al. 1996). Before water injection began, only 1% of the reservoir was above bubblepoint pressure (12.45 MPa). Within less than two years, 45% of the reservoir rose above bubblepoint pressure. Finally, 77% was above bubblepoint pressure after 17 years of water injection. However, despite the high sweep efficiency of water injection, approximately 1.2 billion STB of oil were still left at the end of the water injection period. In addition, the repressurization plan eventually resulted in high reservoir pressure in the center of the unit and low pressure towards the eastern and western margins (Figure 4.5; Dicharry et al. 1973). Because of the tremendous volume of oil still left in the reservoir after waterflooding, other enhanced oil recovery techniques were considered to improve oil recovery. Since 1972, CO_2 has been injected for enhanced oil recovery.

6.3. Quantification of Natural Heterogeneity in SACROC Northern Platform

A high-resolution geocellular model of the SACROC northern platform was constructed by the Texas Bureau of Economic Geology using porosity from wireline logs and three-dimensional seismic data (Wang, Texas Bureau of Economic Geology, *Written Communication*, 2006). This high-resolution geocellular model was

constructed with a broad variety of geologic data (core data, well-log data, sedimentologic and stratigraphic interpretation) and geophysical data (seismic attributes and rock physics data). Consequently, the high-resolution geocellular model includes the detailed heterogeneity and the structure of formations.

Two major methods of incorporating three-dimensional seismic data into a model are inversion and time-depth conversion. Inversion inverts the reflection amplitude into acoustic impedance and time-depth conversion converts amplitude and impedance data from time space to depth space.

6.3.1. Estimation of Porosity from Wireline Log Analysis

The Canyon Formation was formed by shallow water skeletal and oolitic limestone cycles while the Cisco Formation comprises mainly deep-water crinodal mounds and debris wedges (Kerans et al. 2005). The base model utilized here consists of a detailed geologic model that included 23 horizons from early Canyon to the top of the Cisco, and porosity data from 368 wireline logs.

Reservoir quality is better developed in the Canyon than the Cisco (Figure 6.1). In the Canyon Formation, porosity is continuous and increases upward from the mudstone base to the grain-rich top. The reservoir lying in the Cisco Formation is a highly heterogeneous formation, including low porosity zones compartmentalized within one to two well spaces. Heterogeneity in the Cisco Formation can be better resolved by seismic mapping and inversion (Kerans et al. 2005).

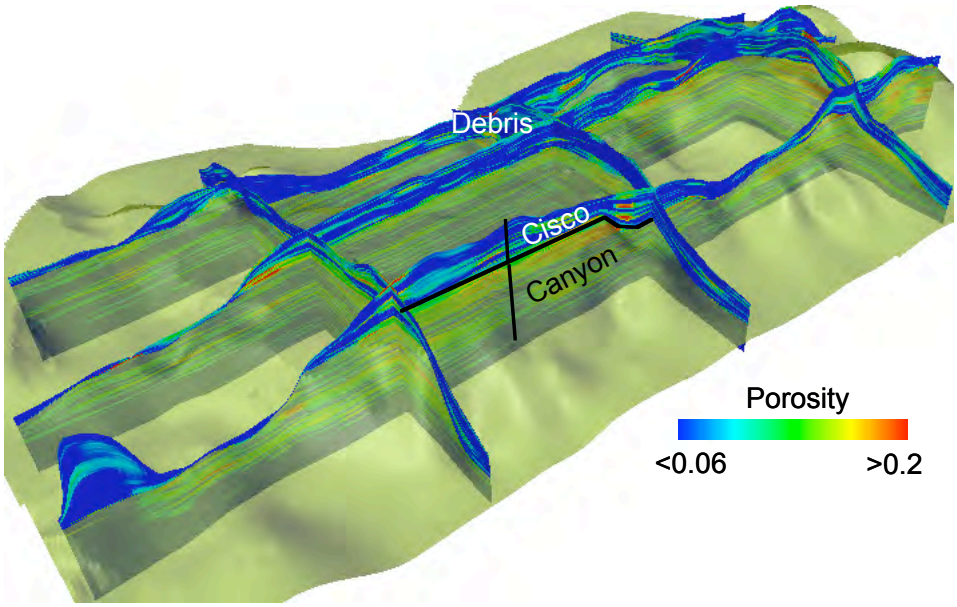

Figure 6.1. Spatial heterogeneity of porosity determined by wireline log.

6.3.2. Estimation of Porosity from both Wireline Logs and Seismic Survey

In the Cisco and Canyon Formations, acoustic impedance decreases linearly with porosity (Figure 6.2). The reflection amplitude, measuring the contrast of impedances of two adjacent media, is not linearly related to porosity. The three-dimensional seismic data in time-space were first inverted from the impedance using the Hampson-Russell package and converted into porosity using the linear relationship in Figure 6.2.

The accuracy of time-depth conversion depends on the number of controlling horizons used. However, the number of controlling seismic horizons is limited by the resolution of the seismic data, which is significantly lower than that of the wireline logs.

Two models, one in time space (time model) and the other in depth (depth model), with 120, 230, and 90 cells in x, y and z directions were built using four

horizons. Seismic attributes, such as amplitude, impedance and porosity, were transferred from the porosity model to the time model, from the time model to the depth model, and from the depth model to the detailed geologic model.

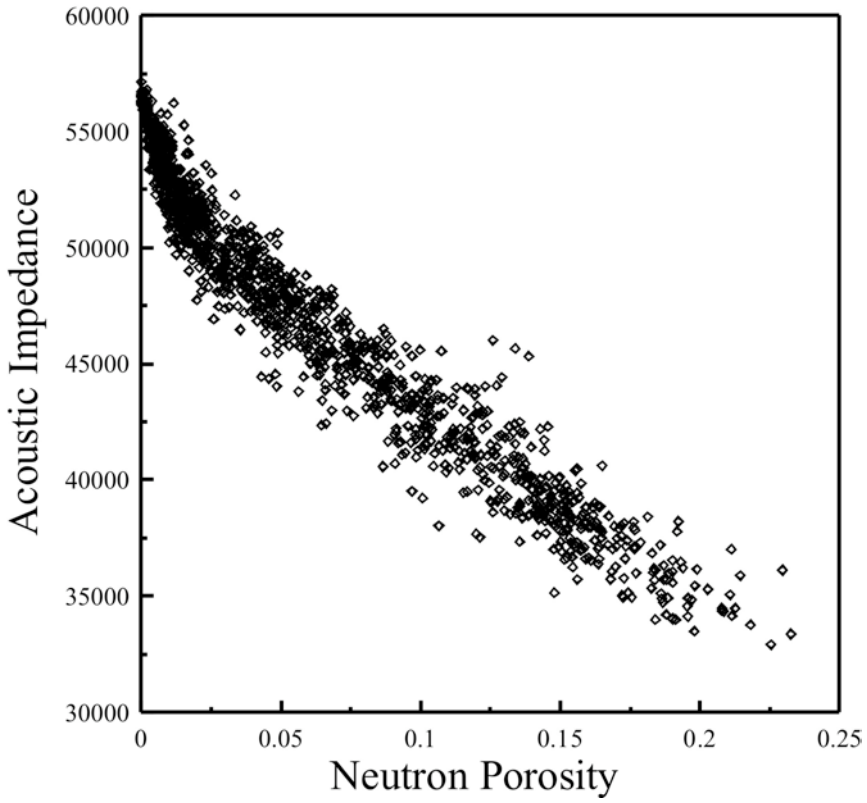

Figure 6.2. Plot of acoustic impedance versus porosity, showing the nearly linear relationship between those properties in well SACROC 27-19.

Seismic porosity values were added to the deterministically interpolated porosity by difference mapping. Since the porosity distribution in the Canyon interval could be mapped deterministically using porosity data from wireline logs, combined seismic and wireline log porosity were only applied to the heterogeneous Cisco interval (Figure 6.3). Compared to the representation shown in Figure 6.1, a

significant increase of porosity distribution was added to the model, which could not be mapped using wireline log data.

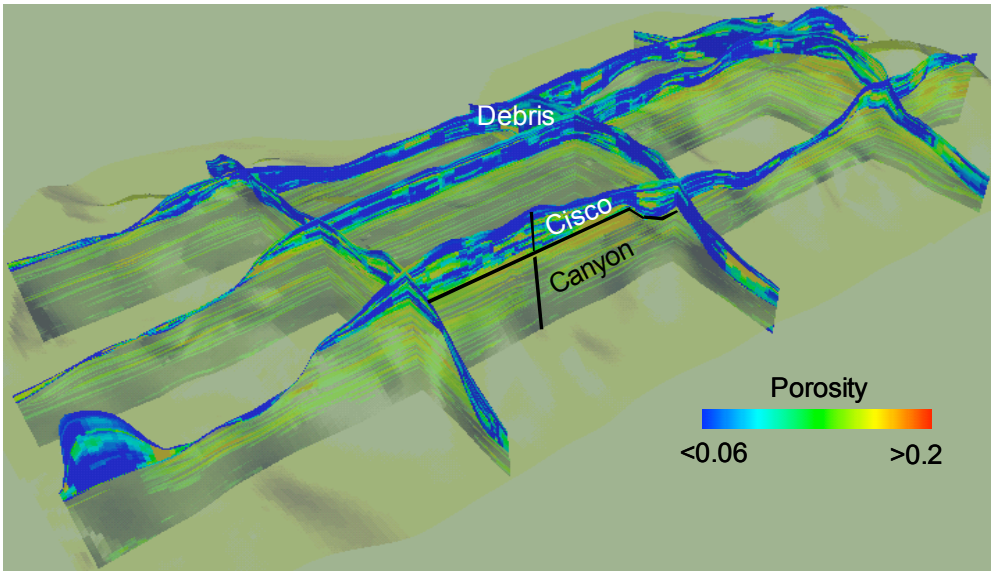

Figure 6.3. Spatial heterogeneity of porosity determined by both wireline log and seismic data.

6.3.3. Estimation of Permeability from Porosity

The prediction of permeability in heterogeneous carbonates from porosity is a difficult and complex problem. A simple correlation cannot describe the relation between permeability and porosity. Babadagli and Al-Salmi (2004) provided an extensive review of existing correlations between porosity and permeability in carbonate rock.

The relationship between porosity and permeability in the high-resolution geocellular model developed by the Texas Bureau of Economic Geology is based on the rock-fabric approach. Lucia, (1995, 1999) discussed this approach, which is based on the premise that pore size distribution related to rock fabric controls permeability in carbonate rock. To determine the relationship between rock fabric and petrophysical parameters, Lucia (1995, 1999) divided pore space into two

categories: interparticle porosity and vuggy porosity. Interparticle porosity includes intergrain and intercrystal pore space. Vuggy pore space is subdivided into separate and touching vugs. Separate vugs are connected through the interparticle pore space (grain molds) and touching vugs form an interconnected pore system independent of the interparticle pore space (caverns and fracture).

Lucia (1995, 1999) suggested that permeability could be related to rock-fabrics, including interparticle porosity, geologic descriptions of particle size and sorting, and suggested that rock fabrics could be divided into three classes. Class I includes interparticle size from 100 to over 500 μm and is dominant in grainstones, dolograinstones, and large crystalline dolostones. Class II includes interparticle size from 20 to 100 μm and is dominant in grain-dominated packstones, fine and medium crystalline, grain-dominated dolopackstones, and medium crystalline, mud-dominated dolostones. Finally, Class III includes interparticle sizes from 20 to 5 μm and is dominant in mud-dominated limestones and fine crystalline, mud-dominated dolostones.

By applying reduced major axis transformation, the classification of carbonate rock by interparticle size is generalized after introducing the rock-fabric number (λ) (Lucia, 1999). The global transforming equation, which calculates permeability from the rock-fabric number and porosity, was developed by Lucia (1999) and Jennings and Lucia (2001):

$$\log(k) = (9.7982 + 12.0838\log(\lambda)) + (8.6711 + 8.2965\log(\lambda))\phi \qquad \text{(Eq. 6.1)}$$

where, λ, k, and ϕ are, respectively, rock-fabric number, permeability, and interparticle porosity. Lucia and Kerans (2004) applied this equation to estimate

permeability distribution in the SACROC northern platform. Permeability is estimated from global transformation using porosity from wire logs and a stratigraphically defined rock-fabric number (Table 6.1).

Table 6.1. Permeability estimation using porosity and rock-fabric number (Lucia and Kerans, 2004).

Formation	Sequence	Rock-fabric number (λ)	Transforming equations	
Cisco	Late		$k = 2.1625 \times 10^6 \times \phi^{3.8844}$	Highest portion of Cisco (Implication of karsting)
	Late	1.7	$k = 1.031 \times 10^7 \times \phi^{6.7592}$	Late Cisco (wide variety of rock fabrics)
	Early	1.9	$k = 2.69 \times 10^6 \times \phi^{6.3584}$	Early Cisco (Characterized by fusulinid/crinoidal/peloid grain dominated packstones, grainstones, and wackestones
Canyon	1	2.5	$k = 97628 \times \phi^{5.3696}$	Early Canyon: (Characterized by moldic ooid grainstone, grain-dominated packstone, and mud-dominated fabrics)
	2	1.75	$k = 38520 \times \phi^{5.0923}$	Late Canyon: (Characterized by crinoidal/fusulinid/peloid, grain-dominated packstones, and mud-dominated fabrics having vuggy porosity)
	3			Below reservoir

6.4. Upscaling: Renormalization Estimating Equivalent Permeability and its Limitation

One goal of this study was to develop a meaningful simulation model based on the Texas Bureau of Economic Geology's high-resolution geocellular model that incorporates natural heterogeneity. The original geocellular model describing the Cisco and Canyon Formations includes 9,450,623 (149 × 287 × 221) elements (Figure 6.4). The approximate size of the model is 4000 m wide and 10,000 m long. The top of the geocellular model describes the top configuration of the Cisco

Formation, which is below approximately 1200 m depth, and the bottom of the model describes the bottom configuration of the Canyon Formation, which is below a depth of approximately 1400 m.

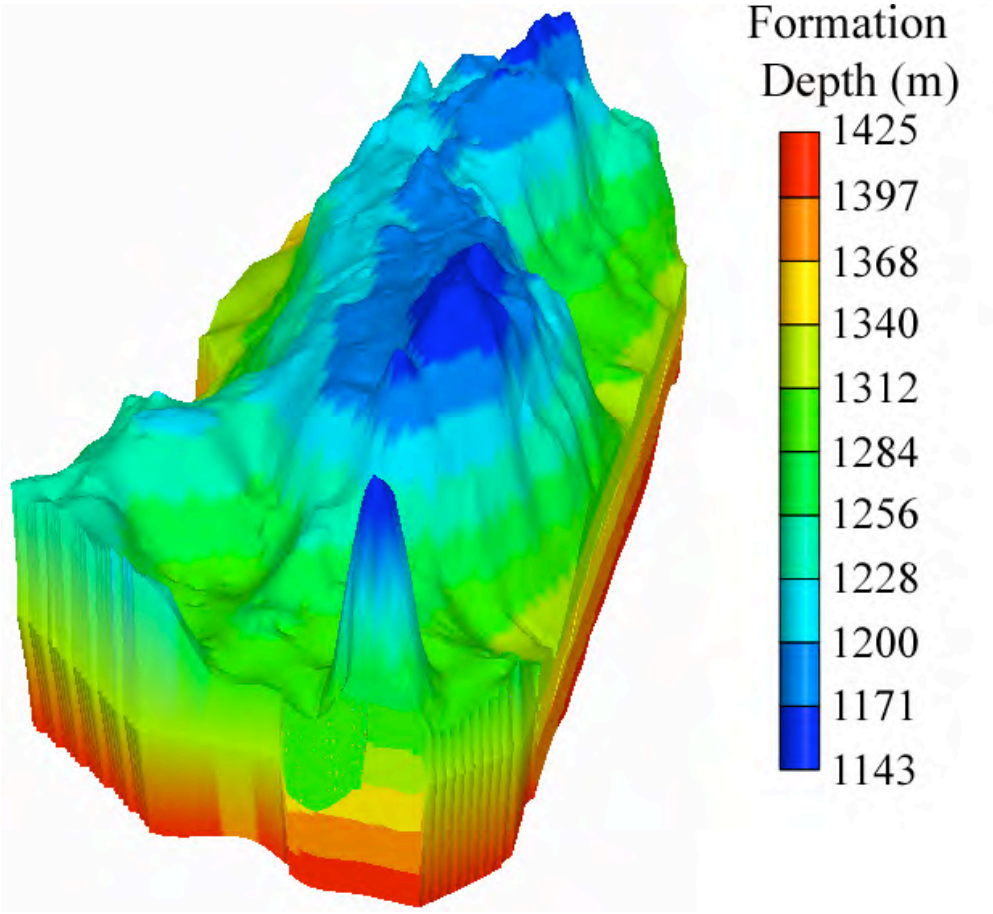

Figure 6.4. High-resolution geocellular model representing the SACROC northern platform.

Although the high-resolution geocellular model provides a quantified characterization of natural heterogeneity in the SACROC northern platform, the development of a multi-phase and -species reactive transport model was hampered due to the large number of elements. For this reason, we elected to upscale the model

to fewer elements. Such upscaling invariably leads to less resolution of heterogeneity, but we tried to preserve as much of the heterogeneity as possible.

Upscaling obtains a description of spatially variable permeability in denser grids that reproduces average values of permeability in sparse grids. The currently available upscaling techniques are reviewed in detail in the literature (Fayers and Hewett, 1992; Christie, 1996; Wen and Gomez-Hernandez, 1996; Renard and de Marsily, 1997; Noetinger et al. 2005). Upscaling can be divided into two categories: local techniques and nonlocal techniques, based on the assumptions that intrinsic permeability is an explicit function of cell conductivities or not (Wen and Gomez-Hernandez, 1996). Local techniques assume that average permeability is intrinsic to the cell permeability in denser grids. Therefore, average permeability is generally expressed as an explicit function of the cell permeability in a denser grid. Nonlocal techniques assume that that average permeability is intrinsic to the cell permeability in a denser gird and it also depends on the boundary conditions. Generally, a solution based on Laplace's equation falls within this category.

We adapted a local technique for upscaling the high-resolution geocelluar model of SACROC. Among several local techniques considered, we obtained upscaling algorithms developed through an equivalent resistor network model (King, 1989). This technique is generally called "renormalization" because it successively upscales the symmetric grid blocks using self-repetitive geometry until the final block size is reached. Renormalization is fast and computationally cheap because it does not require solutions to the differential equations. In addition, it is not constrained by the number of blocks. Because of these practical advantages, many researchers have

studied and updated the renormalization technique (Hinrichsen et al. 1993; King et al. 1993; Christie et al. 1995; King, 1996; Gautier and Noetinger, 1997; Hansen et al. 1997; Wallstrom et al. 1999; Li and Beckner, 2001; Renard et al. 2000).

Despite its many advantages, renormalization has several drawbacks. If there is a high contrast between neighboring permeabilities, it will underestimate average permeabilities (King, 1989; Renard and de Marsily, 1997). In addition, this method does have some limitations with respect to applicable boundary conditions (Malick, 1995, for a detailed discussion of such limitations). Finally, renormalization is specially designed for orthogonal grids.

Although our model satisfies several conditions to apply renormalization, the grid is not completely orthogonal. Although the grid is orthogonal in both the x- and y-detraction, the z-direction is irregular, which induces some error in the resulting upscaled permeabilities. It is extremely difficult to quantify the error due to the non-orthogonality, although we estimate the accrued error to be less than the uncertainty associated with seismic and wireline data used to calibrate the model. Therefore, some errors will accumulate during the renormalization process. Although upscaling generates some errors, the analysis indicates that grid non-orthogonality does not affect the flow simulation (Appendix. XIII).

Sequential results of permeability distributions by renormalization are shown in Figure 6.5. For the model development of CO_2 sequestration simulation, we obtained 15,470 cells after a series of three renormalizations.

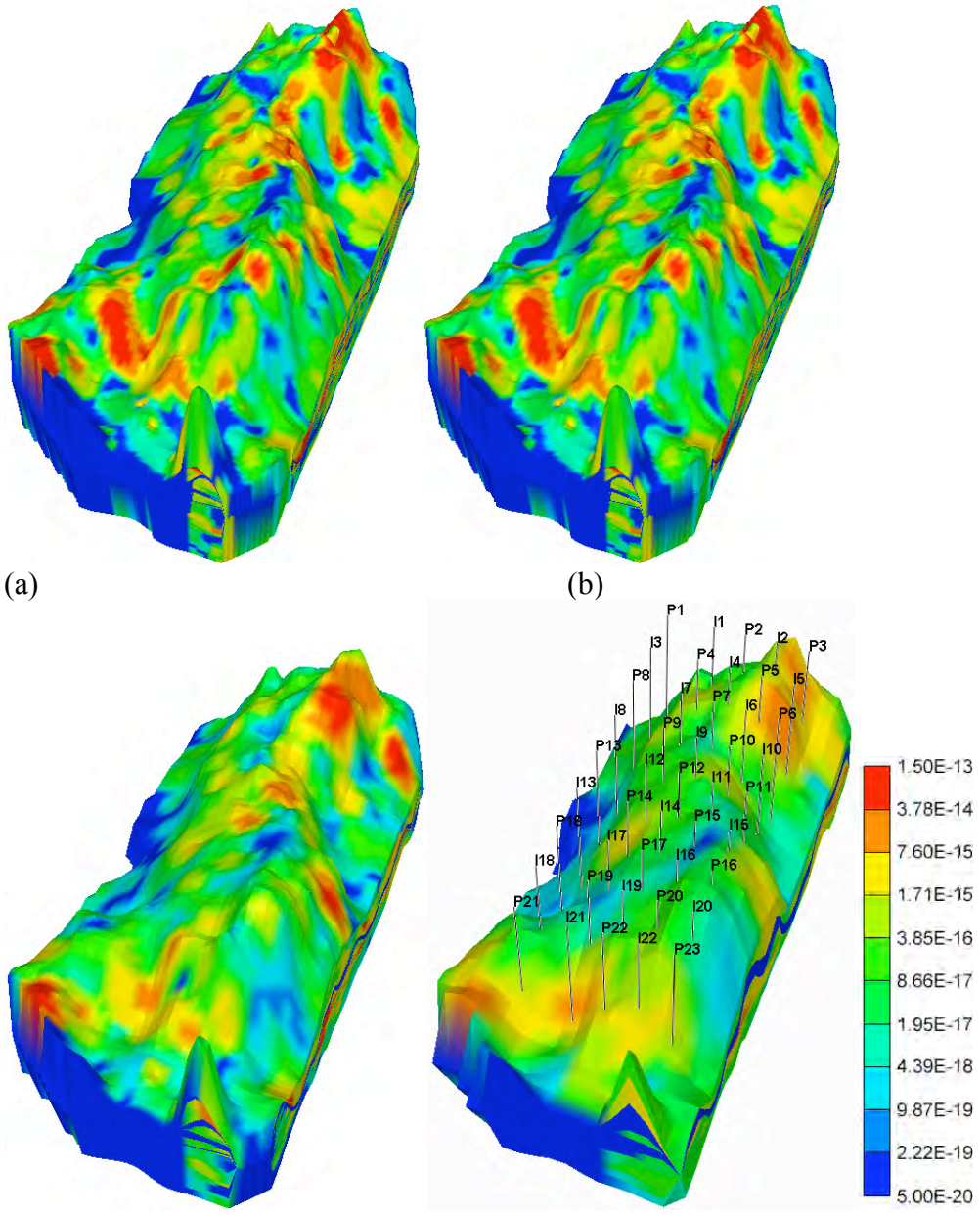

Figure 6.5. Permeability distribution during each renormalization procedure. (a) 149x287x221(=9,450,623): Mean 5.62E-15m^2 and Std. 4.20E-14, (b) 74x143x110(= 1,164,020): Mean 3.64E-15m^2 and Std. 2.40E-14, (c) 36x71x54(=139,968): Mean 2.02E-15m^2 and Std. 1.38E-14, and (d) 17x35x26(=15,470): Mean 5.86E-16m^2 and Std. 3.94E-15.

6.5. Evaluation of the Wolfcamp Shale as a Suitable Seal in SACROC

The purpose of water chemistry data and $\delta^{13}C$ data analyses is to determine the potential sealing effect of Wolfcamp Shale Formation. These chemical analyses

do not provide the definitive proof to whether CO_2 leaks through the Wolfcamp shale because SACROC comprises a huge area, 356 km_2 (Figure 4.1). Therefore, even the most detailed datasets will not cover the entire SACROC area. As such, the ultimate goal of these analyses is to evaluate the overall performance of the Wolfcamp Shale and evaluate the likelihood that the Wolfcamp Shale currently acts as a suitable seal in this area.

6.5.1. Analysis of Water Chemistry from Brine and Shallow Groundwater

The Wolfcamp Shale Formation, about 150 m thick, is the caprock overlying the Cisco and Canyon Formations (Vest, 1970; Raines et al. 2001). Previously, there has been no indication of CO_2 leakage in this field although CO_2 has been injected for enhanced oil recovery for the last 35 years. Carey et al. (2007) measured the permeability of the Wolfcamp shale and indicated that the permeability perpendicular to shale layer is <0.05 mD (k_z) and that parallel to the shale layer is 9 mD (k_x). Furthermore, they performed X-ray diffraction analyses. Based on their mineralogical analysis, CO_2 has not interacted with Wolfcamp shale; the carbonate in the Wolfcamp shale appears to derive from primarily diagenetic processes. In addition, carbon and oxygen isotope measurement from Wolfcamp shale also shows that carbonates in shale are typical marine-originated $\delta^{13}C$ values. The experiments from Carey et al. (2007) suggest that CO_2 is probably effectively stored in the Cisco and Canyon Formations and does not leak through the Wolfcamp shale.

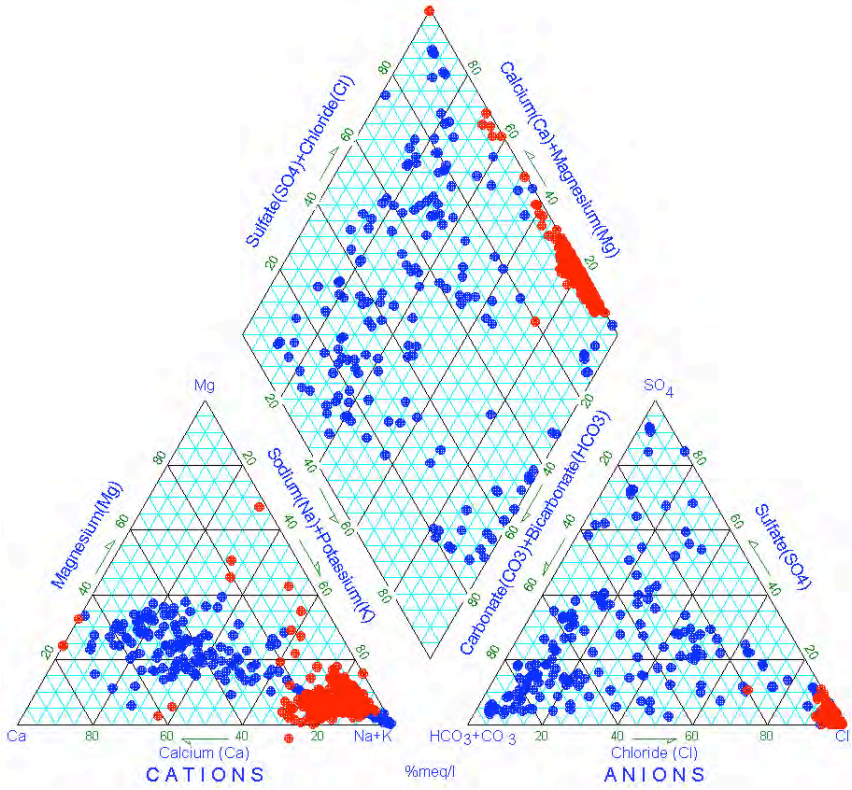

Figure 6.6. Piper diagram showing the classification of both brine and shallow groundwater.

Here, we gathered and analyzed the available water chemistry data, which are a compilation of water analysis reports from various sources such as the Martin Water Laboratory, Unichem, the Texas Water Board, Permian Production Chemical, and the United States Geological Survey (Bowden, Kinder Morgan CO_2, *personal communication*, 2006). Brine samples (840) were gathered from the Cisco and Canyon Formations and shallow groundwater samples (173) were gathered from the Dockum Formation above the Wolfcamp Formation. Generally, while most of the brine is the Na-Cl type, shallow groundwater is shown to be distributed from Na-HCO_3 to Ca-HCO_3 (Figure 6.6).

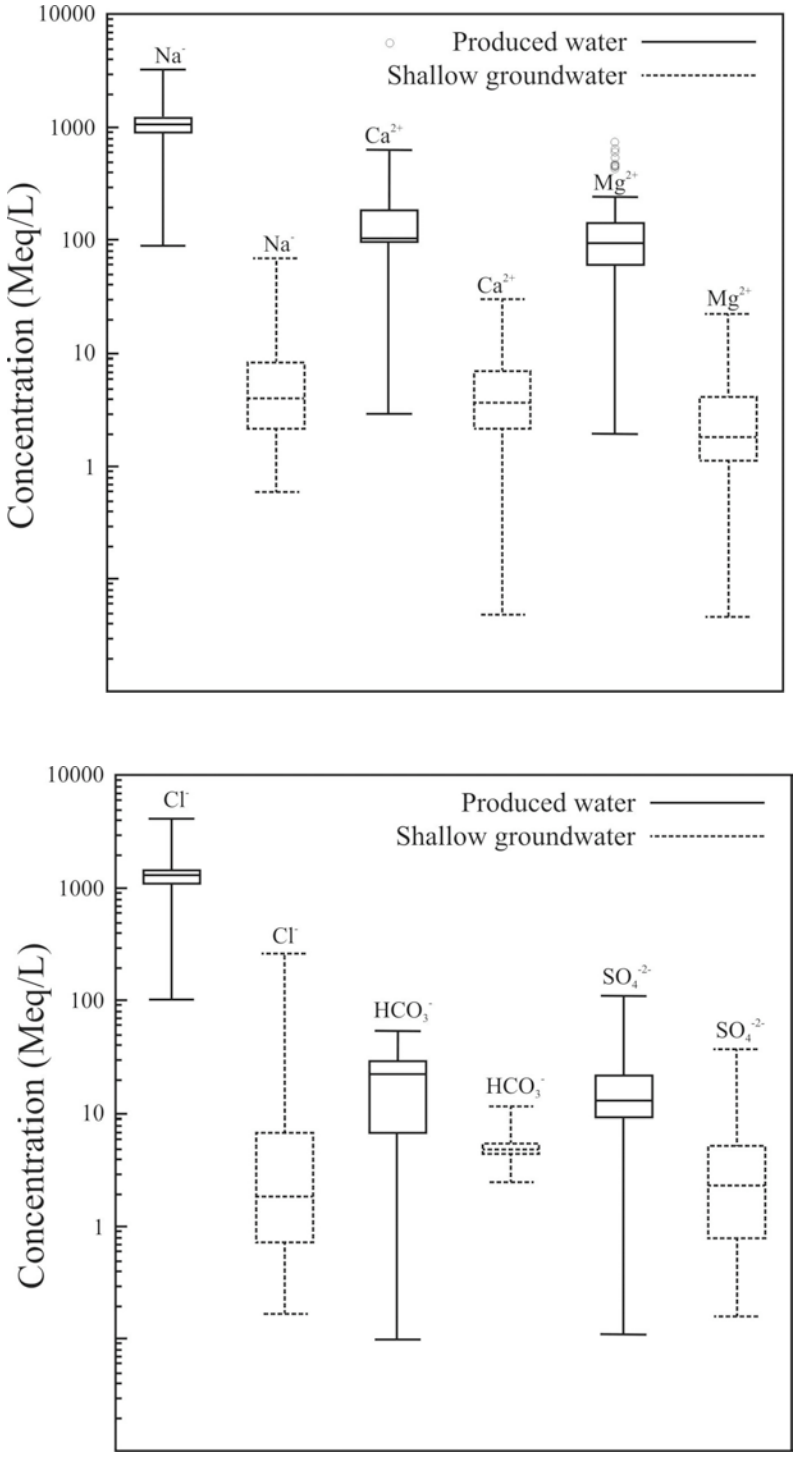

Figure 6.7. Box-and-whisker diagram showing the distinctive difference between brine and shallow groundwater.

We hypothesized that the concentrations of brine and shallow groundwater become more similar to each other if they communicate through high permeability conduits such as faults or fractures. The fluid flow in the Cisco and Canyon Formations are advective-dominant due to the alteration of pressure by injection/production activities for the last 35 years. Therefore, highly advective flow conditions may accelerate mixing the CO_2-saturated brine in the Cisco and Canyon Formations. Additionally, if preferential pathways exist, CO_2-saturated brine in an advective-dominant system may easily migrate to the above shallow groundwater zone.

To evaluate this hypothesis, we compared the concentrations of individual species of brine and shallow groundwater (Figure 6.7). A Box-and-whisker diagram shows that species concentration between brine and shallow groundwater is distinctively different and generally provides no distinct indication of communication between the brine and shallow groundwater. This result suggests that Wolfcamp Shale Formation generally acts as suitable seal in this area.

6.5.2. Analysis of $\delta^{13}C$ Isotope

Since June 1996, CO_2 has been delivered from McElmo Dome, which is the natural CO_2 reservoir in Colorado (Figure 4.6). The delivered CO_2 was injected into the Cisco and Canyon Formations over the last 10 years. The CO_2 from McElmo Dome is magmatically originated with isotope values of around -4 ‰ (Cappa and Rice, 1995). Therefore, we hypnotize that if quickly leaking CO_2 from Cisco and Canyon Formations reaches the surface, $\delta^{13}C$ measured at the surface will show

neither atmospherically-originated values (-9 ~ -8 ‰) nor biologically-originated values (-16 ~ -10 ‰). Rather, $\delta^{13}C$ values will tend toward magmatically originated values (-4 ‰) in McElmo Dome due to the mixing effect. To test the hypothesis, both CO_2 concentrations and $\delta^{13}C$ in air and soil were collected from around five wells and CO_2 pipelines at the SACROC production site 207 (Figure 6.8). The CO_2 concentrations and $\delta^{13}C$ were collected and analyzed during the Research Experience in Carbon Sequestration Field Trip (Fessenden, Los Alamos National Laboratory, *personal communication*, 2006).

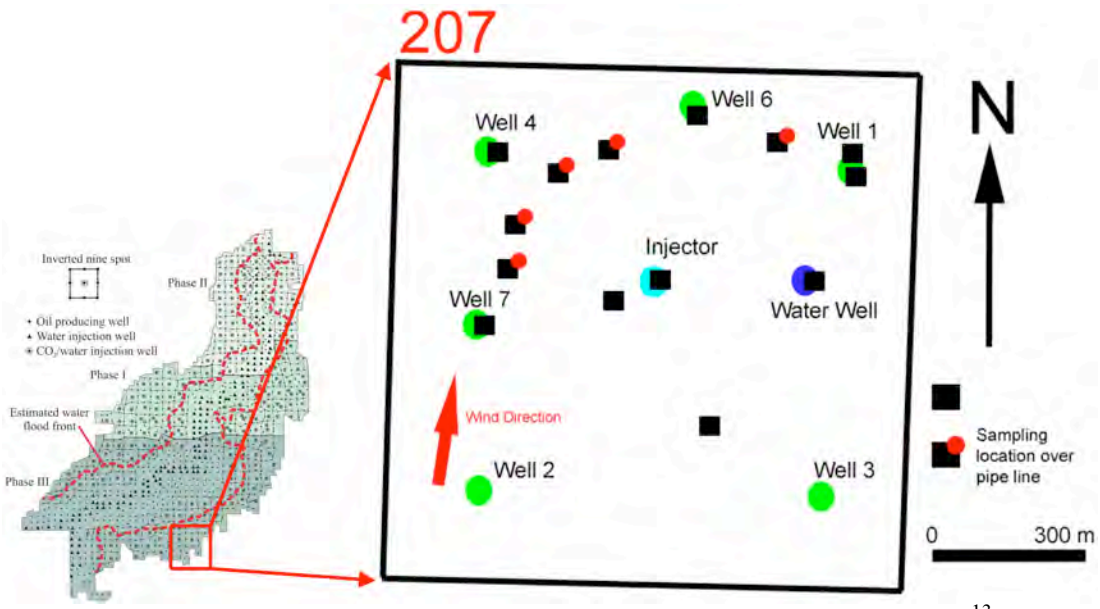

Figure 6.8. Sampling locations for collecting both CO_2 concentration and $\delta^{13}C$ in soil and atmosphere.

To investigate whether $\delta^{13}C$ collected at the surface originates from vegetation/atmosphere or is leaked from the Cisco and Canyon Formations, measured $\delta^{13}C$ data were plotted with magmatically-deriven $\delta^{13}C$ data in Figure 6.9. Magmatically-deriven data from several different sites such as McElmo Dome (Cappa and Rice, 1995), Mammoth Mountain (Bergfeld et al. 2006), Grand Wash

Fault Zone (Heath, 2004), and JM-Brown Bassett field (Ballentine et al. 2001) were chosen for comparison. The original $\delta^{13}C$ data with spatial distribution are provided in Appendix XI.

Measured $\delta^{13}C$ from the atmosphere in SACROC sector 207 is clearly affected by C4 plants (Buffalo grass), having a range from -14 to -12 (Figure 6.9). Values of $\delta^{13}C$ from soil have a wider range, indicating the mixing effect of plants, atmosphere and organic matters in the soil. The $\delta^{13}C$ data from the soil and atmosphere shows a clear distinction with magmatically-derived $\delta^{13}C$ values (-7~-2).

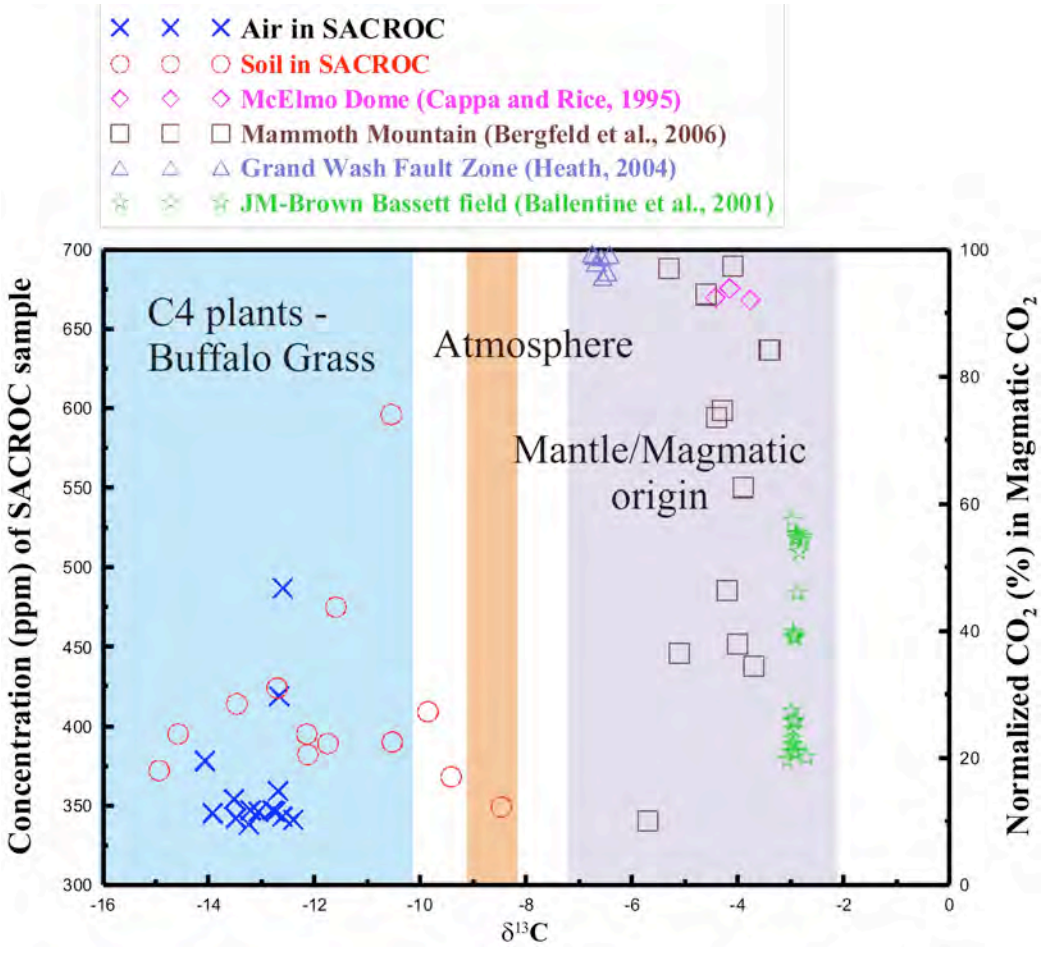

Figure 6.9. Analysis of CO_2 origin in SACROC sector 207.

Although the sampling location for $\delta^{13}C$ only covers sector 207, comparison of $\delta^{13}C$ in SACROC with other magmatically-driven $\delta^{13}C$ suggests that Wolfcamp shale acts as a suitable seal in SACROC (Figure 6.9), consistent with the brine-shallow groundwater data described in the previous section.

6.6. Analysis of CO_2 Injection and Production History in SACROC Northern Platform

Through rigorous analysis of CO_2 injection/production histories provided by Kinder Morgan CO_2, we found that 97 wells were used as CO_2 injectors at the SACROC northern platform from 1972 to 2002, shown in Figure 6.10 (Han et al. 2007). Among them, 51 wells have been actively used to inject about 13 million tons of CO_2 (13,048,845,748 kg) into the Cisco and Canyon Formations. Another 219 wells were CO_2 producers during the same period. Among them, 124 wells were used to produce about 6 million tons of CO_2 (6,104,258,074 kg). A simple mass balance analysis suggests a net of about 7 million tons of CO_2 (6,944,587,674 kg) are sequestered in the SACROC northern platform.

In the next chapter, we will detail results of a study of the ultimate forms of storage of this CO_2, e.g., how much CO_2 exists in a free-flowing phase (hydrostratigraphic trapping), how much is dissolved in the reservoir brine (solubility trapping), how much is trapped in minerals (mineral trapping), and how much is trapped in pores by capillarity (residual gas trapping).

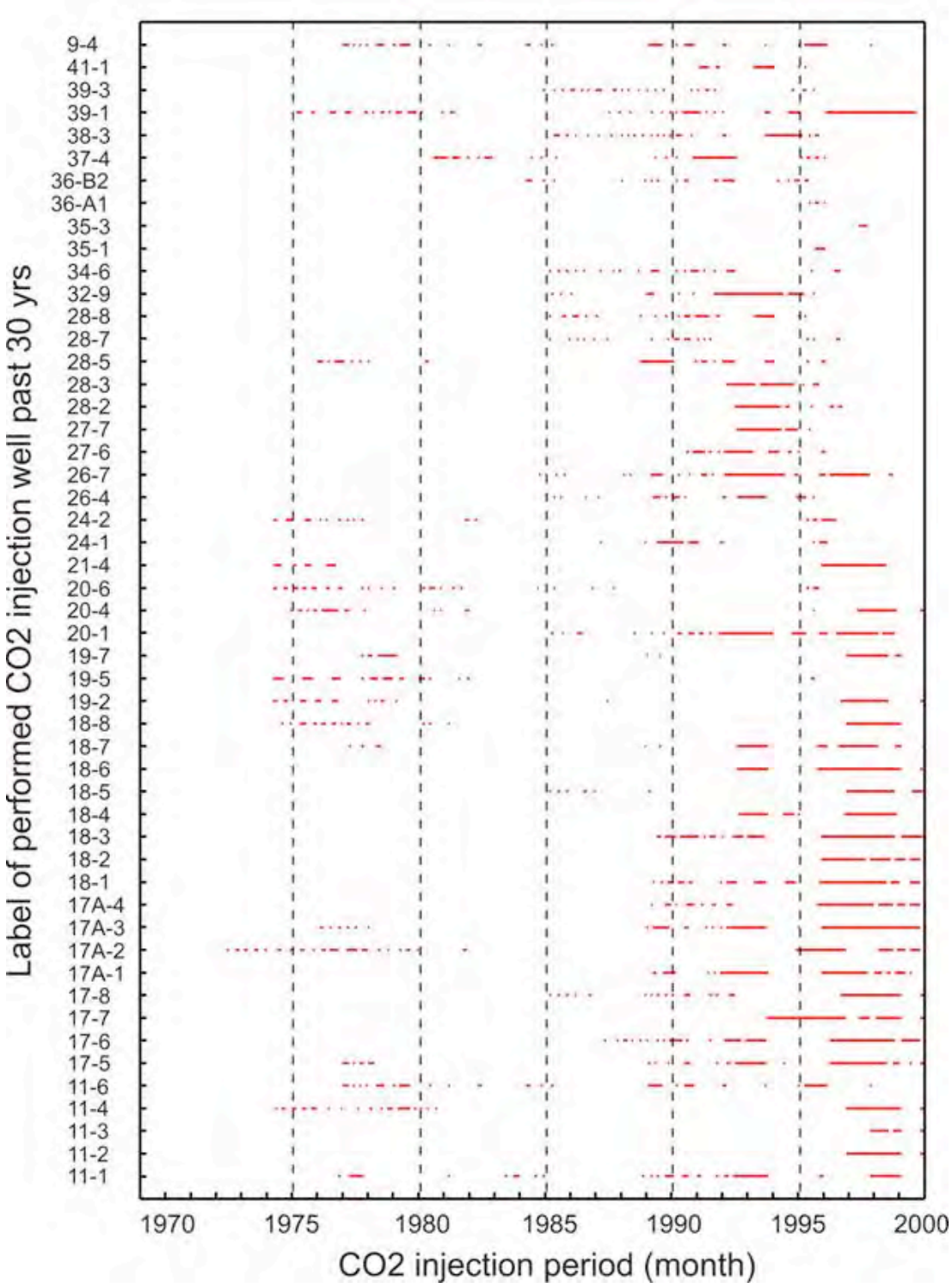

(a)

Figure 6.10. CO_2 injection/production history in the SACROC northern platform from 1972 to 2000 year: (a) CO_2 injection history, (b) CO_2 production history.

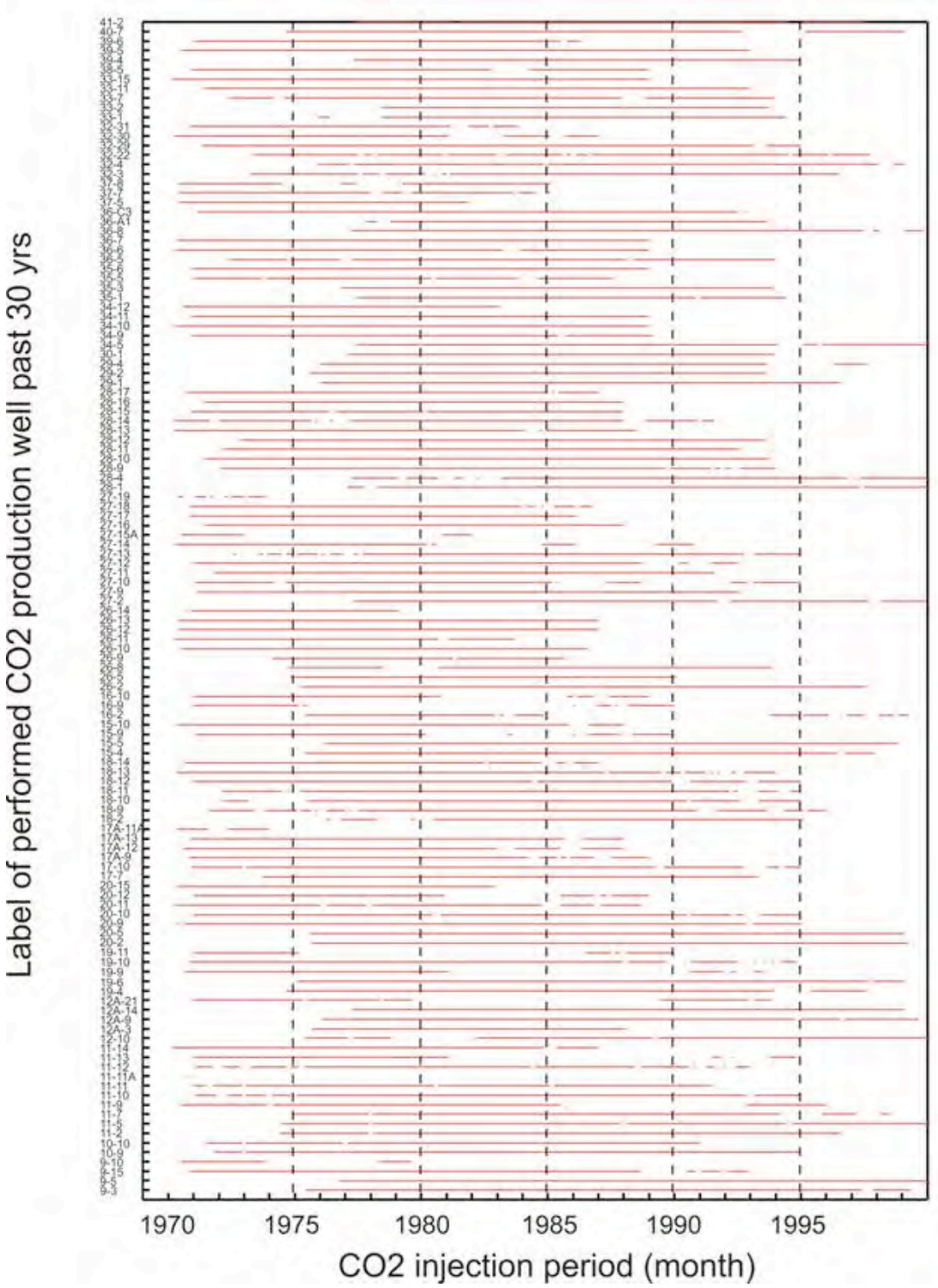

(b)

Figure 6.10. *Continued*

6.7. Summary and Conclusion

Both porosity and permeability vary naturally as a result of complex geological processes. The variability of these rock properties greatly affects the subsurface migration of injected CO_2 and trapping mechanisms such as hydrostratigraphic (mobile), residual, solubility, and mineral trapping. Furthermore, chemical reactions (precipitation/dissolution) induced by CO_2 injection will cause changes in rock properties. Therefore, it is essential to understand the heterogeneity of CO_2 injection sites to predict CO_2 migration and trapping mechanisms. Previously, Doughty and Pruess (2004) recognized the importance of heterogeneity and used stochastic techniques to develop a three-dimensional model representing fluvial/deltaic Frio Formations with TProGS (Carle and Fogg, 1996; 1997).

Although quantification of natural heterogeneity using diverse techniques has been discussed in detail in the hydrology and petroleum literature (Lake and Carroll, 1986; Lake et al. 1991; Anderson, 1996; Kolterman, 1996; de Marsily et al. 2006), the application of these techniques to CO_2 sequestration has not yet been widely performed. Therefore, we successfully adapted a geocelluar model describing reservoir heterogeneity to facilitate a detailed numerical modeling study of sequestration processes.

It is generally regarded that the application of wireline log analysis provides good vertical resolution of porosity only in a small portion of the reservoir. However, a combination of seismic data with wireline log data may represent natural heterogeneity better over a larger scale (Behrens and Tran, 1998; Doyen, 1988). Therefore, researchers at the Texas of Bureau of Economic Geology built a high-

resolution geocellular model based on both seismic modeling and wireline log, which reproduced porosity distribution within the SACROC northern platform. With the porosity distribution, permeability was estimated using a rock-fabric method. The number of elements accounting for the porosity and permeability distribution from this high-resolution geocellular model exceeded 9.4 million elements.

Although the geocellular model appears to provide an effective characterization of natural heterogeneity in the SACROC northern platform, using these data to develop a practical numerical model is difficult because of the large number of elements. Therefore, we applied a renormalization technique to reduce the number of elements from over 9.4 million to 15,470 elements. This grid was then used to develop a numerical model of practical size, as detailed in the next chapter.

Major conclusions in this chapter that can be drawn are as follows.

1. Heterogeneity varying with stratification, deposition, and diagenesis processes is complex to identify at the field/reservoir scale. This study suggests that incorporating geologic knowledge, geophysical logs, and seismic surveys provides an advantage to interpret three-dimensional subsurface structure.
2. The quantified three-dimensional porosity distribution indicates that porosity is continuous and increases upward from base to top in the Canyon Formation. Compared to the Canyon Formation, the Cisco Formation shows high heterogeneity with low compartmentalized porosity zones.

3. Direct application of the subsurface structure model to developing the flow and transport models is constrained because of currently available computer resources. Among the several upscaling techniques, renormalization is the most promising, although some error may be accumulated during renormalization process.
4. Analysis of both water chemistry and $\delta^{13}C$ does not provide a definitive answer but suggests that the Wolfcamp Shale Formation currently acts as a suitable seal in SACROC.
5. A mass balance analysis using field data shows that about 7 million tons of CO_2 (6,944,587,674 kg) are sequestered in the SACROC northern platform.

For the sake of brevity, this chapter is restricted to the characterization and analysis of the reservoir, and application of upscaling techniques required to assemble numerical models of practical size from seismic and other extremely large data sets. Details of the modeling study facilitated by this analysis are provided in the next chapter.

References

Allen, H.H., LaRue, C.R., 1957. SACROC Unit operations. Society of Petroleum Engineers Journal 829.

Allen, H.H., Thomas, J.B., 1959. Pressure maintenance in SACROC Unit operations January 1, 1959. Society of Petroleum Engineers Journal 1259.

Anderson, M.P., 1996. Characterization of geologic heterogeneity. In G. Dagan and S.P. Neumann, eds., Subsurface Flow and Transport: A Stochastic Approach. Cambridge University Press

Babadagli, T., Al-Salmi, S., 2004. A review of permeability-prediction methods for carbonate reservoirs using well-log data. Society of Petroleum Engineers Journal 87824.

Ballentine, C.J., Schoell, M., Coleman, D., Cain, B.A., 2001. 300-Myr old magmatic CO_2 in natural gas reservoirs of the west Texas Permian basin. Nature 409(6818), 327-331.

Bayat, M.G., Pickard, C.D., Benvegnu, A.J., Wingate, T.P., Larkin, R., 1996. Linking reservoir characteristics and recovery processes at SACROC-controlling wasteful cycling of fluids at SACROC while maximizing reserves. Second Annual Subsurface Fluid Control Symposium and Conference.

Behrensm R.A., Tran, T.T., 1998. Incorporating seismic data of intermediate vertical resolution into 3D reservoir models. Society of Petroleum Engineers Journal 49143.

Bergenback, R.E., Terriere, R.T., 1953. Petrography and petrology of Scurry reef, Scurry County, Texas. American Association of Petroleum Geologists Bulletin 37(5), 1014-1029.

Bergfeld, D., Evans, W.C., Howle, J.F., Farrar, C.D., 2006. Carbon dioxide emissions from vegetation-kill zones around the resurgent dome of Long Valley caldera, eastern California, USA. Journal of Volcanology and Geothermal Research 152, 140-156.

Brummett, Jr., W.M., Emanuel, A.S., Ronquille, J.D., 1976. Reservoir description by simulation at SACROC-a case history. Society of Petroleum Engineers Journal 5536.

Burnside, R.J., 1959. Geology of part of Horseshoe Atoll in Borden and Howard Counties, Texas. Geological Survey Professional Paper 315-B, 34.

Cappa, J.A., Rice, D.D., 1995. Carbon dioxide in Mississippian rocks of the Paradox Basin and adjacent areas, Colorado, Utah, New Mexico, and Arizona. Bulletin 2000-H, U.S. Geological Survey, Reston, pp. H1-H21.

Carey, J.W., Wigand, M., Chipera, S., Woldegabriel, G., Pawar, R., Lichtner, P., Wehner, S., Raines, M., Guthrie, J., 2007. Analysis and performance of oil well cement with 30 years of CO_2 exposure from the SACROC unit, west Texas. International Journal of Greenhouse Gas Control 1, 75-85.

Carle, S.F., Fogg, G.E., 1996. Transition probability based indicator geostatistics. Mathematical Geology 28, 437-464.

Carle, S.F., Fogg, G.E., 1997. Modeling spatial variability with one and multidimensional continuous-lag Markov chains. Mathematical Geology 29, 891-917.

Christie, M.A., 1996. Upscaling for reservoir simulation. Society of Petroleum Engineers Journal 37324

Christie, M.A., Mansfield, M., King, P.R., Barker, J.W., Culverwell., I.D., 1995. A renormalization-based upscaling technique for WAG floods in heterogeneous reservoirs. Society of Petroleum Engineers Journal 29127.

De Marsily, G., Delay, F., Goncalves, J., Renard, P., Teles, V., Violette, S., 2005. Dealing with spatial heterogeneity. Hydrogeology Journal 13, 161-183

Dicharry, R.M., Pettyman, T.L., Ronquille, J.D., 1973. Evaluation and design of a CO_2 miscible flood project-SACROC Unit, Kelly-Snyder field. Society of Petroleum Engineers Journal 4083.

Dixon, B.P., Newton, Jr., L.E., 1965. Rejection of large volumes of produced water in secondary operations. Society of Petroleum Engineers Journal 1147.

Doughty, C., Pruess, K., 2004. Modeling supercritical carbon dioxide injection in heterogeneous porous media. Vadose Zone Journal 3, 837-847.

Doyen, P.M. 1988. Porosity from seismic data: A geostatistical approach. Geophysics 53(10), 1263-1275.

Fayers, F.J., Hewett, T.A., 1992. A review of current trends in petroleum reservoir description and assessment of the impacts on oil recovery. Advances in Water Resources 15, 341-365.

Gautier, Y., Noetinger, B., 1997. Preferential flow-paths detection for heterogeneous reservoirs using a new renormalization technique. Transport in Porous Media 26, 1-23.

Han, W.S., McPherson, B.J., 2007. Evaluation of CO_2 storage mechanisms at SACROC, site of 35 years of CO_2 injection, Proceedings of the 6th annual conference on carbon capture & sequestration, Pittsburgh, Pennsylvania.

Hansen, A., Roux, S., Aharony, A., Feder, J., Jossang, T., Hardy, H.H., 1997. Real-space renormalization estimates for two-phase flow in porous media. Transport in Porous Media 29(3), 247-279.

Heath, J.E., 2004. Hydrogeochemical characterization of CO_2 charged fault zones in east-central Utah. M.S., Thesis, Utah State University, Logan. 166p.

Hinrichsen , E.L., Aharony, A., Feder, J., Hansen, A., Jossang, T., 1993. A fast algorithm for estimating large-scale permeabilities of correlated anisotropic media. Transport in Porous Media 12, 55-72.

Jennings, Jr.J.W., Lucia, F.J., 2001. Predicting permeability from well logs in carbonate with a link to geology for interwell permeability mapping. Society of Petroleum Engineers Journal 71336.

Kerans, C., Lucia, F.J., Zeng, H. and Wang, F., 2005, Reservoir Modeling of an Icehouse Giant: Horseshoe Atoll Complex, West Texas, U.S.A, Abstract, American Association of Petroleum Geologists International Conference and Exhibition.

King, P.R., 1989. The use of renormalization for calculating effective permeability. Transport in Porous Media 4, 37-58.

King, P.R., 1996. Upscaling permeability: Error analysis for renormalization. Transport in Porous Media 23, 337-354.

King, P.R., Muggeridge, A.H., Price, W.G., 1993. Renormalization calculations of immiscible flow. Transport in Porous Media 12, 237-260.

Koltermann, C.E., Gorelick, S.M., 1996. Heterogeneity in sedimentary deposits: A review of structure-imitating, process-imitating, and descriptive approaches. Water Resources Research 32(9), 2617-2658.

Lake, L.W., Carroll, Jr.H.B., 1986. Reservoir Characterization (eds.) Academic, San Diego, California.

Lake, L.W., Carroll, Jr.H.B., Wesson, T.C., 1991. Reservoir Characterization (eds.) Academic, San Diego, California.

Li, D., Beckner, B., 2001. A new efficient averaging technique for scaleup of multimillion-cell geologic models. Society of Petroleum Engineers Journal 72599.

Lucia, F.J., 1995. Rock-fabric/petrophysical classification of carbonate pore space for reservoir characterization. American Association of Petroleum Geologists Bulletin 79(9), 1275-1300.

Lucia, F.J., 1999. Carbonate Reservoir Characterization, Springer-Verlag, Berlin.

Lucia, J.F.J., Kerans, C., 2004. Permeability estimation using porosity logs and rock fabric stratigraphy: an example from the SACROC (Pennsylvanian) field, Scurry County, Texas. In R. Trentham, eds., Banking on the Permian basin: Plays, field studies, and techniques. West Texas Geological Society Publication 04-112, 271-274.

Malick, K.M., 1995. Boundary effects in the successive upscaling of absolute permeabilities. MS thesis, Stanford University.

Myers, D.A., Stafford, P.T., Burnside, R.J., 1956. Geology of the late Paleozoic Horseshoe Atoll in west Texas. Bureau of Economic Geology Publication 5607, p.113.

Noetinger, B., Artus, V., Zargar, G., 2005. The future of stochastic and upscaling methods in hydrogeology. Hydrogeology Journal 13, 184-201.

Raines, M. 2005. Kelly-Snyder (Cisco-Canyon) Fields/SACROC unit. West Texas Geological Society: Oil and gas fields in west Texas v.8, Publication number 05-114, p.69-78. West Texas Geological Society, Midland, Texas.

Ranies, M.A., Dobitz, J.K., Wehner, S.C., 2001. A review of the Pennsylvanian SACROC Unit. In J.J. Viveros and S.M. Ingram, eds., The Permian basin: Microns to satellites, looking for oil and gas at all scales: West Texas Geological Society Publication 01-110, p.67-74.

Reid, A.M., Reid, S.A.T., 1991. The cogdell field study, Kent and Scurry counties, Texas: A post-mortem. In M. Candelaria, eds., The Permian basin plays: tomorrow's technology today. West Texas Geological Society Publication 91-89, 39-66.

Renard, P., Le Loc'h, G., Ledoux, E., de Marsily, G., Mackay, R., 2000. A fast algorithm for the estimation of the equivalent hydraulic conductivity of heterogeneous media. Water Resource Research 36(12), 3567-3580.

Renard, Ph., De Marsily, G. 1997. Calculating equivalent permeability: a review. Advances in Water resources 20(5-6), 253-278.

Schatzinger, R.A. 1988. Changes in facies and depositional environments along and across the trend of Horseshoe Atoll, Scurry and Kent Counties, Texas. In, B.K., Cunningham, eds., Permian and Pennsylvanian Stratigraphy Midland basin, west Texs: Studies to aid hydrocarbon exploration. Permian Basin Section, society for Economic Paleontologists and Mineralogists Publication 88-28, 79-95.

Stafford, P.T., 1954. Scurry field: Scurry, Kent and Border Counties, Texas, Herald, F.A. (ed.) Occurrence of oil and gas in west Texas, Bureau of Economic Geology, Austin, Texas, 5716, p. 295-302.

Stewart, R.W., 1957. Reef limestones of the north Snyder oil field Scurry County, Texas. Ph.D Dissertation. Department of Geology. Massachusetts Institute of Technology.

Vest, E. L. Jr., 1970. Oil Fields of Pennsylvanian-Permian Horseshoe Atoll, West Texas *in* Halbouty, Michael T. (ed.) Geology of Giant Petroleum Fields, AAPG Memoir # 14. American Association of Petroleum Geologists, Tulsa Oklahoma, pp. 185-203.

Walker, D.A., Golonka, J., Reid, A.M., 1991. The effects of late Paleozic paleolatitute and paleogeography on carbonate sediment in the Midland basin, Texas. Candelaria, M. (ed.) Permian basin plays, tomorrow's technology today. West Texas Geological Society Publication 91-89, 141-162.

Wallstrom, T.C., Hou, S., Christie, M.A., Durlofsky, L.J., Sharp, D.H., 1999. Accurate scale up of two phase flow using renormalization and nonuniform coarsening. Computational Geoscience 3, 69-87.

Wen, X.-H., Gomez-Hernandez, J.J., 1996. Upscaling hydraulic conductivities in heterogeneous media: An overview. Journal of Hydrology 183(1-2), 9-32.

CHAPTER 7

EVALUATION OF CO_2 TRAPPING MECHANISMS AT THE SACROC NORTHERN PLATFORM, PERMIAN BASIN, TEXAS, SITE OF 35 YEARS OF CO_2 INJECTION:

2. MODEL DEVELOPMENT

7.1. Introduction

Carbon dioxide may be sequestered in geologic formations by several different mechanisms (Hitchon, 1996). One option is to store it as a separate phase (gas or supercritical phase) under a low-permeability caprock, a process commonly called hydrostratigraphic trapping. Another option is to store CO_2 as a dissolved phase in saline groundwater, typically called solubility trapping. Another mechanism is called mineral trapping, which refers to the process whereby CO_2 reacts with divalent cations in the reservoir brine to form secondary carbonate minerals. One last mechanism is residual gas trapping, which refers to capillary forces (surface tension) that render CO_2 immobile in reservoir pore space.

In Chapter 7, two models that evaluate these CO_2 trapping mechanisms in the SACROC northern platform are developed using the upscaled geocellular model developed in Chapter 6. Decisions regarding the assignment of the initial conditions, boundary conditions and other parameters in model are made with the results of data

analyses such as groundwater chemistry, isotopes and CO_2 injection/production history.

The first model is designed for simulating CO_2 trapping mechanisms in a reservoir saturated with brine. In this model, relatively complicated chemical reactions are included to accurately predict mineralization with complexation reactions. Therefore, researchers studying CO_2 sequestration with backgrounds in either hydrology or geochemistry will be interested in this work. The other model is designed for simulating CO_2 trapping mechanisms in a reservoir saturated with both brine and oil. In this model, for the sake of computational efficiency, relatively simple chemical reactions are included with the additional oil phase. The latter model provides a relatively realistic representation of CO_2 trapping mechanisms in the SACROC field because this field is a petroleum reservoir subjected to a long history of CO_2 enhanced oil recovery. In addition, researchers working on CO_2 sequestration with backgrounds in petroleum will be interested in this work. Ultimately, we compare CO_2 trapping mechanisms in both cases and investigate how the different reservoir fluids can affect the CO_2 trapping mechanisms.

7.2. Description of GEM-GHG

A commercial simulator, CMG's GEM (Generalized Equation of State Model) simulator is a multi-dimensional, finite-difference, isothermal compositional simulator that can simulate three-phase (oil, water, gas) and multicomponent fluids (Computer Modeling Group, 2006). Recently, the GEM simulator was expanded into a fully coupled geochemical compositional equation-of-state simulator known as

GEM-GHG for simulation of CO_2 storage in saline aquifers (Nghiem et al. 2004). A detailed description of GEM-GHG was provided in Chapter 5. Recently, a number of studies associated with CO_2 sequestration were performed using GEM-GHG. (Noh et al. 2004; Basbug et al. 2005; Kumar et al. 2004; Calabrese et al. 2005; Ozah et al. 2005; Bryant et al. 2006). The simulation in this study is implemented with GEM-GHG.

7.3. Model Describing Reservoir Saturated with Brine

7.3.1. Initial and Boundary Conditions

For evaluating CO_2 trapping mechanisms, we developed a 15,470 upscaled grid model (Chapter 6) describing the Cisco and Canyon Formations, which are the reservoir formations subjected to CO_2 injection for EOR for the past 35 years (Figure 6.5d). The approximate size of the model is 4000 m wide, 10,000 m long and 250 m thick.

Characterization of the porosity and permeability was described previously in section 6.3. Both porosity and permeability were predicted from a combination of data from seismic survey and wireline log interpretations.

From 1954 to 1971, water was injected in a centerline pattern to increase the reservoir pressure back above bubblepoint pressure (12.45 MPa), as illustrated in Figure 4.5. As a result, when CO_2 injection began in 1972, reservoir pressure had risen above 16.55 MPa (Dicharry et al. 1973; Langston et al. 1988). The initial average pressure conditions in the model are assigned as the 1972 reservoir pressure (16.55 MPa) when CO_2 injection began. To achieve this average pressure, reservoir

pressure in the model is assigned as hydrostatic with pressure at the formation top equal to 15.73 MPa and at the bottom pressure is assigned as 17.90 MPa.

Langston et al. (1988) reported the reservoir temperature as 54.5ºC, and we used this value as an assumed average for the reservoir. In the model, initial reservoir temperature is assigned using a conductive gradient with temperature at the top equal to 54.35ºC and temperature assigned at the bottom equal to 59.83ºC.

The upper boundary is designated as a no-flow condition, because I interpret the Wolfcamp shale above the Cisco and Canyon Formations as an effective seal, based on the analyses of both water chemistry data and $\delta^{13}C$ data (Figures. 6.7 and 6.9). In addition, the experiment from Carey et al. (2007) shows that carbonate in the Wolfcamp shale appears to derive from primarily diagenetic processes and its isotope compositions show typical marine-originated $\delta^{13}C$ values. The eastern, western, and northern boundaries are treated as no-flow boundaries, because the Wolfcamp Shale Formation meets these boundaries; the carbonate reef complex, the Cisco and Canyon Formations, is prism-shaped (Figure 4.2; Vest, 1970).

Although both Kaszuba et al. (2005) and Xu et al. (2005) indicate that the caprock can also act as a reactive component and contribute to mineralization, diffusion processes in caprock are very slow. Gaus et al. (2005) concluded that the porosity changes due to diffusion in typical seals occur in the lower 2 m after 3000 years. Consequently, the mineralization within such caprocks will be much less than that in the associated reservoir formation. Therefore, treating the seals as no-flow boundaries will not significantly affect the reservoir trapping mechanisms and capacity estimation. The bottom boundary is also designated as a no-flow boundary

because the Strawn Formation below the Cisco and Canyon Formations is also a low-permeability unit (Raines, Kinder Morgan CO_2, *personal communication*, 2006). Finally, hydrostatic pressure conditions with about 16.55 MPa (Raines, Kinder Morgan CO_2, *personal communication*, 2006) are assumed at the southern boundary because this boundary is connected to the middle part of the reservoir.

7.3.2. Transport Input Data

A relative permeability function (Figure 7.1) was developed by extrapolating relative permeability data measured in similar carbonate rock (Bennion and Bachu, 2005). Bennion and Bachu (2005) measured the relative permeability of supercritical CO_2 and brine in a 0.16 m core of low-permeability carbonate rock collected from Wabamun Lake, with experimental conditions of 41ºC and 22.4 MPa. Although they provided additional relative permeability data measured in different rocks, we chose to use only the relative permeability data measured in carbonate rock because the Cisco and Canyon Formations are a carbonate reef complex of similar mineralogy.

Previous workers evaluated hysteresis effects using a modified Land equation, which had been adapted to account for residual CO_2 trapping mechanisms (Kumar, 2004; Doughty, 2007). To quantify the residual-trapped CO_2, hysteretic effects in this study, we implemented a modified Land equation (Land, 1968) in our relative permeability curve (Figure 7.1a). Adapting the Land equation requires the determination of maximum residual saturation (S_{grmax}). An empirical formulation determining S_{grmax} from porosity was proposed by Holtz (2002). Using this empirical formulation, S_{grmax} is calculated as ~0.4 in this model.

A capillary pressure function measured in carbonate rock (Figure 7.1b) by Bennion and Bachu (2006) was adapted using Parker's function (Parker et al. 1987).

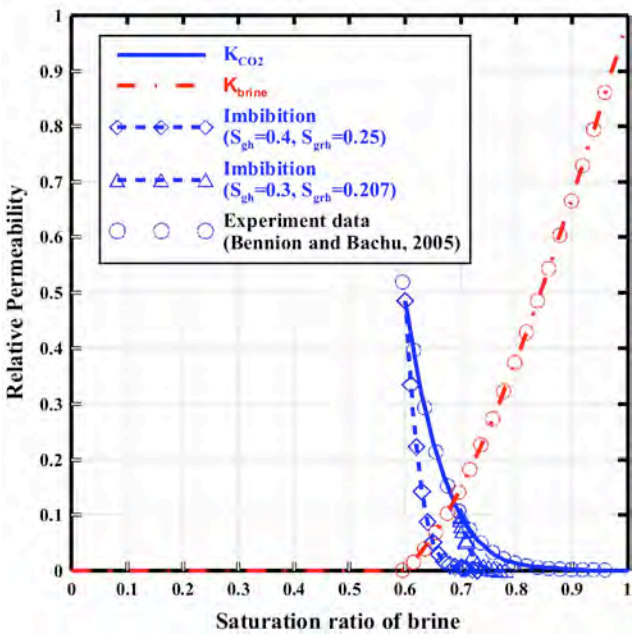

(a)

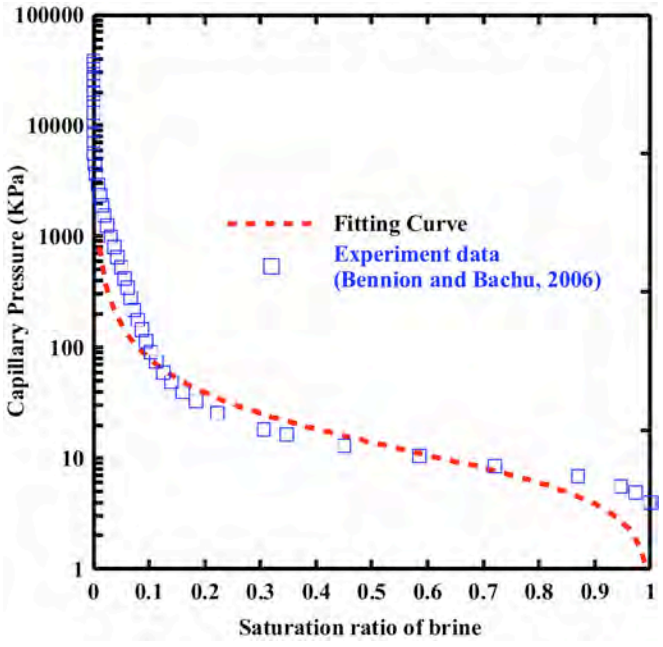

(b)

Figure 7.1. (a) Fitted relative permeability curves with experimental data from Bennion and Bachu (2005). (b) Fitted capillary curve with experimental data from Bennion and Bachu (2006).

The CO_2 density and fugacity coefficients are calculated from the Peng-Robinson equation of state (Peng and Robinson, 1976). Viscosity is estimated from Jossi et al. (1962) and solubility is calculated with Henry's law, adjusted for the effects of salinity using scaled particle theory (Li and Nghiem, 1986).

The density and viscosity of the aqueous mixture (CO_2-H_2O) with effects of brine concentration are, respectively, estimated from Rowe and Chou (1970) and Kestin et al. (1981). In our simulations, the effects of salinity on the brine are calculated from the concentration of Cl^-. Due to the reaction NaCl(aq)=Na^++Cl, the concentration of Cl^- varies at each time step and is updated to adjust brine density, viscosity, and Henry's constant. A detailed discussion of the equations of state implemented in the simulations is provided in Chapter 5.

7.3.3. Chemistry Input Data

A model was constructed using both reservoir fluid and core data collected from the SACROC field. The assignment of mineralogy in Cisco and Canyon Formations is based on X-ray diffraction analyses results (Table 7.1) performed by Carey et al. (2007) who analyzed a core sample from Cisco and Canyon Formations. In their analyses, dolomite and anhydrite were not detected. However, previous geological studies indicated that the Cisco and Canyon Formations highly altered by calcitization and dolomitization included minor amounts of anhydrite, dolomite, sand, and shale (Bergenback and Terriere, 1953; Myers et al. 1956; Raines, et al. 2001). Therefore, we modified mineralogy to include dolomite and anhydrite (Table 7.1).

Dawsonite especially is considered to be a late-stage mineral deposited in natural CO_2 reservoirs (Baker et al. 1995; Moore et al. 2005). Carey et al. (2007) were able to find a single X-ray diffraction peak of dawsonite in SACROC core and indicated the possibility of dawsonite precipitation in the SACROC field. Therefore, dawsonite was chosen for the secondary minerals with siderite.

Table 7.1. Volume fractions, surface areas, and kinetic rates.

Mineral	Weight percent (Carey, 2007)	Modified weight percent	Volume fraction	Surface area (m^2/g)	Activation energy (J/mol)	$Logk_{25}$ (mol/m^2s)	Model kinetic rate	Latest kinetic rate
Calcite	0.82	0.62	0.6063	2.21E-4	41870	-8.80	Svensson and Dreybrodt, (1992)	Lee and Morse, (1999)
Dolomite	0	0.1	0.0933	2.11E-4	41870	-9.22	White, (2005)	Pokrovsky and Schott, (2001)
Kaolinite	0.01	0.01	0.0110	2.49E-3	62760	-13.00	Nagy, (1995)	Nagy, (1995)
Anhydrite	0	0.1	0.0892	2.02E-4	41870	-8.80	Same as calcite	Dove and Czank, (1995)
Quartz	0.03	0.03	0.0303	2.29E-4	87500	-13.90	Tester et al. (1994)	Tester et al. (1994)
Illite	0.02	0.02	0.0193	2.18E-3	58620	-14.00	Knauss and Wolery, (1989)	Knauss and Wolery, (1989)
Ankerite	0.12	0.12	0.1043	1.97E-4	41870	-11.22	Estimated from Dolomite	Estimated from Dolomite
Dawsonite	0	0	0	2.48E-4	62760	-9.09	Hellevang, (2005)	Hellevang, (2005)
Siderite	0	0	0	1.52E-4	41870	-10.22	Estimated from Dolomite	Estimated from Dolomite

Since no direct measurements of BET-surface areas are available, the surface area ($S_a=(A_{grain}xV)/(V_{grain}$ x $M_w)$) was calculated using grain volume (V_{grain}), grain surface area (A_{grain}), molar volume (v), and molecular weight (M_w), as detailed in Table 7.1. To calculate grain volumes and grain surface areas, the mineral grains are assumed to be spherical. An average grain diameter of 0.005 m is assumed for all minerals except clay minerals (0.0005 m) such as kaolinite and illite.

The kinetic rate law for the dissolution and precipitation of minerals is from Lasaga (1984) with a temperature-dependent rate constant derived by Arrhenius' law:

$$r_m = A_m k_{25} \exp\left[-\frac{E_a}{R}\left(\frac{1}{T} - \frac{1}{298.15}\right)\right]\left(1 - \frac{Q_m}{K_m}\right) \qquad \text{(Eq. 7.1)}$$

where m is the mineral index, r is the dissolution/precipitation rate (positive value indicates precipitation and negative value indicates dissolution), A_m is the reactive surface area, k_{25} is the kinetic rate coefficient at 25ºC, E_a is the activation energy, R is the gas constant, K is the equilibrium constant for mineral reaction, and finally, Q is the activity product.

The kinetic rate coefficients of different minerals in this model are summarized in Table 7.1. Although the most recently derived kinetic rates are available from several sources, adapting these values generated a serious numerical convergence problem. It seems that the kinetic rate coefficients are so large that the changes of mineral volume due to precipitation and dissolution occur rapidly. As a result, radical pressure changes lead to quick convergence failure. Coupling this problem with the three-dimensional, heterogeneous model and 45 injection/production wells provided an intractable issue. Therefore, rather than work to identify potential changes to the numerical solver to accommodate a solution with the newer kinetic coefficients, we instead used relatively older coefficients for some minerals (Table 7.1). We did not attempt to calculate the uncertainty associated with using these older coefficients and we concede that this is a limitation of this study.

Thermodynamic parameters including equilibrium constants have been chosen from the SOLMINEQ.88 and PHREEQC databases (Kharaka et al. 1989; Parkhurst and Appelo, 1999). Particularly, the equilibrium constant of ankerite, which is a solid-solution between siderite and dolomite, varies with its composition. In natural system, a binary solution, $Ca(Fe_xMg_{1-x})(CO_3)_2$, where $Mg^{2+} >> Fe^{2+}$ has been observed

(Mozley and Hoernle, 1990), but end-member ankerite has never been observed (Chai and Navrotsky, 1996). Therefore, the composition of ankerite is assumed to be $CaFe_{0.25}Mg_{0.75}(CO_3)_2$ and its equilibrium constant is calculated from a regular solid-solution approach (Wood and Garrels, 1992; Appelo and Postma, 1993). The detail procedure of calculation is shown in Appendix XII.

For the activity coefficient calculation, a B-dot model accounting for the activity coefficient over a wide range of temperatures is implemented (Helgeson, 1969). Although the Pitzer model is more accurate, it does not apply to this model because the model is limited due to the lack of interaction parameters for trace element complexes (Langmuir and Melchior, 1985). Moreover, there are limitations estimating activity coefficients greater than surface temperature with current data. Therefore, researchers associated with CO_2 sequestration frequently used Debye-Huckel-type equations (Kumar et al., 2004; Xu et al., 2004; Gaus et al., 2005; Hellevang et al., 2005; Knauss et al., 2005; Zerai, 2006). Recently, Kervevan et al., (2005) and Andre et al., (2007) applied the Pitzer model to simulate CO_2 sequestration processes.

The initial brine concentration can be obtained after performing equilibrium reactions with an appropriate mineral composition. However, 840 water chemistry data are available for this field. Because the number of water chemistry data provides a statistically meaningful representation of brine concentration, the initial concentration is calculated from the average of the brine water chemistry data (Figure 6.7), expressed in Table 7.2. The charge balance is adjusted less 5% by changing Cl^- concentration.

Table 7.2. Initial brine concentrations.

Primary species	Concentration (mol/l)		Secondary species
H^+	3.981E-7 (pH=6.4)		CO_3^{2-}
K^+	3.981E-7	Estimated	NaCl(aq)
Na^+	1.094E0		$NaCO_3^-$
Ca^{2+}	1.314E-1		$NaHCO_3$(aq)
Mg^{2+}	5.700E-2		$CaCO_3$(aq)
SiO_2(aq)	2.345E-3	Estimated	$CaHCO_3^+$
Al^{3+}	2.318E-11	Estimated	$MgCO_3$(aq)
Fe^{2+}	5.850E-4		$MgHCO_3^+$
Cl^-	1.391E0		$Al(OH)_4^-$
HCO_3^-	5.300E-2		$Al(OH)_3$(aq)
SO_4^{2-}	4.050E-2		$Al(OH)_2^+$
			$Al(OH)^{2+}$
			$FeCl_4^{2-}$
			$FeCl^+$
			$Fe(OH)_2$
			$Fe(OH)^+$
			H_4SiO_4(aq)

7.3.4. Assignment of CO_2 Injection and Production Wells

More than 300 wells have been used for CO_2 injection and production over the last 35 years in the SACROC northern platform (Figure 6.10). Rigorous analyses of CO_2 injection/production histories indicate that 97 wells and 219 wells were respectively used as CO_2 injectors and producers. Because the dimension ($17 \times 35 \times 26 = 15{,}470$) of the upscaled grid used for this simulation is not large enough to assign the total number of wells, wells were lumped together and uniformly assigned a regular pattern (Figure 6.5d). The total numbers of pumping (*P*) and injection (*I*) wells are, respectively, 23 and 22.

Field injection and production were performed for a 30-year period, 1972 - 2002. About 13 million tonnes of CO_2 (13,048,845,748 kg) were injected into the Cisco and Canyon Formations and about 6 million tonnes of CO_2 (6,104,258,074 kg) were produced during this period. Therefore, a simple mass balance analysis suggests

that a net of about 7 million tonnes of CO_2 (6,944,587,674 kg) are sequestered in SACROC northern platform. The calculation of CO_2 net storage in the northern platform of SACROC was addressed in Section 6.6.

In this model, the exact field injection and production history do not match because of issues associated with the upscaled grid scale. In the model, about 7.5 millions tonnes of CO_2 (7,522,860,000 kg) were injected and about 0.4 millions tones of CO_2 (436,833,000 kg) were produced for the 30-year period from 1972 - 2002. The corresponding CO_2 net storage was about 7 million tones (7,059,027,000 kg) in the model. Consequently, the relative error of CO_2 net storage between field and model is 1.65 %.

The detailed injection and production history of wells in this model are shown in Appendix XIII. Finally, to evaluate CO_2 trapping mechanisms of century-scale processes, the total simulation period was 200 years, from 1972 to 2172.

7.3.5. Results and Discussions

7.3.5.1. Quantification of CO_2 Trapping Mechanisms at SACROC Northern Platform

Figure 7.2a summarizes the CO_2 mass stored in different forms, with CO_2 trapping mechanisms detailed in three temporal stages. Figure 7.2b shows the corresponding CO_2 mass flux of CO_2 trapping forms. In Stage I (1972–2002), the injection period, hydrostratigraphic (mobile) trapping is dominant. In this stage, CO_2 is injected into the reservoir by 22 injection wells. The mobile CO_2 mass flux was about 1.7E5 tonnes/year (Figure 7.2b) and total cumulative mass of CO_2 was 5E6

tonnes after 30 years (Year 2002). In this stage, the saturation of CO_2 gradually increases near the injection wells. At the same time, CO_2 migrates either vertically due to buoyancy-driven forces or horizontally through preferential flow paths. Also, solubility-trapped CO_2 increases in this period due to injection-induced high CO_2 partial pressure (Figure 7.2a). The aqueous CO_2 mass flux was about 5E4 tonnes/year (Figure 7.2b).

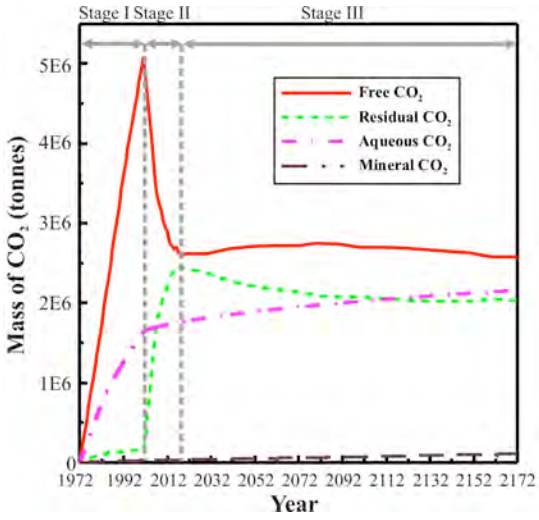

(a) Mass of CO_2 with time

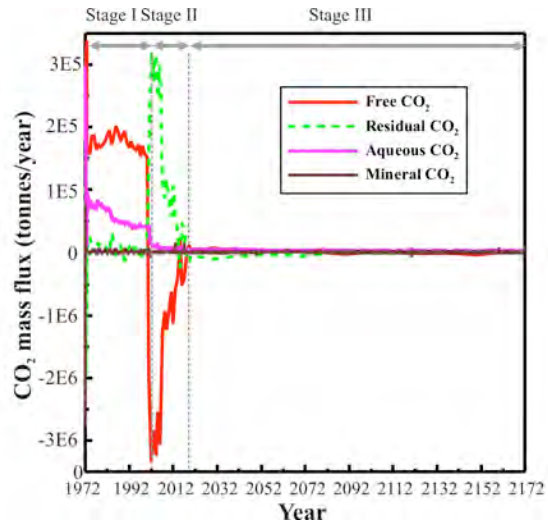

(b) CO_2 mass flux with time

Figure 7.2. CO_2 trapping mechanisms within the reservoir as a function of time.

In Stage II (2002 - 2017), residual trapping becomes important. After injection is halted, the decrease in CO_2 saturation is due to the imbibition process occurring at the tail of the CO_2 plume, where reservoir fluid displaces CO_2. As a result, while CO_2 migrates either vertically or horizontally, some of the mobile CO_2 becomes trapped in pores. At this point, CO_2 changes its phase from free (mobile) CO_2 to residual (immobile) trapped CO_2. In this stage, mobile CO_2 mass flux dramatically decreases while residual CO_2 mass flux dramatically increases (Figure 7.2b). Aqueous CO_2 mass continues to increase at this stage (Figure 7.1a), but at a slower rate because injection-induced CO_2 partial pressure decreases after CO_2 injection ceases. The aqueous CO_2 mass flux was less than 1E4 tonnes/year (Figure 7.2b). Minerals continue to precipitate.

In Stage III (2017–onward), solubility trapping becomes more important as both residual and free CO_2 dissolve in the reservoir brine. Both hydrostratigraphic (mobile) and residual-trapped CO_2 tend to decrease. Therefore, after several hundred years, the amount of solubility-trapped CO_2 will be greater than both hydrostratigraphic (mobile) and residual-trapped CO_2. From 2017 to 2072, the amount of free (mobile) CO_2 slightly increases, corresponding to the reduction of residual-trapped CO_2. This occurs because the free (mobile) CO_2 plume at certain injection wells migrates horizontally to neighboring injection wells where residual CO_2 is trapped. Consequently, the saturation of certain residual-trapped CO_2 becomes greater than the residual saturation value, and residual CO_2 becomes mobile CO_2. At the micro scale, approaching CO_2 plumes from neighboring injection wells increase pressure around pores where residual CO_2 is trapped. When the surrounding pressure

around pores is greater than the capillary entry pressure, the CO_2 blob starts to intrude into the pores where residual CO_2 is trapped; the intruding CO_2 blob is added to the residual-trapped CO_2. Consequently, the saturation of residual-trapped CO_2 increases. When the saturation of residual-trapped CO_2 becomes greater than the residual saturation value, residual-trapped CO_2 becomes mobile.

7.3.5.2. Spatial Distribution of Hydrostratigraphic (Mobile)- and Residual-Trapped CO_2

Figure 7.3a shows the spatial distribution of separate-phase CO_2. Due to the difficulty of showing three-dimensional distributions, two-dimensional cross-sectional views/slices are presented instead. Model results indicate that the spreading pattern of separate-phase CO_2 is different around each injection well due to heterogeneity (Figure 6.5d).

Separate-phase CO_2 reached the top of the Cisco and Canyon Formations (below the Walfcamp shale) within 30 years (year 2002) in injection wells I13 and I22 (Figure 7.3a). For example, CO_2 migrated 84 m from the injection point (I13) to the top of Cisco and Canyon Formations within 30 years due to the presence of a preferential path. In the absence of a high permeability preferential path, more than 30 years are required for CO_2 to reach the top. Well I22 is located on the southern part of the model where the distance from the injection point of Well I22 to the top of Cisco and Canyon Formations was 33 m. The shorter distance meant a preferential (high permeability) pathway was not needed to facilitate CO_2 reaching the top of the formation less than 30 years. Due to the shorter distance, separate-phase CO_2 was

able to reach and laterally spread at the top of the Cisco and Canyon Formations within 30 years.

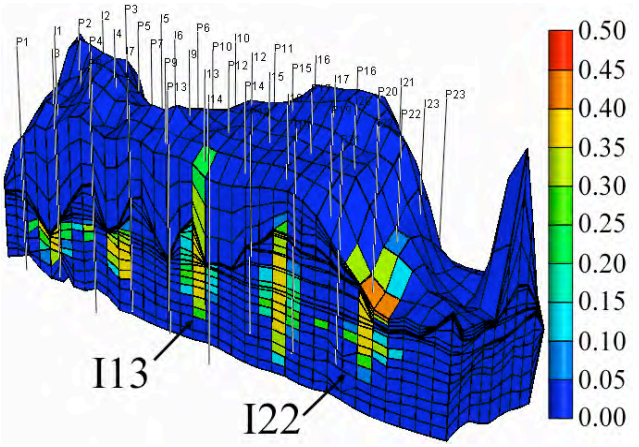

(a)

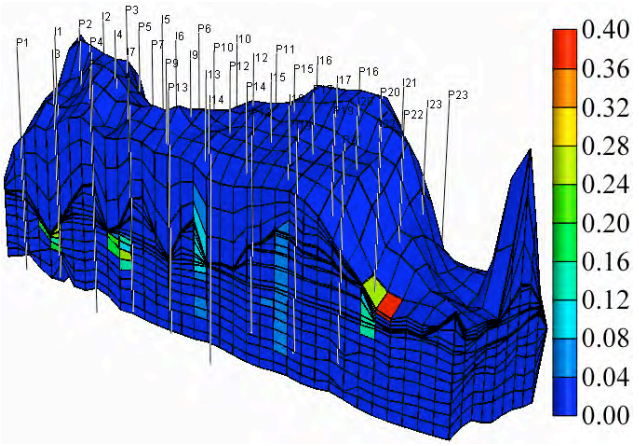

(b)

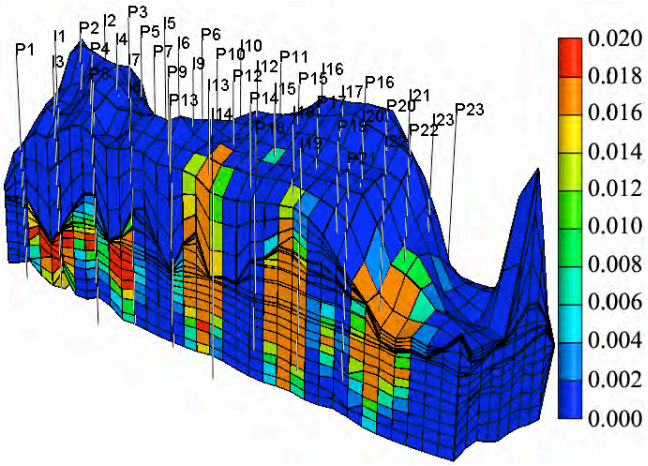

(c)

Figure 7.3. Two-dimensional cross-section view at year 2002 (30 years after CO_2 injection starts): (a) saturation of separate-phase CO_2, (b) relative permeability of separate-phase CO_2, and (c) mole fraction of aqueous-phase CO_2.

In sum, the simulated spatial distribution of separate-phase CO_2 in this model suggests that both the presence of preferential permeability paths and the geometry of the target formation are important factors that determine how fast separate-phase CO_2 reaches a caprock. Additional important factors include the injection pressure (and therefore the hydraulic head gradient) and the fluid composition, especially the presence of oil. We did evaluate the existence of oil and its effects on CO_2 migration, and results are detailed in a section 7.4.

By comparing the spatial distribution between CO_2 saturation (Figure 7.3a) and associated values of relative permeability (Figure 7.3b), it is easy to distinguish the location of free (mobile) CO_2 and residual (immobile) CO_2. When the relative permeability of the separate-phase CO_2 is greater than zero, it becomes mobile. However, when the relative permeability of separate-phase CO_2 is equal to zero, the separate-phase CO_2 becomes immobile and is trapped as residual CO_2. In Figure 7.3a, CO_2 saturation is greater than zero within the CO_2 plumes. However, Figure 7.3b shows that although certain grid blocks have CO_2 saturation greater than zero, they have zero relative permeability. These grid blocks indicate where CO_2 is trapped only as a residual form.

According to Juanes (2006), mobile CO_2 is located at the front of the CO_2 plume, while residual-trapped CO_2 is located at the tail of the CO_2 plume. Similarly, in this simulation, relative permeability was greater than zero at the front of the CO_2 plume around Well I22, indicating the presence of mobile CO_2. However, relative permeability was zero at the tail of the CO_2 plume, although CO_2 saturation was not zero. This indicates that CO_2 was stored in residual form at the tail of the CO_2 plume.

Finally, the distribution of dissolved CO_2 imitates the distribution patterns of separate-phase CO_2, but with a wider extent (Figure 7.3c).

7.3.5.3. Spatial Distribution of Aqueous Species and Minerals

Generally, over the 200-year simulation, calcite is the predominant mineral dissolved. Anhydrite, dolomite and ankerite are the major minerals precipitated. Dawsonite and siderite are also precipitated but in minimal amounts. In addition to the above carbonate minerals, kaolinate and illite respectively precipitated and dissolved. The associated mineral reactions in the model are:

$$CaSO_4(\text{Anhydrite}) = Ca^{2+} + SO_4^{2-} \quad , \qquad \text{(Eq. 7.2)}$$

$$CaCO_3(\text{Calcite}) + H^+ = Ca^{2+} + HCO_3^- \quad , \qquad \text{(Eq. 7.3)}$$

$$CaMg(CO_3)_2(\text{Dolomite}) + 2H^+ = Ca^{2+} + Mg^{2+} + 2HCO_3^- \quad , \qquad \text{(Eq. 7.4)}$$

$$CaFe_{0.25}Mg_{0.75}CO_3(\text{Ankerite})\ 2H^+ = Ca^{2+} + 0.25Fe^{2+} + 0.75Mg^{2+} + 2HCO_3^- \quad , \qquad \text{(Eq. 7.5)}$$

$$FeCO_3(\text{Siderite}) + H^+ = Fe^{2+} + HCO_3^- \quad , \qquad \text{(Eq. 7.6)}$$

$$NaAl(CO_3)(OH)_2(\text{Dawsonite}) + 3H^+ = Na^+ + Al^{3+} + HCO_3^- + 2H_2O \quad , \qquad \text{(Eq. 7.7)}$$

$$Al_2Si_2O_5(OH)_4(\text{Kaolinite}) + 6H^+ = 5H_2O + 2SiO_2(aq) + 2Al^{3+} \quad , \qquad \text{(Eq. 7.8)}$$

$$K_{0.6}(Mg_{0.25}Al_{1.8})(Al_{0.5}Si_{3.5})O_{10}(OH)_2(\text{Illite}) + 8H^+ = 0.25Mg^{2+} + 0.6K^+ + 2.3Al^{3+}$$
$$3.5SiO_2 + 5H_2O \quad , \qquad \text{(Eq. 7.9)}$$

Figure 7.4 shows the mass of mineral changes with time within the model. For most minerals, two hundreds years is insufficient time to reach equilibrium with reservoir fluids. Therefore, after 200 years, all minerals are still dissolving or precipitating. In the case of calcite, about 900 kg is dissolved after 200 years (Figure 7.4a). The precipitations of anhydrite, ankerite, and dolomite are accompanied by

dissolution of calcite, which releases the free Ca^{2+} ions into reservoir fluid. About 1220 kg of anhydrite, 2190 kg of ankerite, and 290 kg of dolomite are precipitated after 200 years. The mass changes of both dawsonite and siderite are relatively small. About 13 kg of dawsonite is precipitated after 200 years. Through their experiment, Carey et al. (2007) indicated the possibility of dawsonite precipitation in the SACROC field. This simulation result is consistent with their observation.

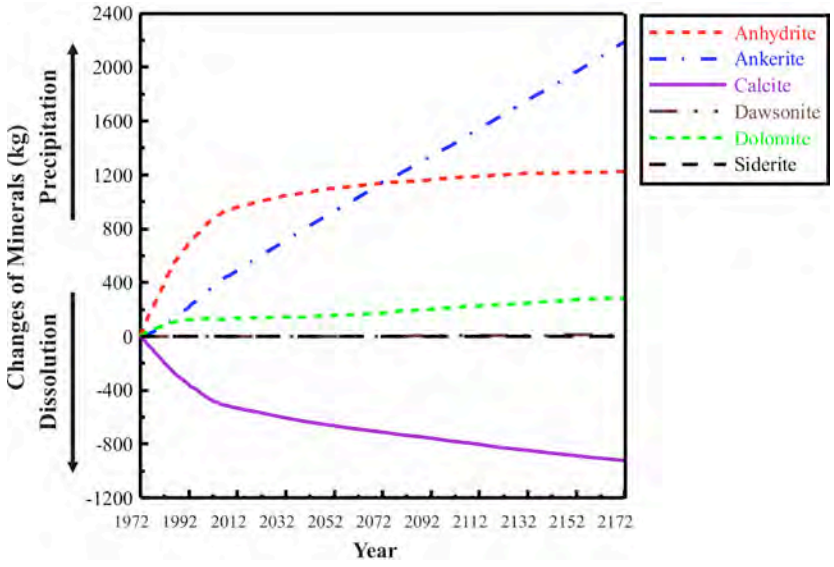

(a) Carbonate minerals

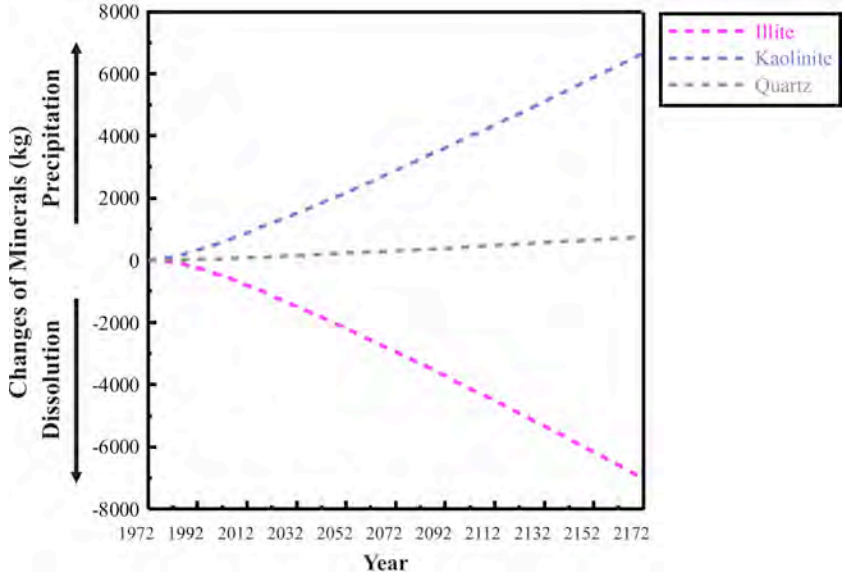

(b) Silicate minerals

Figure 7.4. Changes of minerals mass with time: (a) carbonate minerals, (b) silicate minerals.

Figure 7.4b shows the variation of silicate minerals with over time. Kaolinite and quartz respectively precipitate 6670 kg and 740 kg after 200 years, while about 7000 kg illite dissolves.

The addressed mineral changes initiate as the dissolution of CO_2 lowers the pH of brine (Figure 7.5a), which has also been observed in laboratory and field experiments (Kaszuba et al. 2005; Kharaka et al. 2006). The associated chemical reactions are shown below.

$$CO_2(g) + H_2O = H^+ + HCO_3^- \quad \text{(Eq. 7.10)}$$

$$CO_2(g) + H_2O = 2H^+ + CO_3^{2-} \quad \text{(Eq. 7.11)}$$

Decreasing pH subsequently induces a change of aqueous reactions and minerals. In this simulation, pH is controlled by the buffering of carbonate minerals and does not decrease below 4.5.

Figure 7.5b shows the spatial distribution of Ca^{2+} ions. Ca^{2+} ions are depleted at the boundary of the CO_2 plume where the precipitations of anhydrite (Eq.7.2), dolomite (Eq.7.4), and ankerite (Eq.7.5) are major mechanisms. Figure 7.5c shows the spatial distribution of Mg^{2+} ions. Mg^{2+} ions in reservoir fluids are consumed for the precipitation of dolomite (Eq.7.4) and ankerite (Eq.7.5), and concurrently supplied from the dissolution of illite (Eq.7.9). The initial concentration of Mg^{2+} ions at year 1972 was 0.057 molality (Table 7.2). After 30 years (year 2002), Mg^{2+} ions are depleted at the boundary of the CO_2 plumes where the precipitation of dolomite (Eq.7.4) and ankerite (Eq.7.5) are major mechanisms. However, Mg^{2+} ions are enriched within the CO_2 plumes where the dissolution of illite (Eq.7.9) provides Mg^{2+}

ions to reservoir fluids. Finally, Figure 7.5d shows the spatial distribution of SO_4^{2-} ions, which varies with the precipitation of anhydrite (Eq.7.1).

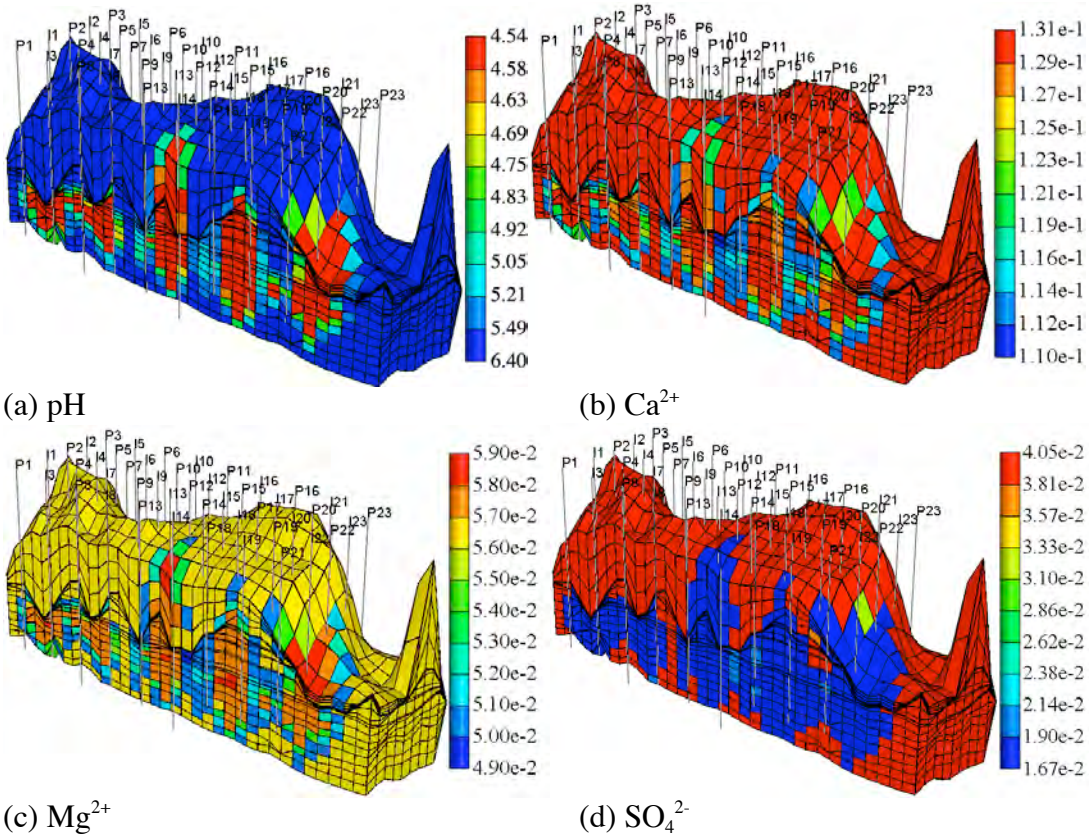

(a) pH (b) Ca^{2+}

(c) Mg^{2+} (d) SO_4^{2-}

Figure 7.5. Two-dimensional cross-section view of aqueous species concentrations (molality) at year 2002 (30 years after CO_2 injection starts).

Figure 7.6 shows the spatial distribution of minerals. Mineral precipitation and dissolution are closely related to the spatial distribution of aqueous species. Calcite dissolution provides more Ca^{2+} ions in the reservoir brine (Figure 7.6a). As a result, Ca^{2+} ions become supersaturated and are triggered to precipitate dolomite (Figure 7.6b), anhydrite (Figure 7.6c), and ankerite (Figure 7.6d). Model results also reveal how much CO_2 is spatially stored as diverse mineral phases. Over 30 years, approximately 0.03 kg of dolomite (Figure 7.6b), 0.20 kg of anhydrite (Figure 7.6c),

and 0.10 kg of ankerite (Figure 7.6d) are precipitated uniformly within CO_2 plumes, and about 0.2 kg of calcite (Figure 7.5a) is dissolved.

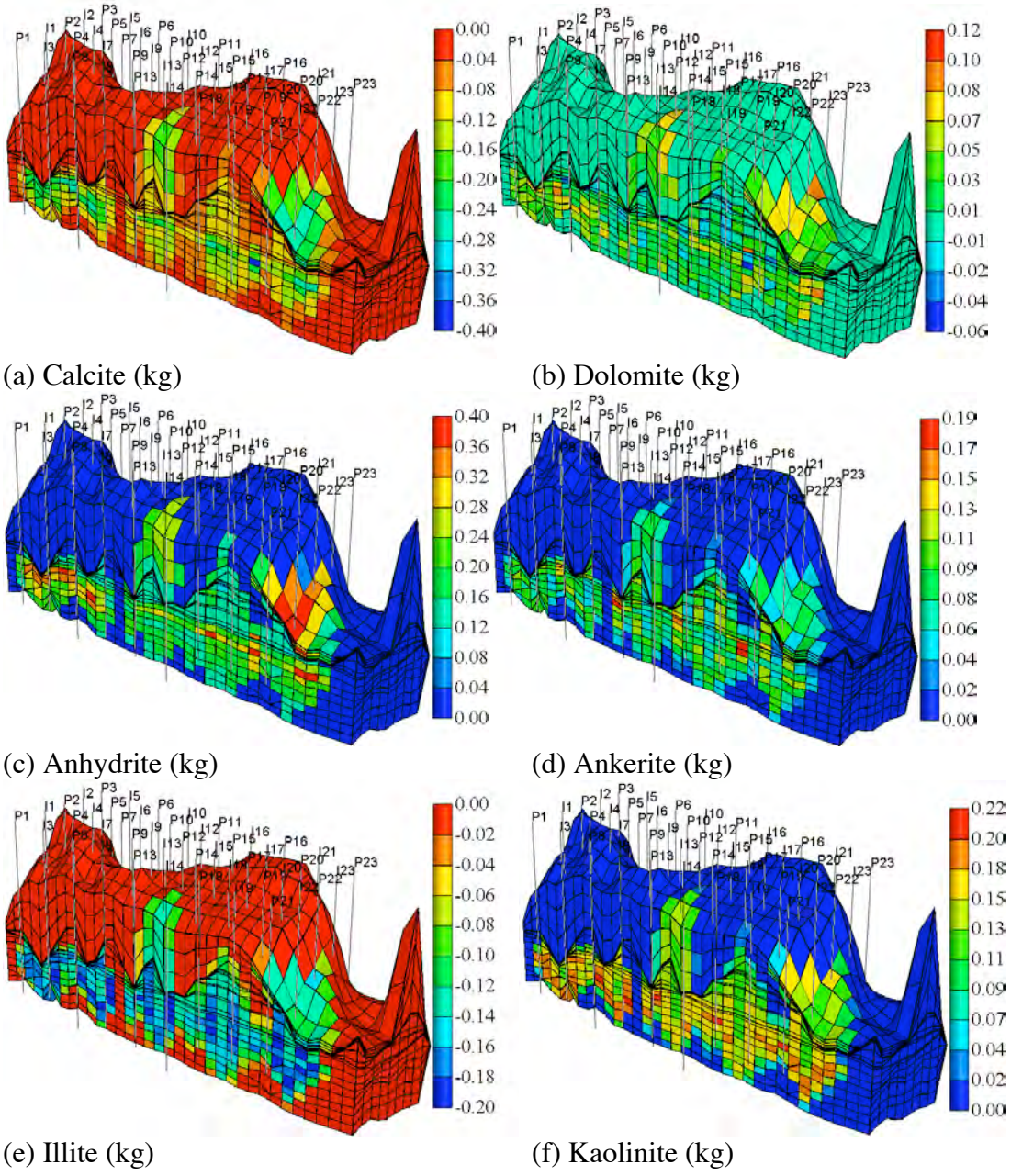

(a) Calcite (kg) (b) Dolomite (kg)

(c) Anhydrite (kg) (d) Ankerite (kg)

(e) Illite (kg) (f) Kaolinite (kg)

Figure 7.6. Two-dimensional cross-section views of minerals at year 2002 (30 years after CO_2 injection starts).

Reactions involving aluminoslicate minerals have been observed experimentally by Bertier et al. (2006). In this simulation, kaolinite and illite respectively precipitated and dissolved (Figure 7.6e and f). Although kinetic rates of aluminosilicate minerals are slow (Table 7.1), the chemical reactions of such aluminosilicate minerals can change the concentration of Al^{3+} ions in brine and cause dawsonite to precipitate (Xu et al. 2004; Hellevang et al. 2005). Through the simulation period, Al^{3+} ions increase from 10^{-11} to 10^{-7} molality due to the reactions with aluminosilicate minerals. Consequently, the change in Al^{3+} ion concentration causes precipitation of a small amount (13 kg) of dawsonite at the end of the simulation time (200 years later).

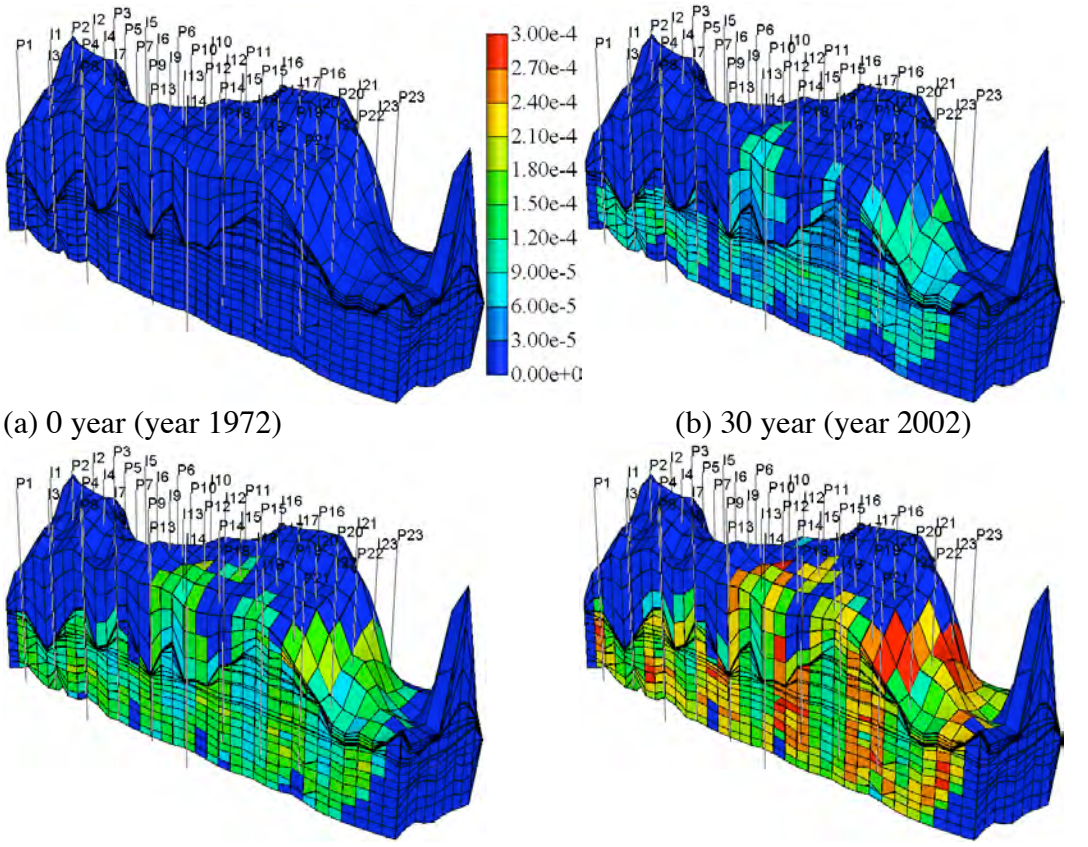

(a) 0 year (year 1972) (b) 30 year (year 2002)

(c) 100 year (year 2072) (b) 200 year (year 2172)

Figure 7.7. Changes of porosity ($\Delta\phi = \phi_{initial} - \phi_{current}$) during simulation period.

The mineral changes of simulated dissolution and precipitation cause changes in porosity. The altered porosity field is shown in Figure 7.7, indicating the net reduction of porosity due to CO_2 injection. After 200 years, mineral precipitation due to CO_2 sequestration causes the reduction of porosity by about 2.4e-4.

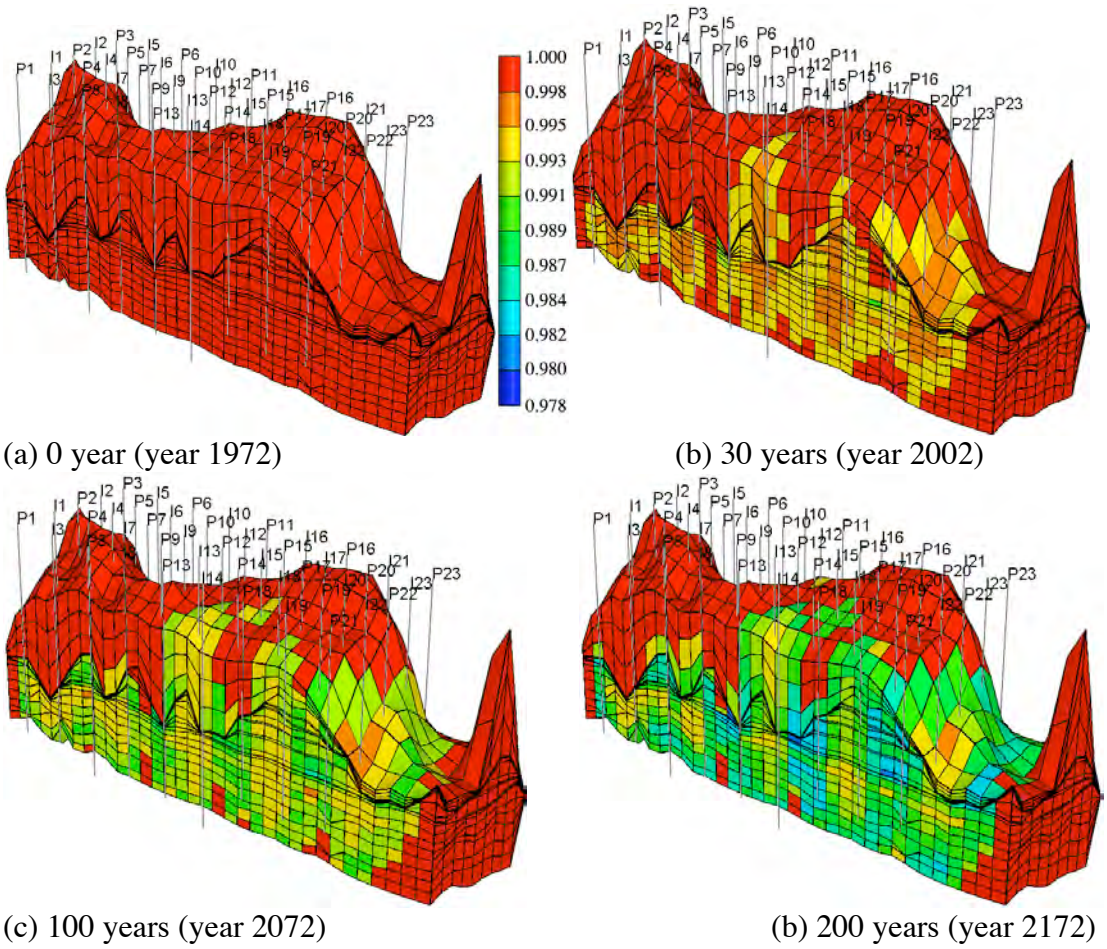

(a) 0 year (year 1972) (b) 30 years (year 2002)

(c) 100 years (year 2072) (b) 200 years (year 2172)

Figure 7.8. Changes of permeability (k/k_0) during simulation period.

The corresponding changes of permeability are calculated from the Kozeny-Carman model:

$$\frac{k}{k_0} = \left(\frac{\phi}{\phi_0}\right)^3 \left(\frac{1-\phi_0}{1-\phi}\right)^2 \qquad \text{(Eq. 7.12)}$$

where ϕ is the porosity, k is the permeability (m^2) and subscript 0 denotes initial values of variables. The altered permeability field (k/k_0) is shown in Figure 7.8, which was calculated from k_x ($=k_y$). k_z can be calculated after multiplying by the anisotropy ratio (0.4). The corresponding permeability reduction was about 0.989 (k/k_0).

7.4. Model Describing Reservoir Saturated with Both Oil and Brine

7.4.1. Initial and Boundary Conditions

The initial conditions for pressure and temperature distribution are the same as those described in section 7.3.1. However, the initial condition for fluid saturation is different from that in the previous model because both oil and brine coexist in this model. The reservoir is assumed to be saturated with both water (0.28) and oil (0.72), following reservoir characterization details provided by Vest (1970). The oil phase is regarded as a mixture of 11 different gas components. The initial oil composition used is from Dicharry et al. (1973), summarized in Table 7.3. The boundary conditions are identical to those of the previous model (Section 7.3.1).

Table 7.3. Initial oil composition of the SACROC reservoir model (Dicharry et al. 1973).

Oil Composition	Mol	Molecular Weight
CO_2	0.0032	44.01
N_2	0.0083	28.01
C1(Methane)	0.2865	16.04
C2(Ethane)	0.1129	30.07
C3(Propane)	0.1239	44.10
I-C4(I-Butane)	0.0136	58.12
N-C4(N-Butane)	0.0646	58.12
I-C5(I-Pentane)	0.0198	72.15
N-C5(N-Pentane)	0.0251	72.15
FC6(Hexane)	0.0406	86.00
C7+(Heptanes plus)	0.3015	275.0

7.4.2. Transport Input Data

The fitted relative permeability curves between supercritical CO_2 and liquid shown in Figure 7.1a were created after extrapolating relative permeability data measured in carbonate rocks (Bennion and Bachu, 2005). Hysteretic effects were included in the relative permeability curve using a modified Land equation (Land, 1968). A relative permeability curve for oil measured from SACROC cores (Core128V) at 50ºC and 1.4 MPa (Rohan and Haggerty, 1996) was used to calibrate oil relative permeability curve in Figure 7.9a. The relative permeability of brine was estimated with irreducible water saturation as 0.1.

Capillary pressure functions between supercritical CO_2 and liquid were adapted from Parker et al. (1987) and calibrated from the data of Bennion and Bachu (2006). Capillary pressure between oil and brine was that measured by Rohan and Haggerty (1996) from SACROC cores (Core128V, 136V, and 191V) at 50ºC and 1.4 MPa. We calibrated capillary pressure functions by Parker et al. (1987) using the Rohan and Haggerty (1996) data (Figure 7.9b). However, using capillary pressure between oil and brine caused serious convergence problems. Additionally, both Aziz and Settari (1979) and Spiteri and Juanes (2006) pointed out that the effects of capillary pressures are often negligible in field-scale simulation, where the characteristic capillary length is much smaller than the grid resolution. Therefore, the effects of capillary pressure between oil and brine were omitted in this simulation.

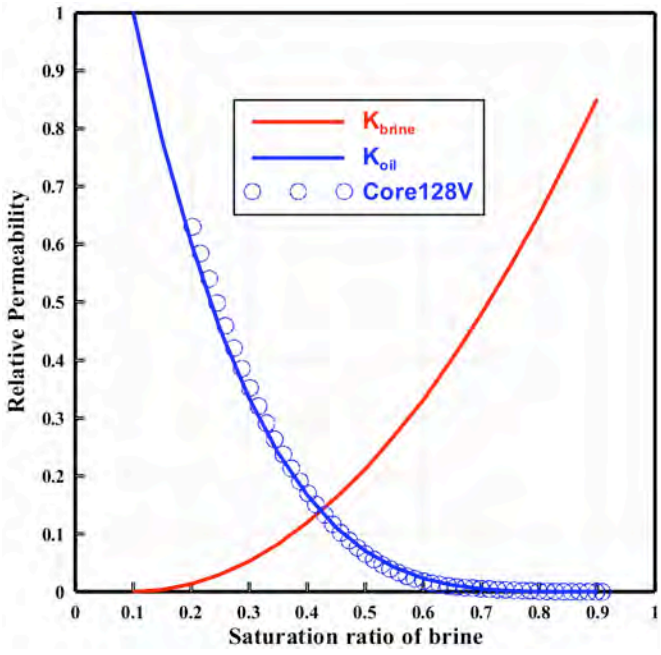

(a)

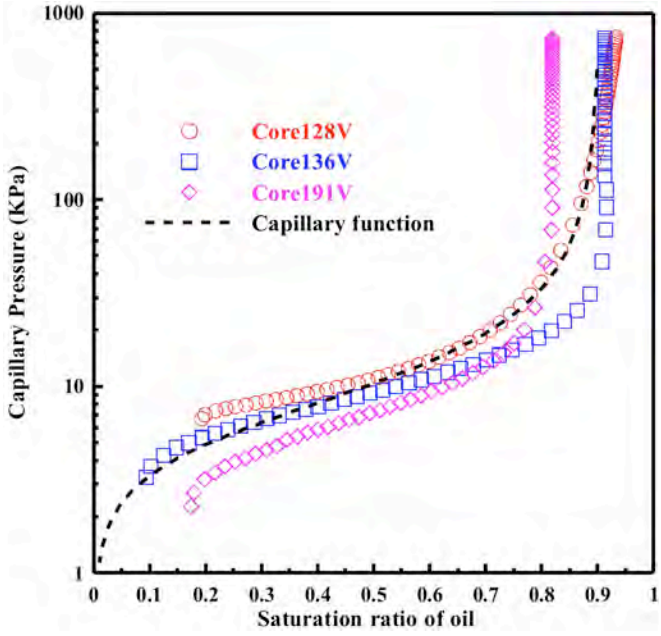

(b)

Figure 7.9. (a) Fitted relative permeability curves between brine and oil; measurements from Rohan and Haggerty (1996). (b) Fitted capillary pressure curve between brine and oil; measurements from Rohan and Haggerty (1996).

7.4.3. Chemistry Input Data

In the previous simulation model describing the reservoir saturated with brine, complex chemical reactions were included for predicting a comprehensive set of

chemical reactions and mineral changes (Table 7.4). However, in this subsequent simulation model describing the reservoir saturated with both brine and oil, some of the reactions have been disregarded because of the high computational expense of including the oil phase. Simulations that include the oil phase are computationally expensive because oil is treated as a mixture of eleven different gas components. The summary of both aqueous species and minerals in both simulations are listed in Table 7.4. Additionally, both mineral parameters and initial brine concentrations are the same as those in the previous model (Table 7.1 and Table 7.2).

Table 7.4. Chemical components in the simulation model describing the reservoir saturated with both brine and oil.

	Simulation describing reservoir saturated with brine	Simulation describing reservoir saturated with both brine and oil
Primary species	CO_2(g),H^+,K^+,Na^+,Ca^{2+},Mg^{2+}, SiO_2(aq), Al^{3+}, Fe^{2+}, Cl^-,SO_4^{2-}	CO_2(g), N_2,C1,C2,C3,I-C4,N-C4,I-C5,N-C5,FC6,C7+,H^+, Na^+, Cl^-
Secondary species	OH^-,HCO_3^-, CO_3^{2-},NaCl(aq), $NaCO_3^-$,$NaHCO_3$(aq),$CaCO_3$(aq),$CaHCO_3^+$,$MgCO_3$(aq),$MgHCO_3^+$,$Al(OH)_4^-$,$Al(OH)_3$(aq),$Al(OH)_2^+$,$Al(OH)^{2+}$,$FeCl_4^{2-}$,$FeCl^+$,$Fe(OH)_2$,$Fe(OH)^+$,H_4SiO_4(aq)	OH^-,HCO_3^-, CO_3^{2-},NaCl(aq)
Mineral	Calcite, dolomite, kaolinite, anhydrite, quartz, illite, ankerite, dawsonite, siderite	Calcite, dolomite, kaolinite, anhydrite, quartz, illite, ankerite, dawsonite, siderite

7.4.4. Assignment of CO_2 Injection and Production Wells

As in the previous model, the 23 pumping (P) and 22 injection (I) wells were respectively assigned in this model (Figure 6.5d). Wells underwent injection and production from 1972 to 2002. Further, this simulation does not intend to analyze oil production history, but rather to evaluate CO_2 trapping mechanisms. Therefore, the actual oil production history was not included but rather only the presence of oil (after Vest, 1970) and its effects on CO_2 migration and trapping mechanisms.

7.4.5. Results and Discussions

7.4.5.1. Quantification of CO_2 Trapping Mechanisms at SACROC Northern Platform

Figure 7.10a shows the CO_2 mass stored as different forms in the reservoir saturated with brine and Figure 7.10b shows the CO_2 mass in the reservoir saturated with both brine and oil.

In the previous brine-only simulation model, CO_2 trapping mechanisms revealed three distinct stages (Figure 7.10a). The CO_2 trapping mechanisms are clearly different within each stage in the brine-only model (Figure 7.10a). However, the trapping mechanisms do not vary so distinctly over time in the brine+oil model (Figure 7.10b). During the full 200-year simulation periods, the dominant CO_2 trapping mechanism is oil trapping, with about 4 million tons of CO_2 dissolved in the oil. In addition, about 2 million tons of CO_2 is stored as a mobile form.

In the brine-only model, the amount of free (mobile) CO_2 dramatically decreases and the amount of residual (immobile) CO_2 suddenly increases after CO_2 injection stops (Figure 7.10a). However, in the brine+oil model reservoir, the relative amounts of both free (mobile) and residual CO_2 generally do not change over time (Figure 7.10b). About 2 millions tons of CO_2 remains as free (mobile) CO_2 during 200 years while about 0.1 million tons of CO_2 stays as residual (immobile) CO_2. Compared to the amount of residual-trapped CO_2 in the brine-only model, residual-trapped CO_2 in the brine+oil model is significantly less (Figure 7.10b).

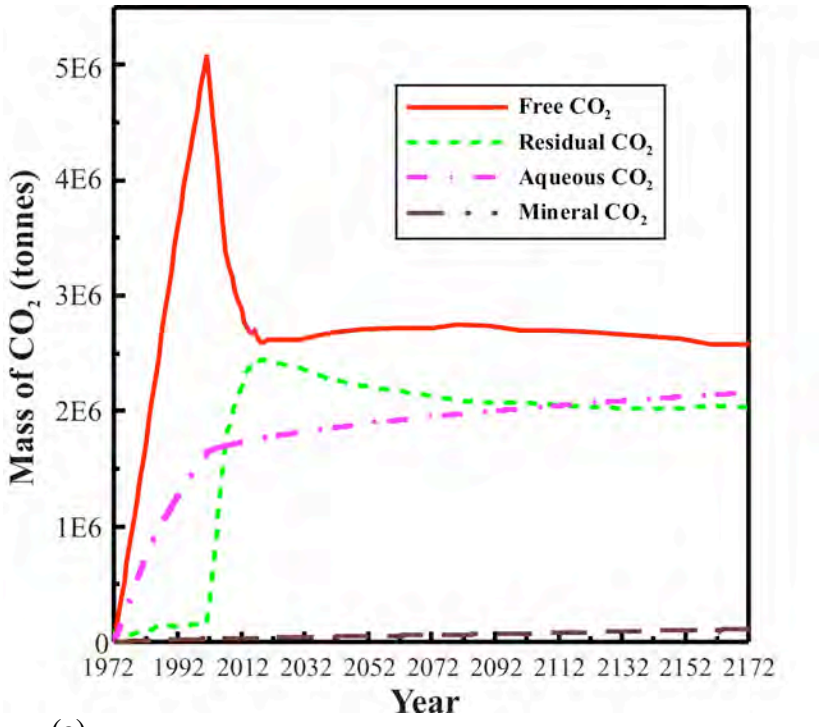

(a)

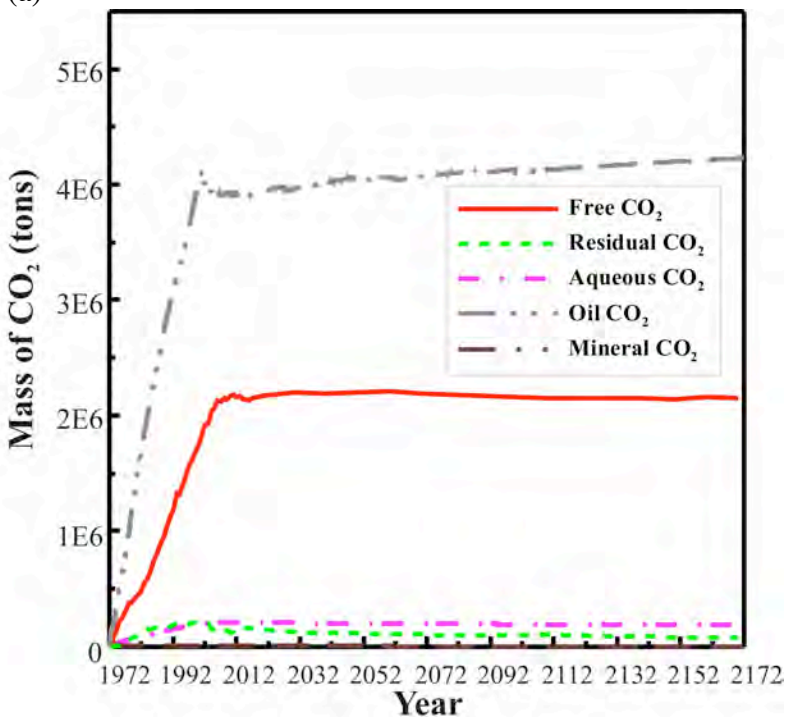

(b)

Figure 7.10. CO_2 trapping mechanisms within reservoir as a function of time: (a) brine-only simulation, (b) brine+oil simulation.

To investigate the difference of the amount of residual-trapped CO_2 in both simulations, the saturations of separate-phase CO_2 at year 2002 were plotted (Figure 7.11).

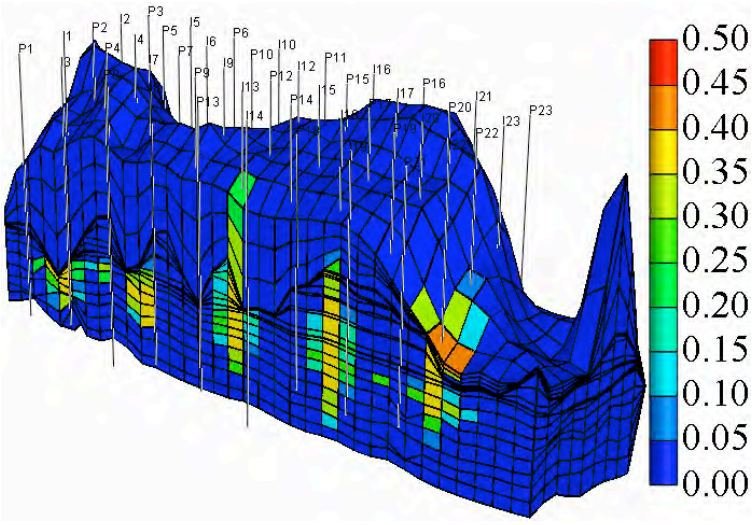

(a)

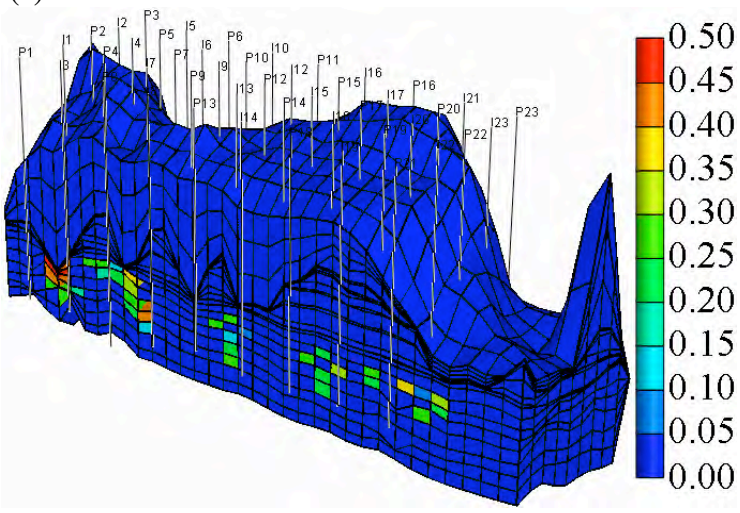

(b)

Figure 7.11. Two-dimensional cross-section view at year 2002 (30 years after CO_2 injection starts): (a) saturation of separate-phase CO_2 in brine-only simulation and (b) saturation of separate-phase CO_2 in brine+oil simulation.

The simulation results show that CO_2 migration behavior is distinctively different in both simulations. Within 30 years, separate-phase CO_2 in the brine-only model tended to migrate vertically and certain CO_2 plumes were able to reach the top

of the Cisco and Canyon Formations (Figure 7.11a). The amount of residual-trapped CO_2 increased at the tail of the CO_2 plumes while separate-phase CO_2 plumes migrated vertically. However, in the brine+oil model, separate-phase CO_2 did not tend to migrate vertically but stayed near the injection wells with high CO_2 saturation (Figure 7.11b). Physically, separate-phase CO_2 is stored as a free (mobile) form due to its high CO_2 saturation, but it does not migrate like residual (immobile) CO_2.

To evaluate the difference of CO_2 vertical migration behavior between the two models (Figure 7.11), the density of gas, brine, and oil phases were compared (Figure 7.12). The density of CO_2 is about 800 kg/m^3 at these reservoir conditions (Figure 7.12a). The brine density ranged from 1040 to 1140 kg/m^3 (Figure 7.12b). An especially higher density of brine is calculated near CO_2 injection wells because of CO_2 dissolution and the increase of salinity induced by subsequent rock-water interaction. The density difference between CO_2 and brine was approximately 300 kg/m^3, which suggests a significant buoyancy force.

Compared to brine density, oil density ranged from 800 to 900 kg/m^3 (Figure 7.12c), very similar to the density of separate-phase CO_2. In the brine+oil reservoir model, the buoyancy-driven force was lower due to the lower contrast in densities. Consequently, stored CO_2 did not migrate vertically but tended to stay closer to the injection wells. In sum, CO_2 is stored as a free (mobile) form but because of the similarity in density and dissolution in oil, the free (mobile) CO_2 does not migrate like residual-trapped CO_2.

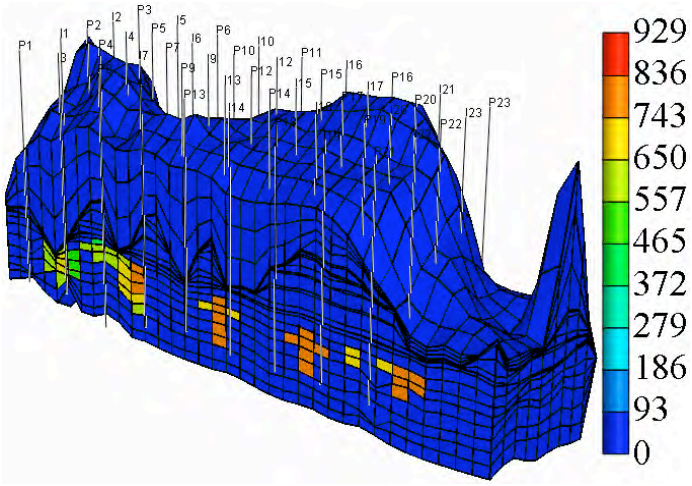

(a)

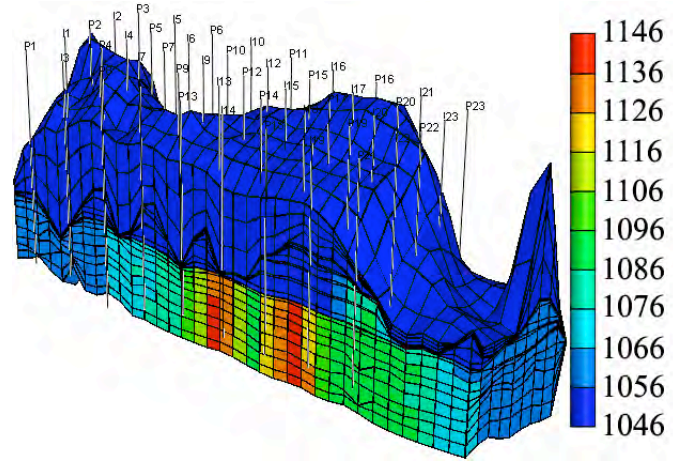

(b)

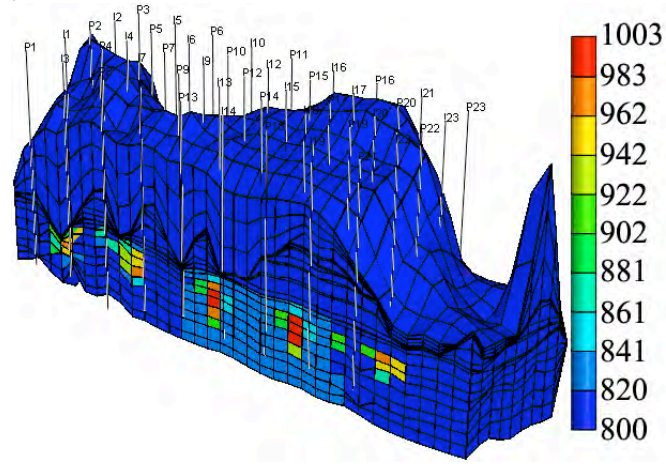

(c)

Figure 7.12. Two-dimensional cross-section view at year 2002 (30 years after CO_2 injection starts): (a) gas density, (kg/m^3), (b) brine density (kg/m^3), and (c) oil density (kg/m^3).

Finally, both aqueous and mineral trapping mechanisms in the oil+brine reservoir model are much less active than those in the brine-only model (Figure 7.10b), because most of the CO_2 dissolved in the oil phase due to higher solubility of CO_2 in oil, and because only 28% of reservoir was occupied by brine. Therefore, the subsequent water-rock interactions decreased.

7.5. Summary and Conclusion

Two models evaluating CO_2 trapping mechanisms in the SACROC northern platform were developed using the upscaled geocellular model developed in Chapter 6. Initial conditions, boundary conditions, and other parameters in this model were carefully chosen based on the results of data analyses such as groundwater chemistry, isotope, and CO_2 injection/production history. The first model was designed for simulating CO_2 trapping mechanisms in a reservoir saturated with brine. The other model was designed for simulating CO_2 trapping mechanisms in a reservoir saturated with both brine and oil.

CO_2 trapping mechanisms in a model of the reservoir saturated only with brine shows distinctive stages (Figure 7.10a). In Stage I (1972~2002), the same as the injection period, hydrostratigraphic (mobile) trapping is dominant. In Stage II (2002~2017), the residual trapping mechanism dramatically increases. In Stage III (2017~after several hundreds years), the solubility trapping mechanism becomes important because both residual and mobile CO_2 will dissolve into brine. Mineral trapping is only important over very long time periods. In sum, the major CO_2

trapping mechanisms were hydrostratigraphic (mobile), residual, and solubility trapping during 200 years.

However, in a reservoir model with oil (72%) and brine (28%) phases, the trapping mechanisms do not vary distinctly over time (Figure 7.10b). The most dominant trapping mechanism is oil trapping. Separate-phase CO_2 is stored as a free (mobile) form due to its high CO_2 saturation, but it does not migrate like residual (immobile) CO_2 because of the similarity in fluid densities. In sum, both oil trapping and hydrostratigraphic (mobile) trapping were the dominant mechanisms over 200 years.

In addition to CO_2 trapping mechanisms, these simulation results from the brine-only model also lead to several different conclusions associated with CO_2 transport and the corresponding chemical reactions.

(1) The simulated spatial distribution of separate-phase CO_2 suggests that both the presence of preferential permeability paths and the geometry of the target formation are important factors that determine how fast separate-phase CO_2 reaches the caprock.

(2) Mobile CO_2 is located at the front of the CO_2 plume where drainage is dominant (CO_2 displaces water), while residual-trapped CO_2 is located at the tail of the CO_2 plume where imbibition is dominant (water displaces CO_2). These results are consistent with Juanes et al. (2006).

(3) Injected CO_2 is stored as several different forms of minerals. Calcite (900 kg) is the predominant mineral dissolved. Anhydrite (1220 kg), dolomite (290 kg), and ankerite (2190 kg) are the major minerals precipitated.

(4) Mineral precipitation due to CO_2 sequestration causes the reduction of porosity by about 2.4e-4 ($=\phi_{initial} - \phi_{current}$) after 200 years. The corresponding permeability reduction calculated from Kozeny-Carman equation was 0.989 (k/k_0)

7.6. Recommendation for Future Injection Plans

The different CO_2 trapping mechanisms in the two models were caused by the contrast of thermophysical properties between oil and brine. Based on the two simulation models, injecting CO_2 into the reservoir saturated with both brine and oil reduces the amount of mobile CO_2, which would otherwise likely migrate vertically to the top seal. Several advantages of CO_2 injection into a reservoir that is both brine and oil-saturated include:

(1) CO_2 solubility in oil is significantly greater than it is in brine. Therefore, most of the CO_2 will dissolve into oil.

(2) Although CO_2 exists in a mobile form, it does not tend to migrate vertically because oil density is similar to CO_2 density, causing less buoyancy-driven vertical migration. In simulation results, separate-phase CO_2 in the reservoir saturated with both brine and oil was stored as mobile CO_2 with higher saturation, but its migration was hindered to the extent that it behaved like residual CO_2.

(3) CO_2 mobility is reduced when three phases coexist, e.g., injecting CO_2 in a brine+oil reservoir, as opposed to injecting into a reservoir with brine only. In this multiphase environment, the vertical movement of separate-

phase CO_2 will be relatively retarded. Although reduction of CO_2 mobility has not been observed directly in oil reservoirs, Pruess (2004) observed in numerical simulation that fluid mobilities are reduced in a three-phase environment (supercritical CO_2, gas CO_2, and water) due to the interference between phases.

(4) The relative permeability of gas also varies with the wettability condition of geologic media. Experimental observation shows that gas relative permeability is about four times lower in oil-wet media than in water-wet media (Moulu et al. 1999; DiCarlo et al. 2000). Therefore, it follows that the vertical migration of injected CO_2 will be slower in an oil reservoir (oil-wet) than in a brine-only formation (purely water-wet).

(5) CO_2 solubility in oil is significantly greater than it is in brine. In addition, although CO_2 exists in a free form, it does not tend to migrate vertically because oil density is similar to CO_2 density. Consequently, it is much less probable that mobile CO_2 reaches the top of the target formation in an oil reservoir. Although mobile CO_2 may reach the top of the target formation, an oil reservoir is always covered by a caprock, whose seal integrality is proven by the presence of oil. Therefore, CO_2 in an oil reservoir cannot escape easily through caprock. However, Li et al. (2006) observed that the seal integrity of the caprock is significantly reduced due to the much lower interfacial tension of the CO_2/water than that of oil/water. Therefore, further research is necessary to investigate the detailed seal integrity of the caprock in an oil reservoir.

Injecting CO_2 into oil reservoirs provides several advantages for minimizing potential CO_2 vertical migration. However, their sizes and volumes are limited for CO_2 storage. Capacity estimation by DOE sponsored Regional Partnership shows that CO_2 capacity in oil and gas reservoirs is about 82.4 billion tonnes, while in brine formations it is about 3378 billion tonnes (NETL, 2007). In comparison, the potential for CO_2 storage in brine formations is immense.

Therefore, to obtain advantages in terms of CO_2 storage capacity and protection from potential leakage from both brine and oil reservoirs, we propose CO_2 injection into brine formations below oil reservoirs. The detailed strategy and study plan for evaluating CO_2 injection below oil reservoir is discussed in Chapter 8.

References

Andre, L., Audigane, P., Azaroual, M., Menjoz, A., 2007. Numerical modeling of fluid-rock chemical interactions at the supercritical CO_2-liquid interface during CO_2 injection into a carbonate reservoir, the Dogger aquifer (Paris basin, France). Energy Conversion and Management 48(6), 1782-1797.

Appelo, C.A.J., Postma, D., 1993. Geochemistry, Groundwater and Pollution. A.A. Balkema Publishers, Rotterdam, Netherlands, 536 pp.

Aziz, K., Settari, A., 1979. Petroleum Reservoir Simulation, Elsevier, New York.

Baker, J.C., Bai, G.P., Hamilton, P.J., Golding, S.D., Keene, J.B., 1995. Continental-scale magmatic carbon dioxide seepage recorded by dawsonite in the Bowen-Gunnedah-Sydney basin system, eastern Australia. Journal of Sedimentary Research 65(3), 522-530.

Basbug, B., Gumrah, F., Oz, B., 2005. Simulating the effects of deep saline aquifer properties on CO_2 sequestration. Petroleum society, Canadian Institute of Mining, Metallurgy & Petroleum, Paper 2005-139, 1-15.

Bennion, B., Bachu, S., 2005. Relative permeability characteristics for supercritical CO_2 displacing water in a variety of potential sequestration zones in the western Canada sedimentary basin. Society of Petroleum Engineers Journal 95547.

Bennion, B., Bachu, S., 2006. The impact of interfacial tension and pore-size distribution/capillary pressure character on CO_2 relative permeability at reservoir conditions in CO_2-brine systems. Society of Petroleum Engineers Journal 99325.

Bergenback, R.E., Terriere, R.T., 1953. Petrography and petrology of Scurry reef, Scurry County, Texas. American Association of Petroleum Geologists Bulletin 37(5), 1014-1029.

Bertier, P., Swennen, R., Laenen, B., Lagrou, D., Dreesen, R., 2006. Experimental identification of CO_2-water-rock interactions caused by sequestration of CO_2 in Westphalian and Buntsandstein sandstones of the Campine basin (NE-Belgium). Journal of Geochemical Exploration 89, 10-14.

Bryant, S.L., Lakshminarasimhan, S., Pope, G.A., 2006. Buoyancy-dominated multiphase flow and its impact on geological sequestration of CO_2. Society of Petroleum Engineers Journal 99938.

Calabrese, M., Masserano, F., Blunt, M.J., 2005. Simulation of physical-chemical processes during carbon dioxide sequestration in geological structures. Society of Petroleum Engineers Journal 95820.

Carey, J.W., Wigand, M., Chipera, S., Woldegabriel, G., Pawar, R., Lichtner, P., Wehner, S., Raines, M., Guthrie, J., 2007. Analysis and performance of oil well cement with 30 years of CO_2 exposure from the SACROC unit, west Texas. International Journal of Greenhouse Gas Control 1, 75-85.

Chai, L., Navrotsky, A., 1996. Synthesis, characterization, and energetics of solid solution along the dolomite-ankerite join, and implications for the stability of ordered $CaFe(CO_3)_2$. American Mineralogist 81, 1141-1147.

Computer Modeling Group, 2006. User's guide GEM, Advanced compositional reservoir simulator (version 2006). Computer modeling Group Ltd.

DiCarlo, D.A., Sahni, A., Blunt, M.J., 2000. Three-phase relative permeability of water-wet, oil-wet, and mixed-wet sandpacks. Society of Petroleum Engineers Journal 60767.

Dicharry, R.M., Pettyman, T.L., Ronquille, J.D., 1973. Evaluation and design of a CO_2 miscible flood project-SACROC Unit, Kelly-Snyder field. Society of Petroleum Engineers Journal 4083.

Doughty, C., 2007. Modeling geologic storage of carbon dioxide: Comparison of non-hysteretic and hysteretic characteristic curves. Energy Conversion and Management 48, 1768-1781.

Dove, P.M., Czank, C.A., 1995. Crystal-chemical controls on the dissolution kinetics of the isostructural surface-celestite anglesite, and barite. Geochimica et Cosmochimica Acta 59(10), 1907-1915.

Gaus, I., Azaroual, M., Czernichowski-Lauriol, I., 2005. Reactive transport modeling of the impact of CO_2 injection on clayey cap rock at Sleipner (North Sea). Chemical Geology 217, 319-337.

Helgeson, H.C., 1969. Thermodynamics of hydrothermal systems at elevated temperatures and pressures. American Journal of Science 267, 729-804.

Hellevang, H., Aagaard, P., Oelkers, E.H., Kvamme, B., 2005. Can dawsonite permanently trap CO_2? Environmental Science and Technology 39, 8281-8287.

Hitchon, B., 1996. Aquifer Disposal of Carbon Dioxide. B. Hitchon (Eds.), Sherwood Park, Alberta, Canada. Geoscience publishing.

Holtz, H.M., 2002. Residual gas saturation to aquifer influx: A calculation method for 3-D computer reservoir model construction. Society of Petroleum Engineers Journal 75502.

Jossi, J.A., Stiel, L.I., Thodos, G., 1962. The viscosity of pure substances in the dense gaseous and liquid phases. AIChe Journal 8(1), 59-62.

Juanes, R. Spiteri, E.J., Orr, F.M., Blunt, M.J., 2006. Impact of relative permeability hysteresis on geological CO_2 storage. Water Resources Research 42, W12418, doi:10.1029/2005WR004806.

Kaszuba, J.P., Janecky, D.R., Snow, M.G., 2005. Experimental evaluation of mixed fluid reactions between supercritical carbon dioxide and NaCl brine: Relevance to the integrity of a geologic carbon repository. Chemical Geology 217, 277-293.

Kestin, J., Khalifa, H.E., Correia, R.J., 1981. Tables of the dynamic and kinematic viscosity of aqueous NaCl solutionsin the temperature range 20-150°C and pressure range 0.1-35 MPa. Journal of Physical and Chemical Reference Data. 10, 71-87.

Kervevan, C., Azaroual, M., Durst, P., 2005. Improvement of the calculation accuracy of acid gas solubility in deep reservoir brines: Application to the geological storage of CO_2. Oil & Gas Science and Technology 60(2), 357-379.

Kharaka, Y.K., Gunter, W.D., Aggarwal, P.K., Perkins, E., Debraal, J.D., 1989. SOLMINEQ.88: A computer program for geochemical modeling of water-rock reactions. USGS Water-Resources Investigations Report 88-4227.

Kharaka, Y.K., Cole, D.R., Tordsen, J.J., Kakouros, E., Nance, H.S., 2006. Gas-water-rock interactions in sedimentary basins: CO_2 sequestration in the Frio formation, Texas, USA. Journal of Geochemical Exploration 89, 183-186.

Knauss, K.G., Wolery, T.J., 1989. Muscovite dissolution kinetics as a function of pH and time at 70ºC. Geochimica et Cosmochimica Acta 53, 1493-1501.

Knauss, K.G., Johnson, J.W., Steefel, C.I., 2005. Evaluation of the impact of CO_2, co-contaminant gas, aqueous fluid and reservoir rock interactions on the geologic sequestration of CO_2. Chemical Geology 217, 339-350.

Kumar, A., Noh, M., Pope, G.A., Bryant, S., Lake, L.W., 2004. Reservoir simulation of CO_2 storage in deep saline aquifers. Society of Petroleum Engineers Journal 89343.

Kumar, A. 2004. A simulation study of carbon sequestration in deep saline aquifer. Master Thesis. University of Texas at Austin.

Land, C.S., 1968. Calculation of imbibition relative permeability for two- and three-phase flow from rock properties. Society of Petroleum Engineers Journal 1942.

Langmuir, D., Melchior, D., 1985. The geochemistry of Ca, Sr, Ba, and Ra sulfates in some deep brines from the Palo Duro basin, Texas. Geochimica et Cosmochimica Acta 49(11), 2423-2432.

Langston, M.V., Hoadley, S.F., Young, D.N., 1988. Definitive CO_2 flooding response in the SACROC unit. Society of Petroleum Engineers Journal 17321.

Lasaga, A.C., 1984. Chemical kinetics of water-rock interaction. Journal of Geophysical Research 89, 4009-4025.

Lee, Y.-J., Morse, J.W., 1999. Calcite precipitation in synthetic veins: Implications for the time and fluid volume necessary for vein filling. Chemical Geology 156, 151-170.

Li, Y.-K., Nghiem, L.X., 1986. Phase equilibria of oil, gas, and water/brine mixtures from a cubic eqaution of state and Henry's law. Canadian Journal of Chemical Engineering 486-496.

Li, Z., Dong, M., Li, S. Huang, S., 2006. CO_2 sequestration in depleted oil and gas reservoirs-caprock characterization and storage capacity. Energy Conversion and Management 47, 1372-1382.

Moore, J., Adams, M., Allis, R., Lutz, S., Rauzi, S., 2005. Mineralogical and geochemical consequences of the long-term presence of CO_2 in natural reservoirs: An example from the Springerville-St. Johns field, Arizona, and New Mexico, U.S.A. Chemical Geology 217, 265-385.

Moulu, J.-C., Vizika, O., Egermann, P., Kalaydjian, F. 1999. A new three-phase relative permeability model for various wettability conditions. Society of Petroleum Engineers Journal 56477.

Mozley, P.S., Hoernle, K., 1990. Geochemistry of carbonate cements in the Sag River and Shublik Formations (Triassic/Jurassic), North Slope, Alaska: Implications for geochemical evolution of formation waters. Sedimentology 37, 817-836.

Myers, D.A., Stafford, P.T., Burnside, R.J., 1956. Geology of the late Paleozoic Horseshoe atoll in west Texas. Bureau of Economic Geology Publication 5607, p.113.

Nagy, K.L., 1995. Dissolution and precipitation kinetics of sheet silicates, in: White, A.F., Brantley, S.L. (Eds.) Chemical Weathering Rates of Silicate Minerals, Reviews in Mineralogy 31, 173-233.

Nghiem, L., Sammon, P., Grabenstetter, J., Ohkuma, H., 2004. Modeling CO_2 storage in aquifers with a fully-coupled geochemiscal EOS compositional simulator. Society of Petroleum Engineers Journal 89474.

National Energy Technology Laboratory, 2007. Carbon sequestration atlas of the United States and Canada (www.netl. Doe.gov/publications/carbon_seq/atlas /index.html)

Noh, M., Lake, L.W., Bryant, S.L., Araque-Martinez, A., 2004. Implications of coupling fractional flow and geochemistry for CO_2 injection in aquifers. Society of Petroleum Engineers Journal 89341.

Ozah, R.C., Lakshminarasimhan, S., Pope, G.A., Sepehrnoori, K., Bryant, S.L., 2005. Numerical simulation of the storage of pure CO_2 and CO_2-H_2S gas mixtures in deep saline aquifers. Society of Petroleum Engineers Journal 97255.

Parker, J.C., Lenhard, R.J., Kuppusamy, T., 1987. A parametric model for constitutive properties governing multiphase flow in porous media. Water Resources Research 23(4), 618-624.

Parkhurst, D.L., Appelo, C.A.J., 1999. User's guide to PHREEQC (version 2) – A computer program for speciation batch-reaction, one-dimensional transport, and inverse geochemical calculations. USGS Water-Resources Investigations Report 99-4259.

Peng, D.Y., Robinson, D.B., 1976. A new two-constant equation of state. Industrial and Engineering Chemistry Fundamentals 15, 59-64.

Pokrovsky, O.S., Schott, J., 2001. Kinetics and mechanisms of dolomite dissolution in neutral to alkaline solutions revisited. American Journal of Science 301, 597-626.

Pruess, K. 2004. Numerical Simulation of CO_2 leakage from a geologic disposal reservoir, including transitions from super- to subcritical conditions, and boiling of liquid CO_2. Society of Petroleum Engineers Journal 86098.

Ranies, M.A., Dobitz, J.K., Wehner, S.C., 2001. A review of the Pennsylvanian SACROC Unit. In J.J. Viveros and S.M. Ingram, eds., The Permian basin: Microns to satellites, looking for oil and gas at all scales. West Texas Geological Society Publication 01-110, p.67-74.

Rohan, J.A., Haggerty, D., 1996. Carbonate special core analysis study for Pennzoil exploration and production company: Elevated temperature centrifuge study. Technical report, Westport Technology Center International, IIT Research Institute.

Rowe, A.M., Chou, J.C.S., 1970. Pressure-volume-temperature-concentration relation of aqueous NaCl solutions. Journal of Chemical and Engineering Data 15, 61-66.

Spiteri, E.J., Juanes, R., 2006. Impact of relative permeability hysteresis on the numerical simulation of WAG injection, Journal of Petroleum Science and Engineering 50(2), 115-139.

Svensson, U., Dreybrodt, W., 1992. Dissolution kinetics of natural calcite minerals in CO_2-water systems approaching calcite equilibrium. Chemical Geology 100, 129-145.

Tester, J.W., Worley, W.G., Robinson, B.A., Grigsby, C.O., Feerer, J.L., 1994. Correlating quartz dissolution kinetics in pure water from 25 to 626ºC. Geochimica et Cosmochimica Acta 58(11), 2407-2420.

Vest, E.L.Jr., 1970. Oil Fields of Pennsylvanian-Permian Horseshoe Atoll, West Texas *in* Halbouty, Michael T. (ed.) Geology of Giant Petroleum Fields, AAPG Memoir # 14. American Association of Petroleum Geologists, Tulsa Oklahoma, pp. 185-203.

Xu, T., Apps, J.A., Pruess, K., 2004. Numerical simulation of CO_2 disposal by mineral trapping in deep aquifers. Applied Geochemistry 19, 917-936.

Xu, T., Apps, J.A., Pruess, K., 2005. Mineral sequestration of carbon dioxide in a sandstone-shale system. Chemical Geology 217, 295-318.

White, S.P., Allis, R.G., Moore, J., Chidsey, T., Morgan, C., Gwynn, W., Adams, M., 2005. Simulation of reactive transport of injected CO_2 on the Colorado Plateau, Utah, USA. Chemical Geology 217, 387-405.

Wood, T.L., Garrels, R.M., 1992. Calculated aqueous-solid-solution reactions in the low-temperature system CaO-MgO-FeO-CO_2-H_2O. Geochimica et Cosmochmica Acta 56, 3031-3043.

Zerai, B., Saylor, B.Z., Matisoff, G., 2006. Computer simulation of CO_2 trapped through mineral precipitation in the Rose Run sandstone, Ohio. Applied Geochemistry 21, 223-240.

CHAPTER 8

SUMMARY, CONCLUSIONS, AND RECOMMENDATIONS

8.1. Epilogue

Much scientific evidence suggests that the global climate has changed over the last 100 years (Figure 8.1a) and that a significant proportion of those changes could be attributed to the release of anthropogenic CO_2 into the atmosphere (Figure 8.1b). To curb the effects of global warming, it is necessary to reduce current CO_2 emissions, which are approximately 7 billion tonnes per year of carbon (Bryant, 2007). To achieve this goal, many countries are beginning to ratify the Kyoto Protocol, a multinational agreement to reduce greenhouse gas emissions, drafted by the United Nations Framework Convention on Climate Change in 1997.

However, reduction of CO_2 emissions is not a straightforward problem, because carbon emission is generally associated with world energy and economy. CO_2 emissions can be reduced predominantly by (1) burning less carbon-containing

fuel, (2) developing technologies for renewable energy, and (3) capturing and storing CO_2 into geological formations.

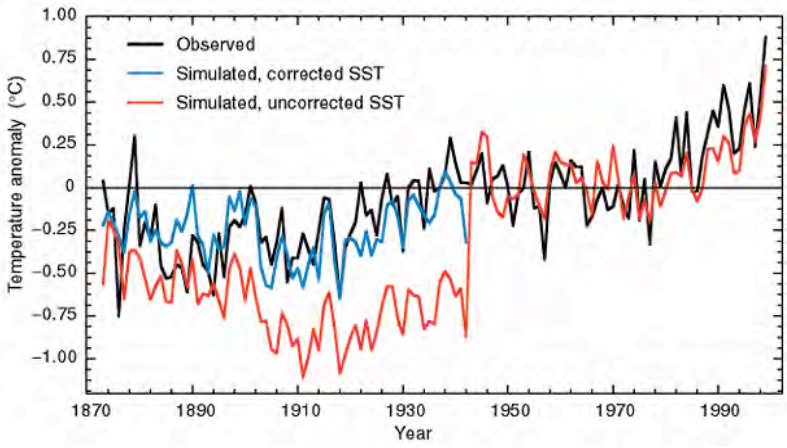

(a)

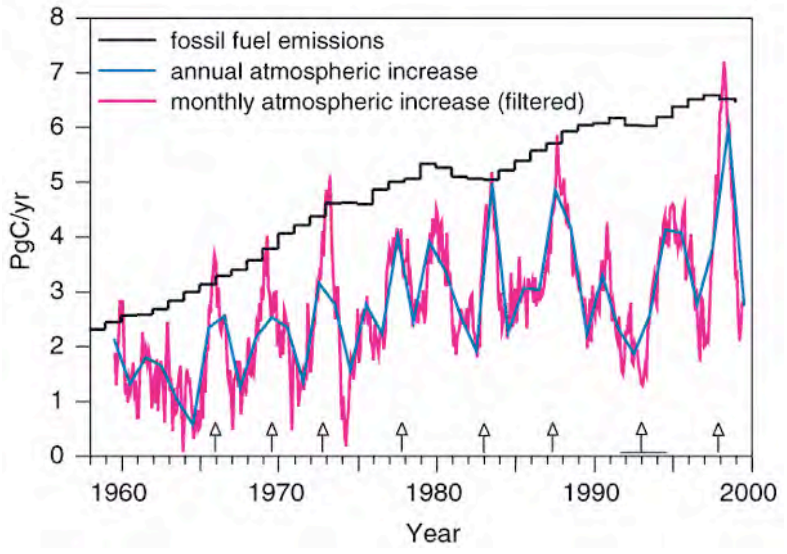

(b)

Figure 8.1. (a) Test of bias adjustments to sea surface temperature (Folland et al., 2001); the black line-annual indicates the annual mean observed land surface air temperature anomaly from 1946 to 1965 (Jones, 1994). (b) Fossil fuel emissions and the rate of increase of CO_2 concentration in the atmosphere (IPCC, 2001); atmospheric data are from Keeling and Whorf, (2000), fossil fuel emissions data from Marland et al., (2000), and British Petroleum (2000).

Although the first option is the most ideal solution for reducing the effects of global warming, it is politically and technically difficult to require all nations on Earth to limit their use of fossil fuels without providing an alternate source of affordable energy. Reducing carbon-emissions from industrial plants indirectly relates to the local and global economy. Moreover, world economy is strongly variable with quantities of energy generating by burning carbon-containing fuel. Therefore, a forced reduction in CO_2 emissions for developing countries such as China and India could be detrimental to their potential growth of gross domestic product (GDP). The second option, development of new technologies for replacing fossil fuel energy such as nuclear, hydrogen, solar, wind, and hydroelectric power is still ongoing. It will potentially take several more decades until the amount of energy generated from these technologies becomes equal to that from carbon-containing fuels. Moreover, the high cost of research and development of alternative energy and its associated infrastructure will be expensive leading to a short term increase in the "carbon tax", which is a tax on energy suppliers emitting carbon dioxide. Consequently, storing CO_2 in geological formations is more attractive than the two aforementioned options because it is relatively inexpensive and uses technology already proven by the oil, gas, and waste disposal industry. For example,

CO_2 has successfully been injected at the Sleipner (Chadwick et al., 2005) and Weyburn (White, 2004) fields in Norway and Canada, respectively, and the chemical/physical impacts on the reservoirs due to CO_2 injection is continuously being studied. In addition, CO_2 has been injected into many oil reservoirs for the purpose of enhanced oil recovery since 1970. Around the world, CO_2 enhanced oil recovery is performing in a total of 420 fields (van Bergen et al., 2004).

It is anticipated that geological sequestration of CO_2 may be the most beneficial, short-term approach to curbing the effects of global warming, after considering aspects of economics and technology. Therefore, the feasibility of geological CO_2 sequestration is currently being tested on a small scale. For examples, the United States Department of Energy created a network of seven Regional Carbon Sequestration Partnerships (Figure 8.2) to develop technology and infrastructure for implementing commercial-scale CO_2 sequestration (Klara et al., 2003; National Energy Technology Laboratory, 2007a). The Partnerships cover 40 states including 160 academic, industrial, governmental and non-governmental entities. In the coming year (2008), over 20 field geologic sequestration tests are being designed and scheduled for deployment in the United States. An additional 23 are ongoing or slated for deployment soon in other countries. For large-scale geologic

sequestration to be deployed and sustainable over the long-term, a meaningful assessment of CO_2 trapping mechanisms is essential.

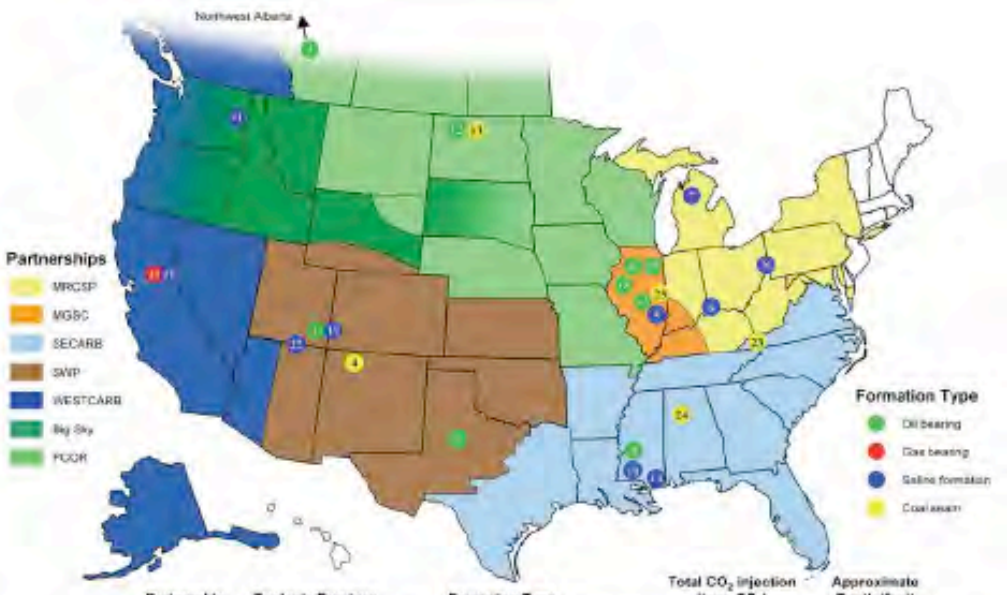

Partnership	Geologic Province	Formation Type	Total CO_2 injection (tons CO_2)	Approximate Depth (feet)
SWP	Paradox Basin, Aneth Field	Oil-bearing	450,000 – 750,000	5,600 – 5,800
SWP	Permian Basin	Oil-bearing	900,000	5,800
PCOR	Keg River Formation	Oil-bearing	250,000 tons CO_2 w/90,000 tons H_2S	5,000
SWP	San Juan Basin	Coal seam	75,000	3,000
MGSC	Illinois Basin	Saline formation	10,000	7,000 – 8,600
MRCSP	Cincinnati Arch	Saline formation	1,000 – 3,000	3,200 – 3,500
MRCSP	Michigan Basin	Saline formation	3,000 – 20,000	3,200 – 3,500
MRCSP	Appalachian Basin	Saline formation	1,000 – 3,000	5,900 – 8,300
SECARB	Gulf Coast	Oil-bearing	500,000	10,000
SECARB	Gulf Coast	Saline formation	30,000	10,300
Big Sky	Columbia Basin	Saline formation (basalt/mafic)	3,000	3,255 – 3,335 & 3,600 – 3,755
PCOR	Duperow Formation	Oil-bearing	5,000	10,000 – 10,500
PCOR	Williston Basin	Coal seam	<1,000	1,600 – 1,800
SECARB	Mississippi Salt Basin	Saline formation	3,000	8,500
MGSC	Illinois Basin	Oil-bearing – Heavy	300	1,550
MGSC	Illinois Basin	Oil-bearing – Well Conversion	300	1,549
MGSC	Illinois Basin	Oil-bearing – Pattern Flood I	300	1,548
MGSC	Illinois Basin	Oil-bearing – Pattern Flood II	300	1,551
SWP	Paradox Basin, Aneth Field	Saline formation	20,000	6,900
WESTCARB	Thorton Gas Field	Saline formation	1,000	3,400 – 3,500
WESTCARB	Thorton Gas Field	Gas-bearing	500	3,050
WESTCARB	Colorado Plateau	Saline formation	2,000	5,000
SECARB	Central Appalachian	Coal seam	1,000	1,600 – 2,300
SECARB	Black Warrior Basin	Coal seam	1,000	1,500 – 2,500
MGSC	Illinois Basin	Coal seam	750	1,000

Figure 8.2. DOE-sponsored regional partnerships in the United States (NETL, 2007a).

Recently, the network of Partnerships assessed the CO_2 storage capacity for three types of geologic formations including saline formations, unmineable coal seams, and hydrocarbon (oil and natural gas) reservoirs in both the United States and Canada (National Energy Technology Laboratory, 2007b).

8.2. Summary and Conclusions

Carbon capture and sequestration may be a key technology pathway to a substantial reduction in greenhouse gas emissions. One of the major tasks of the seven Regional Carbon Sequestration Partnerships is to estimate potential CO_2 storage capacity of geologic formations throughout North America. To estimate CO_2 storage capacity, it is necessary to understand individual CO_2 trapping mechanisms including hydrostratigraphic (mobile), residual, solubility, and mineral trapping. By quantifying the contribution of proportion of each trapping mechanism type, the aggregated regional-scale of CO_2 storage capacity of specific formations can be estimated.

In this dissertation, I assessed the relative roles of these CO_2 trapping mechanisms. Specifically, I carried out a detailed case study of CO_2 sequestration in

the SACROC unit in the Permian basin of Texas, site with a 35 years of CO_2 injection for enhanced oil recovery. This assessment of CO_2 trapping mechanisms was based on evaluation of extensive SACROC data available, including analysis using calibrated numerical simulations that describe multiphase transport coupled with chemical reactions.

In the early part of this dissertation, I assembled and coded two integrated equations of state algorithms to simulate CO_2 migration and transport in brine formations. One is a modified Redlich-Kwong EOS, "MRKEOS," that employs modification of the attractive term from the original van der Waals equation developed in 1873 (van der Waals, 1873; Kerrick and Jacobs 1981; Weir et al, 1996; Cole, 2000). The other algorithm, "SWEOS," is an EOS for CO_2 originally developed by Span and Wagner (1996), who based their algorithm on an empirical representation of the fundamental equation of Helmholtz energy. The assembly of the two fundamentally different EOSs reveals that values for the fugacity coefficient predicted from MRKEOS (Eq.2.12) appear to be systematically lower than those generated by IUPAC and Span and Wagner (1996) (Figure 2.3). This discrepancy occurs due to the treatment of the attractive term (Eq. (2.8)) and covolume (b: 5.8×10^{-5}). Covolume (b) should vary with pressure and temperature instead of remaining

constant. Because of these two parameters, induced error propagates to predicted values of other thermodynamic properties such as compressibility factor, fugacity coefficient, enthalpy, and solubility.

Errors associated with specific thermodynamic variables calculated by the EOS propagate into flow and transport results because the momentum equation (i.e., Darcy's law) includes both density and viscosity. Therefore, I used a generic 1-D model to evaluate the potential CO_2 migration/penetration distance through an unfractured seal and to investigate how EOS variable errors lead to uncertainties in flow and transport simulation results. In general, the results of thermophysical properties for both EOS algorithms are consistent, except for the contrast in the predicted fugacity coefficient of CO_2, which subsequently propagates to a small contrast in predicted solubility. However, simulation results reveal that even minor errors in calculated solubility lead to major uncertainty in flow results, because the error "accumulates." For example, a 0.1% error in solubility can lead to uncertainty in dissolved CO_2 mass that is on the order of hundreds of thousands of tonnes, if millions of tonnes are injected for sequestration in the simulation. Therefore, I suggest that sacrificing EOS accuracy for computational speed is not worth the error introduced in the flow and transport results. Furthermore, I also evaluated impacts

associated with varying (i) the amounts of injected CO_2, (ii) porosity, (iii) permeability, and (iv) brine concentration. These sensitivity analyses were motivated by a desire to understand the relative factors that affect seal integrity and potential CO_2 transport and migration through unfractured seals. The simulation results reveal that the migration/penetration distance of separate-phase CO_2 through an unfractured seal depends linearly on the injected CO_2 mass, logarithmically on caprock permeability, and inversely (1/n) on reservoir porosity.

Finally, a specific case study of CO_2 trapping mechanisms and related processes was conducted using numerical simulation. The site of the case study was the SACROC (Scurry Area Canyon Reef Operators Committee) Unit in the Permian Basin of Texas, the oldest continuous CO_2 enhanced oil recovery (EOR) site in the United States. SACROC has been subjected to CO_2 injection for 35 years, and thus provides an excellent field laboratory for this analysis. A simple mass balance analysis based on field data suggests that approximately 7 million tonnes of CO_2 (6,944,587,674 kg) are sequestered in the SACROC northern platform.

A comprehensive numerical model was developed for analyzing the range of possible trapping mechanisms and other related physical and chemical effects of injected CO_2. In this work, porosity distributions were defined from both seismic

surveys and wire log analyses. Permeability distributions were calculated from seismically-calibrated porosity values using empirical equations derived from rock-fabric classification. To my knowledge, this study marks the first time (in the publicly available literature) that basic geologic information, geophysical logs, and seismic survey data were integrated to create a three-dimensional model of subsurface structure and heterogeneity for a CO_2 sequestration study. The resulting three-dimensional porosity distribution reveals that porosity is continuous and increases upward from base to top in the Canyon Formation. Compared to the Canyon Formation, the Cisco Formation shows a high degree of heterogeneity with compartmentalized low-porosity zones.

The initial goal was to adapt this geo-cellular model to simulate CO_2 trapping mechanisms at SACROC. However, the original geo-cellular model grid developed by geologists and seismologists at the Texas Bureau of Economic Geology consisted of over 9.4 million elements. Therefore, I used an upscaling "renormalization" technique (King, 1989) to reduce the approximate 9.4 million elements down to 15,470. Among the several upscaling techniques I evaluated, renormalization was the most promising and thus was selected for this study. Furthermore, analysis of both

water chemistry and $\delta^{13}C$ isotope data collected from various sources suggest that the Wolfcamp Shale most probably acts as an effective seal.

Based on the upscaled high-resolution geo-cellular model, two separate SACROC reservoir models were developed for the CO_2 trapping mechanism analysis. The first model was designed for simulating CO_2 trapping mechanisms in a reservoir saturated with brine. The other model was designed for simulating CO_2 trapping mechanisms in a reservoir saturated with both brine and oil. CO_2 trapping mechanisms in the brine-only model show a distinctive set of stages. In the first stage (~30 years duration), hydrostratigraphic trapping was dominant, as in the original injection period. In the second stage (~15 years duration), residual trapping dramatically increases. In a third stage (extending hundreds of years), solubility trapping became increasingly important as both the residual and mobile CO_2 dissolved in the brine over time. In a final stage (after several thousand years), mineral trapping is predicted to be greater than any other mechanism. In sum, the major CO_2 trapping mechanisms were hydrostratigraphic (mobile), residual, and solubility trapping over the first 200 years.

In the model that included both brine (28%) and oil (72%), the CO_2 trapping mechanisms did not vary much over time. Separate-phase CO_2 is stored as a free

(mobile) form due to its high saturation, but it behaves like residual (immobile) CO_2 because of the smaller contrast between the densities of oil and CO_2. Furthermore, CO_2 mobility is hindered by other fluids such as brine and oil in the model due to the reduction of relative permeability. In sum, both oil trapping and hydrostratigraphic (mobile) trapping dominated during a 200-year simulation.

The combined results of these two model analyses suggest that injecting CO_2 into brine formations below oil reservoirs will provide several advantages in terms of CO_2 storage capacity and protection from potential leakage. The feasibility of CO_2 injection into brine formations below oil reservoirs is discussed in Section 8.5.

8.3. Limitations and Recommendation from This Study

One of the most limiting aspects of this model is the ignorance of hydromechanical aspects. The importance and application of hydromechanical aspects to earth processes has been extensively discussed in previous studies (Neuzil, 2003). With respect to CO_2 sequestration, a small number of researchers have studied the hydromechanical aspects associated with the stability of caprocks and faults, and these workers attempted to estimate the maximum sustainable fluid pressure for CO_2 injection (Rutqvist et al., 2002; Streit et al., 2004; Li et al., 2006;

Rutqvist et al., 2007). During CO_2 injection, increases in reservoir fluid pressure may induce strain or even fracture in the injection formation. If generated reservoir pressure is less than fracture pressure, the deformation of injection formation will behavior elastically, in general. In this study, elastic behavior is accounted for using a simple porosity formulation that is a function of pressure (Eq. 5.70). However, if the reservoir pressure becomes too large, induced stresses may cause irreversible mechanical (inelastic) changes and create new preferential flow paths. The model simulations developed in this study do not include such inelastic behavior.

In addition, this model is based on a continuum representation of porous media. This approach depends on averaging properties for a porous matrix with solid grains. Specifically, the upscaled grid-blocks are on the order of 100 m x 100 m x 10 m in size. Therefore, heterogeneous features such as faults and fractures that are smaller than this scale are not explicitly represented in this study. In addition, smaller-scale processes such as viscous fingering, convective mixing of dissolved CO_2, and salt precipitation near the injection well are not expressed in this model.

In addition, CO_2 trapping mechanism models for SACROC possess several limitations, including limited knowledge of natural heterogeneity, uncertainty in multiphase flow process parameters, and uncertainty in reactive transport parameters.

Addressing these limitations is recommended for future research. While quantifying natural heterogeneity in high-resolution geo-cellular model, permeability calculated from rock-fabric classification is typically underestimated because the porosity-permeability equations are derived without considering the existence of vug porosity (e.g. caverns and fractures). In addition, the renormalization technique (King, 1989) is derived for orthogonal grids and does not account for effects of non-orthogonality. Therefore, some error may accumulate during as a consequence of the renormalization process.

There are significant limitations dealing with the multiphase processes, which include the effect of interfacial tension, capillary pressure, relative permeability, and hyteresis (Muccino et al., 1998). For example, while simulating CO_2 sequestration processes, modelers often adapt general capillary and relative permeability functions such as Corey, (1954), van Genuchten, (1980), and Parker and Lenhard (1987). In these analytically derived equations, researchers often assume that interfacial tension, the end-point relative permeability, and residual saturation do not vary with pressure, temperature, and salinity. However, recent experimental study shows that such properties strongly depend on the in-situ conditions of pressure, temperature, and

salinity (Bachu and Bennion, 2007). Neglecting these dependencies may lead to excessive error.

Additional difficulties associated with multiphase flow modeling arise from the fluid displacement process (the physical process of one fluid displacing another in void space). Differing displacement processes give rise to varying fluid distributions. This process is generally called "hysteresis". A common approach to hysteresis is to use functions derived by Land (1968), called Land-type hysteresis functions. A Land-type hysteresis function was adapted to predict both hydrostratigraphic (mobile) and residual (immobile) trapping mechanisms in this study. Due to the absence of imbibition data, other researchers (Kumar et al. 2004; Juanes et al. 2006; Doughty, 2007) also adapted a Land-type function for this purpose. However, for better prediction of residual trapping mechanisms, extrapolation of hysteresis curves between known supercritical CO_2 and water data is recommended.

Another limitation associated with multiphase flow and transport is the approximation of phases in relative permeability curves. Systems with oil, brine, and CO_2 phases require three pairs of relative permeability functions (e.g. oil-CO_2, brine-CO_2, and brine-oil). However, current models simplify and only include two pairs of relative permeability functions (gas-liquid and oil-brine). Therefore, three

pairs of relative permeability functions must be explored for better prediction of fluid mobility.

Limitations associated with reactive transport processes including uncertainty associated with kinetic rate constants, activity coefficients, and reactive surface areas, as discussed below. Although researchers acknowledge that observed reaction rates in the field are generally slower than laboratory-measured rates, the reason for this discrepancy is not fully understood (Steefel et al., 2005). In this model, laboratory-determined kinetic rate constants are adapted without considering the discrepancy between field and laboratory values. By adapting laboratory-determined values, it is possible the amount of mineral precipitation is overestimated in these models. Therefore, a detailed error analysis associated with reaction rates must be carried out in the future.

Accurate prediction of chemical concentration can be improved by using the Pitzer model. Specifically, the Pitzer model evaluates the ionic activities of a solution as a function of long-distance interaction, short-distance interaction, pressure, and temperature. This model adequately expresses the thermodynamic properties of a high ionic strength solution over a wide range of concentrations and temperatures. Several studies adapted a generally accepted form of the Pitzer model, one formulated

by Harvie et al. (1984), and proved the accurate prediction of solution properties by that Pitzer model (Bethke, 1996; Lichtner and Felmy, 2003; Zhang et al. 2005). Two recent studies included application of the Pitzer model to simulate CO_2 sequestration (Kervevan et al. 2005; Andre et al. 2007). Although the Pitzer model more accurately predicts activity coefficients in ionic fluids, the models applied in this study are limited because they predict the activity coefficients from Debye-Huckel-type equations.

Finally, uncertainty in reactive surface areas is among the greatest limitations and source of a great deal of uncertainty in my model results. In this study, the reactive surface area data used were taken from studies that estimated the surface areas from geometric calculations, but it is more desirable to obtain direct measurements. In addition, reactive surface areas of minerals also need to be a function of corresponding chemical reactions, including precipitation and dissolution. While this calculation is performed with Eq. (5.67, 5.68), it is not experimentally determined or calibrated. Therefore, future work based on the results of this study would benefit from higher resolution reactive surface area information.

8.4. Contributions to the Science, Engineering, and Society

The performance of CO_2 injection requires a new regulatory framework, long-term monitoring techniques, risk assessments, and finally public acceptance. The scientific results in this dissertation illustrate the essential feasibility of long-term CO_2 sequestration and will aid in assessing these issues directly and indirectly.

8.4.1. Contributions to Science and Engineering

The chapters in this dissertation contribute individual parts of a detailed study of the physical and chemical processes associated with CO_2 trapping mechanisms.

Because CO_2 sequestration is targeted for very deep reservoirs (several kilometers minimum), numerical modeling is an essential tool to test its feasibility. A thorough review of the literature indicates that modeling activity specifically associated with CO_2 sequestration began around 1990. At that time, many researchers used black-oil typed simulators to mimic CO_2 sequestration processes. Later, compositional simulators came to be used, which enabled simulation of dissolution of CO_2 into either oil or brine. Around this same time, other researchers modified geothermal simulators to simulate CO_2 sequestration processes. Consequently, researchers were able to predict the buoyancy-driven migration behavior of both supercritical and dissolved CO_2. However, these approaches were

not able to account for mineral trapping mechanisms, which requires the coupling of transport codes with chemical-reaction codes. Due to the complexity of physical and chemical processes during CO_2 sequestration, these early studies could not address the viability of CO_2 trapping mechanisms such as hydrostratigraphic, residual, solubility, and mineral trapping. Furthermore, these CO_2 trapping mechanisms could not take advantage of the extensive field data as such data just did not exist.

A goal of this dissertation is to provide more understanding of CO_2 trapping mechanisms using now-available extensive field data. The contributions of this dissertation to scientific and engineering communities can be divided into five main parts: (1) a thorough summary of previous modeling approaches associated with CO_2 sequestration, (2) development of the integrated equations-of-state for CO_2 sequestration, (3) quantitative analysis of error propagation from equations-of-state to flow and transport simulations, (4) investigation of time-scales of individual CO_2 trapping mechanisms, and (5) detailed exploration of the relative capacities of CO_2 trapping mechanisms using field data.

Chapter 1 provides a historical overview of modeling approaches used to quantify CO_2 trapping mechanisms and related issues. CO_2 trapping mechanisms are complex physical and chemical processes requiring the understanding of

multiphase effects, hysteresis, phase partitioning, and reactive transport. Many different scientific disciplines and technologies need to be combined to develop simulators that describe CO_2 trapping mechanisms effectively. For example, petroleum researchers have studied extensively both multiphase and hysteresis effects, but typically have not investigated reactive transport processes because they were not important to evaluate oil production. However, reactive transport analysis is essential to evaluate mine tailing geochemistry, ore deposits, rock weathering, geothermal systems, and diagenetic processes. Therefore, reactive transport analysis has long been a tool of geologists and geochemists. Effective numerical models of CO_2 trapping mechanisms are "multi-disciplinary" in nature, and proper implementation of such models requires collaboration among geologists, geochemists, hydrologists, petroleum reservoir modelers and other specialists. The comprehensive discussion in Chapter 1 illustrates how researchers combine knowledge and technology from diverse fields in numerical tools. In addition, this chapter also discusses the current capability and limitation of numerical codes to address CO_2 trapping mechanisms. Currently, multiphase flow (relative permeability and capillary pressure) with hysteresis, reactive transport, heat flow, and phase partitioning were well established in several numerical codes. Such codes

successfully solve specific problems such as convective mixing of dissolved CO_2 (Ennis-King and Paterson, 2007), eruptive CO_2 leakage (Pruess, 2005), salt precipitation due to "drying out" effects near the well bore (Giorgis et al. 2007), and mineralization processes (Xu et al. 2005). However, no publically available codes successfully address both hydrogeomechanical and geochemical aspects at the same time.

In CO_2 and water systems, gravity, viscous, and capillary forces determine mobility of phases. To evaluate explicitly such forces, adequate representation of viscosity and density of water, separate-phase CO_2, and aqueous mixtures of CO_2 over the rage of temperatures and pressures anticipated in typical sedimentary basins is required. Finally, adequate representation of the CO_2 solubility is required. In this dissertation, I assembled two different EOS algorithms and coupled these in a flow and transport simulator, which facilitated simulation of flow and transport of CO_2 as both a separate-phase and an aqueous phase. In detail, both integrated equations of state predict thermodynamic properties (density, fugacity, enthalpy, viscosity) of water, separate-phase CO_2 (gas and supercritical phases), and aqueous mixtures of CO_2 over the range of temperatures and pressures anticipated in a given geologic setting. Source codes are provided including "stand-alone" Matlab ©

scripts and FORTRAN subroutines developed specifically for the TOUGH2 simulator (Pruess, 1999).

Many numerical simulators are available to simulate CO_2 sequestration processes (Table 1.1), and many of these include their own EOS modules. The review by Hu et al. (2007) indicates that only a few EOS models are consistent with results of experimental testing. In general, previous researchers implemented various EOS algorithms in numerical simulators without rigorous comparison and/or calibration to experimental data. The comparison study in this dissertation reveals that minor errors generated from EOS algorithms may accumulate and become significantly large uncertainty in resulting flow and transport simulations. Therefore, based on this comparison study I conclude that the choice of EOS algorithms in numerical simulation studies is critical.

As introduced earlier in this chapter, the seven Regional Carbon Sequestration Partnerships (Figure 8.2) are developing technologies and infrastructure for specific pilot sites. This includes detailed site characterization (sequence stratigraphy and depositional model), injectivity analysis, seal integrity studies, capacity estimation, and development of extensive monitoring plans. One of the major tasks of these projects is to estimate CO_2 storage capacity of potential storage formations, to provide

a ranked set of sequestration options for future industry consideration. However, assessment of trapping mechanisms is extremely difficult because most trapping types and mechanisms apply over different time scales. The most accurate way to estimate storage capacity is through construction of a geologic framework and then use this information in reservoir simulation (Bradshaw et al. 2007). In Chapter 6, I adapted a three-dimensional high-resolution geo-cellular model and upscaled it for quantifying CO_2 trapping mechanisms. Results of this model outlined in Chapter 7 provide reasonable quantitative estimates of relative CO_2 storage trapping mechanisms at the SACROC northern platform study area for a 200-year time period.

This SACROC model is intended to serve as an example or template for evaluating the relative roles of different CO_2 trapping mechanisms at other sites. This study presents the first successful quantification of all significant CO_2 trapping mechanisms (hydrostratigraphic, residual, solubility, mineralization) for a specific site, including effects of heterogeneity, multiphase flow and reactive transport. Figure 8.3 provides a suggested flow chart for building models of CO_2 trapping mechanisms at other CO_2 sequestration sites.

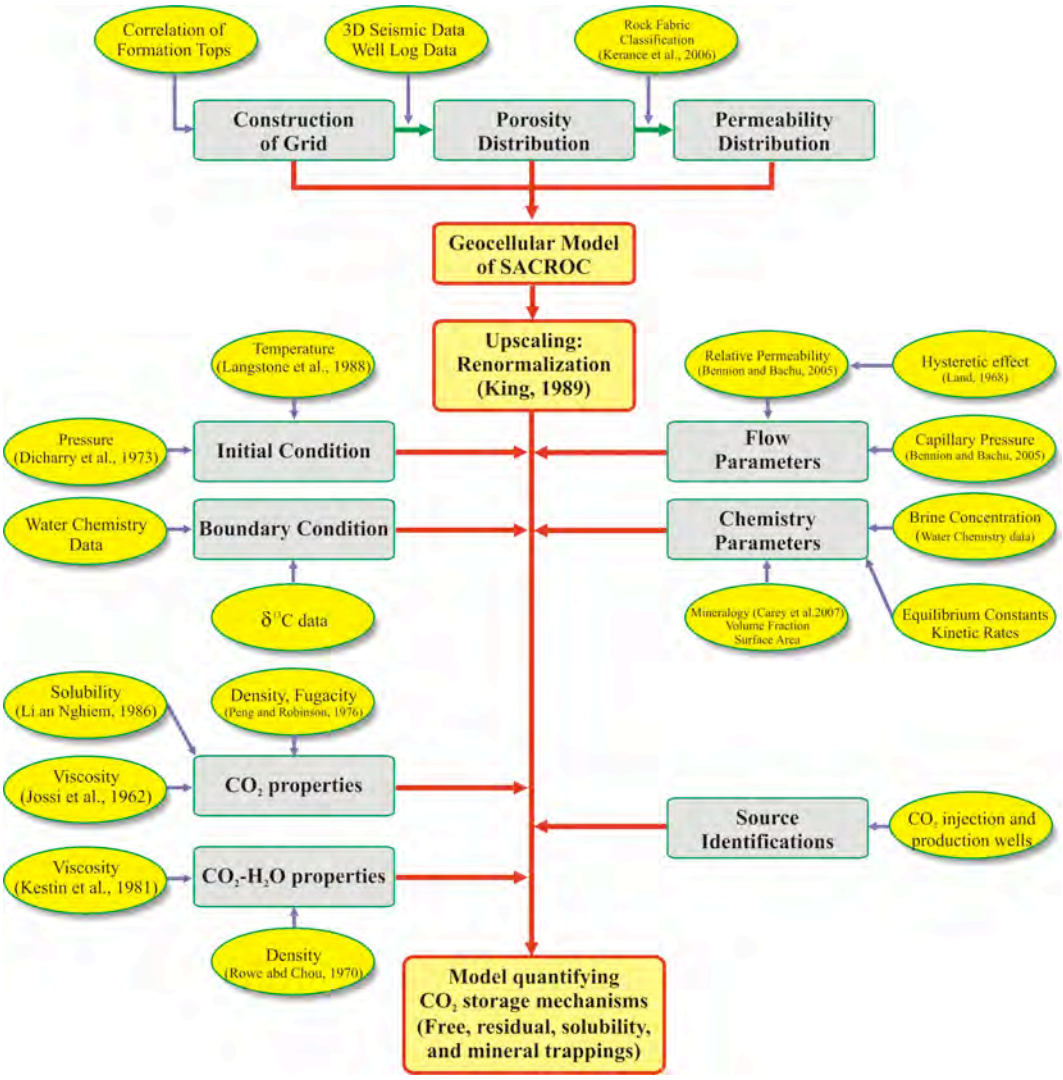

Figure 8.3. Flow chart for quantifying CO_2 trapping mechanisms

In addition, this SACROC model indirectly helps planning for measuring, monitoring, and verification (MMV) technology and protocols. Accurate MMV is essential for (1) health and safety reasons, (2) mass balance verification, (3) improving understanding of behavior and future states of the injected CO_2, and (4)

development of better techniques of subsurface CO_2 storage (Winthaegen et al. 2005). Leakage may also occur either by seal failure or wellbore failure. The efficiency of measuring, monitoring, and verification (MMV) technologies and protocols can be optimized, or at least improved extensively, if results of numerical modeling are incorporated. Finally, this study also examines the feasibility of geological sequestration of several millions tonnes of CO_2. I suggest that numerical simulation tools are the most promising method to evaluate the long-term CO_2 fate and to confirm storage mechanisms.

8.4.2. Contributions to Developing Regulatory Framework

Although CO_2 sequestration is a promising technology, further research is necessary to identify the long-term economic, environmental, health, and safety risks. In addition, a regulatory system will need to manage the sequestration sites and monitor for any potentially leaking CO_2. Although there is no comprehensive legal and regulatory framework for CO_2 sequestration, the United States Environmental Protection Agency (EPA) has a regulatory framework governing underground waste injection, the Underground Injection Control (UIC) framework, for the purpose of protecting clean, shallow ground water by the Safe Drinking Water Act (1974). It is

suggested that a similar framework for CO_2 sequestration be developed based on the regulation of UIC. However, the application will be difficult because of the physical and chemical differences between CO_2 and liquid waste. For example, the viscosity and density of CO_2 is much lower compared to typical liquid waste. As such, the buoyancy driven migration of CO_2 is much greater. In addition, the chemical reactions caused by CO_2, brine, and reservoir rock will be significantly different than those of liquid waste.

The research performed in this dissertation suggests that 30 years of injected CO_2 can be safely sequestered in a typical oilfield site (SACROC) with reducing the potential leakage over the 200 years following injection. In addition, the most important results indicate that the different CO_2 trapping mechanisms can indeed be quantified with time. This finding is very significant and has implications for the now-developing regulatory framework and emerging monitoring technologies. Due to the difficulty of direct adaptation of regulatory frameworks associated with underground waste injection, it may be necessary to develop a separate set of regulations for CO_2 injection based on the results of laboratory and field experiments. Direct experimental methods can only predict short-term sequestration effects, e.g., from several months to several years. However, sequestered CO_2 needs to be stored

safely and monitored over several hundreds years. One definitive way to estimate long-term behavior of injected CO_2 is the approach presented in this dissertation. The prediction of the 200-year CO_2 behavior indicates that both mobile and residual trapping are the major short-term trapping mechanisms. This result indicates that both a regulatory and a monitoring framework need to be designed for these two trapping mechanisms for short-term or immediate applications. For example, because mobile CO_2 (hydrostratigraphic trapping) will be dominant in the short-term (especially with high injection-induced pressure conditions), buoyancy driven CO_2 migration may be very significant, instigating need for a regulatory and monitoring framework focusing on CO_2 buoyancy migration and potential leakage.

8.4.3. Contributions to Public Acceptance

Although the public considers CO_2 sequestration as one way to limit emissions and potential effects of global warming, most may not necessarily want injection of CO_2 in or near their communities ("not-in-my-backyard"). The most significant consideration by the public is the contamination of potential sources of drinking water due to CO_2 leakage. One way to protect shallow groundwater from buoyancy-driven CO_2 is to evaluate the integrity of the overlying seal or caprock.

Analysis of groundwater chemistry and the $\delta^{13}C$ isotope in this dissertation is one way to estimate seal integrity. Furthermore, the newly suggested injection scheme "CO_2 injection into brine formations below oil reservoirs" indicates the possibility of conditions in which CO_2 density is greater than oil density. In this case, CO_2 can be sequestered without any buoyancy-effects. In this hypothetical condition, potential sources of drinking water can be protected from sequestered CO_2.

8.4.4. Potential Cost Benefits

In terms of economic aspects, the aforementioned "below oil reservoir" injection scheme may very well reduce the cost of constructing required infrastructure and monitoring networks, because facilities are often already in place in petroleum fields. Moreover, an oil and gas fields tend to be well–characterized, thus reducing the need for significant additional expense for site characterization.

8.5. Recommendations for Future Work

This section summarized the potential future study based on the results of the trapping mechanism comparison study (Chapter 7). This study analyzed the pros and cons of CO_2 injection scenarios between brine and oil reservoir (Table 8.1).

Injecting CO_2 into oil reservoirs provides several advantages for minimizing potential CO_2 vertical migration. However, their sizes and volumes are limited for CO_2 storage. The capacity estimation by the Regional Partnership shows that CO_2 capacity in oil and gas reservoirs is about 82.4 billion tonnes, while in brine formation it is about 3378 billion tonnes (NETL, 2007). In comparison, the potential for CO_2 storage in brine formations is immense.

Table 8.1. Comparison of CO_2 injection scenarios between in brine and oil reservoir.

Factors	Petroleum Reservoir	Brian Reservoir
CO_2 solubility	Greater	Smaller
Buoyancy flow	Smaller (less risk)	Greater (higher risk)
Mobility	Smaller (Three phase conditions)	Greater (Two phase conditions)
	Smaller (Multiple contact)	Greater (Single contact)
Caprock	Seal integrity is proven by the presence of oil	Presence (sometimes does not)
Infrastructure	Already in place	Needs to be built
Capacity	82.4 billion tonnes (NETL, 2007): not account abandon oil field	3378 billion tonnes (NETL, 2007)

Therefore, to obtain advantages in terms of CO_2 storage capacity and protection from potential leakage from both brine and oil reservoirs, we propose CO_2 injection into brine formations below oil reservoirs. Future research will test our conceptual model and quantify CO_2 trapping mechanisms in a range of reservoir conditions (Figure 8.4).

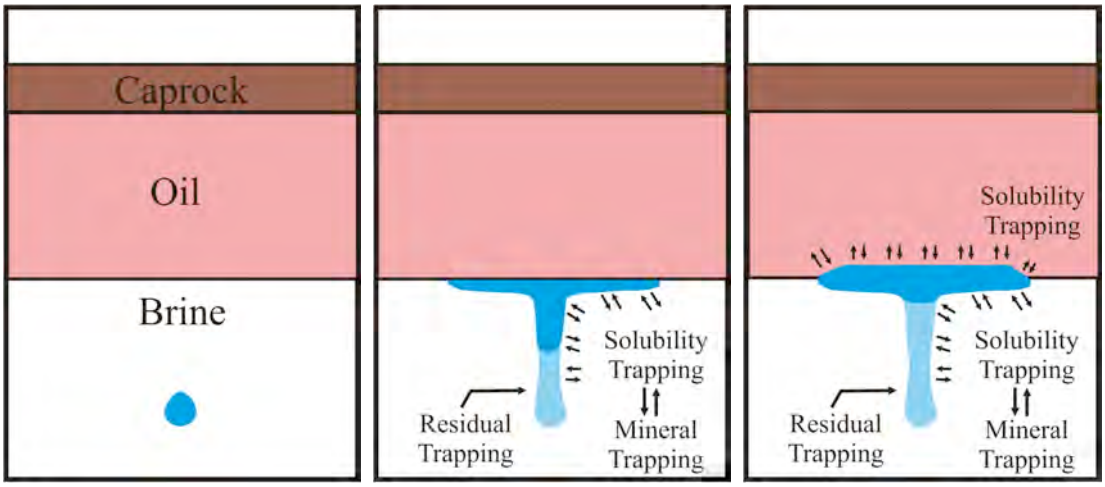

(a) (b) (c)

Figure 8.4. CO_2 injection into brine formations below oil reservoir: (a) Stage I, (b) Stage II, and (c) Stage III.

In Stage I during the injection period, injected CO_2 is expanded from injection location (Figure 8.4a). In Stage II after stopping injection, the decrease in CO_2 saturation is due to the imbibition process occurring at the tail of the CO_2 plume, where brine displaces CO_2. As a result, while CO_2 migrates either vertically or horizontally, some of mobile CO_2 becomes trapped in pores (Figure 8.4b). Once mobile CO_2 reaches the contact boundary between oil and water, the vertical movement of mobile CO_2 is retarded due to the several reasons addressed below;

(1) A smaller density contrast between oil and CO_2

(2) Changes of fluid phases from two phases (brine and CO_2) to three phases conditions (oil, residual brine, and CO_2)

(3) Changes of fluid components from single contact to multiple contact

Theoretically, an oil reservoir above a brine formation becomes a physical barrier and prevents the upward migration of mobile CO_2. The solubility trapping mechanism also occurs because both mobile and immobile CO_2 dissolve into brine (Figure 8.4b). In addition, the mineralization process continues. In sum, the possible trapping mechanisms in Stage II are hydrodynamic, residual, solubility, and mineral trapping into brine.

In Stage III, the oil reservoir keeps acting like a physical barrier. At the same time, the upper part of the mobile CO_2 plume dissolves into the oil reservoir and the bottom part dissolves into the brine (Figure 8.4c). Because CO_2 solubility into oil is greater than oil, oil trapping will keep preventing the vertical movement of CO_2. In sum, the possible trapping mechanisms in Stage III are hydrodynamic, residual, solubility, and mineral trapping into brine, and oil trapping into oil.

Possibly, some of CO_2 is not trapped and keeps migrating as mobile phase CO_2. Although this certain amount of mobile CO_2 moves vertically through the oil reservoir it will stop at the bottom of the caprock, of which seal integrity is proven by the existence of oil.

Although current regional-scale model analyses (Chapter 6 and 7) are very promising for quantifying CO_2 trapping mechanisms, certain physical processes such as viscous fingering, heterogeneity effects, capillary effects and other pore-scale processes are difficult to capture. Therefore, smaller-scale models that evaluate such processes near CO_2 injection wells need to be investigated in more detail.

Additionally, pilot injection tests have demonstrated that injectivity of a well may decrease over time, leading to reduced injection rates. As a result, it may become impossible to inject CO_2 at desired rates and to maintain formation pressures below the maximum allowable fracturing pressure. In the event of elevated pressures associated with injectivity loss, fractures may form, leading to the unintended vertical migration of injected CO_2. Injectivity loss has been the subject of many previous investigations, but primarily for waste disposal activities and CO_2 flooding in oil fields (Saripalli et al., 2000; Xu, et al, 2004). With respect to CO_2 sequestration, Hitchon (1996) investigated injectivity in the Alberta basin using numerical simulation, but this study did not address reactive transport or geomechanical processes.

Well injectivity (I) loss is usually induced by plugging and formation damage during injection. Xu et al., 2004 defined injectivity as the ratio of injection rate (q) to the difference between the borehole pressure (P_b) and initial reservoir pressure (P_i):

$$I = \frac{q}{P_b - P_i} \qquad \text{(Eq. 8.1)}$$

Well-plugging due to migration of fine particles, clay swelling, and chemical dissolution/precipitation may reduce injectivity and the "life" of an injection well. Moreover, severe injectivity loss may increase injection pressures beyond maximum allowable bounds and damage the injection well and associated equipment.

In future work, I plan to investigate the potential for injectivity loss using numerical simulations. The CO_2 injection target formation for this injectivity study is the Canyon Formation in the SACROC Unit and the Entrada Formation in the Uinta basin. The primary purpose of these simulations is to evaluate the role of rock types and brine composition on aqueous reactions that reduce injectivity by changing porosity and permeability. An additional goal of this work will be to evaluate injectivity loss associated with potential changes in mechanical properties caused by these reactions and by fluid pressure changes.

References

Al-Bazali, T.M., Zhang, J., Sharma, M.M., 2005. Measurement of the sealing capacity of shale caprocks. Society of Petroleum Engineers Journal 96100.

Andre, L., Audigane, P., Azaroual, M., Menjoz, A., 2007. Numerical modeling of fluid-rock chemical interactions at the supercritical CO_2-liquid interface during CO_2 injection into a carbonate reservoir, the Dogger aquifer (Paris basin, France). Energy Conversion and Management 48(6), 1782-1797.

Bachu, S., Bennion, B., 2007. Effects of in-situ conditions on relative permeability characteristics of CO_2-brine system. Environmental Geology, DOI 10.1007/s00254-007-0946-9.

Bethke, C.M., 1996. Geochemical Reaction Modeling. Oxford University Press, New York, NY, 397pp.

Bradshaw, J., Bachu, S., Bonijoly, D., Burruss, R., Holloway, S., Christensen, N.P., Mathiassen, O.M., 2007. CO_2 storage capacity estimation: Issues and development of standards. International Journal of Greenhouse Gas Control 1, 62-68.

British Petroleum Company, 2000. BP statistical review of world energy 1999. British Petroleum Company, London, UK.

Bryant, S., 2007. Geologic CO_2 storage−Can the oil and gas industry help to save the planet? Society of Petroleum Engineers Journal 103474.

Chadwick, R.A., Zeigel, P., Gregersen, U., Kirby, G.A., Holloway, S., Johannessen, P.N., 2005. Geological reservoir characterization of a CO_2 storage site: The Utsira sand, Sleipner northern North Sea. Energy 29, 1371-1381.

Cole, B. S., 2000. Sequestration of supercritical carbon dioxide in deep sedimentary basin aquifers: A numerical model. Master's Thesis, New Mexico Institute of Mining and Technology, 124 pp.

Corey, A.T., 1954. The interrelation between has and oil relative permeabilities. Producers Monthly 38-41.

Doughty, C., 2007. Modeling geologic storage of carbon dioxide: Comparison of non-hysteretic and hysteretic characteristic curves. Energy Conversion and Management 48, 1768-1781.

Ennis-King, J., Paterson, L., 2003. Role of convective mixing in the long-term storage of carbon dioxide in deep saline formations. Society of Petroleum Engineers Journal 84344.

Ennis-King, J., Paterson, L., 2007. Coupling of geochemical reactions and convective mixing in the long-term geological storage of carbon dioxide. International Journal of Greenhouse Gas Control 1, 86-93.

Folland, C.K., N.A. Rayner, S.J. Brown, T.M. Smith, S.S. Shen, D.E. Parker, I. Macadam, P.D. Jones, R.N. Jones, N. Nicholls and D.M.H. Sexton, 2001: Global temperature change and it uncertainties since 1861. Geophysical Research Letters 28(13), 2621-2624.

Giorgis, T., Carpita, M., Battistelli, A., 2007. 2D modeling of salt precipitation during the injection of dry CO_2 in a depleted gas reservoir. Energy Conversion and Management 48, 1816-1826.

Harvie, C.E., Moller, N., Weare, J.H., 1994. The prediction of mineral solubilities in natural waters: The Na-K-Mg-Ca-H-Cl-SO_4-OH-HCO_3-CO3-H_2O-system to high ionic strengths at 25°C. Geochimica et COsmochimica Acta 48(4), 723-751.

Houghton, J., 2004. Global Warming. Third edition, Cambridge press.

Hu, J., Duan, Z., Zhu, C., Chou, I., 2007. PVTx properties of the CO_2-H_2O and CO_2-H_2O-NaCl below 647 K: Assessment of experimental data and thermodynamic models. Chemical Geology 238, 249-267.

Intergovernmental Panel on Climate Change. Third Assessment Report: Summary for Policy Makers, 2001. (http://www.grida.no/climate/ipcc_tar/wg1/ index.htm).

Jones. P.D., 1994. Hemispheric surface air temperature variations: A reanalysis and an update to 1993. Journal of Climate 7, 1974-1802.

Juanes, R. Spiteri, E.J., Orr, F.M., Blunt, M.J., 2006. Impact of relative permeability hysteresis on geological CO_2 storage. Water Resources Research 42, W12418, doi:10.1029/2005WR004806.

Keeling, C.D., Whorf, T.P., 2000. Atmospheric CO_2 records from sites in the SIO air sampling network. In: Trends: A compendium of data on global change. Carbon Dioxide Information Analysis Center, Oak Ridge National Laboratory, Oak Ridge, Tenn., USA.

Kerans, C., Lucia, F.J., Zeng, H. and Wang, F., 2005, Reservoir Modeling of an Icehouse Giant: Horseshoe Atoll Complex, West Texas, U.S.A, Abstract, American Association of Petroleum Geologists International Conference and Exhibition.

Kerrick, D. M., Jacobs, G. K., 1981. A modified Redlich–Kwong equation for H_2O, CO_2, and H_2O-CO_2 mixtures. American Journal of Science 281, 735–767.

Kervevan, C., Azaroual, M., Durst, P., 2005. Improvement of the calculation accuracy of acid gas solubility in deep reservoir brines: Application to the geological storage of CO_2. Oil & Gas Science and Technology 60(2), 357-379.

King, P.R., 1989. The use of renormalization for calculating effective permeability. Transport in Porus Media 4, 37-58.

Klara, S.M., Srivastava, R.D., McIlvried, H.G., 2003. Integrated collaborative technology development program for CO_2 sequestration in geologic formations–united States Department of Energy R&D. Energy Conversion and Management 44, 2699-2712.

Kumar, A., Noh, M., Pope, G.A., Bryant, S., Lake, L.W., 2004. Reservoir simulation of CO_2 storage in deep saline aquifers. Society of Petroleum Engineers Journal 89343.

Land, C.S., 1968. Calculation of imbibition relative permeability for two- and three-phase flow from rock properties. Society of Petroleum Engineers Journal 1942.

Langmuir, D., Melchior, D., 1985. The geochemistry of Ca, Sr, Ba, and Ra sulfates in some deep brines from the Palo Duro basin, Texas. Geochimica et Cosmochimica Acta 49(11), 2423-2432.

Li, Q., Wu, Z., Bai, Y., Yin, X., Li, X. 2006. Thermo-hydro-mechanical modellino of CO_2 sequestration system around fault environment. Pure and Applied Geophysics 163, 2585-2593.

Lichtner, P.C., Felmy, A., 2003. Estimations of Hanford SX tank waste compositions from historically derived inventories. Computers and Geosciences 29(3), 371-383.

Marland, G., Boden, T.A., Andres, R.J., 2000. Global, regional, and national CO_2 emissions. In: Trends: A Compendium of Data on Global Change. Carbon Dioxide Information Analysis Center, Oak Ridge National Laboratory, U. S. Department of Energy, Oak Ridge, Tenn., USA.

Muccino, J.C., Gray, W.G., Ferrand, L.A., 1998. Toward an improved understading of multiphase flow in porous media. Reviews of Geophysics 36(3), 401-422.

National Energy Technology Laboratory, 2007a. Carbon sequestration technology roadmap and program plan.

National Energy Technology Laboratory, 2007b. Carbon sequestration atlas of the United States and Canada. (www.netl.doe.gov/publications/carbon_seq /atlas/index. html).

Neuzil, C.E., 2003. Hydromechanical coupling in geologic processes. Hydrogeology Journal 11, 41-83.

Parker, J.C., Lenhard, R.J., 1987. A model for hysteretic constitutive relations governing multiphase flow, 1. Saturation-pressure relations. Water Resources Research 23(12), 2187-2196.

Pruess, K., 1991. TOUGH2-A general purpose numerical simulator for multiphase fluid and heat flow. Report LBNL-29400, Lawrence Berkeley National Laboratory, Berkeley, CA.

Pruess, K., 2005. Numerical studies of fluid leakage from a geologic disposal reservoir for CO_2 show self-limiting feedback between fluid flow and heat transfer. Geophysical Research Letters 32, DOI:10.1029/2005GL023250.

Rutqvist, J., Birkholzer, J., Cappa, F., Tsang, C.-F., 2007. Estimating maximum sustainable injection pressure during geological sequestration of CO_2 using

coupled fluid flow and geomechanical fault-slip analysis. Energy Conversion and Management 48, 1798-1807.

Rutqvist, J., Tsang, C.-F., 2002. A study of caprock hydromechanical changes associated with CO_2 injection into a brine formation. Environmental Geology 42, 296-305.

Saripalli, K.P., Sharma, M.M., Bryant, S.L., 2000. Modeling injection well performance during deep-well injection of liquid wastes. Journal of Hydrology 227, 41-55.

Span, R., Wagner,W., 1996. A new equation of state for carbon dioxide covering the fluid region from the triple-point temperature to 1100 K at pressures up to 800 Mpa. Journal of Physical and Chemical Reference Data 25(6), 1509-1596.

Steefel, C.I., DePaolo, D.J., Lichtner, P.C., 2005. Reactive transport modeling: An essential tool and a new research approach for the Earth sciences. Earth and Planetary Science Letters 240, 539-558.

Streit, J.E., Hillis, R.R., 2004. Estimating fault stability and sustainable fluid pressures for underground storage of CO_2 in porous rock. Energy 29, 1445-1456.

Van Bergen, F., Gale, J., Damen, K.J., Wildenborg, A.F.B., 2004. Worldwide selection of early opportunities for CO_2-enhanced oil recovery and CO_2-enhanced coal bed methane production. Energy 29, 1611-1621.

Van der Waals, J.D. 1873. De continuiteit van den gas en vloeistoftoestand. Ph. D. dissertation, University Leiden, pp. 134.

Van Genuchten, M.Th., 1980. A closed-form equation for predicting the hydraulic conductivity of unsaturated soils. Soil Science Society of America Jounral 44(5), 892-898.

Weir, G. J., White, S. P., Kissling, W. M., 1996. Reservoir storage and containment of greenhouse gases. Transport in Porous Media 23, 37–60.

White, D.J., Burrowes, G., Davis, T., Hajnal, Z., Jirsche, K., Hutcheon, I., Majer, E., Rostron, B., Whittaker, S., 2004. Greenhouse gas sequestration in abandoned

oil reservoirs: The international energy agency Weyburn pilot project. GSA Today 14(7), doi:10.1130/1052-513(2004)014<4:GGSIAO>20.CO;2.

Winthaegen, P., Arts, R., Schroot, B., 2005. Monitoring subsurface CO_2 storage. Oil & Gas Science and Technology 60(3), 573-582.

Xu, T., Ontoy, Y., Molling, P., Spycher, N., Parini, M., Pruess, K., 2004. Reactive transport modeling of injection well scaling and acidizing at Tiwi field, Philippines. Geothermics 33, 477-491.

Xu, T., Apps, J.A., Pruess, K., 2005. Mineral sequestration of carbon dioxide in a sandstone-shale system. Chemical Geology 217, 295-318.

Zhang, G., Zheng, Z., Wan, J., 2005. Modeling reactive geochemical transport of concentrated aqueous solutions. Water Resources Research 41, W02018, doi:10.1029/2004WR003097.

Appendix I. Nomenclature in Chpater 2

Alphabet

a Attractive term
b Covolume [m^3/mol]: 5.8×10^{-5}
c Fitting parameter [cm^3/g]: -9.3134
c_v^* Molar heat capacity at constant volume
d Fitting parameter [$cm^3K^{0.5}$/g]: 11.5477
F The degree of freedom
f Fugacity [Pa]
f_{H_2O} Fugacity of water [Pa]
g Gas phase
H Molar enthalpy of CO_2 [J/mol]
H_{ref}^* Molar enthalpy of CO_2 at the reference state [J/mol]: 0
H_{CO_2} Specific enthalpies of CO_2 [J/kg]
H_{H_2O} Specific enthalpies of pure water [J/kg]
H_{mix} Specific enthalpies of aqueous mixture of CO_2 [J/kg]
H_{sol} Specific enthalpy of solution for CO_2 [J/kg]
$H_{2,1}^{Pvp1}$ Henry's coefficient [Pa]
l Liquid phase
M_w Molecule weight of CO_2 [kg/mole] : 4.40098×10^{-2}
$H_w^{H_2O}$ Molecule weight of H_2O [kg/mole] : 1.80153×10^{-2}
N_α The number of component
N_β The number of phase
n The number of mole
P Pressure [Pa]
P_{sat} Water saturated pressure [Pa]
R Universal gas constant [m^3Pa/molK] : 8.31441
S_β Saturation of fluid phase
t Temperature [°C]
T Temperature [K]
T_{ref} Temperature at the reference state [K] : 273.16
T^* Reduced temperature [K]
U Molar internal energy of CO_2 [J]
U_{ref}^* Molar internal energy at the reference state CO_2 [J]: $-RT_{ref}$
V Total volume [m^3]
$\overline{V_2^\infty}$ Partial molar volume of CO_2 at infinite dilution [m^3/mol]: 3×10^{-5}
v Molar volume of CO_2 [m^3/mol]
$X_{co_2}^{non}$ Mole fraction of CO_2 in non-aqueous phase [-]
$X_{co_2}^{mod\,el}$ Mole fraction of CO_2 in aqueous phase [-]
X_{co_2} Mole fraction of CO_2 in aqueous phase [-]
X_β^α Mass fraction of component α present in fluid β
y Dimensionless variable (=b/4v)
Z Compressibility factor [-]

Greek

α Component (H_2O or CO_2)
β Fluid phase
ϕ Fugacity coefficient [-]
γ_{non} Activity coefficient of CO_2 in non-aqueous phase [-]
γ_{CO_2} Activity coefficient of CO_2 in aqueous phase [-]
γ^* Empirical corrected function
η Viscosity of CO_2 [μPa-s]
η_0 Zero-density viscosity [μ Pa-s]
$\Delta\eta$ Excess Viscosity of CO_2 [μ Pa-s]
$\Delta_c\eta$ Critical point enhancement viscosity of CO_2 [μ Pa-s]
ρ Density of CO_2 [kg/m^3]
$\rho_{CO_2}^{sat}$ Density of CO_2 at saturation pressure [kg/m^3]
ρ_{H_2O} Density of water [kg/m^3]
ρ_{mix} Density of aqueous mixtures of CO_2 and water [kg/m^3]
ξ Scaling factor: -0.088
ψ_η^* Reduced effective cross-section [$T^{0.5}$/μ Pa-s]

Appendix II. Mathematical representation of equation of states (Span and Wagner, 1996).

1. Density algorithms

$$\rho = \frac{p(\delta,\tau)}{RT(1+\phi_\delta^r)}$$

$$\phi_\delta^r = \sum_{i=1}^{7} n_i d_i \delta^{d_1-1}\tau^{t_i} + \sum_{i=8}^{34} n_i e^{-\delta^{c_i}}\left[\delta^{d_i-1}\tau^{t_i}\left(d_i - c_i\delta^{c_i}\right)\right] +$$

$$\sum_{i=35}^{39} n_i \delta^{d_i}\tau^{t_i} e^{-\alpha_i(\delta-\varepsilon_i)^2-\beta_i(\tau-\gamma_i)^2}\left[\frac{d_i}{\delta} - 2\alpha_i(\delta-\varepsilon_i)\right] + \sum_{i=40}^{42} n_i\left[\Delta^{b_i}\left(\Psi + \delta\frac{\partial\Psi}{\partial\delta}\right) + \frac{\partial\Delta^{b_i}}{\partial\delta}\delta\Psi\right]$$

$$\Delta = \theta^2 + B_i\left[(\delta-1)^2\right]^{a_i},\ \theta = (1-\tau) + A_i\left[(\delta-1)^2\right]^{1/(2\beta_i)},\ \Psi = e^{-C_i(\delta-1)^2 - D_i(\tau-1)^2}$$

$$\frac{\partial\Psi}{\partial\delta} = -2C_i(\delta-1)\psi,\ \frac{\partial\Delta^{b_i}}{\partial\delta} = b_i\Delta^{b_i-1}\frac{\partial\Delta}{\partial\delta}$$

2. Fugacity Coefficient algorithms

$$\varphi = \exp\left(\phi^r + \delta\phi_\delta^r - \ln\left(1 + \delta\phi_\delta^r\right)\right)$$

$$\phi^r = \sum_{i=1}^{7} n_i \delta^{d_i} \tau^{t_i} + \sum_{i=8}^{34} n_i \delta^{d_i} \tau^{t_i} e^{-\delta^{c_i}} + \sum_{i=35}^{39} n_i \delta^{d_i} \tau^{t_i} e^{-\alpha_i(\delta-\varepsilon_i)^2 - \beta_i(\tau-\gamma_i)^2} + \sum_{i=40}^{42} n_i \Delta^{b_i} \delta\psi$$

$$\phi_\delta^r = \sum_{i=1}^{7} n_i d_i \delta^{d_1 - 1} \tau^{t_i} + \sum_{i=8}^{34} n_i e^{-\delta^{c_i}} \left[\delta^{d_i - 1} \tau^{t_i} \left(d_i - c_i \delta^{c_i}\right)\right] +$$

$$\sum_{i=35}^{39} n_i \delta^{d_i} \tau^{t_i} e^{-\alpha_i(\delta-\varepsilon_i)^2 - \beta_i(\tau-\gamma_i)^2} \left[\frac{d_i}{\delta} - 2\alpha_i\left(\delta - \varepsilon_i\right)\right] + \sum_{i=40}^{42} n_i \left[\Delta^{b_i}\left(\Psi + \delta\frac{\partial\Psi}{\partial\delta}\right) + \frac{\partial\Delta^{b_i}}{\partial\delta}\delta\Psi\right]$$

$$\Delta = \theta^2 + B_i\left[\left(\delta - 1\right)^2\right]^{a_i},\ \theta = \left(1 - \tau\right) + A_i\left[\left(\delta - 1\right)^2\right]^{1/(2\beta_i)},\ \Psi = e^{-C_i(\delta-1)^2 - D_i(\tau-1)^2}$$

$$\frac{\partial\Psi}{\partial\delta} = -2C_i\left(\delta - 1\right)\psi,\ \frac{\partial\Delta^{b_i}}{\partial\delta} = b_i\Delta^{b_i - 1}\frac{\partial\Delta}{\partial\delta}$$

3. Enthalpy algorithms

$$h = RT\left(1 + \tau\left(\phi_\tau^0 + \phi_\tau^r\right) + \delta\phi_\delta^r\right)$$

$$\phi_r^0 = a_2^0 + \frac{a_3^0}{\tau} + \sum_{i=4}^{8} a_i^0\theta_i^0\left[\left(1 - e^{-\theta_i^0\tau}\right)^{-1} - 1\right]$$

$$\phi_\tau^r = \sum_{i=1}^{7} n_i t_i \delta^{d_i}\tau^{t_i - 1} + \sum_{i=8}^{34} n_i t_i \delta^{d_i}\tau^{t_i - 1}e^{-\delta^{c_i}} + \sum_{i=35}^{39} n_i \delta^{d_i}\tau^{t_i} e^{-\alpha_i(\delta-\varepsilon_i)^2 - \beta_i(\tau-\gamma_i)^2}\left[\frac{t_i}{\tau} - 2\beta_i(\tau - \gamma_i)\right]$$

$$+ \sum_{i=40}^{42} n_i \delta\left[\frac{\partial\Delta^{b_i}}{\partial\tau}\psi + \Delta^{b_i}\frac{\partial\psi}{\partial\tau}\right]$$

$$\phi_\delta^r = \sum_{i=1}^{7} n_i d_i \delta^{d_1 - 1}\tau^{t_i} + \sum_{i=8}^{34} n_i e^{-\delta^{c_i}}\left[\delta^{d_i - 1}\tau^{t_i}\left(d_i - c_i\delta^{c_i}\right)\right] +$$

$$\sum_{i=35}^{39} n_i \delta^{d_i}\tau^{t_i} e^{-\alpha_i(\delta-\varepsilon_i)^2 - \beta_i(\tau-\gamma_i)^2}\left[\frac{d_i}{\delta} - 2\alpha_i(\delta - \varepsilon_i)\right] + \sum_{i=40}^{42} n_i\left[\Delta^{b_i}\left(\Psi + \delta\frac{\partial\Psi}{\partial\delta}\right) + \frac{\partial\Delta^{b_i}}{\partial\delta}\delta\Psi\right]$$

$$\frac{\partial\Delta^{b_i}}{\partial\tau} = -2\theta b_i\Delta^{b_i - 1},\ \frac{\partial\psi}{\partial\tau} = -2D_i(\tau - 1)\psi,\ \Delta = \theta^2 + B_i\left[(\delta - 1)^2\right]^{a_i}$$

$$\theta = (1 - \tau) + A_i\left[(\delta - 1)^2\right]^{1/(2\beta_i)},\ \Psi = e^{-C_i(\delta-1)^2 - D_i(\tau-1)^2},\ \frac{\partial\Psi}{\partial\delta} = -2C_i(\delta - 1)\psi$$

$$\frac{\partial\Delta^{b_i}}{\partial\delta} = b_i\Delta^{b_i - 1}\frac{\partial\Delta}{\partial\delta}$$

I	a_i^0	θ_i^0	I	a_i^0	θ_i^0
1	8.37304456		5	0.62105248	6.11190
2	-3.70454304		6	0.41195293	6.77708
3	2.50000000		7	1.04028922	11.32384
4	1.99427042	3.15163	8	0.08327678	27.08792

i	n_i	d_i	t_i
1	$0.38856823203161 \times 10^{0}$	1	0.00
2	$0.29385475942740 \times 10^{1}$	1	0.75
3	$-0.55867188534934 \times 10^{1}$	1	1.00
4	$-0.76753199592477 \times 10^{0}$	1	2.00
5	$0.31729005580416 \times 10^{0}$	2	0.75
6	$0.54803315897767 \times 10^{0}$	2	2.00
7	$0.12279411220335 \times 10^{0}$	3	0.75

i	n_i	d_i	t_i	c_i
8	$0.21658961543220 \times 10^{1}$	1	1.50	1
9	$0.15841735109724 \times 10^{1}$	2	1.50	1
10	$-0.23132705405503 \times 10^{0}$	4	2.50	1
11	$0.58116916431436 \times 10^{-1}$	5	0.00	1
12	$-0.55369137205382 \times 10^{0}$	5	1.50	1
13	$0.48946615909422 \times 10^{0}$	5	2.00	1
14	$-0.24275739843501 \times 10^{-1}$	6	0.00	1
15	$0.62494790501678 \times 10^{-1}$	6	1.00	1
16	$-0.12175860225246 \times 10^{0}$	6	2.00	1
17	$-0.37055685270086 \times 10^{0}$	1	3.00	2
18	$-0.16775879700426 \times 10^{-1}$	1	6.00	2
19	$-0.11960736637987 \times 10^{0}$	4	3.00	2
20	$-0.45619362508778 \times 10^{-1}$	4	6.00	2
21	$0.35612789270346 \times 10^{-1}$	4	8.00	2
22	$-0.74427727132052 \times 10^{-2}$	7	6.00	2
23	$-0.17395704902432 \times 10^{-2}$	8	0.00	2
24	$-0.21810121289527 \times 10^{-1}$	2	7.00	3
25	$0.24332166559236 \times 10^{-1}$	3	12.00	3
26	$-0.37440133423463 \times 10^{-1}$	3	16.00	3
27	$0.14338715756878 \times 10^{0}$	5	22.00	4
28	$-0.13491969083286 \times 10^{0}$	5	24.00	4
29	$-0.23151225053480 \times 10^{-1}$	6	16.00	4
30	$0.12363125492901 \times 10^{-1}$	7	24.00	4
31	$0.21058321972940 \times 10^{-2}$	8	8.00	4
32	$-0.33958519026368 \times 10^{-3}$	10	2.00	4
33	$0.55993651771592 \times 10^{-2}$	4	28.00	5
34	$-0.30335118055646 \times 10^{-3}$	8	14.00	6

i	n_i	d_i	t_i	α_i	β_i	γ_i	ε_i
35	$-0.21365488688320 \times 10^{3}$	2	1.00	25	325	1.16	1.00
36	$0.26641569149272 \times 10^{5}$	2	0.00	25	300	1.19	1.00
37	$-0.24027212204557 \times 10^{5}$	2	1.00	25	300	1.19	1.00
38	$-0.28341603423999 \times 10^{3}$	3	3.00	15	275	1.25	1.00
39	$0.21247284400179 \times 10^{3}$	3	3.00	20	275	1.22	1.00

i	n_i	a_i	b_i	β_i	A_i	B_i	C_i	D_i
40	$-0.66642276540751 \times 10^{0}$	3.500	0.875	0.300	0.700	0.3	10.0	275
41	$0.72608632349897 \times 10^{0}$	3.500	0.925	0.300	0.700	0.3	10.0	275
42	$0.55068668612842 \times 10^{-1}$	3.000	0.875	0.300	0.700	1.0	12.5	275

Appendix III. Fortran version: MRKEOS.

```
      BLOCK DATA EQOS
C          .....................................................
C          .                                                   .
C          . TOUGH2, MODULE EOSCO2, VERSION 1.0, SEPTEMBER 1999 .
C          .....................................................

COMMON/NN/NEL,NCON,NOGN,NK,NEQ,NPH,NB,NK1,NEQ1,NBK,NSEC,NFLUX
      DATA NK,NEQ,NPH,NB/3,4,3,6/
C----- NK IS THE NUMBER OF COMPONENTS.
C----- NEQ IS THE NUMBER OF EQUATIONS PER GRID BLOCK.
C        USUALLY WE HAVE NEQ = NK+1, FOR NK MASS- AND ONE ENERGY-BALANCE.
C----- NPH IS THE NUMBER OF PHASES WHICH CAN BE PRESENT.
C----- NB IS THE NUMBER OF SECONDARY PARAMETERS OTHER THAN MASS
C      FRACTIONS.
C----- THE TOTAL NUMBER OF SECONDARY PARAMETERS IS NBK = NB+NK.
      END
C********1*********2*********3*********4*********5*********6*********7**
      SUBROUTINE EOS
      IMPLICIT DOUBLE PRECISION(A-H,O-Z)
C
C-----THIS ROUTINE COMPUTES ALL THERMOPHYSICAL PROPERTIES OF AQUEOUS AND
C        TWO-PHASE MIXTURES OF WATER AND CARBON DIOXIDE.
C
      COMMON/P1/X(1)
      COMMON/P2/DX(1)
      COMMON/P3/DELX(1)
      COMMON/E1/ELEM(1)
      COMMON/E2/MATX(1)
      COMMON/E3/EVOL(1)
      COMMON/E4/PHI(1)
      COMMON/E5/P(1)
      COMMON/E6/T(1)
      COMMON/SECPAR/PAR(1)

COMMON/NN/NEL,NCON,NOGN,NK,NEQ,NPH,NB,NK1,NEQ1,NBK,NSEC,NFLUX

COMMON/CONTST/RE1,RE2,RERM,NER,KER,DFAC
      COMMON/KONIT/KON,DELT,IGOOD

COMMON/CYC/KCYC,ITER,ITERC,TIMIN,SUMTIM,GF,TIMOUT
      COMMON/KC/KC
      COMMON/SVZ/NOITE,MOP(24)
      COMMON/GASLAW/R,AMS,AMA,CVAIR
      COMMON/FAIL/IHALVE

COMMON/SOLID/NM,DROK(27),POR(27),PER(3,27),CWET(27),SPHT(27)
      COMMON/SOCH/MAT(27)

COMMON/RPCAP/IRP(27),RP(7,27),ICP(27),CP(7,27),IRPD,RPD(7),
     >  ICPD,CPD(7)
      COMMON/BC/NELA
      COMMON/FF/H1
      CHARACTER*1 H1
      CHARACTER*5 ELEM,MAT
      DIMENSION XX(4),DP(29)
      SAVE ICALL,ZERO
      DATA ZERO/1.D-13/
      DATA ICALL/0/
      ICALL = ICALL + 1
      IF(ICALL.EQ.1) THEN
        WRITE(11,899)
      END IF
      IF (MOP(5).GE.4) THEN
        PRINT 32,KCYC,ITER
      END IF
C
C********1*********2*********3*********4*********5*********6*********7**
C
C-----COME HERE FOR INITIAL CONDITIONS.
C
      IF (KC.EQ.0) THEN
        H1    = CHAR(12)
C
C-----COME HERE TO INITIALIZE SOME DATA.
C
        R     = 8314.7295D0
        AMS   = 18.01534D0
        AMA   = 44.0098D0
C
C-----COME HERE TO ASSIGN DEFAULT RELATIVE PERMEABILITY AND CAPILLARY
C          PRESSURE PARAMETERS TO DOMAINS WITHOUT SPECIAL ASSIGNMENTS.
C
        DO N=1,NM
          IF (IRP(N).EQ.0) THEN
            IRP(N) = IRPD
            ICP(N) = ICPD
            DO M=1,7
              RP(M,N) = RPD(M)
              CP(M,N) = CPD(M)
            END DO
          END IF
        END DO
C
C-----COME HERE TO GENERATE SOME PRINTOUT CONCERNING THE EQUATION-OF-STATE
C-----PACKAGE.
C
        PRINT 300,H1
        PRINT 301,NK,NEQ,NPH,NB
        PRINT 302,NK,NEQ,NPH,NB
        PRINT 303
        PRINT 306
        PRINT 304
        PRINT 305
        PRINT 307
        PRINT 306
C
C-----COME HERE TO ASSIGN INITIAL CONDITIONS.
C
```

```
      DO N=1,NEL
        NLOC  = (N-1) * NK1
        NLOC2 = (N-1) * NSEC*NEQ1
        PX    = X(NLOC+1)
        P(N)  = X(NLOC+1)
        XCO2  = X(NLOC+2)
        IF (XCO2.LT.0.D0.OR.XCO2.GT.1.D0) THEN
          GOTO 202
        END IF
        SCO2  = X(NLOC+3)
        IF (SCO2.LT.0.D0.OR.SCO2.GT.1.D0) THEN
          GOTO 202
        END IF
        TX    = X(NLOC+4)
        IF (TX.LE.0.D0.OR.TX.GE.374.15D0) THEN
          GOTO 202
        END IF
        T(N)  = TX
      END DO
    END IF
C
    IF (MOP(5).GE.7) THEN
      PRINT 31
    END IF
C
C-----COME HERE WHEN MARCHING IN TIME.
C
    IF (KC.GT.0) THEN
      N1 = NELA
    ELSE
      N1 = NEL
    END IF
    DO N=1,N1
      NMAT  = MATX(N)
      NLOC  = (N-1) * NK1
      NLOC2 = (N-1) * NSEC * NEQ1
C
C-----COME HERE TO UPDATE PRIMARY
VARIABLES.
C
      DO M=1,NK1
        IF (ITER.EQ.0) THEN
          XINCR = 0.D0
        ELSE
          XINCR = DX(NLOC+M)
        END IF
        XX(M) = X(NLOC+M) + XINCR
      END DO
C
C-----COME HERE TO PRINT UPDATED PRIMARY
VARIABLES.
C
      IF (MOP(5).GE.7) THEN
        PRINT 35,ELEM(N),(XX(M),M=1,NK1)
      END IF
C
C-----COME HERE TO COMPUTE ALL SECONDARY
VARIABLES. NOTE THAT SECONDARY
C-----PARAMETERS MUST BE CALCULATED
NEQ+1 TIMES; ONCE FOR THE STATE POINT
C-----AND NEQ TIMES FOR EACH OF THE NEQ
PRIMARY VARIABLES INCREMENTED
C-----(X+DX+DELX).
C
      DO K=1,NEQ1
        NLK2  = NLOC2 + (K-1) * NSEC
        NLK2L = NLK2 + NBK
        NLK2S = NLK2L + NBK
        PX    = XX(1)
        XCO2  = XX(2)
        SCO2  = XX(3)
        TX    = XX(4)
C
C-----COME HERE TO CALCULATE SECONDARY
PARAMETERS AT THE STATE POINT.
C
        IF (K.EQ.1) THEN
          IF (XCO2.LT.0.D0) THEN
C
C-----COME HERE TO ENFORCE MASS FRACTION
CONSTRAINT.
C
            XX(2)     = 0.D0
            XCO2      = 0.D0
            DX(NLOC+2) = -X(NLOC+2)
          END IF
          IF (SCO2.LT.0.D0) THEN
C
C-----COME HERE TO ENFORCE SATURATION
CONSTRAINT.
C
            XX(3)     = 0.D0
            SCO2      = 0.D0
            DX(NLOC+3) = -X(NLOC+3)
          END IF
          GO TO 101
        END IF
C
C-----COME HERE TO CALCULATE SECONDARY
PARAMETERS FOR EACH (NEQ) INCREMENTED
C-----(X+DX+DELX) PRIMARY VARIABLE.
C
        DELX(NLOC+K-1) = DFAC * XX(K-1) + 1.D-10
        IF (K.EQ.2) THEN
          PX    = XX(1) + DELX(NLOC+1)
        ELSE IF (K.EQ.3) THEN
          DELX(NLOC+2) = DFAC
          XCO2 = XX(2) + DELX(NLOC+2)
        ELSE IF (K.EQ.4) THEN
          DELX(NLOC+3) = DFAC
          SCO2 = XX(3) + DELX(NLOC+3)
        ELSE IF (K.EQ.5) THEN
          TX    = XX(4) + DELX(NLOC+4)
        END IF
C
 101    CONTINUE
C
C-----COME HERE TO CALCULATE SATURATION
OF H2O.
C
        SH2O = 1.D0 - SCO2
C
C-----COME HERE TO CALCULATE SATURATION
PRESSURE OF H2O.
C
        CALL SAT(TX,PSAT)
        IF (IGOOD.NE.0) THEN
          PRINT *, 'IGOOD = ', IGOOD
          PRINT *, '4444444'
          GO TO 200
        END IF
C
C-----COME HERE TO CALCULATE DENSITY AND
INTERNAL ENERGY OF H2O.
C
        CALL COWAT(TX,PX,DH2O,UH2O)
        IF (IGOOD.NE.0) THEN
          PRINT *, 'IGOOD = ', IGOOD
          PRINT *, '5555555'
          GO TO 200
```

```
        END IF
C
C-----COME HERE TO CALCULATE VISCOSITY OF
H2O.
C
        CALL VISW(TX,PX,PSAT,VH2O)
C
C-----COME HERE TO CALCULATE DENSITY OF
AQUEOUS MIXTURE OF H2O
C-----AND DISSOLVED PHASE CO2.
C
        IF (XCO2.GT.0.D0) THEN
          CALL DENMIX(TX,DH2O,XCO2,DMIX)
        ELSE
          DMIX = DH2O
        END IF
C
C-----COME HERE TO CALCULATE CAPILLARY
PRESSURE.
C
         IF (SCO2.GE.0.01D0) THEN
           CALL PCAPBSC(SH2O,PCAP,NMAT)
         ELSE
           PCAP = 0.D0
         ENDIF
C
C-----COME HERE TO CALCULATE DENSITY,
FUGACITY, AND ENTHALPY OF
C-----SEPARATE PHASE CO2.
C
        PCO2 = PX
        IF (SCO2.GT.0.D0.OR.XCO2.GT.0.D0) THEN
          CALL CO2(TX,PCO2,DCO2,dummy,HCO2)
          IF (IGOOD.NE.0) THEN
            PRINT *, 'IGOOD = ', IGOOD
            PRINT *, '6666666'
            GO TO 200
          END IF
        ELSE
          DCO2 = 0.D0
          HCO2 = 0.D0
        END IF
C
C-----COME HERE TO CALCULATE VISCOSITY OF
SEPARATE PHASE CO2.
C
        IF (SCO2.GT.0.D0) THEN
          CALL VISCO2(TX,DCO2,VCO2)
        ELSE
          VCO2 = 1.D0
        END IF
C
C-----COME HERE TO CALCULATE ENTHALPY OF
DISSOLUTION OF CO2 IN WATER.
C
        IF (XCO2.GT.0.D0) THEN
          CALL SOLUT(PCO2,TX,HSOL)
        ELSE
          HSOL = 0.D0
        END IF
C
C-----COME HERE TO CALCULATE RELATIVE
PERMEABILITIES.
C
        IF (SCO2.GE.0.001D0) THEN
          CALL
RELPBSC(SH2O,SCO2,REPW,REPC,NMAT)
        ELSE
          REPW = 1.D0
          REPC = 0.D0
        END IF
C
C-----COME HERE TO ASSIGN SECONDARY
PARAMETERS FOR WATER.
C-----IN ORDER: SATURATION, RELATIVE
PERMEABILITY, VISCOSITY, DENSITY,
C-----ENTHALPY, CAPILLARY PRESSURE, MASS
FRACTION WATER, MASS FRACTION
C-----DISSOLVED CO2, MASS FRACTION DUMMY
COMPONENT.
C
        PAR(NLK2L+1)   = SH2O
        PAR(NLK2L+2)   = REPW
        PAR(NLK2L+3)   = VH2O
        PAR(NLK2L+4)   = DMIX
        PAR(NLK2L+5)     =(UH2O+PX/DMIX)*(1.D0-
XCO2)+(HCO2+HSOL)*XCO2
        PAR(NLK2L+6)   = PCAP
        PAR(NLK2L+NB+1) = 1.D0 - XCO2
        PAR(NLK2L+NB+2) = XCO2
        PAR(NLK2L+NB+3) = 0.D0
C
C-----COME HERE TO ASSIGN SECONDARY
PARAMETERS FOR DUMMY PHASE (GAS SLOTS).
C-----IN ORDER: SATURATION, RELATIVE
PERMEABILITY, VISCOSITY, DENSITY,
C-----ENTHALPY, CAPILLARY PRESSURE, MASS
FRACTION STEAM, MASS FRACTION
C-----GASEOUS CO2, MASS FRACTION DUMMY
COMPONENT.
C
        PAR(NLK2+1)   = 0.D0
        PAR(NLK2+2)   = 0.D0
        PAR(NLK2+3)   = 1.D0
        PAR(NLK2+4)   = 0.D0
        PAR(NLK2+5)   = 0.D0
        PAR(NLK2+6)   = 0.D0
        PAR(NLK2+NB+1) = 0.D0
        PAR(NLK2+NB+2) = 0.D0
        PAR(NLK2+NB+3) = 0.D0
C
C-----COME HERE TO ASSIGN SECONDARY
PARAMETERS FOR SEPARATE PHASE CO2.
C-----IN ORDER: SATURATION, RELATIVE
PERMEABILITY, VISCOSITY, DENSITY,
C-----ENTHALPY, CAPILLARY PRESSURE, MASS
FRACTION DISSOLVED WATER, MASS
C-----FRACTION DISSOLVED CO2, MASS
FRACTION SEPARATE PHASE CO2.
C
        PAR(NLK2S+1)   = SCO2
        PAR(NLK2S+2)   = REPC
        PAR(NLK2S+3)   = VCO2
        PAR(NLK2S+4)   = DCO2
        PAR(NLK2S+5)   = HCO2
        PAR(NLK2S+6)   = 0.D0
        PAR(NLK2S+NB+1) = 0.D0
        PAR(NLK2S+NB+2) = 0.D0
        PAR(NLK2S+NB+3) = 1.D0
C
C------COME HERE TO STORE LATEST
TEMPERATURE AND ZERO DUMMY SLOT.
C
        PAR(NLK2+NSEC-1) = TX
        PAR(NLK2+NSEC)   = 0.D0
      END DO
    END DO
C
C-----COME HERE TO PRINT SECONDARY
PARAMETERS AT STATE POINT.
```

```
C
      IF (MOP(5).GE.8) THEN
        PRINT 27
        DO N=1,NEL
          NLOC2 = (N-1) * NSEC * NEQ1
          PRINT
30,ELEM(N),(PAR(NLOC2+M),M=1,NSEC)
C
C-----COME HERE TO PRINT INCREMENTED
PARAMETERS.
C
          IF (MOP(5).EQ.8) THEN
            DO K=2,NEQ1
              PRINT                    37,(PAR(NLOC2+(K-
1)*NSEC+M),M=1,NSEC)
            END DO
          END IF
C
C-----COME HERE TO PRINT DERIVATIVES.
C
          IF (MOP(5).EQ.9) THEN
            NLOC = (N-1) * NK1
            DO K=2,NEQ1
              DO M=1,NSEC
                DP(M) = (PAR(NLOC2+(K-1)*NSEC+M)-
PAR(NLOC2+M))
     <                / DELX(NLOC+K-1)
              END DO
              PRINT 37,(DP(M),M=1,NSEC)
            END DO
          END IF
        END DO
      END IF
      RETURN
C
C********1*********2*********3*********4******
***5*********6*********7**
C
C-----COME HERE IF FAILURE IN SAT, COWAT, OR
CO2 (IGOOD NE 0).
C
  200 CONTINUE
      PRINT 201,ELEM(N),(XX(M),M=1,NK1)
      IF(KC.EQ.0) THEN
                GOTO 202
      END IF
      RETURN
C
C-----COME HERE IF INITIAL CONDITIONS ARE
BOGUS.
C
  202 PRINT 203
      STOP
C
C********1*********2*********3*********4******
***5*********6*********7**
C           FORMAT STATEMENTS FOR SUBROUTINE
EOS

  201  FORMAT(' +++++++++          CANNOT FIND
PARAMETERS AT ELEMENT *',A5,
     1  '*          XX(M) =',4(1X,E12.6))
  203  FORMAT(' !!!!!!!!!!! ERRONEOUS DATA
INITIALIZATION !!!!!!!!!!',
     1  11X,'STOP EXECUTION----------')
  899  FORMAT(/6X,'EOSCO2      1.0              1  SEPT
1999',6X,
     X'*EOSCO2* ... THERMOPHYSICAL PROPERTIES
MODULE FOR WATER/CO2')
   32  FORMAT(/' %%%%%%%%%%  E  O  S
%%%%%%%%%% E O S %%%%%%%%%%',
     1  '  [KCYC,ITER] = [',I4,',',I3,']'/)
   31 FORMAT(/' PRIMARY VARIABLES'/)
   35          FORMAT(' AT ELEMENT *',A5,'* ---
',(4(2X,E12.6)))
   27 FORMAT(/' SECONDARY PARAMETERS')
   30  FORMAT(/' ELEMENT ',A5/(10(1X,E12.6)))
   37  FORMAT(/(10(1X,E12.6)))
  300  FORMAT(A1/'  ',121('*')/'  *',27X,'EOSCO2:
EQUATION',
     X' OF STATE FOR MIXTURES OF WATER/CO2
',40X,'*'/
     X' ',121('*')//)
  301  FORMAT(//4X,'OPTIONS SELECTED ARE:
(NK,NEQ,NPH,NB) = (',I1,',',
     XI1,',',I1,',',I1,')'/)
  302  FORMAT(10X,'NK   = ',I2,'    - NUMBER OF
FLUID COMPONENTS'/
     X10X,'NEQ = ',I2,'    - NUMBER OF EQUATIONS
PER GRID BLOCK'/
     X10X,'NPH = ',I2,'    - NUMBER OF PHASES THAT
CAN BE PRESENT'/
     X10X,'NB  = ',I2,'    - NUMBER OF SECONDARY
PARAMETERS (OTHER THAN',
     X' COMPONENT MASS FRACTIONS)'/)
  303          FORMAT(/4X,'AVAILABLE          OPTIONS
ARE:'//4X,'(NK,NEQ,NPH,NB) =
     >(3,3,3,6) - WATER, DISSOLVED CO2, SEPARATE
PHASE CO2;
     > ISOTHERMAL (DEFAULT)'/,
     >34X,'VARIABLES (P, XCO2, SCO2, T)'//
     >4X,'(NK,NEQ,NPH,NB) =
     >(3,4,3,6) - WATER, DISSOLVED CO2, SEPARATE
PHASE CO2;
     > NON-ISOTHERMAL'/,
     >34X,'VARIABLES (P, XCO2, SCO2, T)'/)
  304  FORMAT(/26H THE PRIMARY VARIABLES
ARE/'  P - PRESSURE        ',
     A'XCO2 - MASS FRACTION OF DISSOLVED CO2
',
     B'SCO2 - SEPARATE PHASE CO2 SATURATION'/)
  305 FORMAT(/
     X' ',20('*'),30X,45('*')/
     X' *        COMPONENTS        *',29X,
     X' *   FLUID PHASE CONDITION        PRIMARY
VARIABLES    *'/
     X' ',20('*'),30X,45('*')/
     X' *',18X,'*',30X,'*',43X,'*'/
     X' *      # 1  -  WATER        *',29X,
     X' *   two-phase gas/oil          P,     X,    SCO2,   T *'/
     X' *',18X,'*',30X,'*',43X,'*')
  306 FORMAT(' ',121('*'))
  307 FORMAT(
     X' *      # 2  -  AIR          *',29X,
     X' *   two-phase aqueous/oil       P,     X,    SCO2,   T
*'/
     X' *',18X,'*',30X,'*',43X,'*'/
     X' *      # 3  -  COM3 (oil)   *',29X,
     x' *   three-phase gas/aqueous/oil  P,   S+10,    SCO2,
T *'/
     X' *',18X,'*',30X,'*',43X,'*'/
     X' *      # 4  -  HEAT         *',29X,' ',45('*')/
     x' *',18X,'*')
C
      END
C********1*********2*********3*********4******
***5*********6*********7**
      SUBROUTINE
RELPBSC(SW,SC,REPW,REPC,NMAT)
```

```
      IMPLICIT DOUBLE PRECISION(A-H,O-Z)
C
C-----This routine computes relative permeabilities for liquid
C     (CO2 and water) phases.  From Parker et al. (1987)
C

COMMON/RPCAP/IRP(27),RP(7,27),ICP(27),CP(7,27),I
RPD,RPD(7),
     >  ICPD,CPD(7)

C      Come here to assign the irreducible saturation of water.
      SR = RP(1,NMAT)
C
C     Come here to assign the van Genuchten N parameter.
C     This is a curve-shaping parameter.
      XN = RP(2,NMAT)
C
C       Come here to calculate the van Genuchten M parameter.
C     This is another curve-shaping parameter.
      XM = 1.D0 - 1.D0 / XN
C
C       Come here to calculate the inverse of the van Genuchten M parameter.
      XMINV = 1.D0 / XM
C
C      Come here to calculate the effective saturation of water.
      SWBAR = (SW-SR) / (1.D0-SR)
      IF (SWBAR.LT.0.D0) SWBAR = 0.D0
      IF (SWBAR.GT.1.D0) SWBAR = 1.D0
C
C     Come here to calculate the effective total saturation.
      STBAR = (SW+SC-SR) / (1.D0-SR)
      IF (STBAR.LT.0.D0) STBAR = 0.D0
      IF (STBAR.GT.1.D0) STBAR = 1.D0
C
C     Come here to calculate the relative permeability of water.
      A = SWBAR**.5D0
      B = 1.D0 - (SWBAR**XMINV)
      REPW = A * ((1.D0-(B**XM))**2.D0)
      IF (REPW.LT.0.D0) REPW = 0.D0
      IF (REPW.GT.1.D0) REPW = 1.D0
C
C     Come here to calculate the relative permeability of CO2.
      C = (STBAR-SWBAR)**.5D0
      D = 1.D0 - (STBAR**XMINV)
      REPC = C * (((B**XM)-(D**XM))**7.D0)
      IF (REPC.LT.0.D0) REPC = 0.D0
      IF (REPC.GT.1.D0) REPC = 1.D0
      RETURN
      END
C********1*********2*********3*********4*********5*********6*********7**
      SUBROUTINE PCAPBSC(SW,PC,NMAT)
      IMPLICIT DOUBLE PRECISION(A-H,O-Z)
C
C-----This routine computes capillary pressure as function of water
C     saturation (SW). From Parker et al. (1987).
C

COMMON/RPCAP/IRP(27),RP(7,27),ICP(27),CP(7,27),I
RPD,RPD(7),
     >  ICPD,CPD(7)
C
C      Come here to assign the irreducible saturation of water.
      SR = CP(1,NMAT)
C
C     Come here to assign the van Genuchten N parameter.
C     This is a curve-shaping parameter.
      XN = CP(2,NMAT)
C
C       Come here to assign the van Genuchten alpha parameter.
C     This is a curve-shaping parameter.
      ALPHA = CP(3,NMAT)
C
C     Come here to assign the fluid pair-dependent scaling factor:
      BETA = CP(4,NMAT)
C
C       Come here to calculate the inverse of the van Genuchten N parameter.
      XNINV = 1.D0 / XN
C
C       Come here to calculate the van Genuchten M parameter.
      XM = 1.D0 - XNINV
C
C       Come here to calculate the inverse of the van Genuchten M parameter.
      XMINV = 1.D0 / XM
C
C      Come here to calculate the effective saturation of water.
      SWBAR = (SW-SR) / (1.D0-SR)
      IF (SWBAR.LE.0.D0) SWBAR = 1.D-05
C
C     Come here to calculate the capillary pressure.
      A = -1.D0/(ALPHA*BETA)
            B = SWBAR**(-XMINV)
      PC = A*((B-1)**XNINV)
      RETURN
      END
C********1*********2*********3*********4*********5*********6*********7**
      SUBROUTINE CO2(TX,PCX,DC,FC,HC)
      IMPLICIT DOUBLE PRECISION(A-H,O-Z)
C
C       This subroutine calculates the specific density, fugacity, and
C     specific enthalpy of gaseous and supercritical CO2 as a function of
C       the pressure of CO2 (PCX) and temperature (TX) using a Modified
C     Redlich-Kwong (MRK) equation of state (EOS) and standard thermo-
C       dynamic equations.  This formulation of the MRK EOS is based on the
C       work of Kerrick and Jacobs (1981) and Weir et al. (1996). Weir et al.
C     extended the MRK EOS of Kerrick and Jacobs to low temperatures.
C       Accuracy is suspect outside the temperature and pressure ranges of
C       50 < T < 350 deg C and 0.1 < PCX < 45 MPa, respectively.
C
C             Input:
C                       TX   = Temperature in degrees C
C                       PCX  = Pressure of CO2 in Pa
C
C             Output:
```

```
C                       DC    = Specific density of CO2 in
kg/m3
C                       HC    = Specific enthalpy of CO2 in
J/kg
C                       FC    = Fugacity of CO2 in Pa
C
C             Constants:
C                       XMWC = Molecular weight of CO2
in Kg/mol
C                       R     = Universal gas constant in
m3Pa/molK
C                       B     = Covolume in m3/mol (value
from K&J)
C
C             Variables:
C                       T     = Temperature in K
C                       V     = Molar volume of CO2 in
m3/mol
C                       Y     = Dimensionless variable
(B/4V)
C                       Z     = Compressibility factor [-]
C                       PHI   = Fugacity coefficient [-]
C                       H     = Molar enthalpy in J/mol
C
      COMMON/E1/ELEM(1)
      PARAMETER(XMWC = 4.40098D-02)
      PARAMETER(R    = 8.3147295D0)
      PARAMETER(B    = 5.8D-05)
C
      COMMON/KONIT/KON,DELT,IGOOD
C
      SAVE ICALL
      DATA ICALL/0/
      ICALL=ICALL+1
      IF(ICALL.EQ.1) WRITE(11,899)
  899 FORMAT(6X,'CO2     2.0      1 SEPT     1999',6X,
     X'CALCULATE SPECIFIC DENSITY, ENTHALPY,
AND FUGACITY OF CO2')
C
      IF(PCX.LE..1D6)THEN
        DC=0.D0
              FC=0.D0
              HC=0.D0
              RETURN
      END IF

C     Convert temperature from degrees C to K:
      T   = TX + 2.7315D+02
C
C     First calculate V as a function of T and PCX using
Newton Iteration
C     with tolerance TOL:
       TOL = 1.0D-06
C
C     Initial guess of V, DV, and Y from ideal gas law:
      V = (R*T) / PCX
      DV = V
      Y = B / (4.D0*V)
C
C     Initialize attractive term (AT) of MRK EOS:
      AT  = 0.D0
C
C     Newton Iteration for V as a function of T and PCX:
      KOUNT = 0
      DO WHILE(DABS(DV/V).GT.TOL)
        CALL MRK(Y,T,PCX,V,DV,AT)
        V = V - DV
        Y = B / (4.D0*V)
        KOUNT = KOUNT + 1
        IF(KOUNT.GT.25000) GO TO 5
      END DO
C
C     Calculate density (DC) in kg/m3 from V in m3/mol:
      DC = XMWC / V

C
C     Calculate Y to the 2nd and 3rd powers for later use:
      Y2 = Y * Y
      Y3 = Y2 * Y
C
C     Calculate compressibility factor (Z) by substituting
MRK EOS
C     into Z=PV/RT:
      Z     =   ((1.D0+Y+Y2-Y3)/((1.D0-Y)**3.D0))   -
(AT/(R*T*DSQRT(T)*(V+B)))
C
C     Initialize fugacity coefficient (PHI):
      PHI = 0.D0
C
C     Calculate fugacity (FC):
      CALL FUGACITY(Y,T,V,Z,PHI)
      FC = PHI * PCX

C     Initialize molar enthalpy (H):
      H = 0.D0
C
C     Calculate specific enthalpy (HC):
      CALL ENTHALPY(T,V,Z,H)
      HC = (H/XMWC)+8.0924807D+05
      RETURN
C
C     Come here when no convergence:
5     CONTINUE
      PRINT 6
6     FORMAT('NO CONVERGENCE IN SUBROUTINE
CO2')
      print*, PCX,T,V,Y,DV
      IGOOD = 2
      RETURN
      END
C********1*********2*********3*********4******
***5*********6*********7**
      SUBROUTINE MRK(Y,T,PCX,V,DV,AT)
      IMPLICIT DOUBLE PRECISION(A-H,O-Z)
C
C     This subroutine is called from subroutine CO2 during
the Newton
C     Iteration for the molar volume (V) of CO2 as function
of temperature
C     (T) and pressure of CO2 (PCX).  This subroutine
calculates
C     the V for which the MRK EOS is 0 at the given T and
PCX, and the
C     value of the derivative of the MRK EOS wrt V for the
calculated V.
C
C             Input:
C                       Y     = Dimensionless variable
(B/4V)
C                       T     = Temperature in K
C                       PCX = Pressure of CO2 in Pa
C                       V     = Prev. estimate of molar
volume of CO2 in m3/mol
C
C             Output:
C                       DV    = Change in molar volume of
CO2 in m3/mol
C
C             Constants:
```

```
C                       R     = Universal gas constant in
m3Pa/molK
C                       B     = Covolume in m3/mol (value
from K&J)
C             Ci thru Fi= Coefficients of the MRK EOS
(i=1,2,3)
C                     Values from Weir et al. (1996)
C
C             Variables:
C             CT thru FT= Temperature-dependent functions
for evaluating
C                           attractive term of MRK EOS
C                       AT  = Attractive term of MRK EOS

C                       FV  = V at which MRK EOS is 0
for T and PCX
C                       DV  = -FV / Value of derivative wrt
V of MRK EOS
C
      PARAMETER(R   = 8.3147295D0)
      PARAMETER(B   = 5.8D-05)
      PARAMETER(C1  = 2.39534D+01)
      PARAMETER(C2  = -4.55309D-02)
      PARAMETER(C3  = 3.65168D-05)
      PARAMETER(D1  = -4.09844D-03)
      PARAMETER(D2  = 1.23158D-05)
      PARAMETER(D3  = -8.99791D-09)
      PARAMETER(E1  = 2.89224D-07)
      PARAMETER(E2  = -8.02594D-10)
      PARAMETER(E3  = 7.30975D-13)
      PARAMETER(F1  = -6.43556D-12)
      PARAMETER(F2  = 2.01284D-14)
      PARAMETER(F3  = -2.17304D-17)
C
      SAVE ICALL
      DATA ICALL/0/
      ICALL=ICALL+1
      IF(ICALL.EQ.1) WRITE(11,899)
  899 FORMAT(6X,'MRK          2.0          1 SEPT
1999',6X,
     X'MODIFIED REDLICH-KWONG EQUATION OF
STATE FOR CO2')
C
C     Calculate T squared for later use:
      T2 = T * T
C
C     Calculate V to the 2nd, 3rd, and 4th powers for later
use:
      V2 = V * V
      V3 = V2 * V
      V4 = V3 * V
C
C     Calculate Y to the 2nd and 3rd powers for later use:
      Y2 = Y * Y
      Y3 = Y2 * Y
C
C     Calculate B to the 2nd and 3rd powers for later use:
      B2 = B * B
      B3 = B2 * B
C
C           Calculate temperature-dependent functions for
evaluating attractive
C     term in MRK EOS:
      CT = C1 + (C2*T) + (C3*T2)
      DT = D1 + (D2*T) + (D3*T2)
      ET = E1 + (E2*T) + (E3*T2)
      FT = F1 + (F2*T) + (F3*T2)
C
C     Calculate attractive term in MRK EOS:
      AT = CT + (DT/V) + (ET/V2) + (FT/V3)
C
C     Calculate V at which MRK EOS equals 0:
      FV = PCX - (((R*T*(1.D0+Y+Y2-Y3))/(V*((1.D0-
Y)**3.D0)))-
     >     (AT/(DSQRT(T)*V*(V+B))))
C
C     Calculate -FV / value of derivative wrt V of MRK
EOS
      DV = -FV / (((-3.D0*B*R*T*(1.D0+Y+Y2-
Y3))/(4.D0*V3*
     >     ((1.D0-Y)**4.D0)))-((R*T*(1.D0+Y+Y2-Y3))/
     >                                   (V2*((1.D0-
Y)**3.D0)))+((R*T*(((3.D0*B3)/(64.D0*V4))
     >           -(B2/(8.D0*V3))-(B/(4.D0*V2))))/(V*((1.D0-
Y)**3.D0)))
     >     -(AT/(DSQRT(T)*V*(V+B))))
      RETURN
      END
C********1*********2*********3*********4******
***5*********6*********7**
      SUBROUTINE FUGACITY(Y,T,V,Z,PHI)
      IMPLICIT DOUBLE PRECISION(A-H,O-Z)
C
C     This subroutine is called from subroutine CO2 during
the
C           calculation of fugacity of CO2 as function of
temperature (T),
C     pressure of CO2 (PCX), and molar volume of CO2
(V).  This
C     subroutine calculates the fugacity coefficient of CO2
(PHI) by
C     substituting the MRK EOS into RTln(PHI)=Integral
from V to infinity
C           of (PCX-RT/V)dV - RTln(Z) + RT(Z-1).  This
expression comes from
C     Prausnitz (1969).
C
C             Input:
C                       Y       = Dimensionless variable
(B/4V)
C                       T   = Temperature in K
C                       V     = Molar volume of CO2 in
m3/mol
C                       Z   = Compressibility factor of CO2
[-]
C
C             Output:
C                       PHI = Fugacity coefficient of CO2
[-]
C
C             Constants:
C                       R     = Universal gas constant in
m3Pa/molK
C                       B     = Covolume in m3/mol (value
from K&J)
C             Ci thru Fi= Coefficients of the MRK EOS
(i=1,2,3)
C                           Values from Weir et al. (1996)
C
C             Variables:
C             CT thru FT= Temperature-dependent functions
for evaluating
C                           attractive term of MRK EOS
C
      PARAMETER(R   = 8.3147295D0)
      PARAMETER(B   = 5.8D-05)
      PARAMETER(C1  = 2.39534D+01)
      PARAMETER(C2  = -4.55309D-02)
      PARAMETER(C3  = 3.65168D-05)
      PARAMETER(D1  = -4.09844D-03)
```

```
      PARAMETER(D2  =  1.23158D-05)
      PARAMETER(D3  = -8.99791D-09)
      PARAMETER(E1  =  2.89224D-07)
      PARAMETER(E2  = -8.02594D-10)
      PARAMETER(E3  =  7.30975D-13)
      PARAMETER(F1  = -6.43556D-12)
      PARAMETER(F2  =  2.01284D-14)
      PARAMETER(F3  = -2.17304D-17)
C
      SAVE ICALL
      DATA ICALL/0/
      ICALL=ICALL+1
      IF(ICALL.EQ.1) WRITE(11,899)
  899 FORMAT(6X,'FUGACITY  2.0              1 SEPT
1999',6X,
     X'CALCULATE FUGACITY COEFFICIENT FOR
SEPARATE PHASE CO2')
C
C     Calculate T to the 2nd power for later use:
      T2 = T * T
C
C     Calculate V to the 2nd, 3rd, and 4th powers for later
use:
      V2 = V * V
      V3 = V2 * V
C
C     Calculate B to the 2nd, 3rd, and 4th powers for later
use:
      B2 = B * B
      B3 = B2 * B
      B4 = B3 * B
C
C         Calculate temperature dependent functions for
evaluating attractive
C     term in MRK EOS:
      CT = C1 + (C2*T) + (C3*T2)
      DT = D1 + (D2*T) + (D3*T2)
      ET = E1 + (E2*T) + (E3*T2)
      FT = F1 + (F2*T) + (F3*T2)
C
C     Calculate fugacity coefficient:
      PHI = Y * (8.D0 + Y * (-9.D0 + 3.D0 * Y))/(1.D0-
Y)**3.D0
     >    - DLOG(Z)
     >    - CT / (R * T * DSQRT(T) * (V + B))
     >    - DT / (R * T * DSQRT(T) * V * (V + B))
     >    - ET / (R * T * DSQRT(T) * V2 * (V + B))
     >    - FT / (R * T * DSQRT(T) * V3 * (V + B))
     >     + CT * DLOG(V / (V + B))/ (R * T * DSQRT(T)
* B)
     >    - DT / (R * T * DSQRT(T) * B * V)
     >     + DT * DLOG((V + B) / V) / (R * T * DSQRT(T)
* B2)
     >    - ET / (R * T * DSQRT(T) * 2.D0 * B * V2)
     >    + ET / (R * T * DSQRT(T) * B2 * V)
     >    - ET * DLOG((V + B) / V) / (R * T * DSQRT(T) *
B3)
     >    - FT / (R * T * DSQRT(T) * 3.D0 * B * V3)
     >    + FT / (R * T * DSQRT(T) * 2.D0 * B2 * V2)
     >    - FT / (R * T * DSQRT(T) * B3 * V)
     >    - FT * DLOG(V / (V + B)) / (R * T * DSQRT(T) *
B4)
      PHI = DEXP(PHI)
      RETURN
      END
C********1*********2*********3*********4******
***5*********6*********7**
      SUBROUTINE ENTHALPY(T,V,Z,H)
      IMPLICIT DOUBLE PRECISION(A-H,O-Z)
C
C     This subroutine is called from subroutine CO2 during
the
C         calculation of the specific enthalpy of CO2 as
function of
C     temperature (T), pressure of CO2 (PCX), and molar
volume
C       of CO2 (V).  This subroutine calculates the molar
enthalpy of CO2
C         using residual properties.  A residual prperty is
defined as the
C       difference between the real fluid property and the
perfect gas
C       state property.  Following Patel and Eubank (1988)
for molar enthalpy:
C       H-H'ref = H(T,rho) - H'(Tref,Pref/RTref), where '
indicates the
C     perfect gas state.  Integration is done along the path
C                               H(T,rho)-->H'(T,0)-->H'(Tref,0)--
>H'(Tref,Pref/RTref).
C
C     Determine residual internal energy first: (U-U'ref)/RT
= 1/T integral
C       from 0 to rho of dZ/d(1/T) drho/rho + 1/T integral
from Tref to T of
C       Cv/R dT, where Cv is molar heat capacity in J/(mol
K).  Then determine
C     residual enthalpy: (H-H'ref)/RT = (U-U'ref)/RT + Z -
Tref/T.  Using
C         Tref=273.16 K and Pref=1000 Pa, H'ref=0 (from
Patel and Eubank).
C
C             Input:
C                       T    = Temperature in K
C                       V      = Molar volume of CO2 in
m3/mol
C                       Z    = Compressibility factor of CO2
[-]
C
C             Output:
C                       H      = Molar enthalpy of CO2 in
J/mol
C
C             Constants:
C                       R      = Universal gas constant in
m3Pa/molK
C                       B     = Covolume in m3/mol (value
from K&J)
C             Ci thru Fi = Coefficients of the MRK EOS
(i=1,2,3)
C                               Values from Weir et al. (1996)
C           Gi   = Coefficients of molar heat capacity
C                 Values from Angus et al. (1976)
C                       Tref = Reference temperature in K
(value from P&E)
C
C             Variables:
C                       RHO   = Molar density of CO2 in
mol/m3
C                       XI1   = First Integral (see above)
C                       XI2   = Second Integral (see above)
C                       URES = Residual internal energy
C
      PARAMETER(BETA=  304.21D0)
      PARAMETER(R   = 8.3147295D0)
      PARAMETER(TREF=  2.7316D+02)
      PARAMETER(B   =  5.8D-05)
      PARAMETER(C1  =  2.39534D+01)
      PARAMETER(C2  = -4.55309D-02)
      PARAMETER(C3  =  3.65168D-05)
      PARAMETER(D1  = -4.09844D-03)
```

```
      PARAMETER(D2  =  1.23158D-05)
      PARAMETER(D3  = -8.99791D-09)
      PARAMETER(E1  =  2.89224D-07)
      PARAMETER(E2  = -8.02594D-10)
      PARAMETER(E3  =  7.30975D-13)
      PARAMETER(F1  = -6.43556D-12)
      PARAMETER(F2  =  2.01284D-14)
      PARAMETER(F3  = -2.17304D-17)
      PARAMETER(G0  =  0.769441246D+01)
      PARAMETER(G1  = -0.249610766D+00)
      PARAMETER(G2  = -0.254000397D+02)
      PARAMETER(G3  =  0.651102201D+02)
      PARAMETER(G4  = -0.820863624D+02)
      PARAMETER(G5  =  0.574148450D+02)
      PARAMETER(G6  = -0.212184243D+02)
      PARAMETER(G7  =  0.323362153D+01)
C
      SAVE ICALL
      DATA ICALL/0/
      ICALL=ICALL+1
      IF(ICALL.EQ.1) WRITE(11,899)
  899 FORMAT(6X,'ENTHALPY  2.0          29  JUNE
1999',6X,
     X'CALCULATE  MOLAR  ENTHALPY  OF
SEPARATE PHASE CO2')
C
C     Calculate molar density (RHO):
      RHO = 1.D0 / V
C
C     Calculate rho to the 2nd and 3rd powers for later use:
      RHO2 = RHO * RHO
C
C     Calculate beta to the 2nd thru 7th powers for later use:
      BETA2 = BETA * BETA
      BETA3 = BETA2 * BETA
      BETA4 = BETA3 * BETA
      BETA5 = BETA4 * BETA
      BETA6 = BETA5 * BETA
      BETA7 = BETA6 * BETA
C
C     Calculate Tref to the 2nd thru 6th powers for later use:
      TREF2 = TREF * TREF
      TREF3 = TREF2 * TREF
      TREF4 = TREF3 * TREF
      TREF5 = TREF4 * TREF
      TREF6 = TREF5 * TREF
C
C     Calculate T to the 2nd thru 6th powers for later use:
      T2 = T * T
      T3 = T2 * T
      T4 = T3 * T
      T5 = T4 * T
      T6 = T5 * T
C
C     Calculate B to the 2nd, 3rd, and 4th powers for later
use:
      B2 = B * B
      B3 = B2 * B
      B4 = B3 * B
C
C     Calculate 1/T times the integral from 0 to rho of
dZ/d(1/T) drho/rho:
      XI1   =   (B*RHO*(-6.D0*(3.D0*F1+T*(F2-F3*T))-
B2*(18.D0*D1
     <          +6.D0*T*(D2-D3*T)+3.D0*(3.D0*E1+T*(E2-
E3*T))*RHO
     <                                  +2.D0*(3.D0*F1+T*(F2-
F3*T))*RHO2)+3.D0*B*(6.D0*E1
     <                              +3.D0*F1*RHO+T*(2.D0*E2-
2.D0*E3*T+F2*RHO-F3*T*RHO)))
     <                    +6.D0*(3.D0*F1+T*(F2-F3*T)+B3*(-
3.D0*C1+T*(-C2+C3*T))
     <                     +B2*(3.D0*D1+T*(D2-D3*T))+B*(-
3.D0*E1+T*(-E2+E3*T)))
     <      *DLOG(1+B*RHO))/(12*B4*R*T**1.5)
C
C     Calculate 1/T times the integral from Tref to T of
Cv/R dT, where Cv
C     is molar heat capacity in J/(mol K).  The expression
for Cv is
C     derived an expression from Angus et al. (1976) for
molar
C     heat capacity at constant pressure:
      XI2           =           G0-1.D0+((TREF/T)*(1.D0-
G0))+(((BETA*G1)/T)*DLOG
     <          (T/TREF))+(((BETA2*G2)/T)*((1.D0/TREF)-
(1.D0/T)))
     <          +(((BETA3*G3)/(2.D0*T))*((1.D0/TREF2)-
(1.D0/T2)))
     <          +(((BETA4*G4)/(3.D0*T))*((1.D0/TREF3)-
(1.D0/T3)))
     <          +(((BETA5*G5)/(4.D0*T))*((1.D0/TREF4)-
(1.D0/T4)))
     <          +(((BETA6*G6)/(5.D0*T))*((1.D0/TREF5)-
(1.D0/T5)))
     <          +(((BETA7*G7)/(6.D0*T))*((1.D0/TREF6)-
(1.D0/T6)))
C
C     Calculate residual internal energy (URES):
      URES = XI1+XI2
C
C     Calculate molar enthalpy (H):
      H = (URES+Z-(TREF/T)) * R * T
      RETURN
      END
C********1*********2*********3*********4******
***5*********6*********7**
      SUBROUTINE HENRY(TX,PCX,PS,FC,X1M)
      IMPLICIT DOUBLE PRECISION(A-H,O-Z)
C
C     This subroutine calculates the mass fraction of CO2
in the liquid
C     phase using an extended Henry's Law relationship
from Reid et al.
C     (1987). The relationship is ln(FC/XCO2) = ln(HP) +
VID(PCX-PS)/RT.
C     See below for variable definitions.
C
C          The expression for Henry's Constant is from
O'Sullivan et al. (1985).
C          The expression was created using a piece-wise
quadratic fit to data
C          published by Ellis and Goulding (1963), Malinin
(1959), Takenouchi
C     and Kennedy (1964), and Gibb and Van Ness (1971).
C
C     The value for the the partial molar volume of CO2 at
infinite
C     dilution is assumed to be constant at 30E-6 from the
work of
C     Takenouchi and Kennedy (1964) (and others). This
assumption is
C     reasonable at temperatures below 150 C.
C
C               Input:
C                         TX   = Temperature in degrees C
C                         PCX  = Pressure of CO2 in Pa
C                         PS   = Saturation pressure of water
in Pa
C                         FC   = Fugacity of CO2 in Pa
```

```
C
C            Output:
C                    X1M  = Mass fraction of CO2 in
liquid phase [-]
C
C            Constants:
C                    XMWC = Molecular weight of CO2
in Kg/mol
C                    XMWW = Molecular weight of
H2O in Kg/mol
C                    R    = Universal gas constant in
m3Pa/molK
C                    VID  = Partial molar volume of
CO2 at infinite
C                 dilution in m3/mol (value from T&K)
C
C            Variables:
C                    T    = Temperature in K
C                    TAU  = Temperature variable used
in calculation
C                         of  Henry's  Coefficient  in
degrees C
C                    HP   = Henry's Coefficient in bars,
then Pa
C                    XCO2 = Mole fraction CO2 in
liquid phase [-]
C
     PARAMETER(XMWC = 4.40098D-02)
     PARAMETER(XMWW = 1.801534D-02)
     PARAMETER(R    = 8.3147295D0)
     PARAMETER(VID  = 3.0D-05)
C
     SAVE ICALL
     DATA ICALL/0/
     ICALL=ICALL+1
     IF(ICALL.EQ.1) WRITE(11,899)
  899 FORMAT(6X,'HENRY      2.0          1 SEPT
1999',6X,
    X'CALCULATE MASS FRACTION DISSOLVED
CO2 IN AQUEOUS PHASE')
C
C    Calculate TAU:
     TAU = (TX-1.7D+02) / 1.0D+02
C
C     Calculate TAU to the 2nd and 4th powers for later
use:
     TAU2 = TAU * TAU
     TAU4 = TAU2 * TAU2
C
C    Calculate Henry's Coefficient (HP) in bars:
     IF(TAU.GE.0.D0)THEN
       HP = 6.4D+03 - (2.07778D+03*TAU2) +
(3.1111D+02*TAU4)
     ELSEIF(TAU.LT.0.D0)THEN
       HP = 6.4D+03 - (2.14914D+03*TAU2) -
(1.9543D+02*TAU4)
     ENDIF
C
C    Convert Henry's Coefficient to Pa:
     HP = HP * 1.0D+05
C
C    Convert temperature to K:
     T = TX + 2.7315D+02
C
C    Calculate mole fraction of CO2 (XMOLE):
     XCO2     =     DEXP(DLOG(FC/HP)-(VID*(PCX-
PS))/(R*T))

C    Calculate mass fraction of CO2 (XMASS):
     X1M      =     (XMWC*XCO2)     /     (((1.D0-
XCO2)*XMWW)+(XCO2*XMWC))

     RETURN
     END
C********1*********2*********3*********4*******
***5*********6*********7**
     SUBROUTINE SOLUT(PCX,TX,HSOL)
     IMPLICIT DOUBLE PRECISION(A-H,O-Z)
C
C        This subroutine calculates the enthalpy of CO2
dissolution in
C     liquid water. The expression is from O'Sullivan et al.
(1985).
C      The expression was created using a quadratic fit to
data published
C     by Ellis and Goulding (1963).
C
     SAVE ICALL
     DATA ICALL/0/
     ICALL=ICALL+1
     IF(ICALL.EQ.1) WRITE(11,899)
  899 FORMAT(6X,'SOLUT      1.0          26 JANUARY
1990',6X,
    X'CALCULATE SPECIFIC ENTHALPY OF CO2
DISSOLUTION IN WATER')
C
     T  = 1.D-2 * TX
     T2 = T * T
     T3 = T * T2
     T4 = T * T3
     HSOL = -7.3696D-2 - 5.6405D-1*T + 7.0363D-1*T2
-
    >       2.7882D-1*T3 + 4.2579D-2*T4
     HSOL = HSOL * 1.D6
     RETURN
     END
C********1*********2*********3*********4*******
***5*********6*********7**
     SUBROUTINE DENMIX(TX,DW,X1M,D1M)
     IMPLICIT DOUBLE PRECISION(A-H,O-Z)
C
C      This subroutine returns density of CO2/H2O liquid
mixture. The
C     expression is from Anderson et al. (1992).
C
C            Input:
C                    TX   = Temperature in degrees C
C                    DW   = Density of H2O in kg/m3
C                    X1M  = Mass fraction of CO2 [-]
C
C            Output:
C                    D1M     =     Density     of     CO2/H2O
mixture in kg/m3
C
C            Constants:
C                    XMWC = Molecular weight of CO2
in Kg/mol
C
C            Variables:
C                    RHO     =     Density     of     CO2     at
saturation pressure in mol/cm3
C                    DC   = Density of CO2 at saturation
pressure in kg/m3
C                    X2M  = Mass fraction H2O [-]
C
     PARAMETER(XMWC=4.40098D-02)
C
     SAVE ICALL
     DATA ICALL/0/
```

```
      ICALL=ICALL+1
      IF(ICALL.EQ.1) WRITE(11,899)
  899 FORMAT(6X,'DENMIX      2.0              1 SEPT
1999',6X,'
     XCALCULATE DENSITY OF CO2/H2O AQUEOUS
MIXTURE')
C
      IF(X1M.LE.0.D0) THEN
        D1M = DW
        RETURN
      ENDIF
C
C     Calculate TX to the 2nd, 3rd and 4th powers for later
use:
      TX2 = TX * TX
      TX3 = TX2 * TX
      TX4 = TX3 * TX
C
C     Calculate density of CO2 (RHO) at saturation pressure
in mol/cm3:
      RHO = 1.D0/(3.736D+01 - (7.109D-02*TX) -
(3.812D-05*TX2) +
     <      (3.296D-06*TX3) - (3.702D-09*TX4))
C
C     Convert RHO to kg/m3 (DC):
      DC = RHO * 1.0D+06 * XMWC
C
C     Calculate mass fraction of H2O:
      X2M = 1.D0 - X1M
C
C     Calculate density of CO2/H2O mixture in kg/m3:
      D1M = (DW*DC) / ((X1M*DW)+(X2M*DC))

      RETURN
      END
C********1*********2*********3*********4******
***5*********6*********7**
      SUBROUTINE VISCO2(TX,DC,VC)
      IMPLICIT DOUBLE PRECISION(A-H,O-Z)
C
C      This subroutine calculates the viscosity of pure CO2
as a function
C      of temperature and density of CO2.  The expressions
for calculating
C      the viscosity come from empirical equations provided
in Vesovic et
C      al.(1990) and Fenghour et al. (1998).
C       The critical point enhancement for the viscosity of
CO2
C      has been neglected since it is weak and restricted to a
very small
C      region around the critical point.
C
C             Input:
C                       TX     = Temperature in degrees C
C                       DC     = Density of CO2 in kg/m3
C
C             Output:
C                       VC     = Viscosity of CO2 in Pa-s
C
C             Constants:
C                       Ai           = Coefficients of the
correlation of the
C                              zero-density viscosity
C                       ESCL   = Energy scaling parameter
in K
C                            = epsilon/kappa
C                       Dij          = Coefficients of the
correlation of the
C                              excess viscosity
C
C             Variables:
C                       T      = Temperature in K
C                       TSTAR      = (kappa*T)/epsilon =
T/ESCL [-]
C                       ETA0   = Zero-density viscosity in
muPa-s
C                       DETA       = Excess viscosity in
muPa-s
C
      PARAMETER(A0   =  2.35156D-01)
      PARAMETER(A1   = -4.91266D-01)
      PARAMETER(A2   =  5.211155D-02)
      PARAMETER(A3   =  5.347906D-02)
      PARAMETER(A4   = -1.537102D-02)
      PARAMETER(ESCL =  2.51196D+02)
      PARAMETER(D11  =  0.4071119D-02)
      PARAMETER(D21  =  0.7198037D-04)
      PARAMETER(D64  =  0.2411697D-16)
      PARAMETER(D81  =  0.2971072D-22)
      PARAMETER(D82  = -0.1627888D-22)
C
      SAVE ICALL
      DATA ICALL/0/
      ICALL=ICALL+1
      IF(ICALL.EQ.1) WRITE(11,899)
  899 FORMAT(6X,'VISCO2      2.0              11 DEC
1999',6X,
     X'CALCULATE    VISCOSITY    OF    SEPARATE
PHASE CO2')
C
C     Convert temperature from degrees C to K:
      T = TX + 2.7315D+02
C
C     Calculate DC to 2nd, 6th, and 8th powers:
      DC2 = DC*DC
            DC6 = DC2*DC2*DC2
            DC8 = DC6*DC2
C
C     Calculate TSTAR and 3rd power:
      TSTAR = T/ESCL
            TSTAR3=TSTAR*TSTAR*TSTAR
C
C     Calculate ln(TSTAR) and 2nd, 3rd, and 4th powers:
      BETA1 = DLOG(TSTAR)
      BETA2 = BETA1*BETA1
            BETA3 = BETA2*BETA1
            BETA4 = BETA3*BETA1
C
C     Calculate zero-density limit viscosity in muPa-s:
      EXS                                                =
DEXP(A0+(A1*BETA1)+(A2*BETA2)+(A3*BETA3)+(
A4*BETA4))
      ETA0 = (1.00697D0 * DSQRT(T)) / EXS
C
C     Calculate excess viscosity in muPa-s:
      DETA                                               =
(D11*DC)+(D21*DC2)+((D64*DC6)/TSTAR3)+(D81*D
C8)+
     >      ((D82*DC8)/TSTAR)
C
C     Calculate total viscosity in muPa-s:
      VC = ETA0 + DETA
C
C     Convert viscosity from muPa-s to Pa-s:
      VC = VC * 1.0D-06

      RETURN
      END
```

```
C********1*********2*********3*********4**********5*********6*********7**
      SUBROUTINE OUT
      IMPLICIT DOUBLE PRECISION(A-H,O-Z)
      INCLUDE "PARAM.BSC"
C
C-----THIS SUBROUTINE GENERATES PRINTOUT.
C
C
C$$$$$$$$$ COMMON BLOCKS FOR ELEMENTS $$$$$$$$$$$$$$$$$$$$$$$$$$$$$$$$
C
C     THESE BLOCKS HAVE A LENGTH OF NEL (= NUMBER OF ELEMENTS)
C
      COMMON/E1/ELEM(1)
      COMMON/E2/MATX(1)
      COMMON/E3/EVOL(1)
      COMMON/E4/PHI(1)
      COMMON/E5/P(1)
      COMMON/E6/T(1)
      COMMON/E7/XBC(1)
      COMMON/E8/YBC(1)
      COMMON/E9/ZBC(1)
      COMMON/E10/HHBC(1)
      COMMON/E11/SCO2BC(1)
      COMMON/E12/XCO2BC(1)
      COMMON/E13/FFLOWH(1)
      COMMON/E14/FFLOWV(1)
      COMMON/E15/CFLOWH(1)
      COMMON/E16/CFLOWV(1)
      COMMON/E17/QFLOWH(1)
      COMMON/E18/QFLOWV(1)
      COMMON/E19/DCO2BC(1)
      COMMON/E20/VCO2BC(1)
      COMMON/E21/DH2OBC(1)
      COMMON/E22/HCO2BC(1)
      COMMON/E23/TBC(1)
      COMMON/E24/PHASEBC(1)
      COMMON/E25/FVELH(1)
      COMMON/E26/FVELV(1)
      COMMON/E27/CVELH(1)
      COMMON/E28/CVELV(1)
C
C$$$$$$$$$$$$$$$$$$$$$$$$$$$$$$$$$$$$$$$$$$$$$$$$$$$$$$$$$$$$$$$$$$$$$$$
C
C$$$$$$$$$ COMMON BLOCKS FOR PRIMARY VARIABLES $$$$$$$$$$$$$$$$$$$$$$$$
C
C    THESE BLOCKS HAVE A LENGTH OF 3*NEL
C
      COMMON/P1/X(1)
      COMMON/P2/DX(1)
      COMMON/P3/DELX(1)
      COMMON/P4/R(1)
      COMMON/P5/DOLD(1)
C
C$$$$$$$$$$$$$$$$$$$$$$$$$$$$$$$$$$$$$$$$$$$$$$$$$$$$$$$$$$$$$$$$$$$$$$$
C
C
C$$$$$$$$$ COMMON BLOCKS FOR CONNECTIONS $$$$$$$$$$$$$$$$$$$$$$$$$$$$C
C
      COMMON/C1/NEX1(1)
      COMMON/C2/NEX2(1)
      COMMON/C3/DEL1(1)
      COMMON/C4/DEL2(1)
      COMMON/C5/AREA(1)
      COMMON/C6/BETA(1)
      COMMON/C7/ISOX(1)
      COMMON/C8/GLO(1)
      COMMON/C9/ELEM1(1)
      COMMON/C10/ELEM2(1)
      COMMON/C12/FLOFH1(1)
      COMMON/C13/FLOFH2(1)
      COMMON/C14/FLOFV1(1)
      COMMON/C15/FLOFV2(1)
      COMMON/C16/FLOCH1(1)
      COMMON/C17/FLOCH2(1)
      COMMON/C18/FLOCV1(1)
      COMMON/C19/FLOCV2(1)
      COMMON/C20/GLOH1(1)
      COMMON/C21/GLOH2(1)
      COMMON/C22/GLOV1(1)
      COMMON/C23/GLOV2(1)
      COMMON/C24/VELFH1(1)
      COMMON/C25/VELFH2(1)
      COMMON/C26/VELFV1(1)
      COMMON/C27/VELFV2(1)
      COMMON/C28/VELCH1(1)
      COMMON/C29/VELCH2(1)
      COMMON/C30/VELCV1(1)
      COMMON/C31/VELCV2(1)
C
C$$$$$$$$$$$$$$$$$$$$$$$$$$$$$$$$$$$$$$$$$$$$$$$$$$$$$$$$$$$$$$$$$$$$$$$
C
C$$$$$ COMMON BLOCKS FOR SINKS/SOURCES $$$$$$$$$$$$$$$$$$$$$$$$$$$$$$$$
C
      COMMON/G4/ELEG(1)
      COMMON/G5/SOURCE(1)
      COMMON/G6/LTABG(1)
      COMMON/G7/G(1)
      COMMON/G8/EG(1)
      COMMON/G9/NEXG(1)
      COMMON/G10/ITABG(1)
      COMMON/G11/NGIND(1)
      COMMON/G12/LCOM(1)
      COMMON/G13/PI(1)
      COMMON/G14/PWB(1)
      COMMON/G15/HG(1)
      COMMON/G16/GPO(1)
      COMMON/G17/SDENS(1)
      COMMON/G18/SSAT(1)
      COMMON/G19/GVOL(1)
      COMMON/G20/HL(1)
      COMMON/G21/HS(1)
      COMMON/G22/QVGC(1)
      COMMON/G23/QVWC(1)
      COMMON/G24/QVOC(1)
      COMMON/G25/GRAD(1)
      COMMON/G26/FF(1)
C
C$$$$$$$$$$$$$$$$$$$$$$$$$$$$$$$$$$$$$$$$$$$$$$$$$$$$$$$$$$$$$$$$$$$$$$$
      COMMON/COMPO/FLO(1)
      COMMON/PORVEL/VEL(1)
      COMMON/DM/DELTEN,DELTEX,FOR,FORD
      COMMON/KONIT/KON,DELT,IGOOD
      COMMON/TITLE/ TITLE
      COMMON/DOP/ENTH,KDATA,QUAL
      COMMON/SVZ/NOITE,MOP(24)
      COMMON/POV6/ TSTART

COMMON/NN/NEL,NCON,NOGN,NK,NEQ,NPH,NB,
NK1,NEQ1,NBK,NSEC,NFLUX
```

```
COMMON/CONTST/RE1,RE2,RERM,NER,KER,DFAC
     COMMON/SECPAR/PAR(1)

COMMON/SOLID/NM,DROK(27),POR(27),PER(3,27),
CWET(27),SPHT(27)
     COMMON/SOCH/MAT(27)

COMMON/CYC/KCYC,ITER,ITERC,TIMIN,SUMTIM,
GF,TIMOUT
     COMMON/FF/H1
     CHARACTER*1 H1
     DIMENSION DXM(3)
     CHARACTER*80 TITLE
     CHARACTER*5
ELEM,ELEM1,ELEM2,ELEG,SOURCE,MAT
     CHARACTER*1 ITABG,HB,H0
     CHARACTER*10 PHASE
     real*8 year
     real*8 brvelh(NEL),brvelv(NEL)
C
     SAVE ICALL,HB,H0,ZERO
     DATA HB,H0/' ',' '/
     DATA ICALL,ZERO/0,1.D-13/
     ICALL=ICALL+1
     IF(ICALL.EQ.1) WRITE(11,899)
 899  FORMAT(/6X,'OUT          2.0          1  SEPT
1999',6X,
    X'PRINT RESULTS FOR ELEMENTS,
CONNECTIONS, AND SINKS/SOURCES'/
    x47X,'SPECIAL VERSION FOR *EOSCO2*')
C
C-----COME HERE TO SET UP TECPLOT OUTPUT
FILE.
C
1111      FORMAT(A44,1X,F8.0,A7)
1112
FORMAT('VARIABLES="X","Z","HEAD","TEMP","SC
O2","XCO2","FH2OH",

>"FH2OV","FCO2H","FCO2V","VH2OH","VH2OV","V
CO2H","VCO2V","PHASE"
    >,"MAT"')
1113      FORMAT(/'ZONE T="',E10.5,' YR", I= ',I5,',
J= ',I5,
    >   ',F= POINT')
     IF (ICALL.EQ.1) THEN
       WRITE(80,1111)'TITLE = "CO2 DIAGNOSTICS"'
       WRITE(80,1112)
     END IF
     YEAR=SUMTIM/3.1536E7
     WRITE(80,1113)year,NNZ,NNX
C-----COME HERE TO COMPUTE MAXIMUM
CHANGES.
C
     DO I=1,NK1
       DXM(I) = 0.D0
     END DO
     DO N=1,NEL
       NLOC = (N-1) * NK1
       DO I=1,3
         ADX = DABS(DX(NLOC+I))
         IF (ADX.GT.DXM(I)) DXM(I) = ADX
       END DO
     END DO
C
C-----COME HERE TO PRINT HEADER
INFORMATION.
C
     DAY=SUMTIM/8.64D4
     PRINT 5010,H1,TITLE,KCYC,ITER,KON,DAY
     PRINT 5140,HB
     PRINT
9010,SUMTIM,KCYC,ITER,ITERC,KON,(DXM(I),I=1,3
),
    1  RERM,NER,KER,DELTEX
     PRINT 5140,HB
     PRINT 1000,H0
     PRINT 1001
C
C-----COME HERE TO PRINT VARIABLES AT THE
STATE POINT.
C
     DO N=1,NEL
       NLOC   = (N-1) * NK1
       NLOC2  = (N-1) * NSEC * NEQ1
       NLOC2L = NLOC2 + NBK
       NLOC2S = NLOC2L + NBK
       IF (MOD(N,57).EQ.46) THEN
         PRINT 1002,H1
         PRINT 1001
       END IF
       TX = PAR(NLOC2+NSEC-1)
       PRES = X(NLOC+1)
       IF (KON.NE.2) THEN
         PRES = X(NLOC+1) + DX(NLOC+1)
       END IF
c--APA                                    HHBC(N)    =
PRES/(PAR(NLOC2L+4)*GF)+(ZBC(N)+DEPTH)
       HHBC(N) = PRES
       TBC(N) = TX
              IF (PAR(NLOC2S+1).GT.ZERO) THEN
         SCO2BC(N) = PAR(NLOC2S+1)
       ELSE
         SCO2BC(N) = 0.D0
       END IF
              IF          (PAR(NLOC2L+NB+2).GT.ZERO)
THEN
         XCO2BC(N) = PAR(NLOC2L+NB+2)
       ELSE
         XCO2BC(N) = 0.D0
       END IF
       DH2OBC(N) = PAR(NLOC2L+4)
       IF (SCO2BC(N).EQ.0.D0) THEN
         DCO2BC(N) = 0.D0
         VCO2BC(N) = 0.D0
         HCO2BC(N) = 0.D0
         IF (XCO2BC(N).EQ.0.D0) THEN
           PHASE  = 'NO CO2'
           PHASEBC(N) = 0.D0
         ELSE
           PHASE = 'DISSOLVED'
           PHASEBC(N) = 1.D0
         END IF
       ELSE
         DCO2BC(N) = PAR(NLOC2S+4)
         VCO2BC(N) = PAR(NLOC2S+3)
         HCO2BC(N) = PAR(NLOC2S+5)
         IF (XCO2BC(N).EQ.0.D0) THEN
           IF
(TX.GT.30.957D0.AND.PRES.GT.7.3721D+06) THEN
             PHASE = 'SUPERCRIT'
             PHASEBC(N) = 2.D0
           ELSE
             PHASE = 'GASEOUS'
             PHASEBC(N) = 3.D0
           ENDIF
         ELSE
           IF
(TX.GT.30.957D0.AND.PRES.GT.7.3721D+06) THEN
```

```
            PHASE = 'DISS/SCRIT'
            PHASEBC(N) = 4.D0
          ELSE
            PHASE = 'DISS/GAS'
            PHASEBC(N) = 5.D0
          END IF
        END IF
      END IF
      PRINT
5041,ELEM(N),N,PRES,TX,PAR(NLOC2L+1),SCO2BC
(N),
     >
XCO2BC(N),DH2OBC(N),DCO2BC(N),VCO2BC(N),
     >          HCO2BC(N),PHASE
    END DO
    PRINT 5140,HB
    IF (MOD(KDATA,10).LT.2) THEN
      GO TO 3045
    ENDIF
C
C-----COME HERE TO PRINT FLOW TERMS.
C
    PRINT 5000,H1,TITLE,KCYC,ITER,SUMTIM
    PRINT 5060,H0,HB
    PRINT 5061
    DO 3030 N=1,NCON
      IF (NEX1(N).EQ.0.OR.NEX2(N).EQ.0) THEN
        GO TO 3030
      END IF
      NNP = (N-1) * NPH
      FLOF = 0.D0
      DO NP=1,NPH
        FLOF = FLOF + FLO(NNP+NP)
      END DO
      H = 0.D0
      IF (FLOF.NE.0.D0) THEN
        H = GLO(N) / FLOF
      END IF
      IF (MOD(N,57).EQ.54) THEN
        PRINT 5062,H1,HB
        PRINT 5061
      END IF
      FLOH2O = FLO(NNP+2)
      VELH2O = VEL(NNP+2)
      FLOCO2 = FLO(NNP+3)
      VELCO2 = VEL(NNP+3)
      PRINT
5070,ELEM1(N),ELEM2(N),N,GLO(N),H,FLOF,
     >          FLOH2O,VELH2O,FLOCO2,VELCO2
C
C-----COME HERE TO RECORD FLOW AND
VELOCITY VECTORS FOR TECPLOT OUTPUT FILE.
C
C   See if it is a horizontal connection:
      IF (ISOX(N).EQ.1) THEN
C   Record the heat flow, fluid flow, and velocity out of or
in to the cell of interest:
        FLOFH1(NEX1(N)) = FLOH2O
        FLOFH2(NEX2(N)) = FLOH2O
        FLOCH1(NEX1(N)) = FLOCO2
        FLOCH2(NEX2(N)) = FLOCO2
        VELFH1(NEX1(N)) = VELH2O
        VELFH2(NEX2(N)) = VELH2O
        VELCH1(NEX1(N)) = VELCO2
        VELCH2(NEX2(N)) = VELCO2
        GLOH1(NEX1(N))  = GLO(N)
        GLOH2(NEX2(N))  = GLO(N)
C   See if it is a vertical connection:
      ELSE IF (ISOX(N).EQ.3) THEN
C   Record the heat flow, fluid flow, and velocity out of or
in to the cell of interest:
        FLOFV1(NEX1(N)) = FLOH2O
        FLOFV2(NEX2(N)) = FLOH2O
        FLOCV1(NEX1(N)) = FLOCO2
        FLOCV2(NEX2(N)) = FLOCO2
        VELFV1(NEX1(N)) = VELH2O
        VELFV2(NEX2(N)) = VELH2O
        VELCV1(NEX1(N)) = VELCO2
        VELCV2(NEX2(N)) = VELCO2
        GLOV1(NEX1(N))  = GLO(N)
        GLOV2(NEX2(N))  = GLO(N)
      ENDIF
 3030 CONTINUE
C
C-----COME HERE TO CALCULATE FLOW AND
VELOCITY VECTORS FOR TECPLOT OUTPUT FILE.
C
C    Procedure: (ignore single connections for now). If
signs are the same,
C      set flow direction and magnitude,  if signs are
different, set direction
C    to the same direction as the highest flow rate, and set
magnitude to be
C    the difference between the two i.e. the net flow in the
specified direction.
C
C      Note that if flow magnitude is positive, fluid is
flowing from elem2 into
C    elem1 (i.e. to the left); this holds for both ....H1 and
....H2.
C
     DO 29 N=1,NEL
C   Horizontal connections first:
C   H2O Flow:
C      If the same flow direction, calculate average fluid
flow:
      IF
(FLOFH1(N).GE.0.D0.AND.FLOFH2(N).GE.0.D0)
THEN
        FFLOWH(N) = -(FLOFH1(N)+FLOFH2(N))/2.D0
      ELSE                                          IF
(FLOFH1(N).LT.0.D0.AND.FLOFH2(N).LT.0.D0)
THEN
        FFLOWH(N)                                   =
(DABS(FLOFH1(N))+DABS(FLOFH2(N)))/2.D0
C      If opposing flow directions, calculate the net fluid
flow through:
      ELSE                                          IF
(FLOFH1(N).LT.0.D0.AND.FLOFH2(N).GE.0.D0)
THEN
        IF  (DABS(FLOFH1(N)).GT.DABS(FLOFH2(N)))
THEN
          FFLOWH(N)                                 =
DABS(FLOFH1(N)+FLOFH2(N))
        ELSE
IF(DABS(FLOFH2(N)).GT.DABS(FLOFH1(N))) THEN
          FFLOWH(N)                 =               -
DABS(FLOFH1(N)+FLOFH2(N))
        END IF
      ELSE                                          IF
(FLOFH1(N).GE.0.D0.AND.FLOFH2(N).LT.0.D0)
THEN
        IF  (DABS(FLOFH1(N)).GT.DABS(FLOFH2(N)))
THEN
          FFLOWH(N)                 =               -
DABS(FLOFH1(N)+FLOFH2(N))
        ELSE                                        IF
(DABS(FLOFH2(N)).GT.DABS(FLOFH1(N))) THEN
```

```
            FFLOWH(N)                                   =
DABS(FLOFH1(N)+FLOFH2(N))
          END IF
        END IF
C
C    CO2 Flow:
C      If the same flow direction, calculate average CO2
flow:
        IF (SCO2BC(N).GT.0.D0) THEN
          IF
(FLOCH1(N).GE.0.D0.AND.FLOCH2(N).GE.0.D0)
THEN
            CFLOWH(N)                   =                -
(FLOCH1(N)+FLOCH2(N))/2.D0
          ELSE                                          IF
(FLOCH1(N).LT.0.D0.AND.FLOCH2(N).LT.0.D0)
THEN
            CFLOWH(N)                                   =
(DABS(FLOCH1(N))+DABS(FLOCH2(N)))/2.D0
C       If opposing flow directions, calculate the net CO2
flow through:
          ELSE                                          IF
(FLOCH1(N).LT.0.D0.AND.FLOCH2(N).GE.0.D0)
THEN
            IF
(DABS(FLOCH1(N)).GT.DABS(FLOCH2(N))) THEN
              CFLOWH(N)                                 =
DABS(FLOCH1(N)+FLOCH2(N))
            ELSE
IF(DABS(FLOCH2(N)).GT.DABS(FLOCH1(N))) THEN
              CFLOWH(N)                 =                -
DABS(FLOCH1(N)+FLOCH2(N))
            END IF
          ELSE                                          IF
(FLOCH1(N).GE.0.D0.AND.FLOCH2(N).LT.0.D0)
THEN
            IF
(DABS(FLOCH1(N)).GT.DABS(FLOCH2(N))) THEN
              CFLOWH(N)                 =                -
DABS(FLOCH1(N)+FLOCH2(N))
            ELSE                                        IF
(DABS(FLOCH2(N)).GT.DABS(FLOCH1(N))) THEN
              CFLOWH(N)                                 =
DABS(FLOCH1(N)+FLOCH2(N))
            END IF
          END IF
        ELSE
          CFLOWH(N) = 0.D0
        END IF
C
C    Heat Flow:
C      If the same flow direction, calculate average heat
flow:
        IF
(GLOH1(N).GE.0.D0.AND.GLOH2(N).GE.0.D0) THEN
          QFLOWH(N) = -(GLOH1(N)+GLOH2(N))/2.D0
        ELSE                                            IF
(GLOH1(N).LT.0.D0.AND.GLOH2(N).LT.0.D0) THEN
          QFLOWH(N)                                     =
(DABS(GLOH1(N))+DABS(GLOH2(N)))/2.D0
C    If opposing flow directions, calculate the net heat flow
through:
        ELSE                                            IF
(GLOH1(N).LT.0.D0.AND.GLOH2(N).GE.0.D0) THEN
          IF    (DABS(GLOH1(N)).GT.DABS(GLOH2(N)))
THEN
            QFLOWH(N)                                   =
DABS(GLOH1(N)+GLOH2(N))
          ELSE
IF(DABS(GLOH2(N)).GT.DABS(GLOH1(N))) THEN
            QFLOWH(N)                   =                -
DABS(GLOH1(N)+GLOH2(N))
          END IF
        ELSE                                            IF
(GLOH1(N).GE.0.D0.AND.GLOH2(N).LT.0.D0) THEN
          IF    (DABS(GLOH1(N)).GT.DABS(GLOH2(N)))
THEN
            QFLOWH(N)                   =                -
DABS(GLOH1(N)+GLOH2(N))
          ELSE                                          IF
(DABS(GLOH2(N)).GT.DABS(GLOH1(N))) THEN
            QFLOWH(N)                                   =
DABS(GLOH1(N)+GLOH2(N))
          END IF
        END IF
C
C    H2O Velocity:
C      If the same flow direction, calculate average fluid
velocity:
        IF
(VELFH1(N).GE.0.D0.AND.VELFH2(N).GE.0.D0)
THEN
          FVELH(N) = -(VELFH1(N)+VELFH2(N))/2.D0
        ELSE                                            IF
(VELFH1(N).LT.0.D0.AND.VELFH2(N).LT.0.D0)
THEN
          FVELH(N)                                      =
(DABS(VELFH1(N))+DABS(VELFH2(N)))/2.D0
C       If opposing flow directions, calculate the net fluid
velocity:
        ELSE                                            IF
(VELFH1(N).LT.0.D0.AND.VELFH2(N).GE.0.D0)
THEN
          IF (DABS(VELFH1(N)).GT.DABS(VELFH2(N)))
THEN
            FVELH(N) = DABS(VELFH1(N)+VELFH2(N))
          ELSE
IF(DABS(VELFH2(N)).GT.DABS(VELFH1(N))) THEN
            FVELH(N)                    =                -
DABS(VELFH1(N)+VELFH2(N))
          END IF
        ELSE                                            IF
(VELFH1(N).GE.0.D0.AND.VELFH2(N).LT.0.D0)
THEN
          IF (DABS(VELFH1(N)).GT.DABS(VELFH2(N)))
THEN
            FVELH(N)                    =                -
DABS(VELFH1(N)+VELFH2(N))
          ELSE                                          IF
(DABS(VELFH2(N)).GT.DABS(VELFH1(N))) THEN
            FVELH(N) = DABS(VELFH1(N)+VELFH2(N))
          END IF
        END IF
C
C    CO2 Velocity:
C      If the same flow direction, calculate average CO2
velocity:
        IF (SCO2BC(N).GT.0.D0) THEN
          IF
(VELCH1(N).GE.0.D0.AND.VELCH2(N).GE.0.D0)
THEN
            CVELH(N)                    =                -
(VELCH1(N)+VELCH2(N))/2.D0
          ELSE                                          IF
(VELCH1(N).LT.0.D0.AND.VELCH2(N).LT.0.D0)
THEN
            CVELH(N)                                    =
(DABS(VELCH1(N))+DABS(VELCH2(N)))/2.D0
C       If opposing flow directions, calculate the net CO2
velocity:
```

```
        ELSE                                    IF
(VELCH1(N).LT.0.D0.AND.VELCH2(N).GE.0.D0)
THEN
          IF
(DABS(VELCH1(N)).GT.DABS(VELCH2(N))) THEN
            CVELH(N)                            =
DABS(VELCH1(N)+VELCH2(N))
          ELSE
IF(DABS(VELCH2(N)).GT.DABS(VELCH1(N))) THEN
            CVELH(N)                    =       -
DABS(VELCH1(N)+VELCH2(N))
          END IF
        ELSE                                    IF
(VELCH1(N).GE.0.D0.AND.VELCH2(N).LT.0.D0)
THEN
          IF
(DABS(VELCH1(N)).GT.DABS(VELCH2(N))) THEN
            CVELH(N)                    =       -
DABS(VELCH1(N)+VELCH2(N))
          ELSE                                  IF
(DABS(VELCH2(N)).GT.DABS(VELCH1(N))) THEN
            CVELH(N)                            =
DABS(VELCH1(N)+VELCH2(N))
          END IF
        END IF
      ELSE
        CVELH(N) = 0.D0
      END IF
C
C   Now vertical connections:
C   H2O Flow:
C     If the same flow direction, calculate average fluid
flow:
      IF
(FLOFV1(N).GE.0.D0.AND.FLOFV2(N).GE.0.D0)
THEN
        FFLOWV(N) = (FLOFV1(N)+FLOFV2(N))/2.D0
      ELSE                                      IF
(FLOFV1(N).LT.0.D0.AND.FLOFV2(N).LT.0.D0)
THEN
        FFLOWV(N)                   =           -
(DABS(FLOFV1(N))+DABS(FLOFV2(N)))/2.D0
C     If opposing flow directions, calculate the net fluid
flow through:
      ELSE
IF(FLOFV1(N).LT.0.D0.AND.FLOFV2(N).GE.0.D0)
THEN
        IF (DABS(FLOFV1(N)).GT.DABS(FLOFV2(N)))
THEN
          FFLOWV(N)                 =           -
DABS(FLOFV1(N)+FLOFV2(N))
        ELSE
IF(DABS(FLOFV2(N)).GT.DABS(FLOFV1(N))) THEN
          FFLOWV(N)                             =
DABS(FLOFV1(N)+FLOFV2(N))
        END IF
      ELSE
IF(FLOFV1(N).GE.0.D0.AND.FLOFV2(N).LT.0.D0)
THEN
        IF (DABS(FLOFV1(N)).GT.DABS(FLOFV2(N)))
THEN
          FFLOWV(N)                             =
DABS(FLOFV1(N)+FLOFV2(N))
        ELSE                                    IF
(DABS(FLOFV2(N)).GT.DABS(FLOFV1(N))) THEN
          FFLOWV(N)                 =           -
DABS(FLOFV1(N)+FLOFV2(N))
        END IF
      END IF
C
C   CO2 Flow:
C     If the same flow direction, calculate average CO2
flow:
      IF (SCO2BC(N).GT.0.D0) THEN
        IF
(FLOCV1(N).GE.0.D0.AND.FLOCV2(N).GE.0.D0)
THEN
          CFLOWV(N)                             =
(FLOCV1(N)+FLOCV2(N))/2.D0
        ELSE                                    IF
(FLOCV1(N).LT.0.D0.AND.FLOCV2(N).LT.0.D0)
THEN
          CFLOWV(N)                 =           -
(DABS(FLOCV1(N))+DABS(FLOCV2(N)))/2.D0
C     If opposing flow directions, calculate the net CO2
flow through:
        ELSE
IF(FLOCV1(N).LT.0.D0.AND.FLOCV2(N).GE.0.D0)
THEN
          IF
(DABS(FLOCV1(N)).GT.DABS(FLOCV2(N))) THEN
            CFLOWV(N)                   =       -
DABS(FLOCV1(N)+FLOCV2(N))
          ELSE
IF(DABS(FLOCV2(N)).GT.DABS(FLOCV1(N))) THEN
            CFLOWV(N)                           =
DABS(FLOCV1(N)+FLOCV2(N))
          END IF
        ELSE
IF(FLOCV1(N).GE.0.D0.AND.FLOCV2(N).LT.0.D0)
THEN
          IF
(DABS(FLOCV1(N)).GT.DABS(FLOCV2(N))) THEN
            CFLOWV(N)                           =
DABS(FLOCV1(N)+FLOCV2(N))
          ELSE                                  IF
(DABS(FLOCV2(N)).GT.DABS(FLOCV1(N))) THEN
            CFLOWV(N)                   =       -
DABS(FLOCV1(N)+FLOCV2(N))
          END IF
        END IF
      ELSE
        CFLOWV(N) = 0.D0
      END IF
C
C   Heat Flow:
C     If the same flow direction, calculate average heat
flow:
      IF
(GLOV1(N).GE.0.D0.AND.GLOV2(N).GE.0.D0) THEN
        QFLOWV(N) = (GLOV1(N)+GLOV2(N))/2.D0
      ELSE                                      IF
(FLOFV1(N).LT.0.D0.AND.FLOFV2(N).LT.0.D0)
THEN
        QFLOWV(N)                   =           -
(DABS(GLOV1(N))+DABS(GLOV2(N)))/2.D0
C   If opposing flow directions, calculate the net heat flow
through:
      ELSE                                      IF
(GLOV1(N).LT.0.D0.AND.GLOV2(N).GE.0.D0) THEN
        IF    (DABS(GLOV1(N)).GT.DABS(GLOV2(N)))
THEN
          QFLOWV(N)                 =           -
DABS(GLOV1(N)+GLOV2(N))
        ELSE
IF(DABS(GLOV2(N)).GT.DABS(GLOV1(N))) THEN
          QFLOWV(N)                             =
DABS(GLOV1(N)+GLOV2(N))
        END IF
```

```
      ELSE                                          IF
(GLOV1(N).GE.0.D0.AND.GLOV2(N).LT.0.D0) THEN
        IF(DABS(GLOV1(N)).GT.DABS(GLOV2(N)))
THEN
          QFLOWV(N)                                 =
DABS(GLOV1(N)+GLOV2(N))
        ELSE                                        IF
(DABS(GLOV2(N)).GT.DABS(GLOV1(N))) THEN
          QFLOWV(N)                 =               -
DABS(GLOV1(N)+GLOV2(N))
        END IF
      END IF
C
C   H2O Velocity:
C     If the same flow direction, calculate average fluid
velocity:
      IF
(VELFV1(N).GE.0.D0.AND.VELFV2(N).GE.0.D0)
THEN
        FVELV(N) = (VELFV1(N)+VELFV2(N))/2.D0
      ELSE                                          IF
(VELFV1(N).LT.0.D0.AND.VELFV2(N).LT.0.D0)
THEN
        FVELV(N)                    =               -
(DABS(VELFV1(N))+DABS(VELFV2(N)))/2.D0
C     If opposing flow directions, calculate the net fluid
velocity:
      ELSE                                          IF
(VELFV1(N).LT.0.D0.AND.VELFV2(N).GE.0.D0)
THEN
        IF (DABS(VELFV1(N)).GT.DABS(VELFV2(N)))
THEN
          FVELV(N)                  =               -
DABS(VELFV1(N)+VELFV2(N))
        ELSE
IF(DABS(VELFV2(N)).GT.DABS(VELFV1(N))) THEN
          FVELV(N) = DABS(VELFV1(N)+VELFV2(N))
        END IF
      ELSE                                          IF
(VELFV1(N).GE.0.D0.AND.VELFV2(N).LT.0.D0)
THEN
        IF (DABS(VELFV1(N)).GT.DABS(VELFV2(N)))
THEN
          FVELV(N) = DABS(VELFV1(N)+VELFV2(N))
        ELSE                                        IF
(DABS(VELFV2(N)).GT.DABS(VELFV1(N))) THEN
          FVELV(N)                  =               -
DABS(VELFV1(N)+VELFV2(N))
        END IF
      END IF
C
C   CO2 Velocity:
C     If the same flow direction, calculate average CO2
velocity:
      IF (SCO2BC(N).GT.0.D0) THEN
        IF
(VELCV1(N).GE.0.D0.AND.VELCV2(N).GE.0.D0)
THEN
          CVELV(N) = (VELCV1(N)+VELCV2(N))/2.D0
        ELSE                                        IF
(VELCV1(N).LT.0.D0.AND.VELCV2(N).LT.0.D0)
THEN
          CVELV(N)                  =               -
(DABS(VELCV1(N))+DABS(VELCV2(N)))/2.D0
C     If opposing flow directions, calculate the net CO2
velocity:
        ELSE                                        IF
(VELCV1(N).LT.0.D0.AND.VELCV2(N).GE.0.D0)
THEN
          IF
(DABS(VELCV1(N)).GT.DABS(VELCV2(N))) THEN
            CVELV(N)                =               -
DABS(VELCV1(N)+VELCV2(N))
          ELSE
IF(DABS(VELCV2(N)).GT.DABS(VELCV1(N))) THEN
            CVELV(N)                                =
DABS(VELCV1(N)+VELCV2(N))
          END IF
        ELSE                                        IF
(VELCV1(N).GE.0.D0.AND.VELCV2(N).LT.0.D0)
THEN
          IF
(DABS(VELCV1(N)).GT.DABS(VELCV2(N))) THEN
            CVELV(N)                                =
DABS(VELCV1(N)+VELCV2(N))
          ELSE                                      IF
(DABS(VELCV2(N)).GT.DABS(VELCV1(N))) THEN
            CVELV(N)                =               -
DABS(VELCV1(N)+VELCV2(N))
          END IF
        END IF
      ELSE
        CVELV(N) = 0.D0
      END IF
C
C-----COME HERE TO WRITE TECPLOT OUTPUT
FILE.
1114      FORMAT(15(1X,E10.4),1x,i3)
      brvelh(N)=FVELH(N)*3.1536E9
      brvelv(N)=FVELV(N)*3.1536E9

WRITE(80,1114)XBC(N),ZBC(N),HHBC(N),TBC(N),SC
O2BC(N),
     >
XCO2BC(N),FFLOWH(N),FFLOWV(N),CFLOWH(N),C
FLOWV(N),
     >
brvelh(N),brvelv(N),CVELH(N),CVELV(N),DH2OBC(N
),
     >      MATX(N)
29   CONTINUE
C
C-----COME HERE TO PRINT PRIMARY
VARIABLES, LATEST INCREMENTS, AND REL.
PERMS.
C
      PRINT 5140,HB
      IF (MOD(KDATA,10).LT.3) THEN
        GO TO 3045
      END IF
      PRINT 5000,h1,TITLE,KCYC,ITER,SUMTIM
      PRINT 5030,H0
      DO 3020 N = 1,NEL
        NLOC=(N-1)*NK1
        NLOC2=(N-1)*NSEC*NEQ1
        NLOC2L=NLOC2+NBK
        IF (MOD(N,57) .EQ. 54) PRINT 5032,H1
        PRINT
5040,ELEM(N),N,(X(NLOC+I),I=1,NK1),(DX(NLOC+I)
,I=1,NK1),
     >      PAR(NLOC2L+2),PAR(NLOC2S+2)
 3020 CONTINUE
      PRINT 5140,HB
 3045 CONTINUE
C
C-----COME HERE TO PRINT SOURCE/SINK TERMS.
C
      IF (NOGN.EQ.0) RETURN
      PRINT 5000,h1,TITLE,KCYC,ITER,SUMTIM
```

```
      PRINT 5120,H0
      PRINT 5121
      GC=0.D0
      HGC=0.D0
      DO 3050 N=1,NOGN
        J = NEXG(N)
        IF (J.EQ.0) THEN
          GO TO 3050
        END IF
        IF (MOD(N,58).EQ.54) THEN
          PRINT 5122,H1
          PRINT 5121
        END IF
        IF (GPO(N).GT.0.D0) THEN
          PRINT
5130,ELEG(N),SOURCE(N),N,GPO(N),EG(N)
        END IF
        IF   (GPO(N).LE.0.D0.AND.LCOM(N).NE.NK1+1)
THEN
          PRINT
5130,ELEG(N),SOURCE(N),N,GPO(N),EG(N),
     >          (FF((N-1)*NPH+NP),NP=1,NPH)
        END IF
        IF   (GPO(N).LE.0.D0.AND.LCOM(N).EQ.NK1+1)
THEN
          PRINT
5130,ELEG(N),SOURCE(N),N,GPO(N),EG(N),
     >          (FF((N-1)*NPH+NP),NP=1,NPH),PWB(N)
        END IF
        IF (LCOM(N).NE.NK1+1) THEN
          GO TO 102
        END IF
C
C-----NOW FOR A LITTLE SECTION WHICH
COMPUTES TOTAL FLOWRATE
C       AND FLOWING ENTHALPY FOR WELLS ON
DELIVERABLITY WITH COMPLE-
C             TIONS IN DIFFERENT LAYERS (OR,
GENERALLY, ELEMENTS)
C
C     ALL OPEN INTERVALS OF A WELL MUST BE
KNOWN BY THE SAME SOURCE
C             NAME, AND MUST BE GIVEN IN
UNINTERRUPTED SEQUENCE.
C
        IF (NOGN.EQ.1) THEN
          GO TO 102
        END IF
        IF  (N.EQ.1.AND.SOURCE(N+1).NE.SOURCE(N))
THEN
          GO TO 102
        END IF
        IF (N.EQ.1) THEN
          GO TO 100
        END IF
        IF                                    (SOURCE(N-
1).EQ.SOURCE(N).OR.SOURCE(N).EQ.SOURCE(N+1)
) THEN
          GO TO 100
        END IF
        GO TO 103
C
C-----COME HERE FOR SOURCE IN A CHAIN AND
ACCUMULATE TERMS.
C
  100   GC = GC + GPO(N)
        HGC = HGC + GPO(N) * EG(N)
C
C-----FIND OUT WHETHER CHAIN TERMINATES.
C
        IF (N.EQ.NOGN) THEN
          GO TO 101
        END IF
        IF (SOURCE(N+1).EQ.SOURCE(N)) THEN
          GO TO 102
        END IF
C
C-----COME HERE FOR END OF CHAIN.
C
  101   IF (GC.NE.0.D0) THEN
          HGC=HGC/GC
        END IF
        PRINT 110,SOURCE(N),GC,HGC
  110 FORMAT(' ***** SOURCE  $',A5,'$       RATE
=',E12.5,
     1    ' KG/S    FLOWING ENTHALPY =',E12.5,' J/KG
*****'/)
C
C-----COME  HERE  FOR  SOURCES  OUTSIDE
CHAINS, AND AT END OF CHAIN.
C
  103   GC = 0.D0
        HGC = 0.D0
C
  102   CONTINUE
C
C-----END OF SECTION FOR MULTI-LAYER WELLS
ON DELIVERABILITY
C
 3050 CONTINUE
      PRINT 5140,HB
      RETURN
C
C---*----1----*----2----*----3----*----4----*----5----*----6---
-*----7----*----8
 5000  FORMAT(A1/10X,A80//80X,'KCYC  =',I5,'  -
ITER =',I5,
     1  '  -  TIME =',E12.5/)
 5010  FORMAT(A1/'  ',A80//10X,'OUTPUT  DATA
AFTER (',I4,',',I3,')-',I1,
     1    '-TIME  STEPS',52('  '),'THE  TIME  IS  ',E12.5,'
DAYS')
 9010 FORMAT(' TOTAL TIME       KCYC  ITER
ITERC  KON      DX1M',9X,
     1      'DX2M',9X,'DX3M',10X,'MAX.  RES.',6X,'NER
KER       DELTEX'/
     2
1X,E12.5,3I7,I6,5X,3E13.5,2X,E13.5,4X,I4,I6,5X,E13.5)
 5030          FORMAT(A1,'ELEM.                INDEX
X1',10X,'X2',10X,'X3',10X,' X1',9X,
     1'DX1',9X,'DX2',9X,'DX3',9X,'DX4',8X,'K(LIQ)
K(CO2)'/)
 5032          FORMAT(A1/'  ELEM.               INDEX
X1',10X,'X2',10X,'X3',10X,' X1',9X,
     1'DX1',9X,'DX2',9X,'DX3',9X,'DX4',8X,'K(GAS)
K(LIQ.)'/)
 1000          FORMAT(A1,'ELEM.                INDEX
P',10X,'T',8X,'SH2O',7X,'SCO2',

x7X,'XCO2',7X,'DH2O',7X,'DCO2',7X,'VCO2',7X,'HCO2
',6X,'PHASE')
 1001       FORMAT(16X,'(Pa)',6X,'(deg-C)',5X,'(-)',8X,'(-
)',8X,'(-)',
     x7X,'(kg/m3)',4X,'(kg/m3)',4X,'(Pa-s)',5X,'(J/kg)',6X,'(-
)'/)
 1002          FORMAT(A1/,'ELEM.                INDEX
P',10X,'T',8X,'SH2O',7X,'SCO2',

x7X,'XCO2',7X,'DH2O',7X,'DCO2',7X,'VCO2',7X,'HCO2
',6X,'PHASE')
```

```
 5040 FORMAT(1X,A5,I6,10(1X,E10.5))
 5041 FORMAT(1X,A5,I6,9(1X,E10.5),1X,A10)
 5060 FORMAT(A1,1X,'ELEM1 ELEM2 INDEX
FLOH',A6,'FLOH/FLOF',7X,
    1 'FLOF',7X,'FLO(LIQ) VEL(LIQ) FLO(CO2)
VEL(CO2)')
 5061
FORMAT(25X,'(W)',8X,'(J/KG)',8X,'(KG/S)',7X,'(KG/S)',
7X,
    1 '(M/S) (KG/S) (M/S)'/)
 5062 FORMAT(A1/2X,'ELEM1 ELEM2 INDEX
FLOH',A6,'FLOH/FLOF',7X,
    1 'FLOF',7X,'FLO(LIQ) VEL(LIQ.) FLO(CO2)
VEL(CO2)')
 5070 FORMAT(2A7,1X,I5,(7(1X,E12.5)))
 5120 FORMAT(A1,'ELEMENT SOURCE INDEX
GENERATION RATE ',
    1 ' ENTHALPY FF(GAS) FF(LIQ.) FF(CO2)
P(WB)')
 5121 FORMAT(29X,'(KG/S) OR (W)
(J/KG)',46X,'(PA)'/)
 5122 FORMAT(A1/' ELEMENT SOURCE INDEX
GENERATION RATE ',
    1 ' ENTHALPY FF(GAS) FF(LIQ.) FF(CO2)
P(WB)')
 5130
FORMAT(2X,A5,3X,A5,3X,I2,10X,E12.5,2X,6(1X,E12.
5))
 5140 FORMAT(/' ',131('@')/A1)
C
      END
C********1*********2*********3*********4******
***5*********6*********7**
      SUBROUTINE BALLA
      IMPLICIT DOUBLE PRECISION(A-H,O-Z)
C
C-----THIS SUBROUTINE PERFORMS VOLUME-
AND MASS-BALANCES.
C
C
      COMMON/E2/MATX(1)
      COMMON/E3/EVOL(1)
      COMMON/E4/PHI(1)
      COMMON/P1/X(1)
      COMMON/SECPAR/PAR(1)

COMMON/SOLID/NM,DROK(27),POR(27),PER(3,27),
CWET(27),SPHT(27)
      COMMON/SOCH/MAT(27)

COMMON/CYC/KCYC,ITER,ITERC,TIMIN,SUMTIM,
GF,TIMOUT

COMMON/NN/NEL,NCON,NOGN,NK,NEQ,NPH,NB,
NK1,NEQ1,NBK,NSEC,NFLUX
      COMMON/BC/NELA
      COMMON/FF/H1
      CHARACTER*1 H1
      CHARACTER*5 MAT
C
      SAVE ICALL
      DATA ICALL/0/
      ICALL=ICALL+1
      IF(ICALL.EQ.1) WRITE(11,899)
  899 FORMAT(/6X,'BALLA 0.9 7 JANUARY
1992',6X,
     X'PERFORM SUMMARY BALANCES FOR
VOLUME, MASS, AND ENERGY')
C
      DAY = SUMTIM / 8.64D4
      PRINT 1,H1
    1 FORMAT(A1/' ********** VOLUME- AND
MASS-BALANCES **',80('*')/)
      PRINT 2,KCYC,ITER,SUMTIM,DAY
    2 FORMAT(' ********** [KCYC,ITER] = [',I4,',',I3,']
*****',34X,
     1 'THE TIME IS ',E12.5,' SECONDS, OR ',E12.5,'
DAYS'/)
C
      VOLG = 0.D0
      VOLL = 0.D0
      VOLC = 0.D0
      AMG = 0.D0
      AML = 0.D0
      AMV = 0.D0
      AMA = 0.D0
      AMW = 0.D0
      AMC = 0.D0
      DO 10 N=1,NELA
        NMAT = MATX(N)
        IF (SPHT(NMAT).GE.1.D4) THEN
          GO TO 10
        END IF
        NLOC2 = (N-1) * NSEC * NEQ1
C-->    PHIV = porosity*grid block volume
        PHIV  = PHI(N) * EVOL(N)
C-->                DVOLG=gas vol.,DVOLL=liquid
vol.,DVOLC=CO2 vol. (all in m**3)
        DVOLG = PHIV * PAR(NLOC2+1)
        DVOLL = PHIV * PAR(NLOC2+NBK+1)
        DVOLC = PHIV * PAR(NLOC2+2*NBK+1)
C
C-->   update (initialize vol. parameters)
        VOLG = VOLG + DVOLG
        VOLL = VOLL + DVOLL
        VOLC = VOLC + DVOLC
C
        DAMG = DVOLG * PAR(NLOC2+4)
        AMG  = AMG + DAMG
        DAML = DVOLL * PAR(NLOC2+NBK+4)
        AML  = AML + DAML
        DAMV = DAMG * PAR(NLOC2+NB+1)
        AMV  = AMV + DAMV
        DAMA = DAMG * PAR(NLOC2+NB+2) + DAML
* PAR(NLOC2+NBK+NB+2)
        AMA  = AMA + DAMA
        DAMW = DAML * PAR(NLOC2+NBK+NB+1)
        AMW  = AMW + DAMW
        DAMC = DVOLC * PAR(NLOC2+2*NBK+4) *
PAR(NLOC2+2*NBK+NB+3)
        AMC  = AMC + DAMC
   10   CONTINUE
C
      PRINT 3,VOLL,VOLC
    3 FORMAT(/' PHASE VOLUMES IN PLACE:'/'
AQUEOUS ',E12.5,
     1 ' M**3;  SEPARATE PHASE CO2 ',E12.5,'
M**3')
C
      PRINT 4,AML,AMW,AMA,AMC,AMA+AMC
    4 FORMAT(/' MASS IN PLACE:'/' AQUEOUS
',E12.5,
     1 ' KG;  WATER ',E18.10,' KG;  DISSOLVED CO2
',E18.10,
     2 ' KG;  SEPARATE CO2 ',E18.10,' KG'/
     x' TOTAL CO2 ',E18.10,' KG')
C
      PRINT 5
    5 FORMAT(/1X,119('*')//)
      RETURN
```

```
      END
C********1*********2*********3*********4**********5*********6*********7**
      SUBROUTINE QLOSS
C       DUMMY SUBROUTINE (IF ACTIVE, WOULD DO HEAT EXCHANGE WITH
C     CONFINING LAYERS)
      COMMON/SVZ/NOITE,MOP(24)
C
      SAVE ICALL
      DATA ICALL/0/
      ICALL=ICALL+1
      IF(ICALL.EQ.1) WRITE(11,899)
  899 FORMAT(6X,'QLOSS      1.0          25 JANUARY 1990',6X,
     X'INACTIVE (DUMMY) SUBROUTINE')
C
C     INACTIVATE QLOSS
      MOP(15)=0
      RETURN
      END
C********1*********2*********3*********4**********5*********6*********7**
      SUBROUTINE MASSTRANS
      IMPLICIT DOUBLE PRECISION(A-H,O-Z)
C
C       This subroutine handles the transfer of mass from separate phase CO2
C            to dissolved phase and vice-versa. This is accomplished by having
C       sources and sinks of separate and dissolved phase CO2 in each element,
C         as appropriate.  This subroutine is called from MULTI just after
C     calling QU.  No other modifications are necessary.
C
      COMMON/E3/EVOL(1)
      COMMON/E4/PHI(1)
      COMMON/E9/ZBC(1)
      COMMON/P1/X(1)

      COMMON/NN/NEL,NCON,NOGN,NK,NEQ,NPH,NB,NK1,NEQ1,NBK,NSEC,NFLUX

      COMMON/CYC/KCYC,ITER,ITERC,TIMIN,SUMTIM,GF,TIMOUT

      COMMON/CONTST/RE1,RE2,RERM,NER,KER,DFAC
      COMMON/FAIL/IHALVE
      COMMON/BC/NELA
      COMMON/P4/R(1)
      COMMON/SECPAR/PAR(1)
C
      SAVE ICALL,ZERO
      DATA ICALL,ZERO/0,1.D-13/
      ICALL=ICALL+1
      IF(ICALL.EQ.1) WRITE(11,899)
  899 FORMAT(6X,'TRANSFER  2.0              1 SEPT 1999',6X,
     X'MASS TRANSFER BETWEEN SEPARATE AND DISSOLVED PHASE CO2')
C
      DO 200 N=1,NELA
        NLOC  = (N-1) * NEQ
        NLOCP = (N-1) * NK1
        NLOC2 = (N-1) * NSEC * NEQ1
        PX    = X(NLOCP+1)
        XCO2  = X(NLOCP+2)
        SCO2  = X(NLOCP+3)
        TX    = X(NLOCP+4)
        RHOL  = PAR(NLOC2+NBK+4)
        RHOC  = PAR(NLOC2+2*NBK+4)
        PCO2 = PX
        IF (SCO2.LE.DFAC) THEN
          SCO2 = 0.D0
        END IF
        IF (XCO2.LE.DFAC) THEN
          XCO2 = 0.D0
        END IF
C
        IF (SCO2.EQ.0.D0) THEN
C     Come here if there is no separate phase CO2 present in the element.
C
          IF (XCO2.EQ.0.D0) THEN
C     Come here if there is no dissolved phase CO2 present in the element.
C     In this case, no mass needs to be transferred.
C
            GO TO 200
C
          ELSE IF (XCO2.GT.0.D0) THEN
C     Come here if dissolved mass fraction of CO2 (XCO2) in the element is
C       greater than zero. In this case, must first determine what the dissolved
C       mass fraction of CO2 (XCO2N) should be at the ambient temperature (TX)
C     and pressure (PX).
C
C     Determine the fugacity (FCO2) of CO2 at the ambient temperature (TX)
C     and pressure (PX).
            CALL CO2(TX,PCO2,dummy,FCO2,dummy)

C     Determine the saturation pressure of water (PSAT) at the ambient
C     temperature (TX).
            CALL SAT(TX,PSAT)
C
C     Determine what the dissolved mass fraction of CO2 (XCO2N) should be at
C     the ambient temperature (TX) and pressure (PX).
            CALL HENRY(TX,PCO2,PSAT,FCO2,XCO2N)

            IF (XCO2.LE.XCO2N) THEN
C       Come here if the dissolved mass fraction of CO2 (XCO2) present in the
C       element is less than or equal to what the dissolved mass fraction of CO2
C     (XCO2N) should be at the ambient temperature (TX) and pressure (PX).  In
C     this case, no mass needs to be transferred.
C
              GO TO 200
C
            ELSE IF (XCO2.GT.XCO2N) THEN
C       Come here if the dissolved mass fraction of CO2 (XCO2) in the element
C       is greater than what the dissolved mass fraction of CO2 (XCO2N) should
C     be at the ambient temperature (TX) and pressure (PX).  In this case, CO2
C       will evolve from the dissolved phase forming a separate phase.  Therefore,
C     need to transfer mass from dissolved phase to separate phase.
C
```

```
C      Determine the dissolved mass of CO2 (DMOLD)
present in the element.
            DMOLD = PHI(N) * EVOL(N) * RHOL *
XCO2
C
C    Determine the dissolved mass of CO2 (DMNEW) that
should be present in the
C    element.
            DMNEW = PHI(N) * EVOL(N) * RHOL *
XCO2N
C
C    The mass of CO2 that needs to be transferred from the
dissolved phase
C     to separate phase is the difference between DMNEW
and DMOLD.
C      Note that DMOLD should always be greater than
DMNEW.
            DMDIF = DMNEW - DMOLD
            R(NLOC+2)      =      R(NLOC+2)      -
DMDIF/EVOL(N)
            R(NLOC+3)      =      R(NLOC+3)      +
DMDIF/EVOL(N)
          END IF
        END IF
C
       ELSE IF (SCO2.GT.0.D0) THEN
C     Come here if there is separate phase CO2 present in
the element.
C
C    Determine the fugacity (FCO2) of CO2 at the ambient
temperature (TX)
C    and pressure (PX).
         CALL CO2(TX,PCO2,dummy,FCO2,dummy)

C
C    Determine the saturation pressure of water (PSAT) at
the ambient
C    temperature (TX).
         CALL SAT(TX,PSAT)
C
C     Determine what the dissolved mass fraction of CO2
(XCO2N) should be at
C    the ambient temperature (TX) and pressure (PX).
         CALL HENRY(TX,PCO2,PSAT,FCO2,XCO2N)

C
         IF (XCO2.EQ.XCO2N) THEN
C      Come here if the dissolved mass fraction of CO2
(XCO2) present in the
C    element is equal to what the dissolved mass fraction of
CO2 (XCO2N)
C       should be at the ambient temperature (TX) and
pressure (PX).  In this
C    case, no mass needs to be transferred.
C
           GO TO 200
C
         ELSE IF (XCO2.GT.XCO2N) THEN
C      Come here if the dissolved mass fraction of CO2
(XCO2) in the element
C      is greater than what the dissolved mass fraction of
CO2 (XCO2N) should
C    be at the ambient temperature (TX) and pressure (PX).
In this case, CO2
C      will evolve from the dissolved phase adding to the
separate phase.
C    Therefore, need to transfer mass from dissolved phase
to separate phase.
C
C      Determine the dissolved mass of CO2 (DMOLD)
present in the element.
            DMOLD = PHI(N) * EVOL(N) * (1.D0-SCO2)
* RHOL * XCO2
C
C    Determine the dissolved mass of CO2 (DMNEW) that
should be present in the
C    element.
            DMNEW = PHI(N) * EVOL(N) * (1.D0-SCO2)
* RHOL * XCO2N
C
C    The mass of CO2 that needs to be transferred from the
dissolved phase to
C    separate phase is the difference between DMNEW and
DMOLD.  Note that DMOLD
C    should always be greater than DMNEW.
            DMDIF = DMNEW - DMOLD
            R(NLOC+2) = R(NLOC+2) - DMDIF/EVOL(N)
            R(NLOC+3)      =      R(NLOC+3)      +
DMDIF/EVOL(N)
C
         ELSE IF (XCO2.LT.XCO2N) THEN
C      Come here if the dissolved mass fraction of CO2
(XCO2) in the element
C      is less than what the dissolved mass fraction of CO2
(XCO2N) should
C    be at the ambient temperature (TX) and pressure (PX).
In this case, CO2
C      will dissolve from the separate phase adding to the
dissolved phase.
C    Therefore,need to transfer mass from separate phase to
dissolved phase.
C
C      Determine the dissolved mass of CO2 (DMOLD)
present in the element.
            DMOLD = PHI(N) * EVOL(N) * (1.D0-SCO2)
* RHOL * XCO2
C
C      Determine the dissolved mass of CO2 (DMNEW)
corresponding to the new
C    dissolved mass fraction of CO2 (XCO2).
            DMNEW = PHI(N) * EVOL(N) * (1.D0-SCO2)
* RHOL * XCO2N
C
C    The mass of CO2 that needs to be transferred from the
separate phase to the
C      dissolved phase is the difference between DMNEW
and DMOLD.  Note that DMNEW
C    should always be greater than DMOLD.
            DMDIF = DMNEW - DMOLD
C
C    However, need to determine the total mass of separate
phase CO2 present in
C    the element.
            SMCO2 = PHI(N) * EVOL(N) * SCO2   *
RHOC
C
            IF (DMDIF.GT.SMCO2) THEN
C      Come here if the mass that needs to be transferred
from the separate phase
C      to dissolved phase is greater than the total separate
phase mass present
C      in the element.  In this case, transfer all the separate
phase mass to
C    dissolved phase.
C
              DMDIF = SMCO2
            END IF
            R(NLOC+2) = R(NLOC+2) - DMDIF/EVOL(N)
```

```
            R(NLOC+3)          =          R(NLOC+3)          +
DMDIF/EVOL(N)
          ENDIF
        END IF
200   CONTINUE
      RETURN
      END
C********1*********2*********3*********4******
***5*********6*********7**
```

Appendix IV. Fortran version: SWEOS.

```
      BLOCK DATA EQOS
C         .....................................................
C         .                                                   .
C         . TOUGH2, MODULE EOSCO2, VERSION 1.0,
AUGUST 2005    .
C         .....................................................
C

COMMON/NN/NEL,NCON,NOGN,NK,NEQ,NPH,NB,
NK1,NEQ1,NBK,NSEC,NFLUX
      DATA NK,NEQ,NPH,NB/3,4,3,6/
C
C----- NK IS THE NUMBER OF COMPONENTS.
C----- NEQ IS THE NUMBER OF EQUATIONS PER
GRID BLOCK.
C       USUALLY WE HAVE NEQ = NK+1, FOR NK
MASS- AND ONE ENERGY-BALANCE.
C----- NPH IS THE NUMBER OF PHASES WHICH
CAN BE PRESENT.
C----- NB IS THE NUMBER OF SECONDARY
PARAMETERS OTHER THAN MASS
C     FRACTIONS.
C----- THE TOTAL NUMBER OF SECONDARY
PARAMETERS IS NBK = NB+NK.
C
      END
C
C********1*********2*********3*********4******
***5*********6*********7**
C
      SUBROUTINE EOS
      IMPLICIT DOUBLE PRECISION(A-H,O-Z)
C
C-----THIS ROUTINE COMPUTES ALL
THERMOPHYSICAL PROPERTIES OF AQUEOUS
AND
C       TWO-PHASE MIXTURES OF WATER AND
CARBON DIOXIDE.
C
      COMMON/P1/X(1)
      COMMON/P2/DX(1)
      COMMON/P3/DELX(1)
      COMMON/E1/ELEM(1)
      COMMON/E2/MATX(1)
      COMMON/E3/EVOL(1)
      COMMON/E4/PHI(1)
      COMMON/E5/P(1)
      COMMON/E6/T(1)
      COMMON/SECPAR/PAR(1)

COMMON/NN/NEL,NCON,NOGN,NK,NEQ,NPH,NB,
NK1,NEQ1,NBK,NSEC,NFLUX

COMMON/CONTST/RE1,RE2,RERM,NER,KER,DFAC
      COMMON/KONIT/KON,DELT,IGOOD

COMMON/CYC/KCYC,ITER,ITERC,TIMIN,SUMTIM,
GF,TIMOUT
      COMMON/KC/KC
      COMMON/SVZ/NOITE,MOP(24)
      COMMON/GASLAW/R,AMS,AMA,CVAIR
      COMMON/FAIL/IHALVE

COMMON/SOLID/NM,DROK(27),POR(27),PER(3,27),
CWET(27),SPHT(27)
      COMMON/SOCH/MAT(27)

COMMON/RPCAP/IRP(27),RP(7,27),ICP(27),CP(7,27),I
RPD,RPD(7),
     >  ICPD,CPD(7)
      COMMON/BC/NELA
      COMMON/FF/H1
C
      CHARACTER*1 H1
      CHARACTER*5 ELEM,MAT
      DIMENSION XX(4),DP(29)
      SAVE ICALL,ZERO
      DATA ZERO/1.D-13/
      DATA ICALL/0/
C
      ICALL = ICALL + 1
      IF(ICALL.EQ.1) THEN
        WRITE(11,899)
      END IF
      IF (MOP(5).GE.4) THEN
        PRINT 32,KCYC,ITER
      END IF
C
C********1*********2*********3*********4******
***5*********6*********7**
C
C-----COME HERE FOR INITIAL CONDITIONS.
C
      IF (KC.EQ.0) THEN
        H1    = CHAR(12)
C
C-----COME HERE TO INITIALIZE SOME DATA.
C
        R     = 8314.7295D0
        AMS   = 18.01534D0
        AMA   = 44.0098D0
C
C-----COME HERE TO ASSIGN DEFAULT RELATIVE
PERMEABILITY AND CAPILLARY
C          PRESSURE PARAMETERS TO DOMAINS
WITHOUT SPECIAL ASSIGNMENTS.
C
        DO N=1,NM
          IF (IRP(N).EQ.0) THEN
            IRP(N) = IRPD
            ICP(N) = ICPD
            DO M=1,7
              RP(M,N) = RPD(M)
              CP(M,N) = CPD(M)
            END DO
          END IF
        END DO
C
C-----COME HERE TO GENERATE SOME PRINTOUT
CONCERNING THE EQUATION-OF-STATE
C-----PACKAGE.
C
        PRINT 300,H1
        PRINT 301,NK,NEQ,NPH,NB
        PRINT 302,NK,NEQ,NPH,NB
        PRINT 303
```

```
      PRINT 306
      PRINT 304
      PRINT 305
      PRINT 307
      PRINT 306
C
C-----COME HERE TO ASSIGN INITIAL CONDITIONS.
C
      DO N=1,NEL
        NLOC  = (N-1) * NK1
        NLOC2 = (N-1) * NSEC*NEQ1
        PX    = X(NLOC+1)
        P(N)  = X(NLOC+1)
        XCO2  = X(NLOC+2)
        IF (XCO2.LT.0.D0.OR.XCO2.GT.1.D0) THEN
          GOTO 202
        END IF
        SCO2  = X(NLOC+3)
        IF (SCO2.LT.0.D0.OR.SCO2.GT.1.D0) THEN
          GOTO 202
        END IF
        TX    = X(NLOC+4)
        IF (TX.LE.0.D0.OR.TX.GE.374.15D0) THEN
          GOTO 202
        END IF
        T(N)  = TX
      END DO
    END IF

    IF (MOP(5).GE.7) THEN
      PRINT 31
    END IF
C
C-----COME HERE WHEN MARCHING IN TIME.
C
    IF (KC.GT.0) THEN
      N1 = NELA
    ELSE
      N1 = NEL
    END IF
    DO N=1,N1
      NMAT  = MATX(N)
      NLOC  = (N-1) * NK1
      NLOC2 = (N-1) * NSEC * NEQ1
C
C-----COME HERE TO UPDATE PRIMARY VARIABLES.
C
      DO M=1,NK1
        IF (ITER.EQ.0) THEN
          XINCR = 0.D0
        ELSE
          XINCR = DX(NLOC+M)
        END IF
        XX(M) = X(NLOC+M) + XINCR
      END DO
C
C-----COME HERE TO PRINT UPDATED PRIMARY VARIABLES.
C
      IF (MOP(5).GE.7) THEN
        PRINT 35,ELEM(N),(XX(M),M=1,NK1)
      END IF
C
C-----COME HERE TO COMPUTE ALL SECONDARY VARIABLES. NOTE THAT SECONDARY
C-----PARAMETERS MUST BE CALCULATED NEQ+1 TIMES; ONCE FOR THE STATE POINT
C-----AND NEQ TIMES FOR EACH OF THE NEQ PRIMARY VARIABLES INCREMENTED
C-----(X+DX+DELX).
C
      DO K=1,NEQ1
        NLK2  = NLOC2 + (K-1) * NSEC
        NLK2L = NLK2 + NBK
        NLK2S = NLK2L + NBK
        PX    = XX(1)
        XCO2  = XX(2)
        SCO2  = XX(3)
        TX    = XX(4)
C
C-----COME HERE TO CALCULATE SECONDARY PARAMETERS AT THE STATE POINT.
C
        IF (K.EQ.1) THEN
          IF (XCO2.LT.0.D0) THEN
C
C-----COME HERE TO ENFORCE MASS FRACTION CONSTRAINT.
C
            XX(2)     = 0.D0
            XCO2      = 0.D0
            DX(NLOC+2) = -X(NLOC+2)
          END IF
          IF (SCO2.LT.0.D0) THEN
C
C-----COME HERE TO ENFORCE SATURATION CONSTRAINT.
C
            XX(3)     = 0.D0
            SCO2      = 0.D0
            DX(NLOC+3) = -X(NLOC+3)
          END IF
          GO TO 101
        END IF
C
C-----COME HERE TO CALCULATE SECONDARY PARAMETERS FOR EACH (NEQ) INCREMENTED
C-----(X+DX+DELX) PRIMARY VARIABLE.
C
        DELX(NLOC+K-1) = DFAC * XX(K-1) + 1.D-10
        IF (K.EQ.2) THEN
          PX   = XX(1) + DELX(NLOC+1)
        ELSE IF (K.EQ.3) THEN
          DELX(NLOC+2) = DFAC
          XCO2 = XX(2) + DELX(NLOC+2)
        ELSE IF (K.EQ.4) THEN
          DELX(NLOC+3) = DFAC
          SCO2 = XX(3) + DELX(NLOC+3)
        ELSE IF (K.EQ.5) THEN
          TX   = XX(4) + DELX(NLOC+4)
        END IF

 101    CONTINUE
C
C-----COME HERE TO CALCULATE SATURATION OF H2O.
C
        SH2O = 1.D0 - SCO2
C
C-----COME HERE TO CALCULATE SATURATION PRESSURE OF H2O.
C
        CALL SAT(TX,PSAT)
        IF (IGOOD.NE.0) THEN
          PRINT *, 'IGOOD = ', IGOOD
          PRINT *, '4444444'
          GO TO 200
```

```
        END IF
C
C-----COME HERE TO CALCULATE DENSITY AND
INTERNAL ENERGY OF H2O.
C
        CALL COWAT(TX,PX,DH2O,UH2O)
        IF (IGOOD.NE.0) THEN
          PRINT *, 'IGOOD = ', IGOOD
          PRINT *, '5555555'
          GO TO 200
        END IF
C
C-----COME HERE TO CALCULATE VISCOSITY OF
H2O.
C
        CALL VISW(TX,PX,PSAT,VH2O)
C
C-----COME HERE TO CALCULATE DENSITY OF
AQUEOUS MIXTURE OF H2O
C-----AND DISSOLVED PHASE CO2.
C
        IF (XCO2.GT.0.D0) THEN
          CALL DENMIX(TX,DH2O,XCO2,DMIX)
        ELSE
          DMIX = DH2O
        END IF
C
C-----COME HERE TO CALCULATE CAPILLARY
PRESSURE.
C
         IF (SCO2.GE.0.01D0) THEN
           CALL PCAPBSC(SH2O,PCAP,NMAT)
         ELSE
           PCAP = 0.D0
         ENDIF
C
C-----COME HERE TO CALCULATE DENSITY AND
ENTHALPY OF
C-----SEPARATE PHASE CO2.
C
        PCO2 = PX
        IF (SCO2.GT.0.D0.OR.XCO2.GT.0.D0) THEN

            CALL CO2(TX,PCO2,DCO2)
            CALL
ENTHALPY(TX,PCO2,dummy,HCO2)

          IF (IGOOD.NE.0) THEN
            PRINT *, 'IGOOD = ', IGOOD
            PRINT *, '6666666'
            GO TO 200
          END IF
        ELSE
          DCO2 = 0.D0
          HCO2 = 0.D0
        END IF
C
C-----COME HERE TO CALCULATE VISCOSITY OF
SEPARATE PHASE CO2.
C
        IF (SCO2.GT.0.D0) THEN
          CALL VISCO2(TX,DCO2,VCO2)
        ELSE
          VCO2 = 1.D0
        END IF
C
C-----COME HERE TO CALCULATE ENTHALPY OF
DISSOLUTION OF CO2 IN WATER.
C
        IF (XCO2.GT.0.D0) THEN
          CALL SOLUT(PCO2,TX,HSOL)
        ELSE
          HSOL = 0.D0
        END IF
C
C-----COME HERE TO CALCULATE RELATIVE
PERMEABILITIES.
C
        IF (SCO2.GE.0.001D0) THEN
          CALL
RELPBSC(SH2O,SCO2,REPW,REPC,NMAT)
        ELSE
          REPW = 1.D0
          REPC = 0.D0
        END IF
C
C-----COME HERE TO ASSIGN SECONDARY
PARAMETERS FOR WATER.
C-----IN ORDER: SATURATION, RELATIVE
PERMEABILITY, VISCOSITY, DENSITY,
C-----ENTHALPY, CAPILLARY PRESSURE, MASS
FRACTION WATER, MASS FRACTION
C-----DISSOLVED CO2, MASS FRACTION DUMMY
COMPONENT.
C
        PAR(NLK2L+1)   = SH2O
        PAR(NLK2L+2)   = REPW
        PAR(NLK2L+3)   = VH2O
        PAR(NLK2L+4)   = DMIX
        PAR(NLK2L+5)     =(UH2O+PX/DMIX)*(1.D0-
XCO2)+(HCO2+HSOL)*XCO2
        PAR(NLK2L+6)   = PCAP
        PAR(NLK2L+NB+1) = 1.D0 - XCO2
        PAR(NLK2L+NB+2) = XCO2
        PAR(NLK2L+NB+3) = 0.D0
C
C-----COME HERE TO ASSIGN SECONDARY
PARAMETERS FOR DUMMY PHASE (GAS SLOTS).
C-----IN ORDER: SATURATION, RELATIVE
PERMEABILITY, VISCOSITY, DENSITY,
C-----ENTHALPY, CAPILLARY PRESSURE, MASS
FRACTION STEAM, MASS FRACTION
C-----GASEOUS CO2, MASS FRACTION DUMMY
COMPONENT.
C
        PAR(NLK2+1)   = 0.D0
        PAR(NLK2+2)   = 0.D0
        PAR(NLK2+3)   = 1.D0
        PAR(NLK2+4)   = 0.D0
        PAR(NLK2+5)   = 0.D0
        PAR(NLK2+6)   = 0.D0
        PAR(NLK2+NB+1) = 0.D0
        PAR(NLK2+NB+2) = 0.D0
        PAR(NLK2+NB+3) = 0.D0
C
C-----COME HERE TO ASSIGN SECONDARY
PARAMETERS FOR SEPARATE PHASE CO2.
C-----IN ORDER: SATURATION, RELATIVE
PERMEABILITY, VISCOSITY, DENSITY,
C-----ENTHALPY, CAPILLARY PRESSURE, MASS
FRACTION DISSOLVED WATER, MASS
C-----FRACTION DISSOLVED CO2, MASS
FRACTION SEPARATE PHASE CO2.
C
        PAR(NLK2S+1)   = SCO2
        PAR(NLK2S+2)   = REPC
        PAR(NLK2S+3)   = VCO2
        PAR(NLK2S+4)   = DCO2
        PAR(NLK2S+5)   = HCO2
        PAR(NLK2S+6)   = 0.D0
```

```
          PAR(NLK2S+NB+1) = 0.D0
          PAR(NLK2S+NB+2) = 0.D0
          PAR(NLK2S+NB+3) = 1.D0
C
C------COME HERE TO STORE LATEST TEMPERATURE AND ZERO DUMMY SLOT.
C
          PAR(NLK2+NSEC-1) = TX
          PAR(NLK2+NSEC)   = 0.D0
        END DO
      END DO
C
C-----COME HERE TO PRINT SECONDARY PARAMETERS AT STATE POINT.
C
      IF (MOP(5).GE.8) THEN
        PRINT 27
        DO N=1,NEL
          NLOC2 = (N-1) * NSEC * NEQ1
          PRINT
30,ELEM(N),(PAR(NLOC2+M),M=1,NSEC)
C
C-----COME HERE TO PRINT INCREMENTED PARAMETERS.
C
          IF (MOP(5).EQ.8) THEN
            DO K=2,NEQ1
              PRINT                    37,(PAR(NLOC2+(K-
1)*NSEC+M),M=1,NSEC)
            END DO
          END IF
C
C-----COME HERE TO PRINT DERIVATIVES.
C
          IF (MOP(5).EQ.9) THEN
            NLOC = (N-1) * NK1
            DO K=2,NEQ1
              DO M=1,NSEC
                DP(M)  =  (PAR(NLOC2+(K-1)*NSEC+M)-
PAR(NLOC2+M))
     <                  / DELX(NLOC+K-1)
              END DO
              PRINT 37,(DP(M),M=1,NSEC)
            END DO
          END IF
        END DO
      END IF
      RETURN
C
C********1*********2*********3*********4*********5*********6*********7**
C
C-----COME HERE IF FAILURE IN SAT, COWAT, OR CO2 (IGOOD NE 0).
C
  200 CONTINUE
      PRINT 201,ELEM(N),(XX(M),M=1,NK1)
      IF(KC.EQ.0) THEN
                GOTO 202
      END IF
      RETURN
C
C-----COME HERE IF INITIAL CONDITIONS ARE BOGUS.
C
  202 PRINT 203
      STOP
C
C********1*********2*********3*********4*********5*********6*********7**
C          FORMAT STATEMENTS FOR SUBROUTINE EOS

  201 FORMAT(' +++++++++          CANNOT FIND
PARAMETERS AT ELEMENT *',A5,
     1 '*          XX(M) =',4(1X,E12.6))
  203 FORMAT(' !!!!!!!!!! ERRONEOUS DATA
INITIALIZATION !!!!!!!!!!',
     1  11X,'STOP EXECUTION----------')
  899 FORMAT(/6X,'EOSCO2      2.0             1 JUNE
2005',6X,
     X'*EOSCO2* ... THERMOPHYSICAL PROPERTIES
MODULE FOR WATER/CO2')
   32 FORMAT(/' %%%%%%%%%% E O S
%%%%%%%%%% E O S %%%%%%%%%%',
     1  '  [KCYC,ITER] = [',I4,',',I3,']'/)
   31 FORMAT(/' PRIMARY VARIABLES'/)
   35          FORMAT(' AT ELEMENT *',A5,'* ---
',(4(2X,E12.6)))
   27 FORMAT(/' SECONDARY PARAMETERS')
   30  FORMAT(/' ELEMENT ',A5/(10(1X,E12.6)))
   37  FORMAT(/(10(1X,E12.6)))
  300  FORMAT(A1/'  ',121('*')/'  *',27X,'EOSCO2:
EQUATION',
     X' OF STATE FOR MIXTURES OF WATER/CO2
',40X,'*'/
     X' ',121('*')//)
  301  FORMAT(//4X,'OPTIONS SELECTED ARE:
(NK,NEQ,NPH,NB) = (',I1,',',
     XI1,',',I1,',',I1,')'/)
  302  FORMAT(10X,'NK   = ',I2,'   - NUMBER OF
FLUID COMPONENTS'/
     X10X,'NEQ = ',I2,'   - NUMBER OF EQUATIONS
PER GRID BLOCK'/
     X10X,'NPH = ',I2,'   - NUMBER OF PHASES THAT
CAN BE PRESENT'/
     X10X,'NB  = ',I2,'   - NUMBER OF SECONDARY
PARAMETERS (OTHER THAN',
     X' COMPONENT MASS FRACTIONS)'/)
  303          FORMAT(/4X,'AVAILABLE          OPTIONS
ARE:'//4X,'(NK,NEQ,NPH,NB) =
     >(3,3,3,6) - WATER, DISSOLVED CO2, SEPARATE
PHASE CO2;
     > ISOTHERMAL (DEFAULT)'/,
     >34X,'VARIABLES (P, XCO2, SCO2, T)'//
     >4X,'(NK,NEQ,NPH,NB) =
     >(3,4,3,6) - WATER, DISSOLVED CO2, SEPARATE
PHASE CO2;
     > NON-ISOTHERMAL'/,
     >34X,'VARIABLES (P, XCO2, SCO2, T)'/)
  304  FORMAT(/26H  THE PRIMARY VARIABLES
ARE/'  P - PRESSURE          ',
     A'XCO2 - MASS FRACTION OF DISSOLVED CO2
',
     B'SCO2 - SEPARATE PHASE CO2 SATURATION'/)
  305 FORMAT(/
     X' ',20('*'),30X,45('*')/
     X' *         COMPONENTS         *',29X,
     X' *    FLUID PHASE CONDITION          PRIMARY
VARIABLES     *'/
     X' ',20('*'),30X,45('*')/
     X' *',18X,'*',30X,'*',43X,'*'/
     X' *       # 1  -  WATER         *',29X,
     X' *   two-phase gas/oil          P,     X,   SCO2,   T *'/
     X' *',18X,'*',30X,'*',43X,'*')
  306 FORMAT(' ',121('*'))
  307 FORMAT(
     X' *       # 2  -  AIR           *',29X,
     X' *   two-phase aqueous/oil      P,     X,   SCO2,   T
*'/
```

```
     X' *',18X,'*',30X,'*',43X,'*'/
     X' *       # 3  -  COM3 (oil)   *',29X,
     x' *   three-phase gas/aqueous/oil  P,   S+10,    SCO2,
T *'/
     X' *',18X,'*',30X,'*',43X,'*'/
     X' *       # 4  -  HEAT         *',29X,' ',45('*')/
     x' *',18X,'*')
C
      END
C********1*********2*********3*********4*********5*********6*********7**
      SUBROUTINE
RELPBSC(SW,SC,REPW,REPC,NMAT)
      IMPLICIT DOUBLE PRECISION(A-H,O-Z)
C
C-----This routine computes relative permeabilities for
liquid
C     (CO2 and water) phases.  From modification of
C     Parker et al. (1987)
C

COMMON/RPCAP/IRP(27),RP(7,27),ICP(27),CP(7,27),I
RPD,RPD(7),
     >  ICPD,CPD(7)

C      Come here to assign the irreducible saturation of
water.
      SR = RP(1,NMAT)
C
C    Come here to assign the van Genuchten N parameter.
C    This is a curve-shaping parameter.
      XN = RP(2,NMAT)
C
C       Come here to calculate the van Genuchten M
parameter.
C    This is another curve-shaping parameter.
      XM = 1.D0 - 1.D0 / XN
C
C       Come here to calculate the inverse of the van
Genuchten M parameter.
      XMINV = 1.D0 / XM
C
C      Come here to calculate the effective saturation of
water.
      SWBAR = (SW-SR) / (1.D0-SR)
      IF (SWBAR.LT.0.D0) SWBAR = 0.D0
      IF (SWBAR.GT.1.D0) SWBAR = 1.D0
C
C    Come here to calculate the effective total saturation.
      STBAR = (SW+SC-SR) / (1.D0-SR)
      IF (STBAR.LT.0.D0) STBAR = 0.D0
      IF (STBAR.GT.1.D0) STBAR = 1.D0
C
C     Come here to calculate the relative permeability of
water.
      A = SWBAR**.5D0
      B = 1.D0 - (SWBAR**XMINV)
      REPW = A * ((1.D0-(B**XM))**2.D0)
      IF (REPW.LT.0.D0) REPW = 0.D0
      IF (REPW.GT.1.D0) REPW = 1.D0
C
C     Come here to calculate the relative permeability of
CO2.
      C = (STBAR-SWBAR)**.5D0
      D = 1.D0 - (STBAR**XMINV)
      REPC = C * (((B**XM)-(D**XM))**7.D0)
      IF (REPC.LT.0.D0) REPC = 0.D0
      IF (REPC.GT.1.D0) REPC = 1.D0
      RETURN
      END
C********1*********2*********3*********4*********5*********6*********7**

      SUBROUTINE PCAPBSC(SW,PC,NMAT)
      IMPLICIT DOUBLE PRECISION(A-H,O-Z)
C
C-----This routine computes capillary pressure as function
of water
C     saturation (SW). From modification of
C     Parker et al. (1987).
C

COMMON/RPCAP/IRP(27),RP(7,27),ICP(27),CP(7,27),I
RPD,RPD(7),
     >  ICPD,CPD(7)
C
C      Come here to assign the irreducible saturation of
water.
      SR = CP(1,NMAT)
C
C    Come here to assign the van Genuchten N parameter.
C    This is a curve-shaping parameter.
      XN = CP(2,NMAT)
C
C       Come here to assign the van Genuchten alpha
parameter.
C    This is a curve-shaping parameter.
      ALPHA = CP(3,NMAT)
C
C     Come here to assign the fluid pair-dependent scaling
factor:
      BETA = CP(4,NMAT)
C
C       Come here to calculate the inverse of the van
Genuchten N parameter.
      XNINV = 1.D0 / XN
C
C       Come here to calculate the van Genuchten M
parameter.
      XM = 1.D0 - XNINV
C
C       Come here to calculate the inverse of the van
Genuchten M parameter.
      XMINV = 1.D0 / XM
C
C      Come here to calculate the effective saturation of
water.
      SWBAR = (SW-SR) / (1.D0-SR)
      IF (SWBAR.LE.0.D0) SWBAR = 1.D-05
C
C    Come here to calculate the capillary pressure.
      A = -1.D0/(ALPHA*BETA)
            B = SWBAR**(-XMINV)
      PC = A*((B-1)**XNINV)
      RETURN
      END
C********1*********2*********3*********4*********5*********6*********7**
      SUBROUTINE CO2(TX,PCX,DC)
      IMPLICIT DOUBLE PRECISION(A-H,L,O-Z)
C
C       This subroutine calculates the specific density of
gaseous and
C       supercritical CO2 as a function of the pressure of
CO2 (PCX)
C       and temperature (TX) using a Span and Wagner
(1996) equation of state (EOS)
C       This formulation of the Spand and Wagner EOS is
based on the curve fitting
```

```
C          of numerous experimental data. The EOS is
developed on the Helmholtz fuction.
C     Because the primary variables of Span and Wagner's
EOS ara Temperature and
C          density, The primary variables are switched into
temperatuer and pressure
C          using iteration method (Diamond and Akinfiev,
2003).
C     The EOS can be applied the temperature and pressure
ranges
C      of 0 < T < 826.85 deg C and 0 < PCX < 800 MPa,
respectively.
C
C            Input:
C                        TX   = Temperature in degrees C
C                        PCX  = Pressure of CO2 in Pa
C
C            Output:
C                        DC   = Specific density of CO2 in
kg/m3
C
C            Constants:
C                R      = Specific gas constant (188.9241
[J/kg*K])
C                = RM/M
C                   RM    = Molar gas constant (8.314510
[J/molK])
C               PC   = PRESSURE AT CRITICAL POINT (
7.3773 [MPa])
C                  TC    = TEMPERATURE AT CRITICAL
POINT (304.1282 [K])
C                  DCC  = DENSITY AT CRITICAL POINT
(467.6 [kg/m3])
C
C
      COMMON/E1/ELEM(1)
            PARAMETER(TC   = 304.1282D0)
            PARAMETER(DCC  = 467.6D0)
            PARAMETER(PC   = 7.3773D+6)
       PARAMETER(R    = 188.9241)

C     TABLE 31 (Span and Wagner Coefficient, 1996)

            DOUBLE PRECISION NN(42), D(39),
TT(39), C(34), ALPHA(35:39)
     1, BETA(35:42), GAMMA(35:39), EPSLON(35:39),
SMALLA(40:42)
     2, SMALLB(40:42), BIGA(40:42), BIGB(40:42),
BIGC(40:42)
     3,                                  BIGD(40:42),
CRITICAL_VAPOR_PRESSURE_A(4)
     4,              CRITICAL_VAPOR_PRESSURE_T(4),
CRITICAL_LIQUID_DENSITY_A(4)
     5,               CRITICAL_LIQUID_DENSITY_T(4),
CRITICAL_VAPOR_DENSITY_A(5)
     6, CRITICAL_VAPOR_DENSITY_T(5)



            DATA      NN      /      0.38856823203161,
2.938547594274
     1,       -5.5867188534934,       -0.76753199592477,
0.31729005580416
     2,       0.54803315897767,       0.12279411220335,
2.165896154322
     3,       1.5841735109724,       -0.23132705405503,
0.058116916431436
     4, -0.55369137205382, 0.48946615909422
     5, -0.024275739843501, 0.062494790501678
     6, -0.12175860225246, -0.37055685270086
     7, -0.016775879700426, -0.11960736637987
     8, -0.045619362508778, 0.035612789270346
     9, -0.0074427727132052, -0.0017395704902432
     1, -0.021810121289527, 0.024332166559236
     2, -0.037440133423463, 0.14338715756878
     3, -0.13491969083286, -0.02315122505348
     4, 0.012363125492901, 0.002105832197294
     5, -0.00033958519026368, 0.0055993651771592
     6, -0.00030335118055646, -213.65488688320
     7, 26641.569149272, -24027.212204557
     8, -283.41603423999, 212.47284400179
     9, -0.66642276540751, 0.72608632349897
     1, 0.055068668612842 /

      DATA D / 1, 1, 1, 1, 2, 2, 3, 1, 2, 4, 5, 5, 5, 6, 6, 6,
     1      1, 1, 4, 4, 4, 7, 8, 2, 3, 3, 5, 5, 6, 7, 8, 10, 4, 8,
     2      2, 2, 2, 3, 3 /

      DATA TT / 0, 0.75, 1, 2, 0.75, 2, 0.75, 1.5, 1.5, 2.5, 0,
     1    1.5, 2, 0, 1, 2, 3, 6, 3, 6, 8, 6, 0, 7, 12, 16, 22, 24,
     2    16, 24, 8, 2, 28, 14, 1, 0, 1, 3, 3 /

      DATA C / 0, 0, 0, 0, 0, 0, 0, 1, 1, 1, 1, 1, 1, 1, 1, 1, 2,
     1          2, 2, 2, 2, 2, 2 ,3, 3, 3, 4, 4, 4, 4, 4, 5, 6  /

      DATA (ALPHA(ii), ii=35,39) / 25, 25, 25, 15, 20 /
            DATA (BETA(ii), ii=35,42) / 325, 300, 300,
275, 275, 0.3, 0.3,
     1         0.3 /
            DATA (GAMMA(ii), ii=35,39) / 1.16, 1.19,
1.19, 1.25, 1.22 /
            DATA (EPSLON(ii), ii=35,39) / 1., 1., 1., 1.,
1. /
            DATA (SMALLA(ii), ii=40,42) / 3.5, 3.5, 3. /
            DATA (SMALLB(ii), ii=40,42) / 0.875, 0.925,
0.875 /
            DATA (BIGA(ii), ii=40,42) / 0.7, 0.7, 0.7 /
            DATA (BIGB(ii), ii=40,42) / 0.3, 0.3, 1.0 /
            DATA (BIGC(ii), ii=40,42) / 10.0, 10.0, 12.5 /
            DATA (BIGD(ii), ii=40,42) / 275, 275, 275 /

      COMMON/KONIT/KON,DELT,IGOOD

      SAVE ICALL
            DATA ICALL/0/
            ICALL=ICALL+1
            IF(ICALL.EQ.1) WRITE(11,899)
  899 FORMAT(6X,'CO2     2.0      1 JUNE     2005',6X,
     X'CALCULATE SPECIFIC DENSITY OF CO2')

            IF(PCX.LT..1D6)THEN
              DC=0.D0
              print *,'returning DC = 0, pcx =',pcx
              pause
              RETURN
            END IF

C     Convert temperature from degrees C to K:
            T   = TX + 2.7315D+02
C
C           %%%%%%%%%%%%%%%%%%%%%%%%%%
CRITICAL                              RANGE
%%%%%%%%%%%%%%%%%%%%%%%%%%%%%%%%%%
C
C     Calculate vapor pressure (Eq. 3.13: Span and Wagner)
C
C
C IF THE TEMPERATURE IS SMALLER THAN THE
CRITICAL TEMPERATURE
C THE DENSITY OF THE SATURATED VAPOR IS
CALCULATED USING MODIFIED GAS LAW
```

```
            IF (T.LT.TC) THEN

      DATA      (CRITICAL_VAPOR_PRESSURE_A(ii),
ii=1,4) / -7.0602087,
     1   1.9391218, -1.6463597, -3.2995634 /
      DATA      (CRITICAL_VAPOR_PRESSURE_T(ii),
ii=1,4) / 1.0, 1.5,
     1   2.0, 4.0 /

              LN_P_SAT_CO2 = 0

            DO 1500 i = 1,4
       LN_P_SAT_CO2      =      LN_P_SAT_CO2      +
CRITICAL_VAPOR_PRESSURE_A(i)
     1                  *      (1      -      T      /
TC)**CRITICAL_VAPOR_PRESSURE_T(i)
 1500    CONTINUE

            P_SAT_CO2 = PC * DEXP(TC / T *
LN_P_SAT_CO2)
C
C    Saturated liquid density (Eq. 3.14: Span and Wagner)
C
       DATA      (CRITICAL_LIQUID_DENSITY_A(ii),
ii=1,4) / 1.9245108,
     1   -0.62385555, -0.32731127, 0.39245142 /
       DATA      (CRITICAL_LIQUID_DENSITY_T(ii),
ii=1,4) / 0.340,
     1   0.5, 1.6666666667, 1.833333333 /

       LN_LIQUID_CO2 = 0

       DO 1501 i = 1,4
        LN_LIQUID_CO2      =      LN_LIQUID_CO2      +
CRITICAL_LIQUID_DENSITY_A(i)
     1                  *      (1      -      T      /
TC)**CRITICAL_LIQUID_DENSITY_T(i)
 1501    CONTINUE

        D_LIQUID_CO2      =      DCC      *
DEXP(LN_LIQUID_CO2)
C
C    Saturated vapor density (Eq. 3.15: Span and Wagner)
C
       DATA      (CRITICAL_VAPOR_DENSITY_A(ii),
ii=1,5) / -1.7074879,
     1   -0.82274670, -4.6008549, -10.111178, -29.742252 /
       DATA      (CRITICAL_VAPOR_DENSITY_T(ii),
ii=1,5) / 0.340,
     1   0.5, 1.0, 2.3333333333, 4.6666666667 /

       LN_VAP_CO2 = 0

       DO 1502 i = 1,5
        LN_VAP_CO2      =      LN_VAP_CO2      +
CRITICAL_VAPOR_DENSITY_A(i)
     1                  *      (1      -      T      /
TC)**CRITICAL_VAPOR_DENSITY_T(i)
 1502    CONTINUE

       D_VAPOR_CO2 = DCC * DEXP(LN_VAP_CO2)

C
C    INITIAL APPROXIMATION

       IF (PCX.GE.P_SAT_CO2) THEN

C IN CASE PRESSURE IS GREATER THAN VAPOR
PRESSURE, THIS WILL CALCULATE
C THE DENSITY OF THE SATURATED LIQUID

         DC = D_LIQUID_CO2

       ELSE

C IN CASE PRESSURE IS LESS THAN VAPOR
PRESSURE, THIS WILL CALCULATE
C THE DENSITY OF THE SATURATED VAPOR IS
CALCULATED USING IDEAL GAS LAW

         DC = PCX / (R * T)

       ENDIF

      ELSE

C IF THE TEMPERATURE IS GREATER THAN THE
CRITICAL TEMPERATURE
C THE DENSITY OF THE SATURATED VAPOR IS
CALCULATED USING MODIFIED GAS LAW

         DC = 1 / (30 + R * T / PCX)
       ENDIF

C AFTER MAKING INITIAL APPROXIAMTION
DEPENDING ON TEMPERATURE AND PRESSURE
C CONDITION THE ITERATION METHOD WAS
ADAPTED TO SWITCH THE PRIMARY
VARILABLES
C AT HERE

       KOUNT=0

        DO 1503 K=1,1000

        KOUNT = KOUNT + 1

        IF(KOUNT.GT.999) GO TO 5

C The calculation of tau and delta term

         SP_TAU = TC / T
         SP_DELTA = DC / DCC

C%%%%%%%%%%%%%%%%%%%%%%%%%%%%
%%%%%%%%%%%%%%%%%%%%%%%%%%%%
%%%%%%%%%%%%%%%%%%%%
C%      THE CALCULATION OF PHI_R_DELTA AND
PHI_R_DELTA_DELTA TERM      %%
C%                (TABLE 32 IN SPAN AND WAGNER,
1996)              %%
C%%%%%%%%%%%%%%%%%%%%%%%%%%%%
%%%%%%%%%%%%%%%%%%%%%%%%%%%%
%%%%%%%%%%%%%%%%%%%%

C Calculation of first term in PHI_R and PHI_R_DELTA

       PHI_R_FIR_DELTA = 0
       PHI_R_FIR_DELTA_DELTA = 0

      DO 1504 i=1,7

        PHI_R_FIR_DELTA_TERM = NN(i) * D(i) *
SP_DELTA**(D(i)-1)
     1 * SP_TAU**TT(i)

        PHI_R_FIR_DELTA_DELTA_TERM = NN(i) *
D(i) * (D(i) - 1)
     1 * SP_DELTA**(D(i) - 2) * SP_TAU**TT(i)
```

```
      PHI_R_FIR_DELTA = PHI_R_FIR_DELTA +
PHI_R_FIR_DELTA_TERM

      PHI_R_FIR_DELTA_DELTA                =
PHI_R_FIR_DELTA_DELTA
   1 + PHI_R_FIR_DELTA_DELTA_TERM

 1504 CONTINUE

      PHI_R_FIR_DELTA = PHI_R_FIR_DELTA
      PHI_R_FIR_DELTA_DELTA                =
PHI_R_FIR_DELTA_DELTA

C Calculation of second term in PHI_R and
PHI_R_DELTA

      PHI_R_SEC_DELTA = 0
      PHI_R_SEC_DELTA_DELTA = 0

      DO 1505 i = 8,34

       PHI_R_SEC_DELTA_TERM = NN(i) * DEXP(-
SP_DELTA**C(i))
   1 * (SP_DELTA**(D(i) - 1) * SP_TAU**TT(i)
   2 * (D(i)- C(i) * SP_DELTA**C(i)))

       PHI_R_SEC_DELTA_DELTA_TERM = NN(i) *
DEXP(-SP_DELTA**C(i))
   1 * (SP_DELTA**(D(i) - 2) * SP_TAU**TT(i)
   2 * ((D(i)-C(i) * SP_DELTA**C(i)) * (D(i)-1-C(i) *
SP_DELTA**C(i))
   3 - C(i)**2 * SP_DELTA**C(i)))

       PHI_R_SEC_DELTA = PHI_R_SEC_DELTA +
PHI_R_SEC_DELTA_TERM;

       PHI_R_SEC_DELTA_DELTA                =
PHI_R_SEC_DELTA_DELTA
   1 + PHI_R_SEC_DELTA_DELTA_TERM

 1505 CONTINUE

       PHI_R_SEC_DELTA = PHI_R_SEC_DELTA
       PHI_R_SEC_DELTA_DELTA                =
PHI_R_SEC_DELTA_DELTA

C Calculation of third term in PHI_R and PHI_R_DELTA

      PHI_R_THI_DELTA = 0
      PHI_R_THI_DELTA_DELTA = 0

      DO 1506 i = 35,39

       PHI_R_THI_DELTA_TERM = NN(i) *
SP_DELTA**D(i)
   1 * SP_TAU**TT(i) * DEXP(-ALPHA(i)
   2 * (SP_DELTA - EPSLON(i))**2 - BETA(i) *
(SP_TAU - GAMMA(i))**2)
   3 * (D(i) / SP_DELTA - 2 * ALPHA(i) * (SP_DELTA
- EPSLON(i)))

       PHI_R_THI_DELTA_DELTA_TERM = NN(i) *
SP_DELTA**D(i)
   1       *       SP_TAU**TT(i)       *       DEXP(-
ALPHA(i)*(SP_DELTA - EPSLON(i))**2
   2 - BETA(i) * (SP_TAU - GAMMA(i))**2) * (-2 *
ALPHA(i)
   3 * SP_DELTA**D(i) + 4 * ALPHA(i)**2 *
SP_DELTA**D(i)
   4 * (SP_DELTA - EPSLON(i))**2 - 4 * D(i) *
ALPHA(i)
   5 * SP_DELTA**(D(i)-1) * (SP_DELTA -
EPSLON(i)) + D(i) * (D(i)-1)
   6 * SP_DELTA**(D(i)-2))

       PHI_R_THI_DELTA = PHI_R_THI_DELTA +
PHI_R_THI_DELTA_TERM;

       PHI_R_THI_DELTA_DELTA                =
PHI_R_THI_DELTA_DELTA
   1 + PHI_R_THI_DELTA_DELTA_TERM

 1506   CONTINUE

       PHI_R_THI_DELTA = PHI_R_THI_DELTA
       PHI_R_THI_DELTA_DELTA                =
PHI_R_THI_DELTA_DELTA

C Calculation of forth term in PHI_R and PHI_R_DELTA

      PHI_R_FOR_DELTA = 0
      PHI_R_FOR_DELTA_DELTA = 0

      DO 1507 i = 40,42

       GG = 1.0d00 / (2* BETA(i))

      THETA = 1 - SP_TAU + BIGA(i) * ((SP_DELTA-
1)**2)**(GG)

      BGPHI = DEXP(-BIGC(i) * (SP_DELTA-1)**2 -
BIGD(i)
   1 * (SP_TAU - 1)**2)

      D_BGPHI_D_DELTA = -2 * BIGC(i) *
(SP_DELTA-1) * BGPHI

      DD_BGPHI_DD_DELTA = (2 * BIGC(i) *
(SP_DELTA-1)**2 - 1) * 2
   1 * BIGC(i) * BGPHI

      BGDELTA = THETA**2 + BIGB(i) *
((SP_DELTA-1)**2)**SMALLA(i)

      D_BGDELTA_D_DELTA = (SP_DELTA-1) *
(BIGA(i)*THETA*2/BETA(i)
   1 * ((SP_DELTA-1)**2)**(GG-1) + 2 * BIGB(i) *
SMALLA(i)
   2 * ((SP_DELTA-1)**2)**(SMALLA(i)-1))

      DD_BGDELTA_DD_DELTA = 1/(SP_DELTA-1)
* D_BGDELTA_D_DELTA
   1 + (SP_DELTA - 1)**2 * (4 * BIGB(i) * SMALLA(i)
* (SMALLA(i) - 1)
   2 * ((SP_DELTA - 1)**2)**(SMALLA(i)-2) + 2 *
BIGA(i)**2
   3 * (1 / BETA(i))**2 * (((SP_DELTA - 1)**2)**(GG-
1))**2 + BIGA(i)
   4 * THETA * 4 / BETA(i) * (GG - 1) * ((SP_DELTA -
1)**2)**(GG-2))

      D_BGDELTA_D_DELTA_SMALLB             =
SMALLB(i) * BGDELTA**(SMALLB(i)-1)
   1 * D_BGDELTA_D_DELTA

      DD_BGDELTA_DD_DELTA_SMALLB           =
SMALLB(i)
   1          *          (BGDELTA**(SMALLB(i)-1)*
DD_BGDELTA_DD_DELTA + (SMALLB(i) -1)
```

```
   2        *        BGDELTA**(SMALLB(i)-2)        *
(D_BGDELTA_D_DELTA)**2)

      PHI_R_FOR_DELTA_TERM      =      NN(i)      *
(BGDELTA**SMALLB(i)
   1 * (BGPHI + SP_DELTA * D_BGPHI_D_DELTA)
   2     +     D_BGDELTA_D_DELTA_SMALLB     *
SP_DELTA * BGPHI)

      PHI_R_FOR_DELTA_DELTA_TERM = NN(i) *
(BGDELTA**SMALLB(i)
   1 * (2 * D_BGPHI_D_DELTA + SP_DELTA *
DD_BGPHI_DD_DELTA) + 2
   2 * D_BGDELTA_D_DELTA_SMALLB
   3 * (BGPHI + SP_DELTA * D_BGPHI_D_DELTA)
   4    +    DD_BGDELTA_DD_DELTA_SMALLB    *
SP_DELTA * BGPHI)

      PHI_R_FOR_DELTA = PHI_R_FOR_DELTA +
PHI_R_FOR_DELTA_TERM
      PHI_R_FOR_DELTA_DELTA                =
PHI_R_FOR_DELTA_DELTA
   1 + PHI_R_FOR_DELTA_DELTA_TERM

 1507   CONTINUE

      PHI_R_FOR_DELTA = PHI_R_FOR_DELTA
      PHI_R_FOR_DELTA_DELTA                =
PHI_R_FOR_DELTA_DELTA

C Sum of each term and this value will be PHI_R_DELTA
and PHI_R_DELTA_DELTA

      PHI_R_DELTA     =     PHI_R_FIR_DELTA     +
PHI_R_SEC_DELTA
   1 + PHI_R_THI_DELTA + PHI_R_FOR_DELTA

      PHI_R_DELTA_DELTA                        =
PHI_R_FIR_DELTA_DELTA
   1       +       PHI_R_SEC_DELTA_DELTA       +
PHI_R_THI_DELTA_DELTA
   2 + PHI_R_FOR_DELTA_DELTA

C From here, this part calculate density using iteration
method

      F = DC * (1 + SP_DELTA * PHI_R_DELTA)
      DF = 1 + 2 * SP_DELTA * PHI_R_DELTA +
SP_DELTA**2
   1 * PHI_R_DELTA_DELTA
      DEVIATION = F / (PCX / (R * T)) - 1

      IF (DABS(DEVIATION) .GE. 0.001) THEN

       DC = DC - 0.5 * PCX / (R * T) * DEVIATION /
(DF)

      ELSE

      GO TO 1508

      ENDIF

 1503   CONTINUE

 1508   DC = DC

      RETURN
C
C    Come here when no convergence:
C
 5    CONTINUE
      PRINT 6
 6                FORMAT('NO                CONVERGENCE                IN
SUBROUTINE CO2')
      print*, PCX,T,DC
      IGOOD = 2
      RETURN
      END

C********1*********2*********3*********4******
***5*********6*********7**

      SUBROUTINE FUGACITY(TX,PCX,DC,PHI,FC)
      IMPLICIT DOUBLE PRECISION(A-H,O-Z)
C
C       This subroutine calculates the specific fuagcity of
gaseous and
C       supercritical CO2 as a function of the pressure of
CO2 (PCX)
C       and temperature (TX) using a Span and Wagner
(1996) equation of state (EOS)
C      The primary variables adapted from temperature and
density, which was
C     calculated from subroutine CO2
C
C             Input:
C                      TX   = Temperature in degrees C
C                      PCX  = Pressure of CO2 in Pa
C             DC   = Specific density of CO2 in kg/m3
C
C             Output:
C             PHI = Fugacity coefficient of CO2 [-]
C
C             Constants:
C                   R      = Specific gas constant (188.9241
[J/kg*K])
C                = RM/M
C                     RM     = Molar gas constant (8.314510
[J/molK])
C               PC    = PRESSURE AT CRITICAL POINT (
7.3773 [MPa])
C                  TC     = TEMPERATURE AT CRITICAL
POINT (304.1282 [K])
C                 DCC    = DENSITY AT CRITICAL POINT
(467.6 [kg/m3])
C
      PARAMETER(TC   = 304.1282D0)
      PARAMETER(DCC  =  467.6D0)
      PARAMETER(PC   =  7.3773D+6)
      PARAMETER(R    = 188.9241)

C     TABLE 31 (Span and Wagner Coefficient, 1996)

      DOUBLE PRECISION NN(42), D(39), TT(39),
C(34), ALPHA(35:39)
   1, BETA(35:42), GAMMA(35:39), EPSLON(35:39),
SMALLA(40:42)
   2, SMALLB(40:42), BIGA(40:42), BIGB(40:42),
BIGC(40:42)
   3, BIGD(40:42)

       DATA NN / 0.38856823203161, 2.938547594274,
1 -  2
   1        -5.5867188534934,        -0.76753199592477,
0.31729005580416,        3 -  5
   2        0.54803315897767,        0.12279411220335,
2.165896154322,          6 -  8
   3        1.5841735109724,         -0.23132705405503,
0.058116916431436,       9 - 11
```

```
    4        -0.55369137205382,          0.48946615909422,   12 - 13
    5       -0.024275739843501,         0.062494790501678,   14 - 15
    6        -0.12175860225246,         -0.37055685270086,   16 - 17
    7       -0.016775879700426,         -0.11960736637987,   18 - 19
    8       -0.045619362508778,         0.035612789270346,   20 - 21
    9     -0.0074427727132052,      -0.0017395704902432,   22 - 23
    1     -0.021810121289527,           0.024332166559236,   24 - 25
    2       -0.037440133423463,          0.14338715756878,   26 - 27
    3        -0.13491969083286,         -0.02315122505348,   28 - 29
    4        0.012363125492901,         0.002105832197294,   30 - 31
    5     -0.00033958519026368,       0.0055993651771592,   32 - 33
    6      -0.00030335118055646,       -213.65488688320,   34 - 35
    7          26641.569149272,          -24027.212204557,   36 - 37
    8         -283.41603423999,           212.47284400179,   38 - 39
    9        -0.66642276540751,          0.72608632349897,   40 - 41
    1 0.055068668612842 /                                    42

      DATA D / 1, 1, 1, 1, 2, 2, 3, 1, 2, 4, 5, 5, 5, 6, 6, 6,   1  - 16
    1        1, 1, 4, 4, 4, 7, 8, 2, 3, 3, 5, 5, 6, 7, 8, 10, 4, 8,   17 - 34
    2      2, 2, 2, 3, 3 /                               35 - 39

      DATA TT / 0, 0.75, 1, 2, 0.75, 2, 0.75, 1.5, 1.5, 2.5, 0,     1 - 11
    1     1.5, 2, 0, 1, 2, 3, 6, 3, 6, 8, 6, 0, 7, 12, 16, 22, 24,   12 - 28
    2    16, 24, 8, 2, 28, 14, 1, 0, 1, 3, 3 /                  29 - 39

      DATA C / 0, 0, 0, 0, 0, 0, 0, 1, 1, 1, 1, 1, 1, 1, 1, 1, 2,   1 - 17
    1         2, 2, 2, 2, 2, 2 ,3, 3, 3, 4, 4, 4, 4, 4, 4, 5, 6  /  18 - 34

      DATA (ALPHA(ii), ii=35,39) / 25, 25, 25, 15, 20 /
      DATA  (BETA(ii), ii=35,42) / 325, 300, 300, 275, 275, 0.3, 0.3,
    1         0.3 /
      DATA  (GAMMA(ii), ii=35,39) / 1.16, 1.19, 1.19, 1.25, 1.22 /
      DATA (EPSLON(ii), ii=35,39) / 1., 1., 1., 1., 1. /
      DATA (SMALLA(ii), ii=40,42) / 3.5, 3.5, 3. /
      DATA (SMALLB(ii), ii=40,42) / 0.875, 0.925, 0.875 /
      DATA (BIGA(ii), ii=40,42) / 0.7, 0.7, 0.7 /
      DATA (BIGB(ii), ii=40,42) / 0.3, 0.3, 1.0 /
      DATA (BIGC(ii), ii=40,42) / 10.0, 10.0, 12.5 /
      DATA (BIGD(ii), ii=40,42) / 275, 275, 275 /
C
     SAVE ICALL
     DATA ICALL/0/
     ICALL=ICALL+1
     IF(ICALL.EQ.1) WRITE(11,899)
 899  FORMAT(6X,'FUGACITY  2.0               1  JUNE 2005',6X,
    X'CALCULATE  FUGACITY  COEFFICIENT  FOR SEPARATE PHASE CO2')
C
C  Convert temperature from degrees C to K:
       T   = TX + 2.7315D+02

C  The calculation of TAU and DELTA term

          SP_TAU = TC / T

          CALL CO2(TX,PCX,DC)

          SP_DELTA = DC / DCC

C%%%%%%%%%%%%%%%%%%%%%%%%%%%%%%%%%%%%%%%%%%%%%%%%%%%%%%%%%%%%%%%%%%%%%%
C%                   THE CALCULATION OF PHI_R AND PHI_R_DELTA TERM          %%
C%                    (TABLE 32 IN SPAN AND WAGNER, 1996)                %%
C%%%%%%%%%%%%%%%%%%%%%%%%%%%%%%%%%%%%%%%%%%%%%%%%%%%%%%%%%%%%%%%%%%%%%%

C Calculation of first term in PHI_R and PHI_R_DELTA

      PHI_R_FIR = 0
      PHI_R_FIR_DELTA = 0

       DO 1600 i=1,7
        PHI_R_FIR_TERM = NN(i) * SP_DELTA**(D(i)) * SP_TAU**TT(i)

        PHI_R_FIR_DELTA_TERM = NN(i) * D(i) * SP_DELTA**(D(i)-1)
    1 * SP_TAU**TT(i)

        PHI_R_FIR = PHI_R_FIR + PHI_R_FIR_TERM

        PHI_R_FIR_DELTA = PHI_R_FIR_DELTA + PHI_R_FIR_DELTA_TERM
 1600    CONTINUE

C  Calculation  of  second  term  in  PHI_R  and  PHI_R_DELTA

      PHI_R_SEC = 0
      PHI_R_SEC_DELTA = 0

       DO 1601 i = 8,34
        PHI_R_SEC_TERM = NN(i) * SP_DELTA**(D(i)) * SP_TAU**TT(i)
    1 * DEXP(-SP_DELTA**C(i))

        PHI_R_SEC_DELTA_TERM = NN(i) * exp(-SP_DELTA**C(i))
    1 * (SP_DELTA**(D(i)-1) * SP_TAU**TT(i)
    2 * (D(i)- C(i) * SP_DELTA**C(i)))

        PHI_R_SEC = PHI_R_SEC + PHI_R_SEC_TERM

        PHI_R_SEC_DELTA = PHI_R_SEC_DELTA + PHI_R_SEC_DELTA_TERM
 1601    CONTINUE

C Calculation of third term in PHI_R and PHI_R_DELTA
```

```
      PHI_R_THI = 0
      PHI_R_THI_DELTA = 0

      DO 1602 i = 35,39

       PHI_R_THI_TERM = NN(i) * SP_DELTA**D(i)
* SP_TAU**TT(i)
   1 * DEXP(-ALPHA(i)*(SP_DELTA - EPSLON(i))**2
- BETA(i)
   2 * (SP_TAU-GAMMA(i))**2)

       PHI_R_THI_DELTA_TERM = NN(i) *
SP_DELTA**D(i) * SP_TAU**TT(i)
   1 * DEXP(-ALPHA(i)*(SP_DELTA - EPSLON(i))**2
- BETA(i)
   2 * (SP_TAU-GAMMA(i))**2) * (D(i) / SP_DELTA -
2 * ALPHA(i)
   3 * (SP_DELTA-EPSLON(i)))

       PHI_R_THI = PHI_R_THI + PHI_R_THI_TERM

       PHI_R_THI_DELTA = PHI_R_THI_DELTA +
PHI_R_THI_DELTA_TERM

 1602   CONTINUE

C% Calculation of forth term in PHI_R and
PHI_R_DELTA

      PHI_R_FOR = 0
      PHI_R_FOR_DELTA = 0

      DO 1603 i = 40,42

       GG = 1.0d00 / (2* BETA(i))

       THETA = 1 - SP_TAU + BIGA(i) * ((SP_DELTA-
1)**2)**(GG)

       BGPHI = DEXP(-BIGC(i) * (SP_DELTA-1)**2 -
BIGD(i)
   1 * (SP_TAU - 1)**2)

       D_BGPHI_D_DELTA = -2 * BIGC(i) *
(SP_DELTA - 1) * BGPHI

       BGDELTA = THETA**2 + BIGB(i) *
((SP_DELTA-1)**2)**SMALLA(i)

       D_BGDELTA_D_DELTA = (SP_DELTA-1) *
(BIGA(i) * THETA * 2
   1 / BETA(i) * ((SP_DELTA-1)**2)**(GG - 1) + 2 *
BIGB(i)
   2 * SMALLA(i) * ((SP_DELTA-
1)**2)**(SMALLA(i)-1))

       D_BGDELTA_D_DELTA_SMALLB =
SMALLB(i) * BGDELTA**(SMALLB(i)-1)
   1 * D_BGDELTA_D_DELTA

       PHI_R_FOR_TERM=NN(i) *
BGDELTA**SMALLB(i) * SP_DELTA * BGPHI
       PHI_R_FOR_DELTA_TERM = NN(i) *
(BGDELTA**SMALLB(i)
   1 * (BGPHI + SP_DELTA *
D_BGPHI_D_DELTA)+D_BGDELTA_D_DELTA_SM
ALLB
   2 * SP_DELTA * BGPHI)

       PHI_R_FOR = PHI_R_FOR + PHI_R_FOR_TERM
       PHI_R_FOR_DELTA = PHI_R_FOR_DELTA +
PHI_R_FOR_DELTA_TERM

 1603   CONTINUE

C% SUM OF EACH TERM AND THIS VALUE WILL
BE PHI_R AND PHI_R_DELTA

      PHI_R = PHI_R_FIR + PHI_R_SEC + PHI_R_THI
+ PHI_R_FOR
      PHI_R_DELTA = PHI_R_FIR_DELTA +
PHI_R_SEC_DELTA
   1 + PHI_R_THI_DELTA + PHI_R_FOR_DELTA

C %%%%% Calculate fugacity coefficient (PHI) %%%%

      PHI = DEXP( PHI_R + SP_DELTA *
PHI_R_DELTA
   1 - DLOG(1 + SP_DELTA * PHI_R_DELTA))

C %%%%% Calculate fugacity (FC) %%%%

      FC = PHI * PCX

    RETURN
    END


C********1*********2*********3*********4******
***5*********6*********7**
    SUBROUTINE ENTHALPY(TX,PCX,DC,H)
    IMPLICIT DOUBLE PRECISION(A-H,O-Z)
C
C       This subroutine calculates the specific enthalpy of
gaseous and
C       supercritical CO2 as a function of the pressure of
CO2 (PCX)
C       and temperature (TX) using a Span and Wagner
(1996) equation of state (EOS)
C       The primary variables adapted from temperature and
density, which was
C     calculated from subroutine CO2
C
C             Input:
C                     TX   = Temperature in degrees C
C                     PCX  = Pressure of CO2 in Pa
C             DC   = Specific density of CO2 in kg/m3
C
C             Output:
C                     H      = Molar enthalpy of CO2 in
J/kg
C
C             Constants:
C                  R      = Specific gas constant (188.9241
[J/kg*K])
C                = RM/M
C                    RM     = Molar gas constant (8.314510
[J/molK])
C               PC    = PRESSURE AT CRITICAL POINT (
7.3773 [MPa])
C                    TC    = TEMPERATURE AT CRITICAL
POINT (304.1282 [K])
C                   DCC   = DENSITY AT CRITICAL POINT
(467.6 [kg/m3])
C
    PARAMETER(TC   = 304.1282D0)
    PARAMETER(DCC  = 467.6D0)
    PARAMETER(PC   = 7.3773D+6)
    PARAMETER(R    = 188.9241)
```

```
C    TABLE 31 (Span and Wagner Coefficient, 1996)
     DOUBLE PRECISION NN(42), D(39), TT(39),
C(34), ALPHA(35:39)
    1, BETA(35:42), GAMMA(35:39), EPSLON(35:39),
SMALLA(40:42)
    2, SMALLB(40:42), BIGA(40:42), BIGB(40:42),
BIGC(40:42)
    3, BIGD(40:42), A_ZERO(8), THETA_ZERO(8)

       DATA NN / 0.38856823203161, 2.938547594274,
1 - 2
    1      -5.5867188534934,      -0.76753199592477,
0.31729005580416,        3 - 5
    2      0.54803315897767,      0.12279411220335,
2.165896154322,        6 - 8
    3      1.5841735109724,       -0.23132705405503,
0.058116916431436,        9 - 11
    4      -0.55369137205382,     0.48946615909422,
12 - 13
    5      -0.024275739843501,    0.062494790501678,
14 - 15
    6      -0.12175860225246,     -0.37055685270086,
16 - 17
    7      -0.016775879700426,    -0.11960736637987,
18 - 19
    8      -0.045619362508778,    0.035612789270346,
20 - 21
    9      -0.0074427727132052,   -0.0017395704902432,
22 - 23
    1      -0.021810121289527,    0.024332166559236,
24 - 25
    2      -0.037440133423463,    0.14338715756878,
26 - 27
    3      -0.13491969083286,     -0.02315122505348,
28 - 29
    4      0.012363125492901,     0.002105832197294,
30 - 31
    5      -0.00033958519026368,  0.0055993651771592,
32 - 33
    6      -0.00030335118055646,  -213.65488688320,
34 - 35
    7      26641.569149272,       -24027.212204557,
36 - 37
    8      -283.41603423999,      212.47284400179,
38 - 39
    9      -0.66642276540751,     0.72608632349897,
40 - 41
    1 0.055068668612842 /                        42

      DATA D / 1, 1, 1, 1, 2, 2, 3, 1, 2, 4, 5, 5, 5, 6, 6, 6,
1 - 16
    1    1, 1, 4, 4, 4, 7, 8, 2, 3, 3, 5, 5, 6, 7, 8, 10, 4, 8,
17 - 34
    2    2, 2, 2, 3, 3 /                        35 - 39

      DATA TT / 0, 0.75, 1, 2, 0.75, 2, 0.75, 1.5, 1.5, 2.5,
0,    1 - 11
    1    1.5, 2, 0, 1, 2, 3, 6, 3, 6, 8, 6, 0, 7, 12, 16, 22, 24,
12 - 28
    2    16, 24, 8, 2, 28, 14, 1, 0, 1, 3, 3 /          29 -
39

      DATA C / 0, 0, 0, 0, 0, 0, 0, 1, 1, 1, 1, 1, 1, 1, 1, 1, 2,
1 - 17
    1        2, 2, 2, 2, 2, 2 ,3, 3, 3, 4, 4, 4, 4, 4, 4, 5, 6  /  18
- 34

      DATA (ALPHA(ii), ii=35,39) / 25, 25, 25, 15, 20 /
```

```
       DATA (BETA(ii), ii=35,42) / 325, 300, 300, 275,
275, 0.3, 0.3,
    1       0.3 /
       DATA (GAMMA(ii), ii=35,39) / 1.16, 1.19, 1.19,
1.25, 1.22 /
       DATA (EPSLON(ii), ii=35,39) / 1., 1., 1., 1., 1. /
       DATA (SMALLA(ii), ii=40,42) / 3.5, 3.5, 3. /
       DATA (SMALLB(ii), ii=40,42) / 0.875, 0.925, 0.875
/
       DATA (BIGA(ii), ii=40,42) / 0.7, 0.7, 0.7 /
       DATA (BIGB(ii), ii=40,42) / 0.3, 0.3, 1.0 /
       DATA (BIGC(ii), ii=40,42) / 10.0, 10.0, 12.5 /
       DATA (BIGD(ii), ii=40,42) / 275, 275, 275 /

C  TABLE 27 (Span and Wagner Coefficient, 1996)

       DATA (A_ZERO(ii), ii=1,8) / 8.37304456, -
3.70454304
    1, 2.50000000, 1.99427042, 0.62105248, 0.41195293,
1.04028922
    2, 0.08327678 /
       DATA (THETA_ZERO(ii), ii=1,8) / 0, 0, 0,
3.15163, 6.11190
    1, 6.77708, 11.32384, 27.08792 /
C
    SAVE ICALL
    DATA ICALL/0/
    ICALL=ICALL+1
    IF(ICALL.EQ.1) WRITE(11,899)
 899 FORMAT(6X,'ENTHALPY 2.0          1 JUNE
2005',6X,
   X'CALCULATE MOLAR ENTHALPY OF
SEPARATE PHASE CO2')

C  Convert temperature from degrees C to K:
       T   = TX + 2.7315D+02

C The calculation of TAU and DELTA term

       SP_TAU = TC / T

       CALL CO2(TX,PCX,DC)

       SP_DELTA = DC / DCC

C%%%%%%%%%%%%%%%%%%%%%%%%%%
%%%%%%%%%%%%%%%%%%%%%%%%%%%
%%%%%%%%%%%%%%%
C%              THE CALCULATION OF
PHI_TAU_ZERO              %%
C%          (Eq. 6.3 IN SPAN AND WAGNER, 1996)
%%
C%%%%%%%%%%%%%%%%%%%%%%%%%%
%%%%%%%%%%%%%%%%%%%%%%%%%%%
%%%%%%%%%%%%%%%

       PHI_TAU_ZERO = 0

       DO 1701 i=4,8

        PHI_TAU_ZERO_TERM = A_ZERO(i) *
THETA_ZERO(i)
    1 * ((1 - DEXP(-1 * THETA_ZERO(i) *
SP_TAU))**(-1) - 1)

        PHI_TAU_ZERO = PHI_TAU_ZERO +
PHI_TAU_ZERO_TERM

 1701  CONTINUE
```

```
        PHI_TAU_ZERO = A_ZERO(2) + A_ZERO(3) / SP_TAU + PHI_TAU_ZERO

C%%%%%%%%%%%%%%%%%%%%%%%%%%%%%%%%%%%%%%%%%%%%%%%%%%%%%%%%%%%%%%%%%%%%
C%          THE CALCULATION  OF PHI_R_DELTA AND PHI_R_TAU TERM        %%
C%                (TABLE 32 IN SPAN AND WAGNER, 1996)                %%
C%%%%%%%%%%%%%%%%%%%%%%%%%%%%%%%%%%%%%%%%%%%%%%%%%%%%%%%%%%%%%%%%%%%%

C Calculation of first term in PHI_R_DELTA and PHI_R_TAU

       PHI_R_FIR_DELTA = 0
       PHI_R_FIR_TAU = 0

       DO 1702 i=1,7

        PHI_R_FIR_DELTA_TERM = NN(i) * D(i) * SP_DELTA**(D(i)-1)
    1 * SP_TAU**TT(i)
        PHI_R_FIR_TAU_TERM = NN(i) * TT(i) * SP_DELTA**(D(i))
    1 * SP_TAU**(TT(i)-1)

        PHI_R_FIR_DELTA = PHI_R_FIR_DELTA + PHI_R_FIR_DELTA_TERM

        PHI_R_FIR_TAU = PHI_R_FIR_TAU + PHI_R_FIR_TAU_TERM

 1702   CONTINUE

C Calculation of second term in PHI_R_DELTA and PHI_R_TAU

       PHI_R_SEC_DELTA = 0
       PHI_R_SEC_TAU = 0

       DO 1703 i = 8,34

        PHI_R_SEC_DELTA_TERM = NN(i) * DEXP(-SP_DELTA**C(i))
    1 * (SP_DELTA**(D(i)-1) * SP_TAU**TT(i) * (D(i)-C(i)
    2 * SP_DELTA**C(i)))

        PHI_R_SEC_TAU_TERM = NN(i) * TT(i) * SP_DELTA**(D(i))
    1 * SP_TAU**(TT(i)-1) * DEXP(-SP_DELTA**C(i))

        PHI_R_SEC_DELTA = PHI_R_SEC_DELTA + PHI_R_SEC_DELTA_TERM

        PHI_R_SEC_TAU = PHI_R_SEC_TAU + PHI_R_SEC_TAU_TERM

 1703   CONTINUE

C Calculation of third term in PHI_R_DELTA and PHI_R_TAU

       PHI_R_THI_DELTA = 0
       PHI_R_THI_TAU = 0

       DO 1704 i = 35,39

        PHI_R_THI_DELTA_TERM = NN(i) * SP_DELTA**D(i)
    1 * SP_TAU**TT(i) * DEXP(-ALPHA(i) * (SP_DELTA - EPSLON(i))**2
    2 - BETA(i) * (SP_TAU - GAMMA(i))**2) * (D(i)/SP_DELTA - 2
    3 * ALPHA(i) * (SP_DELTA-EPSLON(i)))

        PHI_R_THI_TAU_TERM = NN(i) * SP_DELTA**D(i) * SP_TAU**TT(i)
    1 * DEXP(-ALPHA(i) * (SP_DELTA - EPSLON(i))**2 - BETA(i)
    2 * (SP_TAU - GAMMA(i))**2) * (TT(i) / SP_TAU - 2 * BETA(i)
    3 * (SP_TAU-GAMMA(i)))

        PHI_R_THI_DELTA = PHI_R_THI_DELTA + PHI_R_THI_DELTA_TERM

        PHI_R_THI_TAU = PHI_R_THI_TAU + PHI_R_THI_TAU_TERM

 1704   CONTINUE

C Calculation of forth term in PHI_R_DELTA and PHI_R_TAU

       PHI_R_FOR_DELTA = 0
       PHI_R_FOR_TAU = 0

       DO 1705 i = 40,42

        GG = 1.0d00 / (2* BETA(i))

        THETA = 1 - SP_TAU + BIGA(i) * ((SP_DELTA-1)**2)**(GG)

        BGPHI = DEXP(-BIGC(i) * (SP_DELTA-1)**2 - BIGD(i)
    1 * (SP_TAU - 1)**2)

        D_BGPHI_D_DELTA = -2 * BIGC(i) * (SP_DELTA-1) * BGPHI

        D_BGPHI_D_TAU = -2 * BIGD(i) * (SP_TAU-1) * BGPHI

        BGDELTA = THETA**2 + BIGB(i) * ((SP_DELTA-1)**2)**SMALLA(i)

        D_BGDELTA_D_DELTA = (SP_DELTA-1) * (BIGA(i) * THETA * 2
    1 / BETA(i) * ((SP_DELTA-1)**2)**(GG-1) + 2 * BIGB(i) * SMALLA(i)
    2 * ((SP_DELTA-1)**2)**(SMALLA(i)-1))

        D_BGDELTA_D_DELTA_SMALLB = SMALLB(i) * BGDELTA**(SMALLB(i)-1)
    1 * D_BGDELTA_D_DELTA

        D_BGDELTA_D_TAU_SMALLB = -2 * THETA * SMALLB(i)
    1 * BGDELTA**(SMALLB(i)-1)

        PHI_R_FOR_DELTA_TERM = NN(i) * (BGDELTA**SMALLB(i) * (BGPHI
    1 + SP_DELTA * D_BGPHI_D_DELTA) + D_BGDELTA_D_DELTA_SMALLB
    2 * SP_DELTA * BGPHI)
```

```
      PHI_R_FOR_TAU_TERM = NN(i) * SP_DELTA
     1 * (D_BGDELTA_D_TAU_SMALLB * BGPHI +
BGDELTA**SMALLB(i)
     2 * D_BGPHI_D_TAU)

      PHI_R_FOR_DELTA = PHI_R_FOR_DELTA +
PHI_R_FOR_DELTA_TERM
      PHI_R_FOR_TAU = PHI_R_FOR_TAU +
PHI_R_FOR_TAU_TERM

 1705   CONTINUE

C     Sum of each term and this value will be
PHI_R_DELTA and PHI_R_TAU

      PHI_R_DELTA = PHI_R_FIR_DELTA +
PHI_R_SEC_DELTA
     1 + PHI_R_THI_DELTA + PHI_R_FOR_DELTA

      PHI_R_TAU = PHI_R_FIR_TAU +
PHI_R_SEC_TAU + PHI_R_THI_TAU
     2 + PHI_R_FOR_TAU

C CALCULATE ETHALPY

      H = 1 * R * T * (1 + SP_TAU * (PHI_TAU_ZERO
+ PHI_R_TAU)
     1 + SP_DELTA * PHI_R_DELTA)+8.0924807D+05

      RETURN
      END
C********1*********2*********3*********4******
***5*********6*********7**
      SUBROUTINE H2O(TX,PCX,ro,at,t_1,pp,A)
      IMPLICIT DOUBLE PRECISION(A-H,O-Z)

C     Instead of using H2O thermodynamic properties from
International formulation
C       committee, the H2O subroutine was adapted from
Hill EOS (1990)to increase
C     the accuracy in SW EOSCO2 algorithms.
C     This EOS is also developed on the Helmholtz fuction.
Because the primary
C       variables of Hill's EOS ara Temperature and density,
The primary variables
C       are switched into temperature and pressure using
iteration method.
C
C             Input:
C                     TX   = Temperature in degrees C
C                     PCX  = Pressure of CO2 in Pa
C             Output:
C                     ro  = Density of water [kg/m3]
C
C             Constants:
C                     dcr = Density at the critical state
[kg/m3]
C                     tcr = Temperature at the critical
state [K]
C                     RGasH2O = Universal gas constant
in [J/g/K]
C
C           [P.G. Hill. A unified fundamental equation for
thermodynamic pro-
C       perties of H2O  J. Phys. Chem. Ref. Data, 1990, v.
19, N 5, pp. 1233-1274]
C
      PARAMETER(dcr = .322778)
      PARAMETER(tcr = 647.067)
      PARAMETER(RGasH2O = 4.61521937)

C     The coefficient of Hill' EOS

      PARAMETER(C001 = -.000034631815)
      PARAMETER(C002 = -.000030378112)
      PARAMETER(delta = 1.028667)
      PARAMETER(dlro0 = .23)
      PARAMETER(dlT0 = .05)

      PARAMETER(alpha = 80)
      PARAMETER(beta = 1)
      PARAMETER(gamma = 130)
      PARAMETER(dlta = 12)
      PARAMETER(nu = 4)

      DIMENSION C(8), A1(7,7), A2(7,12), A3(5,5),
A4(5,10)

      DATA C / 7.07501275112, -8.34240569963, -
0.364601380,
     +  -0.036897043, 0.003033815, 0.000390109,
0.113592870,
     + 2.413178500 /

      DO 1801 i = 1,7
        DO 1802 j = 1,7
          A1(i,j) = 0
 1802   CONTINUE
 1801 CONTINUE

        A1(4, 1) = .3384249125
        A1(5, 1) = -.07153393406
        A1(7, 1) = .0005493680814
        A1(3, 2) = .04933218501
        A1(6, 2) = -.02328491212
        A1(7, 2) = .002402095181
        A1(1, 3) = .7529422956
        A1(3, 3) = -2.28026007
        A1(2, 4) = 1.142004144
        A1(3, 4) = -2.619059624
        A1(5, 4) = .4395237702
        A1(6, 4) = -.03161046646
        A1(7, 4) = .0006814467692
        A1(1, 5) = -.3924227294
        A1(3, 5) = -.2738770648
        A1(4, 6) = -.01943443857
        A1(5, 6) = .003048860434
        A1(3, 7) = .003946510403

      DO 1803 i=1,7
        DO 1804 j=1,12
          A2(i,j) = 0
 1804   CONTINUE
 1803 CONTINUE

        A2(1, 1) = .2243610314
        A2(2, 1) = .1193250201
        A2(5, 1) = .06582959348
        A2(5, 2) = .1651430628
        A2(1, 3) = -2.178969357
        A2(2, 3) = .2674090542
        A2(3, 3) = .8647490995
        A2(1, 4) = -.1530432257
        A2(3, 4) = 2.059881454
        A2(6, 4) = -.4888628703
        A2(7, 4) = .1375328753
        A2(5, 5) = -.9015180666
        A2(6, 5) = -.1444258609
        A2(7, 5) = .1558046279
```

```
      A2(4, 6) = -2.740652563
      A2(6, 6) = .4983771706
      A2(4, 7) = -3.261978564
      A2(5, 7) = 1.609338784
      A2(1, 8) = .03484674963
      A2(2, 8) = -1.537646434
      A2(5, 8) = .2316225257
      A2(2, 9) = -1.419249232
      A2(3, 9) = .7969984635
      A2(5, 10) = .007510544627
      A2(1, 12) = .0005364384732

    DO 1805 i=1,5
      DO 1806 j=1,5
        A3(i, j) = 0
1806   CONTINUE
1805 CONTINUE
      A3(1, 1) = .6109381296
      A3(3, 1) = -.01906644459
      A3(5, 1) = .007976092188
      A3(1, 2) = 1.934466766
      A3(1, 3) = 1.921820547
      A3(3, 3) = -.04410105919
      A3(1, 4) = .6130354419
      A3(2, 4) = -.2855258689
      A3(5, 4) = .0252613708
      A3(2, 5) = -.2374074642
      A3(4, 5) = .03855866402
      A3(5, 5) = .00804167215

    DO 1808 i = 1,5
      DO 1809 j = 1,10
        A4(i, j) = 0
1809   CONTINUE
1808  CONTINUE

      A4(3, 1) = -16.35439033
      A4(1, 2) = -50.25818675
      A4(2, 4) = .164900304
      A4(1, 5) = -.8499893502
      A4(1, 9) = .008314382544
      A4(2, 9) = .0008781327858
      A4(2, 10) = .001537391213
      A4(3, 10) = -.0009016873786
      A4(5, 10) = .0003326628664

C  Convert temperature from degrees C to K:
      T   = TX + 2.7315D+02

C  Convert pressure from [Pa] to [Bar]:
      Pbar = PCX * 10 / 10**6

C HelmholtzCalculation:

      t_1 = -Tcr / T
      dlT = 1 + t_1
      stepro = 1

C From here, Iteration part

      KOUNT=0

      DO WHILE (DABS(stepro).GT.0.000001)

      KOUNT=KOUNT+1

      IF(KOUNT.GT.999) GO TO 5

       dlro = ro - 1
       dlAn = C001 + C002 * dlT
       dlAnT = C002
       dlAnTT = 0
       ksi = ((dlro / dlro0)**2 + (dlT / dlT0)**2)**0.5
       tmp = (ksi / delta)**4

      IF (tmp.GT.88) THEN
         Z = 1E+38
      ELSE IF (tmp.LT..01) THEN
         Z = tmp
      ELSE
         Z = EXP(tmp) - 1
      ENDIF

         tmp = -1 / Z

       IF (tmp.LT.-88) THEN
          exp1Z = 1.01E-38
       ELSE
          exp1Z = EXP(tmp)
       ENDIF

        FF = 1 - exp1Z

       IF (FF.EQ.0) THEN
          Fro = 0
          Froro = 0
          Frororo = 0
          FT = 0
          FTT = 0
          FroT = 0
          FroTT = 0
       ELSE
          Fksi = -4 / delta * exp1Z * (1 / Z + 1 / Z**2)
     +* (log(1 + Z))**(3 / 4)
          ksiro = dlro / ( ksi * dlro0**2 )
          ksiT = dlT / ksi / dlT0**2
          ksiroro = (1 / ksi - (dlro / dlro0)**2 / ksi**3) /
dlro0**2
          ksiTT = (1 / ksi - (dlT / dlT0)**2 / ksi**3) /
dlT0**2
          ksiroT = -dlro * dlT / ksi**3 / (dlro0 * dlT0)**2

          Fro = Fksi * ksiro
          Fksiksi = -12 / delta**2 * exp1Z * (1 / Z + 1 /
Z**2)
     +* (log(1 + Z))**0.5
          Fksiksi = Fksiksi * (1 + 4 / 3 * (1 / Z**2 - 1 / Z - 1)
     + * log(1 + Z))
          Froro = Fksiksi * ksiro**2 + Fksi * ksiroro
          Frororo = 0
          FT = Fksi * ksiT
          FTT = Fksiksi * ksiT**2 + Fksi * ksiTT
          FroT = Fksiksi * ksiro * ksiT + Fksi * ksiroT
          FroTT = 0
       ENDIF

        A0 = 0
        A0T = 0
        A0TT = 0

       DO 1810 i = 1,6
          A0 = A0 + C(i) * (-1*t_1)**(2 - i)
          A0T = A0T - C(i) * (2 - i) * (-1*t_1)**(1 - i)
          A0TT = A0TT + C(i) * (2 - i) * (1 - i) * (-
1*t_1)**(-i)
 1810  CONTINUE

          A0 = A0 + (C(7) * t_1 + C(8)) * log(-1*t_1)
          A0T = A0T + C(7) * (1 + log(-1*t_1)) + C(8) / t_1
          A0TT = A0TT + C(7) / t_1 - C(8) / t_1**2
```

```
      IF (ro .LT. .00002) THEN
         UnitMinusE = ro**2
      ELSE
         UnitMinusE = 1 - e
      ENDIF

         tmp = -alpha * dlT - beta * dlro - gamma * dlT**2
     +- dlta * dlro**2
         e = EXP(-ro**2)
         Ero = -2 * ro * e
         Eroro = -2 * e - 2 * ro * Ero
         Erororo = -4 * Ero - 2 * ro * Eroro

      IF (tmp .GT. 88) THEN
        G = 1.01E+38
      ELSE IF (tmp .LT. -88) THEN
        G = -1.01E-38
      ELSE
        G = EXP(tmp)
      ENDIF

      Gro = G * (-beta - 2 * dlta * dlro)
      Groro = Gro * (-beta - 2 * dlta * dlro) - 2 * dlta * G
      Grororo = Groro * (-beta - 2 * dlta * dlro) - 2 * dlta *
Gro
      GT = G * (-alpha - 2 * gamma * dlT)
      GTT = GT * (-alpha - 2 * gamma * dlT) - 2 * gamma
* G
      GroT = GT * (-beta - 2 * dlta * dlro)
      GroroT = GroT * (-beta - 2 * dlta * dlro) - 2 * dlta *
GT
      GroTT = GTT * (-beta - 2 * dlta * dlro)

      H = exp(-nu * (t_1 + 3))
      HT = -nu * H
      HTT = nu**2 * H

      W1 = 0
      W1ro = 0
      W1roro = 0
      W1rororo = 0
      W1roroT = 0
      W1T = 0
      W1TT = 0
      W1roT = 0
      W1roTT = 0

C%%%%%%%% The calculation of R1 function in
Appendix D %%%%%%%%%%%%%

      DO 1811 i = 1,7
        R1 = UnitMinusE * ro**(i - 2)
        R1ro = UnitMinusE * (i - 2) * ro**(i - 3) - Ero
     +* ro**(i - 2)
        R1roro = UnitMinusE * (i - 2) * (i - 3) * ro**(i - 4)
     +- 2 * Ero * (i - 2) * ro**(i - 3) - Eroro * ro**(i - 2)
        R1rororo = UnitMinusE * (i - 2) * (i - 3) * (i - 4)
     +* ro**(i - 5) - 3 * Ero * (i - 2) * (i - 3) * ro**(i - 4)
        R1rororo = R1rororo - 3 * Eroro * (i - 2) * ro**(i -
3)
     +- Erororo * ro**(i - 2)

C%%%%%%%% IF R(2), follow below claculation
%%%%%%%%%%%%%%%%%%

        IF (i.EQ.2) THEN
          R1 = UnitMinusE * log(ro) - ro**2 * log(ro) +
ro**2 / 2
          R1ro = UnitMinusE / ro - Ero * log(ro) - 2 * ro *
log(ro)
          R1roro = -UnitMinusE / ro**2 - 2 * Ero / ro -
Eroro
     +* log(ro) - 2 * log(ro) - 2
          R1rororo = 2 * UnitMinusE / ro**3 + 3 * Ero /
ro**2
          R1rororo = R1rororo - 3 * Eroro / ro - Erororo *
log(ro)
     +- 2 / ro
        ENDIF

C%%%%%%%% The calculation of T1 and W1 function
in Appendix D %%%%%%%%%%%%%

        DO 1812 j = 1,7
          T1 = t_1**(j - 1)
          T1T = (j - 1) * t_1**(j - 2)
          T1TT = (j - 1) * (j - 2) * t_1**(j - 3)
          W1 = W1 + A1(i, j) * R1 * T1
          W1ro = W1ro + A1(i, j) * R1ro * T1
          W1roro = W1roro + A1(i, j) * R1roro * T1
          W1roroT = W1roroT + A1(i, j) * R1roro * T1T
          W1rororo = W1rororo + A1(i, j) * R1rororo * T1
          W1T = W1T + A1(i, j) * R1 * T1T
          W1TT = W1TT + A1(i, j) * R1 * T1TT
          W1roT = W1roT + A1(i, j) * R1ro * T1T
          W1roTT = W1roTT + A1(i, j) * R1ro * T1TT
 1812   CONTINUE
 1811 CONTINUE
      W2 = 0
      W2ro = 0
      W2roro = 0
      W2rororo = 0
      W2roroT = 0
      W2T = 0
      W2TT = 0
      W2roT = 0
      W2roTT = 0

C%%%%%%%% The calculation of R2 function in
Appendix D %%%%%%%%%%%%%

      DO 1813 i = 1,7
        R2 = ro**i
        R2ro = i * ro**(i - 1)
        R2roro = i * (i - 1) * ro**(i - 2)
        R2rororo = i * (i - 1) * (i - 2) * ro**(i - 3)

C%%%%%%%% The calculation of T1 and W2 function
in Appendix D %%%%%%%%%%%%%

        DO 1814 j = 1,12
          T1 = t_1**(j - 1)
          T1T = (j - 1) * t_1**(j - 2)
          T1TT = (j - 1) * (j - 2) * t_1**(j - 3)
          W2 = W2 + A2(i, j) * R2 * T1
          W2ro = W2ro + A2(i, j) * R2ro * T1
          W2roro = W2roro + A2(i, j) * R2roro * T1
          W2roroT = W2roroT + A2(i, j) * R2roro * T1T
          W2rororo = W2rororo + A2(i, j) * R2rororo * T1
          W2T = W2T + A2(i, j) * R2 * T1T
          W2TT = W2TT + A2(i, j) * R2 * T1TT
          W2roT = W2roT + A2(i, j) * R2ro * T1T
          W2roTT = W2roTT + A2(i, j) * R2ro * T1TT

 1814   CONTINUE
 1813 CONTINUE

      W3 = 0
```

```
      W3ro = 0
      W3roro = 0
      W3rororo = 0
      W3roroT = 0
      W3T = 0
      W3TT = 0
      W3roT = 0
      W3roTT = 0

C%%%%%%%% The calculation R3 function in
Appendix D %%%%%%%%%%%%

      DO 1815 i = 1,5
        R3 = ro**(i + 1)
        R3ro = (i + 1) * ro**i
        R3roro = (i + 1) * i * ro**(i - 1)
        R3rororo = (i + 1) * i * (i - 1) * ro**(i - 2)

C%%%%%%%% The calculation of T2 and W3 function
in Appendix D %%%%%%%%%%%%

        DO 1816 j = 1,5
          T2 = t_1**(j + 1)
          T2T = (j + 1) * t_1**j
          T2TT = (j + 1) * j * t_1**(j - 1)
          W3 = W3 + A3(i, j) * R3 * T2
          W3ro = W3ro + A3(i, j) * R3ro * T2
          W3roro = W3roro + A3(i, j) * R3roro * T2
          W3roroT = W3roroT + A3(i, j) * R3roro * T2T
          W3rororo = W3rororo + A3(i, j) * R3rororo * T2
          W3T = W3T + A3(i, j) * R3 * T2T
          W3TT = W3TT + A3(i, j) * R3 * T2TT
          W3roT = W3roT + A3(i, j) * R3ro * T2T
          W3roTT = W3roT + A3(i, j) * R3ro * T2TT
1816      CONTINUE
1815  CONTINUE

      W4 = 0
      W4ro = 0
      W4roro = 0
      W4rororo = 0
      W4roroT = 0
      W4T = 0
      W4TT = 0
      W4roT = 0
      W4roTT = 0

C%%%%%%%% The calculation of R1 function in
Appendix D %%%%%%%%%%%%

      DO 1817 i = 1,5
        R1 = UnitMinusE * ro**(i - 2)
        R1ro = UnitMinusE * (i - 2) * ro**(i - 3) - Ero
     +* ro**(i - 2)
        R1roro = UnitMinusE * (i - 2) * (i - 3) * ro**(i - 4) -
2
     +* Ero * (i - 2) * ro**(i - 3) - Eroro * ro**(i - 2)
        R1rororo = UnitMinusE * (i - 2) * (i - 3) * (i - 4)
     +* ro**(i - 5) - 3 * Ero * (i - 2) * (i - 3) * ro**(i - 4)
        R1rororo = R1rororo - 3 * Eroro * (i - 2)
     +* ro**(i - 3) - Erororo * ro**(i - 2)

C%%%%%%%% IF R(2), follow below claculation
%%%%%%%%%%%%%%%%%%%%

        IF (i.EQ.2) THEN
          R1 = UnitMinusE * log(ro) - ro**2 * log(ro) +
ro**2 / 2
          R1ro = UnitMinusE / ro - Ero * log(ro) - 2 * ro *
log(ro)
          R1roro = -UnitMinusE / ro**2 - 2 * Ero / ro -
Eroro
     +* log(ro) - 2 * log(ro) - 2
          R1rororo = 2 * UnitMinusE / ro**3 + 3 * Ero /
ro**2
          R1rororo = R1rororo - 3 * Eroro / ro - Erororo *
log(ro)
     +- 2 / ro
        ENDIF

C%%%%%%%% The calculation of T1 and W4 function in
Appendix D %%%%%%%%%%%%

        DO 1818 j = 1,10
          T1 = t_1**(j - 1)
          T1T = (j - 1) * t_1**(j - 2)
          T1TT = (j - 1) * (j - 2) * t_1**(j - 3)
          W4 = W4 + A4(i, j) * R1 * T1
          W4ro = W4ro + A4(i, j) * R1ro * T1
          W4roro = W4roro + A4(i, j) * R1roro * T1
          W4roroT = W4roroT + A4(i, j) * R1roro * T1T
          W4rororo = W4rororo + A4(i, j) * R1rororo * T1
          W4T = W4T + A4(i, j) * R1 * T1T
          W4TT = W4TT + A4(i, j) * R1 * T1TT
          W4roT = W4roT + A4(i, j) * R1ro * T1T
          W4roTT = W4roTT + A4(i, j) * R1ro * T1TT
1818      CONTINUE
1817  CONTINUE
C********1*********2*********3*********4**********5*********6*********7**
      A = A0 + log(ro) + W1 + e * W2 + G * W3 + H *
W4 + FF * dlAn
      Aro = 1 / ro + W1ro + Ero * W2 + e * W2ro + Gro *
W3 + G
     +* W3ro
      Aro = Aro + H * W4ro + dlAn * Fro
      Aroro = -1 / ro**2 + W1roro + Eroro * W2 + 2 * Ero
* W2ro
      Aroro = Aroro + e * W2roro + Groro * W3 + 2 * Gro
* W3ro
     ++ G * W3roro
      Aroro = Aroro + H * W4roro + dlAn * Froro
      Arororo = 2 / ro ** 3 + W1rororo + Erororo * W2 + 3
* Eroro
     +* W2ro
      Arororo = Arororo + 3 * Ero * W2roro + e *
W2rororo
      Arororo = Arororo + Grororo * W3 + 3 * Groro *
W3ro + 3
     +* Gro * W3roro + G * W3rororo
      Arororo = Arororo + H * W4rororo + dlAn * Frororo
      AroroT = W1roroT + Eroro * W2T + 2 * Ero *
W2roT
      AroroT = AroroT + e * W2roroT + GroroT * W3 +
Groro * W3T
      AroroT = AroroT + 2 * GroT * W3ro + 2 * Gro *
W3roT
      AroroT = AroroT + GT * W3roro + G * W3roroT
      AroroT = AroroT + HT * W4roro + H * W4roroT
      AT = A0T + W1T + e * W2T + GT * W3 + G * W3T
+ HT * W4 + H
     +* W4T
      AT = AT + FT * dlAn + FF * dlAnT
      ATT = A0TT + W1TT + e * W2TT + GTT * W3 + 2
* GT * W3T + G
     +* W3TT
      ATT = ATT + HTT * W4 + 2 * HT * W4T + H *
W4TT
      ATT = ATT + FTT * dlAn + 2 * FT * dlAnT + FF *
dlAnTT
```

```
      AroT = W1roT + Ero * W2T + e * W2roT + GroT *
W3 + Gro * W3T
      AroT = AroT + GT * W3ro + G * W3roT + HT *
W4ro + H * W4roT
      AroT = AroT + dlAnT * Fro + dlAn * FroT
      AroTT = W1roTT + Ero * W2TT + e * W2roTT +
GroTT * W3 + GroT
     +* W3T
      AroTT = AroTT + GroT * W3T + Gro * W3TT +
GTT * W3ro + GT
     +* W3roT
      AroTT = AroTT + GT * W3roT + G * W3roTT +
HTT * W4ro + HT
     +* W4roT
      AroTT = AroTT + HT * W4roT + H * W4roTT

      pp = ro * ro * Aro
      dPdro = 2 * ro * Aro + ro * ro * Aroro

      dev = pp - Pbar / dcr / RGasH2O / T
      stepro = -dev / dPdro
      ro = ro + stepro

      IF (ro .GT. 9.2) THEN
        DO WHILE (ro .LT. 9.2)
          ro = ro / 3
        END DO
      ENDIF
      IF (ro .LT. 0) THEN
        ro = .05
      ENDIF

      END DO

      RETURN

 5    CONTINUE
      PRINT 6
 6                FORMAT('NO CONVERGENCE IN
SUBROUTINE CO2')
      print*, PCX,T,ro
      IGOOD = 2
      RETURN
      END


C********1*********2*********3*********4******
***5*********6*********7**
      SUBROUTINE HENRY(TX,PCX,FC,X1M)
      IMPLICIT DOUBLE PRECISION(A-H,K,M,O-Z)
C
C     This subroutine calculates the mass fraction of CO2
in the liquid
C      phase using an extended Henry's Law relationship
from Diamond and
C     Akinfiev (2003). The expression for Henry's Constant
is from the
C      virial-like equation of state Akinfiev and Diamond,
2003.The fugacity of CO2
C     are from Span and Wagner EOS (subroutine fugacity)
and the fugacity of H2O
C     are from Hill EOS (subroutine H2O)
C
C            Input:
C                        TX   = Temperature [degrees C]
C                        PCX  = Pressure of CO2 [Pa]
C                        PS   = Saturation pressure of water
[Pa]
C                        FC   = Fugacity of CO2 [Pa]
C
C            Output:
C                        X1M  = Mass fraction of CO2 in
liquid phase [-]
C
C            Constants:
C                        dcr = Density at the critical state
[kg/m3]
C                        Tcr = Temperature at the critical
state [K]
C            Pcr = Pressure at the critical state [bar]
C                        RGasH2O = Universal gas constant
in [J/g/K]
C            Trk = Temperature at the critical state [K]
C
C
C            Constants:
C                        XMWC = Molecular weight of CO2
[Kg/mol]
C                        MH2O = Molecular weight of H2O
[Kg/mol]
C            Scale = Scaling factor
C               G0H2Ogas = Gibbs's free energy of H2O at
steady state [J/mol]
C                SH2Ogas = Entropy of H2O at steady state
[J/mol]
C
C            Variables:
C                        T    = Temperature in K
C                        kH   = Henry's Coefficient in bars,
then Pa
C                        XCO2 = Mole fraction CO2 in
liquid phase [-]
C

      PARAMETER(dcr = 0.322778)
      PARAMETER(Tcr = 647.067)
      PARAMETER(Pcr = 220.46)
      PARAMETER(Trk = 298.15)

      PARAMETER(RgasJbar = 83.14410002)
      PARAMETER(RGasH2O = 4.61521937)
      PARAMETER(Rgascal = 1.987191683)
      PARAMETER(RgasJ = 8.314410002)

      PARAMETER(Coef1 = -9.3134)
      PARAMETER(Coef2 = 11.5477)
      PARAMETER(Scale = -.088)

      PARAMETER(G0H2Ogas = -228581.9)
      PARAMETER(SH2Ogas = 188.835)

      PARAMETER(MH2O = 18.0152)
      PARAMETER(aH2O = 27.057)
      PARAMETER(bH2OE3 = 17.584)
      PARAMETER(cH2OEmin5 = 2.7696)
      PARAMETER(dH2OE6 = -2.5097)
      PARAMETER(eH2OEmin1 = -2.7656)

      PARAMETER(XMWC = 4.40098D-02)

     DIMENSION asat(6),bsat(6)
C
     SAVE ICALL
     DATA ICALL/0/
     ICALL=ICALL+1
     IF(ICALL.EQ.1) WRITE(11,899)
  899  FORMAT(6X,'HENRY        2.0          1 JUNE
2005',6X,
    X'CALCULATE MASS FRACTION DISSOLVED
CO2 IN AQUEOUS PHASE')
```

```
C           Saul A., Wagner W. International Equations for
the Saturation
C         Properties of Ordinary Water Substances.
C         J. Phys. Chem. Ref. Data, 1987, v. 16, pp. 893-901

      DATA asat /-7.85823,1.83991,-11.7811,22.6705,-
15.9393,1.77516/
      DATA bsat /1.99206, 1.10123, -5.12506E-1, -
1.75263, -45.4485
     +, -6.75615E5/

C  Convert temperature from degrees C to K:
        T  = TX + 2.7315D+02

C  Convert pressure from [MPa] to [Bar]:
        Pbar = PCX * 10 / 10**6

C  FROM HERE, INITIAL APPROXIMATION


C  IF THE TEMPERATURE IS LESS THAN CRITICAL
TEMPERATUE (647.067), IT WILL
C  CACULATE VAPOR PRESSURE

      IF (T .LT. Tcr) THEN
        tausat = 1 - T / Tcr
        sum = asat(1) * tausat + asat(2) * tausat**1.5 +
asat(3)
     +* tausat**3
        sum = sum + asat(4) * tausat**3.5 + asat(5) *
tausat**4
     ++ asat(6) * tausat**7.5
        Psat = EXP(Tcr / T * sum) * Pcr
      ENDIF

      IF (Pbar.EQ.0) THEN
        Pbar = Psat
      ENDIF

C   IF THE PRESSURE IS LESS THAN THE VAPOR
PRESSURE, THE WATER WILL BOIL
C   THEREFORE, THE VOLUME OF VAPOR PHASE
WILL CALCULATE

      IF (Pbar .LT. Psat) THEN
        Vs = RgasJbar * T / Pbar
      ENDIF

C   IF THE PRESSURE IS EQUAL TO THE VAPOR
PRESSURE, IT WILL CALCULTE
C  THE THE DENSITY OF THE SATURATED LIQUID

      IF (Pbar.EQ.Psat) THEN
        sum = 1 + bsat(1) * tausat**(1/3) + bsat(2) *
tausat**(2/3)
        sum = sum + bsat(3) * tausat**(5/3) + bsat(4)
     +* tausat**(16/3)
        sum = sum + bsat(5) * tausat**(43/3) + bsat(6)
     +* tausat**(110/3)
        ro = sum
      ENDIF


      IF (Pbar .GT. Psat) THEN
        IF (Pbar .LE. 1000) THEN
          Vs = 116.271 - 1.03596 * T + 3.90561E-03 * T *
T
     +- 6.2842E-06 * T**3
          Vs = Vs + 3.7039E-09 * T**4
          ro = 18.0152 / Vs / dcr
        ENDIF

        IF (Pbar .LE. 2000) THEN
          Vs = 5.851212 + .0822269 * T - 1.99974E-04 * T
* T
     ++ 1.82853E-07 * T**3
          ro = 18.0152 / Vs / dcr
        ENDIF

        IF (Pbar .LE. 3000) THEN
          Vs = 23.666 - .04115 * T + .0000696 * T * T
     +- 1.462E-08 * T**3
          ro = 18.0152 / Vs / dcr
        ENDIF

        IF (Pbar .LE. 5000) THEN
          Vs = 13.956 + .002059 * T + 1.3935E-05 * T * T
          ro = 18.0152 / Vs / dcr
        ENDIF

        IF (Pbar .LE. 10000) THEN
          Vs = 13.737 + .0032645 * T + 4.822E-06 * T * T
          ro = 18.0152 / Vs / dcr
        ENDIF

        IF (Pbar .GT. 10000) THEN
          Vs = 11.894 + .007639 * T
        ENDIF
      ENDIF

      CALL H2O(TX,PCX,ro,at,t_1,pp,A)

C H2O density calculation

      dH2O = ro * dcr

C H2O enthropy calculation

      SH2O = MH2O * RGasH2O * (t_1 * AT - A) * 0.1 +
63.19949

C H2O enthalpy calculation

      HH2O = MH2O * RGasH2O * Tcr * (-AT - pp / ro /
t_1) * 0.1
     + - 287757.32

C H2O Gibb's free energy calculation

      GH2O = HH2O - T * SH2O + 69495.6

      GTH2Ogas = G0H2Ogas - SH2Ogas * (T - TrK) -
aH2O * T
     +* log(T / TrK) + aH2O * (T - TrK)
      GTH2Ogas = GTH2Ogas - .5 * (bH2OE3) / 1000 * (T
- TrK)**2
     +- .5 * (cH2OEmin5) * 100000 / T * (T / TrK - 1)**2
      GTH2Ogas = GTH2Ogas - 1 / 6 * (dH2OE6) /
1000000 * (T**3
     +- TrK**3 - 3 * TrK**2 * (T - TrK))
      GTH2Ogas = GTH2Ogas - 2 * (eH2OEmin1) * 10 *
((T - TrK)
     +/ (TrK)**0.5 - 2 * ((T)**0.5 - (TrK)**0.5))

C H2O fugacuty calculation [bar]

      fH2O = EXP((GH2O - GTH2Ogas) / RgasJ / T)

C Concentration of dissolved CO2 in CO2-rich phase
```

```
      yH2Oideal = Psat / Pbar

      yH2Orough = (.1256 * (T-273.15) - .0212) * .001 +
(.065
     +* (T-273.15) + 1.21) * .000001 * Pbar

      IF (yH2Oideal .GT. yH2Orough) THEN

        yCO2 = 1 - yH2Oideal
      ELSE
        yCO2 = 1 - yH2Orough
      ENDIF

      dB12 = .5 * (Coef1 + Coef2 * (1000 / T)**.5)
      dB12d = 2 * dH2O * dB12

C Henry's coefficient calculation

      kH = 1
      kH = EXP(log(kH) + (1 - Scale) * log(fH2O) + Scale
     +* log(RgasJbar / MH2O * T * dH2O) + dB12d)

C Mole fraction of CO2 in the aquesous phase

      XCO2_RAW = (FC/10**6) / (kH * yCO2 / 10)

      molalCO2 = 1000 / MH2O * XCO2_RAW / (1 -
XCO2_RAW)

C Empirical correction for CO2 solubility by Diamond
and Akinfiev, 2003

      EmpirFunc = 3.63579E-05 - 4.47782E-06 * (T-
273.15) + .0073101
     +* (XCO2_RAW * 100) + 1.18833E-04 * (T-273.15) *
(XCO2_RAW * 100)
     +- 7.49356E-03 * (XCO2_RAW * 100)**2 +
5.41469E-05 * (T-273.15)
     +* (XCO2_RAW * 100)**2

      XCO2 = XCO2_RAW * (1 + EmpirFunc)

C    Calculate mass fraction of CO2 (XMASS):

     X1M = (XMWC*XCO2) / (((1.D0-
XCO2)*MH2O/1000)+(XCO2*XMWC))

     RETURN
     END
C********1*********2*********3*********4*******
***5*********6*********7**
     SUBROUTINE SOLUT(PCX,TX,HSOL)
     IMPLICIT DOUBLE PRECISION(A-H,O-Z)
C
C        This subroutine calculates the enthalpy of CO2
dissolution in
C     liquid water. The expression is from O'Sullivan et al.
(1985).
C      The expression was created using a quadratic fit to
data published
C     by Ellis and Goulding (1963).
C
     SAVE ICALL
     DATA ICALL/0/
     ICALL=ICALL+1
     IF(ICALL.EQ.1) WRITE(11,899)
  899 FORMAT(6X,'SOLUT      1.0          26 JANUARY
1990',6X,
     X'CALCULATE SPECIFIC ENTHALPY OF CO2
DISSOLUTION IN WATER')
C
     T  = 1.D-2 * TX
     T2 = T * T
     T3 = T * T2
     T4 = T * T3
     HSOL = -7.3696D-2 - 5.6405D-1*T + 7.0363D-1*T2
-
    >       2.7882D-1*T3 + 4.2579D-2*T4
     HSOL = HSOL * 1.D6
     RETURN
     END
C********1*********2*********3*********4*******
***5*********6*********7**
     SUBROUTINE DENMIX(TX,DW,X1M,D1M)
     IMPLICIT DOUBLE PRECISION(A-H,O-Z)
C
C      This subroutine returns density of CO2/H2O liquid
mixture. The
C     expression is from Anderson et al. (1992).
C
C            Input:
C                    TX   = Temperature [degrees C]
C                    DW   = Density of H2O [kg/m3]
C                    X1M  = Mass fraction of CO2 [-]
C
C            Output:
C                    D1M    = Density of CO2/H2O
mixture [kg/m3]
C
C            Constants:
C                    XMWC = Molecular weight of CO2
[Kg/mol]
C
C            Variables:
C                    RHO    = Density of CO2 at
saturation pressure [mol/cm3]
C                    DC   = Density of CO2 at saturation
pressure [kg/m3]
C                    X2M  = Mass fraction H2O [-]
C
     PARAMETER(XMWC=4.40098D-02)
C
     SAVE ICALL
     DATA ICALL/0/
     ICALL=ICALL+1
     IF(ICALL.EQ.1) WRITE(11,899)
  899 FORMAT(6X,'DENMIX      2.0          1 SEPT
1999',6X,'
    XCALCULATE DENSITY OF CO2/H2O AQUEOUS
MIXTURE')
C
     IF(X1M.LE.0.D0) THEN
       D1M = DW
       RETURN
     ENDIF
C
C    Calculate TX to the 2nd, 3rd and 4th powers for later
use:
     TX2 = TX * TX
     TX3 = TX2 * TX
     TX4 = TX3 * TX
C
C    Calculate density of CO2 (RHO) at saturation pressure
in mol/cm3:
     RHO = 1.D0/(3.736D+01 - (7.109D-02*TX) -
(3.812D-05*TX2) +
    <      (3.296D-06*TX3) - (3.702D-09*TX4))
C
```

```
C    Convert RHO to kg/m3 (DC):
     DC = RHO * 1.0D+06 * XMWC
C
C    Calculate mass fraction of H2O:
     X2M = 1.D0 - X1M
C
C    Calculate density of CO2/H2O mixture in kg/m3:
     D1M = (DW*DC) / ((X1M*DW)+(X2M*DC))

     RETURN
     END
C********1*********2*********3*********4*********5*********6*********7**
     SUBROUTINE VISCO2(TX,DC,VC)
     IMPLICIT DOUBLE PRECISION(A-H,O-Z)
C
C     This subroutine calculates the viscosity of pure CO2 as a function
C     of temperature and density of CO2.  The expressions for calculating
C     the viscosity come from empirical equations provided in Vesovic et
C     al.(1990) and Fenghour et al. (1998).
C      The critical point enhancement for the viscosity of CO2
C     has been neglected since it is weak and restricted to a very small
C     region around the critical point.
C
C            Input:
C                    TX     = Temperature [degrees C]
C                    DC     = Density of CO2 [kg/m3]
C
C            Output:
C                    VC     = Viscosity of CO2 [Pa-s]
C
C            Constants:
C                    Ai          = Coefficients of the correlation of the
C                          zero-density viscosity
C                    ESCL   = Energy scaling parameter [K]
C                         = epsilon/kappa
C                    Dij         = Coefficients of the correlation of the
C                          excess viscosity
C
C            Variables:
C                    T      = Temperature [K]
C                    TSTAR      = (kappa*T)/epsilon = T/ESCL [-]
C                    ETA0       = Zero-density viscosity [muPa-s]
C                    DETA    = Excess viscosity [muPa-s]
C
     PARAMETER(A0   =  2.35156D-01)
     PARAMETER(A1   = -4.91266D-01)
     PARAMETER(A2   =  5.211155D-02)
     PARAMETER(A3   =  5.347906D-02)
     PARAMETER(A4   = -1.537102D-02)
     PARAMETER(ESCL =  2.51196D+02)
     PARAMETER(D11  =  0.4071119D-02)
     PARAMETER(D21  =  0.7198037D-04)
     PARAMETER(D64  =  0.2411697D-16)
     PARAMETER(D81  =  0.2971072D-22)
     PARAMETER(D82  = -0.1627888D-22)
C
     SAVE ICALL
     DATA ICALL/0/
     ICALL=ICALL+1
     IF(ICALL.EQ.1) WRITE(11,899)
 899  FORMAT(6X,'VISCO2       2.0              11  DEC 1999',6X,
    X'CALCULATE  VISCOSITY  OF  SEPARATE PHASE CO2')
C
C    Convert temperature from degrees C to K:
     T = TX + 2.7315D+02
C
C    Calculate DC to 2nd, 6th, and 8th powers:
      DC2 = DC*DC
          DC6 = DC2*DC2*DC2
          DC8 = DC6*DC2
C
C    Calculate TSTAR and 3rd power:
     TSTAR = T/ESCL
          TSTAR3=TSTAR*TSTAR*TSTAR
C
C    Calculate ln(TSTAR) and 2nd, 3rd, and 4th powers:
     BETA1 = DLOG(TSTAR)
     BETA2 = BETA1*BETA1
          BETA3 = BETA2*BETA1
          BETA4 = BETA3*BETA1
C
C    Calculate zero-density limit viscosity in muPa-s:
     EXS                                                  =
DEXP(A0+(A1*BETA1)+(A2*BETA2)+(A3*BETA3)+(A4*BETA4))
     ETA0 = (1.00697D0 * DSQRT(T)) / EXS
C
C    Calculate excess viscosity in muPa-s:
     DETA                                                 =
(D11*DC)+(D21*DC2)+((D64*DC6)/TSTAR3)+(D81*DC8)+
    >      ((D82*DC8)/TSTAR)
C
C    Calculate total viscosity in muPa-s:
     VC = ETA0 + DETA
C
C    Convert viscosity from muPa-s to Pa-s:
     VC = VC * 1.0D-06

     RETURN
     END
C********1*********2*********3*********4*********5*********6*********7**
     SUBROUTINE OUT
     IMPLICIT DOUBLE PRECISION(A-H,O-Z)
     INCLUDE "PARAM.BSC"
C
C-----THIS SUBROUTINE GENERATES PRINTOUT.
C
C
C$$$$$$$$$ COMMON BLOCKS FOR ELEMENTS $$$$$$$$$$$$$$$$$$$$$$$$$$$$$$$
C
C      THESE BLOCKS HAVE A LENGTH OF NEL (= NUMBER OF ELEMENTS)
C
     COMMON/E1/ELEM(1)
     COMMON/E2/MATX(1)
     COMMON/E3/EVOL(1)
     COMMON/E4/PHI(1)
     COMMON/E5/P(1)
     COMMON/E6/T(1)
     COMMON/E7/XBC(1)
     COMMON/E8/YBC(1)
     COMMON/E9/ZBC(1)
     COMMON/E10/HHBC(1)
```

```
      COMMON/E11/SCO2BC(1)
      COMMON/E12/XCO2BC(1)
      COMMON/E13/FFLOWH(1)
      COMMON/E14/FFLOWV(1)
      COMMON/E15/CFLOWH(1)
      COMMON/E16/CFLOWV(1)
      COMMON/E17/QFLOWH(1)
      COMMON/E18/QFLOWV(1)
      COMMON/E19/DCO2BC(1)
      COMMON/E20/VCO2BC(1)
      COMMON/E21/DH2OBC(1)
      COMMON/E22/HCO2BC(1)
      COMMON/E23/TBC(1)
      COMMON/E24/PHASEBC(1)
      COMMON/E25/FVELH(1)
      COMMON/E26/FVELV(1)
      COMMON/E27/CVELH(1)
      COMMON/E28/CVELV(1)
C
C$$$$$$$$$$$$$$$$$$$$$$$$$$$$$$$$$$$$$$$$$$$$$$$$$
$$$$$$$$$$$$$$$$$$$$$$$$$$$$
C
C$$$$$$$$$ COMMON BLOCKS FOR PRIMARY
VARIABLES $$$$$$$$$$$$$$$$$$$$$$$$$$
C
C   THESE BLOCKS HAVE A LENGTH OF 3*NEL
C
      COMMON/P1/X(1)
      COMMON/P2/DX(1)
      COMMON/P3/DELX(1)
      COMMON/P4/R(1)
      COMMON/P5/DOLD(1)
C
C$$$$$$$$$$$$$$$$$$$$$$$$$$$$$$$$$$$$$$$$$$$$$$$$$
$$$$$$$$$$$$$$$$$$$$$$$$$$$$
C
C
C$$$$$$$$$ COMMON BLOCKS FOR
CONNECTIONS $$$$$$$$$$$$$$$$$$$$$$$$$$$$$$C
C
      COMMON/C1/NEX1(1)
      COMMON/C2/NEX2(1)
      COMMON/C3/DEL1(1)
      COMMON/C4/DEL2(1)
      COMMON/C5/AREA(1)
      COMMON/C6/BETA(1)
      COMMON/C7/ISOX(1)
      COMMON/C8/GLO(1)
      COMMON/C9/ELEM1(1)
      COMMON/C10/ELEM2(1)
      COMMON/C12/FLOFH1(1)
      COMMON/C13/FLOFH2(1)
      COMMON/C14/FLOFV1(1)
      COMMON/C15/FLOFV2(1)
      COMMON/C16/FLOCH1(1)
      COMMON/C17/FLOCH2(1)
      COMMON/C18/FLOCV1(1)
      COMMON/C19/FLOCV2(1)
      COMMON/C20/GLOH1(1)
      COMMON/C21/GLOH2(1)
      COMMON/C22/GLOV1(1)
      COMMON/C23/GLOV2(1)
      COMMON/C24/VELFH1(1)
      COMMON/C25/VELFH2(1)
      COMMON/C26/VELFV1(1)
      COMMON/C27/VELFV2(1)
      COMMON/C28/VELCH1(1)
      COMMON/C29/VELCH2(1)
      COMMON/C30/VELCV1(1)
      COMMON/C31/VELCV2(1)
C
C$$$$$$$$$$$$$$$$$$$$$$$$$$$$$$$$$$$$$$$$$$$$$$$$$
$$$$$$$$$$$$$$$$$$$$$$$$
C
C$$$$$ COMMON BLOCKS FOR SINKS/SOURCES
$$$$$$$$$$$$$$$$$$$$$$$$$$$$$$$$$$
C
      COMMON/G4/ELEG(1)
      COMMON/G5/SOURCE(1)
      COMMON/G6/LTABG(1)
      COMMON/G7/G(1)
      COMMON/G8/EG(1)
      COMMON/G9/NEXG(1)
      COMMON/G10/ITABG(1)
      COMMON/G11/NGIND(1)
      COMMON/G12/LCOM(1)
      COMMON/G13/PI(1)
      COMMON/G14/PWB(1)
      COMMON/G15/HG(1)
      COMMON/G16/GPO(1)
      COMMON/G17/SDENS(1)
      COMMON/G18/SSAT(1)
      COMMON/G19/GVOL(1)
      COMMON/G20/HL(1)
      COMMON/G21/HS(1)
      COMMON/G22/QVGC(1)
      COMMON/G23/QVWC(1)
      COMMON/G24/QVOC(1)
      COMMON/G25/GRAD(1)
      COMMON/G26/FF(1)
C
C$$$$$$$$$$$$$$$$$$$$$$$$$$$$$$$$$$$$$$$$$$$$$$$$$
$$$$$$$$$$$$$$$$$$$$$$$$$$
      COMMON/COMPO/FLO(1)
      COMMON/PORVEL/VEL(1)
      COMMON/DM/DELTEN,DELTEX,FOR,FORD
      COMMON/KONIT/KON,DELT,IGOOD
      COMMON/TITLE/ TITLE
      COMMON/DOP/ENTH,KDATA,QUAL
      COMMON/SVZ/NOITE,MOP(24)
      COMMON/POV6/ TSTART

COMMON/NN/NEL,NCON,NOGN,NK,NEQ,NPH,NB,
NK1,NEQ1,NBK,NSEC,NFLUX

COMMON/CONTST/RE1,RE2,RERM,NER,KER,DFAC
      COMMON/SECPAR/PAR(1)

COMMON/SOLID/NM,DROK(27),POR(27),PER(3,27),
CWET(27),SPHT(27)
      COMMON/SOCH/MAT(27)

COMMON/CYC/KCYC,ITER,ITERC,TIMIN,SUMTIM,
GF,TIMOUT
      COMMON/FF/H1
      CHARACTER*1 H1
      DIMENSION DXM(3)
      CHARACTER*80 TITLE
      CHARACTER*5
ELEM,ELEM1,ELEM2,ELEG,SOURCE,MAT
      CHARACTER*1 ITABG,HB,H0
      CHARACTER*10 PHASE
      real*8 year
      real*8 brvelh(NEL),brvelv(NEL)
C
      SAVE ICALL,HB,H0,ZERO
      DATA HB,H0/' ',' '/
      DATA ICALL,ZERO/0,1.D-13/
      ICALL=ICALL+1
      IF(ICALL.EQ.1) WRITE(11,899)
```

```
 899  FORMAT(/6X,'OUT            2.0            1  SEPT
1999',6X,
     X'PRINT      RESULTS      FOR      ELEMENTS,
CONNECTIONS, AND SINKS/SOURCES'/
     x47X,'SPECIAL VERSION FOR *EOSCO2*')
C
C-----COME HERE TO SET UP TECPLOT OUTPUT
FILE.
C
1111       FORMAT(A44,1X,F8.0,A7)
1112
FORMAT('VARIABLES="X","Z","HEAD","TEMP","SC
O2","XCO2","FH2OH",

>"FH2OV","FCO2H","FCO2V","VH2OH","VH2OV","V
CO2H","VCO2V","PHASE"
    >,"MAT"')
1113       FORMAT(/'ZONE T="',E10.5,' YR", I= ',I5,',
J= ',I5,
    >    ',F= POINT')
      IF (ICALL.EQ.1) THEN
        WRITE(80,1111)'TITLE = "CO2 DIAGNOSTICS"'
        WRITE(80,1112)
      END IF
      YEAR=SUMTIM/3.1536E7
      WRITE(80,1113)year,NNZ,NNX
C-----COME HERE TO COMPUTE MAXIMUM
CHANGES.
C
      DO I=1,NK1
        DXM(I) = 0.D0
      END DO
      DO N=1,NEL
        NLOC = (N-1) * NK1
        DO I=1,3
          ADX = DABS(DX(NLOC+I))
          IF (ADX.GT.DXM(I)) DXM(I) = ADX
        END DO
      END DO
C
C-----COME HERE TO PRINT HEADER
INFORMATION.
C
      DAY=SUMTIM/8.64D4
      PRINT 5010,H1,TITLE,KCYC,ITER,KON,DAY
      PRINT 5140,HB
      PRINT
9010,SUMTIM,KCYC,ITER,ITERC,KON,(DXM(I),I=1,3
),
     1  RERM,NER,KER,DELTEX
      PRINT 5140,HB
      PRINT 1000,H0
      PRINT 1001
C
C-----COME HERE TO PRINT VARIABLES AT THE
STATE POINT.
C
      DO N=1,NEL
        NLOC   = (N-1) * NK1
        NLOC2  = (N-1) * NSEC * NEQ1
        NLOC2L = NLOC2 + NBK
        NLOC2S = NLOC2L + NBK
        IF (MOD(N,57).EQ.46) THEN
          PRINT 1002,H1
          PRINT 1001
        END IF
        TX = PAR(NLOC2+NSEC-1)
        PRES = X(NLOC+1)
        IF (KON.NE.2) THEN
          PRES = X(NLOC+1) + DX(NLOC+1)
        END IF
c--APA                                    HHBC(N)     =
PRES/(PAR(NLOC2L+4)*GF)+(ZBC(N)+DEPTH)
        HHBC(N) = PRES
        TBC(N) = TX
              IF (PAR(NLOC2S+1).GT.ZERO) THEN
          SCO2BC(N) = PAR(NLOC2S+1)
        ELSE
          SCO2BC(N) = 0.D0
        END IF
              IF        (PAR(NLOC2L+NB+2).GT.ZERO)
THEN
          XCO2BC(N) = PAR(NLOC2L+NB+2)
        ELSE
          XCO2BC(N) = 0.D0
        END IF
        DH2OBC(N) = PAR(NLOC2L+4)
        IF (SCO2BC(N).EQ.0.D0) THEN
          DCO2BC(N) = 0.D0
          VCO2BC(N) = 0.D0
          HCO2BC(N) = 0.D0
          IF (XCO2BC(N).EQ.0.D0) THEN
            PHASE  = 'NO CO2'
            PHASEBC(N) = 0.D0
          ELSE
            PHASE = 'DISSOLVED'
            PHASEBC(N) = 1.D0
          END IF
        ELSE
          DCO2BC(N) = PAR(NLOC2S+4)
          VCO2BC(N) = PAR(NLOC2S+3)
          HCO2BC(N) = PAR(NLOC2S+5)
          IF (XCO2BC(N).EQ.0.D0) THEN
            IF
(TX.GT.30.957D0.AND.PRES.GT.7.3721D+06) THEN
              PHASE = 'SUPERCRIT'
              PHASEBC(N) = 2.D0
            ELSE
              PHASE = 'GASEOUS'
              PHASEBC(N) = 3.D0
            ENDIF
          ELSE
            IF
(TX.GT.30.957D0.AND.PRES.GT.7.3721D+06) THEN
              PHASE = 'DISS/SCRIT'
              PHASEBC(N) = 4.D0
            ELSE
              PHASE = 'DISS/GAS'
              PHASEBC(N) = 5.D0
            END IF
          END IF
        END IF
        PRINT
5041,ELEM(N),N,PRES,TX,PAR(NLOC2L+1),SCO2BC
(N),
     >
XCO2BC(N),DH2OBC(N),DCO2BC(N),VCO2BC(N),
     >           HCO2BC(N),PHASE
      END DO
      PRINT 5140,HB
      IF (MOD(KDATA,10).LT.2) THEN
        GO TO 3045
      ENDIF
C
C-----COME HERE TO PRINT FLOW TERMS.
C
      PRINT 5000,H1,TITLE,KCYC,ITER,SUMTIM
      PRINT 5060,H0,HB
      PRINT 5061
      DO 3030 N=1,NCON
```

```
      IF (NEX1(N).EQ.0.OR.NEX2(N).EQ.0) THEN
        GO TO 3030
      END IF
      NNP = (N-1) * NPH
      FLOF = 0.D0
      DO NP=1,NPH
        FLOF = FLOF + FLO(NNP+NP)
      END DO
      H = 0.D0
      IF (FLOF.NE.0.D0) THEN
        H = GLO(N) / FLOF
      END IF
      IF (MOD(N,57).EQ.54) THEN
        PRINT 5062,H1,HB
        PRINT 5061
      END IF
      FLOH2O = FLO(NNP+2)
      VELH2O = VEL(NNP+2)
      FLOCO2 = FLO(NNP+3)
      VELCO2 = VEL(NNP+3)
      PRINT
5070,ELEM1(N),ELEM2(N),N,GLO(N),H,FLOF,
     >          FLOH2O,VELH2O,FLOCO2,VELCO2
C
C-----COME HERE TO RECORD FLOW AND
VELOCITY VECTORS FOR TECPLOT OUTPUT FILE.
C
C   See if it is a horizontal connection:
      IF (ISOX(N).EQ.1) THEN
C   Record the heat flow, fluid flow, and velocity out of or
in to the cell of interest:
        FLOFH1(NEX1(N)) = FLOH2O
        FLOFH2(NEX2(N)) = FLOH2O
        FLOCH1(NEX1(N)) = FLOCO2
        FLOCH2(NEX2(N)) = FLOCO2
        VELFH1(NEX1(N)) = VELH2O
        VELFH2(NEX2(N)) = VELH2O
        VELCH1(NEX1(N)) = VELCO2
        VELCH2(NEX2(N)) = VELCO2
        GLOH1(NEX1(N))  = GLO(N)
        GLOH2(NEX2(N))  = GLO(N)
C   See if it is a vertical connection:
      ELSE IF (ISOX(N).EQ.3) THEN
C   Record the heat flow, fluid flow, and velocity out of or
in to the cell of interest:
        FLOFV1(NEX1(N)) = FLOH2O
        FLOFV2(NEX2(N)) = FLOH2O
        FLOCV1(NEX1(N)) = FLOCO2
        FLOCV2(NEX2(N)) = FLOCO2
        VELFV1(NEX1(N)) = VELH2O
        VELFV2(NEX2(N)) = VELH2O
        VELCV1(NEX1(N)) = VELCO2
        VELCV2(NEX2(N)) = VELCO2
        GLOV1(NEX1(N))  = GLO(N)
        GLOV2(NEX2(N))  = GLO(N)
      ENDIF
 3030 CONTINUE
C
C-----COME HERE TO CALCULATE FLOW AND
VELOCITY VECTORS FOR TECPLOT OUTPUT FILE.
C
C     Procedure: (ignore single connections for now). If
signs are the same,
C        set flow direction and magnitude,  if signs are
different, set direction
C     to the same direction as the highest flow rate, and set
magnitude to be
C     the difference between the two i.e. the net flow in the
specified direction.
C
C       Note that if flow magnitude is positive, fluid is
flowing from elem2 into
C     elem1 (i.e. to the left); this holds for both ....H1 and
....H2.
C
      DO 29 N=1,NEL
C    Horizontal connections first:
C    H2O Flow:
C      If the same flow direction, calculate average fluid
flow:
       IF
(FLOFH1(N).GE.0.D0.AND.FLOFH2(N).GE.0.D0)
THEN
         FFLOWH(N) = -(FLOFH1(N)+FLOFH2(N))/2.D0
       ELSE                                          IF
(FLOFH1(N).LT.0.D0.AND.FLOFH2(N).LT.0.D0)
THEN
         FFLOWH(N)                                   =
(DABS(FLOFH1(N))+DABS(FLOFH2(N)))/2.D0
C      If opposing flow directions, calculate the net fluid
flow through:
       ELSE                                          IF
(FLOFH1(N).LT.0.D0.AND.FLOFH2(N).GE.0.D0)
THEN
         IF (DABS(FLOFH1(N)).GT.DABS(FLOFH2(N)))
THEN
           FFLOWH(N)                                 =
DABS(FLOFH1(N)+FLOFH2(N))
         ELSE
IF(DABS(FLOFH2(N)).GT.DABS(FLOFH1(N))) THEN
           FFLOWH(N)                 =               -
DABS(FLOFH1(N)+FLOFH2(N))
         END IF
       ELSE                                          IF
(FLOFH1(N).GE.0.D0.AND.FLOFH2(N).LT.0.D0)
THEN
         IF (DABS(FLOFH1(N)).GT.DABS(FLOFH2(N)))
THEN
           FFLOWH(N)                 =               -
DABS(FLOFH1(N)+FLOFH2(N))
         ELSE                                        IF
(DABS(FLOFH2(N)).GT.DABS(FLOFH1(N))) THEN
           FFLOWH(N)                                 =
DABS(FLOFH1(N)+FLOFH2(N))
         END IF
       END IF
C
C    CO2 Flow:
C      If the same flow direction, calculate average CO2
flow:
       IF (SCO2BC(N).GT.0.D0) THEN
         IF
(FLOCH1(N).GE.0.D0.AND.FLOCH2(N).GE.0.D0)
THEN
           CFLOWH(N)                 =               -
(FLOCH1(N)+FLOCH2(N))/2.D0
         ELSE                                        IF
(FLOCH1(N).LT.0.D0.AND.FLOCH2(N).LT.0.D0)
THEN
           CFLOWH(N)                                 =
(DABS(FLOCH1(N))+DABS(FLOCH2(N)))/2.D0
C      If opposing flow directions, calculate the net CO2
flow through:
         ELSE                                        IF
(FLOCH1(N).LT.0.D0.AND.FLOCH2(N).GE.0.D0)
THEN
           IF
(DABS(FLOCH1(N)).GT.DABS(FLOCH2(N))) THEN
             CFLOWH(N)                               =
DABS(FLOCH1(N)+FLOCH2(N))
```

```
          ELSE
IF(DABS(FLOCH2(N)).GT.DABS(FLOCH1(N))) THEN
            CFLOWH(N)          =          -
DABS(FLOCH1(N)+FLOCH2(N))
          END IF
        ELSE                                IF
(FLOCH1(N).GE.0.D0.AND.FLOCH2(N).LT.0.D0)
THEN
          IF
(DABS(FLOCH1(N)).GT.DABS(FLOCH2(N))) THEN
            CFLOWH(N)          =          -
DABS(FLOCH1(N)+FLOCH2(N))
          ELSE                              IF
(DABS(FLOCH2(N)).GT.DABS(FLOCH1(N))) THEN
            CFLOWH(N)                      =
DABS(FLOCH1(N)+FLOCH2(N))
          END IF
        END IF
      ELSE
        CFLOWH(N) = 0.D0
      END IF
C
C   Heat Flow:
C     If the same flow direction, calculate average heat
flow:
      IF
(GLOH1(N).GE.0.D0.AND.GLOH2(N).GE.0.D0) THEN
        QFLOWH(N) = -(GLOH1(N)+GLOH2(N))/2.D0
      ELSE                                IF
(GLOH1(N).LT.0.D0.AND.GLOH2(N).LT.0.D0) THEN
        QFLOWH(N)                          =
(DABS(GLOH1(N))+DABS(GLOH2(N)))/2.D0
C   If opposing flow directions, calculate the net heat flow
through:
      ELSE                                IF
(GLOH1(N).LT.0.D0.AND.GLOH2(N).GE.0.D0) THEN
        IF    (DABS(GLOH1(N)).GT.DABS(GLOH2(N)))
THEN
          QFLOWH(N)                        =
DABS(GLOH1(N)+GLOH2(N))
        ELSE
IF(DABS(GLOH2(N)).GT.DABS(GLOH1(N))) THEN
          QFLOWH(N)          =          -
DABS(GLOH1(N)+GLOH2(N))
        END IF
      ELSE                                IF
(GLOH1(N).GE.0.D0.AND.GLOH2(N).LT.0.D0) THEN
        IF    (DABS(GLOH1(N)).GT.DABS(GLOH2(N)))
THEN
          QFLOWH(N)          =          -
DABS(GLOH1(N)+GLOH2(N))
        ELSE                              IF
(DABS(GLOH2(N)).GT.DABS(GLOH1(N))) THEN
          QFLOWH(N)                        =
DABS(GLOH1(N)+GLOH2(N))
        END IF
      END IF
C
C   H2O Velocity:
C     If the same flow direction, calculate average fluid
velocity:
      IF
(VELFH1(N).GE.0.D0.AND.VELFH2(N).GE.0.D0)
THEN
        FVELH(N) = -(VELFH1(N)+VELFH2(N))/2.D0
      ELSE                                IF
(VELFH1(N).LT.0.D0.AND.VELFH2(N).LT.0.D0)
THEN
        FVELH(N)                           =
(DABS(VELFH1(N))+DABS(VELFH2(N)))/2.D0
C     If opposing flow directions, calculate the net fluid
velocity:
      ELSE                                IF
(VELFH1(N).LT.0.D0.AND.VELFH2(N).GE.0.D0)
THEN
        IF (DABS(VELFH1(N)).GT.DABS(VELFH2(N)))
THEN
          FVELH(N) = DABS(VELFH1(N)+VELFH2(N))
        ELSE
IF(DABS(VELFH2(N)).GT.DABS(VELFH1(N))) THEN
          FVELH(N)          =          -
DABS(VELFH1(N)+VELFH2(N))
        END IF
      ELSE                                IF
(VELFH1(N).GE.0.D0.AND.VELFH2(N).LT.0.D0)
THEN
        IF (DABS(VELFH1(N)).GT.DABS(VELFH2(N)))
THEN
          FVELH(N)          =          -
DABS(VELFH1(N)+VELFH2(N))
        ELSE                              IF
(DABS(VELFH2(N)).GT.DABS(VELFH1(N))) THEN
          FVELH(N) = DABS(VELFH1(N)+VELFH2(N))
        END IF
      END IF
C
C   CO2 Velocity:
C     If the same flow direction, calculate average CO2
velocity:
      IF (SCO2BC(N).GT.0.D0) THEN
        IF
(VELCH1(N).GE.0.D0.AND.VELCH2(N).GE.0.D0)
THEN
          CVELH(N)          =          -
(VELCH1(N)+VELCH2(N))/2.D0
        ELSE                              IF
(VELCH1(N).LT.0.D0.AND.VELCH2(N).LT.0.D0)
THEN
          CVELH(N)                         =
(DABS(VELCH1(N))+DABS(VELCH2(N)))/2.D0
C     If opposing flow directions, calculate the net CO2
velocity:
        ELSE                              IF
(VELCH1(N).LT.0.D0.AND.VELCH2(N).GE.0.D0)
THEN
          IF
(DABS(VELCH1(N)).GT.DABS(VELCH2(N))) THEN
            CVELH(N)                       =
DABS(VELCH1(N)+VELCH2(N))
          ELSE
IF(DABS(VELCH2(N)).GT.DABS(VELCH1(N))) THEN
            CVELH(N)          =          -
DABS(VELCH1(N)+VELCH2(N))
          END IF
        ELSE                              IF
(VELCH1(N).GE.0.D0.AND.VELCH2(N).LT.0.D0)
THEN
          IF
(DABS(VELCH1(N)).GT.DABS(VELCH2(N))) THEN
            CVELH(N)          =          -
DABS(VELCH1(N)+VELCH2(N))
          ELSE                            IF
(DABS(VELCH2(N)).GT.DABS(VELCH1(N))) THEN
            CVELH(N)                       =
DABS(VELCH1(N)+VELCH2(N))
          END IF
        END IF
      ELSE
        CVELH(N) = 0.D0
      END IF
```

```
C
C   Now vertical connections:
C   H2O Flow:
C     If the same flow direction, calculate average fluid
flow:
      IF
(FLOFV1(N).GE.0.D0.AND.FLOFV2(N).GE.0.D0)
THEN
        FFLOWV(N) = (FLOFV1(N)+FLOFV2(N))/2.D0
      ELSE                                          IF
(FLOFV1(N).LT.0.D0.AND.FLOFV2(N).LT.0.D0)
THEN
        FFLOWV(N)                 =                 -
(DABS(FLOFV1(N))+DABS(FLOFV2(N)))/2.D0
C     If opposing flow directions, calculate the net fluid
flow through:
      ELSE
IF(FLOFV1(N).LT.0.D0.AND.FLOFV2(N).GE.0.D0)
THEN
        IF (DABS(FLOFV1(N)).GT.DABS(FLOFV2(N)))
THEN
          FFLOWV(N)                 =                 -
DABS(FLOFV1(N)+FLOFV2(N))
        ELSE
IF(DABS(FLOFV2(N)).GT.DABS(FLOFV1(N))) THEN
          FFLOWV(N)                                   =
DABS(FLOFV1(N)+FLOFV2(N))
        END IF
      ELSE
IF(FLOFV1(N).GE.0.D0.AND.FLOFV2(N).LT.0.D0)
THEN
        IF (DABS(FLOFV1(N)).GT.DABS(FLOFV2(N)))
THEN
          FFLOWV(N)                                   =
DABS(FLOFV1(N)+FLOFV2(N))
        ELSE                                          IF
(DABS(FLOFV2(N)).GT.DABS(FLOFV1(N))) THEN
          FFLOWV(N)                 =                 -
DABS(FLOFV1(N)+FLOFV2(N))
        END IF
      END IF
C
C   CO2 Flow:
C     If the same flow direction, calculate average CO2
flow:
      IF (SCO2BC(N).GT.0.D0) THEN
        IF
(FLOCV1(N).GE.0.D0.AND.FLOCV2(N).GE.0.D0)
THEN
          CFLOWV(N)                                   =
(FLOCV1(N)+FLOCV2(N))/2.D0
        ELSE                                          IF
(FLOCV1(N).LT.0.D0.AND.FLOCV2(N).LT.0.D0)
THEN
          CFLOWV(N)                 =                 -
(DABS(FLOCV1(N))+DABS(FLOCV2(N)))/2.D0
C     If opposing flow directions, calculate the net CO2
flow through:
        ELSE
IF(FLOCV1(N).LT.0.D0.AND.FLOCV2(N).GE.0.D0)
THEN
          IF
(DABS(FLOCV1(N)).GT.DABS(FLOCV2(N))) THEN
            CFLOWV(N)                 =                 -
DABS(FLOCV1(N)+FLOCV2(N))
          ELSE
IF(DABS(FLOCV2(N)).GT.DABS(FLOCV1(N))) THEN
            CFLOWV(N)                                   =
DABS(FLOCV1(N)+FLOCV2(N))
          END IF
        ELSE
IF(FLOCV1(N).GE.0.D0.AND.FLOCV2(N).LT.0.D0)
THEN
          IF
(DABS(FLOCV1(N)).GT.DABS(FLOCV2(N))) THEN
            CFLOWV(N)                                   =
DABS(FLOCV1(N)+FLOCV2(N))
          ELSE                                        IF
(DABS(FLOCV2(N)).GT.DABS(FLOCV1(N))) THEN
            CFLOWV(N)                 =                 -
DABS(FLOCV1(N)+FLOCV2(N))
          END IF
        END IF
      ELSE
        CFLOWV(N) = 0.D0
      END IF
C
C   Heat Flow:
C     If the same flow direction, calculate average heat
flow:
      IF
(GLOV1(N).GE.0.D0.AND.GLOV2(N).GE.0.D0) THEN
        QFLOWV(N) = (GLOV1(N)+GLOV2(N))/2.D0
      ELSE                                          IF
(FLOFV1(N).LT.0.D0.AND.FLOFV2(N).LT.0.D0)
THEN
        QFLOWV(N)                 =                 -
(DABS(GLOV1(N))+DABS(GLOV2(N)))/2.D0
C   If opposing flow directions, calculate the net heat flow
through:
      ELSE                                          IF
(GLOV1(N).LT.0.D0.AND.GLOV2(N).GE.0.D0) THEN
        IF    (DABS(GLOV1(N)).GT.DABS(GLOV2(N)))
THEN
          QFLOWV(N)                 =                 -
DABS(GLOV1(N)+GLOV2(N))
        ELSE
IF(DABS(GLOV2(N)).GT.DABS(GLOV1(N))) THEN
          QFLOWV(N)                                   =
DABS(GLOV1(N)+GLOV2(N))
        END IF
      ELSE                                          IF
(GLOV1(N).GE.0.D0.AND.GLOV2(N).LT.0.D0) THEN
        IF(DABS(GLOV1(N)).GT.DABS(GLOV2(N)))
THEN
          QFLOWV(N)                                   =
DABS(GLOV1(N)+GLOV2(N))
        ELSE                                          IF
(DABS(GLOV2(N)).GT.DABS(GLOV1(N))) THEN
          QFLOWV(N)                 =                 -
DABS(GLOV1(N)+GLOV2(N))
        END IF
      END IF
C
C   H2O Velocity:
C     If the same flow direction, calculate average fluid
velocity:
      IF
(VELFV1(N).GE.0.D0.AND.VELFV2(N).GE.0.D0)
THEN
        FVELV(N) = (VELFV1(N)+VELFV2(N))/2.D0
      ELSE                                          IF
(VELFV1(N).LT.0.D0.AND.VELFV2(N).LT.0.D0)
THEN
        FVELV(N)                  =                 -
(DABS(VELFV1(N))+DABS(VELFV2(N)))/2.D0
C     If opposing flow directions, calculate the net fluid
velocity:
```

```
      ELSE                                          IF
(VELFV1(N).LT.0.D0.AND.VELFV2(N).GE.0.D0)
THEN
        IF (DABS(VELFV1(N)).GT.DABS(VELFV2(N)))
THEN
          FVELV(N)                  =             -
DABS(VELFV1(N)+VELFV2(N))
        ELSE
IF(DABS(VELFV2(N)).GT.DABS(VELFV1(N))) THEN
          FVELV(N) = DABS(VELFV1(N)+VELFV2(N))
        END IF
      ELSE                                          IF
(VELFV1(N).GE.0.D0.AND.VELFV2(N).LT.0.D0)
THEN
        IF (DABS(VELFV1(N)).GT.DABS(VELFV2(N)))
THEN
          FVELV(N) = DABS(VELFV1(N)+VELFV2(N))
        ELSE                                        IF
(DABS(VELFV2(N)).GT.DABS(VELFV1(N))) THEN
          FVELV(N)                  =             -
DABS(VELFV1(N)+VELFV2(N))
        END IF
      END IF
C
C   CO2 Velocity:
C     If the same flow direction, calculate average CO2
velocity:
      IF (SCO2BC(N).GT.0.D0) THEN
        IF
(VELCV1(N).GE.0.D0.AND.VELCV2(N).GE.0.D0)
THEN
          CVELV(N) = (VELCV1(N)+VELCV2(N))/2.D0
        ELSE                                        IF
(VELCV1(N).LT.0.D0.AND.VELCV2(N).LT.0.D0)
THEN
          CVELV(N)                  =             -
(DABS(VELCV1(N))+DABS(VELCV2(N)))/2.D0
C     If opposing flow directions, calculate the net CO2
velocity:
        ELSE                                        IF
(VELCV1(N).LT.0.D0.AND.VELCV2(N).GE.0.D0)
THEN
          IF
(DABS(VELCV1(N)).GT.DABS(VELCV2(N))) THEN
            CVELV(N)                =             -
DABS(VELCV1(N)+VELCV2(N))
          ELSE
IF(DABS(VELCV2(N)).GT.DABS(VELCV1(N))) THEN
            CVELV(N)                              =
DABS(VELCV1(N)+VELCV2(N))
          END IF
        ELSE                                        IF
(VELCV1(N).GE.0.D0.AND.VELCV2(N).LT.0.D0)
THEN
          IF
(DABS(VELCV1(N)).GT.DABS(VELCV2(N))) THEN
            CVELV(N)                              =
DABS(VELCV1(N)+VELCV2(N))
          ELSE                                      IF
(DABS(VELCV2(N)).GT.DABS(VELCV1(N))) THEN
            CVELV(N)                =             -
DABS(VELCV1(N)+VELCV2(N))
          END IF
        END IF
      ELSE
        CVELV(N) = 0.D0
      END IF
C
C-----COME HERE TO WRITE TECPLOT OUTPUT
FILE.
1114      FORMAT(15(1X,E10.4),1x,i3)
c--> APA convert vel. from m/s to cm/yr
      brvelh(N)=FVELH(N)*3.1536E9
      brvelv(N)=FVELV(N)*3.1536E9
cbsc      If (EVOL(N).NE.0.) THEN

WRITE(80,1114)XBC(N),ZBC(N),HHBC(N),TBC(N),SC
O2BC(N),
     >
XCO2BC(N),FFLOWH(N),FFLOWV(N),CFLOWH(N),C
FLOWV(N),
     >
brvelh(N),brvelv(N),CVELH(N),CVELV(N),DH2OBC(N
),
     >        MATX(N)
cbsc      ENDIF
29   CONTINUE
C
C-----COME HERE TO PRINT PRIMARY
VARIABLES, LATEST INCREMENTS, AND REL.
PERMS.
C
     PRINT 5140,HB
     IF (MOD(KDATA,10).LT.3) THEN
       GO TO 3045
     END IF
     PRINT 5000,h1,TITLE,KCYC,ITER,SUMTIM
     PRINT 5030,H0
     DO 3020 N = 1,NEL
       NLOC=(N-1)*NK1
       NLOC2=(N-1)*NSEC*NEQ1
       NLOC2L=NLOC2+NBK
       IF (MOD(N,57) .EQ. 54) PRINT 5032,H1
       PRINT
5040,ELEM(N),N,(X(NLOC+I),I=1,NK1),(DX(NLOC+I)
,I=1,NK1),
     >          PAR(NLOC2L+2),PAR(NLOC2S+2)
 3020 CONTINUE
     PRINT 5140,HB
 3045 CONTINUE
C
C-----COME HERE TO PRINT SOURCE/SINK TERMS.
C
     IF (NOGN.EQ.0) RETURN
     PRINT 5000,h1,TITLE,KCYC,ITER,SUMTIM
     PRINT 5120,H0
     PRINT 5121
     GC=0.D0
     HGC=0.D0
     DO 3050 N=1,NOGN
       J = NEXG(N)
       IF (J.EQ.0) THEN
         GO TO 3050
       END IF
       IF (MOD(N,58).EQ.54) THEN
         PRINT 5122,H1
         PRINT 5121
       END IF
       IF (GPO(N).GT.0.D0) THEN
         PRINT
5130,ELEG(N),SOURCE(N),N,GPO(N),EG(N)
       END IF
       IF   (GPO(N).LE.0.D0.AND.LCOM(N).NE.NK1+1)
THEN
         PRINT
5130,ELEG(N),SOURCE(N),N,GPO(N),EG(N),
     >          (FF((N-1)*NPH+NP),NP=1,NPH)
       END IF
       IF   (GPO(N).LE.0.D0.AND.LCOM(N).EQ.NK1+1)
THEN
```

```
        PRINT
5130,ELEG(N),SOURCE(N),N,GPO(N),EG(N),
   >         (FF((N-1)*NPH+NP),NP=1,NPH),PWB(N)
      END IF
      IF (LCOM(N).NE.NK1+1) THEN
        GO TO 102
      END IF
C
C-----NOW FOR A LITTLE SECTION WHICH COMPUTES TOTAL FLOWRATE
C     AND FLOWING ENTHALPY FOR WELLS ON DELIVERABLITY WITH COMPLE-
C           TIONS IN DIFFERENT LAYERS (OR, GENERALLY, ELEMENTS)
C
C     ALL OPEN INTERVALS OF A WELL MUST BE KNOWN BY THE SAME SOURCE
C           NAME, AND MUST BE GIVEN IN UNINTERRUPTED SEQUENCE.
C
      IF (NOGN.EQ.1) THEN
        GO TO 102
      END IF
      IF  (N.EQ.1.AND.SOURCE(N+1).NE.SOURCE(N)) THEN
        GO TO 102
      END IF
      IF (N.EQ.1) THEN
        GO TO 100
      END IF
      IF                                  (SOURCE(N-1).EQ.SOURCE(N).OR.SOURCE(N).EQ.SOURCE(N+1)) THEN
        GO TO 100
      END IF
      GO TO 103
C
C-----COME HERE FOR SOURCE IN A CHAIN AND ACCUMULATE TERMS.
C
  100   GC = GC + GPO(N)
      HGC = HGC + GPO(N) * EG(N)
C
C-----FIND OUT WHETHER CHAIN TERMINATES.
C
      IF (N.EQ.NOGN) THEN
        GO TO 101
      END IF
      IF (SOURCE(N+1).EQ.SOURCE(N)) THEN
        GO TO 102
      END IF
C
C-----COME HERE FOR END OF CHAIN.
C
  101   IF (GC.NE.0.D0) THEN
          HGC=HGC/GC
      END IF
      PRINT 110,SOURCE(N),GC,HGC
  110 FORMAT(' ***** SOURCE  $',A5,'$       RATE =',E12.5,
     1    ' KG/S    FLOWING ENTHALPY =',E12.5,' J/KG *****'/)
C
C-----COME HERE FOR SOURCES OUTSIDE CHAINS, AND AT END OF CHAIN.
C
  103   GC = 0.D0
      HGC = 0.D0
C
  102   CONTINUE
C
C-----END OF SECTION FOR MULTI-LAYER WELLS ON DELIVERABILITY
C
 3050 CONTINUE
      PRINT 5140,HB
      RETURN
C
C---*----1----*----2----*----3----*----4----*----5----*----6----*----7----*----8
 5000  FORMAT(A1/10X,A80//80X,'KCYC =',I5,'  -ITER =',I5,
     1  ' - TIME =',E12.5/)
 5010  FORMAT(A1/' ',A80//10X,'OUTPUT DATA AFTER (',I4,',',I3,')-',I1,
     1    '-TIME STEPS',52(' '),'THE TIME IS ',E12.5,' DAYS')
 9010 FORMAT(' TOTAL TIME      KCYC  ITER ITERC  KON      DX1M',9X,
     1     'DX2M',9X,'DX3M',10X,'MAX.  RES.',6X,'NERKER      DELTEX'/
     2
1X,E12.5,3I7,I6,5X,3E13.5,2X,E13.5,4X,I4,I6,5X,E13.5)
 5030          FORMAT(A1,'ELEM.          INDEX X1',10X,'X2',10X,'X3',10X,' X1',9X,
     1'DX1',9X,'DX2',9X,'DX3',9X,'DX4',8X,'K(LIQ)  K(CO2)'/)
 5032          FORMAT(A1/' ELEM.          INDEX X1',10X,'X2',10X,'X3',10X,' X1',9X,
     1'DX1',9X,'DX2',9X,'DX3',9X,'DX4',8X,'K(GAS)  K(LIQ.)'/)
 1000          FORMAT(A1,'ELEM.          INDEX P',10X,'T',8X,'SH2O',7X,'SCO2',

x7X,'XCO2',7X,'DH2O',7X,'DCO2',7X,'VCO2',7X,'HCO2',6X,'PHASE')
 1001       FORMAT(16X,'(Pa)',6X,'(deg-C)',5X,'(-)',8X,'(-)',8X,'(-)',
     x7X,'(kg/m3)',4X,'(kg/m3)',4X,'(Pa-s)',5X,'(J/kg)',6X,'(-)'/)
 1002          FORMAT(A1/,'ELEM.          INDEX P',10X,'T',8X,'SH2O',7X,'SCO2',

x7X,'XCO2',7X,'DH2O',7X,'DCO2',7X,'VCO2',7X,'HCO2',6X,'PHASE')
 5040 FORMAT(1X,A5,I6,10(1X,E10.5))
 5041 FORMAT(1X,A5,I6,9(1X,E10.5),1X,A10)
 5060  FORMAT(A1,1X,'ELEM1    ELEM2    INDEX FLOH',A6,'FLOH/FLOF',7X,
     1  'FLOF',7X,'FLO(LIQ)    VEL(LIQ)    FLO(CO2)    VEL(CO2)')
 5061
FORMAT(25X,'(W)',8X,'(J/KG)',8X,'(KG/S)',7X,'(KG/S)',7X,
     1  '(M/S)    (KG/S)    (M/S)'/)
 5062  FORMAT(A1/2X,'ELEM1    ELEM2    INDEX FLOH',A6,'FLOH/FLOF',7X,
     1  'FLOF',7X,'FLO(LIQ)    VEL(LIQ.)    FLO(CO2)    VEL(CO2)')
 5070 FORMAT(2A7,1X,I5,(7(1X,E12.5)))
 5120  FORMAT(A1,'ELEMENT  SOURCE  INDEX  GENERATION RATE  ',
     1  ' ENTHALPY    FF(GAS)    FF(LIQ.)    FF(CO2)    P(WB)')
 5121          FORMAT(29X,'(KG/S)      OR      (W)  (J/KG)',46X,'(PA)'/)
 5122  FORMAT(A1/' ELEMENT  SOURCE  INDEX  GENERATION RATE  ',
     1  ' ENTHALPY    FF(GAS)    FF(LIQ.)    FF(CO2)    P(WB)')
```

```
 5130
FORMAT(2X,A5,3X,A5,3X,I2,10X,E12.5,2X,6(1X,E12.
5))
 5140 FORMAT(/' ',131('@')/A1)
C
      END
C********1*********2*********3*********4******
***5*********6*********7**
      SUBROUTINE BALLA
      IMPLICIT DOUBLE PRECISION(A-H,O-Z)
C
C-----THIS SUBROUTINE PERFORMS VOLUME-
AND MASS-BALANCES.
C
C
      COMMON/E2/MATX(1)
      COMMON/E3/EVOL(1)
      COMMON/E4/PHI(1)
      COMMON/P1/X(1)
      COMMON/SECPAR/PAR(1)

COMMON/SOLID/NM,DROK(27),POR(27),PER(3,27),
CWET(27),SPHT(27)
      COMMON/SOCH/MAT(27)

COMMON/CYC/KCYC,ITER,ITERC,TIMIN,SUMTIM,
GF,TIMOUT

COMMON/NN/NEL,NCON,NOGN,NK,NEQ,NPH,NB,
NK1,NEQ1,NBK,NSEC,NFLUX
      COMMON/BC/NELA
      COMMON/FF/H1
      CHARACTER*1 H1
      CHARACTER*5 MAT
C
      SAVE ICALL
      DATA ICALL/0/
      ICALL=ICALL+1
      IF(ICALL.EQ.1) WRITE(11,899)
 899  FORMAT(/6X,'BALLA      0.9          7 JANUARY
1992',6X,
     X'PERFORM SUMMARY BALANCES FOR
VOLUME, MASS, AND ENERGY')
C
      DAY = SUMTIM / 8.64D4
      PRINT 1,H1
    1 FORMAT(A1/' ********** VOLUME- AND
MASS-BALANCES **',80('*')/)
      PRINT 2,KCYC,ITER,SUMTIM,DAY
    2 FORMAT(' ********** [KCYC,ITER] = [',I4,',',I3,']
*****',34X,
     1 'THE TIME IS ',E12.5,' SECONDS, OR ',E12.5,'
DAYS'/)
C
      VOLG = 0.D0
      VOLL = 0.D0
      VOLC = 0.D0
      AMG = 0.D0
      AML = 0.D0
      AMV = 0.D0
      AMA = 0.D0
      AMW = 0.D0
      AMC = 0.D0
      DO 10 N=1,NELA
        NMAT = MATX(N)
        IF (SPHT(NMAT).GE.1.D4) THEN
          GO TO 10
        END IF
        NLOC2 = (N-1) * NSEC * NEQ1
c--> APA PHIV = porosity*grid block volume
        PHIV  = PHI(N) * EVOL(N)
c-->  APA  DVOLG=gas  vol.,DVOLL=liquid
vol.,DVOLC=CO2 vol. (all in m**3)
        DVOLG = PHIV * PAR(NLOC2+1)
        DVOLL = PHIV * PAR(NLOC2+NBK+1)
        DVOLC = PHIV * PAR(NLOC2+2*NBK+1)
C
c--> APA update (initialize vol. parameters)
        VOLG = VOLG + DVOLG
        VOLL = VOLL + DVOLL
        VOLC = VOLC + DVOLC
C
        DAMG = DVOLG * PAR(NLOC2+4)
        AMG  = AMG + DAMG
        DAML = DVOLL * PAR(NLOC2+NBK+4)
        AML  = AML + DAML
        DAMV = DAMG * PAR(NLOC2+NB+1)
        AMV  = AMV + DAMV
        DAMA = DAMG * PAR(NLOC2+NB+2) + DAML
* PAR(NLOC2+NBK+NB+2)
        AMA  = AMA + DAMA
        DAMW = DAML * PAR(NLOC2+NBK+NB+1)
        AMW  = AMW + DAMW
        DAMC  =  DVOLC  *  PAR(NLOC2+2*NBK+4)  *
PAR(NLOC2+2*NBK+NB+3)
        AMC  = AMC + DAMC
 10   CONTINUE
C
      PRINT 3,VOLL,VOLC
    3 FORMAT(/' PHASE VOLUMES IN PLACE:'/'
AQUEOUS ',E12.5,
     1   ' M**3;          SEPARATE PHASE CO2 ',E12.5,'
M**3')
C
      PRINT 4,AML,AMW,AMA,AMC,AMA+AMC
    4 FORMAT(/' MASS IN PLACE:'/' AQUEOUS
',E12.5,
     1 ' KG;    WATER ',E18.10,' KG;    DISSOLVED CO2
',E18.10,
     2 ' KG;   SEPARATE CO2 ',E18.10,' KG'/
     x' TOTAL CO2 ',E18.10,' KG')
C
C--> WEONSHIK, HAN
      WRITE(100,910)
SUMTIM,AML,AMW,AMA,AMC,AMA+AMC
 910   FORMAT(6(1x,E10.4))

      PRINT 5
    5 FORMAT(/1X,119('*')//)
      RETURN
      END
C********1*********2*********3*********4******
***5*********6*********7**
      SUBROUTINE QLOSS
C       DUMMY SUBROUTINE (IF ACTIVE, WOULD
DO HEAT EXCHANGE WITH
C     CONFINING LAYERS)
      COMMON/SVZ/NOITE,MOP(24)
C
      SAVE ICALL
      DATA ICALL/0/
      ICALL=ICALL+1
      IF(ICALL.EQ.1) WRITE(11,899)
 899  FORMAT(6X,'QLOSS      1.0          25 JANUARY
1990',6X,
     X'INACTIVE (DUMMY) SUBROUTINE')
C
C    INACTIVATE QLOSS
      MOP(15)=0
      RETURN
```

```
      END
C********1*********2*********3*********4*********5*********6*********7**
      SUBROUTINE MASSTRANS
      IMPLICIT DOUBLE PRECISION(A-H,O-Z)
C
C       This subroutine handles the transfer of mass from separate phase CO2
C            to dissolved phase and vice-versa. This is accomplished by having
C       sources and sinks of separate and dissolved phase CO2 in each element,
C          as appropriate.  This subroutine is called from MULTI just after
C     calling QU.  No other modifications are necessary.
C
      COMMON/E3/EVOL(1)
      COMMON/E4/PHI(1)
      COMMON/E9/ZBC(1)
      COMMON/P1/X(1)

COMMON/NN/NEL,NCON,NOGN,NK,NEQ,NPH,NB,
NK1,NEQ1,NBK,NSEC,NFLUX

COMMON/CYC/KCYC,ITER,ITERC,TIMIN,SUMTIM,
GF,TIMOUT

COMMON/CONTST/RE1,RE2,RERM,NER,KER,DFAC
      COMMON/FAIL/IHALVE
      COMMON/BC/NELA
      COMMON/P4/R(1)
      COMMON/SECPAR/PAR(1)
C
      SAVE ICALL,ZERO
      DATA ICALL,ZERO/0,1.D-13/
      ICALL=ICALL+1
      IF(ICALL.EQ.1) WRITE(11,899)
  899 FORMAT(6X,'TRANSFER  2.0              1  SEPT
1999',6X,
     X'MASS TRANSFER BETWEEN SEPARATE AND
DISSOLVED PHASE CO2')
C
      DO 200 N=1,NELA
        NLOC  = (N-1) * NEQ
        NLOCP = (N-1) * NK1
        NLOC2 = (N-1) * NSEC * NEQ1
        PX    = X(NLOCP+1)
        XCO2  = X(NLOCP+2)
        SCO2  = X(NLOCP+3)
        TX    = X(NLOCP+4)
        RHOL  = PAR(NLOC2+NBK+4)
        RHOC  = PAR(NLOC2+2*NBK+4)
        PCO2 = PX
        IF (SCO2.LE.DFAC) THEN
          SCO2 = 0.D0
        END IF
        IF (XCO2.LE.DFAC) THEN
          XCO2 = 0.D0
        END IF
C
        IF (SCO2.EQ.0.D0) THEN
C     Come here if there is no separate phase CO2 present in the element.
C
          IF (XCO2.EQ.0.D0) THEN
C     Come here if there is no dissolved phase CO2 present in the element.
C     In this case, no mass needs to be transferred.
C
            GO TO 200
C
          ELSE IF (XCO2.GT.0.D0) THEN
C     Come here if dissolved mass fraction of CO2 (XCO2) in the element is
C       greater than zero. In this case, must first determine what the dissolved
C       mass fraction of CO2 (XCO2N) should be at the ambient temperature (TX)
C     and pressure (PX).
C
C     Determine the fugacity (FCO2) of CO2 at the ambient temperature (TX)
C     and pressure (PX).
C-->          BARRET                    CALL
CO2(TX,PCO2,dummy,FCO2,dummy)

            CALL
FUGACITY(TX,PCO2,dummy,dummy,FCO2)

C     Determine the saturation pressure of water (PSAT) at the ambient
C     temperature (TX).
            CALL SAT(TX,PSAT)
C
C     Determine what the dissolved mass fraction of CO2 (XCO2N) should be at
C     the ambient temperature (TX) and pressure (PX).
            CALL HENRY(TX,PCO2,FCO2,XCO2N)


C
            IF (XCO2.LE.XCO2N) THEN
C       Come here if the dissolved mass fraction of CO2 (XCO2) present in the
C       element is less than or equal to what the dissolved mass fraction of CO2
C     (XCO2N) should be at the ambient temperature (TX) and pressure (PX).  In
C     this case, no mass needs to be transferred.
C
              GO TO 200
C
            ELSE IF (XCO2.GT.XCO2N) THEN
C       Come here if the dissolved mass fraction of CO2 (XCO2) in the element
C       is greater than what the dissolved mass fraction of CO2 (XCO2N) should
C     be at the ambient temperature (TX) and pressure (PX).  In this case, CO2
C       will evolve from the dissolved phase forming a separate phase.  Therefore,
C     need to transfer mass from dissolved phase to separate phase.
C
C       Determine the dissolved mass of CO2 (DMOLD) present in the element.
              DMOLD = PHI(N) * EVOL(N) * RHOL *
XCO2
C
C     Determine the dissolved mass of CO2 (DMNEW) that should be present in the
C     element.
              DMNEW = PHI(N) * EVOL(N) * RHOL *
XCO2N
C
C     The mass of CO2 that needs to be transferred from the dissolved phase
C       to separate phase is the difference between DMNEW and DMOLD.
C       Note that DMOLD should always be greater than DMNEW.
```

```
            DMDIF = DMNEW - DMOLD
            R(NLOC+2)      =      R(NLOC+2)      -
DMDIF/EVOL(N)
            R(NLOC+3)      =      R(NLOC+3)      +
DMDIF/EVOL(N)
          END IF
        END IF
C
       ELSE IF (SCO2.GT.0.D0) THEN
C     Come here if there is separate phase CO2 present in
the element.
C
C    Determine the fugacity (FCO2) of CO2 at the ambient
temperature (TX)
C    and pressure (PX).
C--->BARRET                                        CALL
CO2(TX,PCO2,dummy,FCO2,dummy)

          CALL
FUGACITY(TX,PCO2,dummy,dummy,FCO2)
C
C    Determine the saturation pressure of water (PSAT) at
the ambient
C    temperature (TX).
          CALL SAT(TX,PSAT)
C
C     Determine what the dissolved mass fraction of CO2
(XCO2N) should be at
C    the ambient temperature (TX) and pressure (PX).
          CALL HENRY(TX,PCO2,FCO2,XCO2N)

          IF (XCO2.EQ.XCO2N) THEN
C      Come here if the dissolved mass fraction of CO2
(XCO2) present in the
C    element is equal to what the dissolved mass fraction of
CO2 (XCO2N)
C       should be at the ambient temperature (TX) and
pressure (PX).  In this
C    case, no mass needs to be transferred.
C
            GO TO 200
C
          ELSE IF (XCO2.GT.XCO2N) THEN
C      Come here if the dissolved mass fraction of CO2
(XCO2) in the element
C      is greater than what the dissolved mass fraction of
CO2 (XCO2N) should
C    be at the ambient temperature (TX) and pressure (PX).
In this case, CO2
C      will evolve from the dissolved phase adding to the
separate phase.
C    Therefore, need to transfer mass from dissolved phase
to separate phase.
C
C       Determine the dissolved mass of CO2 (DMOLD)
present in the element.
            DMOLD = PHI(N) * EVOL(N) * (1.D0-SCO2)
* RHOL * XCO2
C
C    Determine the dissolved mass of CO2 (DMNEW) that
should be present in the
C    element.
            DMNEW = PHI(N) * EVOL(N) * (1.D0-SCO2)
* RHOL * XCO2N
C
C    The mass of CO2 that needs to be transferred from the
dissolved phase to
C    separate phase is the difference between DMNEW and
DMOLD.  Note that DMOLD
C    should always be greater than DMNEW.
            DMDIF = DMNEW - DMOLD
            R(NLOC+2) = R(NLOC+2) - DMDIF/EVOL(N)
            R(NLOC+3)      =      R(NLOC+3)      +
DMDIF/EVOL(N)
C
          ELSE IF (XCO2.LT.XCO2N) THEN
C      Come here if the dissolved mass fraction of CO2
(XCO2) in the element
C     is less than what the dissolved mass fraction of CO2
(XCO2N) should
C    be at the ambient temperature (TX) and pressure (PX).
In this case, CO2
C      will dissolve from the separate phase adding to the
dissolved phase.
C    Therefore,need to transfer mass from separate phase to
dissolved phase.
C
C       Determine the dissolved mass of CO2 (DMOLD)
present in the element.
            DMOLD = PHI(N) * EVOL(N) * (1.D0-SCO2)
* RHOL * XCO2
C
C       Determine the dissolved mass of CO2 (DMNEW)
corresponding to the new
C    dissolved mass fraction of CO2 (XCO2).
            DMNEW = PHI(N) * EVOL(N) * (1.D0-SCO2)
* RHOL * XCO2N
C
C    The mass of CO2 that needs to be transferred from the
separate phase to the
C      dissolved phase is the difference between DMNEW
and DMOLD.  Note that DMNEW
C    should always be greater than DMOLD.
            DMDIF = DMNEW - DMOLD
C
C    However, need to determine the total mass of separate
phase CO2 present in
C    the element.
            SMCO2 = PHI(N) * EVOL(N) * SCO2   *
RHOC
C
            IF (DMDIF.GT.SMCO2) THEN
C      Come here if the mass that needs to be transferred
from the separate phase
C      to dissolved phase is greater than the total separate
phase mass present
C     in the element.  In this case, transfer all the separate
phase mass to
C    dissolved phase.
C
              DMDIF = SMCO2
            END IF
            R(NLOC+2) = R(NLOC+2) - DMDIF/EVOL(N)
            R(NLOC+3)      =      R(NLOC+3)      +
DMDIF/EVOL(N)
          ENDIF
        END IF
200   CONTINUE
      RETURN
      END
C********1*********2*********3*********4******
***5*********6*********7**
```

Appendix V. Matlab version: MRKEOS.

1. MRK_EOSCO2: main m file

2. MRK: This subroutine is called from MRK_EOSCO2 during the Newton iteration for the molar volume (V) of CO2 as function of temperature (T) and pressure of CO2 (PCX). This subroutine calculates the V for which the MRK EOS is 0 at the given T and PCX, and the value of the derivative of the MRK EOS wrt V for the calculated V.

3. FUGACITY_COEFFICIENT: This subroutine is called from MRK_EOSCO2 during the calculation of fugacity of CO2 as function of temperature (T), pressure of CO2 (PCX), and molar volume of CO2 (V). This subroutine calculates the fugacity coefficient of CO2 (PHI) by substituting the MRK EOS into RTln(PHI)=Integral from V to infinity of (PCX-RT/V)dV - RTln(Z) + RT(Z-1). This expression comes from Prausnitz (1969).

4. SPECIFIC_ENTHALPY: This subroutine is called from MRK_EOSCO2 during the calculation of the specific enthalpy of CO2 as function of temperature (T), pressure of CO2 (PCX), and molar volume of CO2 (V). This subroutine calculates the molar enthalpy of CO2 using residual properties. A residual property is defined as the difference between the real fluid property and the perfect gas state property (Patel and Eubank, 1988).

5. HENRY: This subroutine calculates the mass fraction of CO2 in the liquid phase using an extended Henry's Law relationship from Reid et al (1987). The relationship is ln(FC/XCO2) = ln(HP) + VID(PCX-PS)/RT.

See below for variable definitions.

The expression for Henry's Constant is from O'Sullivan et al. (1985). The expression was created using a piece-wise quadratic fit to data published by Ellis and Goulding (1963), Malinin (1959), Takenouchi and Kennedy (1964), and Gibb and Van Ness (1971).

6. SOLUTE: This subroutine calcualtes the enthalpy of CO2 dissolution in liquid water. The expression is from O'Sullivan et al., (1985). The expression was created using a quadratic fit to data published by Ellis and Goulding (1963).

7. DENMIX: This subroutine returns density of CO2/H2O liquid mixture. The expression is from Anderson et al. (1992).

8. VISCO2: This subroutine calculates the viscosity of pure CO2 as a function of temperature and density of CO2. The expressions for calculating the viscosity come from empirical equations provided in Vesovic et al.(1990) and Fenghour et al. (1998).

MRK_EOSCO2.m

```
clear

%C      This subroutine calculates the specific density, fugacity, and
%C    specific enthalpy of gaseous and supercritical CO2 as a function of
%C    the pressure of CO2 (PCX) and temperature (TX) using a Modified
%C     Redlich-Kwong (MRK) equation of state (EOS) and standard thermo-
%C    dynamic equations.  This formulation of the MRK EOS is based on the
%C    work of Kerrick and Jacobs (1981) and Weir et al. (1996). Weir et al.
%C    extended the MRK EOS of Kerrick and Jacobs to low temperatures.
%C     Accuracy is suspect outside the temperature and pressure ranges of
%C    50 < T < 350 deg C and 0.1 < PCX < 45 MPa, respectively.

%C        Input:
%C                TX  = Temperature in degrees C
%C                PCX  = Pressure of CO2 in Pa

%C        Output:
%C                DC   = Specific density of CO2 in kg/m3
%C                HC   = Specific enthalpy of CO2 in J/kg
%C                FC   = Fugacity of CO2 in Pa

%C        Constants:
%C                XMWC = Molecular weight of CO2 in Kg/mol
%C                R    = Universal gas constant in m3Pa/molK
%C                B    = Covolume in m3/mol (value from K&J)

%C        Variables:
%C                T   = Temperature in K
%C                V    = Molar volume of CO2 in m3/mol
%C                Y       = Dimensionless variable (B/4V)
%C                Z   = Compressibility factor [-]
%C                PHI  = Fugacity coefficient [-]
%C                H    = Molar enthalpy in J/mol

T=input('temperature (K) >>')

global T PCX V Y DV DC PHI Z AT H FC XCO2 X1M HSOL D1M VC

    XMWC = 4.40098D-02;
    XMWW = 1.801534D-02;
    R   = 8.3147295D0;
    B   = 5.8D-05;

    PCX=1;
    n=100001:100000:100000001;
for i=1:1000;
    PCX=PCX+100000;

%C    First calculate V as a function of T and PCX using Newton Iteration
%C    with tolerance TOL:

    TOL = 1.0D-06;

%C    Initial guess of V, DV, and Y from ideal gas law:
    V = (R*T) / PCX;
    DV = V;
    Y = B / (4.D0*V);
%C
%C    Initialize attractive term (AT) of MRK EOS:
    AT  = 0.D0;
%C
%C    Newton Iteration for V as a function of T and PCX:
    KOUNT = 0;
    while abs(DV/V)>TOL
      MRK;
      V = V - DV;
      Y = B / (4.D0*V);
      KOUNT = KOUNT + 1;
    end

%C    Calculate density (DC) in kg/m3 from V in m3/mol:
    DC= XMWC / V;
    CO2_DENSITY(i)=DC;

%C    Calculate Y to the 2nd and 3rd powers for later use:
    Y2 = Y * Y;
    Y3 = Y2 * Y;

%C    Calculate compressibility factor (Z) by substituting MRK EOS into Z=PV/RT:
    Z=          ((1.D0+Y+Y2-Y3)/((1.D0-Y)^3.D0))          -(AT/(R*T*sqrt(T)*(V+B)));
    COMPRESSIBILITY_FACTOR(i)=Z;

%C     Calculate fugacity (FC): Call fugacity coefficient calculation from FUGACITY_COEFFICIENT subroutine.
    FUGACITY_COEFFICIENT;

    FUG(i)=PHI;
    FC = PHI * PCX;
    CO2_FUGACITY(i)=FC;

%C       Calculate specific enthalpy (H): Call specific enthalpy calculation from SPECIFIC_ENTHALPY subroutine.
    SPECIFIC_ENTHALPY;

    CO2_ENTHALPY(i)=H;

%C    Calculate mole fraction (XCO2) and mass fraction (X1M): Call mass fraction calculation from HENRY subroutine.
    HENRY;

    CO2_MOLE_FRACTION(i)=XCO2;

%C    Calculate mass fraction of CO2 (XMASS):
    X1M     =     (XMWC*XCO2)     /     (((1.D0-XCO2)*XMWW)+(XCO2*XMWC));

    CO2_MASS_FRACTION(i)=X1M;
```

```
%C     Calculate the enthalpy of CO2 dissolution in liquid water (HSOL): Call the enthalpy of CO2 dissolution calculation from SOLUT subroutine.
      SOLUT;
      ENTHALPY_CO2_DISSOLUTION(i)=HSOL;

%C     Calculate the mixture density of CO2/H2O liquid mixture (D1M): Call the mixture density of CO2/H2O calculation from DENMIX subroutine.
      DENMIX;
      MIXTURE_DENSITY(i)=D1M;

%C     Calculate the dynamic viscosity of CO2 (VC): Call the dynamic viscosity of CO2 calculation from VISCO2 subroutine.
      VISCO2;
      CO2_VISCOSITY(i)=VC;

end

PCX=n./10^6;

title('Pressure vs. CO2 density')
plot(PCX,CO2_DENSITY)
axis([1 100 0 1200])
xlabel('Pressure [MPa]')
ylabel('CO2 density [kg/m3]')

figure
title('Pressure vs. Compressibility factor')
plot(PCX,COMPRESSIBILITY_FACTOR)
axis([0 100 0 2])
xlabel('Pressure [MPa]')
ylabel('Compressibility factor [-]')

figure
title('pressure vs. fugacity coefficient')
plot(PCX,FUG)
axis([1 100 0 1])
xlabel('Pressure [MPa]')
ylabel('Fugacity coefficient [-]')

figure
title('pressure vs. specific enthalpy')
plot(PCX,CO2_ENTHALPY)
xlabel('Pressure [MPa]')
ylabel('Specific enthalpy [J/Kg]')

figure
title('pressure vs. Mole fraction of CO2')
plot(PCX,CO2_MOLE_FRACTION)
axis([0 100 0 0.1])
xlabel('Pressure [MPa]')
ylabel('Mole fraction of CO2 [-]')

figure
title('pressure vs. enthalpy of CO2 dissolution')
plot(PCX,ENTHALPY_CO2_DISSOLUTION)
xlabel('Pressure [MPa]')
ylabel('Enthalpy of CO2 dissolution [J/Kg]')

figure
title('pressure vs. Mixture density of CO2/H2O')
plot(PCX,MIXTURE_DENSITY)
xlabel('Pressure [MPa]')
ylabel('Mixture density of CO2/H2O [kg/m3]')

figure
title('pressure vs. Dynamic viscosity of CO2')
plot(PCX,CO2_VISCOSITY)
xlabel('Pressure [MPa]')
ylabel('Dynamic viscosity of CO2 [Pa-s]')
```

MRK.m

```
function MRK(DV,AT)

%C      This subroutine is called from subroutine CO2 during the Newton
%C      Iteration for the molar volume (V) of CO2 as function of temperature
%C      (T) and pressure of CO2 (PCX).  This subroutine calculates
%C      the V for which the MRK EOS is 0 at the given T and PCX, and the
%C      value of the derivative of the MRK EOS wrt V for the calculated V.

%C          Input:
%C                  Y       = Dimensionless variable (B/4V)
%C                  T   = Temperature in K
%C                  PCX = Pressure of CO2 in Pa
%C                  V       = Prev. estimate of molar volume of CO2 in m3/mol

%C          Output:
%C                  DV  = Change in molar volume of CO2 in m3/mol

%C          Constants:
%C                  R     = Universal gas constant in m3Pa/molK
%C                  B     = Covolume in m3/mol (value from K&J)
%C          Ci thru Fi= Coefficients of the MRK EOS (i=1,2,3)
%C                  Values from Weir et al. (1996)

%C          Variables:
%C          CT thru FT= Temperature-dependent functions for evaluating
%C                      attractive term of MRK EOS
%C                  AT  = Attractive term of MRK EOS

%C                  FV  = V at which MRK EOS is 0 for T and PCX
%C                  DV  = -FV / Value of derivative wrt V of MRK EOS

global T PCX V Y DV DC AT DW H

    R   = 8.3147295D0;
    B   = 5.8D-05;
    C1  = 2.39534D+01;
    C2  = -4.55309D-02;
    C3  = 3.65168D-05;
    D1  = -4.09844D-03;
    D2  = 1.23158D-05;
    D3  = -8.99791D-09;
    E1  = 2.89224D-07;
    E2  = -8.02594D-10;
    E3  = 7.30975D-13;
    F1  = -6.43556D-12;
    F2  = 2.01284D-14;
    F3  = -2.17304D-17;

%C    Calculate T squared for later use:
    T2 = T * T;
%C
%C    Calculate V to the 2nd, 3rd, and 4th powers for later use:
    V2 = V * V;
    V3 = V2 * V;
    V4 = V3 * V;
%C
%C    Calculate Y to the 2nd and 3rd powers for later use:
    Y2 = Y * Y;
    Y3 = Y2 * Y;
%C
%C    Calculate B to the 2nd and 3rd powers for later use:
    B2 = B * B;
    B3 = B2 * B;
%C
%C      Calculate temperature-dependent functions for evaluating attractive
%C    term in MRK EOS:
    CT = C1 + (C2*T) + (C3*T2);
    DT = D1 + (D2*T) + (D3*T2);
    ET = E1 + (E2*T) + (E3*T2);
    FT = F1 + (F2*T) + (F3*T2);

%C    Calculate attractive term in MRK EOS:
    AT = CT + (DT/V) + (ET/V2) + (FT/V3);
%C
%C    Calculate V at which MRK EOS equals 0:
    FV = PCX - (((R*T*(1.D0+Y+Y2-Y3))/(V*((1.D0-Y)^3.D0)))-(AT/(sqrt(T)*V*(V+B))));

%C
%C    Calculate -FV / value of derivative wrt V of MRK EOS
    DV = -FV / (((-3.D0*B*R*T*(1.D0+Y+Y2-Y3))/(4.D0*V3*((1.D0-Y)^4.D0)))-((R*T*(1.D0+Y+Y2-Y3))/(V2*((1.D0-Y)^3.D0)))+((R*T*(((3.D0*B3)/(64.D0*V4))-(B2/(8.D0*V3))-(B/(4.D0*V2))))/(V*((1.D0-Y)^3.D0)))-(AT/(sqrt(T)*V*(V+B))));
```

FUGACITY_COEFFICIENT.m

```
function FUGACITY_COEFFICIENT(PHI)
%     IMPLICIT DOUBLE PRECISION(A-H,O-Z)

%     This subroutine is called from subroutine CO2 during the
%          calculation of fugacity of CO2 as function of temperature (T),
%      pressure of CO2 (PCX), and molar volume of CO2 (V).  This
%     subroutine calculates the fugacity coefficient of CO2 (PHI) by
%     substituting the MRK EOS into RTln(PHI)=Integral from V to infinity
%C       of (PCX-RT/V)dV - RTln(Z) + RT(Z-1).  This expression comes from
%C     Prausnitz (1969).
%C
%C          Input:
%C                         Y       = Dimensionless variable (B/4V)
%C                         T  = Temperature in K
%C                         V      = Molar volume of CO2 in m3/mol
%C                         Z   = Compressibility factor of CO2 [-]
%C
%C          Output:
%C                         PHI = Fugacity coefficient of CO2 [-]
%C
%C          Constants:
%C                         R      = Universal gas constant in m3Pa/molK
%C                         B    = Covolume in m3/mol (value from K&J)
%C          Ci thru Fi= Coefficients of the MRK EOS (i=1,2,3)
%C                              Values from Weir et al. (1996)
%C
%C          Variables:
%C          CT thru FT= Temperature-dependent functions for evaluating
%C                              attractive term of MRK EOS
%C

global T PCX V Y DV DC PHI Z AT H


R  =  8.3147295D0;
B  =  5.8D-05;
C1  =  2.39534D+01;
C2  = -4.55309D-02;
C3  =  3.65168D-05;
D1  = -4.09844D-03;
D2  =  1.23158D-05;
D3  = -8.99791D-09;
E1  =  2.89224D-07;
E2  = -8.02594D-10;
E3  =  7.30975D-13;
F1  = -6.43556D-12;
F2  =  2.01284D-14;
F3  = -2.17304D-17;
%C
%     SAVE ICALL
%     DATA ICALL/0/
%     ICALL=ICALL+1
%     IF(ICALL.EQ.1) WRITE(11,899)
%   899 FORMAT(6X,'FUGACITY  2.0          1 SEPT 1999',6X,
% X'CALCULATE FUGACITY COEFFICIENT FOR SEPARATE PHASE CO2')
%C
%C    Calculate T to the 2nd power for later use:
     T2 = T * T;
%C
%C    Calculate V to the 2nd, 3rd, and 4th powers for later use:
     V2 = V * V;
     V3 = V2 * V;
%C
%C    Calculate B to the 2nd, 3rd, and 4th powers for later use:
     B2 = B * B;
     B3 = B2 * B;
     B4 = B3 * B;
%C
%C       Calculate temperature dependent functions for evaluating attractive
%C    term in MRK EOS:
     CT = C1 + (C2*T) + (C3*T2);
     DT = D1 + (D2*T) + (D3*T2);
     ET = E1 + (E2*T) + (E3*T2);
     FT = F1 + (F2*T) + (F3*T2);
%C
%C    Calculate fugacity coefficient:
     PHI = Y * (8.D0 + Y * (-9.D0 + 3.D0 * Y))/(1.D0-Y)^3.D0...
         - log(Z)...
         - CT / (R * T * sqrt(T) * (V + B))...
         - DT / (R * T * sqrt(T) * V * (V + B))...
         - ET / (R * T * sqrt(T) * V2 * (V + B))...
         - FT / (R * T * sqrt(T) * V3 * (V + B))...
         + CT * log(V / (V + B))/ (R * T * sqrt(T) * B)...
         - DT / (R * T * sqrt(T) * B * V)...
         + DT * log((V + B) / V) / (R * T * sqrt(T) * B2)...
         - ET / (R * T * sqrt(T) * 2.D0 * B * V2)...
         + ET / (R * T * sqrt(T) * B2 * V)...
         - ET * log((V + B) / V) / (R * T * sqrt(T) * B3)...
         - FT / (R * T * sqrt(T) * 3.D0 * B * V3)...
         + FT / (R * T * sqrt(T) * 2.D0 * B2 * V2)...
         - FT / (R * T * sqrt(T) * B3 * V)...
         - FT * log(V / (V + B)) / (R * T * sqrt(T) * B4);
     PHI = exp(PHI);
```

SPECIFIC_ENTHALPY.m

```
function SPECIFIC_ENTHALPY(H)

%C       This subroutine is called from subroutine CO2 during the
%C       calculation of the specific enthalpy of CO2 as function of
%C     temperature (T), pressure of CO2 (PCX), and molar volume
%C     of CO2 (V).  This subroutine calculates the molar enthalpy of CO2
%C       using residual properties.  A residual property is defined as the
%C     difference between the real fluid property and the perfect gas
%C     state property.  Following Patel and Eubank (1988) for molar enthalpy:
%C      H-H'ref = H(T,rho) - H'(Tref,Pref/RTref), where ' indicates the
%C     perfect gas state.  Integration is done along the path
%C                              H(T,rho)-->H'(T,0)-->H'(Tref,0)-->H'(Tref,Pref/RTref).
%C
%C        Determine residual internal energy first: (U-U'ref)/RT = 1/T integral
%C     from 0 to rho of dZ/d(1/T) drho/rho + 1/T integral from Tref to T of
%C     Cv/R dT, where Cv is molar heat capacity in J/(mol K).  Then determine
%C     residual enthalpy: (H-H'ref)/RT = (U-U'ref)/RT + Z - Tref/T.  Using
%C      Tref=273.16 K and Pref=1000 Pa, H'ref=0 (from Patel and Eubank).

%C         Input:
%C                    T    = Temperature in K
%C                    V      = Molar volume of CO2 in m3/mol
%C                    Z    = Compressibility factor of CO2 [-]

%C         Output:
%C                    H      = Molar enthalpy of CO2 in J/mol

%C         Constants:
%C                    R      = Universal gas constant in m3Pa/molK
%C                    B     = Covolume in m3/mol (value from K&J)
%C             Ci thru Fi = Coefficients of the MRK EOS (i=1,2,3)
%C                              Values from Weir et al. (1996)
%C      Gi   = Coefficients of molar heat capacity
%C           Values from Angus et al. (1976)
%C                    Tref = Reference temperature in K (value from P&E)

%C         Variables:
%C                    RHO   = Molar density of CO2 in mol/m3
%C                    XI1  = First Integral (see above)
%C                    XI2  = Second Integral (see above)
%C                    URES = Residual internal energy

global T PCX V Y DV DC PHI Z AT DW H

   XMWC = 4.40098D-02;
   BETA=  304.21D0;
   R   = 8.3147295D0;
   TREF=  2.7316D+02;
   B   = 5.8D-05;
   C1  = 2.39534D+01;
   C2  = -4.55309D-02;
   C3  = 3.65168D-05;
   D1  = -4.09844D-03;
   D2  = 1.23158D-05;
   D3  = -8.99791D-09;
   E1  = 2.89224D-07;
   E2  = -8.02594D-10;
   E3  = 7.30975D-13;
   F1  = -6.43556D-12;
   F2  = 2.01284D-14;
   F3  = -2.17304D-17;
   G0  = 0.769441246D+01;
   G1  = -0.249610766D+00;
   G2  = -0.254000397D+02;
   G3  = 0.651102201D+02;
   G4  = -0.820863624D+02;
   G5  = 0.574148450D+02;
   G6  = -0.212184243D+02;
   G7  = 0.323362153D+01;

%C    Calculate molar density (RHO):
    RHO = 1.D0 / V;

%C     Calculate rho to the 2nd and 3rd powers for later use:
    RHO2 = RHO * RHO;

%C     Calculate beta to the 2nd thru 7th powers for later use:
    BETA2 = BETA * BETA;
    BETA3 = BETA2 * BETA;
    BETA4 = BETA3 * BETA;
    BETA5 = BETA4 * BETA;
    BETA6 = BETA5 * BETA;
    BETA7 = BETA6 * BETA;

%C    Calculate Tref to the 2nd thru 6th powers for later use:
    TREF2 = TREF * TREF;
    TREF3 = TREF2 * TREF;
    TREF4 = TREF3 * TREF;
    TREF5 = TREF4 * TREF;
    TREF6 = TREF5 * TREF;

%C    Calculate T to the 2nd thru 6th powers for later use:
    T2 = T * T;
    T3 = T2 * T;
    T4 = T3 * T;
    T5 = T4 * T;
    T6 = T5 * T;

%C    Calculate B to the 2nd, 3rd, and 4th powers for later use:
    B2 = B * B;
    B3 = B2 * B;
    B4 = B3 * B;

%C     Calculate 1/T times the integral from 0 to rho of dZ/d(1/T) drho/rho:
```

```
    XI1    =    (B*RHO*(-6.D0*(3.D0*F1+T*(F2-F3*T))-
B2*(18.D0*D1...
         +6.D0*T*(D2-D3*T)+3.D0*(3.D0*E1+T*(E2-
E3*T))*RHO...
         +2.D0*(3.D0*F1+T*(F2-
F3*T))*RHO2)+3.D0*B*(6.D0*E1...
         +3.D0*F1*RHO+T*(2.D0*E2-
2.D0*E3*T+F2*RHO-F3*T*RHO)))...
         +6.D0*(3.D0*F1+T*(F2-F3*T)+B3*(-
3.D0*C1+T*(-C2+C3*T))...
         +B2*(3.D0*D1+T*(D2-D3*T))+B*(-
3.D0*E1+T*(-E2+E3*T)))...
         *log(1+B*RHO))/(12*B4*R*T^1.5);

%C     Calculate 1/T times the integral from Tref to T of
Cv/R dT, where Cv
%C     is molar heat capacity in J/(mol K).  The expression
for Cv is
%C     derived an expression from Angus et al. (1976) for
molar
%C     heat capacity at constant pressure:
    XI2              =              G0-1.D0+((TREF/T)*(1.D0-
G0))+(((BETA*G1)/T)*log(T/TREF))+(((BETA2*G2)/T)
*((1.D0/TREF)-(1.D0/T)))...
         +(((BETA3*G3)/(2.D0*T))*((1.D0/TREF2)-
(1.D0/T2)))...
         +(((BETA4*G4)/(3.D0*T))*((1.D0/TREF3)-
(1.D0/T3)))...
         +(((BETA5*G5)/(4.D0*T))*((1.D0/TREF4)-
(1.D0/T4)))...
         +(((BETA6*G6)/(5.D0*T))*((1.D0/TREF5)-
(1.D0/T5)))...
         +(((BETA7*G7)/(6.D0*T))*((1.D0/TREF6)-
(1.D0/T6)));
%C
%C     Calculate residual internal energy (URES):
    URES = XI1+XI2;

%C     Calculate molar enthalpy (H):
    H    =    (URES+Z-(TREF/T))    *    R    *    T    /    XMWC
+809248.07;
```

HENRY.m

```
function HENRY(X1M)

global T PCX V Y DV DC PHI Z AT DW H FC X1M
XCO2


%C     This subroutine calculates the mass fraction of CO2
in the liquid
%C     phase using an extended Henry's Law relationship
from Reid et al.
%C     (1987). The relationship is ln(FC/XCO2) = ln(HP)
+ VID(PCX-PS)/RT.
%C     See below for variable definitions.

%C          The expression for Henry's Constant is from
O'Sullivan et al. (1985).
%C          The expression was created using a piece-wise
quadratic fit to data
%C       published by Ellis and Goulding (1963), Malinin
(1959), Takenouchi
%C          and Kennedy (1964), and Gibb and Van Ness
(1971).

%C     The value for the the partial molar volume of CO2
at infinite
%C     dilution is assumed to be constant at 30E-6 from the
work of
%C     Takenouchi and Kennedy (1964) (and others). This
assumption is
%C     reasonable at temperatures below 150 C.

%C          Input:
%C                    TX   = Temperature in degrees C
%C                    PCX  = Pressure of CO2 in Pa
%C                    PS   = Saturation pressure of water
in Pa
%C                    FC   = Fugacity of CO2 in Pa

%C          Output:
%C                    X1M  = Mass fraction of CO2 in
liquid phase [-]

%C          Constants:
%C                    XMWC = Molecular weight of CO2
in Kg/mol
%C                    XMWW = Molecular weight of
H2O in Kg/mol
%C                    R    = Universal gas constant in
m3Pa/molK
%C                    VID  = Partial molar volume of
CO2 at infinite
%C               dilution in m3/mol (value from T&K)

%C          Variables:
%C                    T    = Temperature in K
%C                    TAU  = Temperature variable used
in calculation
%C                         of Henry's Coefficient in
degrees C
%C                    HP   = Henry's Coefficient in bars,
then Pa
%C                    XCO2 = Mole fraction CO2 in
liquid phase [-]

XMWC = 4.40098D-02;
XMWW = 1.801534D-02;
R1   = 8.3147295D0;
VID  = 3.0D-05;

% Saturation pressure as function of temperature
   A=[-7.691234564,-2.608023696E1,-
1.681706546E2,6.423285504E1,-
1.189646225E2,4.167117320,2.097506760E1,1.E9,6.];

    TCC=T/647.3;
    SC=0.;
    for J=1:5
    SC=SC+A(J)*(1.-TCC)^J;
    PCC=exp(SC/(TCC*(1+A(6)*(1-TCC)+A(7)*(1-
TCC)^2))-(1.-TCC)/(A(8)*(1-TCC)^2+A(9)));
    PS=PCC*2.212E7;
    end

     TTAU = ((T-273.15)-1.7D+02) / 1.0D+02;

%C    Calculate TAU to the 2nd and 4th powers for later
use:
    TAU2 = TTAU * TTAU;
    TAU4 = TAU2 * TAU2;

%C    Calculate Henry's Coefficient (HP) in bars:
    if TTAU>=0.D0;

      HP   =  6.4D+03  -  (2.07778D+03*TAU2)  +
(3.1111D+02*TAU4);

   else
      HP   =  6.4D+03  -  (2.14914D+03*TAU2)  -
(1.9543D+02*TAU4);

   end

%C    Convert Henry's Coefficient to Pa:
    HP = HP * 1.0D+05;

%C    Calculate mole fraction of CO2 (XMOLE):
    XCO2 = exp(log(FC/HP)-(VID*(PCX-PS))/(R1*T));
```

SOLUTE.m

```
function SOLUT(HSOL)

%       This subroutine calcualtes the enthalpy of CO2
dissolution in liquid water.
%     The expression is from O'Sullivan et al., (1985). The
expression was created
%       using a quadratic fit to data published by Ellis and
Goulding (1963).

global T PCX V Y DV DC PHI Z AT H HSOL

%     Convert temperature from kelvin [K] to degree [C]

     TX = T-2.7315D+02;
     T1  = 1.D-2 * TX;
     T2 = T1 * T1;
     T3 = T1 * T2;
     T4 = T1 * T3;
     HSOL = -7.3696D-2 - 5.6405D-1*T1 + 7.0363D-1*T2
- 2.7882D-1*T3 + 4.2579D-2*T4;
     HSOL = HSOL * 1.D6;
```

DENMIX.m

```
function DENMIX(D1M)

%C     This subroutine returns density of CO2/H2O liquid mixture. The
%C     expression is from Anderson et al. (1992).

%C          Input:
%C                    TX   = Temperature in degrees C
%C                    DW   = Density of H2O in kg/m3
%C                    X1M  = Mass fraction of CO2 [-]

%C          Output:
%C                    D1M    = Density of CO2/H2O mixture in kg/m3

%C          Constants:
%C                    XMWC = Molecular weight of CO2 in Kg/mol

%C          Variables:
%C                    RHO    = Density of CO2 at saturation pressure in mol/cm3
%C                    DC   = Density of CO2 at saturation pressure in kg/m3
%C                    X2M  = Mass fraction H2O [-]

global T PCX V Y DV DC PHI Z AT H D1M X1M

      XMWC=4.40098D-02;

%C     Calculate TX to the 2nd, 3rd and 4th powers for later use:
      TX=T-273.15;
      TX2 = TX * TX;
      TX3 = TX2 * TX;
      TX4 = TX3 * TX;

%C      Calculate density of CO2 (RHO) at saturation pressure in mol/cm3:
      RHO1 = 1.D0/(3.736D+01 - (7.109D-02*TX) - (3.812D-05*TX2) + (3.296D-06*TX3) - (3.702D-09*TX4));

%C    Convert RHO to kg/m3 (DC):
      DC1 = RHO1 * 1.0D+06 * XMWC;

%C    Calculate mass fraction of H2O:
      X2M = 1.D0 - X1M;

% From here, calcualte pure water density (International Formulation Committee, 1967)

    A1=[6.824687741E3,-5.422063673E2,-2.096666205E4,3.941286787E4,...
      -6.733277739E4,9.902381028E4,-1.093911774E5,8.590841667E4,...
      -4.511168742E4,1.418138926E4,-2.017271113E3,7.982692717E0,...
      -2.616571843E-2,1.522411790E-3,2.284279054E-2,2.421647003E2,...
      1.269716088E-10,2.074838328E-7,2.174020350E-8,1.105710498E-9,...
      1.293441934E1,1.308119072E-5,6.047626338E-14];

    SA=[8.438375405E-1,5.362162162E-4,1.720000000E0,7.342278489E-2,...
      4.975858870E-2,6.537154300E-1,1.150E-6,1.51080E-5,...
      1.41880E-1,7.002753165E0,2.995284926E-4,2.040E-1];

      TKR=T/647.3;

      PNMR=PCX/2.212E7;

      Y=1.-SA(1)*TKR*TKR-SA(2)/TKR^6;

      ZP=(SA(3)*Y*Y-2.*SA(4)*TKR+2.*SA(5)*PNMR);

      Z=Y+sqrt(ZP);

      PAR1=A1(12)*SA(5)/Z^(5./17.);

PAR2=A1(13)+A1(14)*TKR+A1(15)*TKR*TKR+A1(16)*(SA(6)-TKR)^10+A1(17)/(SA(7)+TKR^19);

PAR3=(A1(18)+2.*A1(19)*PNMR+3.*A1(20)*PNMR*PNMR)/(SA(8)+TKR^11);

      PAR4=A1(21)*TKR^18*(SA(9)+TKR*TKR)*(-3./(SA(10)+PNMR)^4+SA(11));

      PAR5=3.*A1(22)*(SA(12)-TKR)*PNMR*PNMR+4.*A1(23)/TKR^20*PNMR^3;

      VMKR=PAR1+PAR2-PAR3-PAR4+PAR5;

      V=VMKR*3.17E-3;

      DW=1./V;

%C    Calculate density of CO2/H2O mixture in kg/m3:

      D1M = (DW*DC1) / ((X1M*DW)+(X2M*DC1));
```

VISCO2.m

```
function VISCO2(VC)

%C       This subroutine calculates the viscosity of pure
CO2 as a function
%C        of temperature and density of CO2.  The
expressions for calculating
%C        the viscosity come from empirical equations
provided in Vesovic et
%C    al.(1990) and Fenghour et al. (1998).
%C     The critical point enhancement for the viscosity of
CO2
%C    has been neglected since it is weak and restricted to
a very small
%C    region around the critical point.

%C        Input:
%C                  TX    = Temperature in degrees C
%C                  DC    = Density of CO2 in kg/m3

%C        Output:
%C                  VC    = Viscosity of CO2 in Pa-s

%C        Constants:
%C                  Ai          = Coefficients of the
correlation of the
%C                        zero-density viscosity
%C                  ESCL  = Energy scaling parameter
in K
%C                       = epsilon/kappa
%C                  Dij         = Coefficients of the
correlation of the
%C                        excess viscosity

%C        Variables:
%C                  T     = Temperature in K
%C                  TSTAR     = (kappa*T)/epsilon =
T/ESCL [-]
%C                  ETA0    = Zero-density viscosity in
muPa-s
%C                  DETA      = Excess viscosity in
muPa-s

global T PCX V Y DV DC PHI Z AT H VC

      A0   =  2.35156D-01;
      A1   = -4.91266D-01;
      A2   =  5.211155D-02;
      A3   =  5.347906D-02;
      A4   = -1.537102D-02;
      ESCL =  2.51196D+02;
      D11  =  0.4071119D-02;
      D21  =  0.7198037D-04;
      D64  =  0.2411697D-16;
      D81  =  0.2971072D-22;
      D82  = -0.1627888D-22;

      DC2 = DC*DC;
            DC6 = DC2*DC2*DC2;
          DC8 = DC6*DC2;

%C    Calculate TSTAR and 3rd power:
      TSTAR = T/ESCL;
      TSTAR3=TSTAR*TSTAR*TSTAR;

%C    Calculate ln(TSTAR) and 2nd, 3rd, and 4th powers:
      BETA1 = log(TSTAR);
      BETA2 = BETA1*BETA1;
            BETA3 = BETA2*BETA1;
            BETA4 = BETA3*BETA1;

%C    Calculate zero-density limit viscosity in muPa-s:
      EXS                                                =
exp(A0+(A1*BETA1)+(A2*BETA2)+(A3*BETA3)+(A4
*BETA4));
      ETA0 = (1.00697D0 * sqrt(T)) / EXS;

%C    Calculate excess viscosity in muPa-s:
      DETA                                               =
(D11*DC)+(D21*DC2)+((D64*DC6)/TSTAR3)+(D81*D
C8)+((D82*DC8)/TSTAR);

%C    Calculate total viscosity in muPa-s:
      VC = ETA0 + DETA;

%C    Convert viscosity from muPa-s to Pa-s:
      VC = VC * 1.0D-06;
```

Appendix VI. Matlab version: SWEOS.

1. SW_EOSCO2: main m file

2. SPECIFIC_DENSITY: This subroutine calculates the specific density of gaseous and supercritical CO2 as a function of the pressure of CO2 (PCX) and temperature (TX) using a Span and Wagner (1996). This EOS is based on the curve fitting of numerous experimental data and is developed from the Helmholtz fuction. Because the primary variables of Span and Wagner's EOS are temperature (T) and density (ρ), the primary variables are switched into temperature and pressure using iteration method. The EOS can be applied the temperature and pressure ranges of $0 < T < 826.85$ deg C and $0 < PCX < 800$ MPa, respectively.

3. FUGACITY_COEFFICIENT: This subroutine calculates the specific fugacity of gaseous and supercritical CO2 as a function of the pressure of CO2 (PCX) and temperature (TX) using a Span and Wagner (1996). The primary variables adapted from temperature and density, which was calculated from subroutine SPECIFIC_DENSITY.

4. SPECIFIC_ENTHALPY: This subroutine calculates the specific enthalpy of gaseous and supercritical CO2 as a function of the pressure of CO2 (PCX) and temperature (TX) using a Span and Wagner (1996). The primary variables adapted from temperature and density, which was calculated from subroutine SPECIFIC_DENSITY.

5. HENRY: This subroutine calculates the mass fraction of CO2 in the aqueous phase using an extended Henry's Law relationship from Diamond and Akinfiev (2003). The expression for Henry's Constant is from the virial-like equation of state Akinfiev and Diamond, 2003.The fugacity of CO2 are from Span and Wagner EOS (subroutine FUGACITY_COEFFICIENT) and the fugacity of H2O are from Hill EOS (subroutine WATER)

6. WATER: Instead of using H2O thermodynamic properties from International formulation committee, the H2O subroutine was adapted from Hill EOS (1990) to increase the accuracy in SW EOSCO2 algorithms. This EOS is also developed on the Helmholtz fuction. Because the primary variables of Hill's EOS ara Temperature and density, The primary variables are switched into temperature and pressure using iteration method.

7. SOLUTE: This subroutine calcualtes the enthalpy of CO2 dissolution in liquid water. The expression is from O'Sullivan et al., (1985). The expression was created using a quadratic fit to data published by Ellis and Goulding (1963).

8. DENMIX: This subroutine returns density of CO2/H2O liquid mixture. The expression is from Anderson et al. (1992).

9. VISCO2: This subroutine calculates the viscosity of pure CO2 as a function of temperature and density of CO2. The expressions for calculating the viscosity come from empirical equations provided in Vesovic et al.(1990) and Fenghour et al. (1998).

SW_EOSCO2.m

```
T=input('TEMPERATURE [K] >>')
% PCX=input('PRESSURE [Pa] >>')

global T PCX P DC TC RHOC FUG H X1M X1MM FC
XCO2 HSOL D1M VC

%      Global constant
       TC  =  304.1282;
       RHOC =  467.6;

% Caution: When changing the pressure range, need to
chect HENRY and DENMIX subroutine.
% In those subrouine, pressure assinged as P variables,
which is not [Pa].
% Thus, those unit should change at the same time.

%PCX=100001:100000:100000001;
       PCX=[1*10^6:1*10^6:10*10^7];
%for P=1:1000
       for P=1:100;

%C       Calculate density (DC) in kg/m3 from SPECIFIC
DENSITY subroutine
       SPECIFIC_DENSITY;

       CO2_DENSITY(P)=DC;

%C       Calculate fugacity coefficient (FUG) and fugacity
(FC): Call fugacity coefficient calculation from
FUGACITY_COEFFICIENT subroutine.
       FUGACITY_COEFFICIENT;

       FUG_COEFF(P)=FUG;
       FC=FUG*PCX(P);

%C       Calculate specific enthalpy (H): Call specific
enthalpy calculation from SPECIFIC_ENTHALPY
subroutine.
     SPECIFIC_ENTHALPY;

     CO2_ENTHALPY(P)=H;

%C     Calculate mole fraction (X1M) and mass fraction:
Call mole fraction calculation from HENRY subroutine.
     HENRY;
     CO2_MOLE_FRACTION(P)=X1M; % mole fraction

     X1MM  =  (4.40098D-02*X1M)  /  (((1.D0-
XCO2)*18.015/1000)+(X1M*4.40098D-02));  %  mass
fraction
     CO2_MASS_FRACTION(P) = X1MM;

%C     Calculate the enthalpy of CO2 dissolution in liquid
water (HSOL): Call the enthalpy of CO2 dissolution
calculation from SOLUT subroutine.
     SOLUT;

     ENTHALPY_CO2_DISSOLUTION(P)=HSOL;

%C     Calculate the mixture density of CO2/H2O liquid
mixture (D1M): Call the mixture density of CO2/H2O
calculation from DENMIX subroutine.
     DENMIX;

     MIXTURE_DENSITY(P)=D1M;

%C     Calculate the dynamic viscosity of CO2 (VC): Call
the dynamic viscosity of CO2 calculation from VISCO2
subroutine.
     VISCO2;

     CO2_VISCOSITY(P)=VC;
end

PCX=PCX./10^6;

title('Pressure vs. CO2 density')
plot(PCX,CO2_DENSITY)
axis([1 100 0 1200])
xlabel('Pressure [MPa]')
ylabel('CO2 density [kg/m3]')

title('Pressure vs. Fugacity coefficient')
plot(PCX,FUG_COEFF)
axis([1 100 0 1])
xlabel('Pressure [MPa]')
ylabel('Fugacity coefficient [-]')

figure
title('Pressure vs. Specific enthalpy')
plot(PCX,CO2_ENTHALPY)
axis([1 100 5*10^5 1*10^6])
xlabel('Pressure [MPa]')
ylabel('Specific enthalpy [J/Kg]')

figure
title('Pressure vs. Mole fraction of CO2')
plot(PCX,CO2_MOLE_FRACTION)
axis([0 100 0 0.05])
xlabel('Pressure [MPa]')
ylabel('Mole fraction of CO2 [-]')

figure
title('Pressure vs. Enthalpy of CO2 dissolution')
plot(PCX,ENTHALPY_CO2_DISSOLUTION)
xlabel('Pressure [MPa]')
ylabel('Enthalpy of CO2 dissolution [J/Kg]')

figure
title('Pressure vs. Mixture density of CO2/H2O')
plot(PCX,MIXTURE_DENSITY)
xlabel('Pressure [MPa]')
ylabel('Mixture density of CO2/H2O [kg/m3]')

figure
title('Pressure vs. Dynamic viscosity of CO2')
plot(PCX,CO2_VISCOSITY)
axis([0 100 0 2.0E-4])
xlabel('Pressure [MPa]')
ylabel('Dynamic viscosity of CO2 [Pa-s]')
```

SPECIFIC_DENSITY.m

```
function SPECIFIC_DENSITY(DC)

global T PCX P DC TC RHOC

%%%%%%%%%%%%%%%%%%%%%%%%%%%%
%%%%%%%%%%%%%%%%%%%%%%%%%%%%
%%%%%%%%%%%%%%%%%
%% This subroutine calculate the specific density of CO2
using %%
%% Span and Wagner EOS (1996)
%%
%% The primary variable is temerature [K] and pressure
[Pa] %%
%%%%%%%%%%%%%%%%%%%%%%%%%%%%
%%%%%%%%%%%%%%%%%%%%%%%%%%%%
%%%%%%%%%%%%%%%%%

%C       Input:
%C                   T   = TEMPERATURE in [K]
%C     PCX = PRESSURE in [Pa]
%C
%C       Output:
%C                   RHO   = SPECIFIC DENSITY of
CO2 in [kg/m3]
%C
%C       Constants:
%C                   R   = SPECIFIC GAS CONSTANT
gas constant (188.9241 [J/kg*K])
%C         = RM/M
%C       RM   = MOLAR GAS CONSTANT (8.314510
[J/molK])
%C     M   = MOLAR MASS (44.0098 [g/mol])
%C       TC   = TEMPERATURE AT CRITICAL POINT
(304.1282 [K])
%C     RHOC= DENSITY AT CRITICAL POINT (467.6
[kg/m3])

%C DEFINE CONSTANTS:

     PC   =  7.3773 * 10^6;  %[Pa]
     R   =  188.9241;

%C  TABLE 31 (Span and Wagner Coefficient, 1996)
%C   NN(42), D(39), TT(39), C(34), ALPHA(35:39),
BETA(35:42), GAMMA(35:39), EPSLON(35:39)
%C  , SMALLA(40:42), SMALLB(40:42), BIGA(40:42),
BIGB(40:42), BIGC(40:42), BIGD(40:42)

NN=[0.38856823203161, 2.938547594274, -
5.5867188534934, -0.76753199592477,
0.31729005580416, 0.54803315897767,
0.12279411220335,...
   2.165896154322, 1.5841735109724, -
0.23132705405503, 0.058116916431436, -
0.55369137205382, 0.48946615909422, -
0.024275739843501, 0.062494790501678,...
   -0.12175860225246, -0.37055685270086, -
0.016775879700426, -0.11960736637987, -
0.045619362508778,...
   0.035612789270346, -0.0074427727132052, -
0.0017395704902432, -0.021810121289527,
0.024332166559236,...
   -0.037440133423463, 0.14338715756878, -
0.13491969083286, -0.02315122505348,
0.012363125492901,...
   0.002105832197294, -0.00033958519026368,
0.0055993651771592, -0.00030335118055646, -
213.65488688320,...
   26641.569149272, -24027.212204557, -
283.41603423999, 212.47284400179, -
0.66642276540751,...
   0.72608632349897, 0.055068668612842];

D=[1, 1, 1, 1, 2, 2, 3, 1, 2, 4, 5, 5, 5, 6, 6, 6, 1, 1, 4, 4, 4, 7,
8, 2, 3, 3, 5, 5, 6, 7, 8, 10, 4, 8,...
  2, 2, 2, 3, 3];
TT=[0, 0.75, 1, 2, 0.75, 2, 0.75, 1.5, 1.5, 2.5, 0, 1.5, 2, 0, 1,
2, 3, 6, 3, 6, 8, 6, 0, 7, 12, 16, 22, 24,...
  16, 24, 8, 2, 28, 14, 1, 0, 1, 3, 3];
C=[0, 0, 0, 0, 0, 0, 0, 1, 1, 1, 1, 1, 1, 1, 1, 1, 2, 2, 2, 2, 2, 2,
2 ,3, 3, 3, 4, 4, 4, 4, 4, 4, 5, 6];
ALPHA=[0, 0, 0, 0, 0, 0, 0, 0, 0, 0, 0, 0, 0, 0, 0, 0, 0, 0, 0,
0, 0 ,0 ,0 ,0, 0, 0, 0, 0, 0, 0, 0, 0, 0, 0, 25, 25, 25, 15, 20];
BETA=[0, 0, 0, 0, 0, 0, 0, 0, 0, 0, 0, 0, 0, 0, 0, 0, 0, 0, 0, 0,
0 ,0 ,0 ,0, 0, 0, 0, 0, 0, 0, 0, 0, 0, 0, 325, 300, 300, 275,
275, 0.3, 0.3, 0.3];
GAMMA=[0, 0, 0, 0, 0, 0, 0, 0, 0, 0, 0, 0, 0, 0, 0, 0, 0, 0, 0,
0, 0 ,0 ,0 ,0, 0, 0, 0, 0, 0, 0, 0, 0, 0, 0, 1.16, 1.19, 1.19,
1.25, 1.22];
EPSLON=[0, 0, 0, 0, 0, 0, 0, 0, 0, 0, 0, 0, 0, 0, 0, 0, 0, 0, 0,
0, 0 ,0 ,0 ,0, 0, 0, 0, 0, 0, 0, 0, 0, 0, 0, 1., 1., 1., 1., 1.];
SMALLA=[0, 0, 0, 0, 0, 0, 0, 0, 0, 0, 0, 0, 0, 0, 0, 0, 0, 0, 0,
0, 0, 0 ,0 ,0 ,0, 0, 0, 0, 0, 0, 0, 0, 0, 0, 0, 0, 0, 0, 0, 0, 3.5,
3.5, 3.];
SMALLB=[0, 0, 0, 0, 0, 0, 0, 0, 0, 0, 0, 0, 0, 0, 0, 0, 0, 0, 0,
0, 0, 0 ,0 ,0 ,0, 0, 0, 0, 0, 0, 0, 0, 0, 0, 0, 0, 0, 0, 0, 0, 0.875,
0.925, 0.875];
BIGA=[0, 0, 0, 0, 0, 0, 0, 0, 0, 0, 0, 0, 0, 0, 0, 0, 0, 0, 0, 0,
0 ,0 ,0 ,0, 0, 0, 0, 0, 0, 0, 0, 0, 0, 0, 0, 0, 0, 0, 0,  0.7, 0.7,
0.7];
BIGB=[0, 0, 0, 0, 0, 0, 0, 0, 0, 0, 0, 0, 0, 0, 0, 0, 0, 0, 0, 0,
0 ,0 ,0 ,0, 0, 0, 0, 0, 0, 0, 0, 0, 0, 0, 0, 0, 0, 0, 0, 0.3, 0.3,
1.0];
BIGC=[0, 0, 0, 0, 0, 0, 0, 0, 0, 0, 0, 0, 0, 0, 0, 0, 0, 0, 0, 0,
0 ,0 ,0 ,0, 0, 0, 0, 0, 0, 0, 0, 0, 0, 0, 0, 0, 0, 0, 0, 10.0, 10.0,
12.5];
BIGD=[0, 0, 0, 0, 0, 0, 0, 0, 0, 0, 0, 0, 0, 0, 0, 0, 0, 0, 0, 0,
0 ,0 ,0 ,0, 0, 0, 0, 0, 0, 0, 0, 0, 0, 0, 0, 0, 0, 0, 0, 275, 275,
275];


%%%%%%%%%%%%%%%%%%%%%%%%%
CRITICAL RANGE
%%%%%%%%%%%%%%%%%%%%%%%%%%%%%
%

%%%% CALCULATE VAPOR PRESSURE (EQ 3.13:
Span and Wagner) %%%%


      if T < TC;                                       %%
CONDITION: TEMPERATURE < CRITICAL
TEMPERATURE


         CRITICAL_VAPOR_PRESSURE_A=[-
7.0602087, 1.9391218, -1.6463597, -3.2995634];
         CRITICAL_VAPOR_PRESSURE_T=[1.0,  1.5,
2.0, 4.0];


          LN_P_SAT_CO2 = 0;
          for i = 1:4
```

```
            LN_P_SAT_CO2 = LN_P_SAT_CO2 +
CRITICAL_VAPOR_PRESSURE_A(i) * (1 - T /
TC)^CRITICAL_VAPOR_PRESSURE_T(i);
         end
            P_SAT_CO2 = PC * exp(TC / T *
LN_P_SAT_CO2);

%%%% SATURATED LIQUID DENSITY (EQ 3.14:
Span and Wagner) %%%%

       CRITICAL_LIQUID_DENSITY_A=[1.9245108, -
0.62385555, -0.32731127, 0.39245142];
       CRITICAL_LIQUID_DENSITY_T=[0.340, 0.5,
1.6666666667, 1.833333333];

         LN_LIQUID_CO2 = 0;
         for i = 1:4
            LN_LIQUID_CO2 = LN_LIQUID_CO2 +
CRITICAL_LIQUID_DENSITY_A(i) * (1 - T /
TC)^CRITICAL_LIQUID_DENSITY_T(i);
         end
            LN_LIQUID_CO2 = LN_LIQUID_CO2;

            D_LIQUID_CO2 = RHOC *
exp(LN_LIQUID_CO2);

%%%% SATURATED VAPOR DENSITY (EQ 3.15:
Span and Wagner) %%%%

       CRITICAL_VAPOR_DENSITY_A=[-1.7074879,
-0.82274670, -4.6008549, -10.111178, -29.742252];
       CRITICAL_VAPOR_DENSITY_T=[0.340, 0.5,
1.0, 2.3333333333, 4.6666666667];

         LNVAPCO2 = 0;
         for i = 1:5
            LNVAPCO2 = LNVAPCO2 +
CRITICAL_VAPOR_DENSITY_A(i) * (1 - T /
TC)^CRITICAL_VAPOR_DENSITY_T(i);
         end

            DVAPORCO2 = RHOC * exp(LNVAPCO2);

         if PCX(P) >= P_SAT_CO2;
            RHO = D_LIQUID_CO2;
         else
            RHO = PCX(P) / (R * T);
         end
      else
            RHO = 1 / (30 + R * T / PCX(P));
end

%RHO = 1;                  % INITIAL GUESS

for K=1:1000

    TAU = TC / T;
    DELTA = RHO / RHOC;

% THE CALCULATION OF TAU AND DELTA TERM

%%%%%%%%%%%%%%%%%%%%%%%%%%%%
%%%%%%%%%%%%%%%%%%%%%%%%%%%%
%%%%%%%%%%%%%%%%
%%     THE CALCULATION OF PHI_R_DELTA AND
PHI_R_DELTA_DELTA TERM     %%
%%              (TABLE 32 IN SPAN AND WAGNER,
1996)            %%
```

```
%%%%%%%%%%%%%%%%%%%%%%%%%%%%
%%%%%%%%%%%%%%%%%%%%%%%%%%%%
%%%%%%%%%%%%%%%%

% CALCULATION OF FIRST TERM IN PHI_R AND
PHI_R_DELTA

     PHI_R_FIR_DELTA = 0;
     PHI_R_FIR_DELTA_DELTA = 0;

    for i=1:7
      PHI_R_FIR_DELTA_TERM = NN(i) * D(i) *
DELTA^(D(i)-1) * TAU^TT(i);
      PHI_R_FIR_DELTA_DELTA_TERM = NN(i) *
D(i) * (D(i) - 1) * DELTA^(D(i) - 2) * TAU^TT(i);

      PHI_R_FIR_DELTA = PHI_R_FIR_DELTA +
PHI_R_FIR_DELTA_TERM;
      PHI_R_FIR_DELTA_DELTA =
PHI_R_FIR_DELTA_DELTA +
PHI_R_FIR_DELTA_DELTA_TERM;
    end
      PHI_R_FIR_DELTA = PHI_R_FIR_DELTA;
      PHI_R_FIR_DELTA_DELTA =
PHI_R_FIR_DELTA_DELTA;

% CALCULATION OF SECOND TERM IN PHI_R
AND PHI_R_DELTA

     PHI_R_SEC_DELTA = 0;
     PHI_R_SEC_DELTA_DELTA = 0;

      for i = 8:34
       PHI_R_SEC_DELTA_TERM = NN(i) * exp(-
DELTA^C(i)) * (DELTA^(D(i) - 1) * TAU^TT(i) * (D(i)-
C(i) * DELTA^C(i)));
       PHI_R_SEC_DELTA_DELTA_TERM = NN(i) *
exp(-DELTA^C(i)) * (DELTA^(D(i) - 2) * TAU^TT(i) *
((D(i) - C(i) * DELTA^C(i)) * (D(i) - 1 - C(i) *
DELTA^C(i)) - C(i)^2 * DELTA^C(i)));

       PHI_R_SEC_DELTA = PHI_R_SEC_DELTA +
PHI_R_SEC_DELTA_TERM;
       PHI_R_SEC_DELTA_DELTA =
PHI_R_SEC_DELTA_DELTA +
PHI_R_SEC_DELTA_DELTA_TERM;
      end
       PHI_R_SEC_DELTA = PHI_R_SEC_DELTA;
       PHI_R_SEC_DELTA_DELTA =
PHI_R_SEC_DELTA_DELTA;

% CALCULATION OF THIRD TERM IN PHI_R AND
PHI_R_DELTA

     PHI_R_THI_DELTA = 0;
     PHI_R_THI_DELTA_DELTA = 0;

     for i = 35:39
      PHI_R_THI_DELTA_TERM = NN(i) *
DELTA^D(i) * TAU^TT(i) * exp(-ALPHA(i)*(DELTA -
EPSLON(i))^2 - BETA(i) * (TAU - GAMMA(i))^2) *
(D(i) / DELTA - 2 * ALPHA(i) * (DELTA -
EPSLON(i)));
      PHI_R_THI_DELTA_DELTA_TERM = NN(i) *
DELTA^D(i) * TAU^TT(i) * exp(-ALPHA(i)*(DELTA -
EPSLON(i))^2 - BETA(i) * (TAU - GAMMA(i))^2)...
      * (-2 * ALPHA(i) * DELTA^D(i) + 4 *
ALPHA(i)^2 * DELTA^D(i) * (DELTA - EPSLON(i))^2
- 4 * D(i) * ALPHA(i) * DELTA^(D(i)-1) * (DELTA -
EPSLON(i))...
```

```
     + D(i) * (D(i)-1) * DELTA^(D(i)-2));

     PHI_R_THI_DELTA = PHI_R_THI_DELTA +
PHI_R_THI_DELTA_TERM;
     PHI_R_THI_DELTA_DELTA =
PHI_R_THI_DELTA_DELTA +
PHI_R_THI_DELTA_DELTA_TERM;
    end
     PHI_R_THI_DELTA = PHI_R_THI_DELTA;
     PHI_R_THI_DELTA_DELTA =
PHI_R_THI_DELTA_DELTA;


 % CALCULATION OF FORTH TERM IN PHI_R AND
PHI_R_DELTA

    PHI_R_FOR_DELTA = 0;
    PHI_R_FOR_DELTA_DELTA = 0;

    for i = 40:42

      GG = 1.0d00 / (2* BETA(i));

      THETA = 1 - TAU + BIGA(i) * ((DELTA-
1)^2)^(GG);

      BGPHI = exp(-BIGC(i) * (DELTA-1)^2 -
BIGD(i) * (TAU - 1)^2);

      D_BGPHI_D_DELTA = -2 * BIGC(i) *
(DELTA-1) * BGPHI;

      DD_BGPHI_DD_DELTA = (2 * BIGC(i) *
(DELTA-1)^2 - 1) * 2 * BIGC(i) * BGPHI;

      BGDELTA = THETA^2 + BIGB(i) * ((DELTA-
1)^2)^SMALLA(i);

      D_BGDELTA_D_DELTA = (DELTA-1) *
(BIGA(i)*THETA*2/BETA(i)*((DELTA-1)^2)^(GG-
1)+2*BIGB(i)*SMALLA(i)...
      *((DELTA-1)^2)^(SMALLA(i)-1));  %
dbgdlta/ddelta

      DD_BGDELTA_DD_DELTA = 1/(DELTA-1) *
D_BGDELTA_D_DELTA + (DELTA - 1)^2 ...
      * (4 * BIGB(i) * SMALLA(i) * (SMALLA(i) - 1)
* ((DELTA - 1)^2)^(SMALLA(i)-2) + 2 * BIGA(i)^2 * (1
/ BETA(i))^2 ...
      * (((DELTA - 1)^2)^(GG-1))^2 + BIGA(i) *
THETA * 4 / BETA(i) * (GG - 1) * ((DELTA -
1)^2)^(GG-2));

      D_BGDELTA_D_DELTA_SMALLB =
SMALLB(i) * BGDELTA^(SMALLB(i)-1)*
D_BGDELTA_D_DELTA;  %
dbidlta**smallb/ddelta
      DD_BGDELTA_DD_DELTA_SMALLB =
SMALLB(i) * (BGDELTA^(SMALLB(i)-1)*
DD_BGDELTA_DD_DELTA + (SMALLB(i) -1)...
      * BGDELTA^(SMALLB(i)-2) *
(D_BGDELTA_D_DELTA)^2) ;  %
dbidlta**smallb/ddelta

      PHI_R_FOR_DELTA_TERM = NN(i) *
(BGDELTA^SMALLB(i) * (BGPHI + DELTA *
D_BGPHI_D_DELTA) +
D_BGDELTA_D_DELTA_SMALLB * DELTA *
BGPHI);

      PHI_R_FOR_DELTA_DELTA_TERM = NN(i)
* (BGDELTA^SMALLB(i) * (2 * D_BGPHI_D_DELTA
+ DELTA * DD_BGPHI_DD_DELTA)...
      + 2 * D_BGDELTA_D_DELTA_SMALLB *
(BGPHI + DELTA * D_BGPHI_D_DELTA) +
DD_BGDELTA_DD_DELTA_SMALLB * DELTA *
BGPHI);

      PHI_R_FOR_DELTA = PHI_R_FOR_DELTA +
PHI_R_FOR_DELTA_TERM;
      PHI_R_FOR_DELTA_DELTA =
PHI_R_FOR_DELTA_DELTA +
PHI_R_FOR_DELTA_DELTA_TERM;

    end
      PHI_R_FOR_DELTA = PHI_R_FOR_DELTA;
      PHI_R_FOR_DELTA_DELTA =
PHI_R_FOR_DELTA_DELTA;

% SUM OF EACH TERM AND THIS VALUE WILL BE
PHI_R_DELTA AND PHI_R_DELTA_DELTA

PHI_R_DELTA = PHI_R_FIR_DELTA +
PHI_R_SEC_DELTA + PHI_R_THI_DELTA +
PHI_R_FOR_DELTA;
PHI_R_DELTA_DELTA =
PHI_R_FIR_DELTA_DELTA +
PHI_R_SEC_DELTA_DELTA +
PHI_R_THI_DELTA_DELTA +
PHI_R_FOR_DELTA_DELTA;

% FROM HERE, THIS PART CALCULATE DENSITY
USING ITERATION METHOD,

%%%%%%%%%%%%%%%%%%%%%%%%%%%
%%%%%%%%%%%%%%%%%%%%%%%%%%%
%%%%%%%%%%%%%%%%%%%%%%%%

     F = RHO * (1 + DELTA * PHI_R_DELTA);
     DF = 1 + 2 * DELTA * PHI_R_DELTA + DELTA
^ 2 * PHI_R_DELTA_DELTA;
     DEVIATION = F / (PCX(P) / (R * T)) - 1;

     if abs(DEVIATION) > .00001
        RHO = RHO - 0.5 * PCX(P) / (R * T) *
DEVIATION / (DF);
      end
RHO;
end
DC=RHO;
```

FUGACITY_COEFFICIENT.m

```
function FUGACITY_COEFFICIENT(FUG)

global T P DC TC RHOC FUG

%%%%%%%%%%%%%%%%%%%%%%%%%%%%
%%%%%%%%%%%%%%%%%%%%%%%%%%%%
%%%%%%%%%%%%%%%%%
%% This subroutine calculate the fugacity coefficient
using %%
%% Span and Wagner EOS
%%
%%%%%%%%%%%%%%%%%%%%%%%%%%%%
%%%%%%%%%%%%%%%%%%%%%%%%%%%%
%%%%%%%%%%%%%%%%%

%C          Input:
%C                          T   = Temperature in K
%C      DC = Density in Kg/m3
%C
%C          Output:
%C                          FUG  = Fugacity coefficient [-]
%C
%C                          R   = SPECIFIC GAS CONSTANT
gas constant (188.9241 [J/kg*K])
%C         = RM/M
%C        RM   = MOLAR GAS CONSTANT (8.314510
[J/molK])
%C     M   = MOLAR MASS (44.0098 [g/mol])
%C       TC  = TEMPERATURE AT CRITICAL POINT
(304.1282 [K])
%C      RHOC= DENSITY AT CRITICAL POINT (467.6
[kg/m3])
%C

R   =  188.9241;

%C  TABLE 31 (Span and Wagner Coefficient, 1996)
%C    NN(42), D(39), TT(39), C(34), ALPHA(35:39),
BETA(35:42), GAMMA(35:39), EPSLON(35:39)
%C   , SMALLA(40:42), SMALLB(40:42), BIGA(40:42),
BIGB(40:42), BIGC(40:42), BIGD(40:42)

NN=[0.38856823203161, 2.938547594274, -
5.5867188534934, -0.76753199592477,
0.31729005580416, 0.54803315897767,
0.12279411220335,...
    2.165896154322, 1.5841735109724, -
0.23132705405503, 0.058116916431436, -
0.55369137205382, 0.48946615909422, -
0.024275739843501, 0.062494790501678,...
   -0.12175860225246, -0.37055685270086, -
0.016775879700426, -0.11960736637987, -
0.045619362508778,...
    0.035612789270346, -0.0074427727132052, -
0.0017395704902432, -0.021810121289527,
0.024332166559236,...
   -0.037440133423463, 0.14338715756878, -
0.13491969083286, -0.02315122505348,
0.012363125492901,...
    0.002105832197294, -0.00033958519026368,
0.0055993651771592, -0.00030335118055646, -
213.65488688320,...
    26641.569149272, -24027.212204557, -
283.41603423999, 212.47284400179, -
0.66642276540751,...
    0.72608632349897, 0.055068668612842];
D=[1, 1, 1, 1, 2, 2, 3, 1, 2, 4, 5, 5, 5, 6, 6, 6, 1, 1, 4, 4, 4, 7,
8, 2, 3, 3, 5, 5, 6, 7, 8, 10, 4, 8,...
   2, 2, 2, 3, 3];
TT=[0, 0.75, 1, 2, 0.75, 2, 0.75, 1.5, 1.5, 2.5, 0, 1.5, 2, 0, 1,
2, 3, 6, 3, 6, 8, 6, 0, 7, 12, 16, 22, 24,...
    16, 24, 8, 2, 28, 14, 1, 0, 1, 3, 3];
C=[0, 0, 0, 0, 0, 0, 0, 1, 1, 1, 1, 1, 1, 1, 1, 1, 2, 2, 2, 2, 2, 2,
2 ,3, 3, 3, 4, 4, 4, 4, 4, 4, 5, 6];
ALPHA=[0, 0, 0, 0, 0, 0, 0, 0, 0, 0, 0, 0, 0, 0, 0, 0, 0, 0, 0,
0, 0 ,0 ,0 ,0, 0, 0, 0, 0, 0, 0, 0, 0, 0, 0, 25, 25, 25, 15, 20];
BETA=[0, 0, 0, 0, 0, 0, 0, 0, 0, 0, 0, 0, 0, 0, 0, 0, 0, 0, 0, 0,
0 ,0 ,0 ,0, 0, 0, 0, 0, 0, 0, 0, 0, 0, 0, 325, 300, 300, 275,
275, 0.3, 0.3, 0.3];
GAMMA=[0, 0, 0, 0, 0, 0, 0, 0, 0, 0, 0, 0, 0, 0, 0, 0, 0, 0, 0,
0, 0 ,0 ,0 ,0, 0, 0, 0, 0, 0, 0, 0, 0, 0, 0, 1.16, 1.19, 1.19,
1.25, 1.22];
EPSLON=[0, 0, 0, 0, 0, 0, 0, 0, 0, 0, 0, 0, 0, 0, 0, 0, 0, 0, 0,
0, 0 ,0 ,0 ,0, 0, 0, 0, 0, 0, 0, 0, 0, 0, 0, 1., 1., 1., 1., 1.];
SMALLA=[0, 0, 0, 0, 0, 0, 0, 0, 0, 0, 0, 0, 0, 0, 0, 0, 0, 0,
0, 0, 0 ,0 ,0 ,0, 0, 0, 0, 0, 0, 0, 0, 0, 0, 0, 0, 0, 0, 0, 0, 3.5,
3.5, 3.];
SMALLB=[0, 0, 0, 0, 0, 0, 0, 0, 0, 0, 0, 0, 0, 0, 0, 0, 0, 0,
0, 0, 0 ,0 ,0 ,0, 0, 0, 0, 0, 0, 0, 0, 0, 0, 0, 0, 0, 0, 0, 0, 0.875,
0.925, 0.875];
BIGA=[0, 0, 0, 0, 0, 0, 0, 0, 0, 0, 0, 0, 0, 0, 0, 0, 0, 0, 0, 0,
0 ,0 ,0 ,0, 0, 0, 0, 0, 0, 0, 0, 0, 0, 0, 0, 0, 0, 0,  0.7, 0.7,
0.7];
BIGB=[0, 0, 0, 0, 0, 0, 0, 0, 0, 0, 0, 0, 0, 0, 0, 0, 0, 0, 0, 0,
0 ,0 ,0 ,0, 0, 0, 0, 0, 0, 0, 0, 0, 0, 0, 0, 0, 0, 0, 0.3, 0.3,
1.0];
BIGC=[0, 0, 0, 0, 0, 0, 0, 0, 0, 0, 0, 0, 0, 0, 0, 0, 0, 0, 0, 0,
0 ,0 ,0 ,0, 0, 0, 0, 0, 0, 0, 0, 0, 0, 0, 0, 0, 0, 0, 10.0, 10.0,
12.5];
BIGD=[0, 0, 0, 0, 0, 0, 0, 0, 0, 0, 0, 0, 0, 0, 0, 0, 0, 0, 0, 0,
0 ,0 ,0 ,0, 0, 0, 0, 0, 0, 0, 0, 0, 0, 0, 0, 0, 0, 0, 275, 275,
275];

% THE CALCULATION OF TAU AND DELTA TERM

         TAU = TC / T;
         DELTA = DC / RHOC;

%%%%%%%%%%%%%%%%%%%%%%%%%%%%
%%%%%%%%%%%%%%%%%%%%%%%%%%%%
%%%%%%%%%%%%%%%%%
%% THE CALCULATION OF PHI_R AND
PHI_R_DELTA TERM %%
%% (TABLE 32 IN SPAN AND WAGNER,
1996) %%
%%%%%%%%%%%%%%%%%%%%%%%%%%%%
%%%%%%%%%%%%%%%%%%%%%%%%%%%%
%%%%%%%%%%%%%%%%%

% CALCULATION OF FIRST TERM IN PHI_R AND
PHI_R_DELTA


      PHI_R_FIR = 0;
      PHI_R_FIR_DELTA = 0;

       for i=1:7
         PHI_R_FIR_TERM = NN(i) * DELTA^(D(i)) *
TAU^TT(i);
         PHI_R_FIR_DELTA_TERM = NN(i) * D(i) *
DELTA^(D(i)-1) * TAU^TT(i);
```

```
     PHI_R_FIR = PHI_R_FIR + PHI_R_FIR_TERM;
     PHI_R_FIR_DELTA = PHI_R_FIR_DELTA +
PHI_R_FIR_DELTA_TERM;
    end

% CALCULATION OF SECOND TERM IN PHI_R
AND PHI_R_DELTA

    PHI_R_SEC = 0;
    PHI_R_SEC_DELTA = 0;

    for i = 8:34
     PHI_R_SEC_TERM = NN(i) * DELTA^(D(i)) *
TAU^TT(i) * exp(-DELTA^C(i));
     PHI_R_SEC_DELTA_TERM = NN(i) * exp(-
DELTA^C(i)) * (DELTA^(D(i)-1) * TAU^TT(i) * (D(i)-
C(i) * DELTA^C(i)));

     PHI_R_SEC = PHI_R_SEC +
PHI_R_SEC_TERM;
     PHI_R_SEC_DELTA = PHI_R_SEC_DELTA +
PHI_R_SEC_DELTA_TERM;
    end

% CALCULATION OF THIRD TERM IN PHI_R AND
PHI_R_DELTA


    PHI_R_THI = 0;
    PHI_R_THI_DELTA = 0;

    for i = 35:39
     PHI_R_THI_TERM = NN(i) * DELTA^D(i) *
TAU^TT(i) * exp(-ALPHA(i)*(DELTA - EPSLON(i))^2
- BETA(i)*(TAU-GAMMA(i))^2);
     PHI_R_THI_DELTA_TERM = NN(i) *
DELTA^D(i) * TAU^TT(i) * exp(-ALPHA(i)*(DELTA -
EPSLON(i))^2 - BETA(i)*(TAU-
GAMMA(i))^2)*(D(i)/DELTA-2*ALPHA(i)*(DELTA-
EPSLON(i)));

     PHI_R_THI = PHI_R_THI + PHI_R_THI_TERM;
     PHI_R_THI_DELTA = PHI_R_THI_DELTA +
PHI_R_THI_DELTA_TERM;
    end

 % CALCULATION OF FORTH TERM IN PHI_R AND
PHI_R_DELTA

    PHI_R_FOR = 0;
    PHI_R_FOR_DELTA = 0;

    for i = 40:42

      GG = 1.0d00 / (2* BETA(i));
      THETA = 1 - TAU + BIGA(i) * ((DELTA-
1)^2)^(GG);
      BGPHI = exp(-BIGC(i) * (DELTA-1)^2 -
BIGD(i) * (TAU - 1)^2);

      D_BGPHI_D_DELTA=-2 * BIGC(i) * (DELTA-
1) * BGPHI;

      BGDELTA = THETA^2 + BIGB(i) * ((DELTA-
1)^2)^SMALLA(i);

      D_BGDELTA_D_DELTA=(DELTA-1) *
(BIGA(i)*THETA*2/BETA(i)*((DELTA-1)^2)^(GG-
1)+2*BIGB(i)*SMALLA(i)...
      *((DELTA-1)^2)^(SMALLA(i)-1)); %
dbgdlta/ddelta

      D_BGDELTA_D_DELTA_SMALLB =
SMALLB(i) * BGDELTA^(SMALLB(i)-1)*
D_BGDELTA_D_DELTA;
% dbidlta**smallb/ddelta

      PHI_R_FOR_TERM = NN(i) *
BGDELTA^SMALLB(i) * DELTA * BGPHI;
      PHI_R_FOR_DELTA_TERM = NN(i) *
(BGDELTA^SMALLB(i)*(BGPHI+DELTA*D_BGPHI_
D_DELTA)+D_BGDELTA_D_DELTA_SMALLB*DEL
TA*BGPHI);

      PHI_R_FOR = PHI_R_FOR +
PHI_R_FOR_TERM;
      PHI_R_FOR_DELTA = PHI_R_FOR_DELTA +
PHI_R_FOR_DELTA_TERM;
    end

% SUM OF EACH TERM AND THIS VALUE WILL BE
PHI_R AND PHI_R_DELTA

PHI_R = PHI_R_FIR + PHI_R_SEC + PHI_R_THI +
PHI_R_FOR;
PHI_R_DELTA = PHI_R_FIR_DELTA +
PHI_R_SEC_DELTA + PHI_R_THI_DELTA +
PHI_R_FOR_DELTA;

%%%%%%%%%%%%%%%%%%%%%%%%%%
%%%%%%%%%%%%%%%%%%%%%%%%%%
%%%%%%%%%%%%%%%%%%%%%

%% CALCULATE FUGACITY_COEFFICIENT

FUG = exp( PHI_R + DELTA * PHI_R_DELTA - log(1 +
DELTA * PHI_R_DELTA));
```

SPECIFIC_ENTHALPY.m

```
function SPECIFIC_ENTHALPY(H)

global T PCX P DC TC RHOC H

%%%%%%%%%%%%%%%%%%%%%%%%%%%
%%%%%%%%%%%%%%%%%%%%%%%%%%%
%%%%%%%%%%%%%%%%%
%% This subroutine calculate the specific enthalpyof CO2
using   %%
%%   Span   and   Wagner   EOS   (1996)
%%
%% The primary variable is temerature [K] and pressure
[Pa]   %%
%%%%%%%%%%%%%%%%%%%%%%%%%%%
%%%%%%%%%%%%%%%%%%%%%%%%%%%
%%%%%%%%%%%%%%%%

%C        Input:
%C                 T   = TEMPERATURE in [K]
%C     PCX = PRESSURE in [Pa]
%C
%C        Output:
%C                 RHO   = SPECIFIC DENSITY of
CO2 in [kg/m3]
%C
%C        Constants:
%C                 R   = SPECIFIC GAS CONSTANT
gas constant (188.9241 [J/kg*K])
%C        = RM/M
%C       RM   = MOLAR GAS CONSTANT (8.314510
[J/molK])
%C     M   = MOLAR MASS (44.0098 [g/mol])
%C       TC   = TEMPERATURE AT CRITICAL POINT
(304.1282 [K])
%C      RHOC= DENSITY AT CRITICAL POINT (467.6
[kg/m3])

%C  TABLE 27 (Span and Wagner Coefficient, 1996)
A_ZERO=[8.37304456,   -3.70454304,   2.50000000,
1.99427042,   0.62105248,   0.41195293,   1.04028922,
0.08327678];
THETA_ZERO=[0,  0,  0,  3.15163,  6.11190,  6.77708,
11.32384, 27.08792];

%C  TABLE 31 (Span and Wagner Coefficient, 1996)
NN=[0.38856823203161,        2.938547594274,        -
5.5867188534934,                  -0.76753199592477,
0.31729005580416,                  0.54803315897767,
0.12279411220335,...
    2.165896154322,        1.5841735109724,        -
0.23132705405503,        0.058116916431436,        -
0.55369137205382,        0.48946615909422,        -
0.024275739843501, 0.062494790501678,...
   -0.12175860225246,       -0.37055685270086,       -
0.016775879700426,       -0.11960736637987,       -
0.045619362508778,...
    0.035612789270346,    -0.0074427727132052,    -
0.0017395704902432,            -0.021810121289527,
0.024332166559236,...
   -0.037440133423463,       0.14338715756878,       -
0.13491969083286,                -0.02315122505348,
0.012363125492901,...
    0.002105832197294,        -0.00033958519026368,
0.0055993651771592,    -0.00030335118055646,    -
213.65488688320,...
    26641.569149272,         -24027.212204557,        -
283.41603423999,              212.47284400179,         -
0.66642276540751,...
    0.72608632349897, 0.055068668612842];
D=[1, 1, 1, 1, 2, 2, 3, 1, 2, 4, 5, 5, 5, 6, 6, 6, 1, 1, 4, 4, 4, 7,
8, 2, 3, 3, 5, 5, 6, 7, 8, 10, 4, 8,...
   2, 2, 2, 3, 3];
TT=[0, 0.75, 1, 2, 0.75, 2, 0.75, 1.5, 1.5, 2.5, 0, 1.5, 2, 0, 1,
2, 3, 6, 3, 6, 8, 6, 0, 7, 12, 16, 22, 24,...
   16, 24, 8, 2, 28, 14, 1, 0, 1, 3, 3];
C=[0, 0, 0, 0, 0, 0, 0, 1, 1, 1, 1, 1, 1, 1, 1, 1, 2, 2, 2, 2, 2, 2,
2 ,3, 3, 3, 4, 4, 4, 4, 4, 4, 5, 6];
ALPHA=[0, 0, 0, 0, 0, 0, 0, 0, 0, 0, 0, 0, 0, 0, 0, 0, 0, 0, 0,
0, 0 ,0 ,0 ,0, 0, 0, 0, 0, 0, 0, 0, 0, 0, 0, 25, 25, 25, 15, 20];
BETA=[0, 0, 0, 0, 0, 0, 0, 0, 0, 0, 0, 0, 0, 0, 0, 0, 0, 0, 0, 0,
0 ,0 ,0 ,0, 0, 0, 0, 0, 0, 0, 0, 0, 0, 0, 325, 300, 300, 275,
275, 0.3, 0.3, 0.3];
GAMMA=[0, 0, 0, 0, 0, 0, 0, 0, 0, 0, 0, 0, 0, 0, 0, 0, 0, 0, 0,
0, 0 ,0 ,0 ,0, 0, 0, 0, 0, 0, 0, 0, 0, 0, 0, 1.16, 1.19, 1.19,
1.25, 1.22];
EPSLON=[0, 0, 0, 0, 0, 0, 0, 0, 0, 0, 0, 0, 0, 0, 0, 0, 0, 0, 0,
0, 0 ,0 ,0 ,0, 0, 0, 0, 0, 0, 0, 0, 0, 0, 0, 1., 1., 1., 1., 1.];
SMALLA=[0, 0, 0, 0, 0, 0, 0, 0, 0, 0, 0, 0, 0, 0, 0, 0, 0, 0,
0, 0, 0 ,0 ,0 ,0, 0, 0, 0, 0, 0, 0, 0, 0, 0, 0, 0, 0, 0, 0, 0, 3.5,
3.5, 3.];
SMALLB=[0, 0, 0, 0, 0, 0, 0, 0, 0, 0, 0, 0, 0, 0, 0, 0, 0, 0,
0, 0, 0 ,0 ,0 ,0, 0, 0, 0, 0, 0, 0, 0, 0, 0, 0, 0, 0, 0, 0, 0.875,
0.925, 0.875];
BIGA=[0, 0, 0, 0, 0, 0, 0, 0, 0, 0, 0, 0, 0, 0, 0, 0, 0, 0, 0, 0,
0 ,0 ,0 ,0, 0, 0, 0, 0, 0, 0, 0, 0, 0, 0, 0, 0, 0, 0, 0,  0.7, 0.7,
0.7];
BIGB=[0, 0, 0, 0, 0, 0, 0, 0, 0, 0, 0, 0, 0, 0, 0, 0, 0, 0, 0, 0,
0 ,0 ,0 ,0, 0, 0, 0, 0, 0, 0, 0, 0, 0, 0, 0, 0, 0, 0, 0, 0.3, 0.3,
1.0];
BIGC=[0, 0, 0, 0, 0, 0, 0, 0, 0, 0, 0, 0, 0, 0, 0, 0, 0, 0, 0, 0,
0 ,0 ,0 ,0, 0, 0, 0, 0, 0, 0, 0, 0, 0, 0, 0, 0, 0, 0, 0, 10.0, 10.0,
12.5];
BIGD=[0, 0, 0, 0, 0, 0, 0, 0, 0, 0, 0, 0, 0, 0, 0, 0, 0, 0, 0, 0,
0 ,0 ,0 ,0, 0, 0, 0, 0, 0, 0, 0, 0, 0, 0, 0, 0, 0, 0, 0, 275, 275,
275];

%C DEFINE CONSTANTS:
      R   =  188.9241;

% THE CALCULATION OF TAU AND DELTA TERM
         TAU = TC / T;
         DELTA = DC / RHOC;

%%%%%%%%%%%%%%%%%%%%%%%%%%%
%%%%%%%%%%%%%%%%%%%%%%%%%%%
%%%%%%%%%%%%%%%%
%%                    THE  CALCULATION  OF
PHI_TAU_ZERO             %%
%%              (Eq. 6.3 IN SPAN AND WAGNER, 1996)
%%
%%%%%%%%%%%%%%%%%%%%%%%%%%%
%%%%%%%%%%%%%%%%%%%%%%%%%%%
%%%%%%%%%%%%%%%%

      PHI_TAU_ZERO = 0;

      for i=4:8
        PHI_TAU_ZERO_TERM   =   A_ZERO(i)   *
THETA_ZERO(i) * ((1 - exp(-1 * THETA_ZERO(i) *
TAU))^(-1) - 1);
```

```
    PHI_TAU_ZERO = PHI_TAU_ZERO +
PHI_TAU_ZERO_TERM;
    end
    PHI_TAU_ZERO = A_ZERO(2) + A_ZERO(3) /
TAU + PHI_TAU_ZERO;

%%%%%%%%%%%%%%%%%%%%%%%%%%
%%%%%%%%%%%%%%%%%%%%%%%%%%
%%%%%%%%%%%%%%%
%%       THE CALCULATION  OF PHI_R_DELTA
AND PHI_R_TAU TERM       %%
%%          (TABLE 32 IN SPAN AND WAGNER,
1996)          %%
%%%%%%%%%%%%%%%%%%%%%%%%%%
%%%%%%%%%%%%%%%%%%%%%%%%%%
%%%%%%%%%%%%%%%

% CALCULATION OF FIRST TERM IN PHI_R AND
PHI_R_DELTA

    PHI_R_FIR_DELTA = 0;
    PHI_R_FIR_TAU = 0;

    for i=1:7
     PHI_R_FIR_DELTA_TERM = NN(i) * D(i) *
DELTA^(D(i)-1) * TAU^TT(i);
     PHI_R_FIR_TAU_TERM = NN(i) * TT(i) *
DELTA^(D(i)) * TAU^(TT(i)-1);

     PHI_R_FIR_DELTA = PHI_R_FIR_DELTA +
PHI_R_FIR_DELTA_TERM;
     PHI_R_FIR_TAU = PHI_R_FIR_TAU +
PHI_R_FIR_TAU_TERM;
    end

% CALCULATION OF SECOND TERM IN PHI_R
AND PHI_R_DELTA

    PHI_R_SEC_DELTA = 0;
    PHI_R_SEC_TAU = 0;

    for i = 8:34
     PHI_R_SEC_DELTA_TERM = NN(i) * exp(-
DELTA^C(i)) * (DELTA^(D(i)-1) * TAU^TT(i) * (D(i)-
C(i) * DELTA^C(i)));
     PHI_R_SEC_TAU_TERM = NN(i) * TT(i) *
DELTA^(D(i)) * TAU^(TT(i)-1) * exp(-DELTA^C(i));

     PHI_R_SEC_DELTA = PHI_R_SEC_DELTA +
PHI_R_SEC_DELTA_TERM;
     PHI_R_SEC_TAU = PHI_R_SEC_TAU +
PHI_R_SEC_TAU_TERM;
    end

% CALCULATION OF THIRD TERM IN PHI_R AND
PHI_R_DELTA

    PHI_R_THI_DELTA = 0;
    PHI_R_THI_TAU = 0;

    for i = 35:39
     PHI_R_THI_DELTA_TERM = NN(i) *
DELTA^D(i) * TAU^TT(i) * exp(-ALPHA(i)*(DELTA -
EPSLON(i))^2 - BETA(i)*(TAU-GAMMA(i))^2) *
(D(i)/DELTA-2*ALPHA(i)*(DELTA-EPSLON(i)));
     PHI_R_THI_TAU_TERM = NN(i) * DELTA^D(i)
* TAU^TT(i) * exp(-ALPHA(i)*(DELTA -
EPSLON(i))^2 - BETA(i)*(TAU-GAMMA(i))^2) *
(TT(i)/TAU-2*BETA(i)*(TAU-GAMMA(i)));
     PHI_R_THI_DELTA = PHI_R_THI_DELTA +
PHI_R_THI_DELTA_TERM;
     PHI_R_THI_TAU = PHI_R_THI_TAU +
PHI_R_THI_TAU_TERM;
    end

 % CALCULATION OF FORTH TERM IN PHI_R AND
PHI_R_DELTA

    PHI_R_FOR_DELTA = 0;
    PHI_R_FOR_TAU = 0;

    for i = 40:42

      GG = 1.0d00 / (2* BETA(i));
      THETA = 1 - TAU + BIGA(i) * ((DELTA-
1)^2)^(GG);
      BGPHI = exp(-BIGC(i) * (DELTA-1)^2 -
BIGD(i) * (TAU - 1)^2);

      D_BGPHI_D_DELTA = -2 * BIGC(i) *
(DELTA-1) * BGPHI;
      D_BGPHI_D_TAU = -2 * BIGD(i) * (TAU-1) *
BGPHI;

      BGDELTA = THETA^2 + BIGB(i) * ((DELTA-
1)^2)^SMALLA(i);

      D_BGDELTA_D_DELTA=(DELTA-1) *
(BIGA(i)*THETA*2/BETA(i)*((DELTA-1)^2)^(GG-
1)+2*BIGB(i)*SMALLA(i)...
      *((DELTA-1)^2)^(SMALLA(i)-1));

      D_BGDELTA_D_DELTA_SMALLB =
SMALLB(i) * BGDELTA^(SMALLB(i)-1)*
D_BGDELTA_D_DELTA;
      D_BGDELTA_D_TAU_SMALLB = -2 *
THETA * SMALLB(i) * BGDELTA^(SMALLB(i)-1);

      PHI_R_FOR_DELTA_TERM = NN(i) *
(BGDELTA^SMALLB(i)*(BGPHI+DELTA*D_BGPHI_
D_DELTA)+D_BGDELTA_D_DELTA_SMALLB*DEL
TA*BGPHI);
      PHI_R_FOR_TAU_TERM = NN(i) * DELTA *
(D_BGDELTA_D_TAU_SMALLB * BGPHI +
BGDELTA^SMALLB(i) * D_BGPHI_D_TAU);

      PHI_R_FOR_DELTA = PHI_R_FOR_DELTA +
PHI_R_FOR_DELTA_TERM;
      PHI_R_FOR_TAU = PHI_R_FOR_TAU +
PHI_R_FOR_TAU_TERM;

    end

% SUM OF EACH TERM AND THIS VALUE WILL BE
PHI_R_DELTA AND PHI_R_TAU

PHI_R_DELTA = PHI_R_FIR_DELTA +
PHI_R_SEC_DELTA + PHI_R_THI_DELTA +
PHI_R_FOR_DELTA;
PHI_R_TAU = PHI_R_FIR_TAU + PHI_R_SEC_TAU +
PHI_R_THI_TAU + PHI_R_FOR_TAU;

%%%%%%%%%%%%%%%%%%%%%%%%%%
%%%%%%%%%%%%%%%%%%%%%%%%%%
%%%%%%%%%%%%%%%%%%%%%

%% CALCULATE ETHALPY
```

```
H = 1 * R * T * (1 + TAU * (PHI_TAU_ZERO +
PHI_R_TAU) + DELTA * PHI_R_DELTA) + 809248.07;
```

HENRY.m

```
function HENRY(X1M)

%%%%%%%%%%%%%%%%%%%%%%%%%%%%%%%%%%%%%%%%%%%%%%%%%%%%%%%%%%%%%%%%%%%%%%%%%%%
%% This subroutine calculate the mole fraction of CO2 using          %%
%%        Diamond        and        Akinfiev        (2003)        %%
%%%%%%%%%%%%%%%%%%%%%%%%%%%%%%%%%%%%%%%%%%%%%%%%%%%%%%%%%%%%%%%%%%%%%%%%%%%

%C          Input:
%C                         T   = TEMPERATURE in [K]
%C     PCX = PRESSURE in [Pa]
%C
%C          Output:
%C     X1M = Mole fraction of Aqueous CO2
%C
%C          Constants:
%C                         R   = SPECIFIC GAS CONSTANT gas constant (188.9241 [J/kg*K])
%C          = RM/M
%C        RM   = MOLAR GAS CONSTANT (8.314510 [J/molK])
%C     M   = MOLAR MASS (44.0098 [g/mol])
%C       TC  = TEMPERATURE AT CRITICAL POINT (304.1282 [K])
%C     RHOC= DENSITY AT CRITICAL POINT (467.6 [kg/m3])
%C

global T Pbar ro P t_1 AT A A0T W1T e W2T GT W3 G W3T HT W4 H W4T pp FC X1M XCO2

%          [P.G. Hill. A unified fundamental equation for thermodynamic pro-
%'       perties of H2O  J. Phys. Chem. Ref. Data, 1990, v. 19, N 5, pp. 1233-1274]

      dcr = .322778; %[kg/m3]
      Tcr = 647.067; %[K]
      Pcr = 220.46; %[bar]
      TrK = 298.15;

      RgasJbar = 1.987191683 * 41.84;
      RGasH2O = 4.61521937;
      Rgascal = 1.987191683;
      RgasJ = Rgascal * 4.184;

      Coef1 = -9.3134;
      Coef2 = 11.5477;

      Scale = -.088;

      MH2O = 18.0152;

       asat=[-7.85823,1.83991,-11.7811,22.6705,-15.9393,1.77516];
       bsat=[1.99206, 1.10123, -5.12506E-1, -1.75263, -45.4485, -6.75615E5];

%    Changing unit to [Bar]
       Pbar=P*10^1;

        if T < Tcr

%          Saul A., Wagner W. International Equations for the Saturation
%          Properties of Ordinary Water Substances.
%          J. Phys. Chem. Ref. Data, 1987, v. 16, pp. 893-901

         tausat = 1 - T / Tcr;
         sum = asat(1) * tausat + asat(2) * tausat ^ 1.5 + asat(3) * tausat ^ 3;
         sum = sum + asat(4) * tausat ^ 3.5 + asat(5) * tausat ^ 4 + asat(6) * tausat ^ 7.5;
         Psat = exp(Tcr / T * sum) * Pcr;
        end

        if Pbar==0
          Pbar = Psat;
        end

        if Pbar < Psat
          Vs = RgasJbar * T / Pbar;
        end

        if Pbar==Psat
         sum = 1 + bsat(1) * tausat ^ (1/3) + bsat(2) * tausat ^ (2/3);
         sum = sum + bsat(3) * tausat ^ (5/3) + bsat(4) * tausat ^ (16/3);
         sum = sum + bsat(5) * tausat ^ (43/3) + bsat(6) * tausat ^ (110/3);
         ro = sum;
        end

        if Pbar > Psat
          if Pbar <= 1000
             Vs = 116.271 - 1.03596 * T + 3.90561E-03 * T * T - 6.2842E-06 * T ^ 3;
             Vs = Vs + 3.7039E-09 * T ^ 4;
             ro = 18.0152 / Vs / dcr;
          end

          if Pbar <= 2000
             Vs = 5.851212 + .0822269 * T - 1.99974E-04 * T * T + 1.82853E-07 * T ^ 3;
             ro = 18.0152 / Vs / dcr;
          end

          if Pbar <= 3000
             Vs = 23.666 - .04115 * T + .0000696 * T * T - 1.462E-08 * T ^ 3;
             ro = 18.0152 / Vs / dcr;
          end

          if Pbar <= 5000
             Vs = 13.956 + .002059 * T + 1.3935E-05 * T * T;
             ro = 18.0152 / Vs / dcr;
          end

          if Pbar <= 10000
             Vs = 13.737 + .0032645 * T + 4.822E-06 * T * T;
             ro = 18.0152 / Vs / dcr;
          end
```

```
        if Pbar > 10000
           Vs = 11.894 + .007639 * T;
        end
      end

%     Call thermodynamic properties of water

      WATER;

%     Density of water [kg/m3]
      dH2O = ro * dcr;

     ddH2O(P)=dH2O;

%     Enthropy of water

      SH2O = MH2O * RGasH2O * (t_1 * AT - A) * 0.1 +
63.19949;

      SSH2O(P)=SH2O;

%     Enthalpy of water

      HH2O = MH2O * RGasH2O * Tcr * (-AT - pp / ro /
t_1) * 0.1 - 287757.32;

      HHH2O(P)=HH2O;

%     Gibbs' free energy of water

      GH2O = HH2O - T * SH2O + 69495.6;

        G0H2Ogas = -228581.9;
        SH2Ogas = 188.835;
        aH2O = 27.057;
        bH2OE3 = 17.584;
        cH2OEmin5 = 2.7696;
        dH2OE6 = -2.5097;
        eH2OEmin1 = -2.7656;

        GTH2Ogas = G0H2Ogas - SH2Ogas * (T - TrK) -
aH2O * T * log(T / TrK) + aH2O * (T - TrK);
        GTH2Ogas = GTH2Ogas - .5 * (bH2OE3) / 1000 *
(T - TrK) ^ 2 - .5 * (cH2OEmin5) * 100000 / T * (T / TrK
- 1) ^ 2;
        GTH2Ogas = GTH2Ogas - 1 / 6 * (dH2OE6) /
1000000 * (T ^ 3 - TrK ^ 3 - 3 * TrK ^ 2 * (T - TrK));
        GTH2Ogas = GTH2Ogas - 2 * (eH2OEmin1) * 10 *
((T - TrK) / (TrK)^0.5 - 2 * ((T)^0.5 - (TrK)^0.5));

       lnfH2O = (GH2O - GTH2Ogas) / RgasJ / T; %[bar]

       fH2O(P)=exp(lnfH2O) / 10;

      yH2Oideal = Psat / Pbar;

      yH2Orough = (.1256 * (T-273.15) - .0212) * .001 +
(.065 * (T-273.15) + 1.21) * .000001 * Pbar;

      if yH2Oideal > yH2Orough

         yCO2 = 1 - yH2Oideal;
      else
         yCO2 = 1 - yH2Orough;
      end

       dB12 = .5 * (Coef1 + Coef2 * (1000 / T) ^ .5);
       dB12d = 2 * dH2O * dB12;

         lnkH = 0;

         lnkH = lnkH + (1 - Scale) * lnfH2O + Scale *
log(RgasJbar / MH2O * T * dH2O) + dB12d;

         XCO2 = (FC/10^6) / (exp(lnkH) * yCO2 / 10);

         molalCO2 = 1000 / MH2O * XCO2 / (1 - XCO2);

%              'Empirical correction for CO2 solubility by
Diamond and Akinfiev (2003)

       EmpirFunc = 3.63579E-05 - 4.47782E-06 * (T-
273.15) + .0073101 * (XCO2 * 100) + 1.18833E-04 * (T-
273.15) * (XCO2 * 100) - 7.49356E-03 * (XCO2 * 100) ^
2 + 5.41469E-05 * (T-273.15) * (XCO2 * 100) ^ 2;
       X1M = XCO2 * (1 + EmpirFunc);
```

WATER.m

```
function WATER

      dcr = .322778;
      Tcr = 647.067; %[K]
      RGasH2O = 4.61521937;

      C001 = -.000034631815;
      C002 = -.000030378112;
      delta = 1.028667;
      dlro0 = .23;
      dlT0 = .05;

      alpha = 80;
      beta = 1;
      gamma = 130;
      dlta = 12;
      nu = 4;

global T Pbar ro AT t_1 pp A A0T W1T e W2T GT W3 G W3T HT W4 H W4T

%    Saul, A., Wagner, W., 1987. International equations for the saturation properties of ordinary water substance.
%    Journal of Physical and Chemical Reference Data 16(4), 893-899.

%    Hill, P.G., 1990. A unified fundamental equation for the thermodynamic properties of H2O.
%    Journal of Physical and Chemical Reference Data 19(5), 1233-1274.

      C=[7.07501275112, -8.34240569963, -0.364601380, -0.036897043,
0.003033815,0.000390109,0.113592870,2.413178500];

     for i=1:7
       for j=1:7
          A1(i,j) = 0;
       end
     end
       A1(4, 1) = .3384249125;
       A1(5, 1) = -.07153393406;
       A1(7, 1) = .0005493680814;
       A1(3, 2) = .04933218501;
       A1(6, 2) = -.02328491212;
       A1(7, 2) = .002402095181;
       A1(1, 3) = .7529422956;
       A1(3, 3) = -2.28026007;
       A1(2, 4) = 1.142004144;
       A1(3, 4) = -2.619059624;
       A1(5, 4) = .4395237702;
       A1(6, 4) = -.03161046646;
       A1(7, 4) = .0006814467692;
       A1(1, 5) = -.3924227294;
       A1(3, 5) = -.2738770648;
       A1(4, 6) = -.01943443857;
       A1(5, 6) = .003048860434;
       A1(3, 7) = .003946510403;

      for i=1:7
        for j=1:12
           A2(i,j) = 0;
        end
     end
       A2(1, 1) = .2243610314;
       A2(2, 1) = .1193250201;
       A2(5, 1) = .06582959348;
       A2(5, 2) = .1651430628;
       A2(1, 3) = -2.178969357;
       A2(2, 3) = .2674090542;
       A2(3, 3) = .8647490995;
       A2(1, 4) = -.1530432257;
       A2(3, 4) = 2.059881454;
       A2(6, 4) = -.4888628703;
       A2(7, 4) = .1375328753;
       A2(5, 5) = -.9015180666;
       A2(6, 5) = -.1444258609;
       A2(7, 5) = .1558046279;
       A2(4, 6) = -2.740652563;
       A2(6, 6) = .4983771706;
       A2(4, 7) = -3.261978564;
       A2(5, 7) = 1.609338784;
       A2(1, 8) = .03484674963;
       A2(2, 8) = -1.537646434;
       A2(5, 8) = .2316225257;
       A2(2, 9) = -1.419249232;
       A2(3, 9) = .7969984635;
       A2(5, 10) = .007510544627;
       A2(1, 12) = .0005364384732;

      for i=1:5
        for j=1:5
           A3(i, j) = 0;
        end
      end
       A3(1, 1) = .6109381296;
       A3(3, 1) = -.01906644459;
       A3(5, 1) = .007976092188;
       A3(1, 2) = 1.934466766;
       A3(1, 3) = 1.921820547;
       A3(3, 3) = -.04410105919;
       A3(1, 4) = .6130354419;
       A3(2, 4) = -.2855258689;
       A3(5, 4) = .0252613708;
       A3(2, 5) = -.2374074642;
       A3(4, 5) = .03855866402;
       A3(5, 5) = .00804167215;

      for i = 1:5
        for j = 1:10
           A4(i, j) = 0;
        end
      end
       A4(3, 1) = -16.35439033;
       A4(1, 2) = -50.25818675;
       A4(2, 4) = .164900304;
       A4(1, 5) = -.8499893502;
       A4(1, 9) = .008314382544;
       A4(2, 9) = .0008781327858;
       A4(2, 10) = .001537391213;
       A4(3, 10) = -.0009016873786;
       A4(5, 10) = .0003326628664;

%HelmholtzCalculation:

      t_1 = -Tcr / T;
      dlT = 1 + t_1;  %deltaT
      stepro = 1;

%Iteration
while abs(stepro) > .000001
      dlro = ro - 1;              %deltaRO in Appendix C
```

```
    dlAn = C001 + C002 * dlT;
    dlAnT = C002;
    dlAnTT = 0;
    ksi = ((dlro / dlro0)^ 2 + (dlT / dlT0)^ 2)^0.5;
    tmp = (ksi / delta) ^ 4;

    if tmp > 88
      Z = 1E+38;
    elseif tmp < .01
      Z = tmp;
    else
      Z = exp(tmp) - 1;
    end

      tmp = -1 / Z;

    if tmp < -88
      exp1Z = 1.01E-38;
    else
      exp1Z = exp(tmp);
    end

    FF = 1 - exp1Z;

    if FF == 0
      Fro = 0;
      Froro = 0;
      Frororo = 0;
      FT = 0;
      FTT = 0;
      FroT = 0;
      FroTT = 0;
    else
      Fksi = -4 / delta * exp1Z * (1 / Z + 1 / Z ^ 2) *
(log(1 + Z)) ^ (3 / 4);  % Appendix E
      ksiro = dlro / ( ksi * dlro0 ^ 2 );
% Appendix E
      ksiT = dlT / ksi / dlT0 ^ 2;
% Appendix E
      ksiroro = (1 / ksi - (dlro / dlro0) ^ 2 / ksi ^ 3) / dlro0
^ 2;          % Appendix E
      ksiTT = (1 / ksi - (dlT / dlT0) ^ 2 / ksi ^ 3) / dlT0 ^
2;             % Appendix E
      ksiroT = -dlro * dlT / ksi ^ 3 / (dlro0 * dlT0) ^ 2;
% Appendix E

      Fro = Fksi * ksiro;
% Appendix E
      Fksiksi = -12 / delta ^ 2 * exp1Z * (1 / Z + 1 / Z ^
2) * (log(1 + Z))^0.5; % Appendix E
      Fksiksi = Fksiksi * (1 + 4 / 3 * (1 / Z ^ 2 - 1 / Z - 1)
* log(1 + Z));   % Appendix E
      Froro = Fksiksi * ksiro ^ 2 + Fksi * ksiroro;
% Appendix E
      Frororo = 0;
% Three time derivative od F function
      FT = Fksi * ksiT;
% Appendix E
      FTT = Fksiksi * ksiT ^ 2 + Fksi * ksiTT;
% Appendix E
      FroT = Fksiksi * ksiro * ksiT + Fksi * ksiroT;
% Appendix E
      FroTT = 0
    end

    A0 = 0;
    A0T = 0;
    A0TT = 0;

    for i = 1:6
      A0 = A0 + C(i) * (-t_1) ^ (2 - i);
% Equation (3)
      A0T = A0T - C(i) * (2 - i) * (-t_1) ^ (1 - i);
% The first derivative by T term of Equation (3)
      A0TT = A0TT + C(i) * (2 - i) * (1 - i) * (-t_1) ^ (-
i);                % The second derivative by T term of
Equation (3)
    end
      A0 = A0 + (C(7) * t_1 + C(8)) * log(-t_1);
% Equation (3) in Appendix A
      A0T = A0T + C(7) * (1 + log(-t_1)) + C(8) / t_1;
% The first derivative by T term of Equation (3)
      A0TT = A0TT + C(7) / t_1 - C(8) / t_1 ^ 2;
% The second derivative by T term of Equation (3)


      e = exp(-ro ^ 2);
% Appendix E
      Ero = -2 * ro * e;
% The derivative term in Appendix E
      Eroro = -2 * e - 2 * ro * Ero;
% The second derivative term in Appendix E
      Erororo = -4 * Ero - 2 * ro * Eroro;
% The third derivative term in Appendix E

    if ro < .00002
      UnitMinusE = ro ^ 2;
    else
      UnitMinusE = 1 - e;
% The (1-E) at R fuction in Appendix D
    end

      tmp = -alpha * dlT - beta * dlro - gamma * dlT ^ 2
- dlta * dlro ^ 2;    % The inside fuction of G in Appendix
E

    if tmp > 88
      G = 1.01E+38;
    elseif tmp < -88
      G = -1.01E-38;
    else
      G = exp(tmp);
    end

    Gro = G * (-beta - 2 * dlta * dlro);
% The first drivative by density in Appendix E
    Groro = Gro * (-beta - 2 * dlta * dlro) - 2 * dlta * G;
% The second derivative by density in Appendix E
    Grororo = Groro * (-beta - 2 * dlta * dlro) - 2 * dlta *
Gro;              % The Third derivative by density in
Appendix E
    GT = G * (-alpha - 2 * gamma * dlT);
% The first derivative by temperature in Appendix E
    GTT = GT * (-alpha - 2 * gamma * dlT) - 2 * gamma
* G;                % The second derivative by
temperature in Appendix E
    GroT = GT * (-beta - 2 * dlta * dlro);
% The derivative by density and temperature in Appendix
E
    GroroT = GroT * (-beta - 2 * dlta * dlro) - 2 * dlta *
GT;                % The derivative by density and
temperature in Appendix E
    GroTT = GTT * (-beta - 2 * dlta * dlro);
% The derivative by density and temperature in Appendix
E

    H = exp(-nu * (t_1 + 3));
% The fuction of H in Appendix E
    HT = -nu * H;
% The first derivative by temperature in Appendix E
```

```
    HTT = nu ^ 2 * H;
% The second derivative by temperature in Appendix E

    W1 = 0;
    W1ro = 0;
    W1roro = 0;
    W1rororo = 0;
    W1roroT = 0;
    W1T = 0;
    W1TT = 0;
    W1roT = 0;
    W1roTT = 0;

%%%%%%%% The calculation of R1 function in Appendix D %%%%%%%%%%%%

    for i = 1:7
      R1 = UnitMinusE * ro ^ (i - 2);
      R1ro = UnitMinusE * (i - 2) * ro ^ (i - 3) - Ero * ro ^ (i - 2);
      R1roro = UnitMinusE * (i - 2) * (i - 3) * ro ^ (i - 4) - 2 * Ero * (i - 2) * ro ^ (i - 3) - Eroro * ro ^ (i - 2);
      R1rororo = UnitMinusE * (i - 2) * (i - 3) * (i - 4) * ro ^ (i - 5) - 3 * Ero * (i - 2) * (i - 3) * ro ^ (i - 4);
      R1rororo = R1rororo - 3 * Eroro * (i - 2) * ro ^ (i - 3) - Erororo * ro ^ (i - 2);

%%%%%%%% IF R(2), follow below claculation %%%%%%%%%%%%%%%%%%

      if i == 2
          R1 = UnitMinusE * log(ro) - ro ^ 2 * log(ro) + ro ^ 2 / 2;
          R1ro = UnitMinusE / ro - Ero * log(ro) - 2 * ro * log(ro);
          R1roro = -UnitMinusE / ro ^ 2 - 2 * Ero / ro - Eroro * log(ro) - 2 * log(ro) - 2;
          R1rororo = 2 * UnitMinusE / ro ^ 3 + 3 * Ero / ro ^ 2;
          R1rororo = R1rororo - 3 * Eroro / ro - Erororo * log(ro) - 2 / ro;
      end

      %%%%%%%% The calculation of T1 and W1 function in Appendix D %%%%%%%%%%%%

      for j = 1:7
        T1 = t_1 ^ (j - 1);
        T1T = (j - 1) * t_1 ^ (j - 2);
        T1TT = (j - 1) * (j - 2) * t_1 ^ (j - 3);
        W1 = W1 + A1(i, j) * R1 * T1;
        W1ro = W1ro + A1(i, j) * R1ro * T1;
        W1roro = W1roro + A1(i, j) * R1roro * T1;
        W1roroT = W1roroT + A1(i, j) * R1roro * T1T;
        W1rororo = W1rororo + A1(i, j) * R1rororo * T1;
        W1T = W1T + A1(i, j) * R1 * T1T;
        W1TT = W1TT + A1(i, j) * R1 * T1TT;
        W1roT = W1roT + A1(i, j) * R1ro * T1T;
        W1roTT = W1roTT + A1(i, j) * R1ro * T1TT;
    end
  end

    W2 = 0;
    W2ro = 0;
    W2roro = 0;
    W2rororo = 0;
    W2roroT = 0;
    W2T = 0;
    W2TT = 0;
    W2roT = 0;
    W2roTT = 0;

%%%%%%%% The calculation of R2 function in Appendix D %%%%%%%%%%%%

    for i = 1:7
      R2 = ro ^ i;
      R2ro = i * ro ^ (i - 1);
      R2roro = i * (i - 1) * ro ^ (i - 2);
      R2rororo = i * (i - 1) * (i - 2) * ro ^ (i - 3);

      %%%%%%%% The calculation of T1 and W2 function in Appendix D %%%%%%%%%%%%

      for j = 1:12
        T1 = t_1 ^ (j - 1);
        T1T = (j - 1) * t_1 ^ (j - 2);
        T1TT = (j - 1) * (j - 2) * t_1 ^ (j - 3);
        W2 = W2 + A2(i, j) * R2 * T1;
        W2ro = W2ro + A2(i, j) * R2ro * T1;
        W2roro = W2roro + A2(i, j) * R2roro * T1;
        W2roroT = W2roroT + A2(i, j) * R2roro * T1T;
        W2rororo = W2rororo + A2(i, j) * R2rororo * T1;
        W2T = W2T + A2(i, j) * R2 * T1T;
        W2TT = W2TT + A2(i, j) * R2 * T1TT;
        W2roT = W2roT + A2(i, j) * R2ro * T1T;
        W2roTT = W2roTT + A2(i, j) * R2ro * T1TT;
    end
  end

    W3 = 0;
    W3ro = 0;
    W3roro = 0;
    W3rororo = 0;
    W3roroT = 0;
    W3T = 0;
    W3TT = 0;
    W3roT = 0;
    W3roTT = 0;

      %%%%%%%% The calculation R3 function in Appendix D %%%%%%%%%%%%

    for i = 1:5
      R3 = ro ^ (i + 1);
      R3ro = (i + 1) * ro ^ i;
      R3roro = (i + 1) * i * ro ^ (i - 1);
      R3rororo = (i + 1) * i * (i - 1) * ro ^ (i - 2);

      %%%%%%%% The calculation of T2 and W3 function in Appendix D %%%%%%%%%%%%

      for j = 1:5
        T2 = t_1 ^ (j + 1);
        T2T = (j + 1) * t_1 ^ j;
        T2TT = (j + 1) * j * t_1 ^ (j - 1);
        W3 = W3 + A3(i, j) * R3 * T2;
        W3ro = W3ro + A3(i, j) * R3ro * T2;
        W3roro = W3roro + A3(i, j) * R3roro * T2;
        W3roroT = W3roroT + A3(i, j) * R3roro * T2T;
        W3rororo = W3rororo + A3(i, j) * R3rororo * T2;
        W3T = W3T + A3(i, j) * R3 * T2T;
        W3TT = W3TT + A3(i, j) * R3 * T2TT;
        W3roT = W3roT + A3(i, j) * R3ro * T2T;
        W3roTT = W3roT + A3(i, j) * R3ro * T2TT;
    end
  end
```

```
    W4 = 0;
    W4ro = 0;
    W4roro = 0;
    W4rororo = 0;
    W4roroT = 0;
    W4T = 0;
    W4TT = 0;
    W4roT = 0;
    W4roTT = 0;

    %%%%%%%% The calculation of R1 function in Appendix D %%%%%%%%%%%%

    for i = 1:5
      R1 = UnitMinusE * ro ^ (i - 2);
      R1ro = UnitMinusE * (i - 2) * ro ^ (i - 3) - Ero * ro ^ (i - 2);
      R1roro = UnitMinusE * (i - 2) * (i - 3) * ro ^ (i - 4) - 2 * Ero * (i - 2) * ro ^ (i - 3) - Eroro * ro ^ (i - 2);
      R1rororo = UnitMinusE * (i - 2) * (i - 3) * (i - 4) * ro ^ (i - 5) - 3 * Ero * (i - 2) * (i - 3) * ro ^ (i - 4);
      R1rororo = R1rororo - 3 * Eroro * (i - 2) * ro ^ (i - 3) - Erororo * ro ^ (i - 2);

%%%%%%%% IF R(2), follow below claculation %%%%%%%%%%%%%%%%%%

      if i == 2
          R1 = UnitMinusE * log(ro) - ro ^ 2 * log(ro) + ro ^ 2 / 2;
          R1ro = UnitMinusE / ro - Ero * log(ro) - 2 * ro * log(ro);
          R1roro = -UnitMinusE / ro ^ 2 - 2 * Ero / ro - Eroro * log(ro) - 2 * log(ro) - 2;
          R1rororo = 2 * UnitMinusE / ro ^ 3 + 3 * Ero / ro ^ 2;
          R1rororo = R1rororo - 3 * Eroro / ro - Erororo * log(ro) - 2 / ro;
        end

      %%%%%%%% The calculation of T1 and W4 function in Appendix D %%%%%%%%%%%%

      for j = 1:10
        T1 = t_1 ^ (j - 1);
        T1T = (j - 1) * t_1 ^ (j - 2);
        T1TT = (j - 1) * (j - 2) * t_1 ^ (j - 3);
        W4 = W4 + A4(i, j) * R1 * T1;
        W4ro = W4ro + A4(i, j) * R1ro * T1;
        W4roro = W4roro + A4(i, j) * R1roro * T1;
        W4roroT = W4roroT + A4(i, j) * R1roro * T1T;
        W4rororo = W4rororo + A4(i, j) * R1rororo * T1;
        W4T = W4T + A4(i, j) * R1 * T1T;
        W4TT = W4TT + A4(i, j) * R1 * T1TT;
        W4roT = W4roT + A4(i, j) * R1ro * T1T;
        W4roTT = W4roTT + A4(i, j) * R1ro * T1TT;
      end
    end

    A = A0 + log(ro) + W1 + e * W2 + G * W3 + H * W4 + FF * dlAn;
    Aro = 1 / ro + W1ro + Ero * W2 + e * W2ro + Gro * W3 + G * W3ro;
    Aro = Aro + H * W4ro + dlAn * Fro;
    Aroro = -1 / ro ^ 2 + W1roro + Eroro * W2 + 2 * Ero * W2ro;
    Aroro = Aroro + e * W2roro + Groro * W3 + 2 * Gro * W3ro + G * W3roro;
    Aroro = Aroro + H * W4roro + dlAn * Froro;
    Arororo = 2 / ro ^ 3 + W1rororo + Erororo * W2 + 3 * Eroro * W2ro;
    Arororo = Arororo + 3 * Ero * W2roro + e * W2rororo;
    Arororo = Arororo + Grororo * W3 + 3 * Groro * W3ro + 3 * Gro * W3roro + G * W3rororo;
    Arororo = Arororo + H * W4rororo + dlAn * Frororo;
    AroroT = W1roroT + Eroro * W2T + 2 * Ero * W2roT;
    AroroT = AroroT + e * W2roroT + GroroT * W3 + Groro * W3T;
    AroroT = AroroT + 2 * GroT * W3ro + 2 * Gro * W3roT;
    AroroT = AroroT + GT * W3roro + G * W3roroT;
    AroroT = AroroT + HT * W4roro + H * W4roroT;
    AT = A0T + W1T + e * W2T + GT * W3 + G * W3T + HT * W4 + H * W4T;
    AT = AT + FT * dlAn + FF * dlAnT;
    ATT = A0TT + W1TT + e * W2TT + GTT * W3 + 2 * GT * W3T + G * W3TT;
    ATT = ATT + HTT * W4 + 2 * HT * W4T + H * W4TT;
    ATT = ATT + FTT * dlAn + 2 * FT * dlAnT + FF * dlAnTT;
    AroT = W1roT + Ero * W2T + e * W2roT + GroT * W3 + Gro * W3T;
    AroT = AroT + GT * W3ro + G * W3roT + HT * W4ro + H * W4roT;
    AroT = AroT + dlAnT * Fro + dlAn * FroT;
    AroTT = W1roTT + Ero * W2TT + e * W2roTT + GroTT * W3 + GroT * W3T;
    AroTT = AroTT + GroT * W3T + Gro * W3TT + GTT * W3ro + GT * W3roT;
    AroTT = AroTT + GT * W3roT + G * W3roTT + HTT * W4ro + HT * W4roT;
    AroTT = AroTT + HT * W4roT + H * W4roTT;

    pp = ro * ro * Aro;
    dPdro = 2 * ro * Aro + ro * ro * Aroro;

    dev = pp - Pbar / dcr / RGasH2O / T;
    stepro = -dev / dPdro;
    ro = ro + stepro;

    if ro > 9.2
       while ro < 9.2
         ro = ro / 3;
       end
    end
    if ro < 0
       ro = .05;
    end
end
```

SOLUTE.m

```
function SOLUT(HSOL)

%       This subroutine calcualtes the enthalpy of CO2
dissolution in liquid water.
%     The expression is from O'Sullivan et al., (1985). The
expression was created
%       using a quadratic fit to data published by Ellis and
Goulding (1963).

global T HSOL

%     Convert temperature from kelvin [K] to degree [C]

     TX = T-2.7315D+02;
     T1  = 1.D-2 * TX;
     T2 = T1 * T1;
     T3 = T1 * T2;
     T4 = T1 * T3;
     HSOL = -7.3696D-2 - 5.6405D-1*T1 + 7.0363D-1*T2
- 2.7882D-1*T3 + 4.2579D-2*T4;
     HSOL = HSOL * 1.D6;
```

DENMIX.m

```
function DENMIX(D1M)

%C     This subroutine returns density of CO2/H2O liquid mixture. The
%C     expression is from Anderson et al. (1992).

%C          Input:
%C     T    = Temperature in Kevin K
%C                    TX   = Temperature in degrees C
%C                    DW   = Density of H2O in kg/m3
%C                    X1MM  = Mass fraction of CO2 [-]

%C          Output:
%C                    D1M    = Density of CO2/H2O mixture in kg/m3

%C          Constants:
%C                    XMWC = Molecular weight of CO2 in Kg/mol

%C          Variables:
%C                    RHO    = Density of CO2 at saturation pressure in mol/cm3
%C                    DC   = Density of CO2 at saturation pressure in kg/m3
%C                    X2M  = Mass fraction H2O [-]

global T P D1M X1MM

     XMWC=4.40098D-02;

%C     Calculate TX to the 2nd, 3rd and 4th powers for later use:
     TX=T-273.15;
     TX2 = TX * TX;
     TX3 = TX2 * TX;
     TX4 = TX3 * TX;

%C      Calculate density of CO2 (RHO) at saturation pressure in mol/cm3:
     RHO1 = 1.D0/(3.736D+01 - (7.109D-02*TX) - (3.812D-05*TX2) + (3.296D-06*TX3) - (3.702D-09*TX4));

%C    Convert RHO to kg/m3 (DC):
     DC1 = RHO1 * 1.0D+06 * XMWC;

%C    Calculate mass fraction of H2O:
     X2M = 1.D0 - X1MM;

% From here, calcualte pure water density (International Formulation Committee, 1967)

    A1=[6.824687741E3,-5.422063673E2,-2.096666205E4,3.941286787E4,...
     -6.733277739E4,9.902381028E4,-1.093911774E5,8.590841667E4,...
     -4.511168742E4,1.418138926E4,-2.017271113E3,7.982692717E0,...
     -2.616571843E-2,1.522411790E-3,2.284279054E-2,2.421647003E2,...
     1.269716088E-10,2.074838328E-7,2.174020350E-8,1.105710498E-9,...
     1.293441934E1,1.308119072E-5,6.047626338E-14];

    SA=[8.438375405E-1,5.362162162E-4,1.720000000E0,7.342278489E-2,...
     4.975858870E-2,6.537154300E-1,1.150E-6,1.51080E-5,...
     1.41880E-1,7.002753165E0,2.995284926E-4,2.040E-1];

     TKR=T/647.3;

     PNMR=(P*10^6)/2.212E7;

     Y=1.-SA(1)*TKR*TKR-SA(2)/TKR^6;

     ZP=(SA(3)*Y*Y-2.*SA(4)*TKR+2.*SA(5)*PNMR);

     Z=Y+sqrt(ZP);

     PAR1=A1(12)*SA(5)/Z^(5./17.);


PAR2=A1(13)+A1(14)*TKR+A1(15)*TKR*TKR+A1(16)*(SA(6)-TKR)^10+A1(17)/(SA(7)+TKR^19);


PAR3=(A1(18)+2.*A1(19)*PNMR+3.*A1(20)*PNMR*PNMR)/(SA(8)+TKR^11);

     PAR4=A1(21)*TKR^18*(SA(9)+TKR*TKR)*(-3./(SA(10)+PNMR)^4+SA(11));

     PAR5=3.*A1(22)*(SA(12)-TKR)*PNMR*PNMR+4.*A1(23)/TKR^20*PNMR^3;

     VMKR=PAR1+PAR2-PAR3-PAR4+PAR5;

     V=VMKR*3.17E-3;

     DW=1./V;

%C    Calculate density of CO2/H2O mixture in kg/m3:

     D1M = (DW*DC1) / ((X1MM*DW)+(X2M*DC1));
```

VISCO2.m

```
function VISCO2(VC)

%C       This subroutine calculates the viscosity of pure
CO2 as a function
%C          of temperature and density of CO2.  The
expressions for calculating
%C          the viscosity come from empirical equations
provided in Vesovic et
%C     al.(1990) and Fenghour et al. (1998).
%C      The critical point enhancement for the viscosity of
CO2
%C     has been neglected since it is weak and restricted to
a very small
%C     region around the critical point.

%C          Input:
%C                    TX     = Temperature in degrees C
%C                    DC     = Density of CO2 in kg/m3

%C          Output:
%C                    VC     = Viscosity of CO2 in Pa-s

%C          Constants:
%C                    Ai          = Coefficients of the
correlation of the
%C                          zero-density viscosity
%C                    ESCL   = Energy scaling parameter
in K
%C                         = epsilon/kappa
%C                    Dij         = Coefficients of the
correlation of the
%C                          excess viscosity

%C          Variables:
%C                    T      = Temperature in K
%C                    TSTAR     = (kappa*T)/epsilon =
T/ESCL [-]
%C                    ETA0    = Zero-density viscosity in
muPa-s
%C                    DETA       = Excess viscosity in
muPa-s

global T DC VC

      A0   =  2.35156D-01;
      A1   = -4.91266D-01;
      A2   =  5.211155D-02;
      A3   =  5.347906D-02;
      A4   = -1.537102D-02;
      ESCL =  2.51196D+02;
      D11  =  0.4071119D-02;
      D21  =  0.7198037D-04;
      D64  =  0.2411697D-16;
      D81  =  0.2971072D-22;
      D82  = -0.1627888D-22;

      DC2 = DC*DC;
            DC6 = DC2*DC2*DC2;
          DC8 = DC6*DC2;

%C    Calculate TSTAR and 3rd power:
      TSTAR = T/ESCL;
      TSTAR3=TSTAR*TSTAR*TSTAR;

%C    Calculate ln(TSTAR) and 2nd, 3rd, and 4th powers:
      BETA1 = log(TSTAR);
      BETA2 = BETA1*BETA1;
            BETA3 = BETA2*BETA1;
            BETA4 = BETA3*BETA1;

%C    Calculate zero-density limit viscosity in muPa-s:
      EXS                                                =
exp(A0+(A1*BETA1)+(A2*BETA2)+(A3*BETA3)+(A4
*BETA4));
      ETA0 = (1.00697D0 * sqrt(T)) / EXS;

%C    Calculate excess viscosity in muPa-s:
      DETA                                               =
(D11*DC)+(D21*DC2)+((D64*DC6)/TSTAR3)+(D81*D
C8)+((D82*DC8)/TSTAR);

%C    Calculate total viscosity in muPa-s:
      VC = ETA0 + DETA;

%C    Convert viscosity from muPa-s to Pa-s:
      VC = VC * 1.0D-06;
```

Appendix VII. Mathematical representation of brine density (Batzel and Wang, 1992).

$$\rho_{brine} = \rho_{water} + S\left(0.668 + 0.44S + 10^{-6}\left(300P - 2400PS + T\left(80 + 3T - 3300S - 13P + 47PS\right)\right)\right)$$

$$\rho_{water} = 1 + 10^{-6}\begin{pmatrix} -80T - 3.3T^2 + 0.00175T^3 + 489P - 2TP + 0.016T^2P - 1.3\times10^{-5}T^3P - \\ 0.333P^2 - 0.002TP^2 \end{pmatrix}$$

ρ_{brine} and ρ_{water} are g/cm^3, S is NaCl mass fraction (ppm/10^6), P is in MPa and T is in ºC.

Appendix VIII. Mathematical representation of brine viscosity (Palliser and McKibbin, 1998).

$$\mu_{brine}(T,P,X) = \frac{\left\{\begin{array}{l}\mu_{water}(T,P)(1+3X)\left((800-T)/800\right)^{9} \\ +(T/800)^{9}\left(\mu_{water}(T,P)(1-X)+\mu_{c}(800)X\right)\end{array}\right\}}{\left(\frac{800-T}{800}\right)^{9}+\left(\frac{T}{800}\right)^{9}}$$

$$\mu_{c}(800) = 4.71624\times10^{-3} - 4.02030\times10^{-6}\times800$$

μ_{brine} and μ_{water} are kg/ms is NaCl mass fraction, P is in bar and T is in ºC.

Appendix IX. Mathematical representation of CO_2 solubility in brine (Duan and Sun, 2003).

$$m_{CO_2} = \frac{y_{CO_2} P}{\exp\left(\frac{\mu^{l(0)}_{CO_2}}{RT} - \ln\varphi_{CO_2} + \sum_{Na=1}^{11} 2\lambda_{CO_2-Na^+} m_{Na^+} + \sum_{Na=1}^{11}\sum_{Cl=1}^{11} \xi_{CO_2-Na^+-Cl^-} m_{Na^+} m_{Cl^-}\right)}$$

$$\frac{\mu^{l(0)}_{CO_2}}{RT} = c_1 + c_2 T + \frac{c_3}{T} + c_4 T^2 + \frac{c_5}{(630 - T)} + c_6 P + c_7 P \ln T + \frac{c_8 P}{T} + \frac{c_9 P}{(630 - T)}$$

$$+ \frac{c_{10} P^2}{(630 - T)^2} + c_{11} T \ln P$$

$$y_{CO_2} = \frac{\left(P - P_{H_2O}\right)}{P}$$

$$P_{H_2O} = \frac{P_c T}{T_c}\left(1 + a_1(-t)^{1.9} + a_2 t + a_3 t^2 + a_4 t^3 + a_5 t^4\right)$$

I	c_i	a_i	λ_{CO_2-Na}	$\lambda_{CO_2-Na-Cl}$
1	$2.8944770600 \times 10^{1}$	-3.8640844×10^{1}	$-0.411370585 \times 10^{0}$	$3.36389723 \times 10^{-4}$
2	$-0.0354581768 \times 10^{0}$	5.8948420×10^{0}	$6.076320130 \times 10^{-4}$	$-1.98298980 \times 10^{-5}$
3	$-4.7706707700 \times 10^{3}$	5.9876516×10^{1}	$9.753477080 \times 10^{1}$	0
4	$1.0278276800 \times 10^{-5}$	2.6654627×10^{1}	0	0
5	$3.3812609800 \times 10^{1}$	1.0637097×10^{1}	0	0
6	$9.0403714000 \times 10^{-3}$		0	0
7	$-1.1493403100 \times 10^{-3}$		0	0
8	$-0.3074057260 \times 10^{0}$		$-0.0237622469 \times 10^{0}$	$2.12220830 \times 10^{-3}$
9	$-0.0907301486 \times 10^{0}$		$0.0170656236 \times 10^{0}$	$-5.24873303 \times 10^{-3}$
10	$9.327133930 \times 10^{-4}$		0	0
11			$1.413358340 \times 10^{-5}$	0

m_{CO2} is mol/kg, P is in bar and T is in ºK.

CO_2 solubility model from Duan and Sun (2003) is based on the Pitzer activity coefficient model (see the equations 5 in Duan and Sun, 2003). If Debye-Huckel model is applied to calculate activity coefficient in Duan and Sun's model, the predictive solubility will be different.

Appendix X. $\delta^{13}C$ values collected from site 207 at SACROC and magmatically-originated.

SACROC (this study)				Ballentine et al. (2001)	
Atmohsphere Concentration (ppm)	$\delta^{13}C$	Soil Concentration (ppm)	$\delta^{13}C$	CO2 fraction	$\delta^{13}C$
338	-13.24	414	-13.47	54.80	-2.77
345	-13.93	382	-12.13	54.60	-2.88
346	-12.74	424	-12.71	55.10	-2.91
359	-12.69	641	-52.09*	55.30	-2.89
419	-12.67	409	-9.86	57.40	-2.97
347	-13.21	349	-8.47	54.60	-2.90
347	-12.79	596	-10.55	54.20	-2.79
354	-13.52	395	-14.58	39.70	-2.95
341	-12.40	390	-10.53	39.10	-2.97
342	-13.49	395	-12.15	38.90	-2.91
487	-12.60	389	-11.75	39.20	-2.92
378	-14.07	475	-11.60	46.00	-2.88
346	-13.06	368	-9.42	52.50	-2.84
				20.80	-2.94
Heath (2004)		Bergfeld et al. (2006)		20.10	-2.70
CO2 fraction	$\delta^{13}C$	CO2 fraction	$\delta^{13}C$	21.00	-2.91
97.85	-6.68	92.90	-4.60	22.20	-2.97
95.66	-6.56	74.70	-4.30	21.90	-2.96
99.41	-6.76	38.00	-4.00	19.70	-3.06
98.75	-6.58	46.30	-4.20	24.60	-2.97
99.16	-6.42	62.60	-3.90	26.10	-2.89
96.45	-6.47	97.40	-4.10	27.30	-2.99
99.07	-6.72	84.20	-3.40	25.80	-2.97
		73.50	-4.40	25.70	-2.93
Cappa and Rice (1995)		36.40	-5.10	23.10	-2.96
CO2 fraction	$\delta^{13}C$	34.40	-3.70	21.10	-3.02
92.02	-3.77	97.00	-5.30		
92.38	-4.43	10.00	-5.70		
93.87	-4.15				

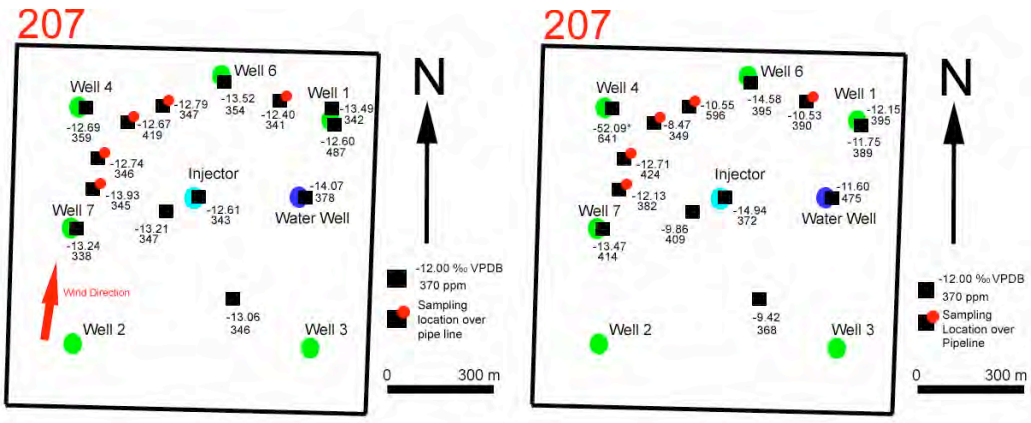

(a) atmosphere (b) soil

Appendix XI. Calculation of equilibrium constant of ankerite.

Equilibrium constant of ankerite is calculated from three ways: (1) mechanical mixing, (2) ideal mixing and (3) regular solid-solution. The equilibrium constants from each approach are compared.

Part I. Mechanical mixing

The chemical reaction of ankerite solid-solution is shown in Eq.1

$$Ca(Mg_xFe_{1-x})(CO_3)_2 = Ca^{2+} + xMg^{2+} (1-x)Fe^{2+} + 2(CO_3^{2-}) \quad \text{(Eq.1)}$$

The equilibrium constant of ankerite solid-solution is expressed as Eq.2

$$K_{ank}^{ss} = \frac{(Ca^{2+})(Mg^{2+})^x(Fe^{2+})^{(1-x)}(CO_3^{2-})^2}{(CaMg_xFe_{1-x}(CO_3)_2)} \quad \text{(Eq.2)}$$

The chemical reaction of end-member dolomite is shown in Eq.3

$$CaMg(CO_3)_2 = Ca^{2+} + Mg^{2+} + 2CO_3^{2-} \quad \text{(Eq.3)}$$

The equilibrium constant of end-member dolomite is expressed as Eq.4

$$K_{dol} = \frac{(Ca^{2+})(Mg^{2+})(CO_3^{2-})^2}{(CaMg(CO_3)_2)} \rightarrow (Mg^{2+}) = \frac{(CaMg(CO_3)_2)K_{dol}}{(Ca^{2+})(CO_3^{2-})^2} \quad \text{(Eq.4)}$$

The equilibrium constant of end-member siderite is expressed as Eq.5

$$CaFe(CO_3)_2 = Ca^{2+} + Fe^{2+} + 2CO_3^{2-} \quad \text{(Eq.5)}$$

The equilibrium constant of end-member siderite is expressed as Eq.6

$$K_{sid} = \frac{(Ca^{2+})(Fe^{2+})(CO_3^{2-})^2}{(CaFe(CO_3)_2)} \rightarrow (Fe^{2+}) = \frac{(CaFe(CO_3)_2)K_{sid}}{(Ca^{2+})(CO_3^{2-})^2} \quad \text{(Eq.6)}$$

Applying logarithm into Eq.1 and the following reaction becomes Eq.7

$$\log(K_{ank}^{ss}) = \log(Ca^{2+}) + x\log(Mg^{2+}) + (1-x)\log(Fe^{2+}) + 2\log(CO_3^{2-}) - \log(CaMg_xFe_{1-x}(CO_3)_2)$$

(Eq.7)

Insert Eq.4 and Eq.6 into Eq.7 and the following equation becomes Eq.8

$$\log(K_{ank}^{ss}) = \log(Ca^{2+}) + x\log(\frac{(CaMg(CO_3)_2)K_{dol}}{(Ca^{2+})(CO_3^{2-})^2}) + (1-x)\log(\frac{CaFe(CO_3)_2K_{sid}}{(Ca^{2+})(CO_3^{2-})^2}) + 2\log(CO_3^{2-}) - \log(CaMg_xFe_{1-x}(CO_3)_2)$$

(Eq.8)

After removing logarithm from Eq.8, the equation expressing the equilibrium constant of ankerite solid-solution is expressed with the end-member dolomite and siderite in Eq.9.

$$K_{ank}^{ss} = K_{dol}^{x}K_{sid}^{1-x}\frac{(CaMg(CO_3)_2)^x(CaFe(CO_3)_2)^{(1-x)}}{(CaMg_xFe_{1-x}(CO_3)_2)} \quad \text{(Eq.9)}$$

Assuming the activity of minerals is 1 will shows the final equation describing mechanical mixing

$$K_{ank}^{ss} = K_{dol}^{x}K_{sid}^{1-x} \quad \text{(Eq.10)}$$

Part II. Ideal mixing

Equation for ideal mixing is derived after assuming $(CaMg(CO_3)_2)$=x, $CaFe(CO_3)_2$=1-x, and $(CaMg_xFe_{1-x}(CO_3)_2)$=1 (Glynn and Reardon, 1990; Lichnter and Carey, 2006)

$$K_{ank}^{ss} = K_{dol}^{x}K_{sid}^{1-x}x^x(1-x)^{(1-x)} = (xK_{dol})^x((1-x)K_{sid})^{(1-x)} \quad \text{(Eq.11)}$$

Part III. Regular solid-solution

Calculation of regular solid-solution model is followed by Appelo and Postma (1993). Reaction for solid-solution of ankerite is defined in Eq.12

$$Fe^{2+} + CaMg(CO_3)_2 = Mg^{2+} + CaFe(CO_3)_2 \quad \text{(Eq.12)}$$

The equilibrium constant of ankerite solid-solution is expressed as Eq.13

$$K_{ank}^{ss} = \frac{K_{dol}}{K_{sid}} = \left(\frac{m_{Mg^{2+}}}{m_{Fe^{2+}}}\right)\left(\frac{\lambda_{Fe^{2+}}}{\lambda_{Mg^{2+}}}\frac{N_{Fe^{2+}}}{N_{Mg^{2+}}}\right) \quad \text{(Eq.13)}$$

After defining the following relationship ($N_{Mg^{2+}} = x$ and $N_{Fe^{2+}} = 1 - x$), λ is determined in Eq.14 and Eq.15

$$\lambda_{Mg^{2+}} = \exp\left(a_0 N_{Fe^{2+}}^2\right) = \exp(a_0(1-x)^2) \quad \text{(Eq.14)}$$

$$\lambda_{Fe^{2+}} = \exp\left(a_0 N_{Mg^{2+}}^2\right) = \exp(a_0 x^2) \quad \text{(Eq.15)}$$

Inserting (Eq.14 and 15) into (eq.13) becomes Eq.16

$$K_{ss} = \frac{K_{dol}}{K_{sid}} = \left(\frac{m_{Mg^{2+}}}{m_{Fe^{2+}}}\right)\left(\frac{(1-x)\exp(a_0 x^2)}{x\exp(a_0(1-x)^2)}\right) \quad \text{(Eq.16)}$$

Rearrange (Eq.16) to compute a_0

$$a_0 = \frac{1}{2x-1}\ln\left\{\frac{m_{Fe^{2+}}}{m_{Mg^{2+}}}\frac{K_{dol}}{K_{sid}}\frac{x}{1-x}\right\} \quad \text{(Eq.17)}$$

Where, the parameters for computing a_0 is defined in Table 1.

Table 1. Parameters to compute a_0

Log(K_{dol}) at 25°C	2.5135
Log(K_{sid}) at 25°C	0.0303
Molality (Fe^{2+})	5.85E-4 (From brine data in SACROC field)
Molality (Mg^{2+})	5.70E-2 (From brine data in SACROC field)

Using these parameters, a_o is computed with a function of Mg^{2+} and plotted in Figure 1.

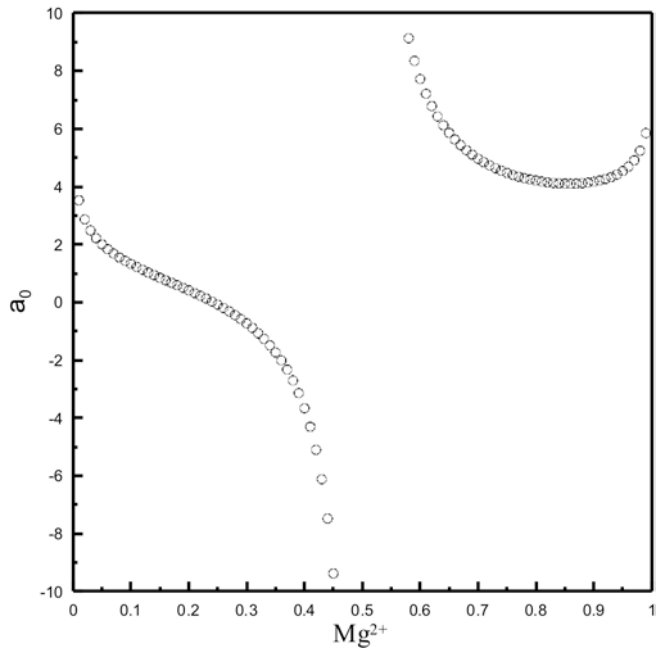

Figure 1. The a_0 parameter plotted as a function of Mg^{2+}

The composition of ankerite in SACROC simulation is $CaMg_{0.75}Fe_{0.25}(CO_3)_2$. Therefore, Mg^{2+} is equal to 0.75 and the corresponding a_0 parameter is computed as 4.474356.

Finally, Eq.18 from Glynn (1990) is applied to calculate the regular solid-solution with the determined a_0 parameter.

$$K_{ss} = (xK_{dol})^{x}((1-x)K_{ank})^{(1-x)}\exp\left(a_0 x(1-x)\right) \qquad \text{(Eq.18)}$$

Part IV. Comparison of each model

Equilibrium constants of ankerite solid-solution are computed and compared in Figure 2 with a function of Mg^{2+}.

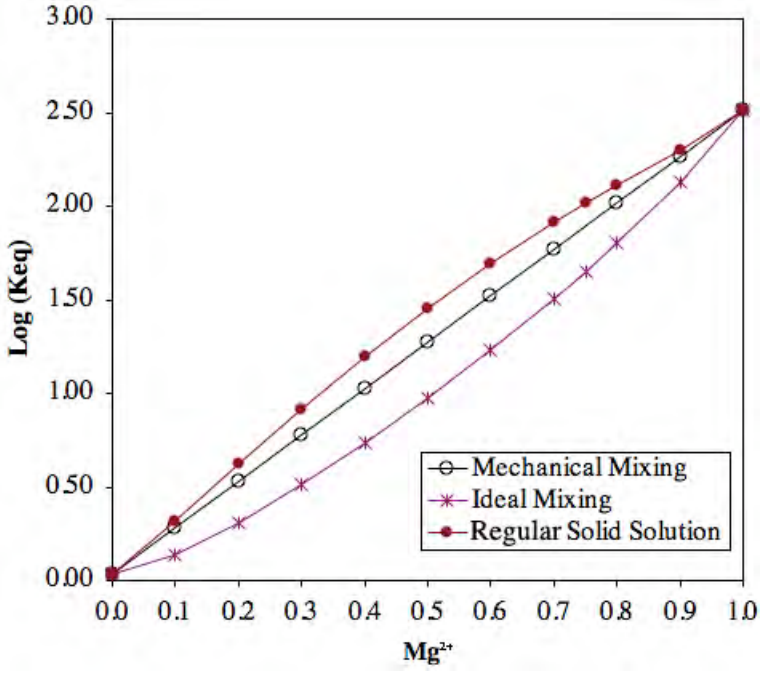

Figure 2. Equilibrium constanst of ankerite solid-solution with a function of Mg^{2+}.

Finally, equilibrium constant of ankerite solid solution ($CaMg_{0.75}Fe_{0.25}(CO_3)_2$) is calculated from regular solid solution model. The computed $\log(K_{eq})$ is 2.01283.

Appendix XII. Injection and production history of wells in SACROC model.

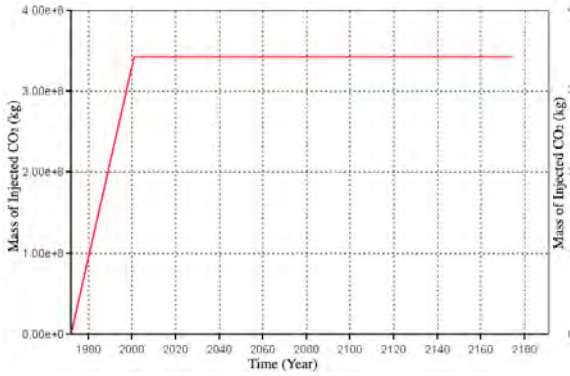

(1) Injection well 1 (I1)

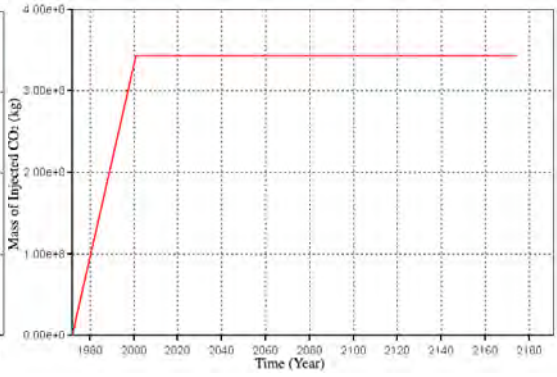

(2) Injection well 2 (I2)

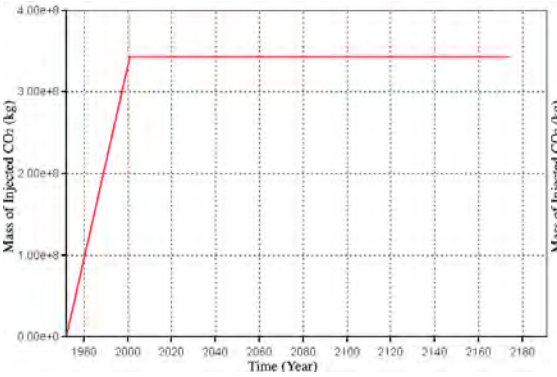

(3) Injection well 3 (I3)

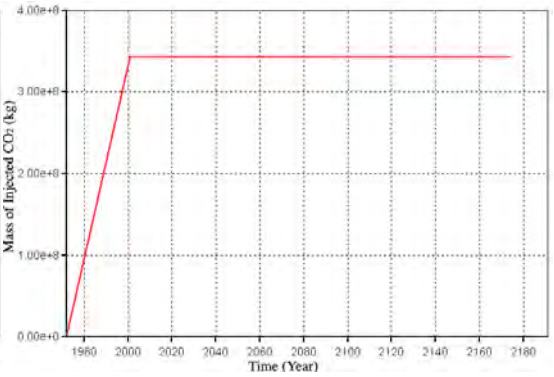

(4) Injection well 4 (I4)

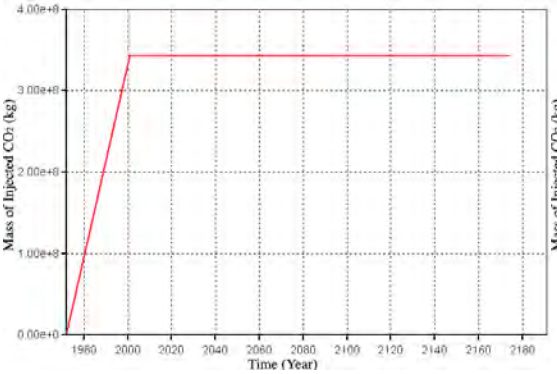

(5) Injection well 5 (I5)

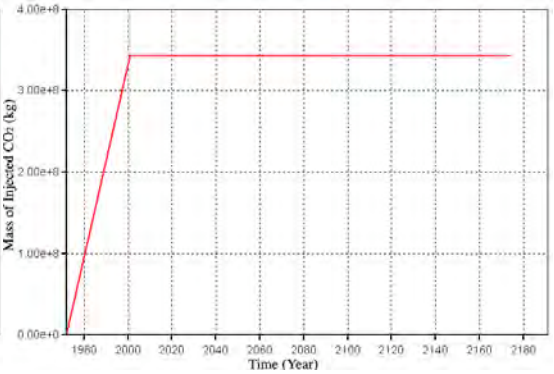

(6) Injection well 6 (I6)

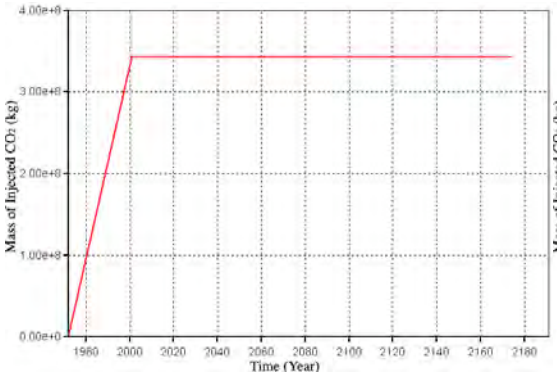

(7) Injection well 7 (I7)

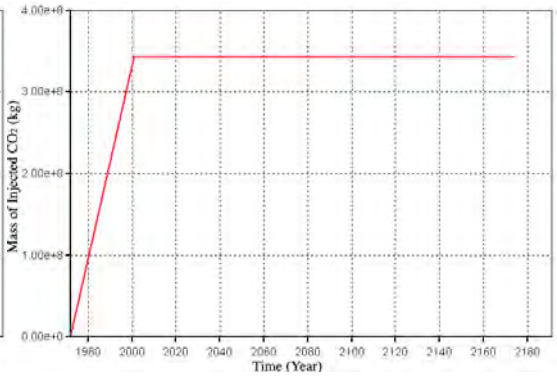

(8) Injection well 8 (I8)

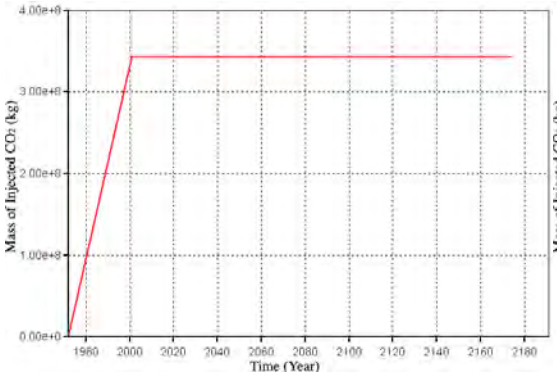

(9) Injection well 9 (I9)

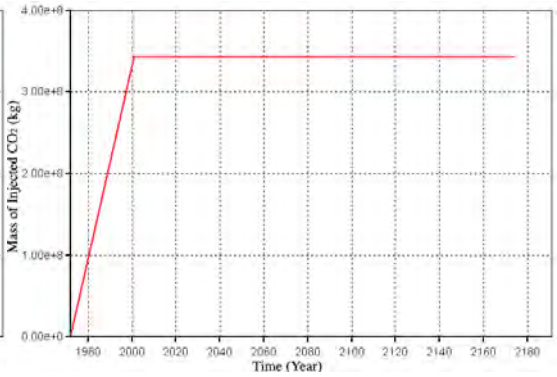

(10) Injection well 10 (I10)

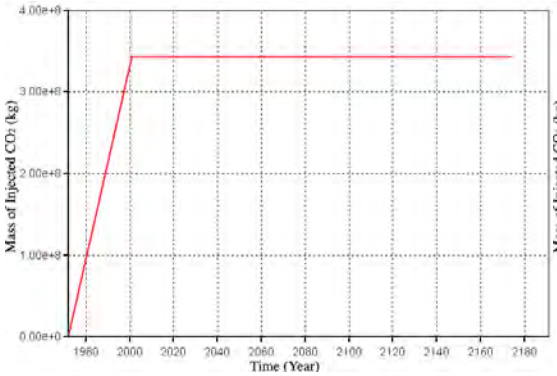

(11) Injection well 11 (I11)

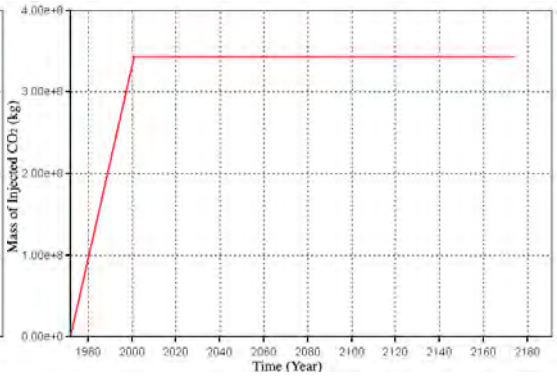

(12) Injection well 12 (I12)

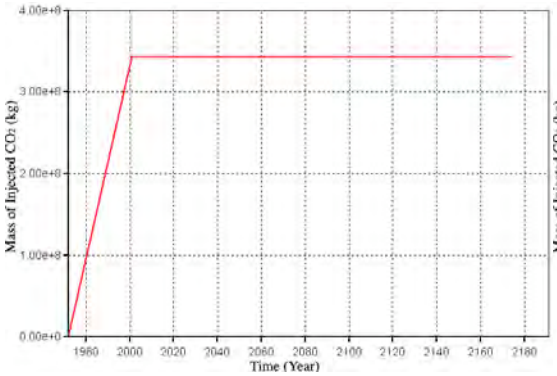

(13) Injection well 13 (I13)

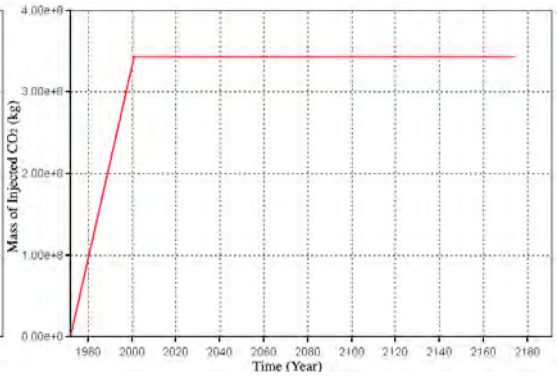

(14) Injection well 14 (I14)

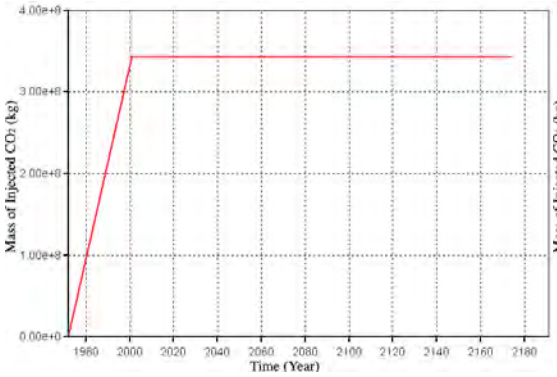

(15) Injection well 15 (I15)

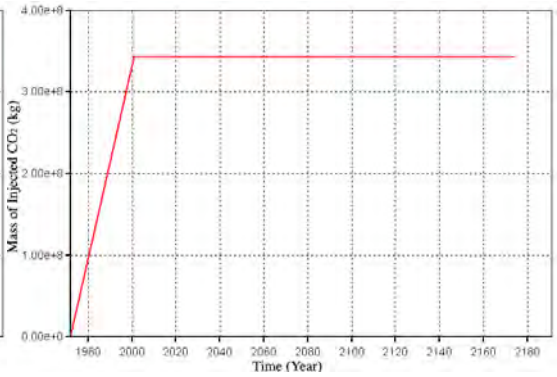

(16) Injection well 16 (I16)

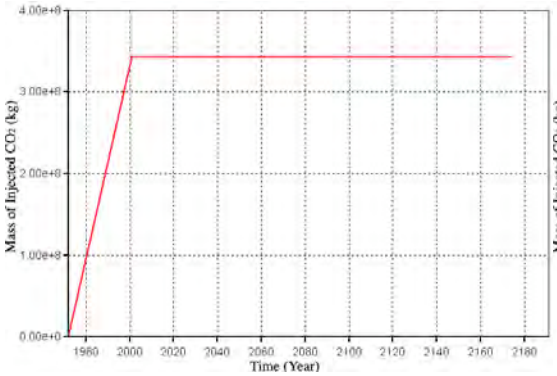

(17) Injection well 17 (I17)

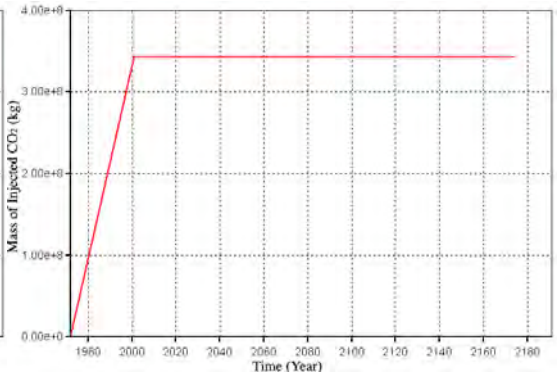

(18) Injection well 18 (I18)

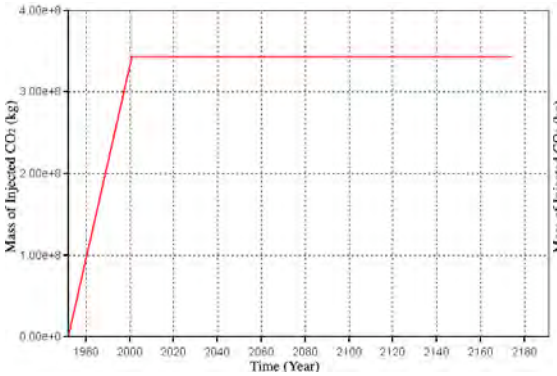

(19) Injection well 19 (I19)

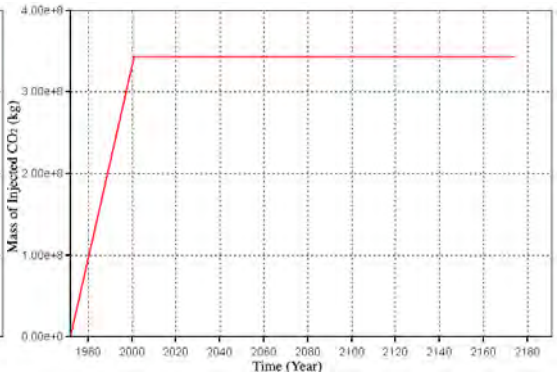

(20) Injection well 20 (I20)

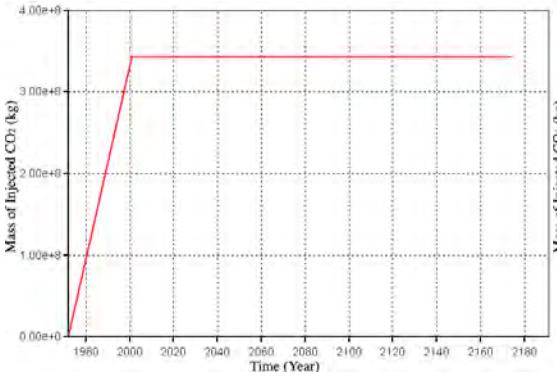

(21) Injection well 21 (I21)

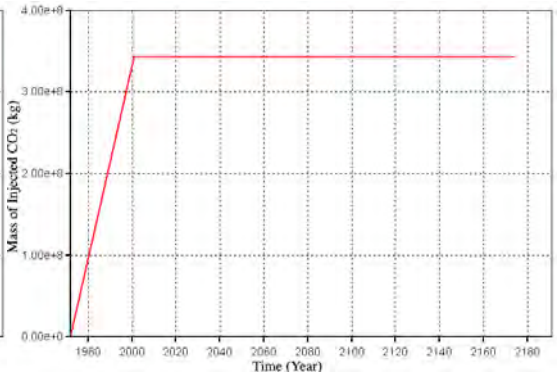

(22) Injection well 22 (I22)

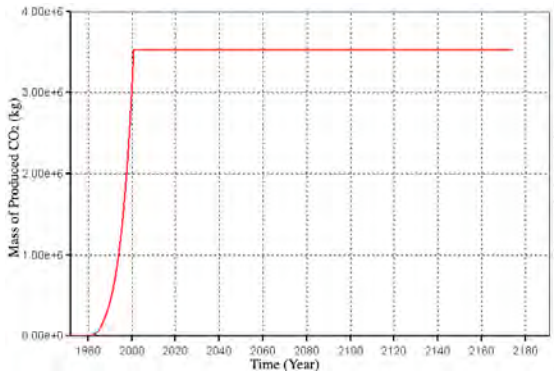

(23) Prodution well 23 (P1)

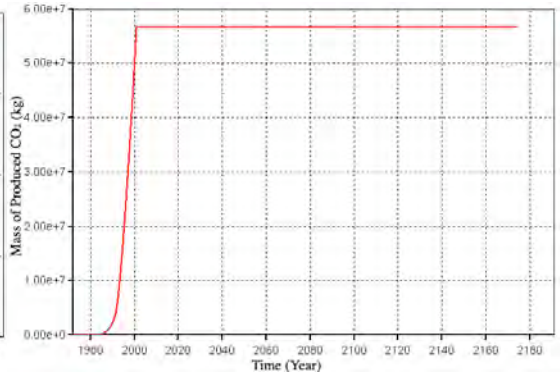

(24) Production well 24 (P2)

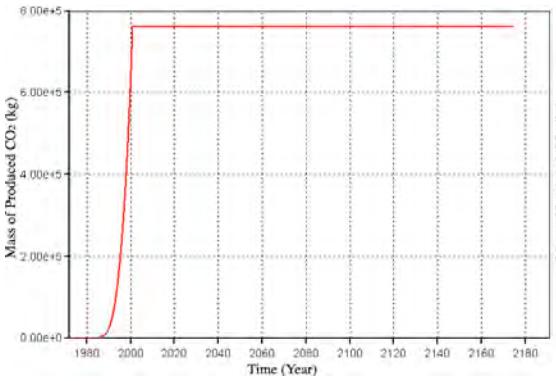

(25) Production well 25 (P3)

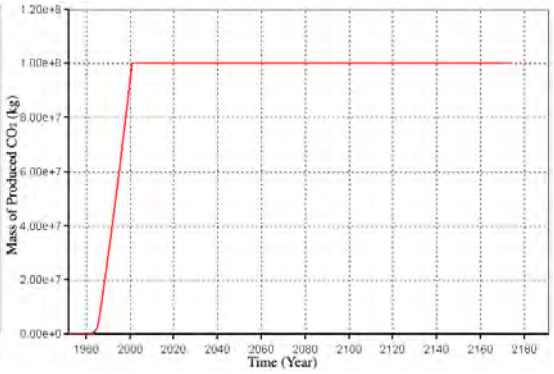

(26) Production well 26 (P4)

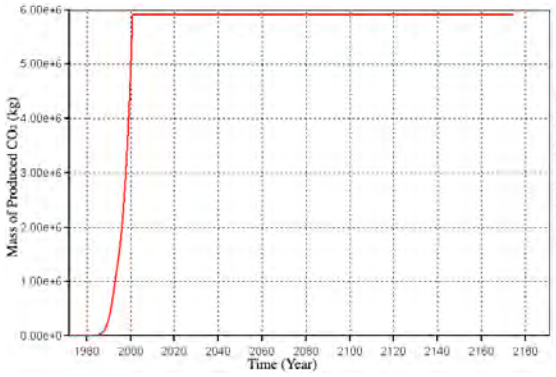

(27) Production well 27 (P5)

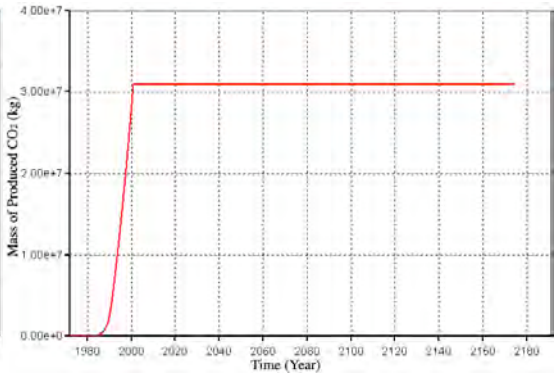

(28) Production well 28 (P6)

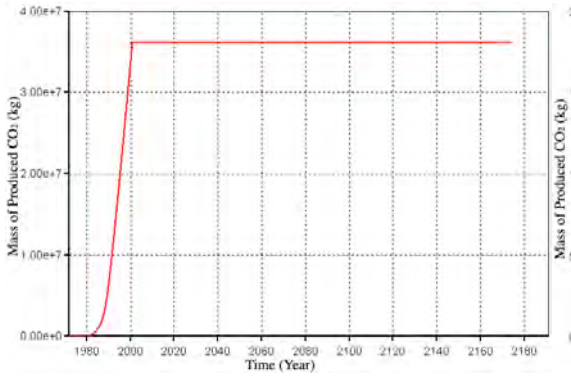

(29) Production well 29 (P7)

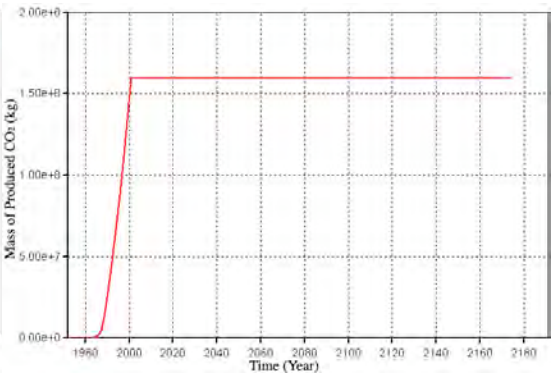

(30) Production well 30 (P8)

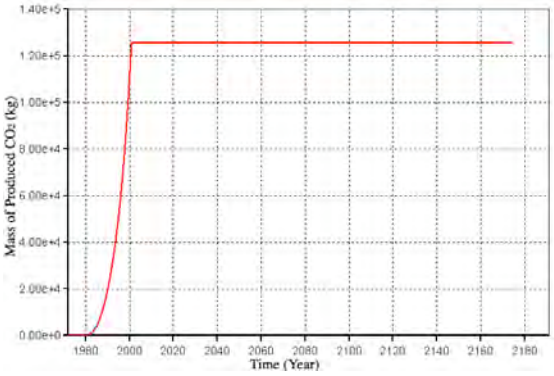

(31) Production well 31 (P9)

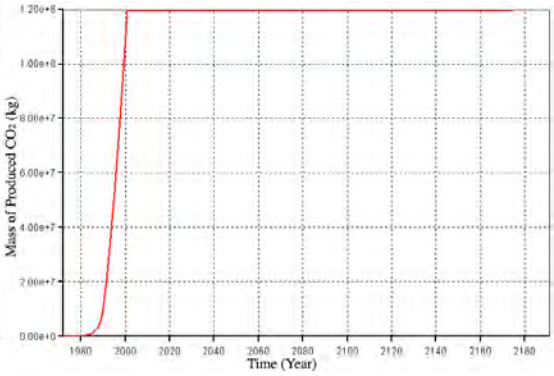

(32) Production well 32 (P10)

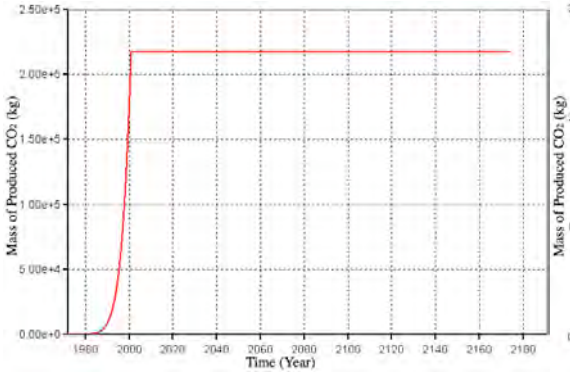

(33) Production well 33 (P11)

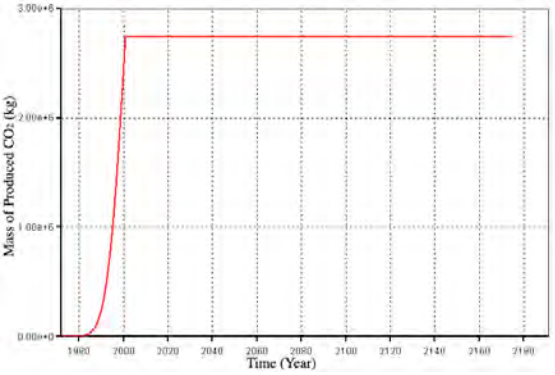

(34) Production well 34 (P12)

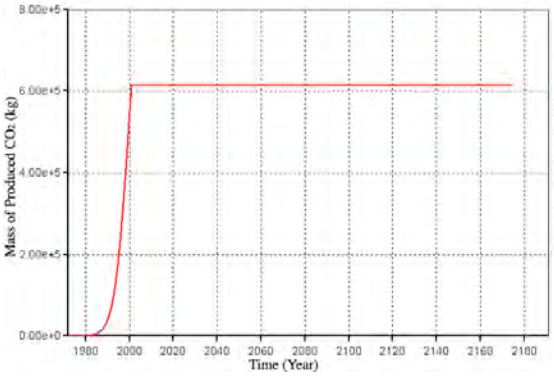

(35) Production well 35 (P13)

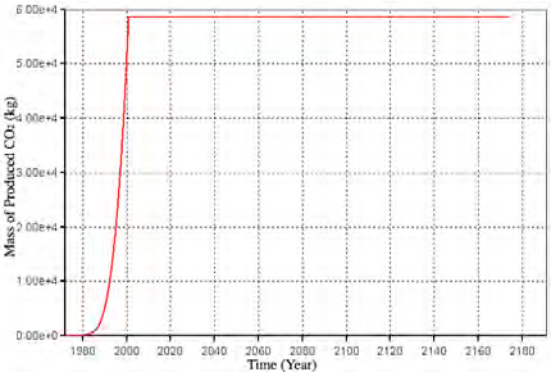

(36) Production well 36 (P14)

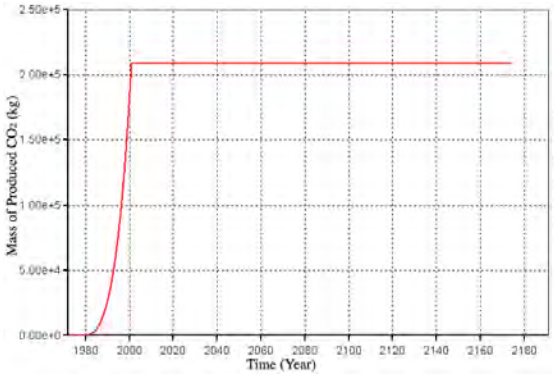

(37) Production well 37 (P15)

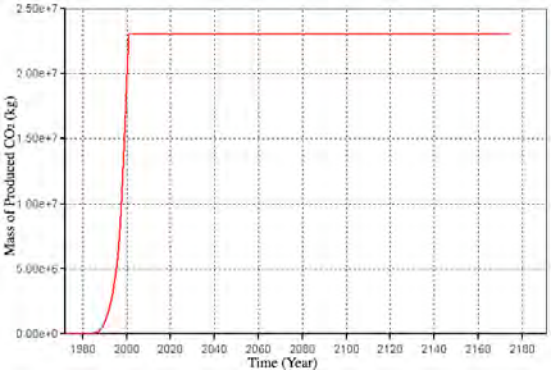

(38) Production well 38 (P16)

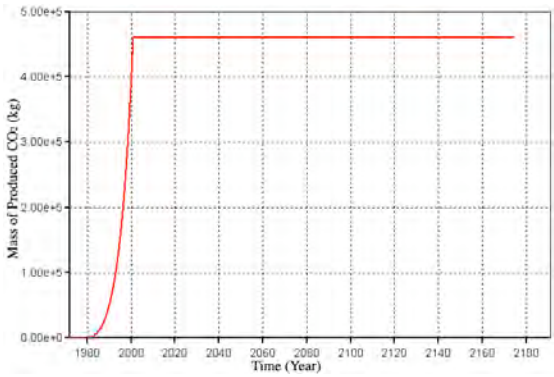

(39) Production well 39 (P17)

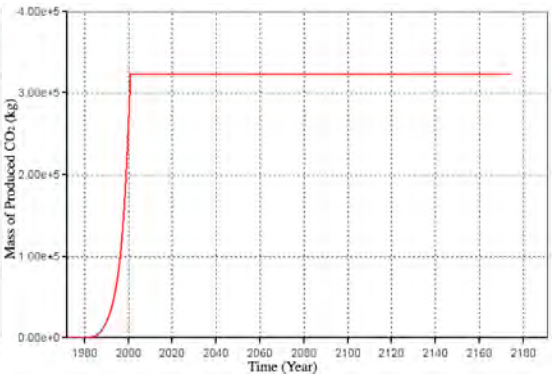

(40) Production well 40 (P18)

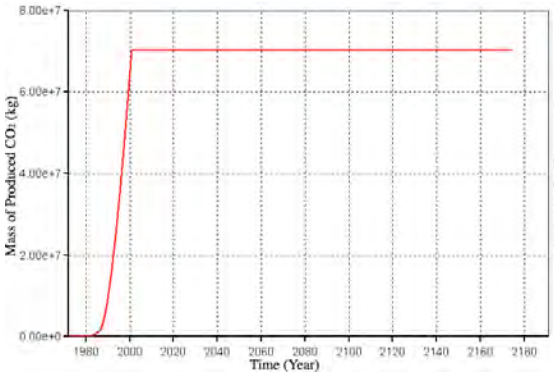

(41) Production well 41 (P19)

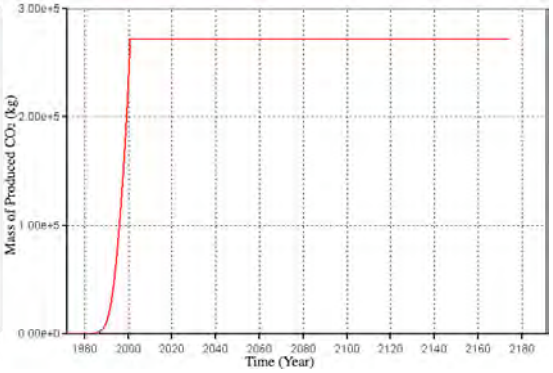

(42) Production well 42 (P20)

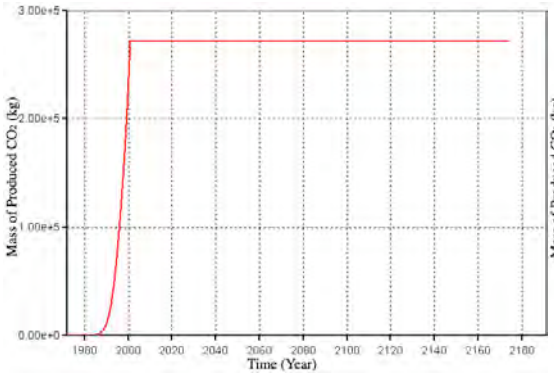

(43) Production well 43 (P21)

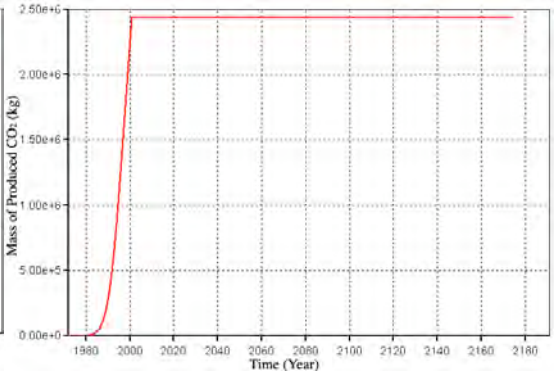

(44) Production well 44 (P22)

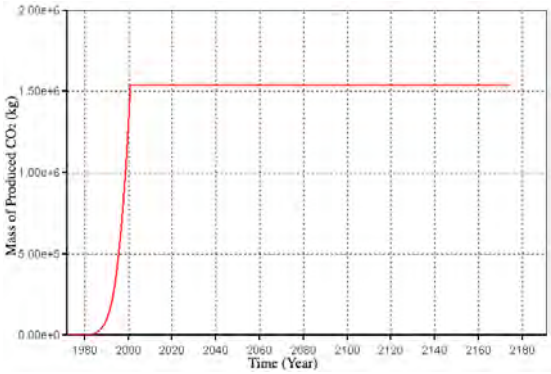

(45) Production well 45 (P23)

Appendix XIII. The effect of grid non-orthogonality.

To investigate potential effects of grid non-orthogonality, a non-orthogonal grid was developed (Figure 1a). Uniform porosity (0.3) and permeability (10^{-14} m^2) were assigned in both models, assuming homogeneous and isotropic conditions to ensure that there are no additional effects other than the effect of grid orientation.

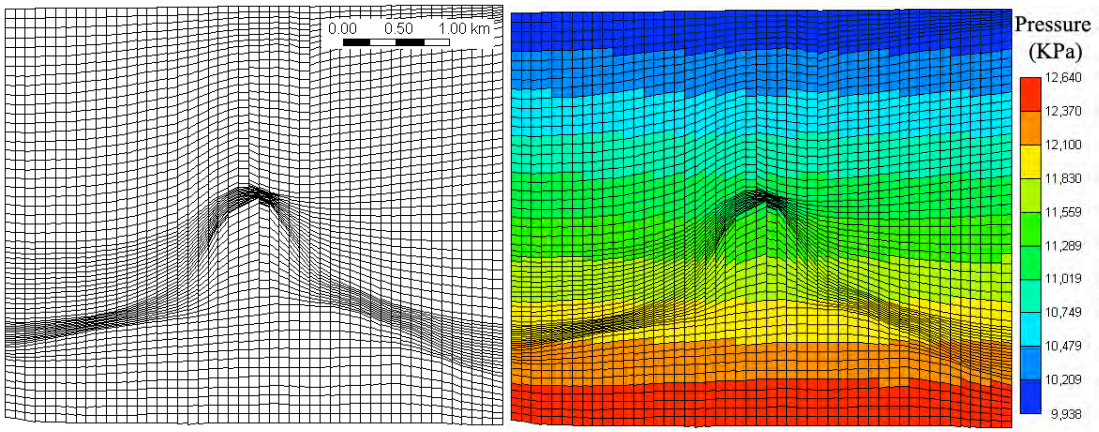

(a) (b)

Figure 1. The effect of grid non-orthogonality: (a) non-orthogonal grid and (b) pressure distribution after steadystate simulation.

Using these initial conditions, simulations describing single-phase and steady-state conditions were performed. Therefore, the solutions of these simulations are to solve the Laplace equation ($\frac{\partial^2 P}{\partial x^2} + \frac{\partial^2 P}{\partial y^2} = 0$). Lateral boundaries are assumed to be no-flow conditions but top (10 MPa) and bottom (12 MPa) boundaries are assumed to be constant pressure conditions. This simulation is performed with CMG's GEM (Computer Modeling Group, 2006)

Simulation results show that the pressure distributions at steady-state conditions are not affected by the non-orthogonality of grid. Pressure distribution shows a hydrostatic pressure condition (Figure 1(b)). In sum, upscaling (Chapter 6) creats a coarse grid, and resolution is reduced. However, grid non-orthorgonality will not significantly affect simulation results.